

Copyright  
by  
John Scott McCartney  
2007

**The Dissertation Committee for John Scott McCartney Certifies that this is the  
approved version of the following dissertation:**

**Determination of the Hydraulic Characteristics of Unsaturated Soils  
Using a Centrifuge Permeameter**

**Committee:**

---

Jorge G. Zornberg, Supervisor

---

Robert B. Gilbert

---

Stephen G. Wright

---

Bridget R. Scanlon

---

Randall J. Charbeneau

**Determination of the Hydraulic Characteristics of Unsaturated Soils  
using a Centrifuge Permeameter**

**by**

**John Scott McCartney, B.S.;M.S.**

**Dissertation**

Presented to the Faculty of the Graduate School of

The University of Texas at Austin

in Partial Fulfillment

of the Requirements

for the Degree of

**Doctor of Philosophy**

**The University of Texas at Austin**

**August 2007**

**To Mary**



## **Acknowledgements**

I would like to acknowledge my supervisor, Jorge Zornberg, for guiding and supporting me throughout my PhD and MS degrees. He has been a great mentor over the past 8 years at CU and UT. I am grateful for the opportunity he gave me to develop the centrifuge permeameter and the unsaturated soils lab at UT Austin. It has been a challenging yet rewarding experience. I would like to thank Bob Gilbert and Steve Wright for their support during my PhD. I really appreciate the time and effort that they and the other geotechnical faculty have put into the coursework at UT. I would also like to thank Bridget Scanlon and Randy Charbeneau for participating on my dissertation committee and providing new ideas on how to apply the centrifuge permeameter.

Several individuals at Thomas Broadbent and Sons, LLC, in Huddersfield, UK helped make the centrifuge permeameter a reality. I am grateful for the stout centrifuge design by Alan Ainsworth and the robust data acquisition design by Neil Baker. I learned about electronics, mechanics, machine installation, proper centrifuge testing techniques, and life from Neil, Paul Hadfield, Andy Hoskin, and Ian Burley of Broadbent.

I would like to thank my friends, fellow graduate students, and professors at UT Austin and CU Boulder for many fruitful discussions and their objective feedback on my research. I would like to thank Eduardo Dell'Avanzi for sharing his experiences with centrifuge testing while we were at CU Boulder. My parents and my fiancée Mary have given their love and support during both the good and trying times of my PhD.

Funding from the National Science Foundation under the Graduate Research Fellowship (2002-2005) and from the University of Texas Thrust fellowship (specifically the E.M. Keck family) is gratefully appreciated. Development of the centrifuge permeameter was possible through National Science Foundation Grant CMS-0401488.

# **Determination of the Hydraulic Characteristics of Unsaturated Soils using a Centrifuge Permeameter**

Publication No. \_\_\_\_\_

John Scott McCartney, PhD

The University of Texas at Austin, 2007

Supervisor: Jorge G. Zornberg

A new experimental approach to determine the hydraulic characteristics of unsaturated soils using a centrifuge permeameter was developed in this study. Specifically, the centrifuge permeameter is used to determine the water retention curve (WRC), which quantifies the energy required to retain water in the soil pores during wetting and drying, and the hydraulic conductivity function (K-function), which quantifies the soil's change in impedance to water flow as it becomes unsaturated. An aim of this study is the promotion of using experimentally-derived hydraulic characteristics in engineering practice. Accordingly, the goals behind development of the centrifuge permeameter were a reasonable testing time, measurement of all variables relevant to water flow in unsaturated soils, and a methodology allowing straightforward interpretation of experimental data to determine the hydraulic characteristics.

Development of the centrifuge permeameter was guided by lessons learned from an evaluation of previous characterization approaches. Specifically, issues such as the use of steady-state or transient water flow, boundary condition effects, and the use of

instrumentation were evaluated in conventional tests to better develop the centrifuge permeameter. Steady-state infiltration of water through a soil specimen instrumented with tensiometers to measure matric suction and time domain reflectometry to infer moisture content was found to be the most reliable means of characterization. Steady-state water flow permits straightforward, repeatable interpretation of instrumentation results, boundary conditions, and flow data to determine the hydraulic characteristics. Centrifugation is employed to decrease the time required to reach steady-state water flow through a soil specimen by imposing a centripetal acceleration on the infiltrating water. The water infiltration rate and centripetal acceleration can be independently controlled in the centrifuge permeameter in order to reach different target hydraulic conductivity values. Continuous, in-flight measurement of the variables relevant to hydraulic characterization is possible through an on-board data acquisition system.

The experimental component of this study is focused on validation of the centrifuge permeameter and verification of the hydraulic characteristics obtained using this approach. Simultaneous determination of the WRC and K-function for a clay of low plasticity was found to be possible in less than a week using the centrifuge permeameter, whereas several months were required in conventional tests. Consistent measurements of hydraulic conductivity were obtained using this approach, and little hysteresis was observed in the hydraulic characteristics. Additional experiments were performed to evaluate the validity of different assumptions required to interpret the experimental data and different issues in centrifuge testing. Two major assumptions required in previous centrifuge permeameter approaches were evaluated using the instrumentation available in the centrifuge permeameter. During steady-state water flow in the centrifuge, the suction and moisture content were found to be relatively uniform along the longitudinal axis of the permeameter, and the outflow boundary was found to have a negligible influence on

the suction profile. Settlement under the increased body forces in the centrifuge were found to be negligible for the soil investigated in this study. The hydraulic characteristics were found to be sensitive to the calibration of the transducers and sensors used to infer the water pressure and moisture content during centrifugation.

Overall, the expeditious, direct determination of the hydraulic characteristics of unsaturated soils was successfully achieved using centrifuge technology. Accordingly, the centrifuge permeameter approach helps promote the use hydraulic characteristics of unsaturated soils in geotechnical engineering design.

## Table of Contents

List of Tables.....	xiv
List of Figures.....	xv
Chapter 1: Introduction.....	1
1.1 Research Motivation.....	1
1.2 Research Objectives.....	4
1.3 Dissertation Organization.....	5
Chapter 2: Hydraulic Characteristics of Unsaturated Soils.....	7
2.1 Overview.....	7
2.2 Important Variables used to Describe Unsaturated Soils.....	7
2.2.1 Water Content of Unsaturated Soils.....	7
2.2.2 Matric Suction.....	9
2.2.3 Impedance to Water Flow through Soils.....	9
2.3 Hydraulic Characteristics of Unsaturated Soils.....	11
2.3.1 Water Retention Curve (WRC).....	11
2.3.2 K-function.....	18
Chapter 3: Water Flow in Unsaturated Soils.....	25
3.1 Overview.....	25
3.2 Flow of Water through Unsaturated Soils.....	25
3.3 Suction Profiles in Soil during Water Flow under Normal Gravity.....	30
3.4 Suction Profiles in Soil during Water Flow in the Centrifuge.....	36
3.5 Boundary Conditions during Water Flow in Unsaturated Soils.....	41
Chapter 4: Materials.....	45
4.1 Soil Selection for Validation of the Centrifuge Permeameter.....	45
4.2 Geotechnical Classification.....	47
4.3 Compaction Characteristics.....	48

Chapter 5: Determination of the Hydraulic Characteristics of Soil using Conventional Techniques .....	50
5.1 Overview .....	50
5.2 Hydraulic Conductivity of Saturated Specimens ( $K_s$ ) .....	51
5.2.1 Flexible Wall Permeameter Technique.....	51
5.2.2 Rigid wall Permeameter Technique.....	53
5.2.3 Centrifuge Permeameter Technique .....	55
5.3 Water Retention Curve (WRC).....	57
5.3.1 Overview .....	57
5.3.2 Axis Translation (Pressure Plate).....	58
5.3.3 Hanging Column.....	62
5.3.4 Thermodynamic Techniques.....	65
5.3.5 Centrifuge Permeameter Techniques.....	68
5.3.6 Summary of Experimental Techniques to Determine the WRC.....	71
5.4 Hydraulic Conductivity Function (K-Function) .....	73
5.4.1 Overview.....	73
5.4.2 Measurement of Outflow during WRC Tests .....	74
5.4.3 Infiltration or Evaporation Techniques.....	77
5.4.4 Centrifuge Permeameter Techniques.....	92
5.4.5 Summary of Experimental Techniques to Determine the K-function .....	105
Chapter 6: The Centrifuge Permeameter for Unsaturated Soils .....	107
6.1 Overview .....	107
6.2 Geotechnical Centrifuge .....	108
6.3 Centrifuge Permeameter Environments.....	110
6.4 Flow Rate Control and Monitoring System .....	115
6.4.1 Fluid Supply System.....	115
6.4.2 Fluid Distribution System.....	118
6.4.3 Outflow Collection System.....	120
6.5 Moisture Content and Suction Instrumentation .....	126
6.5.1 Time Domain Reflectometry .....	126

6.5.2 Tensiometers .....	140
6.5.3 Heat Dissipation Units .....	145
6.6 Data Acquisition System and Auxiliary Centrifuge Components .....	152
Chapter 7: Testing Philosophy and Experimental Procedures.....	159
7.1 Overview .....	159
7.2 Testing Philosophy.....	161
7.2.1 Bridging Theory and Measurement .....	161
7.2.2 Assumptions in the Centrifuge Permeameter Approach.....	164
7.3 Soil Placement and Instrumentation Installation Procedures.....	168
7.3.1 Overview .....	168
7.3.2 Hydraulic Characterization Permeameter .....	168
7.3.3 Prototype Permeameter .....	176
7.4 Procedures Adopted for Hydraulic Characterization .....	180
7.5 Procedures Adopted to Interpret Centrifuge Testing Issues .....	186
7.5.1 Procedures to Evaluate Suction Profiles during Centrifugation.....	186
7.5.2 Procedures to Evaluate Boundary Condition Effects.....	186
7.5.3 Procedures to Evaluate Centrifugation Effects on Hydraulic Characteristics.....	187
7.5.4 Procedures to Evaluate Time Required for Hydraulic Characterization .....	188
7.6 Interpretation of Instrumentation Results .....	188
Chapter 8: Results from Infiltration Test in Prototype Permeameter .....	193
8.1 Testing Scope.....	193
8.2 Test I (porosity of 0.4, $w_c = w_{c,opt}$ ).....	193
Chapter 9: Results from Hydraulic Characterization Tests .....	199
9.1 Testing Scope.....	199
9.2 Test II (porosity of 0.35, $w_c = w_{c,opt} - 3\%$ ).....	202
9.3 Test III (porosity of 0.35, $w_c = w_{c,opt}$ ) .....	221
9.4 Test IV (porosity of 0.35, $w_c = w_{c,opt} + 3\%$ ).....	251

Chapter 10: Determination of the Hydraulic Characteristics of Unsaturated Soils using the Centrifuge Permeameter .....	268
10.1 Overview .....	268
10.2 Determination of the Hydraulic Characteristics .....	268
10.2.1 Determination of the WRC .....	268
10.2.2 Determination of the K-function.....	270
10.3 Evaluation of Hydraulic Characteristics from Centrifuge Tests.....	275
10.3.1 Summary of K-function and WRC Results .....	275
10.3.2 Repeatability of Hydraulic Characteristics from the Centrifuge Permeameter .....	280
10.3.3 Evaluation of Testing Approaches to Determine Hydraulic Characteristics.....	281
10.3.4 Consistency of Hydraulic Characteristics from the Centrifuge Permeameter .....	282
10.3.5 Effect of Hysteresis on the Hydraulic Characteristics .....	284
10.3.6 Effect of Compaction Conditions on Hydraulic Characteristics.....	289
Chapter 11: Verification of the Centrifuge Permeameter Results .....	290
11.1 Overview .....	290
11.2 Comparison between Centrifuge and Conventional Test Results.....	290
11.3 Comparison between Centrifuge Results and Predictive Models.....	292
Chapter 12: Evaluation of Centrifuge Testing Issues .....	295
12.1 Overview .....	295
12.2 Suction and Moisture Content Profiles during Centrifugation .....	295
12.3 Boundary Condition Effects .....	297
12.4 Impact of Centrifugation on the Hydraulic Characteristics .....	300
12.5 Evaluation of Testing Times for Hydraulic Characterization.....	312
Chapter 13: Summary and Conclusions.....	318
13.1 Summary of Research Objectives.....	318
13.2 Conclusions from Hydraulic Characterization.....	321
13.3 Conclusions from Evaluation of Testing Issues.....	324
13.4 Conclusions from Verification of Centrifuge Results .....	325



13.5 Recommendations for Future Research .....	326
Appendix A: Lessons Learned from Preliminary Tests.....	329
A.1 Overview of Preliminary Tests .....	329
A.2 Interpretation of Instrumentation Results .....	332
Appendix B: Solution to Richards' Equation in the Centrifuge .....	341
B.1 Overview .....	341
A.2 Finite Difference Model.....	343
B.3 Boundary Conditions.....	343
A.3.1 Inflow boundary .....	343
A.3.2 Outflow boundary .....	344
B.4 Matrix Format .....	345
B.5 Solution (Modified Picard Iteration).....	346
B.6 RichTexNG .....	347
Glossary .....	355
References.....	356
Vita.....	364

## List of Tables

Table 4.1: Geotechnical properties for RMA Soil Type II .....	48
Table 5.1: Relative humidity and suction values for different saturated salt solutions ....	66
Table 5.2: van Genuchten-Mualem (1980) parameters for CL clay and geotextile .....	72
Table 5.3: Summary of column infiltration test results .....	92
Table 5.4: K-function testing times reported in the literature.....	106
Table 6.1: Calibration equations for TDR in both centrifuge permeameters .....	139
Table 9.1: Purpose of hydraulic characterization tests (with Test I included also) .....	199
Table 9.2: Soil compaction conditions in testing program .....	200
Table 9.3: Range of centrifuge and inflow conditions during each test .....	201
Table 9.4: Summary of the test stages for hydraulic characterization Test II .....	202
Table 9.5: Summary of the first five test stages for hydraulic characterization Test III	221
Table 9.6: Summary of Stage III-6 for hydraulic characterization Test III .....	222
Table 9.7: Summary of Stage III-7 for hydraulic characterization Test III .....	223
Table 9.8: Summary of the test stages for hydraulic characterization Test IV .....	251
Table 12.1: Summary of expected and observed settlements .....	311
Table 12.2: Summary of testing times in hydraulic characterization tests .....	315
Table 12.3: Scaled testing times for large-scale columns.....	317
Table A.1: Summary of test conditions for preliminary centrifuge permeameter tests..	331

## List of Figures

Figure 2.1: Phase diagram for unsaturated soils .....	8
Figure 2.2: Typical water retention curves (WRCs): (a) Logarithmic; (b) Natural.....	11
Figure 2.3: Experimental WRCs for different geotechnical materials .....	12
Figure 2.4: (a) Schematic of a hysteretic WRC (after Lenhard <i>et al.</i> 1991); (b) Hysteretic WRC data for glass bead media (Topp and Miller 1966) .....	14
Figure 2.5: Relationship between capillary rise, pipette size, and moisture storage .....	16
Figure 2.6: Typical K-functions for different materials: (a) Logarithmic; (b) Natural ....	18
Figure 2.7: K-functions for different geotechnical materials: (a) $K-\theta$ ; (b) $K-\psi$ .....	19
Figure 2.8: Hysteresis in the K-function (Topp and Miller 1966): (a) $K-\psi$ ; (b) $K-S$ .....	21
Figure 2.9: Predictive and experimental K-functions: (a) Nimmo and Akstin (1988); (b) Khaleel <i>et al.</i> (1995).....	24
Figure 3.1: Schematic of infiltration through an unsaturated soil layer .....	26
Figure 3.2: (a) Centrifuge control volume (Dell'Avanzi <i>et al.</i> 2004); (b) $N_r$ vs. $z_m/L_m$ ...	28
Figure 3.3: Suction profiles at steady-state flow for different inflow rates .....	32
Figure 3.4: Suction profiles at steady-state flow for different boundary suctions.....	33
Figure 3.5: Total head, suction head, and elevation head profiles for a full-scale (1.5 m) prototype during steady-state flow: (a) Head values; (b) Head gradients...	34
Figure 3.6: Hydraulic conductivity profiles for steady-state water flow .....	35
Figure 3.7: Total head, suction head, and elevation head profiles for a permeameter (0.127 m) during steady-state flow: (a) Head values; (b) Head gradients ..	35
Figure 3.8: Steady state suction profiles for different values of: (a) $N_{r,mid}$ ; (b) $v_m$ ; (c) $\psi_0$ ..	38
Figure 3.9: Head profiles during steady flow in the centrifuge: (a) Values; (b) Gradients .....	39
Figure 3.10: Steady-state $K$ profiles (a) Variation with $N_{r,mid}$ ; (b) Variation with $v_m$ .....	40
Figure 3.11: Interpretation of the hydraulic characteristics to show the capillary break effect, with black arrows showing initial conditions, and gray arrows showing conditions at capillary breakthrough: (a) WRC; (b) K-function ..	44
Figure 4.1: Granulometric curve for RMA Soil Type II.....	47
Figure 4.2: (a) Compaction curve for RMA Soil Type II; (b) Reduced-scale mold.....	49
Figure 4.3: Piston compactor .....	49
Figure 5.1: Flexible wall permeameter: (a) Setup; (b) Typical results .....	52
Figure 5.2: Effect of compaction moisture content on the hydraulic conductivity of saturated RMA Soil Type II specimens .....	53
Figure 5.3: Rigid-wall permeameter: (a) Setup; (b) Typical results .....	54
Figure 5.4: Effect of porosity on the hydraulic conductivity of saturated specimens compacted at the optimum water content.....	55
Figure 5.5: $K_s$ in the centrifuge (Nimmo and Mello 1991) (a) Apparatus; (b) $K_s$ results.	56
Figure 5.6: Pressure plate apparatus .....	58
Figure 5.7: Pressure plate cell: (a) Assembled pressure plate; (b) Components; (c) Assembled without pressure cell; (d) Specimen preparation .....	60
Figure 5.8: Pressure plate results (courtesy of Jeff Kuhn): (a) Outflow data; (b) Discharge velocity data; (c) Moisture content data; (d) WRC .....	61

Figure 5.9: Hanging column apparatus.....	62
Figure 5.10: Hanging column: (a) Setup; (b) Schematic of the top of Mariotte burette...	63
Figure 5.11: Hanging column results; (a) Typical outflow data; (b) $S-\psi$ .....	64
Figure 5.12: Desiccator with salt solution .....	65
Figure 5.13: Desiccator cabinets in a fume hood.....	67
Figure 5.14: WRC from thermodynamic and physical techniques.....	67
Figure 5.15: Steady-state and equilibrium suction profiles: (a) Low $\omega$ ; (b) High $\omega$ .....	69
Figure 5.16: Centrifuge WRCs: (a) Khanzode <i>et al.</i> (2002); (b) Gardner (1938); (c) Conca and Wright (1998).....	70
Figure 5.17: WRC results for soil with different porosities .....	72
Figure 5.18: Comparison between WRC of CL clay and nonwoven geotextile.....	73
Figure 5.19: K-functions predicted from the WRCs in Figure 5.17 and Figure 5.18.....	74
Figure 5.20: Multi-step outflow analysis results for a suction increment of 7 kPa .....	76
Figure 5.21: K-function results from pressure plate results.....	77
Figure 5.22: Infiltration/evaporation column.....	78
Figure 5.23: Soil infiltration column: (a) Schematic; (b) Picture of a column test .....	81
Figure 5.24: (a) Outflow support plate; (b) O-ring seal at the base of the column.....	82
Figure 5.25: Peristaltic pump with graduated cylinder as an inflow reservoir .....	82
Figure 5.26: (a) Inflow distribution system; (b) Schematic of inflow distribution system.....	83
Figure 5.27: (a) Tipping bucket gauge; (b) Tipping bucket with graduated cylinder.....	84
Figure 5.28: Inflow and outflow data for column test .....	85
Figure 5.29: Wetting front progression for column test .....	85
Figure 5.30: Moisture content time series for sensors located at various elevations.....	86
Figure 5.31: Moisture content profiles.....	87
Figure 5.32: Predicted suction time series .....	88
Figure 5.33: Sigmoid curve fitting from data collected in infiltration column tests at various elevations: (a) Moisture content; (b) Suction .....	89
Figure 5.34: K-function calculated using steady-state and transient column test data.....	90
Figure 5.35: (a) Transient drainage data with direct solution using assumed properties (Nimmo 1990) (b) K-function from inverse analysis of drainage data (Simunek and Nimmo 2005).....	93
Figure 5.36: IFC-SSC setup (Nimmo <i>et al.</i> 1987): (a) Permeameter; (b) Centrifuge .....	95
Figure 5.37: UFA setup (Conca and Wright 1998): (a) Schematic of rotor and permeameter; (b) Centrifuge and flow-pump.....	96
Figure 5.38: Moisture content profiles measured after centrifugation: (a) Nimmo <i>et al.</i> (1987); (b) Conca and Wright (1990) .....	99
Figure 5.39: Hydraulic conductivity values measured with the centrifuge approach (a) SSC data (Nimmo <i>et al.</i> 1987); (b) UFA data (Conca and Wright 1998). .....	100
Figure 5.40: Relationship between discharge velocity and g-level (Nimmo <i>et al.</i> 1987) .....	101
Figure 5.41: Variation in hydraulic conductivity with specimen height (a) K profiles for a constant inflow rate; (b) Range in K for different flow rates.....	103
Figure 5.42: Variation in $\chi$ with specimen height (Dell'Avanzi <i>et al.</i> 2004).....	104
Figure 5.43: Effect of flow type on K-function: (a) Steady-state; (b) Transient .....	105
Figure 6.1: Centrifuge setup (Courtesy of Thomas Broadbent and Sons, LLC) .....	108

Figure 6.2: G-ton rating of centrifuge permeameter (with other geotechnical centrifuges)	109
Figure 6.3: Power requirements for centrifugation at different angular velocities.....	110
Figure 6.4: Hydraulic characterization permeameter: (a) Isometric view; (b) Environment	111
Figure 6.5: Variation in $N_{r,mid}$ with $\omega$ for the hydraulic characterization permeameter .	112
Figure 6.6: Prototype permeameter: (a) Schematic view; (b) Environment.....	113
Figure 6.7: Variation in $N_{r,mid}$ with $\omega$ for the prototype permeameter.....	114
Figure 6.8: G-meter calibration curves .....	115
Figure 6.9: (a) Infusion pump setup; (b) Discharge velocities for range of inflow rates	116
Figure 6.10: Low-flow rotary union: (a) Picture; (b) Schematic view .....	117
Figure 6.11: Water conservation test in a mini-centrifuge .....	118
Figure 6.12: Plumbing connection between rotary union and permeameter: (a) Connection with brake tubing; (b) Flexible plastic tubing connector .....	118
Figure 6.13: (a) Schematic of the fluid distribution cap; (b) Top of Prototype permeameter fluid distribution cap; (c) Bottom of prototype permeameter fluid distribution cap during 1-g inflow test; (d) Fluid distribution cap for hydraulic characterization permeameter with TDR hole .....	119
Figure 6.14: Centrifuge inflow fluid distribution test.....	120
Figure 6.15: (a) Outflow support plate for prototype permeameter; (b) Outflow support plate for hydraulic characterization permeameter; (c) Wire mesh filters; (d) Wire mesh filter and outflow support plate.....	121
Figure 6.16: (a) Cross-section of the hydraulic characterization permeameter; (b) Air- release pipe; (c) Air-release pipe connection with the outflow support plate; (d) Air release pipe in outflow plate.....	123
Figure 6.17: Outflow reservoir: (a) Disassembled; (b) Outflow transducer and valve ..	124
Figure 6.18: Outflow transducer results with: (a) Angular velocity (b) g-level .....	125
Figure 6.19: Outflow transducer calibration curve .....	126
Figure 6.20: (a) Picture of TDR waveguide; (b) Schematic; (c) Zone of influence .....	128
Figure 6.21: (a) TDR fitting in prototype permeameter; (b) Schematic view of fittings	129
Figure 6.22: (a) Schematic of TDR waveguide and permeameter; (b) TDR receptacle in permeameter; (c) Top view of TDR waveguide in permeameter; (d) Elevation view of TDR in permeameter .....	130
Figure 6.23: Full TDR waveform .....	131
Figure 6.24: TDR waveform with derivative travel time analysis.....	132
Figure 6.25: TDR waveforms in water and air .....	134
Figure 6.26: TDR waveforms with changing soil water content: (a) Prototype permeameter; (b) Hydraulic characterization permeameter.....	135
Figure 6.27: (a) Embedded TDR compaction data; (b) Compaction mold.....	136
Figure 6.28: Embedded TDR calibration curves .....	136
Figure 6.29: Effect of salinity on TDR measurements: (a) Waveforms; (b) Calibrations .....	137
Figure 6.30: TDR calibration curve for hydraulic characterization permeameter.....	138

Figure 6.31: TDR sensitivity: (a) TDR during centrifugation in empty H.C. permeameter; (b) TDR measurements during steady-state flow in prototype permeameter .....	139
Figure 6.32: Flushing tensiometer for prototype permeameter: (a) Schematic; (b) Disassembled tensiometer; (c) Tensiometer with saturation chamber .....	142
Figure 6.33: Tensiometer for the hydraulic characterization permeameter: (a) Schematic views; (b) Picture; (c) Tensiometer with transducer; (d) Bracket in swinging bucket; (e) Tensiometer in bracket and permeameter .....	143
Figure 6.34: Calibration chamber for the tensiometers .....	144
Figure 6.35: Tensiometer calibration curves: (a) Prototype permeameter tensiometer; (b) Hydraulic characterization permeameter tensiometer .....	145
Figure 6.36: Heat dissipation unit .....	147
Figure 6.37: (a) Constant current source; (b) Cold-junction compensation module .....	147
Figure 6.38: (a) Fitting for prototype permeameter; (b) Fitting for hydraulic characterization permeameter .....	148
Figure 6.39: Typical HDU temperature responses during heating .....	149
Figure 6.40: HDU calibration results reported by Flint <i>et al.</i> (2002) .....	150
Figure 6.41: HDU calibration: (a) Calibration chamber; (b) Calibration curve .....	151
Figure 6.42: HDU measurements: (a) At rest and at high $\omega$ ; (b) At low $\omega$ .....	152
Figure 6.43: On-board data acquisition system .....	153
Figure 6.44: (a) User interface side of DAS; (b) Brackets and Cable stays .....	154
Figure 6.45: (a) Cable tester and multiplexer containment unit; (b) Top of cable tester; (c) Cross section schematic of the cable tester/multiplexer containment unit; (d) Side view of board within cable tester .....	155
Figure 6.46: Temperature monitoring system: (a) Cold-junction compensation circuit; (b) calibration equation .....	156
Figure 6.47: (a) CCD for in-flight visualization; (b) CCD installed in centrifuge; (c) Stroboscope for external visualization .....	157
Figure 6.48: Centrifuge work area .....	158
Figure 6.49: Crane and hoist for exchange of centrifuge permeameter environments ..	158
Figure 7.1: Instrumentation layout in the hydraulic characterization permeameter .....	162
Figure 7.2: Hydraulic characterization permeameter components .....	169
Figure 7.3: Assembled hydraulic characterization permeameter: (a) Installed TDR waveguide; (b) Rubber stoppers; (c) Outflow mesh .....	170
Figure 7.4: Compaction outside the centrifuge: (a) First lift; (b) Scarification; (c) Last lift .....	170
Figure 7.5: Post-compaction: (a) Preparation of the soil surface; (b) Placement of collar and filter papers; (c) Connection of inflow distribution cap .....	171
Figure 7.6: Compaction in the centrifuge .....	172
Figure 7.7: (a) Imposition of constant inflow rate outside centrifuge (with water bath); (b) Removal of rubber stoppers in tensiometer holes after saturation for installation in the centrifuge .....	173
Figure 7.8: (a) Outflow reservoir with initial volume of water; (b) Placement of hydraulic characterization permeameter in the centrifuge bucket .....	174

Figure 7.9: Calibration of tensiometers: (a) Tensiometer profile; (b) Pressure transducer .....	175
Figure 7.10: Installation of tensiometers (a) Support bracket and permeameter ready for tensiometer installation; (b) Installed tensiometers.....	175
Figure 7.11: Prototype permeameter (a) Picture of empty TDR ports and plugged tensiometer ports (lower port plugged with rubber stopper); (b) Schematic of instrument spacing .....	176
Figure 7.12: Prototype permeameter: (a) Installed TDR waveguides with rubber stopper for tensiometer; (b) Permeameters with different boundary conditions ...	177
Figure 7.13: Compaction in the prototype permeameter: (a) First lift with TDR; (b) Finished lift; (c) Intermediate lift with no TDR; (d) Last lift with uppermost TDR (e) Prepared surface; (f) Fiber-glass wicks for inflow distribution; (g) Top fluid distribution cap.....	178
Figure 7.14: (a) Disconnected outflow reservoir; (b) Assembly of permeameter and reservoir in the centrifuge .....	179
Figure 7.15: (a) Air release tube; (b) Placement of permeameter in the centrifuge .....	180
Figure 7.16: (a) Installation of tensiometer; (b) Permeameter ready for centrifugation.	180
Figure 7.17: Ranges in $K_{target}$ as a function of: (a) $Q$ and $\omega$ ; (b) $v_m$ and $N_{r,mid}$ .....	181
Figure 7.18: Test sequences for hydraulic characterization approaches in the centrifuge permeameter: (a) $Q$ and $\omega$ ; (b) $K_{target}$ and $N_{r,mid}$ .....	183
Figure 7.19: Contours of constant $K_{target}$ : (a) Flow rate vs. RPM; (b) $v_m$ vs. $N_{r,mid}$ .....	184
Figure 7.20: Hysteresis testing sequences: (a) $Q$ vs. $\omega$ ; (b) $K_{target}$ vs. $N_{r,mid}$ .....	185
Figure 7.21: Hypothetical data from the different instruments in the centrifuge permeameter: (a) Constant $\omega$ and varying $Q$ ; (b) Constant $Q$ and varying $\omega$ .....	189
Figure 7.22: Hypothetical data from outflow transducer: (a) Constant $\omega$ and varying $Q$ ; (b) Constant $Q$ and varying $\omega$ .....	191
Figure 7.23: Hypothetical data from the TDR .....	191
Figure 7.24: Hypothetical data from the tensiometer: (a) Constant $\omega$ and varying $Q$ ; (b) Constant $Q$ and varying $\omega$ .....	192
Figure 8.1: Test I time series: (a) Flow control variables $Q$ and $\Sigma V$ ; (b) Centrifuge control variables $\omega$ and $N_r$ ; (c) G-meter and thermocouple results .....	194
Figure 8.2: Outflow transducer measurements in Test I.....	195
Figure 8.3: TDR measurements in Test I: (a) Specimen A; (b) Specimen B .....	196
Figure 8.4: Moisture content profiles in Test I: (a) Specimen A; (b) Specimen B.....	196
Figure 8.5: Tensiometer measurements in Test I.....	197
Figure 8.6: Final moisture content profile from destructive samples at the end of testing .....	198
Figure 9.1: Test II: (a) Summary of imposed $Q$ and $\omega$ (arrows denote progression of the test); (b) Summary of steady-state imposed $K$ values with $N_{r,mid}$ .....	203
Figure 9.2: Test II time series: (a) Flow control variables $Q$ and $\Sigma V$ ; (b) Centrifuge control variables $\omega$ and $N_r$ ; (c) G-meter and thermocouple results.....	204
Figure 9.3: Summary of outflow transducer measurements during Test II .....	205

Figure 9.4: Summary of TDR measurements during Test II .....	206
Figure 9.5: Tensiometer measurements during Test II: (a) Specimen A; (b) Specimen B .....	206
Figure 9.6: Control variables in Stage II-1 .....	207
Figure 9.7: Outflow transducer measurements in Stage II-1 .....	208
Figure 9.8: TDR measurements in Stage II-1 .....	208
Figure 9.9: Tensiometer measurements in Stage II-1: (a) Specimen A; (b) Specimen B .....	209
Figure 9.10: Suction profiles in Stage II-1: (a) Specimen A; (b) Specimen B .....	209
Figure 9.11: Control variables in Stage II-2 .....	210
Figure 9.12: Outflow transducer measurements in Stage II-2 .....	210
Figure 9.13: TDR measurements in Stage II-2 .....	211
Figure 9.14: Tensiometer measurements in Stage II-2: (a) Specimen A; (b) Specimen B .....	211
Figure 9.15: Suction profiles in Stage II-2 .....	212
Figure 9.16: Control variables in Stage II-3 .....	212
Figure 9.17: Outflow transducer in Stage II-3: (a) Before drainage; (b) After drainage .....	213
Figure 9.18: Summary of measured values in Stage II-3: (a) TDR; (b) Tensiometer; (c) Outflow transducer .....	214
Figure 9.19: Tensiometer measurements in Stage II-3: (a) Specimen A; (b) Specimen B .....	214
Figure 9.20: Suction profiles in Stage II-3 .....	215
Figure 9.21: Control variables in Stage II-4 .....	215
Figure 9.22: Outflow transducer measurements in Stage II-4 .....	216
Figure 9.23: Summary of measured values in Stage II-4: (a) TDR; (b) Tensiometer; (c) Outflow transducer .....	216
Figure 9.24: Tensiometer measurements in Stage II-4: (a) Specimen A; (b) Specimen B .....	217
Figure 9.25: Suction profiles in Stage II-4 .....	217
Figure 9.26: Control variables in Stage II-5 .....	218
Figure 9.27: Outflow transducer measurements in Stage II-5 .....	218
Figure 9.28: Summary of TDR values in Stage II-5 .....	219
Figure 9.29: Tensiometer measurements in Stage II-5: (a) Specimen A; (b) Specimen B .....	219
Figure 9.30: Suction profiles in Stage II-5 .....	220
Figure 9.31: Final moisture content profile from destructive samples at the end of Test II .....	220
Figure 9.32: Summary of imposed $Q$ and $\omega$ for Test III (arrows denote progression of test): (a) First five stages; (b) Stage III-6; (c) Stage III-7 .....	224
Figure 9.33: Summary of $K_{target}$ values with $N_{r,mid}$ in Test III (arrows denote progression of test): (a) First five stages; (b) Stage 6; (c) Stage III-7 .....	225
Figure 9.34: Test III time series: (a) Flow control variables $Q$ and $\Sigma V$ ; (b) Centrifuge control variables $\omega$ and $N_r$ ; (c) G-meter and thermocouple results .....	226
Figure 9.35: Summary of outflow transducer measurements during Test III .....	227
Figure 9.36: Summary of TDR measurements during Test III .....	228



Figure 9.37: Tensiometer measurements during Test III: (a) Specimen A; (b) Specimen B	228
Figure 9.38: Control variables in Stage III-1	229
Figure 9.39: Outflow transducer measurements in Stage III-1	230
Figure 9.40: TDR measurements in Stage III-1	230
Figure 9.41: Tensiometer measurements in Stage III-1: (a) Specimen A; (b) Specimen B	231
Figure 9.42: Suction profiles in Stage III-1: (a) Specimen A; (b) Specimen B	231
Figure 9.43: Control variables in Stage III-2	232
Figure 9.44: Outflow transducer measurements in Stage III-2	232
Figure 9.45: TDR measurements in Stage III-2	233
Figure 9.46: Tensiometer measurements in Stage III-2: (a) Specimen A; (b) Specimen B	234
Figure 9.47: Suction profiles in Stage III-2: (a) Specimen A; (b) Specimen B	234
Figure 9.48: Control variables in Stage III-3	235
Figure 9.49: Outflow transducer measurements in Stage III-3	235
Figure 9.50: TDR measurements in Stage III-3	236
Figure 9.51: Tensiometer measurements in Stage III-3: (a) Specimen A; (b) Specimen B	236
Figure 9.52: Suction profiles in Stage III-3: (a) Specimen A; (b) Specimen B	237
Figure 9.53: Control variables in Stage III-4	237
Figure 9.54: Outflow transducer measurements in Stage III-4	238
Figure 9.55: TDR measurements in Stage III-4	238
Figure 9.56: Tensiometer measurements in Stage III-4: (a) Specimen A; (b) Specimen B	239
Figure 9.57: Suction profiles in Stage III-4: (a) Specimen A; (b) Specimen B	239
Figure 9.58: Control variables in Stage III-5	240
Figure 9.59: Outflow transducer measurements in Stage III-5	241
Figure 9.60: TDR measurements in Stage III-5	241
Figure 9.61: Tensiometer measurements in Stage III-5: (a) Specimen A; (b) Specimen B	242
Figure 9.62: Suction profiles in Stage III-5: (a) Specimen A; (b) Specimen B	242
Figure 9.63: Control variables in Stage III-6: (a) Inflow rate; (b) $N_{r,mid}$	243
Figure 9.64: Outflow transducer measurements in Stage III-6	244
Figure 9.65: TDR measurements in Stage III-6	245
Figure 9.66: Tensiometer measurements in Stage III-6: (a) Specimen A; (b) Specimen B	245
Figure 9.67: Suction profiles in Stage III-6: (a) Specimen A drying; (b) Specimen B drying; (c) Specimen A wetting; (d) Specimen B wetting	246
Figure 9.68: Control variables in Stage III-7	247
Figure 9.69: Outflow transducer measurements in Stage III-7	247
Figure 9.70: TDR measurements in Stage III-7	248
Figure 9.71: Tensiometer measurements in Stage III-7: (a) Specimen A; (b) Specimen B	249

Figure 9.72: Suction profiles in Stage III-7: (a) Specimen A drying; (b) Specimen B drying; (c) Specimen A wetting; (d) Specimen B wetting .....	250
Figure 9.73: Final moisture content profile from destructive samples at end of Test III	250
Figure 9.74: Test IV: (a) Summary of imposed $Q$ and $\omega$ (arrows denote progression of the test); (b) Summary of steady-state imposed $K$ values with $N_{r,mid}$ .....	252
Figure 9.75: Test IV time series: (a) Flow control variables $Q$ and $\Sigma V$ ; (b) Centrifuge control variables $\omega$ and $N_r$ ; (c) G-meter and thermocouple results .....	253
Figure 9.76: Summary of outflow transducer measurements during Test IV .....	254
Figure 9.77: Summary of TDR measurements during Test IV .....	254
Figure 9.78: Tensiometer measurements in Test IV: (a) Specimen A; (b) Specimen B	255
Figure 9.79: Control variables in Stage IV-1 .....	256
Figure 9.80: Outflow transducer measurements in Stage IV-1 .....	256
Figure 9.81: TDR measurements in Stage IV-1 .....	257
Figure 9.82: Tensiometer measurements in Stage IV-1: (a) Specimen A; (b) Specimen B .....	258
Figure 9.83: Suction profiles in Stage IV-1: (a) Specimen A; (b) Specimen B .....	258
Figure 9.84: Control variables in Stage IV-2 .....	259
Figure 9.85: Outflow transducer measurements in Stage IV-2 .....	259
Figure 9.86: TDR measurements in Stage IV-2 .....	260
Figure 9.87: Tensiometer measurements in Stage IV-2: (a) Specimen A; (b) Specimen B .....	261
Figure 9.88: Suction profiles in Stage IV-2: (a) Specimen A; (b) Specimen B .....	261
Figure 9.89: Control variables in Stage IV-3 .....	262
Figure 9.90: Outflow transducer measurements in Stage IV-3 .....	262
Figure 9.91: TDR measurements in Stage IV-3 .....	263
Figure 9.92: Tensiometer measurements in Stage IV-3: (a) Specimen A; (b) Specimen B .....	263
Figure 9.93: Suction profiles in Stage IV-3: (a) Specimen A; (b) Specimen B .....	264
Figure 9.94: Control variables in Stage IV-4 .....	264
Figure 9.95: Outflow transducer measurements in Stage IV-4 .....	265
Figure 9.96: TDR measurements in Stage IV-4 .....	265
Figure 9.97: Tensiometer measurements in Stage IV-4: (a) Specimen A; (b) Specimen B .....	266
Figure 9.98: Suction profiles in Stage IV-4: (a) Specimen A; (b) Specimen B .....	267
Figure 9.99: Final moisture content profile from destructive samples at end of Test IV	267
Figure 10.1: WRC determined for different suction values in drying path of Stage III-6 .....	269
Figure 10.2: (a) Suction values measured at different elevations at steady-state water flow during Test III; (b) Suction head gradient values for different elevations	271
Figure 10.3: Comparison between suction head gradient and centrifuge elevation head gradient ( $N$ ) at steady-state water flow during Test III .....	272
Figure 10.4: K-functions with $K_{target}$ and $K_{measured}$ : (a) Stage III-7; (b) Stage III-1 .....	273
Figure 10.5: Comparison between $K_{target}$ (without suction head gradient) and $K_{measured}$ (with suction head gradient): (a) Test II; (b) Test III; (c) Test IV; Note:	

$K_{\text{measured}}$ values calculated using the upper and middle tensiometers in Test III and using the upper and lower tensiometers in Tests II and IV .....	274
Figure 10.6: Test II results for Specimen A: (a) $K-\psi$ ; (b) $K-\theta$ ; (c) $K-S_r$ ; (d) WRC .....	275
Figure 10.7: Test II results for Specimen B: (a) $K-\psi$ ; (b) $K-\theta$ ; (c) $K-S_r$ ; (d) WRC.....	276
Figure 10.8: Test III results for Specimen A: (a) $K-\psi$ ; (b) $K-\theta$ ; (c) $K-S_r$ ; (d) WRC .....	277
Figure 10.9: Test III results for Specimen B: (a) $K-\psi$ ; (b) $K-\theta$ ; (c) $K-S_r$ ; (d) WRC .....	278
Figure 10.10: Test IV results for Specimen A: (a) $K-\psi$ ; (b) $K-\theta$ ; (c) $K-S_r$ ; (d) WRC .....	279
Figure 10.11: Test IV results for Specimen B: (a) $K-\psi$ ; (b) $K-\theta$ ; (c) $K-S_r$ ; (d) WRC .....	280
Figure 10.12: Repeatability assessment: (a) K-function; (b) WRC.....	281
Figure 10.13: Comparison of characterization approaches: (a) K-function; (b) WRC...	282
Figure 10.14: Consistency tests during Stage III-5: (a) Specimen A; (b) Specimen B ..	283
Figure 10.15: Consistency tests for Specimen A during Stage III-5: (a) $K-\psi$ ; (b) $K-\theta$ ..	284
Figure 10.16: Constant $K_{\text{target}}$ hysteresis test: (a) Specimen A; (b) Specimen B.....	285
Figure 10.17: Hysteresis tests for Specimen A during Stage III-5: (a) $K-\psi$ ; (b) $K-\theta$ .....	286
Figure 10.18: K-function hysteresis: (a) $K-\psi$ Approach (i); (b) $K-\theta$ Approach (i); (c) $K-\psi$ Approach (ii); (d) $K-\theta$ Approach (ii); (e) $K-\psi$ Approach (iii); (f) $K-\theta$ Approach (iii) .....	287
Figure 10.19: Hysteresis in WRCs: (a) Approach (i); (b) Approach (ii); (c) Approach (iii) .....	288
Figure 10.20: Effect of compaction water content; (a) K-function; (b) WRC.....	289
Figure 11.1: K-functions with centrifuge and column infiltration tests.....	290
Figure 11.2: Comparison of WRC from the centrifuge and pressure plate tests .....	291
Figure 11.3: Comparison of K-functions from the centrifuge and pressure plate tests ..	292
Figure 11.4: Centrifuge data with fitted Campbell model K-functions .....	293
Figure 11.5: (a) Fitted WRC using the van Genuchten model; (b) K-function predicted using the van Genuchten-Mualem model using the WRC parameters .....	294
Figure 12.1: Theoretical and measured suction profiles with boundary condition effects .....	297
Figure 12.2: Boundary effects on moisture content profiles: (a) Column; (b) Centrifuge .....	298
Figure 12.3: RichTexNg results showing de-saturation of the bottom boundary ( $v_m = 0$ ) .....	300
Figure 12.4: Results from oedometer test on a saturated, compacted specimen .....	301
Figure 12.5: Incremental change in slope for the $n\text{-log}\sigma'$ curve in Figure 12.4.....	302
Figure 12.6: Effective stress profiles (Note: geometry is for centrifuge permeameter) ..	303
Figure 12.7: Calculations using $e\text{-log}\sigma'$ curve (a) Void ratio; (b) Surface settlement ...	303
Figure 12.8: Schematic stress-deformation surface for unsaturated soils (Fredlund 2006) .....	304
Figure 12.9: Net normal stress profiles (Note: geometry is for centrifuge permeameter) .....	305
Figure 12.10: Constrained modulus predicted from the model of Mendoza <i>et al.</i> (2005) .....	307
Figure 12.11: Calculated strains with specimen height (for a constant suction of 120 kPa) .....	307

Figure 12.12: Bounds on expected surface settlement with $N_{r,mid}$ .....	308
Figure 12.13: Surface of a dense specimen ( $n = 0.35$ ) after infiltration at 120 g .....	309
Figure 12.14: Effect of g-level on the K-function: (a) $K-\psi$ , (b) $K-\theta$ , (a) $K-S$ ; (b) $\psi-\theta$ .....	310
Figure 12.15: Views of the top of the soil specimen at the end of Test III.....	311
Figure 12.16: Estimated travel times for soils with different initial $K_s$ values .....	313
Figure 13.1: Design K-function: (a) $K-\psi$ , (b) $K-\theta$ .....	327
Figure A.1: Actual outflow data from an infiltration test without soil .....	333
Figure A.2: Outflow transducer results indicating compression of the pore air .....	334
Figure A.3: High outflow measurements: (a) Reservoir full; (b) Transducer capacity ..	335
Figure A.4: Infiltration test on sand; (a) Inflow data; (b) Volumetric moisture content	336
Figure A.5: Changes in moisture content inferred from TDR during an infiltration test (Note: $\omega = 200$ RPM, $N_r = 25$ , dashed lines separate different $v_m$ in ml/hr)	336
Figure A.6: Tensiometer data from an infiltration/drainage test .....	337
Figure A.7: Tensiometer cavitation: (a) Cavitation behavior; (b) Behavior after flushing .....	338
Figure A.8: Flushing needle for an installed tensiometer .....	339
Figure A.9: TDR data indicating a leak and air-pressure build-up .....	340

## **Chapter 1: Introduction**

### **1.1 RESEARCH MOTIVATION**

Unsaturated soils contain both air and water in the pore spaces between solid particles. Three independent variables can be used to characterize the hydraulic behavior of unsaturated soils: the volume of water in the pore spaces, the matric suction (difference in air and water pressures), and the impedance to water flow through the soil. The relationships between these variables are referred to as the hydraulic characteristics of an unsaturated soil. The relationship between the volume of water in a pore spaces and the matric suction is referred to as the “water retention curve” or WRC. The WRC reflects the energy required to remove water from the soil. The relationship between the volume of water in the pore space and the soil’s impedance to water flow is referred to as the “hydraulic conductivity function” or K-function. The hydraulic conductivity of an unsaturated soil is related to the volume of water in the pores because the presence of air restricts the available pathways for water flow. The K-function can also be defined using the matric suction and the WRC.

Geotechnical applications involving unsaturated soils include waste containment systems (landfills), embankments and natural slopes, surficial drainage systems, roadway pavements, and reinforced soil walls, and foundations in expansive soils. Geotechnical engineers are often interested in quantifying the hydraulic characteristics of unsaturated soils in order to evaluate the volume of water moving through the soil, assess stability, and predict soil volume changes. Other fields of engineering are interested in the hydraulic characteristics of unsaturated soils as well. For instance, agricultural engineers are interested in the availability of water for plant growth, and hydrologists are interested in the water balance near the ground surface to quantify natural resources. Further,

knowledge of the hydraulic characteristics of unsaturated soils can be applied to soils that contain mixtures of other liquids and gases in their pore spaces. For instance, environmental engineers are interested in the migration of contaminants through soils, and petroleum engineers are interested in the extraction of oil and natural gas from soils.

The hydraulic characteristics of unsaturated soils are complex. The WRC and K-function may vary with the soil density (or the corresponding pore size distribution), physico-chemical properties of the soil particles, chemistry of the water flowing through the soil, dissolution of gases into the pore water, and environmental variables like temperature and barometric air pressure. Further, the WRC and K-function show hysteretic behavior due to entrapment of air in the pores during wetting and drying.

Because the hydraulic characteristics of unsaturated soils are complex and thus soil-specific, many experimental approaches have been proposed in the technical literature for their determination. Most approaches only allow definition of one of the hydraulic characteristics at a time, require several assumptions, and involve multiple specimens. In general, a flow condition must be imposed on a soil specimen, and the relevant variables (*e.g.*, water volume, water pressure, water flow rate) are measured with time. The measurements must be reduced to determine the WRC and K-function, which often requires simplifying assumptions. For example, some experimental approaches used in practice involve transient water flow, where the variables being measured change with time. Transient approaches yield a significant amount of information in a short period of time. However, as will be discussed in Chapter 5, the data are often difficult to analyze and the results are prone to experimental error and variability. Other experimental approaches involve continuous, steady flow of water through the soil. As will be discussed in Chapter 2, the data from steady flow tests are easier to interpret and the results are often less prone to variability. However, these tests have a long duration.

Although experimentally-derived hydraulic characteristics provide a better representation of a soil's behavior than theoretical predictions, control of the variables that affect the soil's hydraulic characteristics and the required time frame for their determination may result in considerable cost to an engineering project. It is also difficult to appropriately sample or prepare representative soil specimens to account for spatial and temporal variability in soil properties in the field. Alternatively, engineers can estimate the hydraulic characteristics of unsaturated soil using published databases, empirical correlations, or theoretical models. Although estimates of the hydraulic characteristics may be the only feasible alternative for some projects, their use could potentially lead to inadequate, conservative, or costly designs. Also, estimates of the hydraulic characteristics that do not consider soil-specific issues may result in an inadequate understanding of geotechnical systems involving unsaturated soils.

Accordingly, the intention of this study is to promote the use of experimentally-derived hydraulic characteristics in geotechnical engineering practice by presenting a new approach to determine the hydraulic characteristics of unsaturated soils. The goals of this new approach are to determine the hydraulic characteristics in a reasonable time frame using straightforward techniques to interpret the data. The new approach involves development and validation of an instrumented permeameter used to control the flow of water through a soil specimen while spinning in a high-speed geotechnical centrifuge. This permeameter is referred to as the "Centrifuge Permeameter for Unsaturated Soils". Centrifugation is employed to provide an additional driving force for water flow, and steady-state infiltration is used to provide repeatable testing conditions. The behavior noted in a long column of soil in the field during steady-state infiltration, which is easy to interpret to define the hydraulic characteristics, can be replicated in a smaller soil specimen in the centrifuge permeameter with a decreased testing time.

## **1.2 RESEARCH OBJECTIVES**

The specific objectives of this study are to:

- Review the terminology and basic concepts governing the hydraulic behavior of unsaturated soils;
- Review the experimental and predictive techniques that have been used to determine the hydraulic characteristics of unsaturated soils;
- Review the theory of water flow through unsaturated soils in a field setting as well as in a centrifuge permeameter setting;
- Select and characterize a soil useful for verification of the centrifuge permeameter;
- Determine the hydraulic characteristics of the selected soil using conventional experimental and predictive techniques;
- Develop the geometry, layout, and plumbing for the centrifuge permeameter using lessons learned from the theoretical investigation of water flow in the centrifuge;
- Develop, calibrate, and verify the instrumentation used in the centrifuge permeameter to measure the key variables needed to define the hydraulic characteristics in a continuous, non-destructive, and non-intrusive manner during centrifugation;
- Provide a link between the theory of water flow and measurements from the centrifuge permeameter to determine the hydraulic characteristics of an unsaturated soil specimen in the centrifuge permeameter;
- Determine the hydraulic characteristics of a selected clay with different compaction conditions to validate the centrifuge approach and verify assumptions in the analysis;
- Determine the impact of centrifugation on the hydraulic characteristics;
- Assess hysteresis in the hydraulic characteristics during steady-state water flow;
- Compare the results from the centrifuge permeameter approach with those from conventional testing approaches.



### **1.3 DISSERTATION ORGANIZATION**

A review of the important variables used to describe unsaturated soils and an introduction to the Water Retention Curve (WRC) and K-function are presented in Chapter 2. The theoretical basis for water flow through unsaturated soils under normal gravity and in the centrifuge is presented in Chapter 3. This information is used to form the basis for a centrifuge permeameter approach to determine the hydraulic characteristics. Specifically, theoretical solutions are presented for the water pressure profiles during steady-state water flow, which are used to show how the hydraulic characteristics can be defined in an infiltration test. Boundary conditions that may be employed to control the flow of water through a soil specimen during hydraulic characterization are also discussed. The geotechnical properties of the soil used in this study to demonstrate the use of the centrifuge permeameter are described in Chapter 4. Predictive models, empirical correlations, and conventional approaches used to determine the hydraulic characteristics for unsaturated soils are discussed in Chapter 5. Hydraulic characteristics from these approaches were obtained for the soil described in Chapter 4.

The Centrifuge Permeameter for Unsaturated Soils is described in Chapter 6. This chapter also includes a description of the instrumentation used in this study to measure water content, matric suction, and fluid flow rate. Soil-specific calibration of the instrumentation is also discussed. Details of the testing philosophy and experimental procedures adopted for the centrifuge permeameter are described in Chapter 7. This includes a discussion of the variables that are necessary for determination of the hydraulic characteristics, how they can be measured using the instrumentation, and the assumptions required for data analysis. The procedures adopted for hydraulic characterization in the centrifuge permeameter are described, including methods used for specimen preparation, centrifugation and water flow control. Procedures adopted to

validate the assumptions adopted to interpret the centrifuge permeameter results and to evaluate important centrifuge testing issues like settlement and testing time are also presented. In addition, a discussion of the expected measurements from the instrumentation is also included in Chapter 7.

The results of a test conducted in a large centrifuge permeameter focusing on boundary condition effects and moisture content profiles are presented in Chapter 8. The results from three series of tests conducted in a smaller centrifuge permeameter focusing on determination of the hydraulic characteristics are presented in Chapter 9. Chapter 10 includes an analysis and synthesis of the data from these tests, focusing on determination of the WRC and K-function. Chapter 11 includes a comparison of the results from the centrifuge permeameter with those from conventional tests presented in Chapter 5. Finally, Chapter 12 includes an evaluation of different issues in centrifuge determination of the hydraulic characteristics.

A summary of how the research objectives were achieved, conclusions drawn from this study, and issues proposed for future research, are presented in Chapter 13. In addition, two appendices to this dissertation are included. Appendix A includes an evaluation of the results from preliminary centrifuge permeameter tests. The instrumentation results from these tests were shown to be particularly useful in interpreting different testing issues like leaks, instrument sensitivity, and instrument failure. Appendix B includes the theoretical derivation of a computer program useful for analysis of water flow in a centrifuge specimen. Although not the focus of this study, this model was used to interpret boundary condition effects in the centrifuge permeameter.

## **Chapter 2: Hydraulic Characteristics of Unsaturated Soils**

### **2.1 OVERVIEW**

The definitions of the hydraulic characteristics presented in the introduction were presented in general terms. This chapter presents variables commonly used to quantify the hydraulic aspects of unsaturated soils, and how they can be related to define the hydraulic characteristics. Specifically, variables are presented to represent the volume of water in the soil pores, the difference in pressure between the water and air in the soil pores, and the impedance to water flow through the soil. These variables are then related to define the water retention curve (WRC) and the hydraulic conductivity function (K-function). These relationships are not referred to as soil “properties” in this study because they depend on the current state of the soil as well as the past history of wetting and drying. This section describes the important aspects of these relationships and the impact of different variables on their shapes.

### **2.2 IMPORTANT VARIABLES USED TO DESCRIBE UNSATURATED SOILS**

#### **2.2.1 Water Content of Unsaturated Soils**

The relative amounts of water and air within the soil pores has a significant influence on the behavior of unsaturated soils. Some of the common phase relationships used to quantify the relative amounts of water and air in soils are illustrated in Figure 2.1. The gravimetric moisture content  $w$  is defined as the mass of water  $M_w$  divided by the mass of solids  $M_s$ , while the volumetric moisture content  $\theta$  is defined as the volume of water in the voids  $V_w$  divided by the total volume of the soil  $V_T$ . These quantities are linked through the dry density of the soil  $\rho_d$  and the density of water  $\rho_w$ . The porosity  $n$ , which is the ratio of the volume of voids  $V_v$  and the total volume, is also the volumetric

The diagram illustrates a three-phase system consisting of Air, Water, and Solid particles. The mass fractions are defined as follows:

- $M_a$ : Mass of Air
- $M_w$ : Mass of Water
- $M_s$ : Mass of Solid particles

The volume fractions are defined as follows:

- $V_a$ : Volume of Air
- $V_w$ : Volume of Water
- $V_s$ : Volume of Solid particles
- $V_t$ : Total Volume

The densities and specific gravity are defined as follows:

- $\rho_a$ : Density of Air
- $\rho_w$ : Density of Water
- $\rho_s = G_s \rho_w$ : Density of Solid particles, where  $G_s$  is the specific gravity of solid particles.

The mass and volume fractions are related by the following equations:

$$w = \frac{M_w}{M_s} \quad n = \frac{V_w}{V_t}$$

$$\theta = \frac{V_w}{V_t} \quad S_r = \frac{V_w}{V_v} = \frac{\theta}{n}$$

$$e = \frac{V_v}{V_s} = \frac{n}{1-n} \quad S_i e = w G_s$$

$$\rho_{bulk} = \frac{M_t}{V_t} = G_s \rho_w \frac{1+w}{1+e}$$

$$\rho_d = \frac{M_s}{V_t} = \frac{\rho_s}{1+e} = \frac{\rho_{bulk}}{1+w} = \rho_w \frac{\theta}{w}$$

The volumetric moisture content is typically used to quantify changes in water storage of a soil specimen, although this is only strictly true for rigid soils like compacted or overconsolidated soils. The volumetric moisture content is not adequate to fully describe changes in moisture storage of compressible specimens, as there may be changes in the both the total volume of the soil and the volume of water in the pores during water flow. Alternatively, the gravimetric moisture content and void ratio are useful when dealing with compressible porous media because the mass and volume of solids do not change during water flow. Specifically, changes in the gravimetric moisture content reflect changes in the mass of water in a soil, while changes in void ratio reflect changes in the volume of the voids. Nonetheless, the volumetric moisture content is used in this study as the soils investigated are stiff, compacted clays of low plasticity.

### 2.2.2 Matric Suction

In unsaturated soils, water is held within the pores by a combination of adsorptive and capillary pressures (Olson and Langfelder 1965). Adsorptive pressures are present in soils due to electrical fields and short-range attractive forces (van Der Waals forces) that tend to draw water toward the soil particles. These pressures may be significant in highly plastic clays, where the net negative charges on the surface of clay particles interact with water dipoles and cations in the pore water. The capillary pressure is defined as the difference between the pore air pressure and the pore water pressure. Water is a wetting fluid for most soil particles, which implies that the air-water menisci between individual soil particles are convex, tensioned membranes. Accordingly, the air pressure is greater than the water pressure, so the water pressure has a negative magnitude when the air pressure is atmospheric. Because the adsorptive and capillary pressures are difficult to distinguish from each other experimentally, they are often considered together as a single variable, referred to as the matric suction  $\psi$ . The matric suction is thus defined in the same fashion as the capillary pressure, as follows:

$$\psi = P_a - P_w \quad (2.1)$$

where  $P_a$  is the air pressure, and  $P_w$  is the water pressure, and  $\psi$  is the matric suction having units of pressure (kPa). Assuming that the pressure in the air phase is atmospheric (*i.e.*,  $P_a = 0$ ), the suction equals  $\psi = -P_w$ , and is thus a positive quantity for unsaturated soils. This assumption will be used throughout this dissertation. Also, when the term “suction” is used alone, it refers to matric suction.

### 2.2.3 Impedance to Water Flow through Soils

The impedance to water flow through a soil has been investigated by many researchers, most famously by Darcy (1856). Darcy observed that the flow of water

through soil is proportional to the gradient in total hydraulic head, equal to the sum of the water pressure head and elevation head. This relationship is given by Darcy's law:

$$Q = -KiA \quad (2.2)$$

where  $K$  is a constant of proportionality,  $i$  is the gradient in hydraulic head, and  $A$  is the cross-sectional area of flow. The constant of proportionality,  $K$ , is referred to as the hydraulic conductivity, and is typically given the subscript "s" when the soil is water saturated ( $K_s$ ). The hydraulic conductivity has been associated with the characteristics of the soil and fluid. For instance, the Hagen-Poiseuille law for flow of water through a fully-filled capillary tube has been used to investigate the variables that affect  $K_s$  (Mitchell 1979). This model is applied to soils as follows:

$$Q = \left( \frac{cR^2 \rho_w g}{\mu_w} \right) \left( \frac{H}{L} \right) A \quad (2.3)$$

where  $Q$  is the flow rate over an area  $A$ ,  $c$  is a shape coefficient (1/8 for a capillary tube),  $R$  is a characteristic pore radius,  $\rho_w$  is the density of water,  $g$  is the acceleration due to gravity,  $\mu_w$  is the dynamic viscosity of water at constant temperature, and  $H$  is the total head difference over a length  $L$  (gradient). From Equation (2.3),  $K_s$  is defined as:

$$K_s = \frac{cR^2 \rho_w g}{\mu_w} = \frac{\kappa \rho_w g}{\mu_w} \quad (2.4)$$

where  $\kappa = cR^2$  is defined as the intrinsic permeability of the soil. The Hagen-Poiseuille law was used by Kozeny (1927) to predict  $K_s$  for poorly graded soils with a single, measurable pore radius (sand, gravel). However, it has several shortcomings when being used to predict the hydraulic conductivity of clays, where definition of a characteristic pore radius is ambiguous and physico-chemical effects play an important role.

## 2.3 HYDRAULIC CHARACTERISTICS OF UNSATURATED SOILS

### 2.3.1 Water Retention Curve (WRC)

The water retention curve is defined in this study as the relationship between suction ( $\psi$ ) on the abscissa axis and the volumetric moisture content ( $\theta$ ) or degree of saturation ( $S_r$ ) on the ordinate axis. The volumetric moisture content is typically used in situations when the WRC is used to calculate the moisture storage of a soil for a given suction, as the volume of water equals the total volume multiplied by  $\theta$ , or when measurement techniques that are on a volume-averaged basis are used to infer the moisture content (neutron probes, dielectric sensors). The degree of saturation is typically used in situations where the WRC for different soils are being compared, as it normalizes the volumetric moisture content to the porosities of the different materials. Schematic WRCs for different materials are shown in Figure 2.2(a) and Figure 2.2(b), with the suction plotted on logarithmic and natural scales, respectively. The curves shown are “drying” curves, as the degree of saturation decreases from 1.0 as the suction increases.

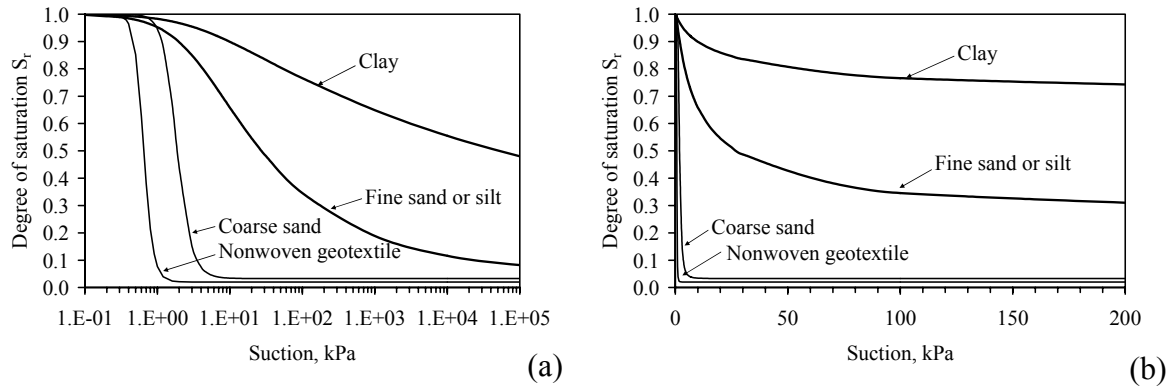


Figure 2.2: Typical water retention curves (WRCs): (a) Logarithmic; (b) Natural

The schematic WRCs for coarse-grained materials (*e.g.*, the coarse sand and nonwoven geotextile) show a relatively sharp decrease in degree of saturation at a low

suction. This occurs because soils have a range of pore sizes, with larger pores storing more water than smaller pores. The suction required to draw water from a pore increases as its size decreases. The coarse-grained materials have a relatively narrow range of pore sizes and drain from saturated conditions to dry conditions over a range of suction from 0 to 10 kPa. The WRCs for fine-grained soil (silt or clay) show a more gradual decrease in moisture content over a wider range of suction, as they have a wider range of pore sizes.

Typical WRCs for different soil types reported in the literature are shown in Figure 2.3. Similar to the observations made from comparison of the schematic WRCs in Figure 2.2, soils having larger pore sizes (sands) generally de-saturate at lower suctions than the soils with smaller pores (silts and clays). However, these data emphasize that there are differences in behavior that can only be assessed from soil-specific testing. For instance, the sand characterized by Conca and Wright (1998) retains an appreciable amount of water up to relatively high suctions. Accordingly, the shapes of the WRCs in Figure 2.3 emphasize the importance of using experimentally derived WRCs instead of schematic curves representative of groups of soil types (such as those in Figure 2.2).

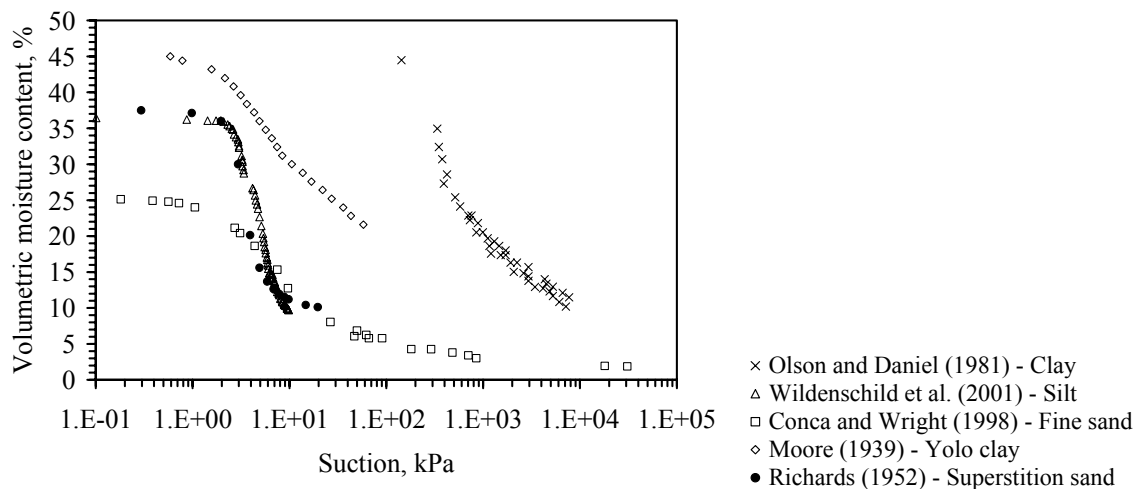


Figure 2.3: Experimental WRCs for different geotechnical materials



When drying a specimen from saturated conditions (zero suction), the specimen will initially remain saturated with water as the suction increases. Specifically, air-water menisci form in the pores on the outer boundaries of the soil specimen, but air does not enter the specimen. The suction is equal to the negative water pressure in this case. As the soil dries further, the suction increases and air enters some of the pores. The suction at which air enters the voids is typically referred to as the “air entry suction”. However, the air-entry suction is not unique for most soils due to the fact that air enters pores with different sizes at different suctions and the pores on the outer surface of the soil may not necessarily drain first. Accordingly, the air-entry suction depends on the arrangement of particles. In geotechnical practice, the air-entry suction is related with the height of the capillary fringe, which is a zone of saturated soil above the water table. The variability of the height of capillary rise reflects the vague definition of the air-entry suction.

As the soil dries further, the degree of saturation will continue to decrease until reaching a value that remains constant with increasing suction. This degree of saturation is often referred to as the residual saturation. Residual saturation is also a vaguely defined quantity. During drying, the water in the soil pores will eventually become occluded, eliminating interconnected pathways available for advective water flow. Occlusion of the water may occur at relatively high degrees of saturation. However, a soil can still be dried further by transporting water in the vapor phase. Accordingly, the residual saturation for a soil will likely depend on how the WRC is determined: via water flow (infiltration) or via vapor flow (evaporation).

The shape of a WRC has been interpreted in different ways to indicate different features about the moisture storage of a soil. When the suction is plotted on a logarithmic scale, the WRC typically has an “S”-shape. This shape is typically not noted when the suction is plotted on a natural scale. Nonetheless, when the WRC is plotted on a

logarithmic scale, researchers typically associate the point of curvature at low suction with the air entry value, and the one at high suction with the residual saturation.

A WRC can also show wetting and drying paths that are significantly different, a phenomenon referred to as hysteresis. Poulovasilis (1962) and Topp and Miller (1966) performed comprehensive investigations of the effects of hysteresis on the hydraulic properties of unsaturated soils. A schematic representation of wetting and drying paths of the WRC for a glass bead media is shown in Figure 2.4(a). During drying from full saturation, the larger pores drain first, followed by the smaller pores, and the WRC follows the primary drying path. During wetting from fully dry conditions, water fills smaller pores first, which may entrap air in larger pores. This leads to the WRC having a different wetting path. Wetting of the soil by reducing the suction may not lead to 100% saturation because entrapped air will prevent saturation of the soil unless positive water pressure is applied. Wetting and drying from different initial conditions follow internal scanning curves, which are typically scaled from the primary wetting and drying curves (Lenhard *et al.* 1991). These features are observed in the results of Topp and Miller (1966) shown in Figure 2.4(b), who investigated wetting and drying of glass beads.

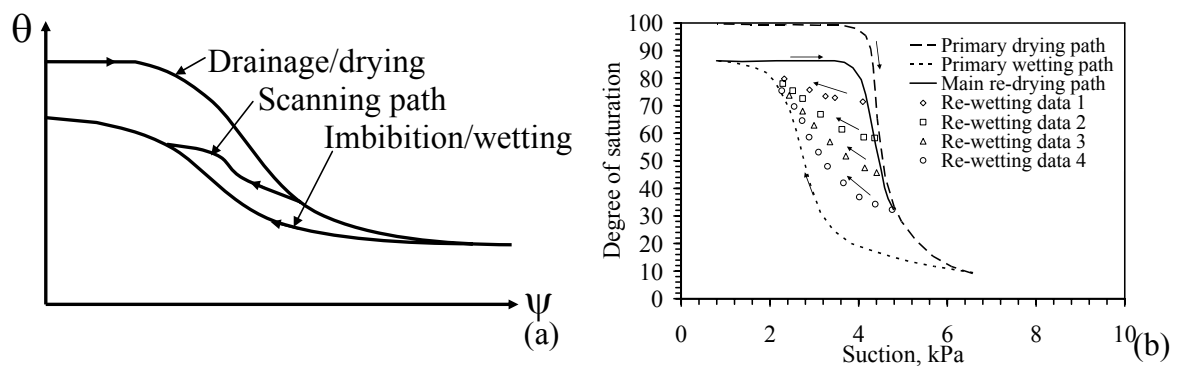


Figure 2.4: (a) Schematic of a hysteretic WRC (after Lenhard *et al.* 1991); (b) Hysteretic WRC data for glass bead media (Topp and Miller 1966)

The moisture storage of a soil depends on its WRC. As mentioned, the storage capacity per unit area can be estimated by multiplying the volumetric moisture content for a given suction by the thickness of a soil layer. The upper limit is the porosity, while the lower limit is the residual moisture content. Another useful moisture storage value is the field capacity, which is the moisture content value above which the soil cannot retain water by capillarity under the effects of gravity (Hillel 1980). When water is added to a soil that is at field capacity, drainage occurs. The field capacity may be obtained from infiltration tests, although a generally accepted value for low plasticity soils is the moisture content corresponding to a suction of 33 kPa (Nachabe 1998).

The capillary rise of water in a pipette is a useful tool to assess the influence of pore size on the WRC. The suction in a pipette is given by the Young-Laplace equation:

$$\psi = h_c \rho_w g = \frac{2\sigma_{aw} \cos \gamma}{R} \quad (2.5)$$

where  $h_c$  is the height of capillary rise in a pipette of radius  $R$ ,  $\rho_w$  is the density of water,  $g$  is the acceleration of gravity,  $\sigma_{aw}$  is the surface tension of water in air (at constant temperature), and  $\gamma$  is the wetting contact angle ( $10^\circ$  for quartz minerals, but typically assumed to be zero). Equation (2.5) indicates that the suction is inversely proportional to the pore radius. Accordingly, for the same volumetric moisture content, it will require a higher suction to remove water from a fine-grained soil (with comparatively small pore radii) than a coarse-grained soil. Further, as the radius of a pore is associated to the volume of water in the pore, increasing the suction applied to a soil specimen will cause a drop in moisture content. The height of capillary rise and the volume of water storage for a series of pipettes, shown in Figure 2.5 for  $\sigma_{aw} = 0.0727$  N/m, highlights the relationship between the WRC and a soil's pore size distribution.

A particular case that highlights the relevance of the relationship between the WRC and the pore size distribution of a soil is the case of dual-porosity soils (Burger and

Shackelford 2001). Clay-sand mixtures or organic soils like diatomaceous earth that consist of particles with internal porosity have two widely different representative pore sizes. In this case, a WRC with a bimodal shape may be obtained.

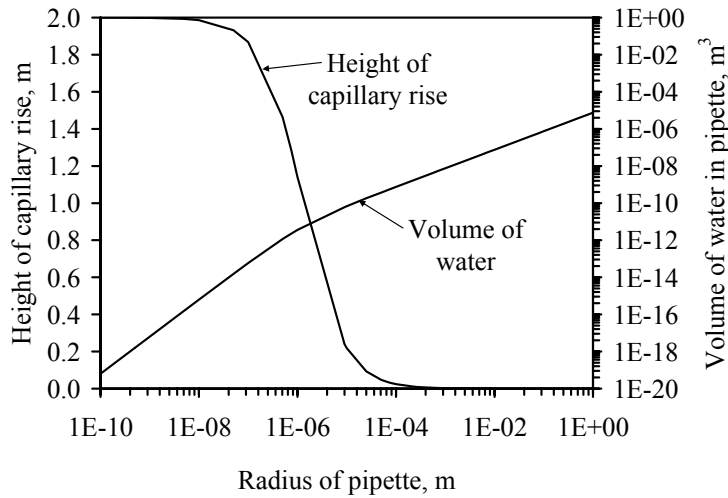


Figure 2.5: Relationship between capillary rise, pipette size, and moisture storage

Some studies have focused on the prediction of the WRC from the grain size distribution of a soil measured by sieve analysis (Fredlund *et al.* 1997; Hwang and Powers 2003) or the pore size distribution measured by mercury porosimetry (Kong and Tan 2000). However, this type of approach is inadequate for clay soils that have very fine pore sizes or when significant physico-chemical effects occur. In this case, the shape of the WRC can be affected by different geotechnical parameters, such as the compaction water content, (Tinjum *et al.* 1997; Miller *et al.* 2002). For such empirical approaches, it is necessary to quantify the shape of the WRC with a continuous function. Researchers have obtained WRCs by fitting experimental data to power law, hyperbolic, or polynomial functions (Brooks and Corey 1964; van Genuchten 1980; Fredlund and Xing 1994). In addition, continuous WRC functions are useful for numerical analyses of water

flow. The Brooks and Corey (1964) model is able to represent a sharp air entry suction, which is realistic for some coarser-grained soils. It is given by:

$$\theta = \theta_r + (\theta_s - \theta_r) \left( \frac{\psi}{\psi_{aep}} \right)^{-\lambda_{BC}} \quad (2.6)$$

where  $\theta_r$  is the residual moisture content,  $\theta_s$  is the saturated moisture content (porosity),  $\psi_{aep}$  is the air entry suction, and  $\lambda_{BC}$  is a fitting parameter. The van Genuchten (1980) model is commonly used in numerical simulations as it is differentiable (without sharp curves) even in the vicinity of the air entry suction. It is given by:

$$\theta = \theta_r + (\theta_s - \theta_r) \left[ 1 + (\alpha_{vG} \psi)^{N_{vG}} \right]^{-\left(1 - \frac{1}{N_{vG}}\right)} \quad (2.7)$$

where  $\alpha_{vG}$  and  $N_{vG}$  are fitting parameters. The Fredlund and Xing (1994) model is similar to the van Genuchten model. It is given by:

$$\theta = \theta_r + (\theta_s - \theta_r) \left\{ \ln \left[ e + \left( \frac{\psi}{a} \right)^n \right] \right\}^m \quad (2.8)$$

where  $e$  is base of the natural logarithm,  $a_{FX}$  represents the air entry suction,  $n_{FX}$  represents the pore size distribution, and  $m_{FX}$  represents the model skew.

The WRC for a given material is not only sensitive to the pore size distribution, but also to soil mineralogy, density, and structure (*e.g.*, flocculated or dispersed) (Olson and Langfelder 1965, Tinjum *et al.* 1997; Miller *et al.* 2002), presence of macro-features such as cracks or fissures (Kleppe and Olson 1985), chemical composition and pH of the pore fluid (Henry and Smith 2003), temperature (Hopmans and Dane 1986b), freezing and thawing (Shoop and Bigl 1997) and sampling effects (Olson and Daniel 1981). Changes in soil volume during water flow may have significant impacts on the WRC, making definition of the WRC difficult. In this case the WRC has been quantified in terms of the gravimetric moisture content (Parent and Cabral 2004; Lu and Likos 2005).

### 2.3.2 K-function

Unlike water-saturated soils, the available pathways for water flow in unsaturated soil decrease as the moisture content decreases. This is quantified by the hydraulic conductivity function  $K(\theta)$ , which accounts for the change in the ratio between flow rate and total hydraulic gradient with decreasing moisture content (or increasing suction). Schematic K-functions for geotechnical materials are shown in Figure 2.6(a) and Figure 2.6(b), with suction plotted on a logarithmic and natural scale, respectively. These K-functions are based on a theoretical model discussed later in this section, and are purposely plotted over a wide range of hydraulic conductivity values to emphasize the differences between the materials. Near saturation, the coarser-grained materials (sand and geotextiles) have high hydraulic conductivity, while the finer-grained materials (silt and clay) have lower hydraulic conductivity. However, the coarse-grained materials are less conductive than the fine-grained materials at suctions greater than 10 kPa. This can be explained using the shapes of the WRCs for these materials. Fine-grained materials can retain more water under higher suctions, so there are more pathways available for water flow. The coarse sand and nonwoven geotextile approach residual saturation for suctions above 10 kPa, so there few (if any) pathways available for water flow.

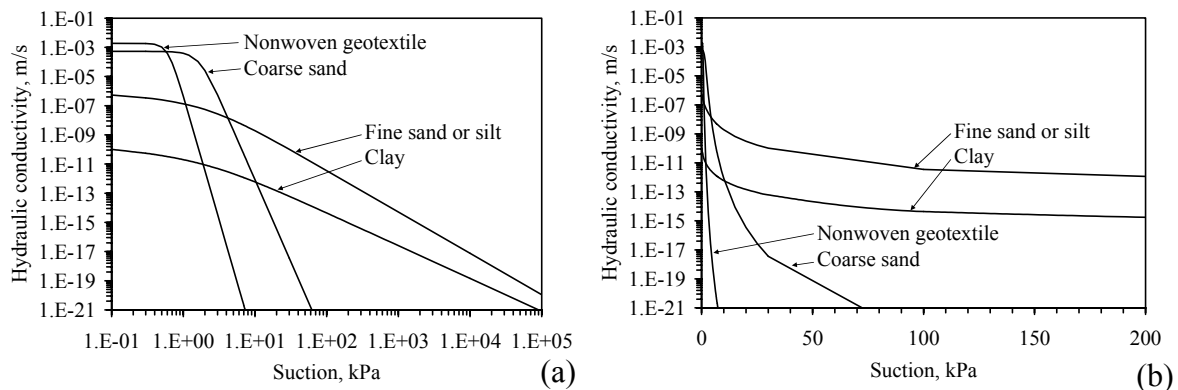


Figure 2.6: Typical K-functions for different materials: (a) Logarithmic; (b) Natural

K-functions of different geotechnical materials reported in the literature are shown in Figure 2.7(a) and Figure 2.7(b) as functions of suction and moisture content, respectively. In general, the K-functions follow similar trends to those shown schematically in Figure 2.6. Most coarse-grained soils have a hydraulic conductivity within an order of magnitude of their saturated value until reaching a volumetric moisture content of about 20%, after which a steep decrease in  $K$  is observed. Clays on the other hand, show a more steady decrease in  $K$  over the full range of moisture contents.

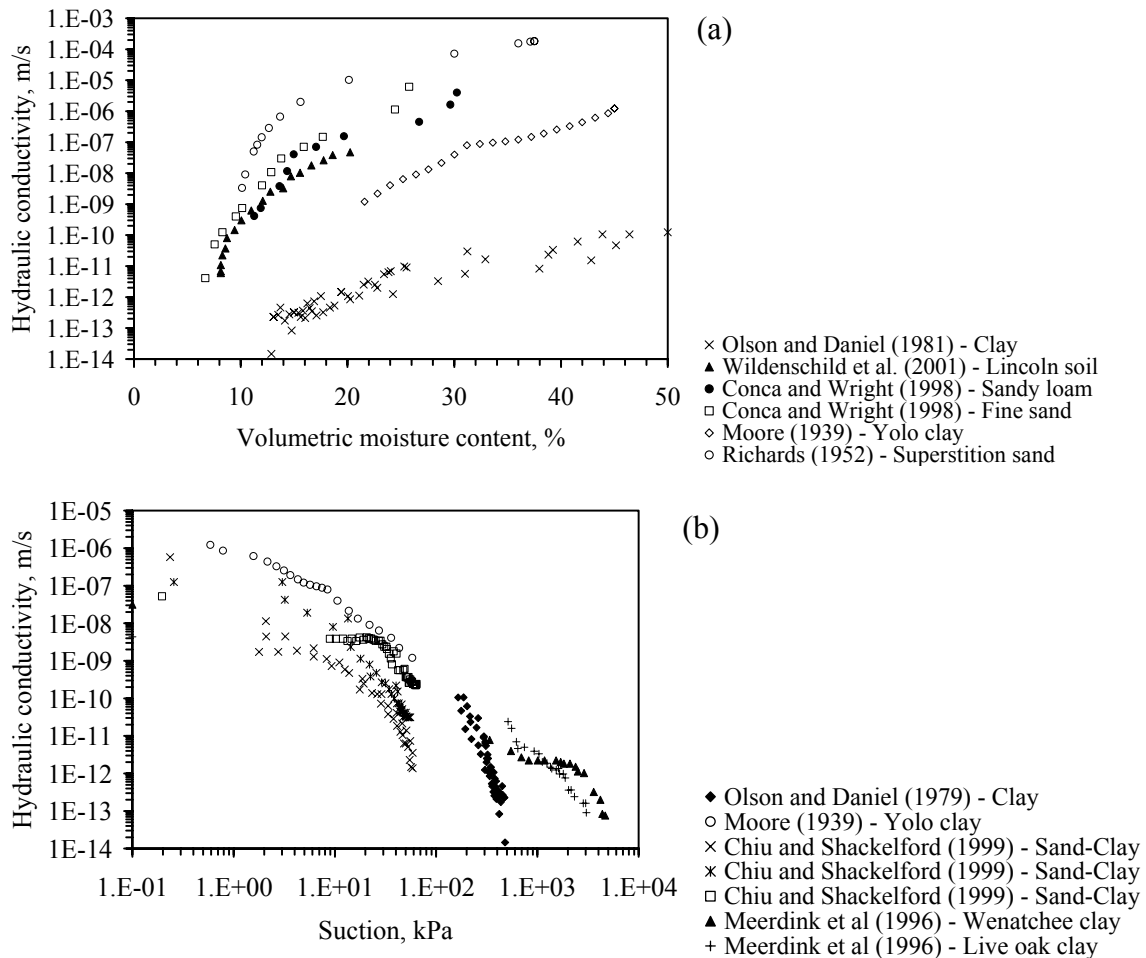


Figure 2.7: K-functions for different geotechnical materials: (a)  $K-\theta$ , (b)  $K-\psi$

The hydraulic conductivity of a soil at low water contents is very difficult to measure, and may be equal to zero for suctions below residual saturation. Hydraulic conductivity values as low as  $10^{-12}$  m/s have been measured using steady-state flow techniques (Conca and Wright 1998) and as low as  $10^{-14}$  m/s using transient flow techniques (Hamilton *et al.* 1981). In addition, at very high suctions clays may desiccate and crack. In this case, flow of water through the intact soil matrix is unimportant compared to flow through the cracks.

The K-function can be represented as a function of  $\theta$  or  $\psi$ , depending on its application. Experimental techniques based on water flow typically yield a K-function that is a function of  $\theta$ , while techniques based on application of suction gradients yield a K-function that is a function of  $\psi$ . Most numerical models solve the governing equation for water flow in terms of suction, making a K-function that is a function of  $\psi$  particularly useful. The K-function has also been shown to have significant hysteresis when plotted as a function of suction (Topp and Miller 1966). This study used steady-state horizontal infiltration of water through a mono-dispersed glass bead media to investigate hysteresis in the K-function, shown in Figure 2.8(a). However, when the K-function was plotted as a function of degree of saturation, shown in Figure 2.8(b), hysteresis is negligible. It is possible that the air-water menisci in the soil will be arranged differently during wetting and drying, resulting in a different suction for the same moisture content upon wetting and drying.



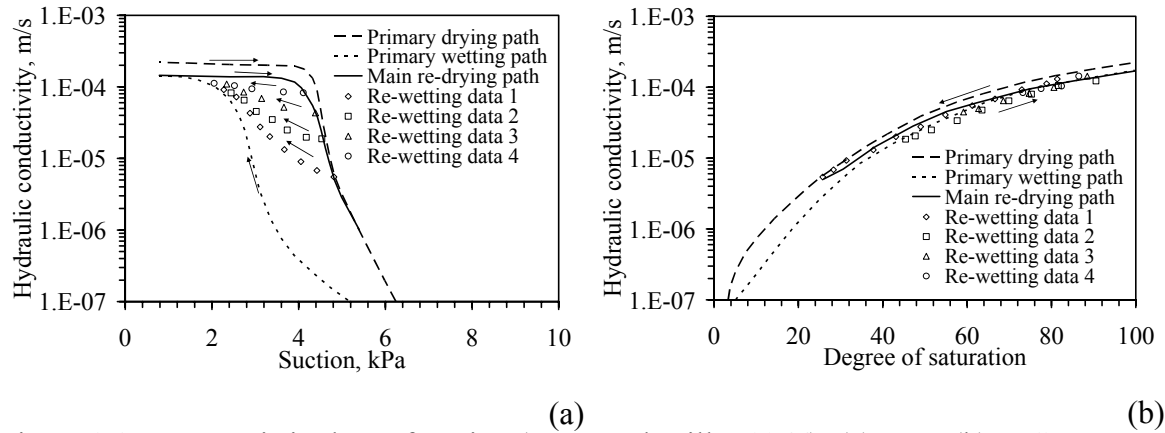


Figure 2.8: Hysteresis in the K-function (Topp and Miller 1966): (a)  $K-\psi$ ; (b)  $K-S$

The hydraulic conductivity of a saturated soil ( $\psi = 0$ ,  $\theta = n$ ) is an important point on the K-function (Mitchell *et al.* 1965; Olson and Daniel 1981). In practice, this is usually the only value that is obtained experimentally on the K-function, and semi-empirical relationships are used to predict the rest of the K-function. Early approaches to predict the K-function were empirical, and were based on a generalization of Kozeny's approach (Mualem 1976). This approach associates the K-function with the hydraulic conductivity of a saturated specimen multiplied by a power function of the normalized volumetric moisture content (*i.e.*, the effective saturation):

$$K(\theta) = K_s \left( \frac{\theta - \theta_r}{n - \theta_r} \right)^\beta \quad (2.9)$$

where  $\beta$  is a fitting parameter that is correlated with experimental K-functions. Irmay (1954) proposed  $\beta = 3.0$  as a general value to use for soils, while Brooks and Corey (1964) indicate that  $\beta = 3.5$  provides a better fit to experimental data.

Gardner (1958) proposed an exponential model for the K-function:

$$K(\psi) = K_s e^{-\alpha\psi} \quad (2.10)$$

where  $\alpha$  is a fitting parameter that was typically correlated with a characteristic pore size of the soil. This model is particularly useful in analysis as it is easily differentiable.

Statistical models based on pore size distributions were used later, with the goal of predicting the K-function from the WRC (Childs and Collis-George 1950; Burdine 1953; Millington and Quirk 1961; Mualem 1976). These approaches assume that the soil is an interconnected series of pores having a size distribution characterized by the shape of the WRC (Mualem 1986). Most models have the form (Leong and Rahardjo 1999):

$$\frac{K(\theta)}{K_s} = \left( \frac{\theta - \theta_r}{\theta_s - \theta_r} \right)^b \left( \frac{\int_0^\theta \frac{dx}{\psi^{2-r}(x)}}{\int_0^1 \frac{dx}{\psi^{2-r}(x)}} \right)^m \quad (2.11)$$

where  $b$ ,  $r$ , and  $m$  are constants related to the pore size distribution, and  $x$  is an integration variable. The first term in Equation (2.11) is a correction factor used to account for tortuosity, while the second term is a ratio between the available, water filled fluid pathways and the total possible number of fluid pathways. Based on statistical considerations, Burdine (1953) suggested that  $b = 2$ ,  $r = 0$ , and  $m = 1$ , while Mualem (1976) suggested that  $b = 0.5$ ,  $r = 1$ , and  $m = 2$ . Mualem's assumption is considered to be more suitable for fine-grained soils (Leong and Rahardjo 1999). Statistical models neglect physicochemical effects on moisture flow (attraction of water to particles) and neglect flow of water in films on particle surfaces. Film transport may be particularly important for low moisture contents (Conca and Wright 1990; Tuller and Or 2001).

The K-function can be predicted from the macroscopic approach by inserting one of Equations (2.6) through (2.8) into Equation (2.11). The K-function can be represented as a function of  $\theta$  or  $\psi$ , depending on the application. Experimental techniques based on outflow typically yield a K-function that is a function of  $\theta$ , while experimental techniques based on suction gradients yield a K-function that is a function of  $\psi$ . The most commonly used predictive K-function is obtained by substituting the Mualem (1976) model into the van Genuchten model (1980), as follows:

$$K(\theta) = K_s \sqrt{\frac{\theta - \theta_r}{\theta_s - \theta_r}} \left[ 1 - \left( 1 - \left( \frac{\theta - \theta_r}{\theta_s - \theta_r} \right)^{1-N_{VG}} \right)^{\frac{1}{1-N_{VG}}} \right]^2 \quad (2.12)$$

where  $N_{VG}$  is the same parameter used for the WRC in Equation (2.7).  $K(\psi)$  can be defined by substituting Equation (2.7) for  $\theta$  into Equation (2.12). Another common relationship incorporates the Burdine (1953) model into the Brooks-Corey (1964) model:

$$K(\theta) = K_s \left( \frac{\theta - \theta_r}{\theta_s - \theta_r} \right)^{3 + \frac{2}{\lambda_{BC}}} \quad (2.13)$$

where  $\lambda_{BC}$  is the same parameter as that used to define the shape of the WRC.

Poulsen *et al.* (1999) presents a comparison of K-function predictions with experimental K-function data collected into the UNSODA database (Leji *et al.* 1996). The authors found statistical correlations between the measured and predicted values of hydraulic conductivity for 191 soils. However, significant scatter was observed, making a statistical approach suitable for preliminary estimation of the K-function. Nimmo and Akstin (1988) and Khaleel *et al.* (1995) compared K-functions obtained from experiments with those from theoretical predictions. Nimmo and Akstin (1988) found that most of the models show a good fit to the data, as shown in Figure 2.9(b). Khaleel *et al.* (1995) found that the K-function predicted by the van Genuchten-Mualem model tends to under-predict the actual data, as shown in Figure 2.9(b). However, the authors found that this model tends to provide a better fit to experimental data when it is scaled linearly by at least one measurement of the hydraulic conductivity of an unsaturated specimen. The K-function in Figure 2.9(b) is scaled to  $K$  at the lowest volumetric moisture content of 5.5%. The K-functions of Nimmo and Akstin (1988) and Khaleel *et al.* (1995) show drops in  $K$  with decreasing moisture content, reflecting that soils are not ideal assemblies of capillary tubes, as assumed by the models.

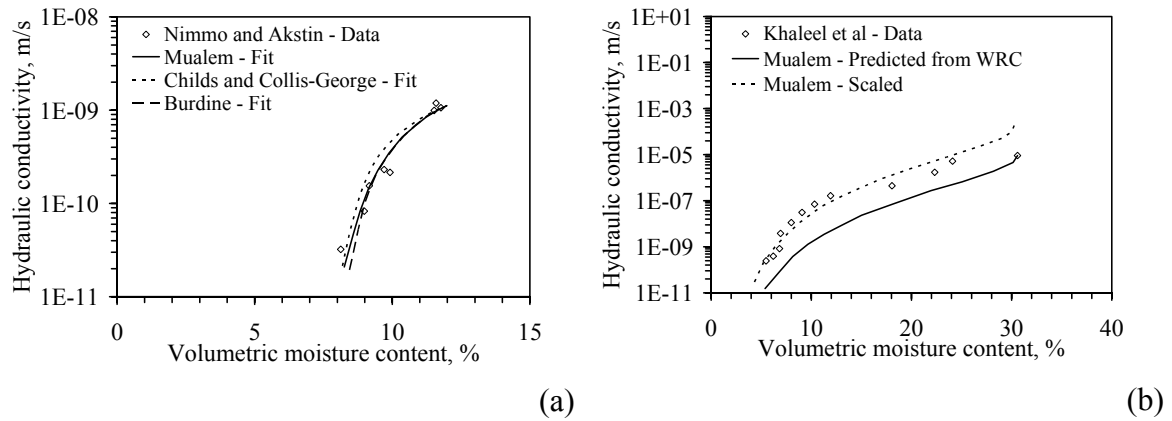


Figure 2.9: Predictive and experimental K-functions: (a) Nimmo and Akstin (1988); (b) Khaleel *et al.* (1995)

There has been a significant amount of research on the K-function from the perspective of soil physics since the early 1900's (Buckingham 1901). Most research has been conducted on predictive and experimental approaches to define the K-function. There have been some experimental studies on the influence of soil variables such as porosity (Nimmo and Akstin 1988), compaction conditions (Meerdink *et al.* 1996), and fines content (Chiu and Shackelford 2001). There have also been some studies on environmental variables such as pore water chemistry (Arulandaran *et al.* 1988) and temperature (Hopmans and Dane 1988). In addition, the lessons learned from studies on the hydraulic conductivity of saturated soils may be used to predict the effects of different variables on the K-function (Olson and Daniel 1981). Due to the difficulty and duration of testing, uncertainty in experimental K-functions has not been assessed in the literature.

## Chapter 3: Water Flow in Unsaturated Soils

### 3.1 OVERVIEW

Centrifugation is used in this study to increase the gradient in hydraulic energy causing water to flow through soils. This chapter describes the theoretical background of water flow through unsaturated soils, under both normal gravity and under a centrifuge acceleration field. Specifically, the components of hydraulic energy in the flowing water and the governing equation for water flow through unsaturated soils, Richards' equation, are described for normal gravity and a centrifuge acceleration field. Analytical solutions to the governing equation assuming steady-state conditions are presented in terms of the distribution in suction along the longitudinal axis of the permeameter. At steady-state, the flow rate and distribution in suction are constant with time. The suction distribution from these solutions can be used to guide the determination of the hydraulic characteristics during infiltration in a permeameter test under normal gravity or in the centrifuge. In addition, the outflow boundary conditions expected during water flow across layered soils (*e.g.*, the interface between a soil and a porous support) is discussed.

### 3.2 FLOW OF WATER THROUGH UNSATURATED SOILS

A schematic a soil layer with thickness  $L_p$  undergoing one-dimensional (1-D), vertically downward, water flow is shown in Figure 3.1. The datum is selected as the base of the soil layer, with  $z_p$  being the height from the base of the profile. The subscript “ $p$ ” indicates that the soil profile is a 1-gravity “prototype”, differentiating it from a centrifuge model, having subscript “ $m$ ”. As  $z_p$  is oriented upward, a positive discharge velocity  $v_p$  is also designated as upward. The boundary conditions and control volume shown in this figure are discussed later.

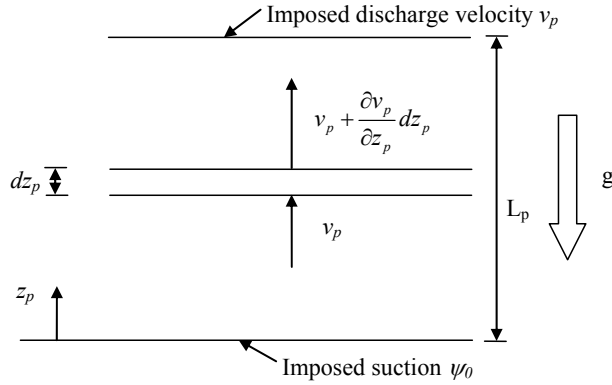


Figure 3.1: Schematic of infiltration through an unsaturated soil layer

To be consistent with the terminology in geotechnical engineering, the energy in the pore water is quantified in this study using the hydraulic head, having units of length. The gradient term “ $i$ ” in Darcy’s law [Equation (2.2)] reflects the change in hydraulic head over a differential length  $\partial z_p$ . In this case, Darcy’s law can be expressed as:

$$Q = -K \left( \frac{\partial h}{\partial z_p} \right) A \quad (3.1)$$

where  $K$  is the hydraulic conductivity,  $g$  is the gravitational constant,  $A$  is the cross-sectional area perpendicular to the flow direction,  $z_p$  is the vertical distance from a selected datum, and  $h$  is the total hydraulic head. A modified form of Bernoulli’s equation can be used to define the different components of  $h$ , as follows:

$$h = z_p + \frac{1}{2g} \left( \frac{v_p}{n} \right)^2 + \frac{P_o}{\rho_w g} + \frac{P_w}{\rho_w g} \quad (3.2)$$

where  $v_p$  is referred to as the discharge velocity equal to  $Q/A$ ,  $n$  is the porosity,  $P_o$  is the pressure in the water due to an osmotic gradient, and  $P_w$  is the pressure in the water due to its self-weight. The term  $v_p/n$  is referred to as the seepage velocity, and reflects the local increase in discharge velocity as water flows around the soil particles. In Equation (3.2), the four terms on the right hand side correspond to the potential energy head (or elevation head), the kinetic energy head, the osmotic pressure head, and the water pressure head.

The seepage velocity is small for soils (typically less than  $10^{-7}$  m/s for fine-grained soils), leading to a negligible contribution of the kinetic energy head to the total hydraulic head. The osmotic pressure arises from the tendency for the electrolyte concentration in the pore water in a soil to reach thermodynamic equilibrium. The concentration of electrolytes is assumed not to change significantly with changes in water content, so the osmotic pressure does not contribute to the hydraulic gradient. The osmotic pressure is thus neglected in the analyses in this study.

Assuming that the air pressure is equal to zero and neglecting the contributions of the osmotic pressure and seepage velocity, the hydraulic head can be simplified:

$$h = z_p - \frac{\psi}{\rho_w g} = h_e + h_p \quad (3.3)$$

where  $h$  is the total hydraulic head having units of length,  $h_e = z_p$  is the elevation head, and  $h_p = -\psi/\rho_w g$  is the suction head. The gradient of hydraulic head with respect to  $z_p$  is:

$$\frac{\partial h}{\partial z_p} = 1 - \frac{1}{\rho_w} \frac{\partial \psi}{\partial z_p} \quad (3.4)$$

Accordingly, the discharge velocity can be calculated using Equation (3.4) and Darcy's law [Equation (3.1)], as follows:

$$v_p = -K(\psi) \left( 1 - \frac{1}{\rho_w g} \frac{\partial \psi}{\partial z_p} \right) \quad (3.5)$$

The dominant components of hydraulic head, the elevation head and the matric suction head, are independent as the elevation head depends on location in an acceleration field (*i.e.*, gravity field) while suction depends on the shape of the air-water meniscus. Unlike the suction head gradient, which can vary over orders of magnitude, the gradient of the elevation head is constant. Centrifugation can be used to increase the relevance of the elevation head component of the hydraulic head compared to the suction head by imposing a centripetal acceleration  $a$  on a spinning specimen:

$$a = \omega^2 r = N_r g \quad (3.6)$$

where  $\omega$  is the angular velocity of the centrifuge,  $r$  is the radius from the axis of rotation to a point in a centrifuge field,  $g$  is the acceleration due to gravity, and  $N_r$  is the ratio between the centripetal acceleration and  $g$ . The  $r$  subscript in  $N_r$  signifies that  $N$  varies (linearly) with radius. The value of  $N_r$  at mid-height in a specimen,  $N_{r,mid}$ , is used in this study to provide a single value of  $N_r$  for a test.  $N_{r,mid}$  referred to as the “g-level”.

A cylindrical soil specimen spinning about a central axis at a rate of  $\omega$  in the centrifuge is shown in Figure 3.2(a). The cylindrical specimen with length  $L_m$  has an inlet face at a radius of  $r_T$ , and an outlet face at a radius of  $r_0$ . To be consistent with the 1-gravity soil profile, it is useful to choose a coordinate  $z_m$  in the centrifuge permeameter having a datum at the base of a specimen, defined as:

$$z_m = r_0 - r \quad (3.7)$$

where  $z_m$  is the distance from the datum at the base of the specimen,  $r$  is the radius from the center of rotation, and  $r_0$  is the radius of the base of the specimen. The variation in  $N_r$  with  $z_m/L_m$  for the geometry of the centrifuge permeameter used in this study is shown in Figure 3.2(b). For this geometry,  $N_{r,mid}$  is 12% of the value of  $N_r$  at the ends of the specimen. As  $z_m$  is defined as positive toward the axis of rotation, the water discharge velocity  $v_m$  is positive in the direction of positive  $z_m$  (toward the axis of rotation).

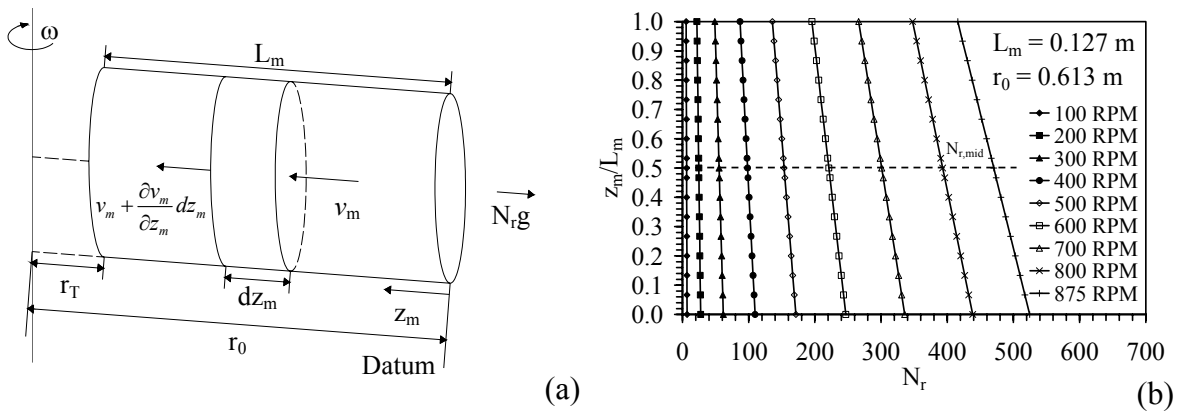


Figure 3.2: (a) Centrifuge control volume (Dell'Avanzi *et al.* 2004); (b)  $N_r$  vs.  $z_m/L_m$



The self-weight of water in the centrifuge acceleration field increases the driving force for water flow. The hydraulic head in the centrifuge model  $h_m$  is quantified as:

$$h_m = -\frac{1}{2} \left( \frac{I\omega^2}{mg} \right) + \frac{1}{2g} \left( \frac{v_m}{n} \right)^2 + \frac{P_w}{\rho_w g} + \frac{P_o}{\rho_w g} \quad (3.8)$$

where  $I$  is the rotational inertia of a point mass  $m$  in a centrifuge field. The components on the right hand side correspond to the rotational potential energy head induced by centrifugation, the kinetic energy head due to the relative linear velocity of the fluid with respect to the solids, the water pressure head, and osmotic pressure head. The sign of the first term is negative as the rotational kinetic energy increases in the opposite direction of the coordinate  $z_m$ . For a point mass  $m$  in a centrifuge field, the moment of inertia is:

$$I = m(r_0 - z_m)^2 \quad (3.9)$$

If centrifugation does not cause turbulent water flow through the soil, the kinetic energy term may be neglected. The air pressure is assumed to be negligible, the suction can be substituted for the water pressure as  $-\psi = P_w$ . The osmotic pressure is assumed not to vary with moisture content for unsaturated soils, so the last term is not considered. Considering these assumptions, the hydraulic head in the centrifuge is:

$$h_m = -\frac{\omega^2}{2g} (r_0 - z_m)^2 - \frac{\psi}{\rho_w g} = h_{em} + h_p \quad (3.10)$$

where  $h_m$  is the total hydraulic head having units of length, the suction head is the same as that in 1-gravity ( $-\psi/\rho_w g$ ), and the centrifuge elevation head is equal to:

$$h_{em} = -\frac{\omega^2}{2g} (r_0 - z_m)^2 \quad (3.11)$$

The gradient of the hydraulic head in the centrifuge with respect to  $z_m$  is:

$$\frac{\partial h_m}{\partial z_m} = \frac{\omega^2}{g} (r_0 - z_m) - \frac{1}{\rho_w g} \frac{\partial \psi}{\partial z_m} \quad (3.12)$$

This equation can be incorporated into Darcy's law to determine the discharge velocity:

$$v_m = -K(\psi) \left[ \frac{\omega^2}{g} (r_0 - z_m) - \frac{1}{\rho_w g} \frac{\partial \psi}{\partial z_m} \right] \quad (3.13)$$

During steady-state water flow, the discharge velocity  $v_m$  is constant with both time and  $z_m$ , so in this case hydraulic conductivity must vary with radius in the centrifuge as  $z_m$  is present in Equation (3.13). This will be discussed later in this chapter. This equation should be valid in the centrifuge as long as Darcy's law is valid in the centrifuge and water flow is laminar. This can be assessed by evaluating Reynolds number:

$$R_e = \left( \frac{v_m}{n} \right) \frac{\rho_w d_{10}}{\mu} \quad (3.14)$$

where  $d_{10}$  is the characteristic particle size and  $\mu$  is the viscosity of water. Laminar flow is typically ensured in soil for Reynolds numbers less than 10. The steady-state inflow rates used in experiments in this study (*i.e.*,  $10^{-7}$  m/s or less) result in Reynolds numbers less than 10. Darcy's law in the centrifuge is further evaluated in Section 5.5.3.

### 3.3 SUCTION PROFILES IN SOIL DURING WATER FLOW UNDER NORMAL GRAVITY

Water flow through the control volume in Figure 3.1 is governed by the continuity principle, as follows:

$$\frac{\partial \theta}{\partial t} = - \frac{\partial v_p}{\partial z_p} \quad (3.15)$$

where the left-hand side represents the change in moisture storage in the control volume having length  $dz_p$ , and the right hand side represents the change in flow rate across the control volume. Substitution of Equation (3.5) into Equation (3.15) and using the chain rule to make  $\psi$  the primary variable permits derivation of the governing equation for water flow in unsaturated soils. This is referred to as Richards' equation, and is given by:

$$\frac{d\theta}{d\psi} \frac{\partial \psi}{\partial t} = \frac{\partial}{\partial z_p} \left[ K(\psi) \left( 1 - \frac{1}{\rho_w g} \frac{\partial \psi}{\partial z_p} \right) \right] \quad (3.16)$$

Richards' equation is a coupled, nonlinear, parabolic equation. For real flow situations, it is often solved numerically using finite differences or finite elements. Solutions can be challenging, as the constitutive functions  $[K(\psi)$  and  $\theta(\psi)]$  are nonlinear and may have undefined or zero derivatives. In addition, boundary conditions are rarely straightforward as there are few instances in nature where there is a constant flow rate or constant head.

Richards' equation can be solved analytically if the K-function is assumed to follow an exponential model, such as Gardner's model [Equation (2.10)]. Srivastava and Yeh (1991) presented a relatively simple approach to solve for suction profiles during transient water flow toward a water table. However, the solution only provides the transient transition in the suction profiles from one steady-state flow rate to another. In this case, their solution is not entirely correct for use in modeling transient infiltration through a compacted soil layer with initially constant suction. Alternatively, Dell'Avanzi *et al.* (2004) presented a simple analytical expression that can be used to predict the suction profile for steady-state water flow. The solution is given by:

$$\begin{aligned} \psi(z_p) &= -\frac{1}{\alpha} \ln \left[ e^{\left( \ln \left( \frac{v_p}{K_s} \right) + e^{-\alpha \psi_0} \right) - \alpha \rho_w g z_p} - \frac{v_p}{K_s} \right] \quad \text{if } \left( \frac{v_p}{K_s} \right) + e^{-\alpha \psi_0} > 0 \\ \psi(z_p) &= -\frac{1}{\alpha} \ln \left[ -e^{\left( \ln \left( \frac{v_p}{K_s} \right) + e^{-\alpha \psi_0} \right) - \alpha \rho_w g z_p} - \frac{v_p}{K_s} \right] \quad \text{if } \left( \frac{v_p}{K_s} \right) + e^{-\alpha \psi_0} < 0 \end{aligned} \quad (3.17)$$

where  $v_p$  is the discharge velocity in a prototype,  $z_p$  is the height of a prototype,  $\alpha$  is a soil-specific fitting parameter for Gardner's model, and  $\psi_0$  is the suction value imposed at the base of the specimen. The two forms of the equation are necessary when different values of  $\psi_0$  are used. The suction profiles for different imposed discharge velocities on a soil layer with a saturated bottom boundary are shown in Figure 3.3.

Given the  $\alpha$  parameter for Gardner's model, the limiting suction in the upper zone of the soil layer,  $\psi_\infty$ , may also be predicted (Dell'Avanzi *et al.* 2004):

$$\psi_{\infty} = -\frac{1}{\alpha} \ln \left( -\frac{v_p}{K_s} \right) \quad (3.18)$$

The limiting suction values for the different profiles are shown in Figure 3.3. Inversely, this model allows the value of  $\alpha$  to be estimated using the imposed flow rate  $v_p$  and a measurement of the suction in the upper portion of the soil profile.

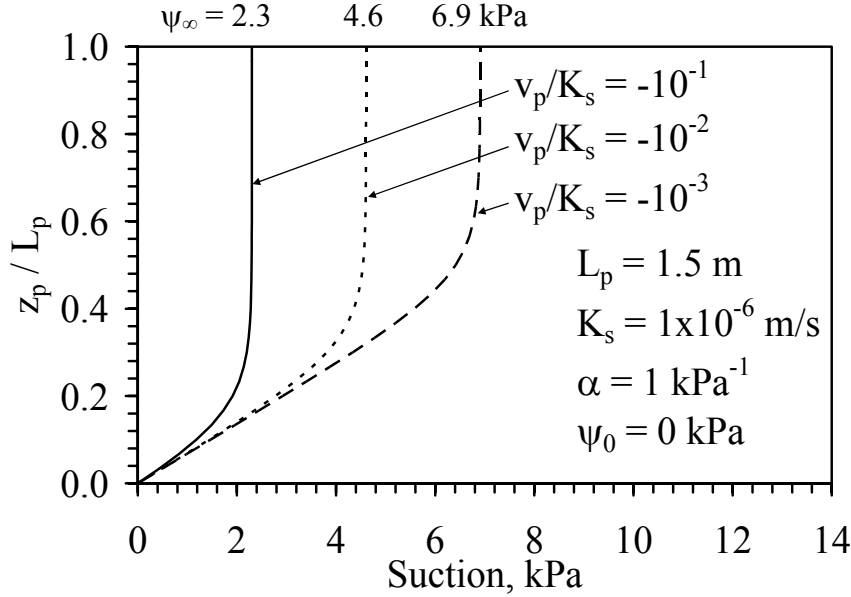


Figure 3.3: Suction profiles at steady-state flow for different inflow rates

Del'Avanzi *et al.* (2004) also found that the limiting suction in the upper zone of the soil layer is independent of the outflow boundary condition for steady-state infiltration, as long as the soil profile has a length greater than the height above which the suction does not vary. Suction profiles for different boundary conditions are shown in Figure 3.4. The height above which the suction does not vary tends to decrease with increasing suction values imposed at the base. The saturated bottom boundary condition has the greatest effect on the suction distribution with specimen height, and provides the “worst” case scenario for hydraulic characterization, which is discussed later.

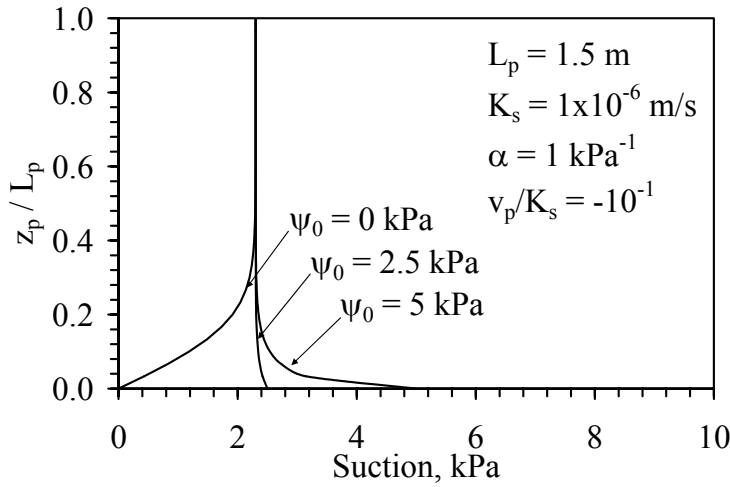


Figure 3.4: Suction profiles at steady-state flow for different boundary suctions

The distribution in total hydraulic head with height in a 1-g prototype during steady-state flow can be determined using the solution for the suction profile (in terms of head) and the elevation head. The total head and pressure head for a 1.5 m long prototype soil profile is shown in Figure 3.5(a). A profile of this length is typical of a column infiltration test or a surficial layer of soil in the field. The analytical solution for the suction indicates that there will be a significant portion of the profile in which the suction is constant with height. In this zone, the magnitude of the total head profile is dominated by the elevation head profile, reflected in the fact that the two profiles are parallel with height. This is better illustrated using the distribution in gradient with height, shown in Figure 3.5(b). It is clear that a “unit gradient” zone exists in the upper portion of the profile, where the suction gradient is negligible and the total head gradient is equal to 1.0. In this case, water flow is almost solely driven by the gradient in elevation except near the base.

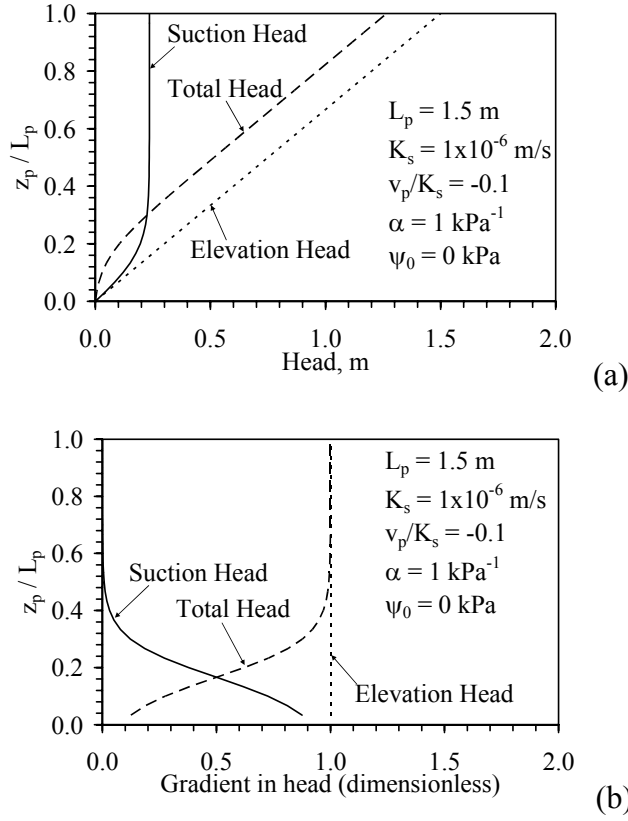


Figure 3.5: Total head, suction head, and elevation head profiles for a full-scale (1.5 m) prototype during steady-state flow: (a) Head values; (b) Head gradients

Using the gradient in total head, the hydraulic conductivity can be defined:

$$K = \frac{-v_p}{1 - \frac{1}{\rho_w g} \frac{d\psi}{dz_p}} \quad (3.19)$$

The distribution in hydraulic conductivity with height for different infiltration rates is shown in Figure 3.6. Measurements of hydraulic conductivity in a column infiltration test can be made near the top of the soil layer, where a zone develops with a unit hydraulic gradient (*i.e.*, constant suction). In this zone, the hydraulic conductivity of the unsaturated soil defined from Equation (3.19) is equal to the imposed infiltration rate. Accordingly, for steady-state flow, measurements of the moisture content and suction in the upper portion of the profile will yield a single point on the K-function.

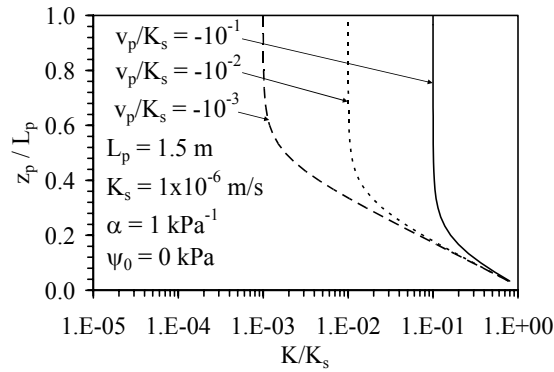


Figure 3.6: Hydraulic conductivity profiles for steady-state water flow

The suction profiles in Figure 3.3 apply to soil layers with thickness  $L_p$  large enough that the boundary does not affect the suction distribution. It is also useful to investigate the distribution in total head for a specimen with the size of a permeameter during steady-state flow under 1-g, as shown in Figure 3.7(a). In this case, the length of the soil profile is significantly smaller (0.127 m) than that shown in Figure 3.3. The suction profile does not approach a limiting suction value in this case, and the total head profile is dominated by the suction head. The gradient distributions in Figure 3.7(b) indicate that a unit hydraulic gradient does not develop in the permeameter.

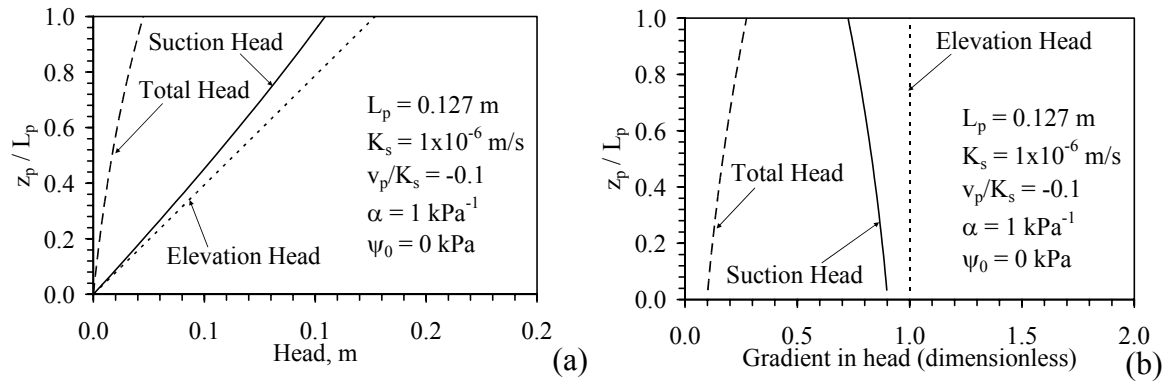


Figure 3.7: Total head, suction head, and elevation head profiles for a permeameter (0.127 m) during steady-state flow: (a) Head values; (b) Head gradients

### 3.4 SUCTION PROFILES IN SOIL DURING WATER FLOW IN THE CENTRIFUGE

Combining the continuity equation [Equation (3.15)] with the discharge velocity [Equation (3.13)], Richards' equation for one-dimensional flow of water through unsaturated soil in a centrifuge permeameter control volume [Figure 3.2(a)] is defined as:

$$\frac{d\theta}{d\psi} \frac{\partial \psi}{\partial t} = \frac{\partial}{\partial z_m} \left[ K(\psi) \left[ \frac{\omega^2}{g} (r_0 - z_m) - \frac{1}{\rho_w g} \frac{\partial \psi}{\partial z_m} \right] \right] \quad (3.20)$$

This equation has been solved numerically by Bear *et al.* (1984) and Simunek and Nimmo (2005). A finite-difference program called RichTexNg was developed as part of this study (Appendix B) to investigate the boundary conditions expected in a centrifuge permeameter. Numerical solution of Richards' equation in the centrifuge is particularly difficult as the slope of the WRC ( $d\theta/d\psi$ ) and the K-function  $K(\psi)$  are nonlinear. Further, the equation contains a quadratic term in the primary variable  $\psi$  (after expansion of the second term on the right hand side using the chain and product rules).

Alternatively, analytical solutions can be derived when using Gardner's (1958) model for the K-function. Due to the added complexity of Richards' equation in the centrifuge, an analytical solution for the suction profile during transient water flow solution is not possible. However, Dell'Avanzi *et al.* (2004) derived an analytical solution for suction profiles during steady state water flow in the centrifuge:

$$\begin{aligned} \psi(z_m) &= -\frac{1}{\alpha} \ln \left[ e^{\left( \ln \left( \frac{v_m}{N_r K_s} \right) + e^{-\alpha \psi_0} \right) - \alpha \omega^2 \rho_w z_m \left( r_0 - \frac{z_m}{2} \right)} - \frac{v_m}{N_r K_s} \right] \quad \text{if } \left( \frac{v_m}{N_r K_s} \right) + e^{-\alpha \psi_0} > 0 \\ \psi(z_m) &= -\frac{1}{\alpha} \ln \left[ -e^{\left( \ln \left( \frac{v_m}{N_r K_s} \right) + e^{-\alpha \psi_0} \right) - \alpha \omega^2 \rho_w z_m \left( r_0 - \frac{z_m}{2} \right)} - \frac{v_m}{N_r K_s} \right] \quad \text{if } \left( \frac{v_m}{N_r K_s} \right) + e^{-\alpha \psi_0} < 0 \end{aligned} \quad (3.21)$$

where  $\psi_0$  is the suction at the outflow face of the centrifuge specimen. Suction profiles for a soil layer with an imposed surface discharge velocity and a saturated bottom boundary are shown in Figure 3.8(a) and Figure 3.8(b) for a values of  $\alpha = 1 \text{ kPa}^{-1}$  and  $K_s = 10^{-6} \text{ m/s}$ , and a normalized specimen geometry representative of the centrifuge permeameter developed in this study. The effect of  $N_{r,mid}$  on the suction profile while



holding  $v_m$  constant is shown in Figure 3.8(a), and the effect of  $v_m$  on the suction profile while holding  $N_r$  constant is shown in Figure 3.8(b). Although the specimen height used in this analysis is relatively small ( $L_m = 0.127$  m), the suction profiles are similar to those observed during steady-state flow through a larger soil profile in a 1-g setting ( $L_p = 1.5$  m in Figure 3.3). The average g-level influences the distribution of suction with height, while both the average g-level and the discharge velocity influence the magnitude of suction in the upper portion of the specimen. Although the magnitudes of suction in this figure depend on the assumed values of  $\alpha$  and  $K_s$ , the distribution of suction with height in the specimen is important to note. Despite the saturated bottom boundary condition, the suction does not vary significantly in the upper portion of the specimen length, even for low  $N_{r,mid}$ . Because  $N_r$  varies with radius, the suction distribution in the upper portion of the specimen is inclined. However, it may be assumed constant for practical purposes.

Centrifugation is therefore a useful tool to obtain the similar suction profiles to those observed during infiltration through a relatively long soil column in a 1-gravity setting. Due to the shorter length of a centrifuge permeameter specimen compared to that of the soil profile in Figure 3.3, the time required to reach these similar suction profiles, even at low flow rates, will be much shorter in the centrifuge permeameter.

Similar to the suction profiles in Figure 3.3, the suction at the outflow boundary does not have a significant effect on the shape of the suction profile in the upper zone of the specimen, as indicated by the suction profiles in Figure 3.8(c). Given the value of  $\alpha$  in the Gardner (1958) model, the limiting suction in the upper zone of the soil layer may also be predicted (Dell'Avanzi *et al.* 2004):

$$\psi_\infty = -\frac{1}{\alpha} \ln \left( -\frac{v_m}{N_{r,mid} K_s} \right) \quad (3.22)$$

Unlike the 1-g case, the limiting suction is valid only when  $N_r = N_{r,mid}$  throughout the profile. Otherwise, Equation (3.21) can be used to predict  $\psi_0$  at a given height  $z_m$ .

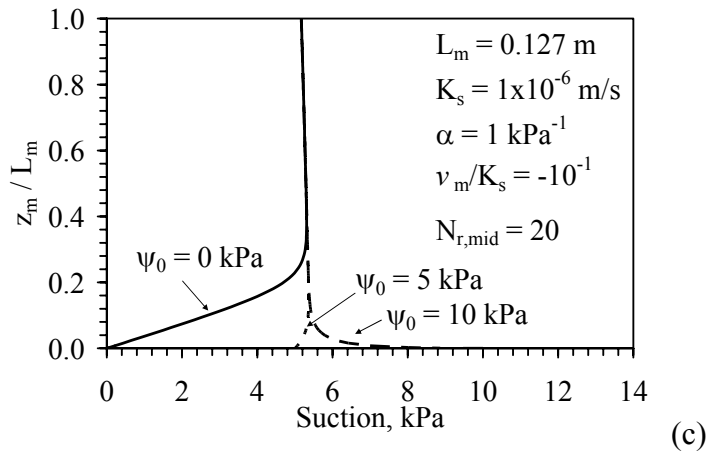
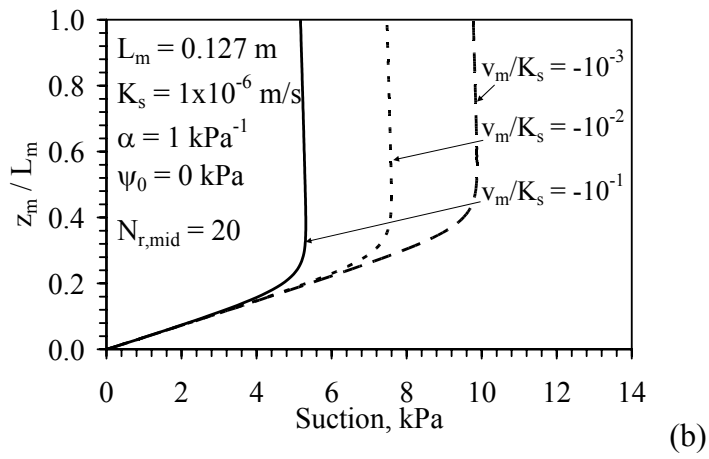
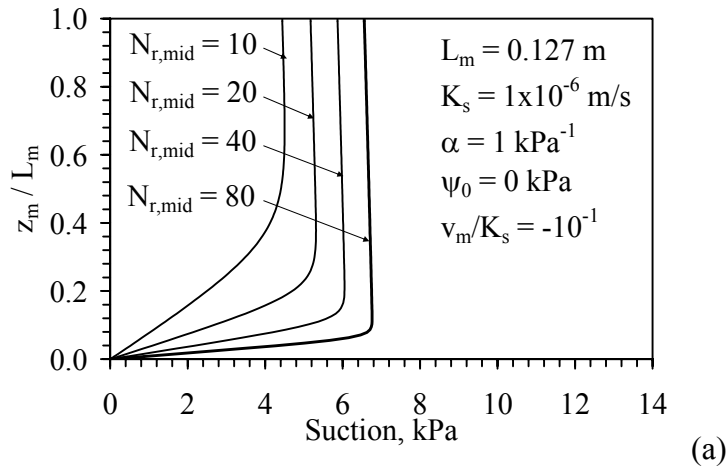


Figure 3.8: Steady state suction profiles for different values of: (a)  $N_{r,mid}$ ; (b)  $v_m$ ; (c)  $\psi_0$

Using the suction head profile quantified for steady-state flow in the centrifuge, the total head and elevation head profiles can be calculated using Equation (3.21), as shown in Figure 3.9(a). The centrifuge elevation head has a much larger magnitude than the suction head. The gradient profiles shown in Figure 3.9(b) indicate that the total head gradient is dominated by the centrifuge elevation head gradient. Also, the suction head gradient is constant in the upper portion of the specimen during steady-state flow. For these conditions, it can be considered negligible.

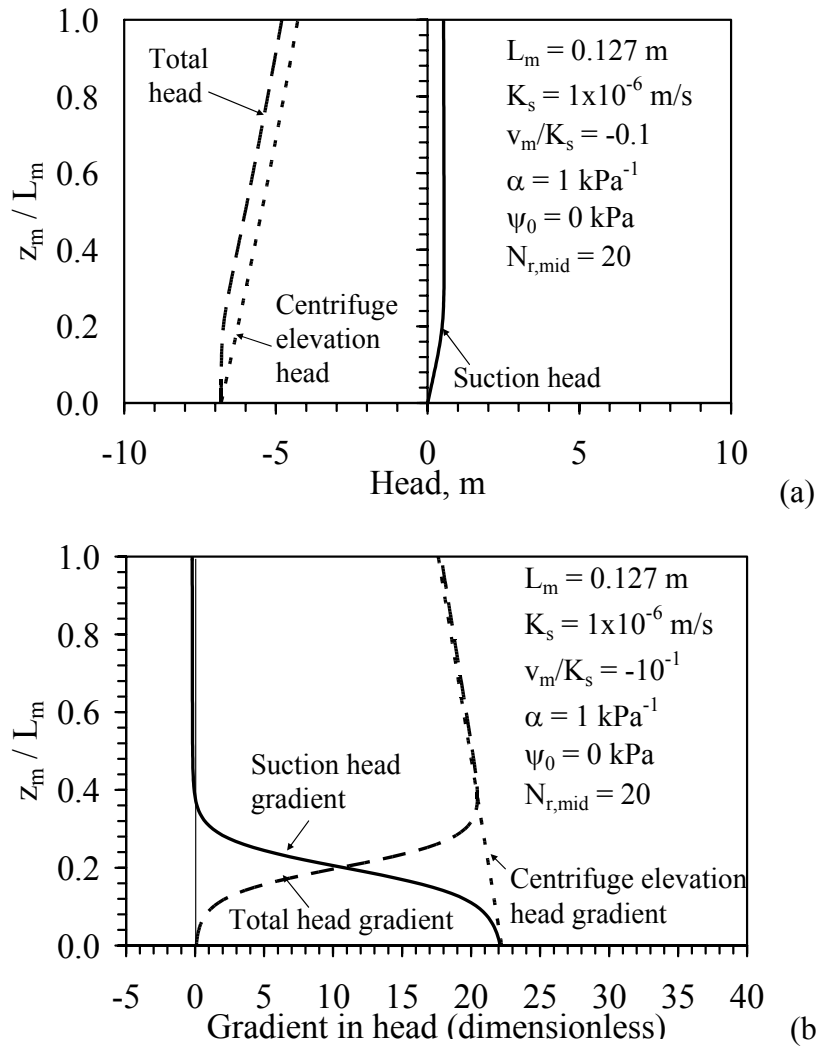


Figure 3.9: Head profiles during steady flow in the centrifuge: (a) Values; (b) Gradients

Using the calculated components of the total head gradient, the distribution in  $K$  at steady state water flow can be determined using Darcy's law, as follows:

$$K(\psi, z_m) = \frac{-v_m}{\left[ \frac{\omega^2}{g} (r_0 - z_m) - \frac{1}{\rho_w g} \frac{d\psi}{dz_m} \right]} \quad (3.23)$$

where  $v_m$  is an imposed, discharge velocity (equal to  $Q/A$ ) and  $\omega$  is an imposed centrifuge angular velocity. Distributions in  $K$  with varying g-level are shown in Figure 3.10(a) and with varying inflow rates shown in Figure 3.10(b) for the permeameter geometry representative of the centrifuge permeameter. Although constant in the upper zone of the profile, there is a slight increase in  $K$  with height because the centrifuge elevation head gradient varies with height. This is not the case for a 1-g soil profile, as “g” is constant.

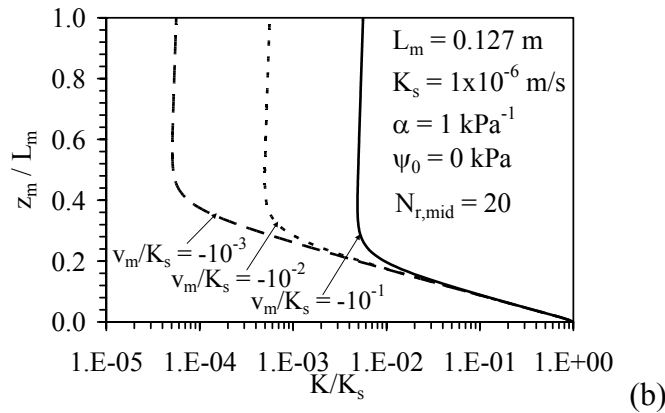
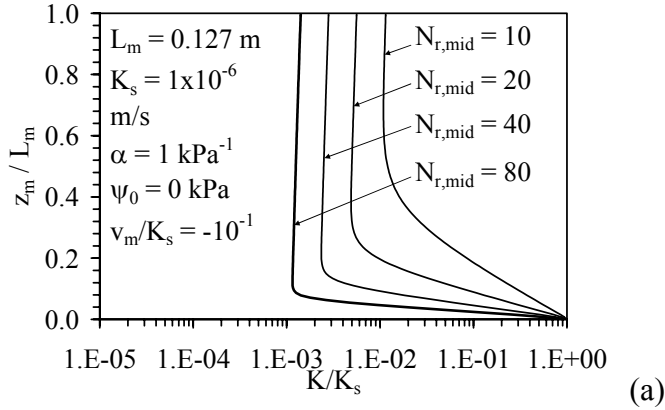


Figure 3.10: Steady-state  $K$  profiles (a) Variation with  $N_{r,mid}$ , (b) Variation with  $v_m$

### 3.5 BOUNDARY CONDITIONS DURING WATER FLOW IN UNSATURATED SOILS

The boundary conditions typically used in hydraulic applications are: imposed total head boundaries (Dirichlet) or imposed flow rate (Neumann) boundaries. However, there are other boundary conditions that may be prescribed, most of which involve the situation in which there are layered materials (Bear *et al.* 1987). For instance, a soil may be placed atop a boundary in which the impedance to water flow (*i.e.*, hydraulic conductivity) is constant. This would be the case in which the soil profile being investigated is underlain by a filter having constant hydraulic conductivity.

In general, the flow situation that will be considered in this study is that of one-dimensional, vertical, downward flow of water through a soil profile. Further, the hydraulic characteristics of unsaturated soils will be determined during steady-state water flow. Assuming that there is no evaporation, the upper surface is considered to be the inflow boundary, and the lower surface is considered to be the outflow boundary.

Both constant head and constant inflow rate boundary conditions can be used to attain steady-state water flow in a soil profile. In the determination of the hydraulic conductivity using rigid-wall permeameters (Mitchell *et al.* 1965) or flexible-wall permeameters (Daniel *et al.* 1985), a constant head boundary condition is used to reach steady-state water flow in saturated soil specimens. However, in unsaturated soils, it is difficult to apply a constant total head to the inflow boundary with the goal of reaching steady state water flow. One approach that uses this boundary condition is the tension disc infiltrometer, which is typically used to measure the K-function in the field. This approach is most suitable for soils with relatively high hydraulic conductivity when unsaturated. It is more common to impose a constant inflow rate to attain steady-state flow in unsaturated soils. In this case, the imposed inflow rate must be less than the hydraulic conductivity of the soil when saturated. The inflow rate can either be

controlled by passing water through a saturated plate placed atop the soil layer, or by using a flow pump. Nimmo *et al.* (1987) summarized several studies that imposed a constant flow rate using a saturated crust or ceramic stone. This approach has the disadvantage that different saturated plates must be used to impose different flow rates. Flow pumps are typically more convenient to supply a constant flow rate, but require special care to evenly distribute low flow rates uniformly across the surface of a specimen. In this study, flow pumps are used as the inflow boundary condition.

The suction profiles in Figure 3.3 and Figure 3.8 indicate that, regardless of the outflow boundary condition used in permeameter, the suction in the unit gradient zone of a soil profile during steady-state flow is insensitive to the suction at the outflow boundary (if the soil profile has sufficient length). Although not explicitly stated in this analysis, this observation is only true for an outflow face that has similar or greater hydraulic conductivity than the soil being drained. For example, the suction profiles in Figure 2.16 would not have been observed had a material with low permeability been placed beneath the soil profile, as positive pressures would need to be generated in the soil to maintain constant water flow through the system. This additional requirement leads to the concept of freely-draining boundary conditions, in which  $K_{\text{outflow}} \gg K_{\text{soil}}$ . Using the idea of freely-draining boundary conditions, Conca and Wright (1998) proposed the concept of open flow. In open flow, water is supplied to a vertically-oriented soil specimen at one end and is allowed to freely exit from another end without imposing suction values on the inflow or outflow faces. Instead, the suction in the upper zone of the specimen reaches a constant value associated with the imposed flow rate, similar to the suction profiles in Figure 3.3 and Figure 3.8. The suction at the base of the profile may be equal to zero (saturated), or it may be greater than zero depending on the flow conditions. The suction

profiles in Figure 3.4 indicate that a suction value greater than zero at the outflow face may lead to a greater length of the specimen having constant suction.

It should be noted that even if a high conductivity material is placed underneath a soil profile to act as an outflow face, the suction at the outflow face may be greater than zero. In the case of downward, transient infiltration through an initially unsaturated soil profile underlain by a filter layer (*e.g.*, a geosynthetic drainage layer, a metal screen, or a piece of filter paper), a capillary break may form. A capillary break prevents water from moving from a fine-grained soil into a coarse-grained soil at a measurable rate until the fine-grained soil becomes nearly saturated at the interface (Shackelford *et al.* 1994; Stormont and Anderson 1999; Khire *et al.* 1999; 2000).

To illustrate the capillary break phenomena, the WRCs and K-functions for a geotextile (coarse-grained) and clay (fine-grained) are shown in Figure 3.11(a) and Figure 3.11(b), respectively. The capillary break concept is based on the continuity of suction at the interface between two different materials. When a clay-geotextile system is at an initially high suction (*e.g.*, 100 kPa, shown by the black arrows), the clay has a degree of saturation of 0.5 while the underlying nonwoven geotextile is at residual conditions. At this high suction, the hydraulic conductivity of the clay is approximately  $1 \times 10^{-13}$  m/s while the geotextile is relatively impermeable. Consequently, moisture passing through the fine-grained material will not progress into the coarse-grained material at a measurable rate. Instead, water will accumulate at the clay-geotextile interface until the suction at the interface reaches a value at which the hydraulic conductivity of the coarse grained material is no longer significantly less than that of the fine-grained material. This suction value is referred to as the breakthrough suction.

The gray arrows in Figure 3.11 indicate the expected breakthrough suction for these materials, based on the interpretation presented by Khire *et al.* (1999). A

breakthrough suction of 1.0 kPa is predicted from the WRCs. Capillary breakthrough for these materials occurs at the suction corresponding to the intersection between the two K-functions. When the breakthrough suction is reached, leakage is observed into the coarse-grained layer at a rate close to the saturated hydraulic conductivity of the fine-grained layer. The degree of saturation in the clay will be relatively high (95%) when breakthrough occurs. It should be noted that a suction of 1 kPa is significantly below the suction corresponding to field capacity (typically considered at 33 kPa for silts and clays with low plasticity). For suctions below that corresponding to field capacity (*i.e.*, wetter soils), water would have drained downwards had the capillary break not occurred.

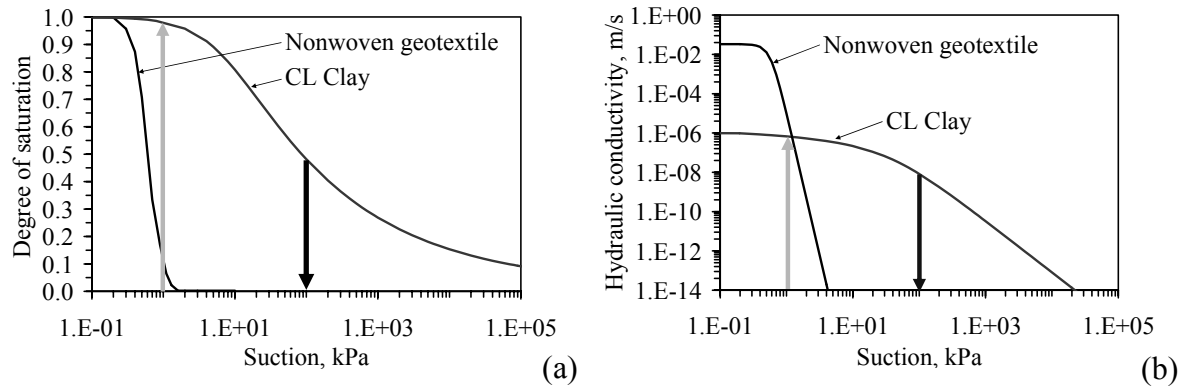


Figure 3.11: Interpretation of the hydraulic characteristics to show the capillary break effect, with black arrows showing initial conditions, and gray arrows showing conditions at capillary breakthrough: (a) WRC; (b) K-function

In summary, ‘open flow’ boundary conditions are likely to result in similar moisture content and suction profiles to that of a saturated (zero suction) boundary condition. For open flow boundary conditions, the suction at the outflow face of the soil will be slightly greater than zero (1 to 4 kPa depending on the outflow plate material), but the suction profile with height will be similar to the profiles shown in Figure 3.3 and Figure 3.8. Further, open flow boundary conditions will not provide significant impedance to water flow through a soil specimen.



## **Chapter 4: Materials**

### **4.1 SOIL SELECTION FOR VALIDATION OF THE CENTRIFUGE PERMEAMETER**

The centrifuge permeameter approach presented in later chapters of this dissertation may present important challenges for determination of the hydraulic characteristics of soils. Although a centrifuge approach can be used for a variety of soils, the conditions under which a given soil should be investigated in the centrifuge may be restricted due to testing issues as well as the soil's hydraulic and mechanical properties. The main testing issues that have implications on the type of soil used in the centrifuge permeameter are the stresses associated with the centrifuge acceleration field, the testing time required for hydraulic characterization, the ability to apply a uniform rate of infiltration to a specimen, and the functionality of instrumentation in the permeameter used to measure moisture content and suction. The main mechanical and hydraulic properties of a soil that may affect their characterization in a centrifuge permeameter are its consolidation curve (*i.e.*, its stiffness), its tendency to swell or shrink upon changes in moisture content, its range in hydraulic conductivity with porosity when saturated, and its range in hydraulic conductivity with moisture content when unsaturated.

There are several examples of how the centrifuge conditions may need to be modified to evaluate a given soil. Characterization of a soft, compressible soil in the centrifuge may cause significant volume change under the increased acceleration field. This change in volume may lead to a change in hydraulic characteristics from that associated with the original soil structure. To use this soil in the centrifuge, lower g-levels may need to be used to limit the amount of volume change. However, because the testing time is associated with the g-level, lower g-levels may not provide a significant enough advantage in testing time over conventional characterization approaches. Characterization

of a coarse sand may be difficult due to the ability of the permeameter to uniformly distribute water across the area of a specimen. Further, the range of suction over which a coarse sand may experience appreciable changes in moisture content and  $K$  can be small, making the resolution of the instrumentation important. Characterization of clays having high plasticity index may be difficult because very low infiltration rates must be imposed to determine low hydraulic conductivity values. This may lead to long testing times unless very high g-levels are imposed, which may in turn cause settlement. Clays of high plasticity may experience swelling during infiltration in the centrifuge under low g-levels. Other soil properties, like electrical conductivity and salinity, may influence instrumentation used to measure moisture content and suction.

The hydraulic characteristics of remolded and compacted specimens of a clay of low plasticity are investigated in this study. This chapter summarizes the geotechnical and index properties of the soil selected to demonstrate the use of the centrifuge permeameter approach. In general, this soil has several characteristics that make it ideal for use in validating the centrifuge permeameter. First, the compacted clay is relatively stiff when saturated, and does shrink or swell during changes in moisture content when unsaturated. This does not place a strong restriction on the g-levels that can be used for characterization. As shown in the next chapter, the hydraulic conductivity of the clay when saturated ( $K_s$ ) is between  $10^{-4}$  and  $10^{-9}$  m/s, depending on its porosity. This range of hydraulic conductivity allows a conventional infusion pump to be used to impose an infiltration rate on the soil. The low hydraulic conductivity compared to sand indicates that lateral migration of moisture will occur during vertical infiltration, improving the distribution of infiltration across the area of the specimen. The clay has low salinity and electrical conductivity, permitting the use of dielectric sensors to infer moisture content. Preliminary tests indicate that the current configuration of the centrifuge permeameter

and its instrumentation work well to measure the hydraulic characteristics of this clay. However, modifications may be necessary to adapt the centrifuge permeameter to the other soil types.

## 4.2 GEOTECHNICAL CLASSIFICATION

The soil used in this study is referred to as RMA Soil Type II, and was obtained in 2001 from the landfill cover testing facility located inside the Rocky Mountain Arsenal (RMA) near Denver, Colorado. Six 55-gallon drums of the soil were dried in a constant humidity room at a temperature of 50 degrees and a relative humidity of 10%. A mortar and pestle was used to break up aggregations of particles. The granulometric curve for this soil, shown in Figure 4.1, was determined using sieve and hydrometer analyses. The soil has approximately 60% passing the #200 sieve. The granulometric curve for sand used in some of the preliminary tests is also included in this figure for comparison.

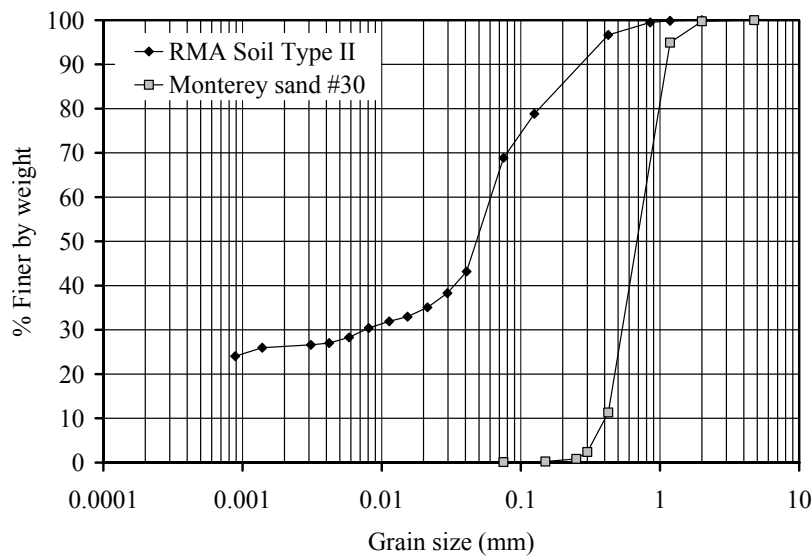


Figure 4.1: Granulometric curve for RMA Soil Type II

The specific gravity of RMA Soil Type II was determined to be 2.7 using the procedures described in ASTM D854-92. The liquid and plastic limits were determined

for Soil Type II according to ASTM D4318. The soil has a liquid limit (LL) of 28.74% and a plasticity index (PI) of 17.18%. These and other geotechnical properties of RMA Soil Type II are summarized in Table 4.1. These properties indicate that this soil classifies as “CL” according to the Unified Soil Classification System (USCS).

Table 4.1: Geotechnical properties for RMA Soil Type II

Variable	Value	Units
$G_s$	2.71	
$D_{10}$	< 0.0009	mm
$D_{50}$	0.05	mm
$D_{90}$	0.2	mm
pH	8.2	
LL	29	
PL	17	
PI	12	

### 4.3 COMPACTION CHARACTERISTICS

The compaction curve for RMA Soil Type II was determined with the standard Proctor effort of 600 kNm/m<sup>3</sup> (ASTM D698) in a reduced-size mold (diameter of 71.1 mm and height of 142.2 mm). The compaction mold was built in two halves, so that that it can be split in half to extract the soil specimen. A hammer with mass of 2.58 kg and a drop height of 0.29 m were used to compact five layers with 23 blows/layer. The gravimetric water content was determined using ASTM D2216. The gravimetric water content at compaction is referred to as “ $w_c$ ”. The standard Proctor compaction curve is shown in Figure 4.2(a), and the compaction mold is shown in Figure 4.2(b). The optimum gravimetric water content at compaction ( $w_{c,opt}$ ) is approximately 12% and the maximum dry density ( $\rho_{d,max}$ ) is 1900 kg/m<sup>3</sup>. A slight variability in dry density at low values of  $w_c$  was observed.

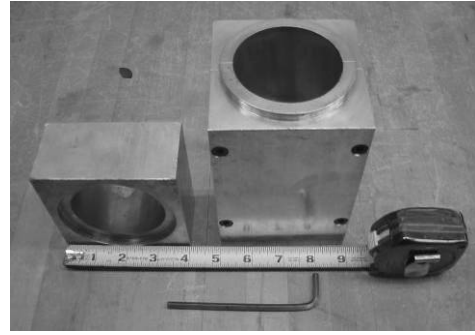
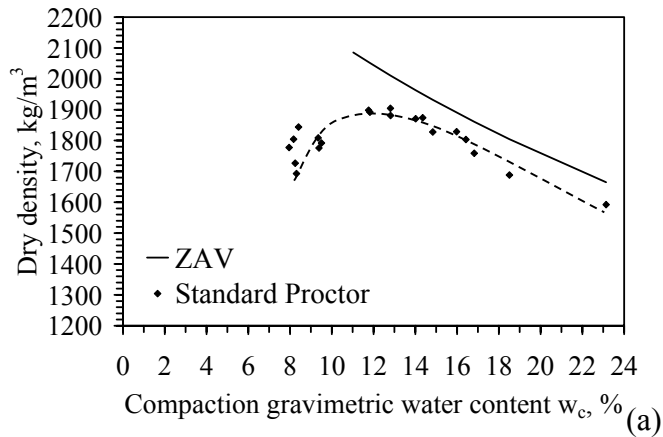


Figure 4.2: (a) Compaction curve for RMA Soil Type II; (b) Reduced-scale mold

The porosity ( $n$ ) is used in this study to classify the density of soil specimens because it reflects the upper bound on the volumetric moisture content. The porosity corresponding to the maximum standard Proctor dry density is equal to 0.30. In the different tests described in this study, higher porosities are often used to investigate the effects of density on the hydraulic characteristics. Specifically, loose specimens were compacted to a porosity of 0.50, medium-dense specimens were compacted to a porosity of 0.45, and dense specimens were compacted to a density of 0.35. These densities correspond to dry densities that 70, 80, and 90% of the maximum standard Proctor dry density. A Bellofram<sup>®</sup> piston compactor, shown in Figure 4.3, was used to change the compaction energy in order to reach different target porosities. The compaction energy was controlled by varying the pressure and cross-sectional area of the piston.



Figure 4.3: Piston compactor

## **Chapter 5: Determination of the Hydraulic Characteristics of Soil using Conventional Techniques**

### **5.1 OVERVIEW**

The goal of this chapter is to provide a baseline evaluation of the hydraulic characteristics of the clay used in this study, and to evaluate the benefits and shortcomings of different techniques used in the past to determine the hydraulic characteristics of soils. This chapter focuses on the procedures and typical results from both 1-gravity and centrifuge tests that have been used in previous studies to characterize (i) the hydraulic conductivity of saturated clay; (ii) the water retention curve for clay, and (iii) the K-function for unsaturated clay. When possible, these tests were conducted on the clay used in the centrifuge permeameter testing program. Otherwise, typical results from the literature are presented. The development of the centrifuge permeameter was guided by the lessons learned from the tests described in this chapter.

The experimental approaches discussed in this chapter for determination of the hydraulic characteristics of unsaturated soils all involve water flow through a soil specimen. Water flow through soil can be controlled by manipulating the gradient in total hydraulic head through the specimen or the flow rate. The value being manipulated in a test is referred to as the control variable. A test based on manipulation of the gradient typically involves measurement of the flow rate, while a test based on manipulation of the flow rate typically involves measurement of the gradient (suction and moisture content distributions). The control variables along with the measurements can be synthesized to determine the hydraulic characteristics. The measurements may be made during transient flow, when the pressure and water content in the soil are adjusting to the boundary conditions, or at steady-state, when the pressure and water content in the soil

have reached a stable distribution during water flow. As will be shown, transient approaches yield a significant amount of data in a short amount of time, but the results are more susceptible to experimental and calculation errors than in steady-state tests (Benson and Gribb 1997). Steady-state approaches generally yield repeatable results, but testing times are long and data is limited. Fingering and water flow through preferential channels play an important role in both steady-state and transient approaches.

## **5.2 HYDRAULIC CONDUCTIVITY OF SATURATED SPECIMENS ( $K_s$ )**

### **5.2.1 Flexible Wall Permeameter Technique**

The hydraulic conductivity of saturated specimens is an important point on the K-function. The hydraulic conductivity values of saturated RMA Soil Type II specimens with different compaction moisture contents were determined using a flexible wall permeameter. The flexible wall permeameter, a Trautwein<sup>®</sup> pressure control panel with inflow, outflow, and cell pressure control, and a pressure transducer to measure back-pressure are shown in Figure 5.1(a).

Compacted specimens with a height of 142.2 mm and diameter of 71.1 mm were saturated using back-pressure in the flexible wall permeameter under an effective stress of 14 kPa. The low effective stress was used to replicate surface soil conditions. The specimens were then permeated under an average gradient of 3.0 (pressure difference of 3.5 kPa). The heights of water in the inflow/outflow burettes were used to calculate the hydraulic gradient. The pressures applied by the panel were measured independently by pressure transducers. The test continued until the ratio of inflow to outflow was equal to one, as shown in Figure 5.1(b). This indicates that steady-state flow has been obtained, at which point the hydraulic conductivity was recorded.

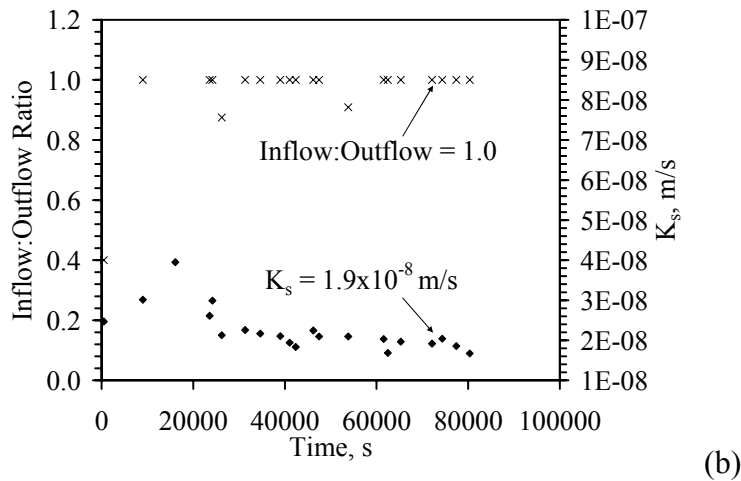
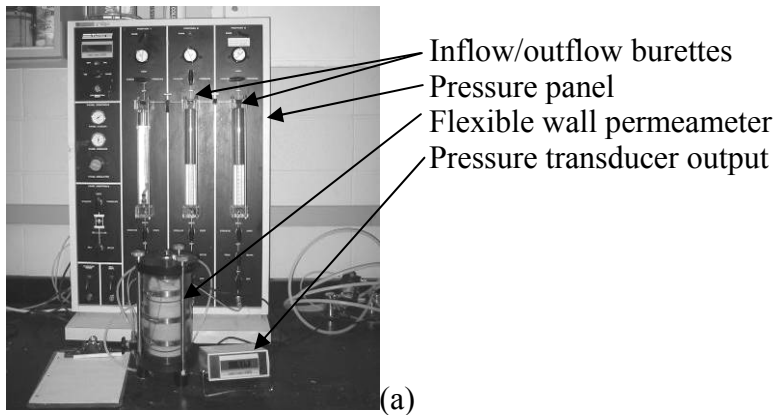


Figure 5.1: Flexible wall permeameter: (a) Setup; (b) Typical results

The hydraulic conductivity values for RMA Soil Type II specimens compacted using the standard Proctor effort with water contents at compaction ranging from 8 to 16.5% are summarized in Figure 5.2. A log-linear decrease in hydraulic conductivity is observed with increasing compaction water content. The saturated hydraulic conductivity values range from  $2 \times 10^{-7}$  m/s for specimens compacted with low compaction water content to  $3.7 \times 10^{-10}$  m/s for specimens compacted using high compaction water content. Some variability in the data is noted. The variability can be attributed to uneven compaction effort throughout the length of the specimen, different



specimen lengths (some specimens were trimmed to obtain specimens for other tests), and slight variation in effective stress attributed to variability in the pressure regulators.

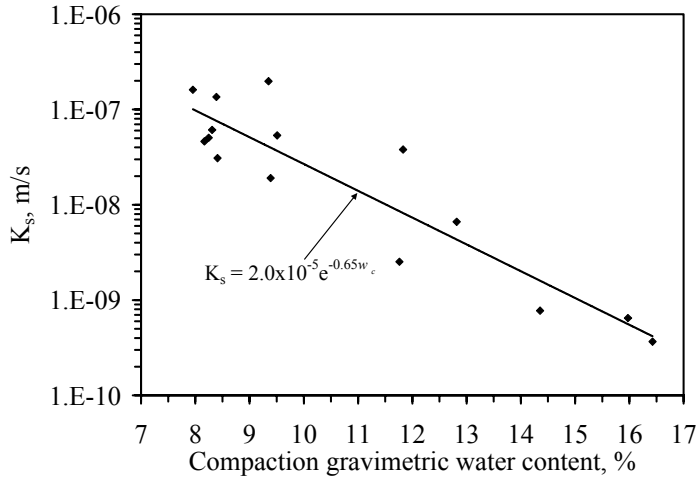


Figure 5.2: Effect of compaction moisture content on the hydraulic conductivity of saturated RMA Soil Type II specimens

### 5.2.2 Rigid wall Permeameter Technique

The hydraulic conductivity values of saturated RMA Soil Type II specimens with different porosities were determined using a rigid-wall permeameter, shown in Figure 5.3(a). The setup can be modified to perform constant-head or falling-head tests. This approach was used to assess the hydraulic conductivity of soils with a wide range of porosities. Specimens were prepared by compacting soil into the rigid-wall permeameter using the piston compactor. The specimens had a height of 127 mm and a diameter of 76.2 mm, and were hydrated by flushing distilled water from the bottom of the specimen. A constant head test was performed by measuring the head loss through the specimen for the constant head reservoir placed at three elevations above the outflow port of the permeameter. The head loss through the specimen was also measured using manometers inserted into the wall of the cell. The relationship between the calculated total hydraulic

gradient and measured outflow rate, shown in Figure 5.3(b), was used to calculate the hydraulic conductivity.

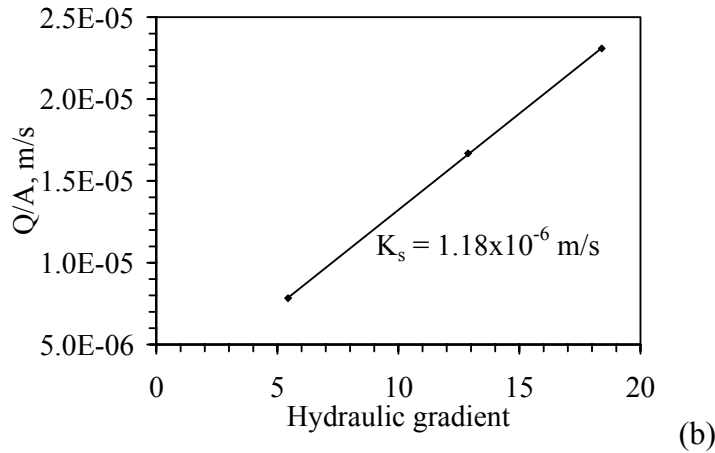
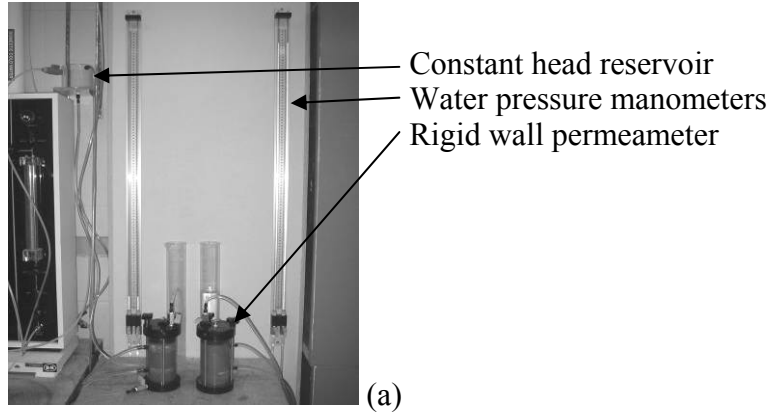


Figure 5.3: Rigid-wall permeameter: (a) Setup; (b) Typical results

The variation in hydraulic conductivity with porosity is shown in Figure 5.4. This figure includes data from specimens compacted into the rigid-wall permeameter with a water content at compaction of  $\pm 1\%$  of the optimum water content ( $w_{c,opt}$ ), as well as data from Figure 5.2 that were compacted at  $w_{c,opt}$ . This data is useful to predict changes in  $K_s$  that can be expected for changes in porosity that may occur during centrifugation due to the increased effective stress. A wide range in  $K_s$  values is obtained for this clay (*i.e.*,  $5 \times 10^{-4} \text{ m/s}$  to  $1 \times 10^{-10} \text{ m/s}$ ), with a non-linear decrease in  $K_s$  with decreasing porosity. The

variation in the hydraulic conductivity with porosity predicted from the Kozeny-Carman model is also shown in Figure 5.4, given by:

$$K = CD_{10}^2 \frac{n^3}{(1-n)^2} \left( \frac{\gamma_w}{\mu} \right) S_r^3 \quad (5.1)$$

where  $C$  is a fitting parameter equal to 1.0,  $D_{10}$  is equal to 0.01 mm,  $\mu$  is the dynamic viscosity of water, and  $S_r$  is the degree of saturation. This model leads to a poor fit. A log-linear curve was found to better fit the data.

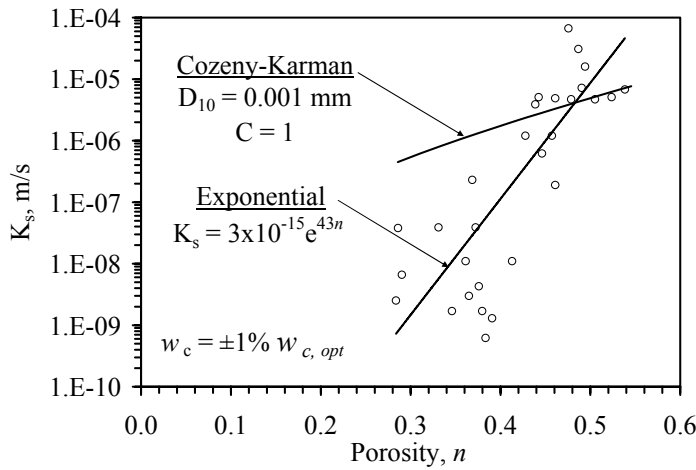


Figure 5.4: Effect of porosity on the hydraulic conductivity of saturated specimens compacted at the optimum water content

### 5.2.3 Centrifuge Permeameter Technique

Although this study does not focus on the determination of the hydraulic conductivity of saturated specimens using a centrifuge permeameter, the lessons learned from research in this area can help interpret results obtained from K-function characterization tests. Several studies have been conducted using centrifuges to measure the hydraulic conductivity of saturated soil specimens (Nimmo and Mello 1982; Singh and Gupta 2000; Singh and Gupta 2001). Constant head and falling head tests have been conducted.  $K_s$  is calculated in the constant head approach as follows:

$$K_s = \frac{2v_m L}{\rho_w \omega^2 (r_0^2 - r_{water}^2)} \quad (5.2)$$

where  $r_{water}$  is the radial position of the constant head water supply, and  $L$  is the length of the specimen. A constant head setup in the centrifuge is cumbersome, as it requires a set of inflow and outflow reservoirs. The falling head approach is easier to implement in the centrifuge, where  $K_s$  can be calculated as follows:

$$K_s = \frac{L}{N_r t} \ln \left( \frac{h_1}{h_2} \right) \quad (5.3)$$

where  $h_1$  is the original height of water above the specimen, and  $h_2$  is the height of water above the specimen after a certain time  $t$  during centrifugation at a g-level  $N_r$ . The apparatus developed by Nimmo and Mello (1982), shown in Figure 5.5(a), was used to perform both constant head and falling head tests.  $K_s$  results are shown in Figure 5.5(b) for three soils tested under 1-g falling head tests (FG) as well as centrifuge constant head (CC) and falling head (FC) tests. A decrease in  $K_s$  is observed with increasing  $N_{r,mid}$  up to 1800 g's. This decrease occurs because the effective stress increases by  $N_{r,mid}$  in the centrifuge, resulting in consolidation and lower  $K_s$ .

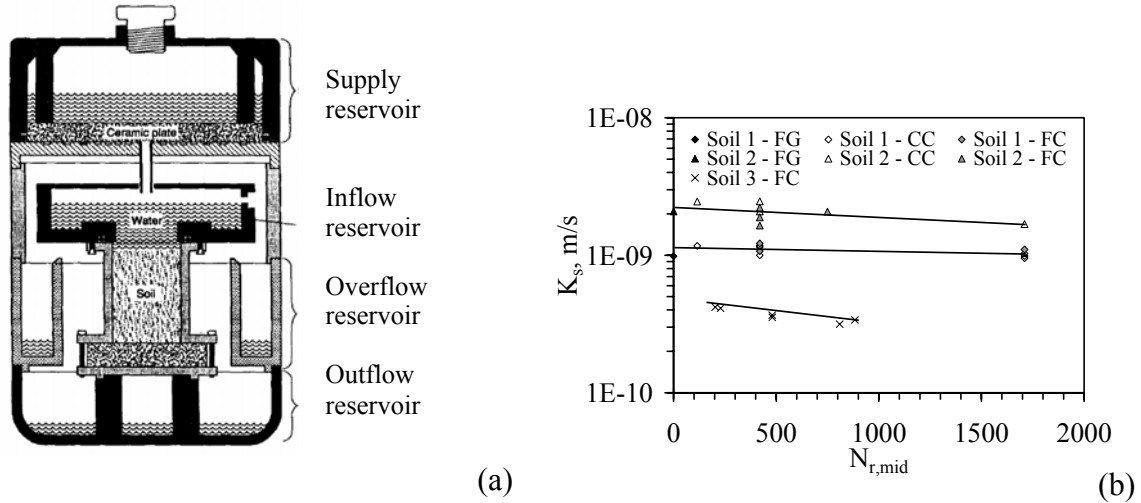


Figure 5.5:  $K_s$  in the centrifuge (Nimmo and Mello 1991) (a) Apparatus; (b)  $K_s$  results

Robinson (2002) noted that several studies that have been presented in the literature do not include the centrifuge driving force in their calculation of  $K_s$  using the falling head centrifuge approach (Singh and Gupta 2000; Singh and Gupta 2001). This error results in  $K_s$  values that increase with  $N_{r,mid}$ . Although  $K_s$  is a proportionality constant and not a scalable quantity, the total hydraulic gradient is affected by the centrifuge driving force. Sharma and Samarasekara (2007) have continued to use the results of Singh and Gupta (2001), so this misunderstanding continues in the literature.

### **5.3 WATER RETENTION CURVE (WRC)**

#### **5.3.1 Overview**

Several techniques are available to determine the WRC experimentally (Klute *et al.* 1986; Wang and Benson 2001) using physical and thermodynamic techniques. Physical techniques involve expulsion of water from a specimen of initially water-saturated soil by imposing a known value of suction on a specimen boundary. Specimens are usually small in size so that the variation in suction within the specimen is minimal. Thermodynamic techniques involve evaporation of water from a specimen inside a closed environment with known relative humidity. In this case, the total suction (*i.e.*, the sum of osmotic pressure and matric suction) within the soil will reach equilibrium with the water vapor pressure in the pore air (related to the relative humidity). However, as water flow is controlled by the matric suction, a correlation must be developed between total and matric suction to use these techniques. In general, physical techniques are used for low suctions (*e.g.*, < 1500 kPa) while thermodynamic techniques are used for higher suctions.

In this section, WRC results for RMA Soil Type II obtained using axis translation, hanging column, and thermodynamic tests are presented. A centrifuge permeameter approach to determine the WRC is also presented, with results from the literature.

### 5.3.2 Axis Translation (Pressure Plate)

The most commonly used physical technique is the axis translation technique. The axis translation technique is described by Hilf (1954) and Olson and Langfelder (1965). This technique takes advantage of the fact that the suction is equal to the difference between the pore air and pore water pressures. Instead of dealing with atmospheric air pressure and negative pore water pressures, the axis translation technique imposes positive air and water pressures, with a difference equal to the imposed suction. An apparatus that employs this technique is the pressure plate, shown in Figure 5.6.

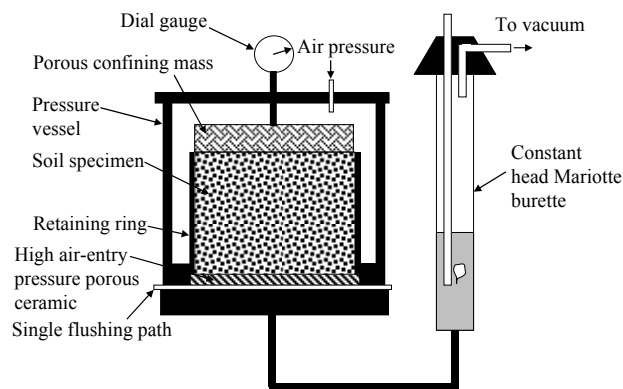


Figure 5.6: Pressure plate apparatus

A pressure plate typical test involves placing a soil specimen on a saturated ceramic disc within a pressure vessel. The air pressure in the vessel is then increased, and the water pressure on the other side of the saturated ceramic is maintained constant. Application of air pressure to the soil in the vessel will cause air to enter the pores and displace water, which will flow from the soil through the saturated ceramic. The air-entry pressure of the ceramic disc must be higher than that of the soil, and should be higher than the maximum air pressure applied to the pressure vessel. The water pressure at the base of the ceramic disc is usually kept at atmospheric pressure, and outflow is measured using a constant-head Mariotte burette. The water level in a constant-head Mariotte

burette can change during outflow from the specimen while maintaining the same water pressure at the base of the ceramic. After outflow is negligible, the system is in equilibrium under the imposed matric suction. The total volume of outflow can be measured for this pressure increment. This approach can be repeated for higher air pressure increments, which will cause gradual drainage of the specimen. After reaching equilibrium at the highest pressure increment, the pressure may be decreased, hysteresis can be investigated by permitting water from the constant-head Mariotte burette to flow back into the specimen. At the end of testing, the final volumetric moisture content can be estimated from the gravimetric water content (measured destructively) and the dry density. The volumetric moisture content at each increment can then be back-calculated from the outflow measured throughout the test. The range of suction for this test is limited by the air-entry value of the porous ceramic disc, which is typically between 300 and 500 kPa. More details for pressure plate testing can be found in ASTM D6836.

The axis translation technique was used to characterize the WRC for the RMA Soil Type II for suctions ranging from 10 to 150 kPa. The pressure plate device used to determine the WRC was developed by at UT by Jeff Kuhn (Personal communication 2007). The device has several advantages over axis translation equipment used in agronomy applications, and provides several enhancements to the device developed by Wang and Benson (2004). Specifically, the device allows measurement of specimen height during testing, limits exposure of the saturated ceramic disc to the soil specimen only (*i.e.*, no direct air-ceramic contact), allows measurement of the outflow volume from the specimen during testing, allows flushing of diffused air that passes through the ceramic via a single drainage path, and can be safely used to pressures of 2000 kPa. Views of the pressure plate device are shown in Figure 5.7.

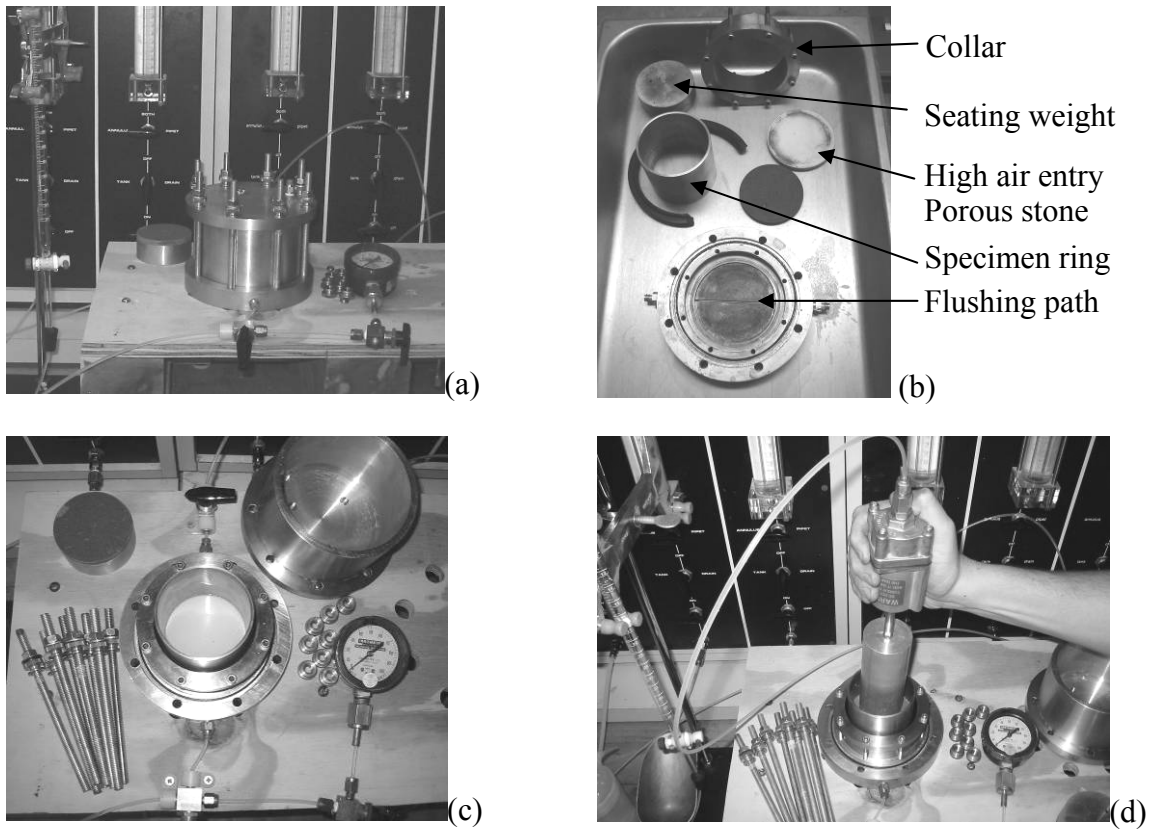


Figure 5.7: Pressure plate cell: (a) Assembled pressure plate; (b) Components; (c) Assembled without pressure cell; (d) Specimen preparation

The axis translation technique was used to define the WRC for intermediate ranges of suction (*i.e.*, 1 kPa to 150 kPa). The outflow time series for four pressure increments are shown in Figure 5.8(a) for a RMA Soil Type II specimen with a porosity of 0.53. This data is similar to that of the hanging column test, and indicates that the outflow reaches an asymptote near equilibrium. Decreasing outflow volume with time was observed at the end of progressively higher pressure increments because the larger pores drain first.



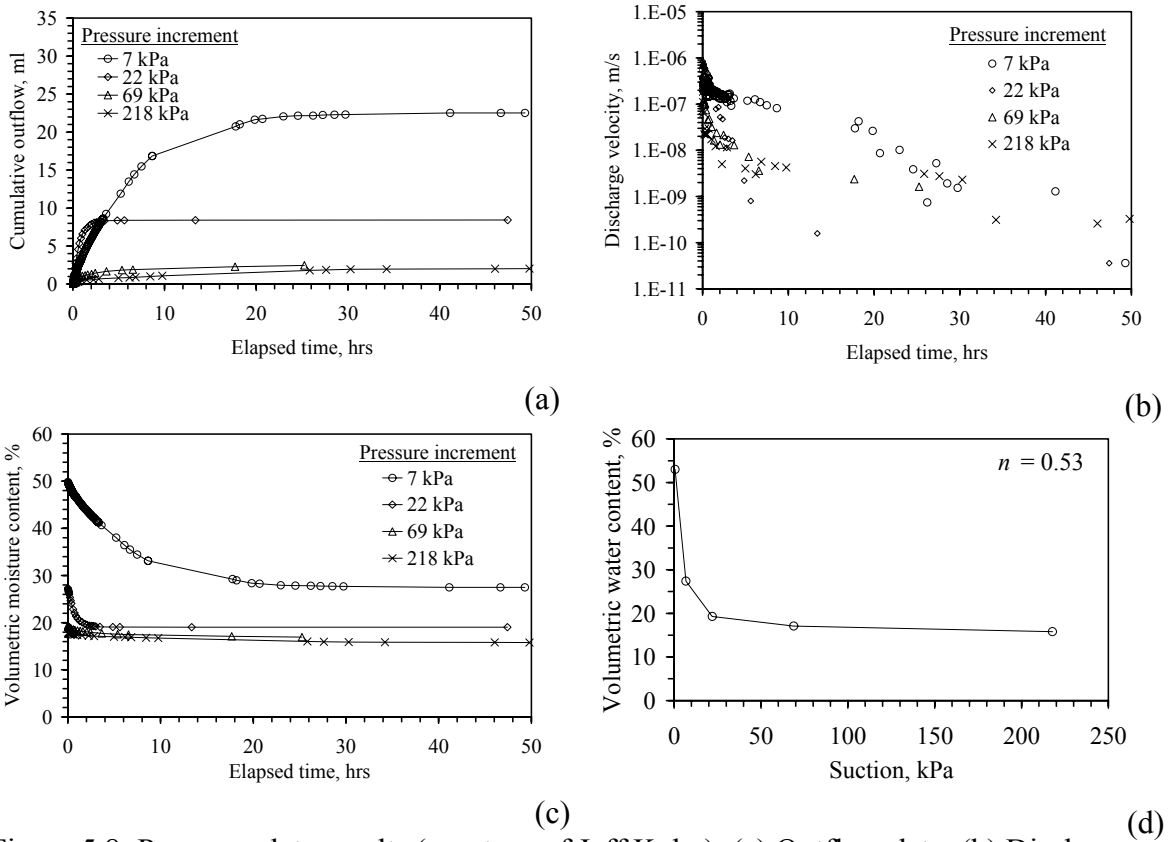


Figure 5.8: Pressure plate results (courtesy of Jeff Kuhn): (a) Outflow data; (b) Discharge velocity data; (c) Moisture content data; (d) WRC

The discharge velocities calculated with time for the pressure increments are shown in Figure 5.8(b). The data shows scatter, especially at large times. The data for the 22 kPa pressure increment shows a linear decrease in discharge velocity up to 10 hours, followed by an asymptotic decrease with time. The volumetric moisture content was back-calculated for each time interval using the outflow data, and is shown in Figure 5.8(c). Finally, the WRC defined using the volumetric moisture content at equilibrium and the suction in the soil (equal to the positive pressure increment) is shown in Figure 5.8(d). The RMA Soil Type II specimen showed negligible volume change.

### 5.3.3 Hanging Column

The hanging column apparatus is another common physical technique (Haines 1932), shown in Figure 5.9. In this test, a specimen is placed on a fritted (porous) glass disc held within a glass Büchner funnel. The air entry pressure of commonly used fritted glass plates is less than 10 kPa so that the response of the water column is rapid, making this approach useful only for low suctions. The bottom of the funnel is connected to a manometer tube, and a negative water pressure is imposed on the disk by fixing the water level in the tube at an elevation below the disk. A constant head can be maintained in the manometer using a Mariotte burette, which allows outflow to be measured with time.

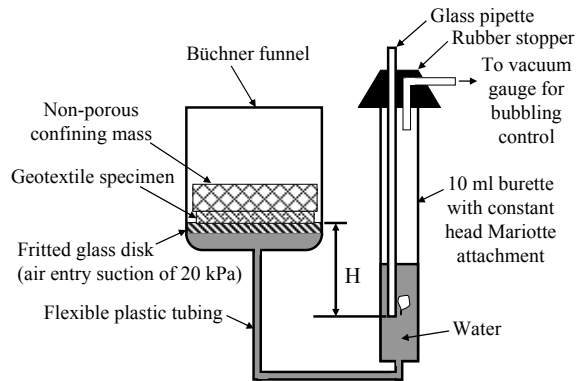


Figure 5.9: Hanging column apparatus

A picture of the hanging column setup used in this study is shown in Figure 5.10(a). The hanging columns consist of a 250 ml Büchner funnel with a fritted glass disc. Fritted glass discs of different porosities were used: a coarse porosity having an air entry suction of 15 kPa, a medium porosity having an air entry suction of 25 m, and a fine porosity having an air entry suction of 50 kPa. The funnels are mounted on a pulley system that is used to apply a water head difference of 4 m (~40 kPa). The lower end of the Büchner funnel is connected to a water-saturated tube, attached to a constant-head Mariotte burette, the top of which is shown schematically in Figure 5.10(b). The

Mariotte burette allows measurement of outflow from the specimen without altering the suction head applied to the specimen. It consists of a graduated burette, a rubber stopper with a hole drilled to fit the burette on its larger end, and a thin glass pipette. To ensure continuous bubbling from the pipette in the Mariotte burette during outflow, a vacuum is applied to the top of the burette. Before testing, a 150 g porous stone is placed above the soil specimen to enhance hydraulic connection between the soil and the fritted glass disc. The soil was compacted within a brass ring with a height of 6.5 mm and diameter of 54 mm. To permit initial saturation, the water level in the hanging column was raised above the top of the specimen and vacuum of 10 kPa was applied to the top of the Büchner funnel for at least 24 hours. Back-calculation of the initial moisture content indicates that the initial saturation exceeded 95%.

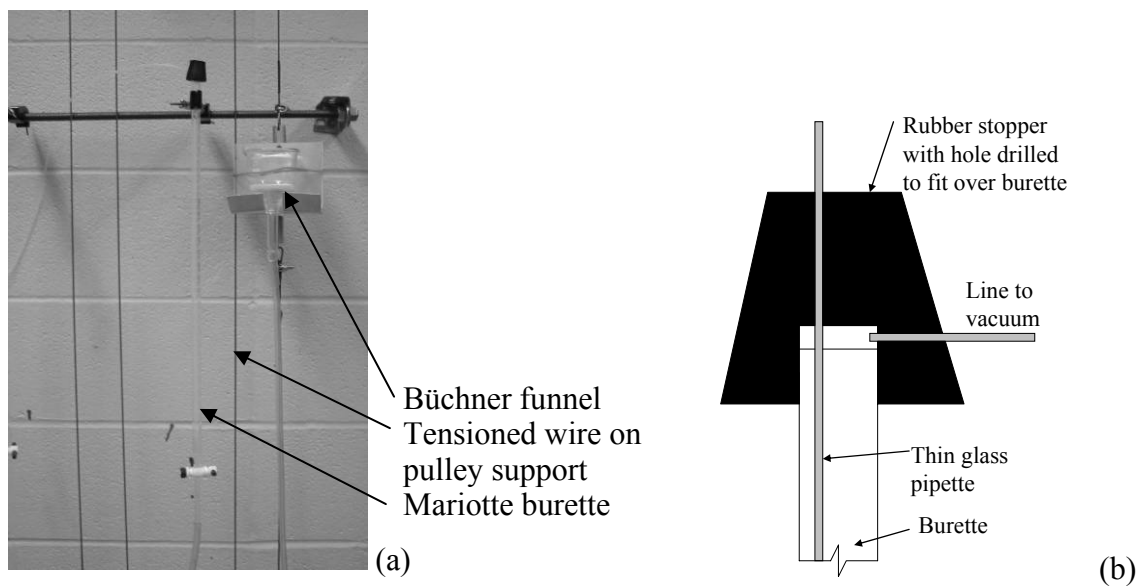


Figure 5.10: Hanging column: (a) Setup; (b) Schematic of the top of Mariotte burette

The hanging column is useful for determining points on the WRC at a range of low suction values (less than 10 kPa). Typical outflow data from a drying WRC test for a nonwoven geotextile are shown in Figure 5.11(a). The volumetric moisture content at

equilibrium is directly correlated with the suction corresponding to the water head difference. Approximately 5 to 20 minutes was required to reach equilibrium for each suction value. The drying portions of the WRCs for RMA Soil Type II compacted to three porosities are shown in Figure 5.11(b) in terms of  $S_r$ . The loose specimen ( $n = 0.5$ ) had an air entry suction of approximately 2.0 kPa, while the denser specimens had not reached their air entry suction at the extents of this test. The data for a nonwoven geotextile is shown to highlight the fact that this test is most appropriate for coarse materials that exhibit large changes in degree of saturation over this suction range.

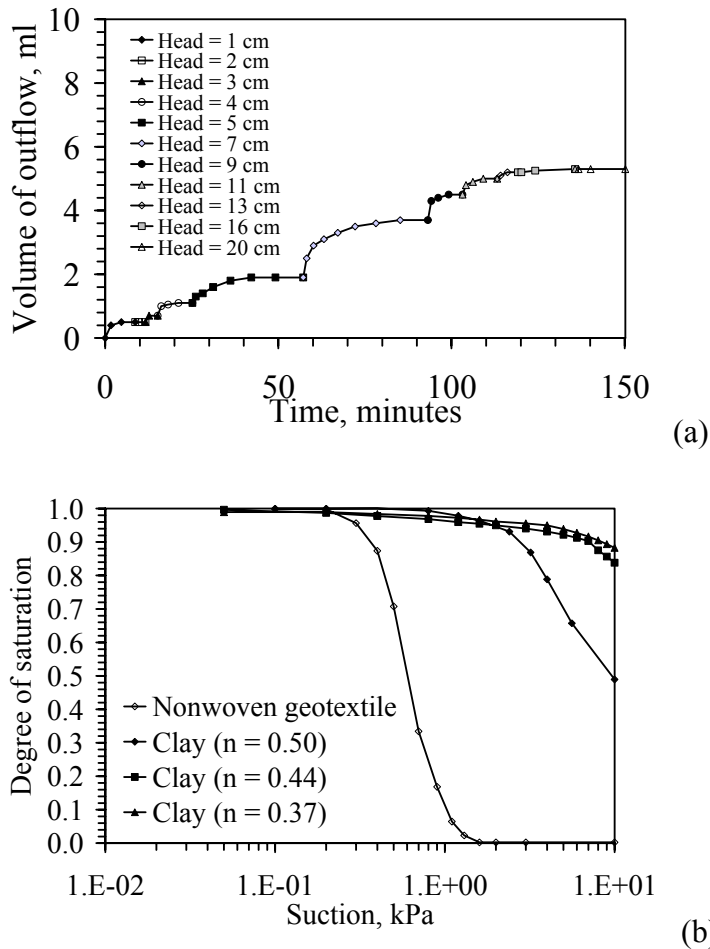


Figure 5.11: Hanging column results; (a) Typical outflow data; (b)  $S$ - $\psi$

### 5.3.4 Thermodynamic Techniques

The most common thermodynamic technique is the filter paper method (Leong and Rahardjo 1999). The approach involves allowing a standardized filter paper (*e.g.*, Whatman #42) to reach thermodynamic equilibrium with a soil specimen. Matric suction can be measured by placing a piece of filter paper in contact with the soil to permit capillary action, while total suction can be measured by placing the filter paper in a hermetically-sealed environment with the soil but preventing direct contact. This method is simple and inexpensive, but it is time consuming and difficult to interpret due to different trends in osmotic pressure and matric suction with moisture content. Another thermodynamic technique is the chilled mirror hygrometer (Wang and Benson 2001). This device also obtains the total suction by inferring the water vapor pressure in the soil after measuring the temperature at which moisture condenses on a mirror. When condensation occurs, a change in the optical properties of the mirror can be detected. The simplest thermodynamic approach is the use of a desiccator (Tang and Cui 2005). The relative humidity in the desiccator is controlled by allowing water to evaporate from a saturated salt solution, as shown in Figure 5.12.

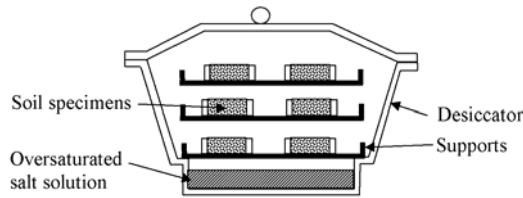


Figure 5.12: Desiccator with salt solution

The relative humidity in the desiccator chamber is related to an equivalent total suction in the soil specimens calculated as:

$$\psi = -\frac{\rho_w RT}{M_w} \ln \left( \frac{R_h}{100\%} \right) \quad (5.4)$$

where  $\psi$  is the equivalent soil total suction in kPa,  $R$  is the universal gas constant equal to  $8.31432 \text{ (kPa m}^3\text{)/(kmol K)}$ ,  $\rho_w$  is the unit weight of water equal to approximately  $1000 \text{ kg/m}^3$ ,  $M_w$  is the molar mass of water vapor equal to  $18.016 \text{ kg/kMol}$ ,  $T$  is the absolute temperature, which was approximately  $296.5 \text{ K (23 }^\circ\text{C)}$  during the testing period, and  $R_h$  is the relative humidity at equilibrium for a given salt solution. The saturated salt solutions used in this study, along with the measured relative humidity values and suctions are shown in Table 5.1. This method is time consuming, and requires rapid measurement of the specimen weight after removal from the desiccator. This approach is useful for determining points on the WRC for high total suctions (greater than  $3500 \text{ kPa}$ ).

Table 5.1: Relative humidity and suction values for different saturated salt solutions

Chemical	$R_h$ (%)	Suction (kPa)
MgCl	33	151528
CuCl <sub>3</sub>	68	51909
KCl	84	23278
KSO <sub>4</sub>	97	3741

The desiccator chambers used in this study are hermetically sealed polycarbonate boxes with 3 shelves upon which soil specimens may be placed, as shown in Figure 5.13. A saturated salt solution is sealed within the desiccator chamber, and the relative humidity of the air within the desiccator chamber comes to equilibrium with the evaporation of water from the saturated salt solution. The air was mixed using a fan placed within the desiccator chamber. The relative humidity and temperature were measured using a Fischer Scientific<sup>®</sup> digital gauge. The specimens were allowed to equilibrate in the chamber for 3 months.



Figure 5.13: Desiccator cabinets in a fume hood

The WRC from the thermodynamic approach along with those from the physical approaches are shown in Figure 5.14. The suction is plotted on a logarithmic scale to capture the wide range of suction values obtained using the different tests. The matric suction results from the hanging column and pressure plate tests align well. The difference in suction values from the desiccator cabinet is likely due to variability and possibly due to osmotic suction effects. Approximately 6 months in total testing time was required to define this curve.

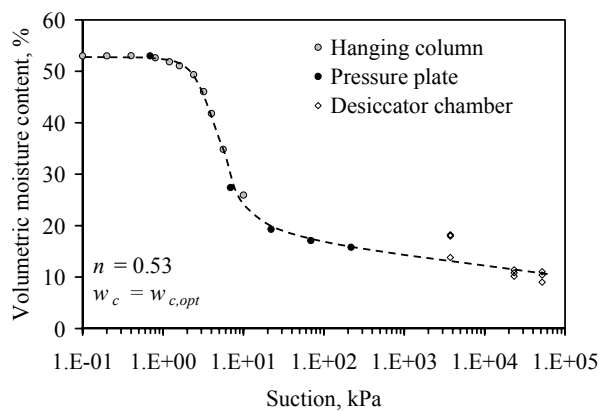


Figure 5.14: WRC from thermodynamic and physical techniques

### 5.3.5 Centrifuge Permeameter Techniques

Centrifuges were first used in the early 1900's to define the WRC by soil scientists (Briggs and McLane 1907; Gardner 1937) and petroleum engineers (Hassler and Bruner 1945; Hoffman 1963). Procedures for determination of the WRC with a centrifuge permeameter have been developed (ASTM 6836). In general, saturated soil specimens are placed in a permeameter with a high-air-entry ceramic plate as the outflow boundary. During centrifugation, the increased hydraulic potential causes water to exit the specimen through the ceramic while air enters the surface of the specimen. No inflow is supplied to the specimen, so flow from the soil is transient. The suction profile with height in the specimen can be defined if the suction at the bottom boundary is known and outflow has ceased (equilibrium). The equilibrium suction profile can be defined by setting both sides of the equation for discharge velocity [Equation (3.13)] equal to zero, signifying that flow has stopped. This implies that the total hydraulic potential is zero, and that the components are equal, as follows::

$$\frac{\partial \psi}{\partial z_m} = \rho_w \omega^2 (r_0 - z_m) \quad (5.5)$$

The suction distribution can be obtained by integrating Equation (5.5) with respect to  $z_m$ :

$$\psi(z_m) - \psi(0) = \int_0^{z_m} \rho_w \omega^2 (r_0 - x) dx \quad (5.6)$$

where  $\psi_0$  is the suction at the outflow boundary (zero for a saturated ceramic plate), and  $x$  is an integration variable. The suction distribution obtained when flow ceases is:

$$\psi(z_m) = \frac{\rho_w \omega^2}{2} [2r_0 z_m - z_m^2] + \psi(0) \quad (5.7)$$

The variation in the equilibrium suction profile with height is quadratic, but may be closer to a linear distribution when the specimen length  $L_m$  is small compared to  $r_0$ . The suction profile predicted from this approach is independent of the WRC and K-function. Suction profiles during steady-state flow and at equilibrium (no flow) are shown in



Figure 5.15(a) and Figure 5.15(b) for low and high values of  $\omega$ . Unlike the steady-state suction profile, the equilibrium suction profile increases steadily with  $z_m$ , and does not tend to a limiting value. Accordingly, selection of a representative suction value for definition of the WRC is not straightforward. Researchers have used the average suction, the suction at mid-height, and the suction at the soil surface. For the specimen geometry shown in Figure 5.15, the average suction and the suction at mid-height are nearly identical. ASTM D6839 recommends use of the suction at the soil surface.

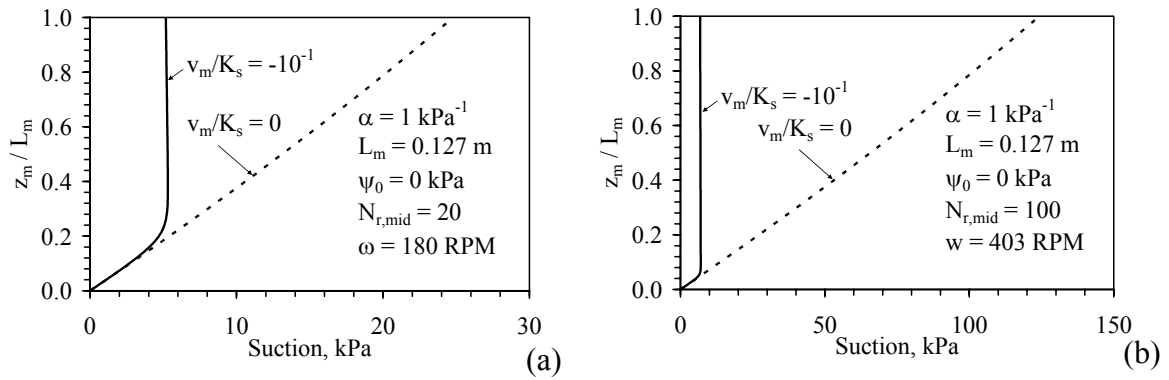


Figure 5.15: Steady-state and equilibrium suction profiles: (a) Low  $\omega$ ; (b) High  $\omega$

The average moisture content at different stages in a centrifuge test can be back-calculated using the measured outflow at the end of each stage and the final moisture content measured destructively at the end of testing. Analytical techniques can be used to associate the average moisture content (measured destructively after equilibrium is reached) with the suction to define the WRC (Forbes 1994). ASTM D6839 recommends correlating the average moisture content directly with a scaled value of the suction at the soil surface, although the scaling process is not described. Khanzode *et al.* (2002) obtained a WRC for a compacted silt using the ASTM D6839 approach, shown in Figure 5.16(a). The results were similar to those obtained using a Tempe cell, although the moisture content values at similar suctions were about 5% lower for the centrifuge

approach. This may have been due to the use of the average moisture content, although Khanzode *et al.* (2002) indicated that de-saturation of the bottom boundary may led to additional drying of the specimen. Data from an early paper by Gardner (1938) using the centrifuge technique are shown in Figure 5.16(b). Although Gardner claimed that the suction values were calibrated using filter paper measurements, the suction range obtained by Gardner is higher than those presented in the literature for similar soils (see Figure 2.3). A similar observation can be made in the results from Conca and Wright (1998), shown in Figure 5.16(c), who report suction values as high as 32000 kPa. This corresponds to  $N_{r,mid} = 26,000$  ( $\omega = 6500$  RPM), which is very high. For comparison, the analysis in Figure 5.15(b) indicates that a suction of 125 kPa corresponds to  $N_{r,mid} = 100$ .

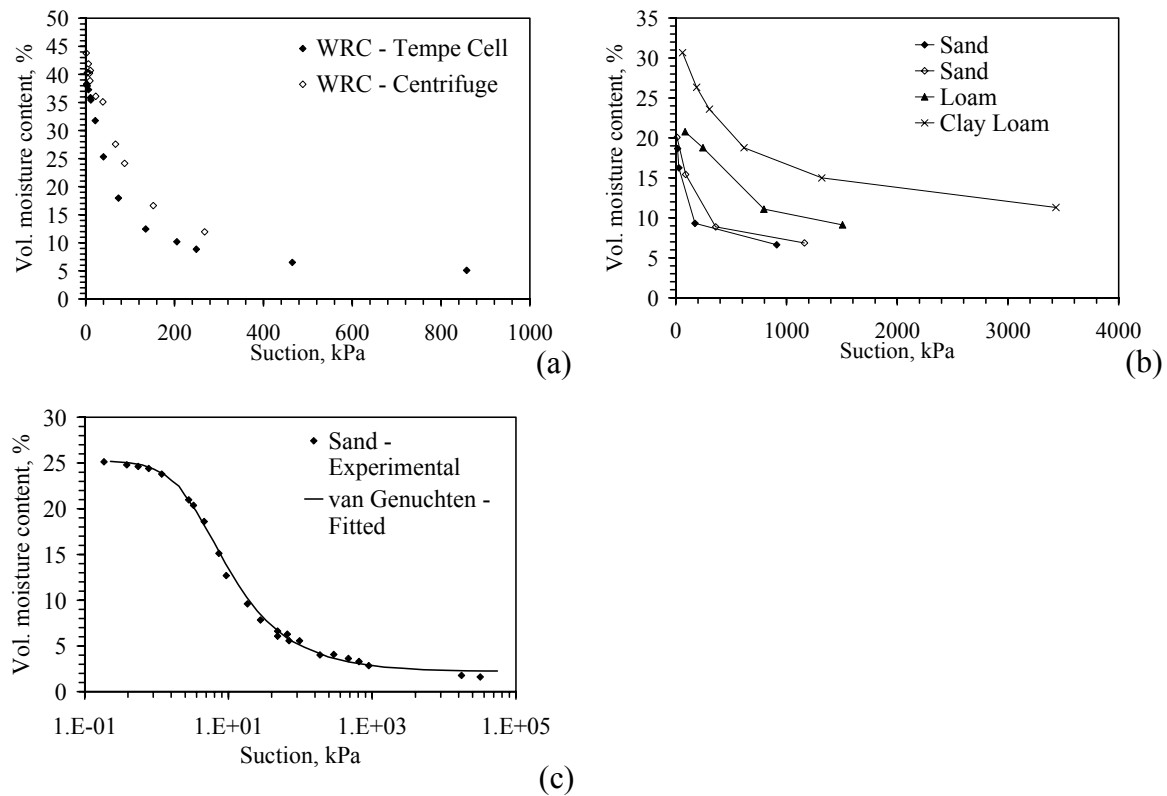


Figure 5.16: Centrifuge WRCs: (a) Khanzode *et al.* (2002); (b) Gardner (1938); (c) Conca and Wright (1998)

### **5.3.6 Summary of Experimental Techniques to Determine the WRC**

In summary, conventional techniques used to define the WRC require significant time to obtain limited data, different approaches may be needed for different suction ranges, several specimens may be required to obtain the full WRC, and the moisture content is typically measured destructively. Another issue that the approaches described above have in common is that they involve transient water flow. Specifically, a suction boundary condition is applied, and water flows until the suction profile within the specimen is in equilibrium with the boundary condition. This transient process often becomes slower with time, and may result in uneven distribution of moisture throughout the specimen (depending on its size). A problem specific to the use of porous ceramics in the axis translation approach is the diffusion of air across the ceramic. In general, most experimental approaches to determine the WRC lack of control of volume change during drying and wetting and have the inability to impose a stress state representative of field conditions. Historically, this is because the soil physicists who developed these techniques dealt with non-deformable surficial soils. However, this aspect is important for geotechnical engineers, who deal with deformable soils like peat and clays of high plasticity, and must consider situations where changes in stress occur.

The effect of porosity on the WRC of the clay was also investigated using pressure plate and filter paper tests. The experimental data, along with fitted curves given by the van Genuchten model are shown in Figure 5.17. The van Genuchten-Mualem parameters for these WRC are shown in Table 5.2. The ordinate intercept of each WRC corresponds to the porosity of the specimens. The WRCs have similar shapes except at low suctions. The denser specimens tend to have slightly higher moisture storage at high suctions than the loose specimens. This suggests that the rationale that loose soils have

higher moisture storage capacity, often advocated in the design of alternative covers, may not be the case for a wide range of suction.

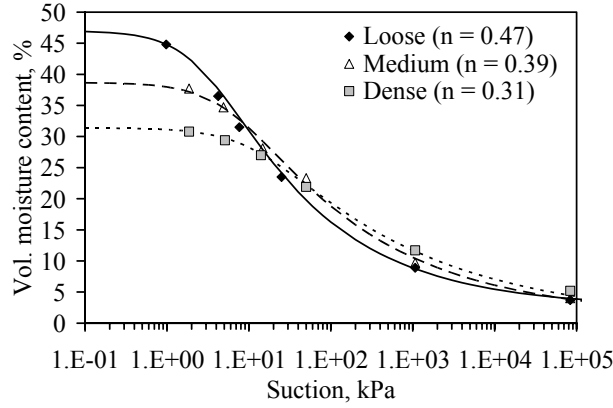


Figure 5.17: WRC results for soil with different porosities

Table 5.2: van Genuchten-Mualem (1980) parameters for CL clay and geotextile

Specimen name	$w_c$ (%)	Porosity $n$ (%)	$\theta_r$ (%)	$\alpha$ (kPa <sup>-1</sup> )	N	$K_s$ (m/s)
Nonwoven geotextile	N/A	99.1	2.0	1.70	6.00	3.3E-02
Low PI clay	11.8	47.0	2.5	0.33	1.33	4.7E-06
Low PI clay	12.0	38.7	0.9	0.16	1.27	1.2E-07
Low PI clay	11.9	31.4	0.3	0.08	1.23	1.7E-09

The possibility of a capillary break effect between a fine-grained soil (such as the CL clay described in this chapter) and an underlying coarse material (such as an outflow support platen) was discussed in Section 3.5. A capillary break will impact the moisture profiles in the soil during infiltration (McCartney *et al.* 2007b). A comparison between the WRCs for the CL clay and different outflow boundary materials is shown in Figure 5.18. Assuming the geotextile is initially dry, and the compacted soil has an initial suction of 120 kPa, water will flow from the soil into the geotextile after the suction at the interface is reduced to about 1 kPa. This corresponds to the point at which the nonwoven geotextile increases in saturation from residual conditions.

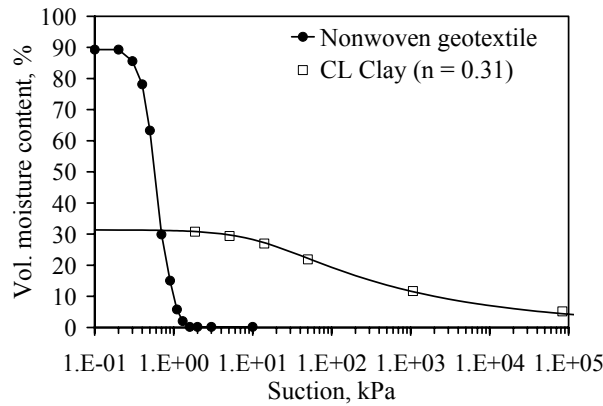


Figure 5.18: Comparison between WRC of CL clay and nonwoven geotextile

## 5.4 HYDRAULIC CONDUCTIVITY FUNCTION (K-FUNCTION)

### 5.4.1 Overview

Several techniques have been proposed for direct determination of the K-function in the laboratory (Benson and Gribb 1997). However, as a first approach the K-function for RMA Soil Type II was predicted from the shapes of the experimentally-derived WRCs using the van Genuchten-Mualem model, shown in Figure 5.19 as functions of suction and volumetric moisture content. The ordinate intercept of the K-functions in Figure 5.19(a) reflects the hydraulic conductivity of saturated specimens. Because the suction is continuous at the interface between a soil and geotextile, the intersections between the K-functions in Figure 5.19(a) may provide an indication of the breakthrough suction. The K-function for the nonwoven geotextile indicates that once capillary break occurs from the soil into the geotextile (around 1 kPa), the geotextile will provide little impedance to flow, as its hydraulic conductivity is much greater than that of the soil. However, because the moisture content is not continuous at the interface between two materials, the intersections between the K-functions shown as a function of moisture content in Figure 5.19(b) cannot be used to predict the breakthrough moisture content.

The van Genuchten-Mualem model tends to show a slight up-turn in the K-function at moisture contents near the porosity, which may not be realistic.

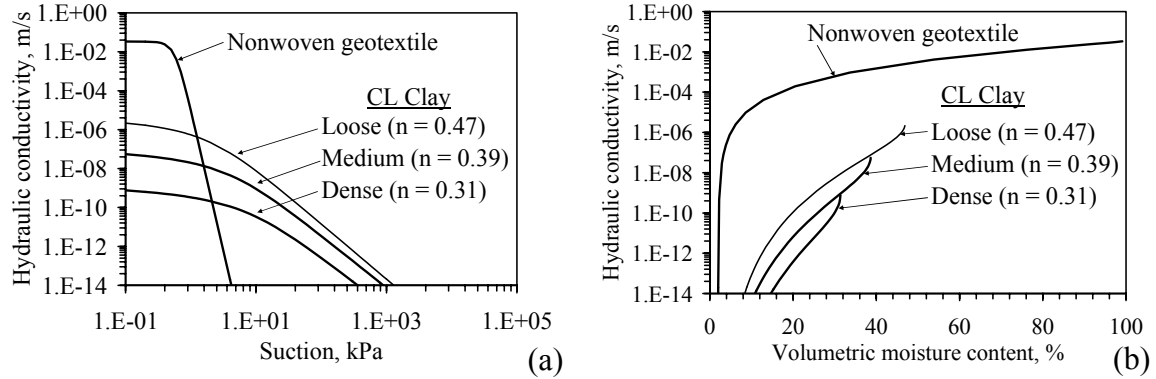


Figure 5.19: K-functions predicted from the WRCs in Figure 5.17 and Figure 5.18

#### 5.4.2 Measurement of Outflow during WRC Tests

The K-function can be defined using the pressure plate or hanging column approaches (Benson and Gribb 1997). These approaches require careful measurement of outflow during an axis translation test, and must account for the impedance to flow due to the ceramic and the impact on volume measurement of air diffusion through the ceramic. The most commonly used technique is the multi-step outflow method, which involves the application of pressure increments selected to ensure a measurable amount of water outflow (Parker *et al.* 1985; Wildenschild *et al.* 2001). Several assumptions have been used to infer the K-function from the outflow results, including analytical techniques (Gardner 1956) and inverse solutions (Eching and Hopmans 1993; van Dam *et al.* 1994). There are other variations of this method that involve either smooth increases in air pressure or a single abrupt pressure increment, but the results of these methods are difficult to interpret and may cause soil volume changes (Butters and Duchateau 2002).

The multi-step outflow method involves calculation of the hydraulic conductivity using a solution to Fick's second law of diffusion, given by:

$$\frac{\partial \psi}{\partial t} = D \frac{\partial^2 \psi}{\partial z^2} \quad (5.8)$$

where  $D$  is a constant equal to:

$$D = K \frac{d\psi}{d\theta} \quad (5.9)$$

Gardner (1956) obtained an analytical solution to Equation (5.8) with time:

$$\ln\left(\frac{V_{\infty} - V}{V_{\infty}}\right) = \ln\left(\frac{8}{\pi^2}\right) - \frac{D\pi^2 t}{4L^2} \quad (5.10)$$

where  $V$  is the outflow time series during an applied suction increment,  $V_{\infty}$  is the final cumulative outflow value,  $L$  is the length of the specimen, and  $t$  is time. Accordingly, a plot of the left-hand-side of Equation (5.10) versus time for an applied suction increment leads to a linear relationship with a slope equal to  $D\pi^2/4L^2$  and intercept  $\ln(8/\pi^2)$ . Using the value of  $D$  and the slope of the WRC obtained from the pressure plate test, the hydraulic conductivity for the suction increment can be obtained using Equation (5.9). This approach is prone to significant errors at low moisture contents, where the diffusivity  $D$  is known to be variable (Hillel 1980). This analytical procedure relies on several simplifying assumptions (Benson and Gribb 1997), which include: (i) constant  $K$  over the applied suction increment, (ii) negligible flow of water due to gravity, (iii) homogeneous and rigid soil, and (iv) negligible impedance to outflow from the specimen due to the porous stone.

The first three assumptions are valid for small specimens, small suction increments, and soils with low plasticity index. The fourth assumption is the main shortcoming of this method, as the small value of the hydraulic conductivity of the stone indicates that it may have a significant impact on the hydraulic conductivity values measured using the multi-step outflow approach. For example, the hydraulic conductivity of a ceramic plate obtained from SoilMoisture, Inc. (having an air-entry value of 300

kPa) is  $2.5 \times 10^{-9}$  m/s. Several approaches have been developed to account for the change in impedance due to the hydraulic conductivity of the porous stone. For instance, Kunze and Kirkham (1962) provide an approach to consider the impedance of the outflow plate, but their approach involves complex graphical techniques that often yield scattered results (McKelvey 1964). The impedance of the outflow plate has been the major drawback of this approach, so Gardner's approach is not used frequently in practice.

The multi-step outflow method was performed using the pressure plate data outflow data (presented in Figure 5.8). The left-hand-side of Equation (5.10) is shown as a function of time in Figure 5.20. A linear relationship with a slope of  $D\pi^2/4L^2 = -0.15$  is observed. The intercept is -0.01, which is smaller than the theoretical value of  $\ln(8/\pi^2) = -0.21$ , indicating that the plate impedance is high. This was also found to occur for higher suction increments where outflow is small.

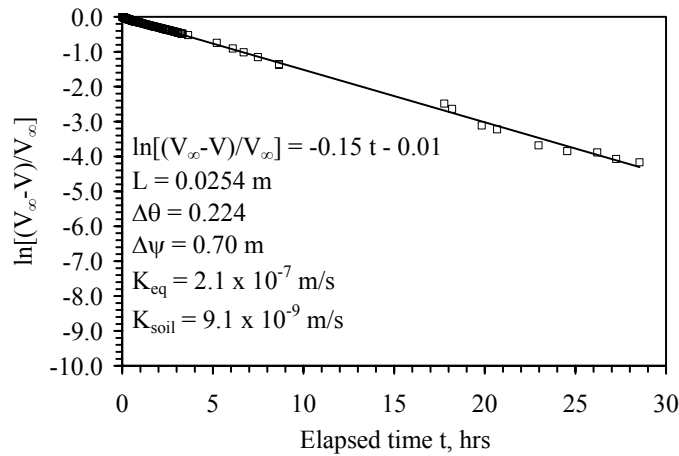


Figure 5.20: Multi-step outflow analysis results for a suction increment of 7 kPa

Using the value of  $D = 3.9 \times 10^{-5}$  m<sup>2</sup>/hr calculated from the data in Figure 5.20 and the WRC slope ( $\Delta\theta/\Delta\psi = 0.32 \text{ m}^{-1}$ ), the hydraulic conductivity for the suction increment was obtained using Equation (5.9). This can be repeated for other suction increments to



define the K-function, as shown in Figure 5.21. The predicted K-function from the WRC of the loose specimen ( $n = 0.53$ ) in Figure 5.17 is also shown. The  $K$  values at low moisture contents are much higher than those predicted from the van Genuchten model. This is likely both because the van Genuchten model does not provide a good prediction, and the experimental K-function is affected by the outflow platen.

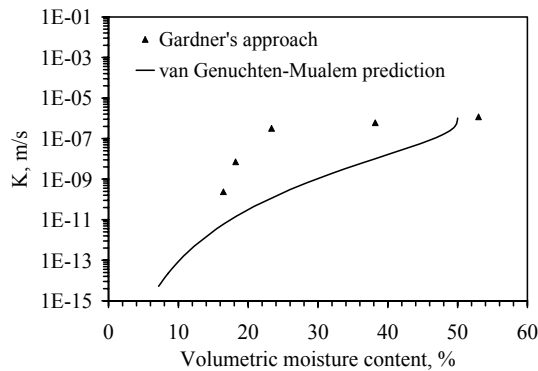


Figure 5.21: K-function results from pressure plate results

### 5.4.3 Infiltration or Evaporation Techniques

#### 5.4.3.1 Overview

A simple alternative used to alleviate the testing problems observed in the multi-step outflow method is the measurement of the K-function during moisture flow through a specimen confined within a column or permeameter (Moore 1939; Richards 1952). Flow is applied to one end of the soil using either a system of saturated ceramics or a flow pump. A typical setup used to measure the K-function is shown in Figure 5.22 (Meerdink *et al.* 1996; Stormont and Anderson 1999; Lu and Likos 2005; McCartney *et al.* 2005). Moisture content and suction time series are measured with distance through the soils during infiltration. The data can either be analyzed from the transient infiltration data or from the steady-state moisture profiles to determine the K-function. Problems

specific to K-function determination using column testing include outflow boundary effects on the suction distribution in the soil column (capillary break) and difficulties in uniformly distributing fluid from pumps to the specimen.

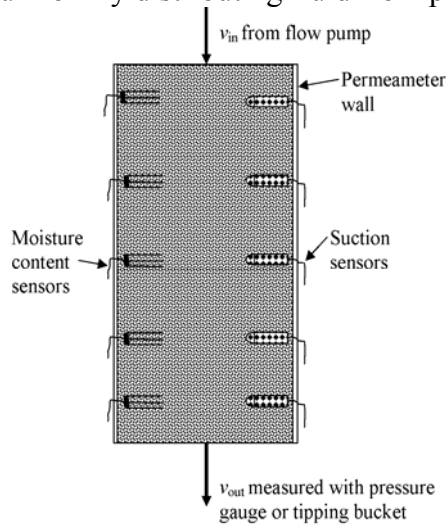


Figure 5.22: Infiltration/evaporation column

#### 5.4.3.2 Steady-State Analysis of Infiltration Data

During steady vertical infiltration with a deep water table, a unit hydraulic gradient (*i.e.*,  $i = 1$ ) is typically observed in the soil profile, which means that the suction does not change with depth and water flow is driven only by gravity. In this case, the hydraulic conductivity equals the imposed steady-state discharge velocity. Points on the K-function can be obtained by changing the imposed flow. Steady state approaches yield repeatable results, but require significant testing times. As will be shown, this is especially the case for measurement of low hydraulic conductivity values in dense soils and clays (where very low flow rates must be imposed).

#### 5.4.3.2 Transient Analysis of Infiltration Data

The most commonly approach to determine the K-function from transient infiltration data is the instantaneous profile method (Watson 1966). This approach can

either involve surface evaporation from an initially saturated soil specimen placed on a laboratory scale (Wendroth *et al.* 1993) or infiltration into an initially dry soil (Hamilton *et al.* 1981; Meerdink *et al.* 1996). The approach may require significant time, and requires good control of the temperature and humidity in the laboratory. This analysis is a discretization of Darcy's law for vertical flow:

$$K_j = \frac{\Delta V_j}{A \Delta t} \left( \frac{-1}{\left( \frac{\Delta h}{\Delta z} \right)_j} \right) \quad (5.11)$$

where  $z$  is the height from the specimen base,  $\Delta V_{w,i}$  is the volume of water that has passed a point  $j$  in the soil profile during an time interval  $\Delta t$ ,  $A$  is the cross-sectional area of the specimen, and  $h$  is the total hydraulic head at a point  $j$ , equal to:

$$h_j = z_j - \frac{\psi_j}{\rho_w g} \quad (5.12)$$

The gradient term in Equation (5.11) can be calculated at each point as follows:

$$i_j = \left( \frac{\Delta h}{\Delta z} \right)_j = -1 - \frac{1}{\gamma_w} \left( \frac{\psi_j - \psi_{j-1}}{z_{j-1} - z_j} \right) \quad (5.13)$$

where  $j = 0$  at the upper soil surface, which is at a constant suction value during infiltration. For vertical downward infiltration, the position  $j$  increases with depth from the surface. The gradient is typically large during transient infiltration into a compacted soil (*i.e.*, with an initial suction typically greater than 150 kPa).

The suction values in Equation (5.13) can be measured using tensiometers or heat dissipation units. However, this approach may lead to significant errors in the calculation of the K-function. For instance, there may be timing issues related to the measurement of suction using tensiometers. Water must flow into or out of the tensiometer as the suction in the soil changes, resulting in a time delay that may not correspond to TDR measurements of  $\Delta V_w$ . Further, heat dissipation units may not provide adequate resolution

at low suction values (< 20 kPa) that occur during infiltration. However, heat dissipation units provide an excellent alternative if evaporation were used instead of infiltration.

Alternatively, the gradient can be inferred from moisture content data measured using TDR by calculating the suction values from the WRC. Hysteresis in the WRC may result in some uncertainty. Specifically, infiltration occurs along a wetting hysteresis scanning curve in the WRC, so using either the primary wetting or drying path WRCs may lead to some uncertainty. Alternatively, the transient WRC can be defined using simultaneous tensiometer and TDR measurements of suction and moisture content.

During a given time interval  $\Delta t$ , the volume of water downstream from a given point can be obtained by integrating the water content profile, as follows:

$$\Delta V_{w,j}^k = A \sum_{i=1}^n (\theta^k - \theta^{k-1}) (z_{j+1} - z_j) \quad (5.14)$$

where  $k$  represents the current time step, and  $n$  is the total number of points.

#### **5.4.3.4 Infiltration Test Results**

The infiltration column used in this study to determine the K-function for RMA Soil Type II is a PVC column permeameter. The column, shown in Figure 5.23, has an inside diameter of 203 mm. The large diameter was selected to minimize the impact of any leakage along the side wall of the permeameter, allow placement of sensors, and provide a large area of water flow. A soil profile having thickness of 0.75 m is presented in this chapter to show how the K-function can be calculated using the instantaneous profile method, although several other columns tests were performed (McCartney *et al.* 2005; McCartney and Zornberg 2007a; 2007b). The length of this profile minimizes the outflow boundary effects on the moisture content profile during infiltration. During infiltration, volumetric moisture content values at different points in the soil column were inferred using time domain reflectometry (TDR). TDR is discussed in detail in Chapter 6.

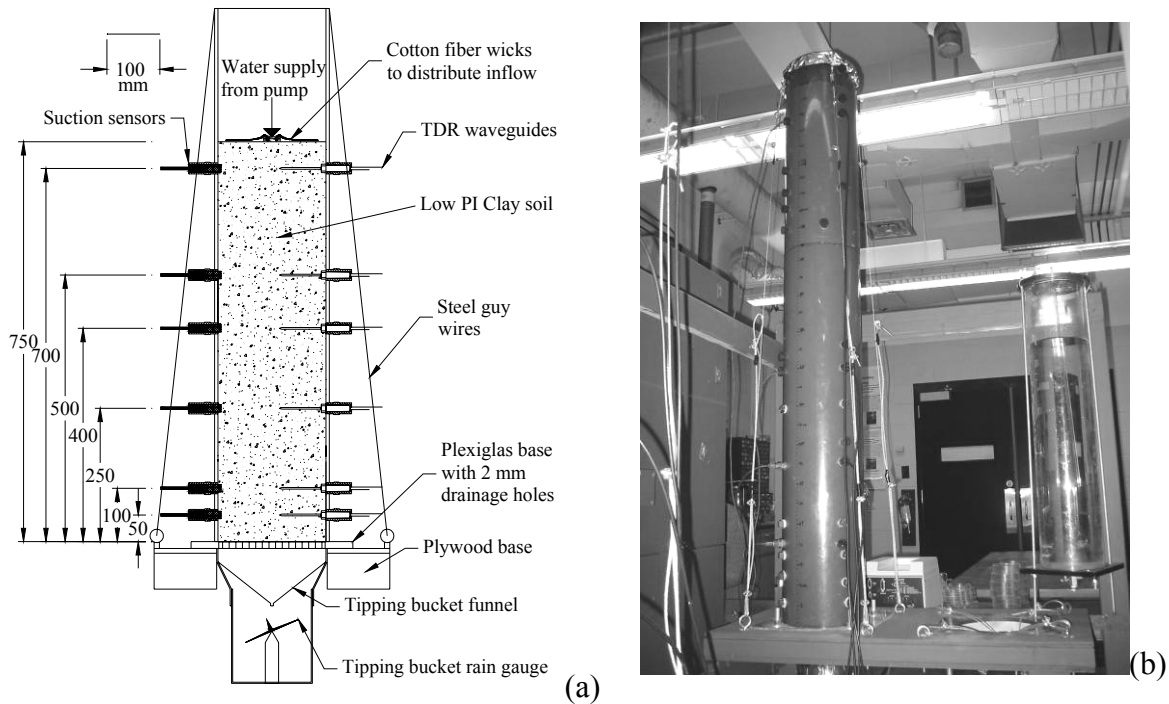


Figure 5.23: Soil infiltration column: (a) Schematic; (b) Picture of a column test

The large size of the columns required several custom-built components to provide hydraulic sealing and a sturdy working environment during preparation of the soil profile. The PVC columns were attached to the frame using tensioned wires. The wires were attached to eye bolts affixed to a plywood support, and hook bolts were placed over the top edge of the column. A turnbuckle was used to tension the wire. The base of the column rests on an acrylic plate with a 195 mm diameter honey-comb pattern of 2 mm holes. The base of the column rests on an acrylic plate with a 195-mm diameter pattern of 1.6 mm holes honey-comb arrangement, as shown in Figure 5.24(a). This acrylic plate was intended to serve as a freely-draining lower boundary to the soil column. The column was sealed to the acrylic plate using an o-ring placed within a groove in the base of the column, shown in Figure 5.24(b).

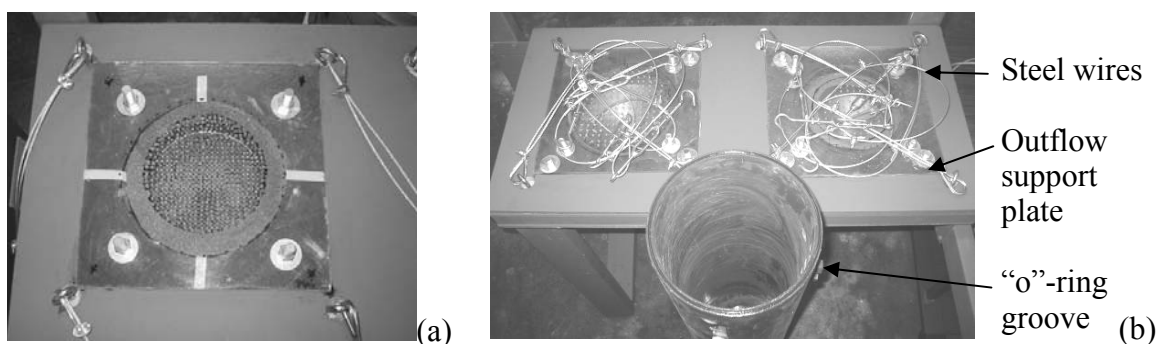


Figure 5.24: (a) Outflow support plate; (b) O-ring seal at the base of the column

A constant water flow rate was applied to the top surface of the soil using a Masterflex® L/S peristaltic pump. The pump functions by compressing a nylon tube against a series of 6.35 mm rolling barrels on a circular frame. The circular frame is rotated about its center by a motor at a constant rate. Small packets of water are trapped in the tube between each rolling barrel, providing a pulsing flow rate. The connection between the tubing and the pump is frictional, so the tubing was refreshed every 3 weeks to prevent changes in the flow rate due wear. The height of water in a 1000 ml graduated cylinder was monitored as a backup. The inflow supply setup is shown in Figure 5.25.



Figure 5.25: Peristaltic pump with graduated cylinder as an inflow reservoir

Due to the low flow rates used in this portion of the study (approximately 10 ml/min), special care was taken to achieve uniform distribution of the fluid over the area

of the column. Specifically, the fluid was distributed across the top of the of the soil surface using a radial assembly of fabric wicks. The inflow line from the peristaltic pump was placed within a small cup at the center of the soil area. Fabric wicks were distributed over the soil surface with one end resting in the cup. In some tests a small confining weight was placed on the wick to improve contact with the soil. Measurements of the moisture content at locations across the soil surface indicate that the water distribution is relatively uniform. A picture of the inflow distribution system for the columns is shown in Figure 5.26(a), while a schematic is shown in Figure 5.26(b).

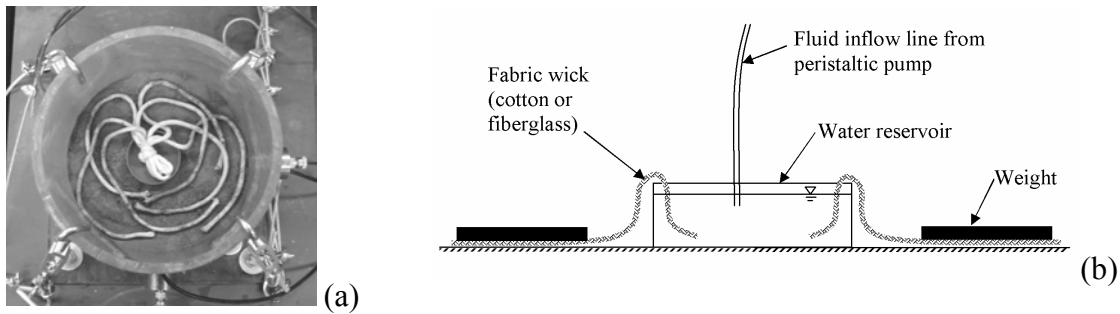


Figure 5.26: (a) Inflow distribution system; (b) Schematic of inflow distribution system

Outflow from the soil profiles was measured using tipping bucket rain gauges. The water passing through the outflow support plate collected in a brass funnel connected to the tipping bucket gauge. The tipping bucket gauge shown in Figure 5.27(a) is a triangular, double-sided bucket that rests upon a pivot. Water dripping from the funnel is channeled into the upper half of the bucket. After a certain volume of water has dripped into the upper bucket, the moment due to the weight of the water causes the bucket to tip on the pivot. The timing of each tip is recorded as a digital signal. Water then drips into the other side of the bucket, and the process is repeated. For redundancy the outflow was also collected in a 1000 ml graduated cylinder, as shown in Figure 5.27(b).

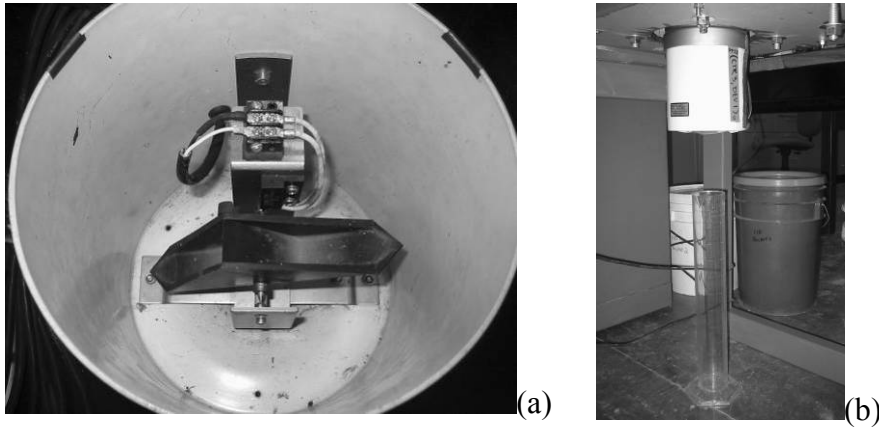


Figure 5.27: (a) Tipping bucket gauge; (b) Tipping bucket with graduated cylinder

Before placement of soil within the column, a thin film of vacuum grease was placed on the inside wall of the column. This was intended to minimize side-wall leakage during infiltration and minimize friction during compaction. Moisture conditioned soil was then compacted in 25 mm lifts using the piston compactor to a porosity of 0.50. TDR waveguides were installed within the middle of lifts during compaction. A rubber stopper with a central hole was used to provide a seal between the TDR wiring and the column. The heights of the TDR waveguides for the different profiles are shown in Figure 5.23(a). The waveguides were initially placed in the loose lift with a slight upward orientation so that they would be horizontal after compaction. Post-test exhumation indicated that this was the case.

The inflow and outflow volumes of water for the soil profile are shown in Figure 5.28. Two inflow stages were used in this study. The first inflow stage involved application of a constant inflow rate of  $8 \times 10^{-8}$  m/s until steady-state seepage was observed, which required about 1500 hrs. The second inflow stage involved application of a higher rate of  $1.5 \times 10^{-7}$  m/s, and continued until steady seepage was observed, after about 2000 hrs. The progression of the wetting front during infiltration is shown in



Figure 5.29. This figure indicates that approximately 550 hrs were required for the wetting front to reach the base of the profile. However, the tipping bucket data in Figure 5.28 indicates that outflow did not occur until 950 hrs. This is because water did not exit from the soil until the base of the profile was nearly saturated due to the capillary break effect. A capillary break forms when there is a contrast in pore sizes at an interface, (*i.e.*, the fine-grained CL clay placed atop the relatively large holes in the outflow platen).

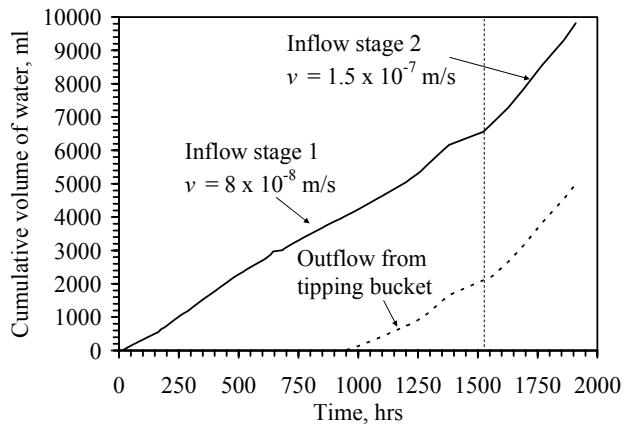


Figure 5.28: Inflow and outflow data for column test

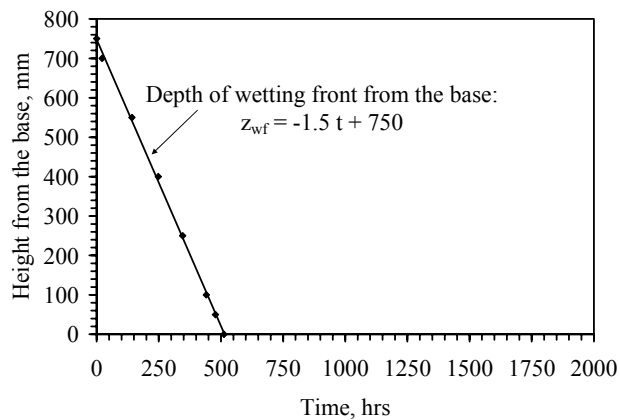


Figure 5.29: Wetting front progression for column test

The moisture content time series inferred from the six TDR waveguides are shown in Figure 5.30. At the beginning of testing, the moisture content in the column is uniformly equal to 14.7% (corresponding to the molding gravimetric water content of 10.7%). As the wetting front passes through the profile, the moisture content measured by TDR increases gradually to approximately 23.5%. After the wetting front reaches the base at a time of 520 hrs (see Figure 5.29), the TDR measurements indicate that moisture begins to accumulate in the lower portion of the profile. The moisture content begins to progressively increase with height in the column up to a height of 500 mm. By the time outflow is collected from the base of the column, the moisture content at a height of 50 mm from the base is 40% (degree of saturation of 0.81). The final gravimetric moisture content at the base after testing was 47% (nearly saturated). During accumulation of moisture at the base of the profile, the upper portion of the profile was relatively unaffected by the boundary, and is only influenced by on going infiltration. For instance, when the infiltration rate was increased after 1500 hrs, the moisture content at 700 mm only increased from 23.5 to 25.4%.

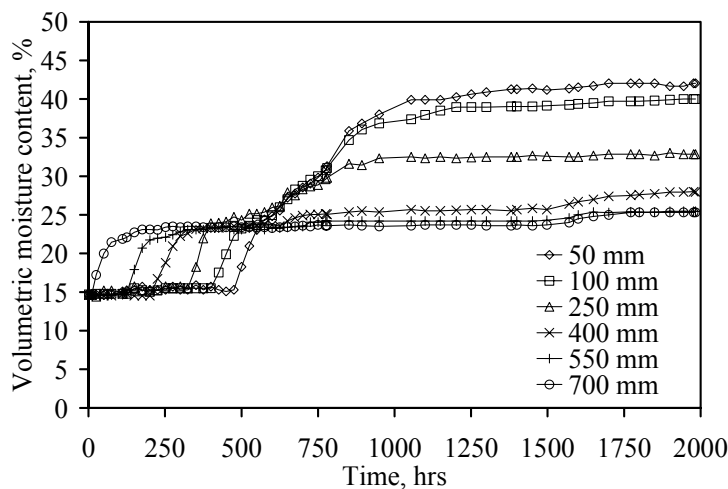


Figure 5.30: Moisture content time series for sensors located at various elevations

The data shown in Figure 5.30 can be interpreted using isochrones of moisture content with height in the permeameter, shown in Figure 5.31. The moisture front gradually progresses vertically downward through the profile at a moisture content of 23.5%. Accumulation of moisture at the base of the profile after 550 hrs is indicated by a bulge in the moisture profile at the base. The steady-state moisture content at the top of the profile is 23.5% after 1200 hrs for the first infiltration rate, and 25.4% after the second infiltration rate. During these two stages, it is clear that a unit hydraulic gradient develops in the upper portion of the soil profile (*i.e.*, the suction does not change with height). In this case the hydraulic conductivity equals the applied flow rate.

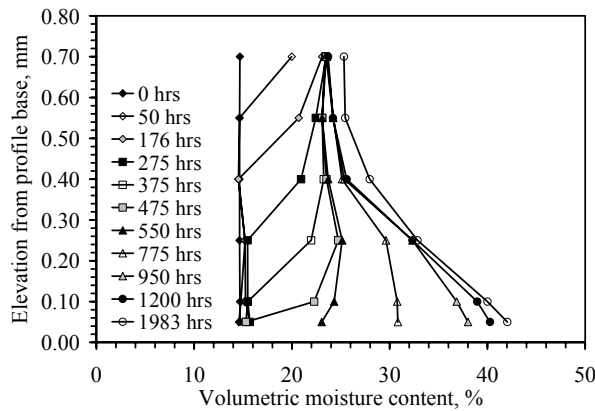


Figure 5.31: Moisture content profiles

The suction measurements in this column were made with heat dissipation units. As will be discussed in Chapter 5, heat dissipation units were unreliable for measurement of suctions less than 50 kPa. Accordingly, the suction time series was predicted from the moisture content time series using the van Genuchten model parameters for the dense specimen ( $n = 0.37$ ) in Table 4.2. The suction time series shown in Figure 5.32 indicates that the initial suction in the profile is approximately 166 kPa. After reaching steady-

state infiltration, the suction in the upper portion of the specimen was about 20 kPa, while the suction at the base was approximately 3 kPa (near saturation).

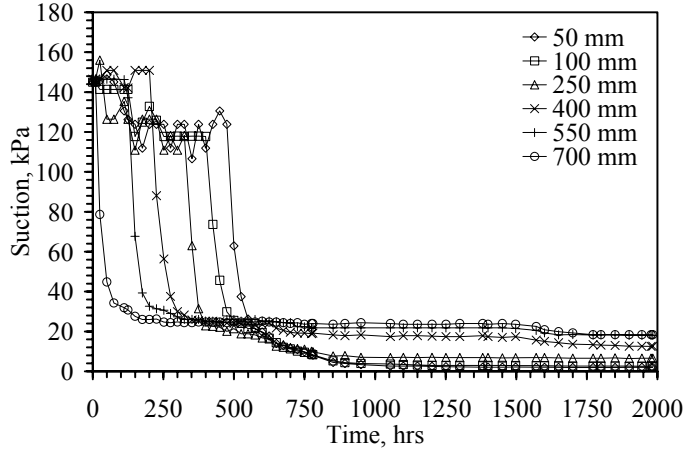


Figure 5.32: Predicted suction time series

Fluctuations in the suction have a large effect on the values of  $K$  calculated from the instantaneous profile approach as the gradient is in the denominator of the equation to predict  $K$  [Equation (5.11)]. Also, the gradient is the difference between two large suction values, which tends to cause increased variability. Fluctuations in the measured moisture content time series were found to lead to negative or underestimated values of  $\Delta V_{w,i}$ . This led to low calculated  $K$  values. An approach to improve these shortcomings of the instantaneous profile method calculations is to fit a smooth function to the moisture content and suction time series. The initial portion of the moisture content time series are the most useful for transient flow calculations, as there is a transition from dry soil to wet soil without the influence of the bottom boundary on the moisture profile. The initial portions of the curves follow an S-shaped curve, which is well represented by a sigmoid curve. The sigmoid curve used for matching the moisture content time series is:

$$\theta(t) = \frac{1}{a + be^{-ct}} \quad (5.15)$$

where  $t$  is time,  $e$  is the base of the natural logarithm, and  $a$ ,  $b$ , and  $c$  are shape parameters. The shape parameter  $a$  may be calculated as:

$$a = \frac{1}{(\theta_{\max} - \theta_{\min})} \quad (5.16)$$

where  $\theta_{\max}$  and  $\theta_{\min}$  are the maximum and minimum moisture contents in an S-shaped time series. If  $c$  is selected to fit the experimental data, then  $b$  can be calculated as:

$$b = \frac{a}{t_{\Delta} c} \quad (5.17)$$

where  $t_{\Delta}$  is the time when the moisture content transitions from dry to wet. The sigmoid-fitted moisture content and suction data are shown in Figure 5.33(a) and Figure 5.33(b).

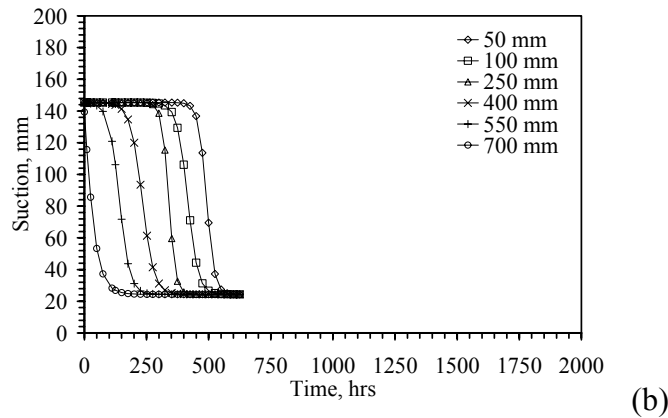
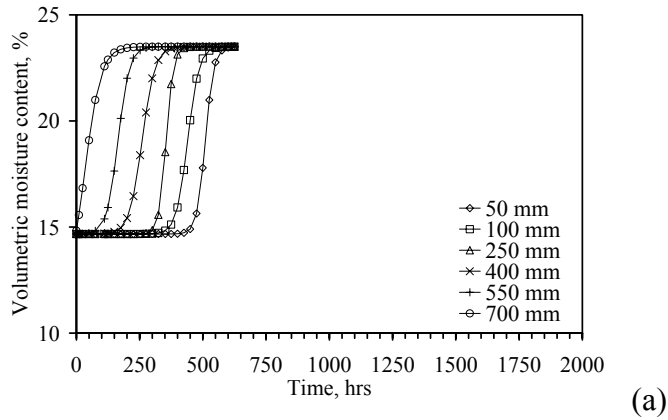


Figure 5.33: Sigmoid curve fitting from data collected in infiltration column tests at various elevations: (a) Moisture content; (b) Suction

These curves are only shown until 550 hrs, when the wetting front reaches the base of the profile. The fitted time series may be used to calculate the K-function with the instantaneous profile method, as shown in Figure 5.34. The K-function calculated using the fitted data and the instantaneous profile method shows some scatter, but a well-defined trend is observed. No negative  $K$  values were calculated after smoothing the data using a sigmoid fitting, and the calculated gradient values were consistent. The van Genuchten-Mualem model K-function prediction is also shown in Figure 5.34, although it cannot be strictly compared with the data from the instantaneous profile method because the WRC was used to calculate the suction values in the gradient term. The K-function data from the steady-state infiltration data is several orders of magnitude greater than the predicted K-function. The transient and steady-state K-functions do not match well as the drying-path WRC was used to calculate the suction values. A K-function was drawn to fit the steady-state  $K$  data and the transient  $K$  data at low moisture contents.

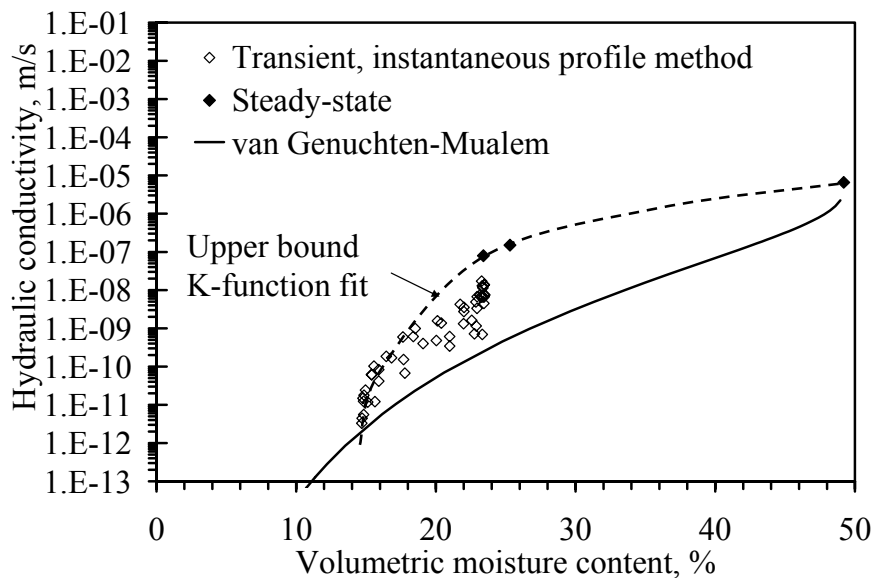


Figure 5.34: K-function calculated using steady-state and transient column test data

Several other large-scale column tests were conducted, and are reported elsewhere (McCartney *et al.* 2005; McCartney and Zornberg 2007a; McCartney and Zornberg 2007b). These tests were conducted to simulate the performance of alternative landfill covers, so the density of the soil is generally looser than that used in the centrifuge permeameter testing program (presented in Chapter 7). However, the lessons learned from these tests are still useful to evaluate the benefits of the centrifuge permeameter (*e.g.*, testing times, shapes of the WRCs and K-functions, outflow boundary effects). In all tests, a constant infiltration rate was applied to the top of an initially dry (as-compacted) soil column. The column geometry, inflow boundary conditions (steady infiltration rate), outflow boundary conditions, and soil densities are summarized in Table 5.3. The testing times for the column tests range from a week to several months. As expected, the time required to reach steady-state water flow increases with height of the soil column as well as with the magnitude of the imposed infiltration rate. Further, this time is greater for looser soils due to their greater moisture storage capacity.

The moisture content and suction at the wetting front were measured near the top of the soil profile, and are assumed to represent the moisture content associated with the imposed infiltration rate through an initially dry soil (*e.g.*, before any outflow boundary effects are observed). The steady-state moisture content and suction values are those measured near the top of the soil profiles after the outflow rate equals the infiltration rate. The boundary condition did not have an effect on the moisture content and suction in the top portion of the longer columns (tests C, D, E), so the moisture content and suction at the wetting front are the same as those at steady-state. In these longer columns, the moisture content and suction were observed not to vary with height in the upper portion of the specimen (consistent with Figure 3.3). In this case, the imposed infiltration rate  $v$  is equal to  $K$  at steady-state, as the gradient in hydraulic head in Darcy's law equals 1.0.

Table 5.3: Summary of column infiltration test results

Column test - stage number	Soil height (mm)	Porosity	Compaction water content (%)	Inflow discharge velocity (m/s)	Outflow boundary condition	Wetting front		Steady-state	
						$\theta$ (%)	$\psi$ (kPa)	$\theta$ (%)	$\psi$ (kPa)
A*	300	0.50	8.0	2.0E-07	Nonwoven geotextile	26.9	N/A	37.0	N/A
B*	300	0.50	8.0	2.0E-07	Monterey sand	27.0	N/A	38.9	N/A
C-1*	750	0.47	11.0	8.00E-08	Filter paper/screen	23.4	N/A	23.5	N/A
C-2*	750	0.47	11.0	1.50E-07	Filter paper/screen	25.4	N/A	25.4	N/A
D-1**	1350	0.48	10.5	3.4E-08	Nonwoven geotextile	24.7	N/A	24.7	N/A
D-2**	1350	0.48	10.5	6.0E-08	Nonwoven geotextile	25.6	N/A	25.6	N/A
E-1	1500	0.47	10.5	3.4E-08	Filter paper/screen	24.7	N/A	24.7	N/A
E-2	1500	0.47	10.5	6.0E-08	Filter paper/screen	26.1	N/A	26.1	N/A
F***	135	0.50	10.8	3.50E-08	Nonwoven geotextile	21	11	41	3.64
G***	135	0.43	11.2	3.50E-08	Nonwoven geotextile	22.4	10	37	3.7
H***	135	0.37	10.5	3.50E-08	Nonwoven geotextile	22	11	30	6.5
I**	135	0.44	11.4	8.50E-08	Nonwoven geotextile	26.5	8	36	4

\* McCartney *et al.* (2005)

\*\* McCartney and Zornberg (2007a)

\*\*\* McCartney and Zornberg (2007b)

## 5.4.4 Centrifuge Permeameter Techniques

### 5.4.4.1 Determination of the *K*-function with Transient Water Flow

Similar to 1-g characterization approaches, both transient and steady-state water flow have been used to determine the *K*-function. Centrifuge approaches were used to define the *K*-function using transient water drainage data from an initially saturated specimen (Nimmo 1990; Singh *et al.* 2001). This approach does not require control of



the inflow into the specimen. The outflow from the specimen is inferred by periodically measuring outflow volume and changes in the specimen mass. The amount of outflow typically decreases with time during centrifugation. The K-function can be determined by matching of the outflow (or moisture content) data with results of a direct numerical solution of Richards' equation using assumed hydraulic characteristics (Nimmo 1990) or using inverse analysis (Simunek and Nimmo 2005). Although transient drainage tests are simple from an experimental point of view, the use of direct and inverse analysis for interpretation of the hydraulic properties relies on several assumptions. Specifically, the models for the WRC and K-function used in the analysis are assumed to have the same shape as the hydraulic characteristics being measured. It is also assumed that the specimen has negligible outflow boundary impedance and is rigid and homogenous.

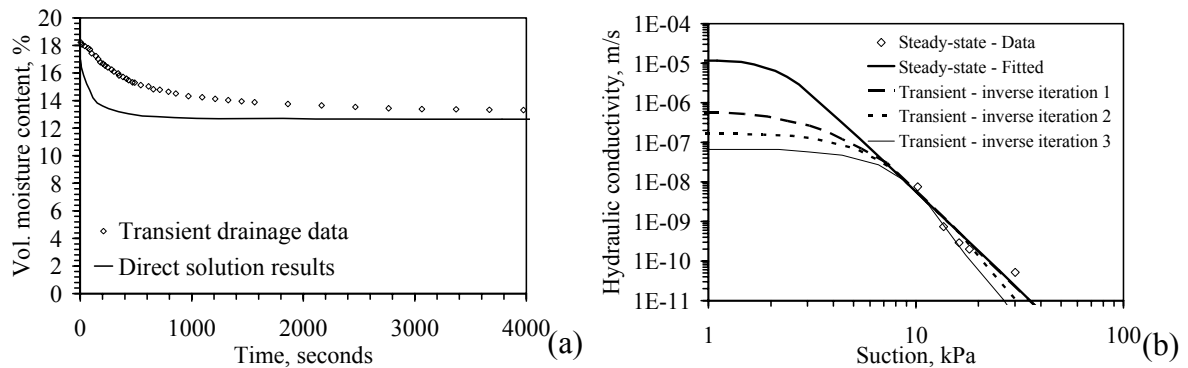


Figure 5.35: (a) Transient drainage data with direct solution using assumed properties (Nimmo 1990) (b) K-function from inverse analysis of drainage data (Simunek and Nimmo 2005)

Typical transient drainage and direct modeling results are shown in Figure 5.35(a). The best-fit modeling results do not match the experimental data well, implying that the assumptions in the analysis are not valid. K-functions from different iterations of an inverse analysis are shown in Figure 5.35(b) along with a steady-state data for the same soil. Although the inverse analysis results provide similar a similar K-function

slope to the fitted K-function, the steady-state results fall into a narrow range of suction, making the comparison difficult to assess.

#### ***5.4.4.2 Determination of the K-function with Steady-State Water Flow***

The K-function can be determined by imposing a constant  $v_m$  on a soil specimen and the spinning the centrifuge at a constant  $\omega$ , then waiting until steady-state flow is attained. After reaching steady-state flow, a point on the K-function can be defined by correlating a measurement of the moisture content or suction at a certain height  $z_m$  with the  $K$  value at this height determined using Equation (3.23). Such an approach requires multiple measurements of suction with height in order to measure the suction head gradient at the height of interest. Further, multiple measurements of suction and moisture content with height can be used to define several points on the K-function. However, depending on the outflow boundary condition and the characteristics of the test, the value of  $K$  may not vary significantly with height. In this case, multiple points on the K-function can be defined by changing the imposed values of  $v_m$  and  $\omega$ .

Centrifugation with steady-state water flow has been used in several studies to define the K-function for a wide range of soils (Nimmo *et al.* 1987, Nimmo 1990, Nimmo and Akstin 1988; Conca and Wright 1990, Nimmo *et al.* 1992; Khaleel *et al.* 1995). These studies were conducted in conjunction with the US Geological survey and the US Department of Energy, with the goal of characterizing the water and contaminant transport characteristics of unsaturated soil profiles.

Nimmo *et al.* (1987) described the development and validation of the Internal Flow Control Steady-State Centrifuge (IFC-SSC) method. This study was complemented with additional studies by Nimmo and Akstin (1988) and Nimmo *et al.* (1992), which described improvements to the experimental technique and investigations into the K-functions of other soils. This approach uses a system of reservoirs and ceramic stones to

supply a constant fluid flow rate to the upper surface of a soil specimen, as shown in the schematic view in Figure 5.36(a). The SSC permeameter is mounted in a medical-size centrifuge, such as the one shown in Figure 5.36(b), having a small radius of 0.1-0.2 m and a maximum angular velocity of 20,000 RPM. Specifically, the uppermost ceramic stone was used to apply a constant influx to a lower reservoir, providing a constant head to a ceramic stone resting directly on the specimen. The stones should remain saturated during centrifugation, so the discharge velocity supplied to the specimen depends on the saturated hydraulic conductivity of the stone and the g-level [using the constant head  $K_s$  expression in Equation (5.2)]. To change flow rates, a different ceramic stone must be installed. Accordingly, increases in the g-level will also cause proportional increases in the flow rate, so these variables cannot be controlled independently. The bottom boundary condition is controlled by either placing the soil on a saturated ceramic stone ( $\psi_0 = 0$ ), or by placing the soil atop an unsaturated ceramic stone in which the suction at the interface is controlled by adjusting the height of a water bath surrounding the stone ( $\psi_0 > 0$ ). The suction at the top of the outflow ceramic stone is given by Equation (5.7).

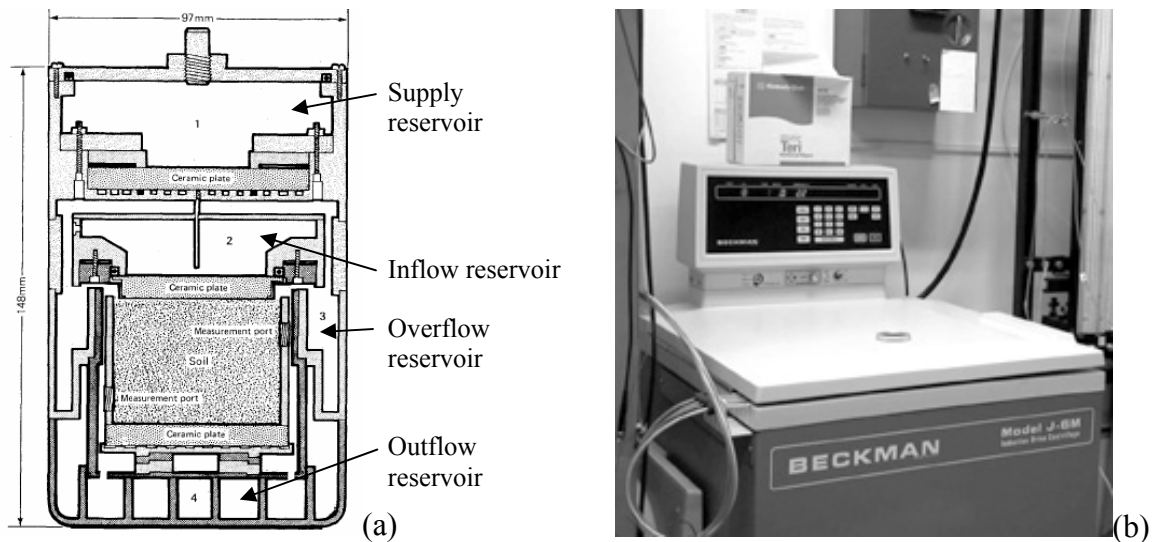


Figure 5.36: IFC-SSC setup (Nimmo *et al.* 1987): (a) Permeameter; (b) Centrifuge

The IFC-SSC experimental setup was developed for use within a small centrifuge container (97 mm diameter by 148 mm height), so instrumentation could not be used during centrifugation (although ports were included to use tensiometers outside of the centrifuge). The centrifuge must be stopped periodically to measure outflow and changes in specimen mass. A major shortcoming of this approach is that the upper ceramic stone and constant head reservoir rest directly on the specimen, which can cause significant settlement at high  $g$ -levels. This was addressed by spinning the centrifuge to the highest  $g$ -level expected in the test, allowing the specimen to consolidate, and then reducing the centrifuge speed to start the  $K$ -function characterization. This approach was found to lead to variability in the porosity of the soil (Nimmo and Akstin 1988).

Conca and Wright (1990; 1998) developed a commercial version of the SSC, referred to as the Unsaturated Flow Apparatus (UFA<sup>TM</sup>). Instead of using a system of reservoirs and ceramic stone, a rotary joint was developed to supply water to the rotating specimen from a flow pump outside the centrifuge. A schematic of the UFA rotor is shown in Figure 5.37(a), and the UFA in a medical centrifuge is shown in Figure 5.37(b).

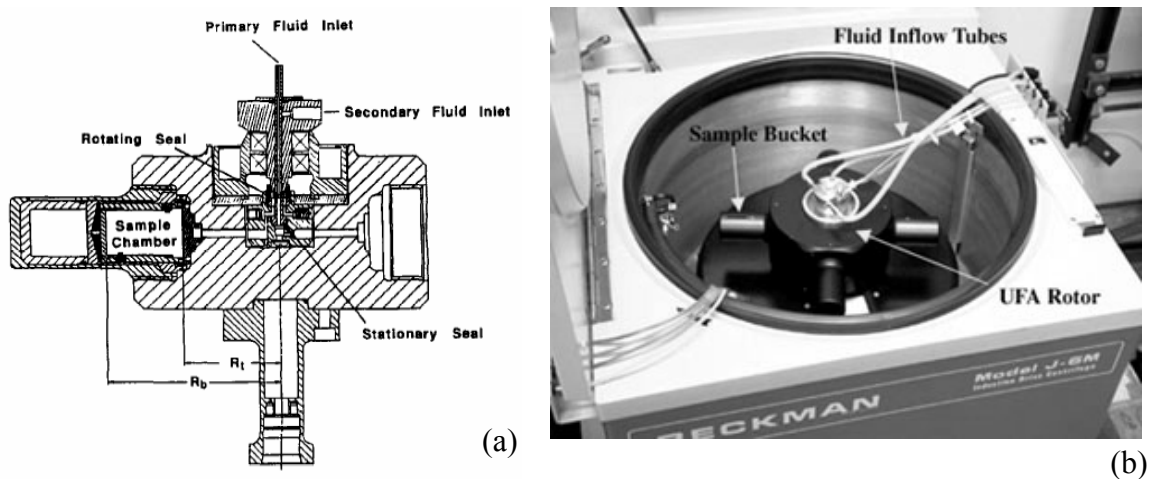


Figure 5.37: UFA setup (Conca and Wright 1998): (a) Schematic of rotor and permeameter; (b) Centrifuge and flow-pump

The UFA employs open-flow boundary conditions, which are described in Section 2.5. In this case, the suction value at the soil surface reaches equilibrium with the imposed inflow, and can be predicted using Equation (3.22). The suction at the base should be close to zero as a capillary break will likely occur at the soil-base plate interface. However, the zone of influence of the outflow plate on the suction profile is likely to be minimal under increased gravity, as indicated from the suction profiles in Figure 3.8(c). An advantage of this approach over the SSC is that the outflow plate provides negligible impedance to outflow. Similar to the SSC, this approach also requires the centrifuge to be stopped to measure outflow and changes in specimen mass.

ASTM D6527 was developed to standardize the procedures for the UFA approach to define the K-function. Several studies have employed the UFA approach to define the K-function for the design of geotechnical structures (Zornberg *et al.* 2003) and the analysis of hydrological systems (Nimmo *et al.* 1994; Sigda and Wilson 2003). During these tests, water content changes are inferred by periodically measuring the outflow from the specimen, determining the gravimetric water content at the end of the test, and back-calculating the water content time series using the mass of outflow collected between each measurement time. In these tests, suction was measured by pressing a tensiometer against the side of the specimen while the centrifuge was stopped. The volume of outflow is used to verify that steady-state has been reached, so outflow from consolidation should be separated from that associated with the imposed flow rate. These values are often small, especially for low  $v_m$  values, resulting in some variability in  $\theta$ .

The UFA and SSC approaches employ an additional simplification to Equation (3.23) to calculate  $K$  by assuming that the gradient in suction head is negligible in the specimen. In this case,  $K$  is inversely proportional to  $N_r$ , as follows:

$$K(\psi, z_m) = \frac{-v_m g}{\omega^2 (r_0 - z_m)} = -\frac{v_m}{N_r} \quad (5.18)$$

Although the  $g$ -level varies with specimen height the UFA and SSC approaches assume that  $N_r$  is constant with radius, and equal to that at mid-height ( $N_{r,mid}$ ) (Nimmo *et al.* 1987; Conca and Wright 1998). Accordingly, the value of  $z_m$  at mid-height is used as the reference point for calculation of the  $K$  value from Equation (5.11) during steady-state infiltration tests. Although the mid-height of the specimen provides a good reference point for the average  $g$ -level in the specimen, it may not provide the best location to characterize the hydraulic conductivity. Specifically, the outflow boundary may impact the  $K$  distribution near mid-height (depending on the  $g$ -level and soil type), so using the mid-height may lead to an overestimation of  $K$  when compared with that in the zone with zero gradient in the suction head.

The assumption of a zero suction gradient in the upper zone of a specimen during steady-state flow is reasonable for certain centrifuge and specimen geometries, as indicated from the theoretical suction profiles shown in Figure 3.8. However, these studies assume that the entire specimen has the same suction during steady-state water flow (Nimmo *et al.* 1987; Conca and Wright 1998). By making this assumption, the researcher could define the  $K$ -function by correlating the average moisture content of the specimen, back-calculated from measurements of specimen mass during testing, with the value of  $K$  from Equation (5.18). Nimmo *et al.* (1987) and Conca and Wright (1990) presented measurements of moisture content versus specimen height, shown in Figure 5.38(a) and Figure 5.38(b), respectively, to support this assumption.

There are several reasons this approach is not reasonable. Specifically, these UFA and SSC do not have in-flight measurements, so moisture re-distribution may have occurred after the centrifuge was stopped. The soils tested in these studies were dense sands, which may have reached residual saturation conditions throughout the profile even during steady-state flow, tending to make the moisture distribution uniform. Further,

although the lengths of specimens used by Nimmo *et al.* (1987) and Conca and Wright (1998) were small, the  $r_0/L_m$  ratios are similar to the specimen geometry used in defining the suction profiles in Figure 3.8. If the assumptions in the analysis were correct, the suction profiles in a UFA or SSC specimen should be similar to those in Figure 3.8. Accordingly, use of the average moisture content for the entire specimen in the UFA approach overestimates the moisture content used to define the K-function.

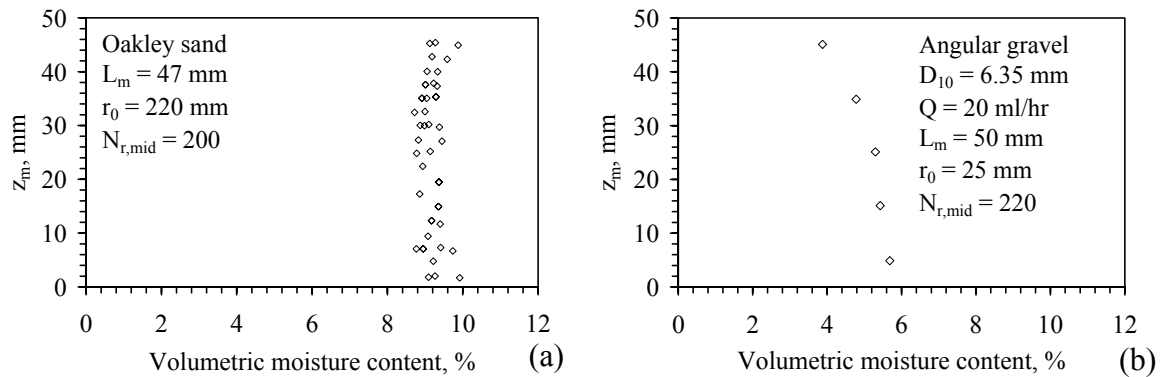


Figure 5.38: Moisture content profiles measured after centrifugation: (a) Nimmo *et al.* (1987); (b) Conca and Wright (1990)

The K-function determined by Nimmo *et al.* (1987) using the SSC is shown in Figure 5.39(a). The centrifuge was only used to determine the five points on the K-function for the dense sand at low moisture content (< 12%), while 1-g column tests were used to determine the K-function for the loose sand and the dense sand at a moisture content of 34%. Despite the difference in densities and g-level, the K data lines up well. Five different ceramic stones were used to determine the five centrifuge data points. A K-function determined by Conca and Wright (1998) is shown in Figure 5.39(b). The sand shows a decrease in moisture content of 20% as the hydraulic conductivity decreases by nearly 7 orders of magnitude. The K-function data lines up well with the K-function predicted using the van Genuchten-Mualem model with parameters defined from

the WRC from a separate centrifugation test [Figure 5.16(c)]. Although the prediction fits the data well, the model over-predicts the K-function by an order of magnitude at low moisture contents. This may be due to the fact that transient flow was used to define the WRC while steady-state flow was used to define the K-function.

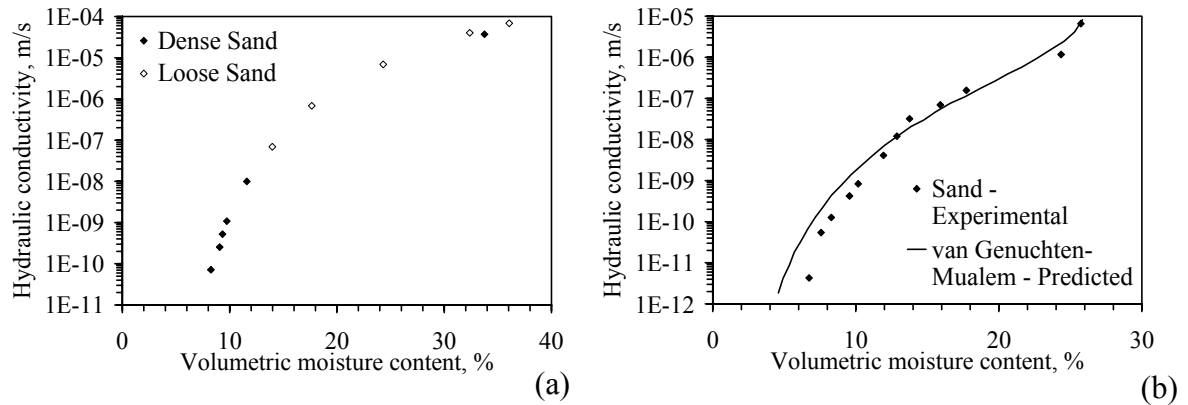


Figure 5.39: Hydraulic conductivity values measured with the centrifuge approach (a) SSC data (Nimmo *et al.* 1987); (b) UFA data (Conca and Wright 1998)

The UFA and SSC analyses assume the validity of Darcy's law in the centrifuge. Nimmo *et al.* (1987) presents one of the few experimental validations of this law using steady-state flow in a centrifuge. This study used a ceramic stone and constant head reservoir to control the flux through the soil profile, which means that the discharge velocity applied to the profile increased proportionally with the g-level applied by the centrifuge. Accordingly, changes in g-level will lead to similar changes in the discharge velocity, making the hydraulic conductivity calculated using Equation (3.23) the same for each g-level. Darcy's law was verified by ensuring that the outflow discharge velocity was proportional to the driving force, as shown in Figure 5.40, and by measuring the suction to ensure that it does not change with each increase in g-level.



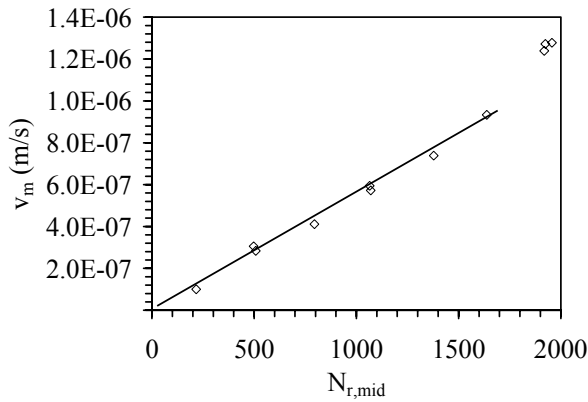


Figure 5.40: Relationship between discharge velocity and g-level (Nimmo *et al.* 1987)

Nimmo *et al.* (1987) observed a negligible suction gradient with specimen height, so only the centrifuge driving force is shown on the abscissa. The researchers observed a linear trend in outflow discharge velocity with driving force up to  $N_{r,mid} = 1650g$ . An increase in discharge velocity was observed at the highest g-level, but this may have been due to additional consolidation of the specimen. The suction at each g-level was not reported, but the authors claim that it was constant. The suction was measured using tensiometers pressed against the specimen, outside of the centrifuge. This approach may have led to some uncertainty in the measured suction and the validity of Darcy's law.

In summary, the SSC and UFA centrifuges must be periodically stopped to measure the specimen mass to ensure steady state flow, and the moisture content must be measured destructively at the end of the test. The SSC and UFA do not allow the direct acquisition of the relevant variables (suction, moisture content, discharge velocity) in-flight during testing. Accordingly, the K-function and WRC cannot be determined without simplifying assumptions about the suction distribution with  $z_m$ , or by measuring the variables outside of the centrifuge. Further, the WRC and K-function cannot be

obtained simultaneously in these approaches. The hydraulic conductivity (or impedance to flow) of the plates used an outflow boundary is also not discussed in these studies.

During steady-state flow in a soil specimen in the centrifuge,  $v_m$  is constant with both time and  $z_m$ . However, the total hydraulic potential and  $N_r$  vary with  $z_m$ . This implies that the hydraulic conductivity  $K$ , which is the coefficient of proportionality between  $v_m$  and the gradient in hydraulic potential, must also vary with radius. There is an added level of complexity because the suction also varies with radius in the specimen (especially near the outflow face), so the hydraulic conductivity must vary according to the shape of the K-function. For the suction profiles shown in Figure 3.8, the hydraulic conductivity will be equal to the saturated hydraulic conductivity at the outflow face, and will be relatively, but not entirely, constant in the upper portion of the specimen.

Assumption of a zero suction gradient throughout the specimen, which is the basis of the SSC and UFA analysis, leads to a paradox. Specifically, if the suction gradient equals zero in the upper portion of the specimen, then the suction and  $K$  would both be constant in this region. However, unless  $N_r$  in Equation (5.18) is uniform throughout the specimen ( $N_r = N_{r,mid}$ ),  $K$  must vary with radius. From a practical point of view, it is reasonable to assume that the suction is constant in the upper portion of the specimen, as the magnitude of the variation is small enough that changes in  $K$  are negligible.

As a first attempt to understand the magnitude of variation in hydraulic conductivity through a specimen during steady state flow, the distribution in the imposed  $K$  values predicted from Equation (5.18) are shown in Figure 5.41(a) for a single discharge velocity and different angular velocities. The geometry variables in the example are representative of the centrifuge permeameter used in this study. To be completely accurate, the bottom portion of these curves should slope toward the hydraulic conductivity of a saturated specimen, and should follow the slope of the suction

profile in the upper portion of the specimen. Nonetheless, there is little change in hydraulic conductivity with radius, especially with high angular velocities. The difference in the  $K$  values at the top and bottom of the specimen for different discharge velocities is shown in Figure 5.41(b). The change in  $K$  throughout the specimen is more significant at low g-levels and high flow rates. This observation is similar to the trends in the suction profiles with  $N_{r,mid}$  and  $v_m$  shown in Figure 3.8.

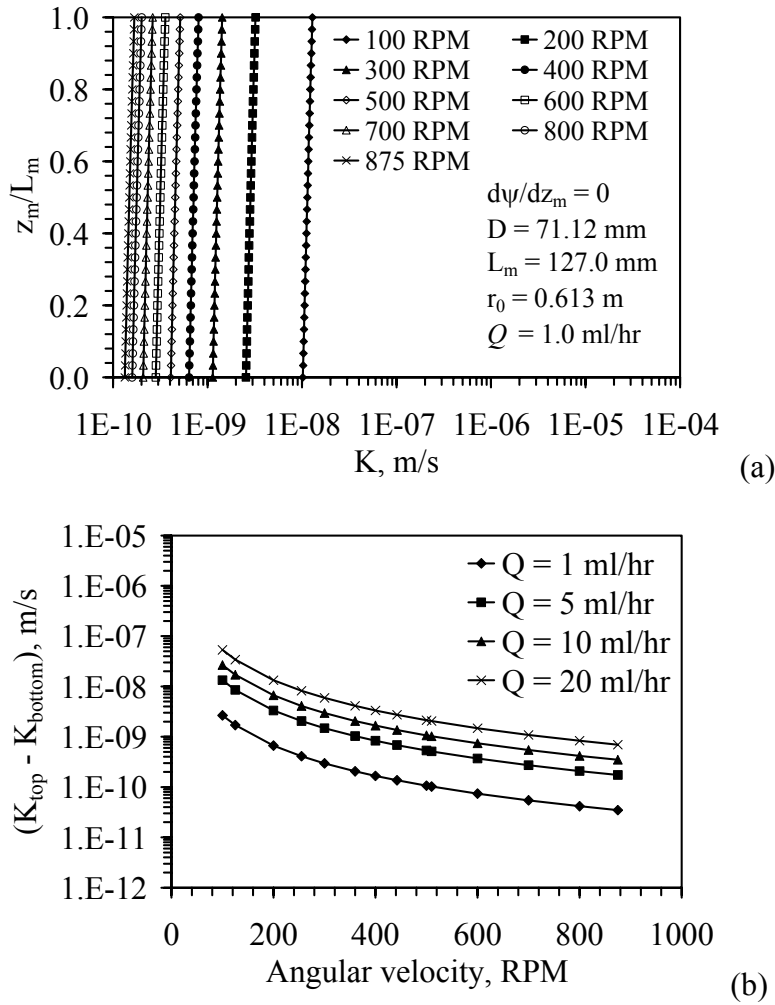


Figure 5.41: Variation in hydraulic conductivity with specimen height (a)  $K$  profiles for a constant inflow rate; (b) Range in  $K$  for different flow rates

The dependence of  $N_r$  and  $K$  on  $z_m$  can be alleviated by using a small specimen height  $L_m$  with respect to the centrifuge radius so that there will be negligible effects of radius on flow. This can be quantified using the uniformity coefficient  $\chi$ , defined as (Dell'Avanzi *et al.* 2004):

$$\chi = 1 + \frac{\frac{z_m}{r_0}}{2 \left( 1 - \frac{z_m}{r_0} \right)} \quad (5.19)$$

If the uniformity coefficient is close to 1.0 throughout the specimen, the  $g$ -level will be effectively constant throughout the specimen ( $N_r$  approaches  $N_{r,mid}$ ). The variations in the uniformity coefficient with specimen with  $r_0/L_m$  for different locations in the centrifuge permeameter are shown in Figure 5.42. The value of  $r_0/L_m$  is used to quantify the length of the permeameter with respect to the outside radius, and large values indicate that the specimen is small compared to the outside radius. The permeameter used in this study for hydraulic characterization of unsaturated soils has an average uniformity coefficient of 1.1 throughout the specimen ( $r_0/L_m = 4.82$ ), which is considered acceptable.

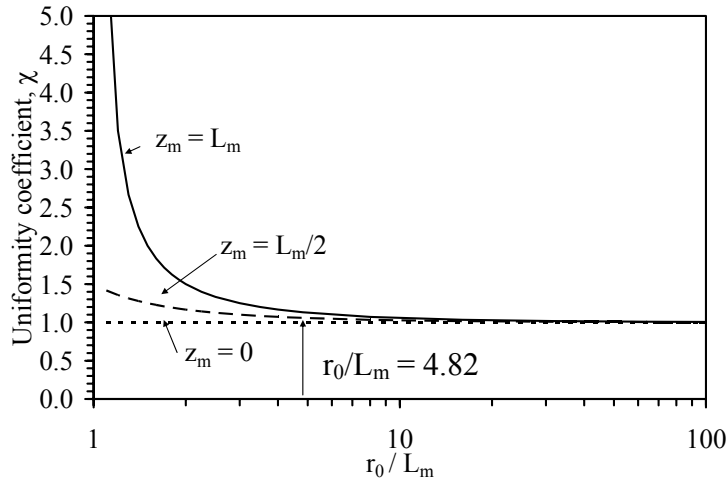


Figure 5.42: Variation in  $\chi$  with specimen height (Dell'Avanzi *et al.* 2004)

### 5.4.5 Summary of Experimental Techniques to Determine the K-function

Overall, there are many approaches to determine the K-function in the laboratory, all of which require flow of water through a soil specimen. There are several other techniques that have been used in the field (Benson and Gribb 1991). Comparing the different laboratory techniques, the centrifuge approaches have the advantage of faster testing times. However, specialized equipment is often necessary. Column tests tend to rely heavily on the accuracy of the measurements made by sensors. Outflow measurements during WRC tests yield both hydraulic characteristics, but there are important shortcomings associated with boundary condition effects.

Typical results from steady-state tests to define the K-function for a sand and clay are shown in Figure 5.43(a) (Moore 1939; Richards 1952). The steady-state K-functions follow a smooth trend with decreasing moisture content. The data for the clay soil required more than 80 days to reach steady-state flow. Results for transient determination of the K-function for clay are shown in Figure 5.43(b) (Olson and Daniel 1981). The K-function was determined in about 20 days using analysis of transient changes in suction during horizontal infiltration.

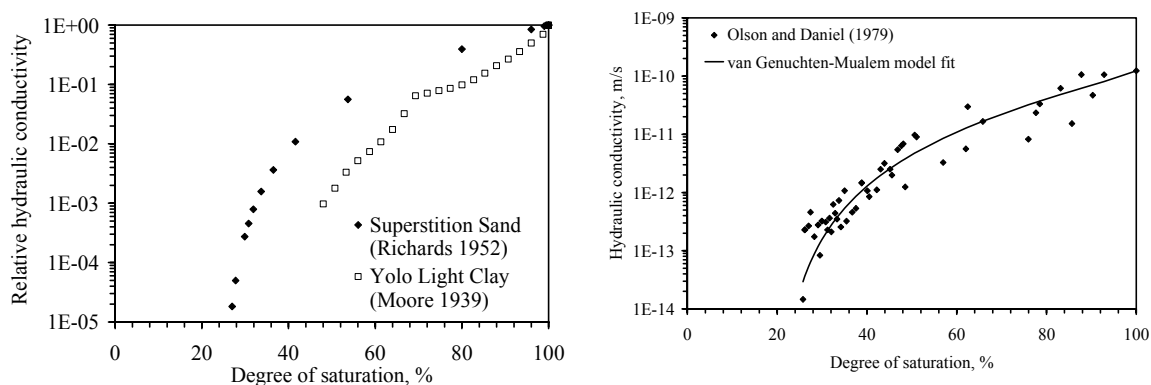


Figure 5.43: Effect of flow type on K-function: (a) Steady-state; (b) Transient

Testing times reported in different experimental studies in the literature are summarized in Table 5.4. Despite the different soil types and analysis approaches, transient tests conducted at 1-g and steady-state tests conducted in the centrifuge allow characterization of the hydraulic characteristics in less than a week. The information required to interpret the K-function is attained in transient approaches before reaching steady state flow, making it as fast as obtaining a single point on the K-function using a steady-state approach. However, the transient data reported in the literature typically shows significant scatter [Figure 2.7 and Figure 5.43(b)]. Steady-state tests at 1-g have been reported to require from one to several months. For example, the infiltration test described in this section had a duration of several weeks. Most of the soils shown in Table 5.4 have hydraulic conductivity values of approximately  $10^{-10}$  m/s at residual saturation. In these soils, the testing times under 1-gravity conditions cannot be decreased below the time required for water to flow through a specimen at steady rate.

Table 5.4: K-function testing times reported in the literature

Researcher	Soil type	Time of testing (days)	Type of testing	Type of flow	Test description	Data analysis
Moore (1939)	Yolo light clay	80+	1-g	Steady state	Column	Direct
Richards (1952)	Superstition sand	10+	1-g	Steady state	Column	Direct
Lu <i>et al.</i> (2001)	SW Sand	26.00	1-g	Steady state	Flow pump	Direct
Lu <i>et al.</i> (2001)	Esperance sand	35.00	1-g	Steady state	Flow pump	Direct
Lu <i>et al.</i> (2001)	SP sand	22.00	1-g	Steady state	Flow pump	Direct
Olson and Daniel (1979)	Fire clay	21.00	1-g	Transient	Instantaneous profile	Direct
Hamilton <i>et al.</i> (1979)	Goose lake clay	21.00	1-g	Transient	Instantaneous profile	Direct
Durner <i>et al.</i> (2001)	Sandy soil	8.33	1-g	Transient	Multistep	Direct
Durner <i>et al.</i> (2001)	Sandy soil	12.50	1-g	Transient	Continuous	Direct
Durner <i>et al.</i> (2001)	Sandy soil	2.92	1-g	Transient	One step	Direct
Wildenschild <i>et al.</i> (2001)	Columbia soil	2.29	1-g	Transient	Multistep	Direct
Wildenschild <i>et al.</i> (2001)	Lincoln soil	2.17	1-g	Transient	Multistep	Direct
Young <i>et al.</i> (2002)	Vinton fine sand	0.07	1-g	Transient	Upward infiltration	Inverse
Young <i>et al.</i> (2002)	Appling sandy loam	0.07	1-g	Transient	Upward infiltration	Inverse
Nimmo (1990)	Superstition sand	0.28	N-g	Steady state	SCA-centrifuge	Direct
Conca and Wright (1998)	Hanford Cores	3.50	N-g	Steady state	UFA-centrifuge	Direct
Conca and Wright (1998)	Sandy loam	4.50	N-g	Steady state	UFA-centrifuge	Direct
Conca and Wright (1998)	Fine sand	5.50	N-g	Steady state	UFA-centrifuge	Direct
Conca and Wright (1998)	Sand	6.50	N-g	Steady state	UFA-centrifuge	Direct
Conca and Wright (1998)	Tuff	7.50	N-g	Steady state	UFA-centrifuge	Direct
Sigda and Wilson (2005)	Fractured rock	1.00	N-g	Steady state	UFA-centrifuge	Direct

## **Chapter 6: The Centrifuge Permeameter for Unsaturated Soils**

### **6.1 OVERVIEW**

The conventional and centrifuge experimental approaches described in Chapter 5 were shown to be useful in determining the hydraulic characteristics of unsaturated soils in Chapter 4. However, these approaches suffer from long testing times, boundary condition effects, lack of instrumentation, and complicated analyses. These shortcomings have driven the development of the Centrifuge Permeameter for Unsaturated Soils. The goal of the centrifuge permeameter is to provide an expedited measurement of the WRC and K-function for a single soil specimen in a single test using steady-state infiltration. The centrifuge permeameter incorporates a high-g centrifuge with an instrumented, rigid wall permeameter. An advantage of the centrifuge permeameter over those developed in the past is that instrumentation was developed to non-destructively and non-intrusively infer suction and volumetric moisture content profiles in a soil specimen during centrifugation. Data can be collected while in-flight using a data acquisition system specifically developed for use in high-g environments. The plumbing developed for the centrifuge permeameter allows control of the infiltration rate imposed on the specimen from outside the centrifuge. This feature of the centrifuge permeameter permits independent control of the infiltration rate and centrifuge acceleration, so flow phenomena such as wetting and drying can be investigated. Open flow boundary conditions are used in the centrifuge permeameter, in which water is supplied to the soil surface at a constant rate (less than  $K_s$ ) and is allowed to freely exit the outflow side of the permeameter. Descriptions of the individual components of the centrifuge permeameter are presented in this chapter, including the centrifuge, permeameter environments, flow control system, instrumentation, and data acquisition system.

## 6.2 GEOTECHNICAL CENTRIFUGE

The centrifuge system was constructed by Thomas Broadbent and Sons, LLC of Huddersfield, UK. A cross section of the centrifuge is shown in Figure 6.1. The centrifuge consists of a spindle and bearing assembly, which rest atop three vibration isolators mounted to a conical base pedestal. The data acquisition system hub is placed atop the spindle, and the permeameter environment is mounted on top of the hub. The central access shaft permits wires and plumbing lines to be passed from the data acquisition system and permeameter environment to the stationary environment via rotary joints (*e.g.*, a electrical slip ring stack, a high pressure fluid union, and a fiber-optic rotary joint). A belt-driven motor is used to spin the centrifuge.

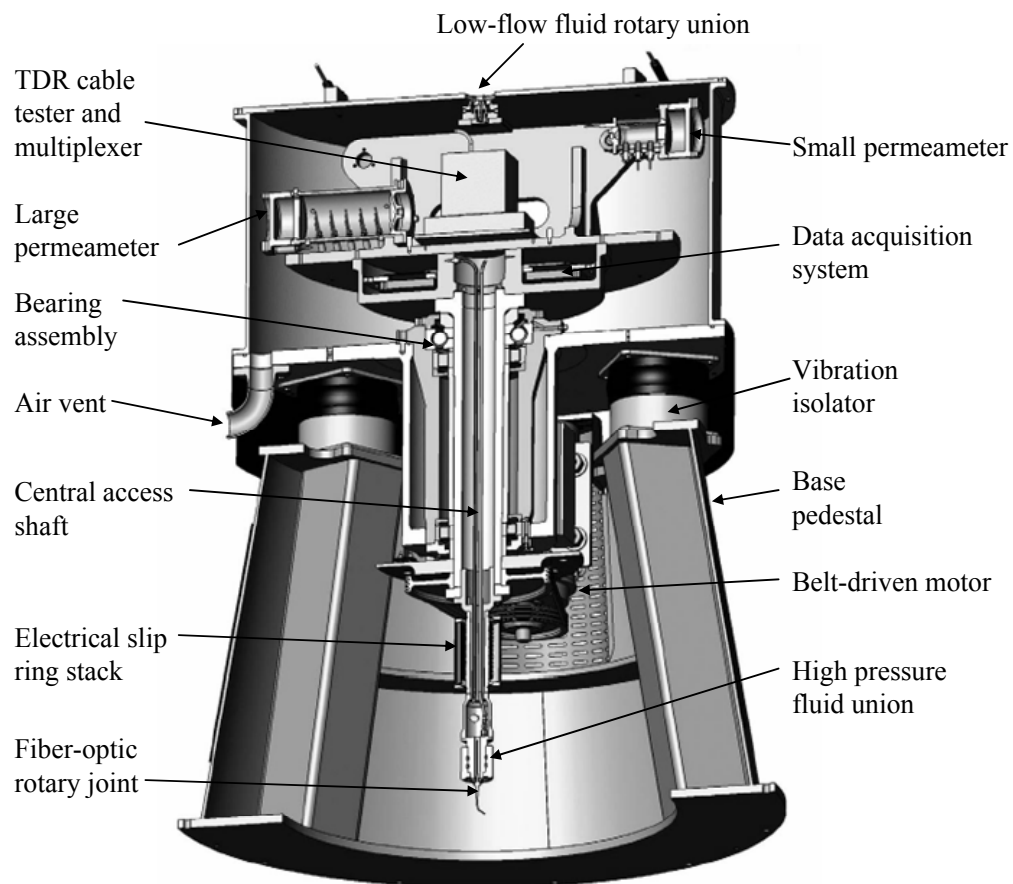


Figure 6.1: Centrifuge setup (Courtesy of Thomas Broadbent and Sons, LLC)



Centrifuges are classified by their g-ton rating, equal to the product of the maximum payload and g-level. The centrifuge has a maximum angular velocity of 875 RPM and an outer radius of 0.7 m, which translate to a g-level of 600. Two permeameter environments with different payloads were developed for this study: (i) a small permeameter used for hydraulic characterization of soil specimens having a maximum payload of 20 kg, and (ii) a larger permeameter used for evaluation of water flow through layered soil profiles having a maximum payload of 55 kg. The g-ton ratings of the centrifuge are shown in Figure 6.2, along with those for other geotechnical centrifuges. This centrifuge has significant differences with conventional geotechnical centrifuges, which have been tailored to address mechanical response of earth structures, rather than investigation of flow phenomena. The only centrifuges that can impose a higher g-level are bench-top medical centrifuge such as those used by UFA and SSC.

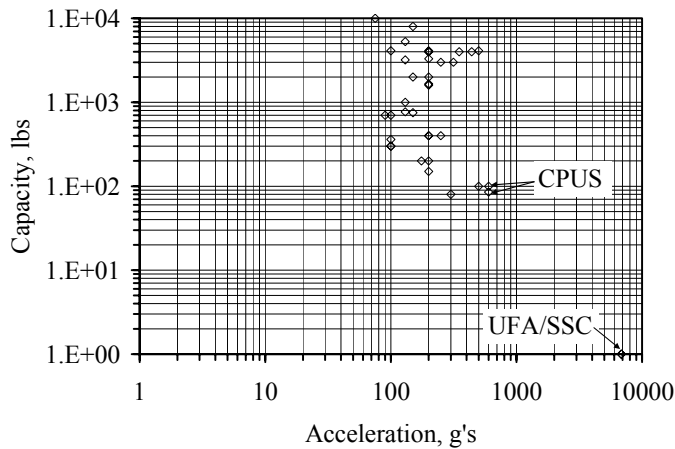


Figure 6.2: G-ton rating of centrifuge permeameter (with other geotechnical centrifuges)

The power requirements for the centrifuge permeameter are related to the centrifuge speed, which leads to proportional increases in frictional wind drag. The energy required to maintain a steady angular velocity observed from factory calibration tests increases quadratically with angular velocity, as shown in Figure 6.3. The motor

can supply up to 22 kW to accelerate the centrifuge, nearly three times the power required to maintain the centrifuge spinning at the maximum speed. Accordingly, the cost of centrifugation depends on the duration of a centrifuge test, the number of changes in centrifuge speed, and local power costs. Energy is not recovered during deceleration.

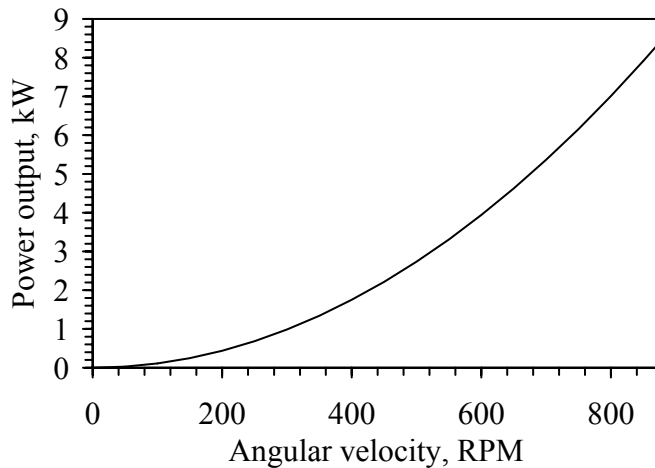


Figure 6.3: Power requirements for centrifugation at different angular velocities

### 6.3 CENTRIFUGE PERMEAMETER ENVIRONMENTS

The small, or hydraulic characterization, permeameter is shown in Figure 6.4(a). This permeameter is used to determine the hydraulic characteristics of a representative element of soil (or other porous material) using steady-state water flow. Two identical, instrumented permeameters are mounted on swinging buckets attached opposite to each other on a steel support frame, as shown in Figure 6.4(b). The flow of a hydraulic characterization test can be explained using the illustration in Figure 6.4(b). Water entering the permeameter environment through the low flow rotary union is passed along the copper brake tubing to the fluid distribution cap. The water then infiltrates through the soil specimen, and is collected in the outflow reservoir. The swinging buckets maintain the same orientation between the longitudinal axis of the permeameter and the resultant of the acceleration field, whether at rest (vertical) or spinning. For example,

when spinning at a g-level of 100, the slope of the permeameter with respect to the horizontal would be 100:1. Distances from the central axis of the centrifuge to different points in the permeameter are shown in Figure 6.4(b). Permeameters at rest (left) and spinning (right) are shown in this figure.

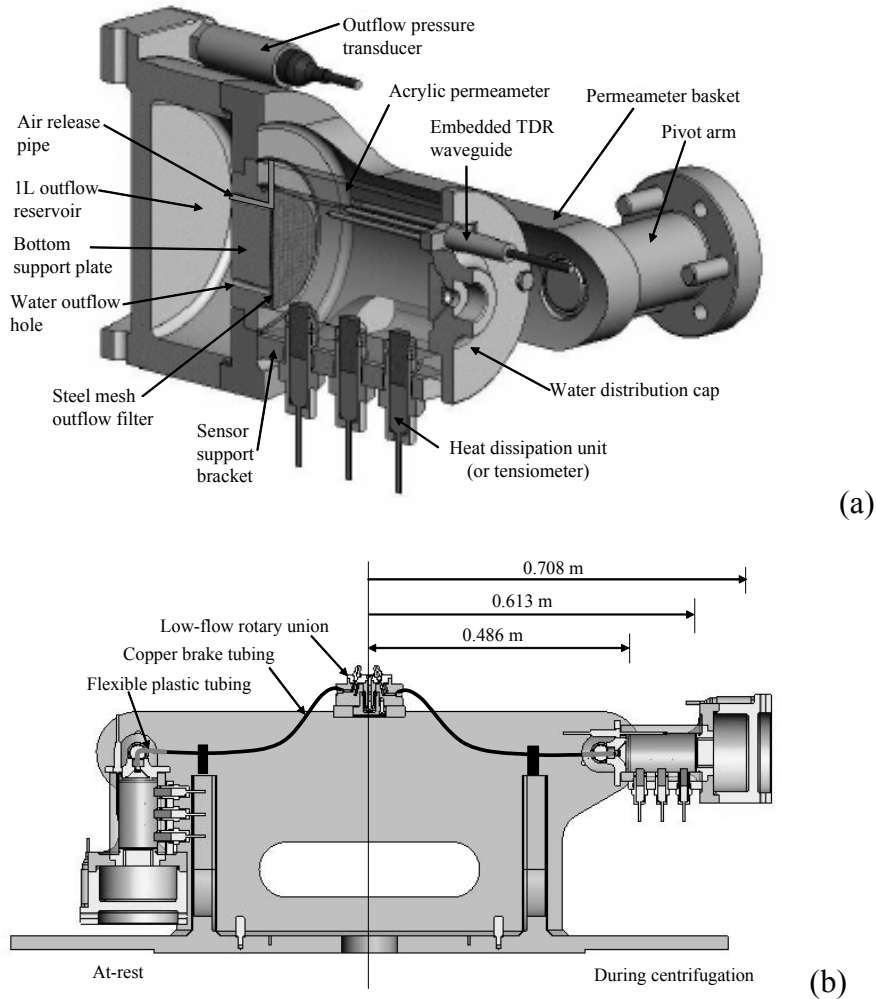


Figure 6.4: Hydraulic characterization permeameter: (a) Isometric view; (b) Environment

The hydraulic characterization permeameter is an acrylic cylinder having an inside diameter of 71.12 mm (2.8 inches) and a specimen height of 127 mm (5.0 inches). The permeameter has a collar with a height of 15.24 mm (0.6 inches) which is present

during testing and allows trimming of compacted specimens to the desired height. Acrylic was selected due to its low electrical conductivity, allowing the use of dielectric sensors to infer the moisture content. A typical specimen has a height  $L_m = 127$  mm, and a 15.24 mm collar used to level compacted specimens. The inside diameter is slightly less than a typical 76.2-mm diameter Shelby tube, which permits an undisturbed specimen to be trimmed into the permeameter. The wall thickness of the permeameter is 25 mm, which was selected to permit placing instrumentation within the walls of the permeameter. The instrumentation layout for this permeameter was designed to minimize inclusions into the specimen. Inclusions may cause disturbance of the soil structure during insertion, may cause or prevent settlement of the soil during centrifugation, and may contribute to an increase in flow path tortuosity, all of which may alter measurement of the soil hydraulic conductivity. The variation in g-level throughout the specimen is shown in Figure 6.5. The g-level varies with the radius in the specimen, although it is approximately uniform up to  $N_{r,mid} = 100$ . As mentioned in Chapter 3, the  $r_0/L_m$  ratio for this specimen is 4.82, which indicates a relatively uniform gravitational field based on the analysis performed by Dell'Avanzi *et al.* (2004).

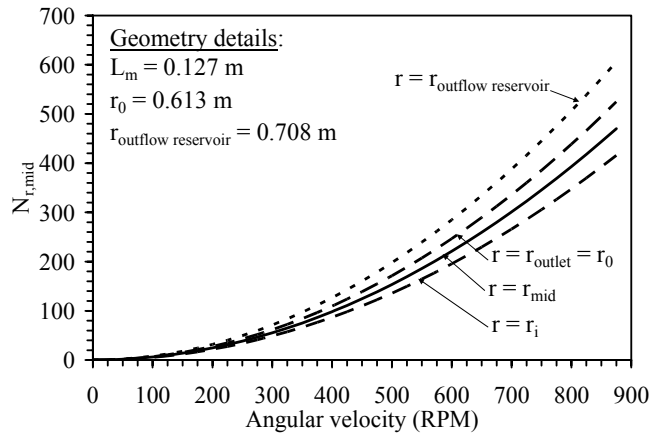


Figure 6.5: Variation in  $N_{r,mid}$  with  $\omega$  for the hydraulic characterization permeameter

The large, or prototype, permeameter is shown in Figure 6.6(a) and Figure 6.6(b). The permeameter was designed as an infiltration column, similar to the one used for the definition of the K-function described in Chapter 5. The permeameter is constructed from a steel tube with a height of 305 mm, a diameter of 152.5 mm, and a wall thickness of 12.7 mm. The term “prototype” is used to describe this permeameter, as its size allows investigation of water flow through scaled models of 1-g soil profiles. The prototype permeameter is used in this study to investigate moisture content and suction profiles in a soil specimen during steady-state flow in the centrifuge permeameter.

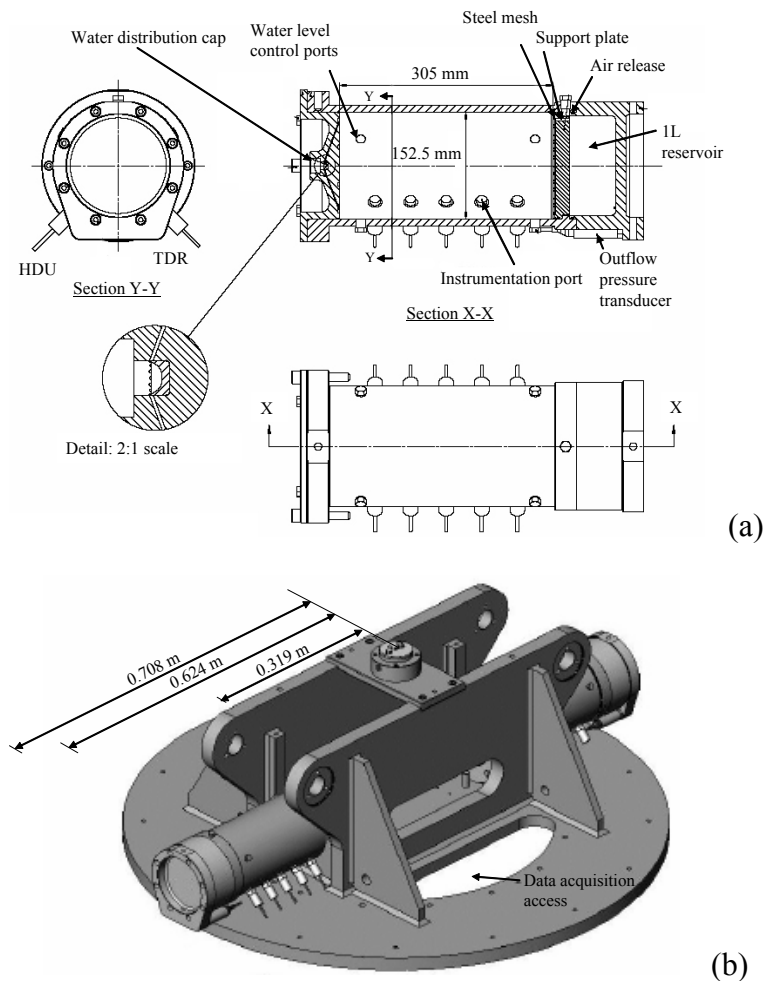


Figure 6.6: Prototype permeameter: (a) Schematic view; (b) Environment

The permeameter is mounted in a permanent horizontal position in the centrifuge due to its size. The prototype permeameter has three vertical arrays of instrumentation ports, so moisture content, suction, or temperature sensors can be embedded within the soil specimen. Because sensors may be embedded, the soil types that can be used in this permeameter must be relatively stiff to limit settlement. The sensor arrays designed to allow determination of suction and moisture content profiles during flow through layered systems. Additional ports are included in the side of the permeameter, which can be used to form a water table. In this case, the outflow plate can be plugged and the tubes in the side of the permeameter can be connected directly to the outflow collection reservoir. Also, air can be pumped through holes near the top of the permeameter to induce evaporation from the upper surface of the soil specimen. As the length of the permeameter with respect to the radius of the centrifuge is greater for the prototype permeameter ( $r_0/L_m = 2.05$ ), the g-level varies more significantly through the specimen, as shown in Figure 6.7. This permeameter is meant to be used with relatively stiff, compacted soils due to the variation in g throughout the specimen.

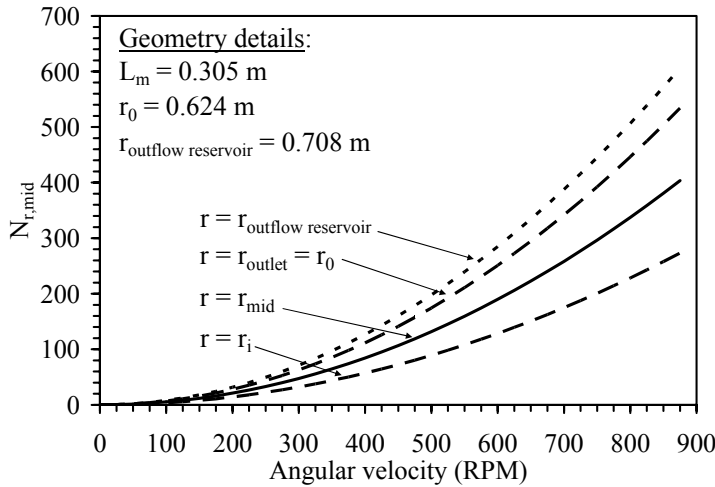


Figure 6.7: Variation in  $N_{r,mid}$  with  $\omega$  for the prototype permeameter

The relationships between  $N_{r,mid}$  and angular velocity shown in Figure 6.5 and Figure 6.7 can be correlated with the voltage output from a load cell mounted on the permeameter environment in order to provide a direct measurement of the g-level during centrifugation. This load cell is referred to as a “g-meter”. The output of the load cell was calibrated with the g-level at different radii in the centrifuge. The calibration curves for the g-meter for different locations within the small permeameter are shown in Figure 6.8. The g-level at mid-height of the specimen is reported in analyses.

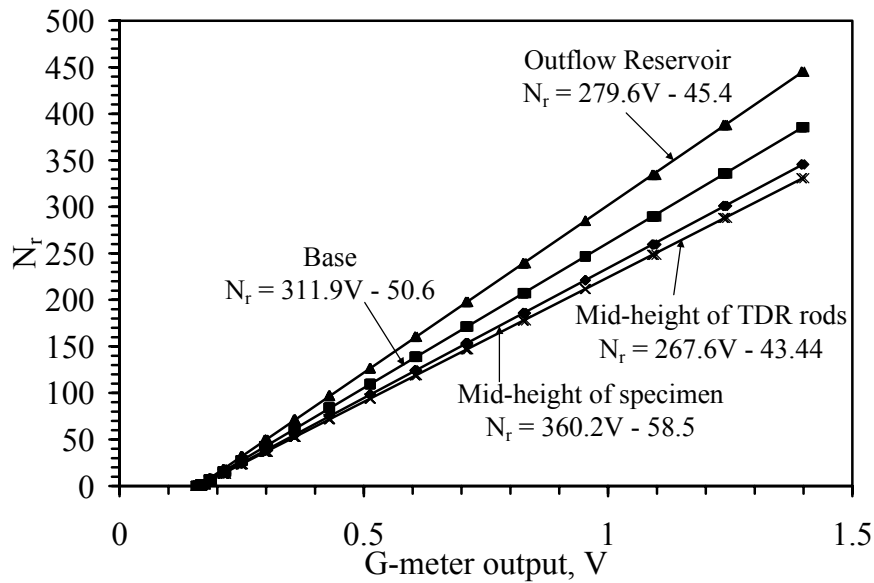


Figure 6.8: G-meter calibration curves

## 6.4 FLOW RATE CONTROL AND MONITORING SYSTEM

### 6.4.1 Fluid Supply System

Fluid is supplied to the permeameters using a Gemini<sup>®</sup> PC-2TX two-channel medical infusion pump, shown in Figure 6.9(a). The pump has an air-bubble detection feature, and measures pressure in the fluid during steady-state supply of water. The infusion pump was selected as it can apply a continuous, steady flow rate that is more

favorable than the “pulsed” flow supplied by peristaltic pumps. Water is supplied to the pump using a medical IV bag. Distilled water was used with all infiltration tests in this study, although the infusion pump allows any type of fluid to be used (tap water, natural pore fluid, oil). The pump has a flow capacity ranging from 0.1 to 1000.0 ml/hr. The discharge velocities calculated for this range of inflow rates are shown in Figure 6.9(b) for the centrifuge permeameters. Syringe pumps that have a screw drive (*e.g.*, the Harvard syringe pump) can be used in studies that require lower discharge velocities.

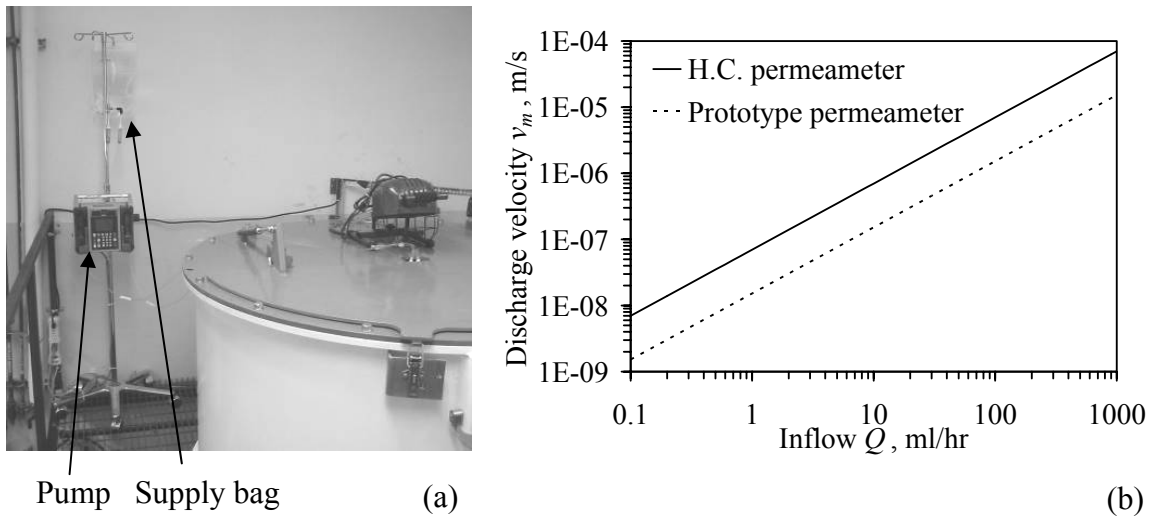


Figure 6.9: (a) Infusion pump setup; (b) Discharge velocities for range of inflow rates

Due to space limitations within the centrifuge, fluid is passed through a 2-channel low-flow rotary union, shown in Figure 6.10. The rotary union was designed to transmit low flow rates while preventing water loss and minimizing heat generation. As discussed later, a flow boundary condition is desired for the permeameters. Accordingly, the rotary union is designed to operate without pressurizing the fluid. This has an added advantage of permitting free movement of air into and out of the specimen during testing.



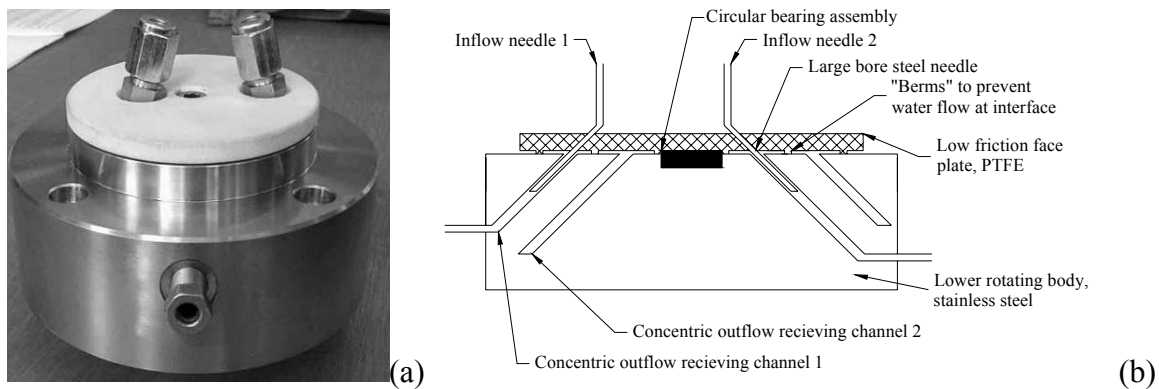


Figure 6.10: Low-flow rotary union: (a) Picture; (b) Schematic view

The rotary union consists of two halves. The lower, rotating half is made from steel and has two inclined, concentric channels. These channels are plumbed to exit ports on opposite sides of the joint, from which water passes to the diametrically opposite permeameters. The upper, stationary half is made from PolyTetraFluoroEthylene (PTFE or Teflon). The PTFE provides a low-friction interface contact with the steel lower chamber and prevents water leakage from the rotating interface. To ensure nominal contact between the PTFE disc and the steel lower chamber, the top chamber is suspended on a bearing assembly. The PTFE disc supports two steel needles that are placed with the same radial location and inclination as the inclined channels in the lower half. Fluid from the infusion pump drips from the steel needles into the concentric channels in the lower half. The centripetal acceleration field pushes the fluid toward the outside radius of the inclined channel, after which it drains through the exit hole. The union also functions while the system is stationary.

Tests for assessment of potential water loss were conducted with the rotary union using the setup shown in Figure 6.11. A flow rate was applied to the stationary side with the pump while the outflow was collected over a period of time in a beaker attached to

the spinning half. No water losses were observed in the tests for different combinations of flow rates and angular velocities (1.0 ml/hr and 100 ml/hr each at 100 and 700 RPM).

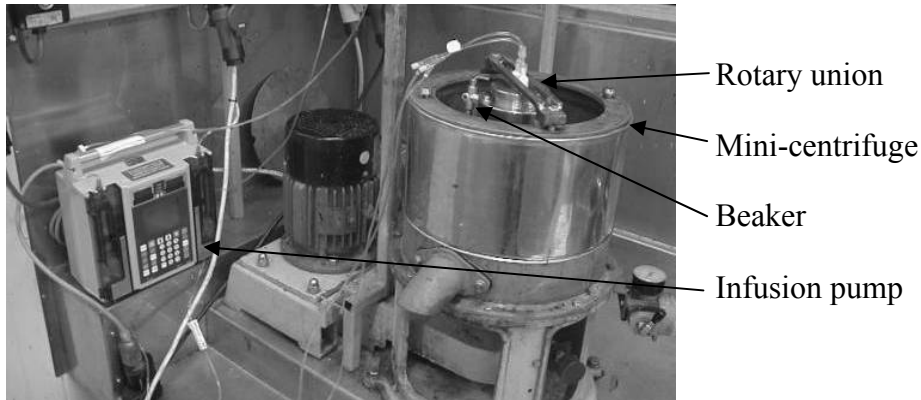


Figure 6.11: Water conservation test in a mini-centrifuge

#### 6.4.2 Fluid Distribution System

Saville<sup>®</sup> copper brake tubing is used to transmit water from the rotary union to the permeameter, shown in Figure 6.12(a). Copper tubing can be bent into shape but remains rigid during centrifugation. Flexible plastic tubing was used as a connector to permit free rotation of the permeameter as it swings up during centrifugation [Figure 6.12(b)].

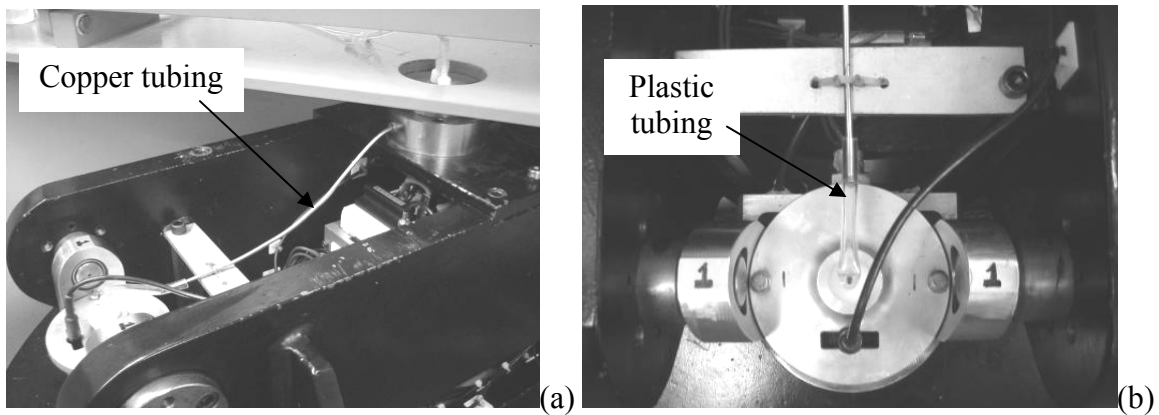


Figure 6.12: Plumbing connection between rotary union and permeameter: (a) Connection with brake tubing; (b) Flexible plastic tubing connector

The permeameter top cap is used to distribute water uniformly across the area of the specimen so that the full area of the specimen receives moisture flow. The copper tubing from the rotary union connects to a 1 ml cylindrical reservoir on the top of the steel top cap, as shown in Section A-A of Figure 6.13(a) and in Figure 6.13(b). After the reservoir fills, water will overflow into a series of holes in the reservoir. The holes are angled to form a concentric circle on the bottom of the top cap. The top cap for the prototype permeameter has 16 1.6-mm-diameter holes evenly distributed in two circles [Figure 6.13(c)], and the hydraulic characterization permeameters has 8 holes [Figure 6.13(d)]. The top cap for the hydraulic characterization permeameter also has a port to allow access for the vertically-oriented TDR waveguide.

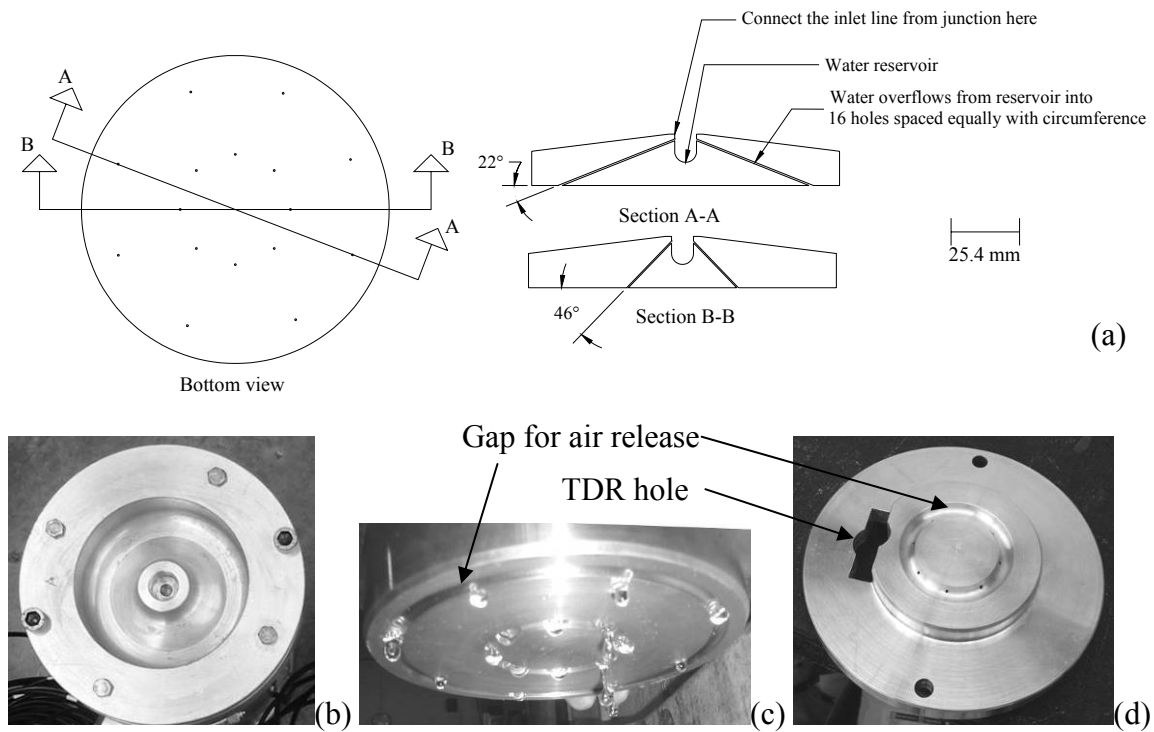


Figure 6.13: (a) Schematic of the fluid distribution cap; (b) Top of Prototype permeameter fluid distribution cap; (c) Bottom of prototype permeameter fluid distribution cap during 1-g inflow test; (d) Fluid distribution cap for hydraulic characterization permeameter with TDR hole

A preliminary 1-g flow test was conducted on the fluid distribution cap outside of the centrifuge. Water dripping from a faucet was successfully distributed to all 16 holes of the large permeameter cap, as shown in Figure 6.13(c). Although qualitative, this test illustrates the functionality of the fluid distribution system. An inflow test was also repeated in the centrifuge using the hydraulic characterization permeameter. Test tubes were embedded in a sand layer, directly under the outlet ports of the distribution cap in order to collect the flow from each hole, as shown in Figure 6.14(a). A flow rate of 5 ml/hr was applied for 5 hours, after which the water collected in each tube was measured. The results indicate that the volume collected by each tube was approximately 1/8 of the total volume, within 0.1 ml, as reflected in the results in Figure 6.14(b).

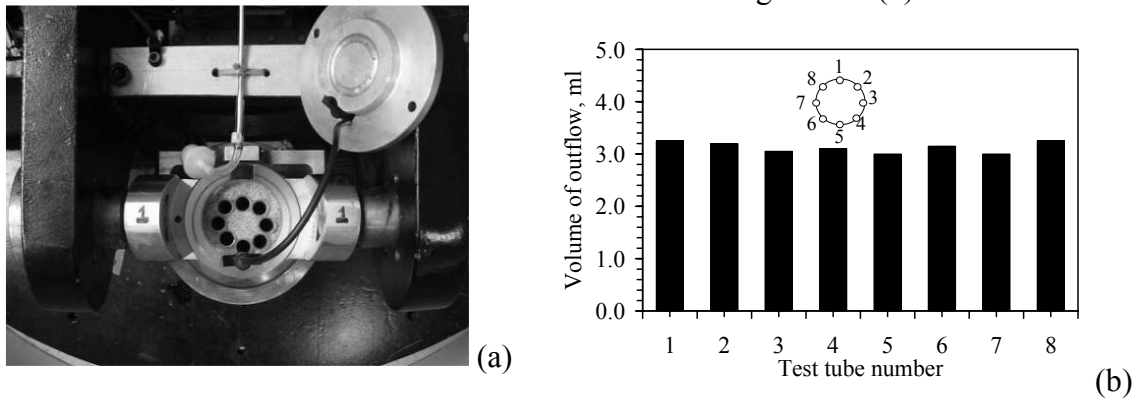


Figure 6.14: Centrifuge inflow fluid distribution test

### 6.4.3 Outflow Collection System

The bottom (outflow) boundary for permeameters consists of a 12 mm steel outflow support plate with a system of fluid collection grooves, sloped slightly toward a 3-mm diameter exit hole, as shown in Figure 6.15(a) and Figure 6.15 (b). An o-ring groove along its perimeter prevents water from leaking around the edges of the plate. In the hydraulic characterization tests, two filter alternatives were used to retain the soil while minimizing hydraulic impedance. A braided wire mesh filter with a porosity of 0.4

was used in some tests, as this porosity is close to that of the soils used in this study. Although this mesh appears free-flowing, an accumulation of fines was noticed in the pores after testing. In later tests, a layer of filter paper underlain by a #100 wire screen was used, as no soil was lost and the hydraulic impedance was minimal. The braided wire mesh filters (flat) and wire screens (curled) shown in Figure 6.15(c) and Figure 6.15(d). A geosynthetic drainage layer was also used as a boundary condition in one of the tests in this study. McCartney *et al.* (2005) found that use of geosynthetic drainage layers under a compacted clay layer tends to cause a capillary break, resulting in accumulation of water near the outflow face of the soil. McCartney *et al.* (2005) found that the suction at capillary breakthrough was 4 kPa for a 6 oz/yd<sup>2</sup> nonwoven geotextile. This allows investigation of suction profiles for different boundary conditions.

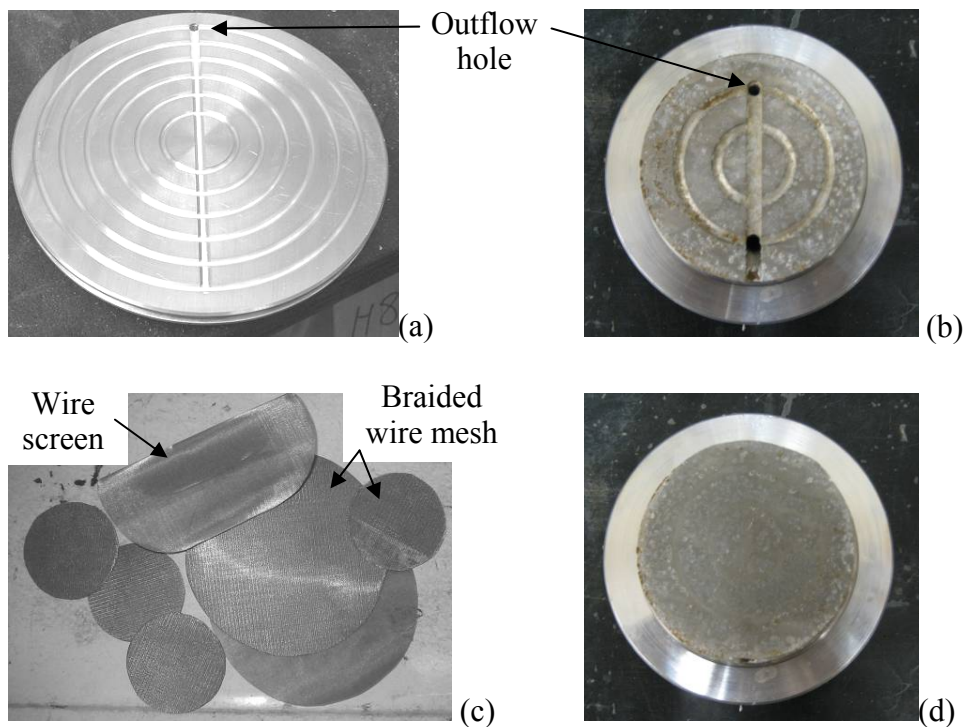


Figure 6.15: (a) Outflow support plate for prototype permeameter; (b) Outflow support plate for hydraulic characterization permeameter; (c) Wire mesh filters; (d) Wire mesh filter and outflow support plate

Although a zero suction boundary condition is not imposed at the base of the profile, it is expected that the soil becomes almost saturated near the outflow face during steady-state water flow. This is postulated because water will not flow out of an unsaturated soil until the pressure in the water overcomes that in the pore air (assumed to be atmospheric). In other words, the water meniscus must become convex for outflow to occur. Accordingly, the use of an outflow support plate without direct control of the water table may still act as a saturated boundary condition for steady-state flow. However, different from a water table, a zone of capillary rise may not occur for a freely-draining outflow plate. Another important point that should be made is that the bottom outflow face will de-saturate if inflow is not supplied to the soil profile (Forbes 1997). This was observed to be a problem in centrifuge tests involving transient drainage of a specimen placed atop a saturated porous stone.

The seal between the outflow support plate and the underlying outflow collection reservoir is air-tight. Consequently, an air escape hole was included in the base of the permeameter, as shown in Figure 6.16. This approach was selected to minimize stress concentrations in the outflow reservoir assembly that may arise if a hole were drilled in the reservoir. A 3-mm-diameter steel pipe was passed through a hole in the support platen, bent into a channel in the support platen so that it would be flush with the level of the permeameter base, and passed then through the permeameter wall. An “o”-ring was used to provide a seal between the pipe and the permeameter wall. This approach was found to successfully allow air to escape from the outflow reservoir as water flows out of the permeameter. Another hole in the outflow support plate transmits water into the outflow reservoir as shown in Figure 6.16(d). Water drips from this hole into the water reservoir, providing further indications that the soil at the base of the permeameter must be nearly saturated for outflow to occur.

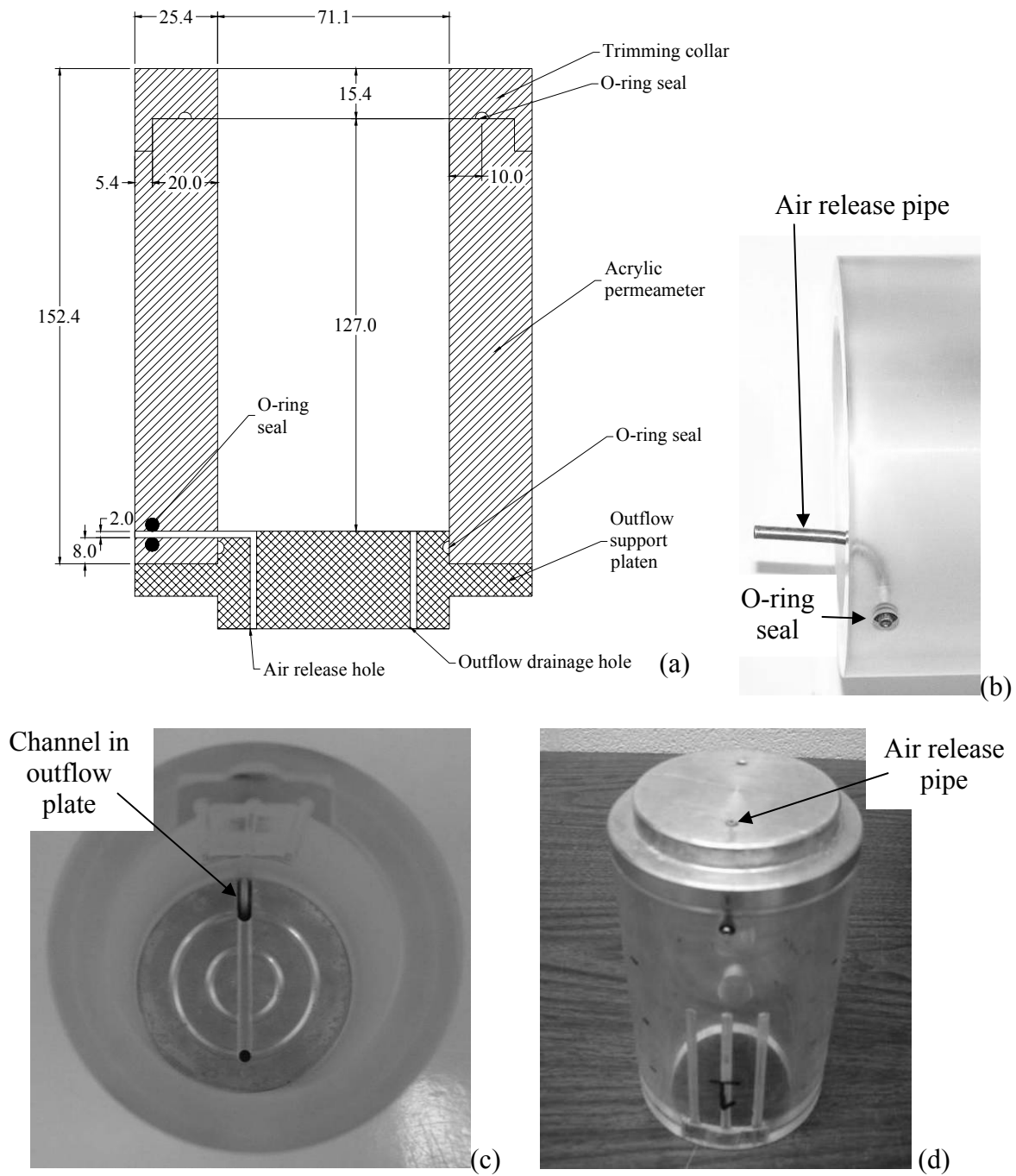


Figure 6.16: (a) Cross-section of the hydraulic characterization permeameter; (b) Air-release pipe; (c) Air-release pipe connection with the outflow support plate; (d) Air release pipe in outflow plate

The outflow collection reservoir shown in Figure 6.17(a) has a 1 liter capacity, and is connected to the base of the permeameter, as shown in Figure 6.17(b). Water is emptied from the reservoir using a ball-valve fitting. The amount of fluid in the collection reservoir is measured using a Druck PMP-4010 pressure transducer having a capacity of 40 kPa. The low capacity of the transducer was adopted to allow good resolution for small changes in pressure ( $\sim 0.007$  kPa). The sensing membrane of the transducer is aligned with the base of the outflow reservoir. The pressure transducer is connected to the outflow reservoir via a machined manometer tube, so that the pressure measured by the transducer is the same as that at the base of the water column in the reservoir.

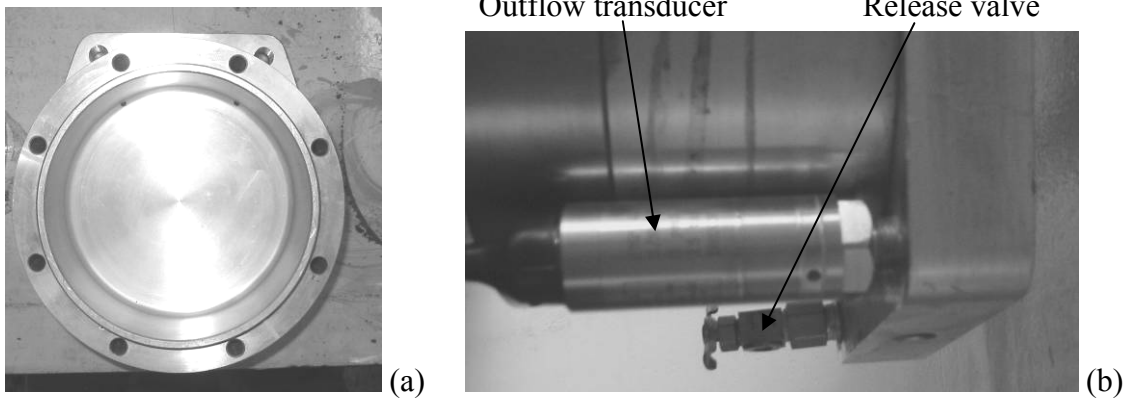


Figure 6.17: Outflow reservoir: (a) Disassembled; (b) Outflow transducer and valve

The water pressure at the base of the reservoir depends on both the g-level at the base of the reservoir and the height of water. The height of water in the outflow reservoir is not straightforward to calculate because non-uniformity in the g-field leads to curvature of the water surface, and small volumes of water may not be sufficient to form a continuous film across the area of the permeameter. Further, as the transducer is aligned vertically in the centrifuge, its diaphragm will deflect downward under its own weight. A volume of 10 ml is maintained in the outflow reservoir to prevent deflection of the transducer diaphragm in the direction of g (and measurement of negative values).



To overcome the aforementioned issues, a conventional calibration procedure outside of the centrifuge could not be performed for the outflow transducer. Instead, calibration was performed by placing a known volume of water in the reservoir, and spinning the centrifuge to several velocities, as shown in Figure 6.18(a). The same data plotted as a function of the g-level is shown in Figure 6.18(b), indicating a linear trend between  $N_{r,mid}$  and the output voltage for volumes of water greater than 400 ml. However, curvature of the water surface and lack of sufficient water to cover the base of the reservoir lead to less deflection of the outflow transducer diaphragm for smaller water volumes. The linear portions of these curves were used to define calibration curves for the two transducers, shown in Figure 6.19, relating the Voltage/ $N_r$  with outflow volume.

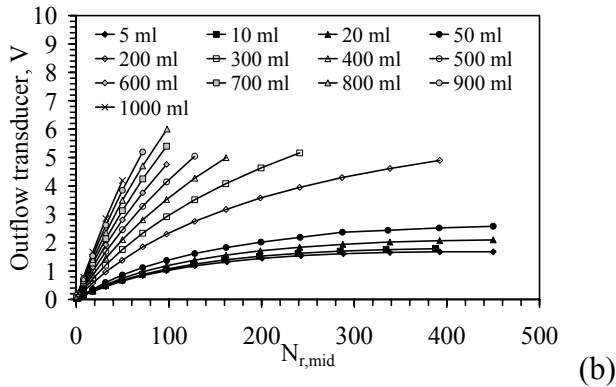
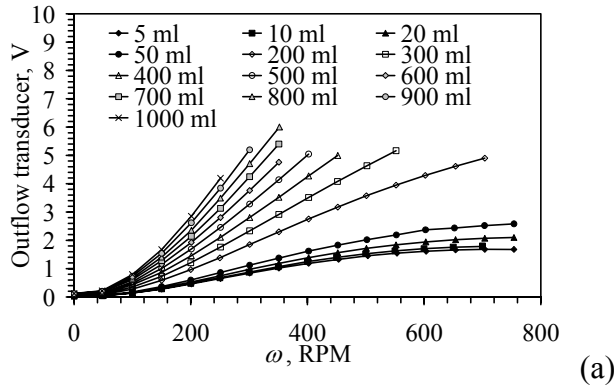


Figure 6.18: Outflow transducer results with: (a) Angular velocity (b) g-level

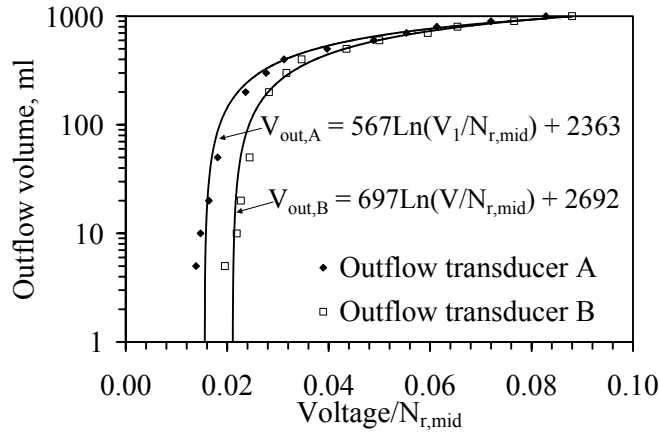


Figure 6.19: Outflow transducer calibration curve

Despite the nonlinearity in the calibration equation, it should be noted that the outflow volume is not used for interpretation of infiltration tests. The main purpose of the data collected from outflow transducer in this study is the assessment of steady state flow has been achieved. During steady state flow, the voltage output from the outflow transducers shows a constant increase with time. This is discussed in Appendix A.

## 6.5 MOISTURE CONTENT AND SUCTION INSTRUMENTATION

### 6.5.1 Time Domain Reflectometry

Time domain reflectometry (TDR) systems are used in geoenvironmental engineering applications to measure the bulk apparent dielectric permittivity  $K_a$  and electrical conductivity of soil, which can in turn be used to infer the volumetric moisture content of the soil (Benson and Bosscher 1999; Siddiqui *et al.* 2000). TDR technology involves measuring the travel time of an electromagnetic pulse applied to a transmission line terminating in a shielded, metallic, waveguide (Topp *et al.* 1980). The waveguide is typically buried within the soil mass. The pulse is reflected at every change in impedance along the transmission line-probe system (*e.g.*, the beginning and end of the waveguide).

The velocity of the reflected pulse is sensitive to the dielectric permittivity of the water within the soil mass, which is an order of magnitude greater than that of air and soil particles. The dielectric permittivity of the soil mass inferred from the velocity of the reflected pulse then can be correlated with the volumetric moisture content of the soil.

Conventional TDR requires the generation of electromagnetic pulses with a frequency on the order of 10-100 GHz. The pulse in conventional TDR is generated by a cable tester, which also digitizes reflected waveforms, uses curve-fitting software to analyze the shape of the waveform, and logs waveforms over time. Use of TDR in field monitoring programs is often limited by the relatively high power requirements and cost of the cable tester, but they are well suited for laboratory measurements. The results of the calibration testing program conducted as part of this study indicate that conventional TDR can infer a wide range of volumetric moisture content values (*i.e.*, 5% to 50%). The precision of the TDR system can be as high as  $\pm 0.1\%$  if careful analysis of the TDR waveforms is made. Benson and Bosscher (1999) indicate that conventional TDR is the least sensitive among available dielectric techniques to environmental variables that may affect measurement of the dielectric permittivity (*e.g.*, temperature, attenuation due to salinity or electrical conductivity of the soil particles, frequency dispersion, *etc.*).

The TDR system used in this study is the Mini-Trase<sup>®</sup>, developed by SoilMoisture, Inc. of Santa Barbara, California. This TDR system includes a cable tester (Model 6050X), a 16-channel coaxial multiplexer (model 6021C16), and mini-buriable waveguides (model 6111). The details of the cable tester will be discussed in the section on data acquisition. The waveguide used in this study has three cylindrical, 80-mm long prongs, as shown in Figure 6.20(a). The center prong is the active transmission line, while the two outer prongs provide shielding. This arrangement is necessary to confine the energy of the electromagnetic pulse to the area around the central probe. The zone of

influence of the electromagnetic pulse was investigated by varying the proximity of the probe to the wall of a steel box filled with wet sand. The approximate zone of influence is shown in Figure 6.20(c). Zegelin *et al.* (1989) presented an assessment of the shape of the electromagnetic fields for soil with varying dielectric permittivity.

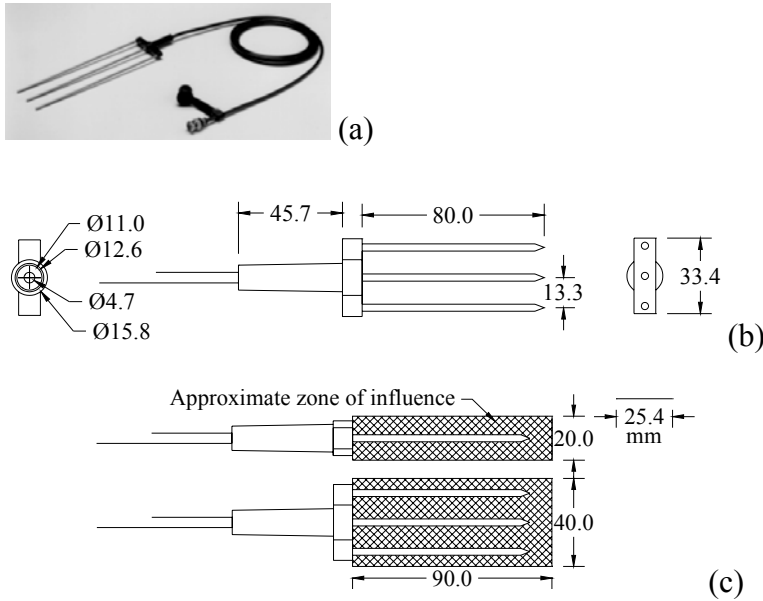


Figure 6.20: (a) Picture of TDR waveguide; (b) Schematic; (c) Zone of influence

Confinement of the TDR waveguide in the permeameters was challenging, and different layouts were adopted for the prototype and the hydraulic characterization permeameters. In the prototype permeameter, the TDR waveguides are embedded horizontally within the soil, and the cable is passed through the side wall of the permeameter, as shown in Figure 6.21(a). To avoid removal of the BNC coaxial connector at the end of the waveguide, a split fitting was developed, shown in Figure 6.21(b). The fitting is sealed using an o-ring placed on the TDR waveguide, and is threaded on the outside to match the  $\frac{1}{2}$ " NPT instrumentation ports in the prototype permeameter. The fitting rigidly grips the waveguide, so it is cantilevered in the specimen. Accordingly, the waveguide should not place significant additional load to the

specimen causing differential settlement. However, compacted soil should be dense enough to minimize settlement around the waveguide.

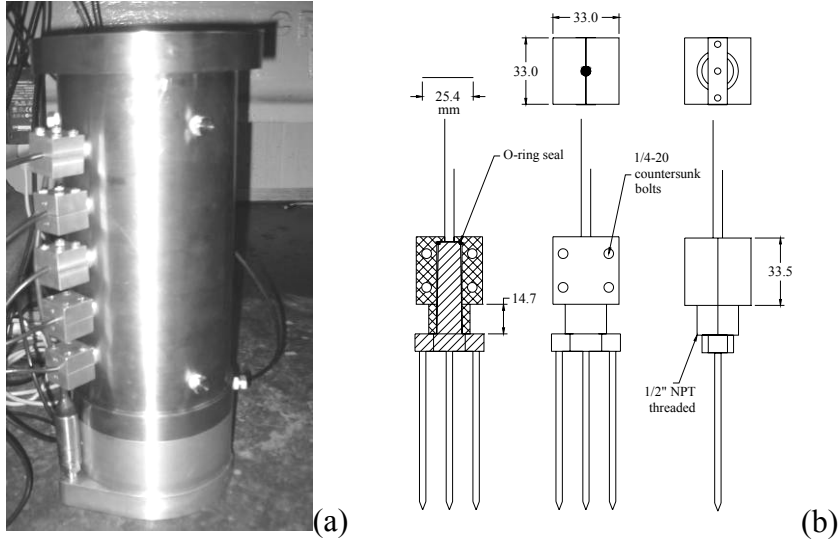


Figure 6.21: (a) TDR fitting in prototype permeameter; (b) Schematic view of fittings

The hydraulic characterization permeameter uses a single TDR waveguide embedded longitudinally within the acrylic wall of the permeameter, as shown in Figure 6.22. This particular orientation of the TDR along the edge of the permeameter was selected due to space constraints and to avoid inclusions into the specimen which may affect the flow behavior under investigation. This orientation has implications on the measurement of moisture profiles during transient infiltration through the permeameter, because TDR infers the average moisture content along the length of the waveguide (McCartney *et al.* 2006). Use of a travel time analysis (described below) does not allow inference of the moisture content profile along the waveguide, only the average moisture content over the length of the waveguide. However, during steady state moisture flow in the centrifuge, the moisture content in the upper portion of the specimen is approximately constant. Accordingly, the average moisture content measured by the TDR in this

Figure 1 consists of four parts: (a) Schematic diagrams of the apparatus components, (b) Photograph of the permeameter assembly, (c) Photograph of the TDR waveguide assembly, and (d) Photograph of the air release hole assembly.

Part (a) includes several detailed drawings:
 

- Top view of the permeameter:** Shows concentric circles with radii R1.6, R35.6, R55.6, and R61.0. A recess cut into the wall of the permeameter is shown, partially embedding the waveguides (70% of metal is exposed to the soil). Dimensions include 13.3, 13.3, and 35.6.
- Side view of the permeameter:** Shows the vertical assembly with dimensions 121.9, 25.4, 71.1, 20.0, 7.9, 5.4, 10.0, and 12.5. A scale bar indicates 25.4 mm.
- Side view of the TDR waveguide:** Shows the waveguide assembly with dimensions 152.4, 127.0, 6.7, 15.0, 21.2, 8.0, 2.0, 10.0, 47.1, 11.0, and 10.0. Labels include "TDR waveguide", "Trimming collar", "O-ring seal", "O-ring seal", "Outflow support platen", "Outflow drainage hole", and "Air release hole".
- Side view of the air release hole:** Shows the air release hole assembly with dimensions 8.0, 2.0, 12.0, 20.0, 10.0, 137.0, 26.7, and 1/8" diameter steel pipe. Labels include "Acrylic permeameter", "Pore water pressure transducer ports", and "O-ring seal".
- Top view of the air release hole:** Shows concentric circles with radii R7.9, R46.1, R50.1, R55.6, and R61.0. Dimensions include 33.4 and 9.0.

Parts (b), (c), and (d) are photographs showing the physical components of the apparatus, corresponding to the schematic diagrams in (a).

130

A complete TDR waveform is shown in Figure 6.23. The pulse is a 2 Volt square wave with an effective rise time of 7 ps. The pulse is applied to the cable for 15 ms, which is significantly longer than the expected time for the first reflection from the waveguide (about 22.5 ns for a 5 m cable). Reflections of the waveform at changes in impedance are measured by an oscilloscope in the cable tester. The reflections are superimposed upon the input pulse, so the composite waveform contains a significant amount of information about the propagation in the cable tester itself, the multiplexer, the cable, and the waveguide embedded in the soil. Measurements of travel time through the waveguide require analysis of the portion of the waveform that corresponds to the waveguide ( $> 18$  ns). However, the shape of the complete waveform will reflect its frequency content. This is important as attenuation (loss of signal) and dispersion (different rates of travel) of the different frequencies present in the square wave change the reflection travel time. This is an important area for future research.

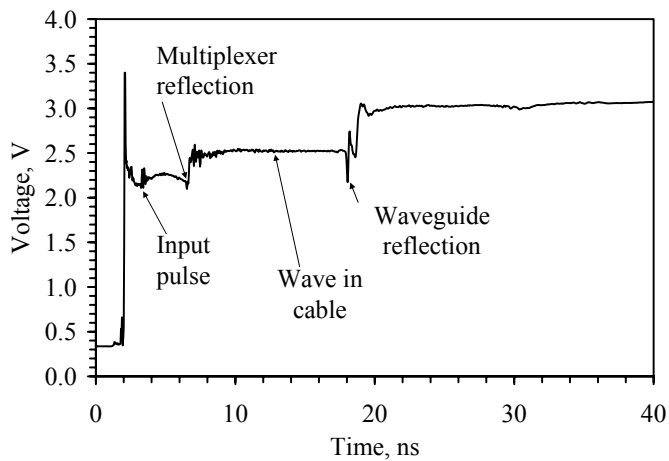


Figure 6.23: Full TDR waveform

The input pulse, reflections as the pulse passes into the multiplexer, and the reflection at the waveguide are shown in Figure 6.23. These aspects of the waveform are specific to the particular setup of the TRASE system. For a brief moment, the waveform

shows a higher voltage than 2V, as the TDR system acts as a low pass filter, attenuating high frequency components of the square wave. This leads to an increase in the voltage of the reflected wave (Zegelin *et al.* 1981). As the pulse passes through the multiplexer into the 50Ω cable, it stabilizes at 2.5 Volts (~2V greater than the initial voltage).

The waveforms used to infer the travel time of the pulse in the waveguide have a window ranging from 18 ns to 30 ns with 1200 data points. The input voltage may vary from waveguide to waveguide because of the multiplexer. Consequently, a normalized form for the voltage on the ordinate, referred to as the reflection coefficient, is defined as:

$$\rho_{RC} = \frac{(V_i - V_C)}{V_C} \quad (6.1)$$

where  $\rho_{RC}$  is the reflection coefficient,  $V_i$  is the reflection voltage at any time and  $V_C$  is the voltage in the cable. To analyze the travel time of the pulse through the waveguide, the derivative approach proposed by Robinson *et al.* (2005) was used. This approach uses the first derivative of the waveform to find the inflection points of the reflected waveform, as shown in Figure 6.24. The inflection points correlate with the location of the maximum energy of the wave as it passes through the waveguide. This leads to a more reliable measure of the travel time than when using the first reflection arrival times.

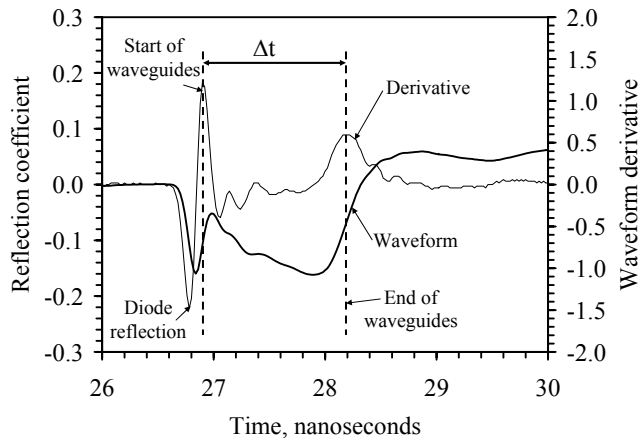


Figure 6.24: TDR waveform with derivative travel time analysis



The times at which the pulses reach the beginning and end of the probes are identified in Figure 6.24 as  $\Delta t$ . This travel time reflects the 1-way travel time through the soil. The average velocity of the reflected pulse in the waveguide can be calculated as:

$$v_{pulse} = \frac{L_{probe}}{\Delta t} \quad (6.2)$$

where  $v_{pulse}$  is the pulse velocity,  $L_{probe}$  is the length of the waveguide, and  $\Delta t$  is the 1-way trip travel time through the waveguide. The buriable waveguides used in this study have diode embedded in the head of the probe which forms a known change in impedance before the beginning of the waveguide. This permits automated identification of the reflected waveform. Accordingly, the reflection from the beginning of the probe can be identified as the trough occurring 0.12 ns after the waveform shows a downward drop in voltage. This diode corresponds to the negative spike in the derivative in Figure 6.24 at a time of 26.8 ns, while the beginning of the waveguide corresponds to the positive spike in the derivative at a time of 26.9 ns.

The velocity of the pulse is also related to the bulk dielectric permittivity of the medium surrounding the waveguide:

$$v_{pulse} = \frac{c}{\sqrt{K_a}} \quad (6.3)$$

where  $c$  is the speed of light in vacuum and  $K_a$  is the dielectric permittivity of the media surrounding the waveguide. Equations (6.2) and (6.3) can be combined to obtain an expression for the apparent dielectric permittivity:

$$K_a = \left( \frac{c\Delta t}{2L} \right)^2 \quad (6.4)$$

The travel time data from the waveforms can be used to determine the dielectric permittivity for different materials.

TDR waveforms for a waveguide in air and water are shown in Figure 6.25. The travel time in air is negligible ( $\sim 0.1$  ns) as it is a good insulator. Accordingly, the wave does not attenuate as it travels through the waveguide. However, the travel time in water is greater ( $\sim 2.2$  ns). The smaller frequencies of the wave (that travel fastest) are attenuated as the wave comes in contact with the water, resulting in a slower travel time. The values of  $K_a$  calculated for air and water are 1.2 and 78, respectively.

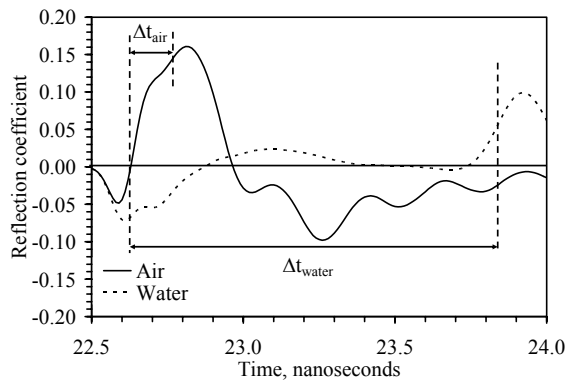
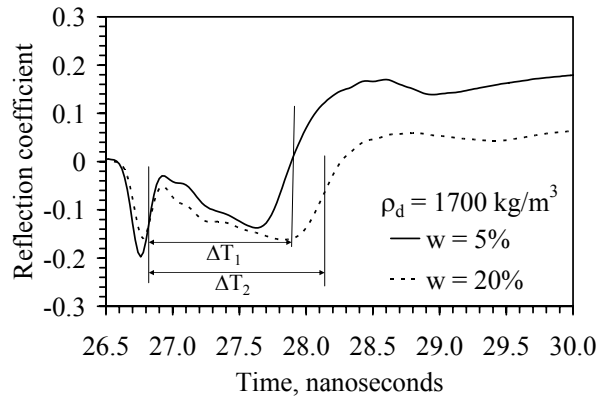
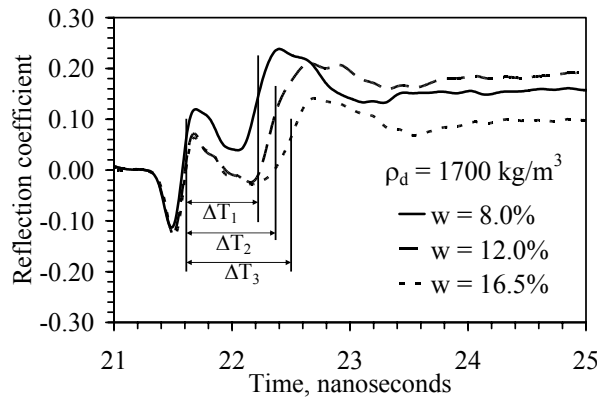


Figure 6.25: TDR waveforms in water and air

Waveforms for waveguides embedded in soil with the same density but different gravimetric water contents are shown in Figure 6.26(a). The travel time increases as the water content of the soil increases. The magnitude of the reflected voltage is typically lower for waveguides in wetter soils, as the higher frequency components of the wave attenuate, causing a decrease in voltage. The wetter soils also show a lower “dip” in voltage after the pulse enters the waveguide because of this same reason. Similar observations can be made for the waveguide embedded in the wall of the hydraulic characterization permeameter, waveforms for which are shown in Figure 6.26(b). The acrylic material is an insulator, so the reflected waveforms are closer to that of a wave in air than a wave in water (*e.g.*, shorter travel times). However, an increase in the travel time is still noted for soils with increasing water content.



(a)



(b)

Figure 6.26: TDR waveforms with changing soil water content: (a) Prototype permeameter; (b) Hydraulic characterization permeameter

A calibration program was conducted to associate measured  $K_a$  values with volumetric moisture content of the RMA Soil Type II soil. This included measurement of the dielectric permittivity of specimens with compaction water contents ranging from 5% to 35% (gravimetric) and porosities of 0.35, 0.45, and 0.5. These porosities correspond to 90, 80, and 70% of the maximum dry density for the standard Proctor compaction energy ( $1900 \text{ kg/m}^3$ ), respectively. The standard Proctor compaction curve and the reduced-effort compaction data are shown in Figure 6.27(a). The compaction mold used for calibration of embedded TDR waveguides is shown in Figure 6.27(b).

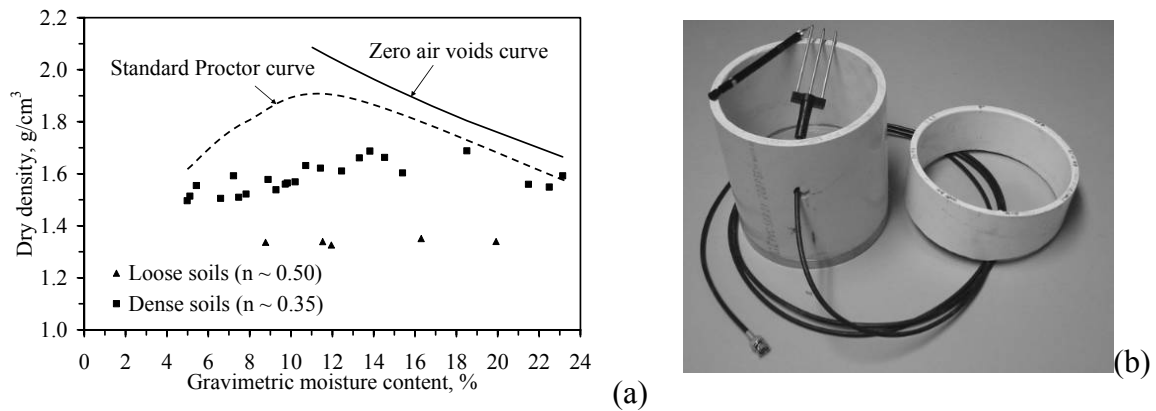


Figure 6.27: (a) Embedded TDR compaction data; (b) Compaction mold

To define calibration curves for the prototype permeameter, the TDR waveguide was buried within the middle lift of the compaction mold. Results of the calibration program for three porosities are shown in Figure 6.28. Linear calibration curves were obtained for the clay. Lower porosities lead to greater changes in dielectric permittivity with changes in volumetric moisture content. In other words, the travel time is less sensitive to changes in moisture content for looser soils.

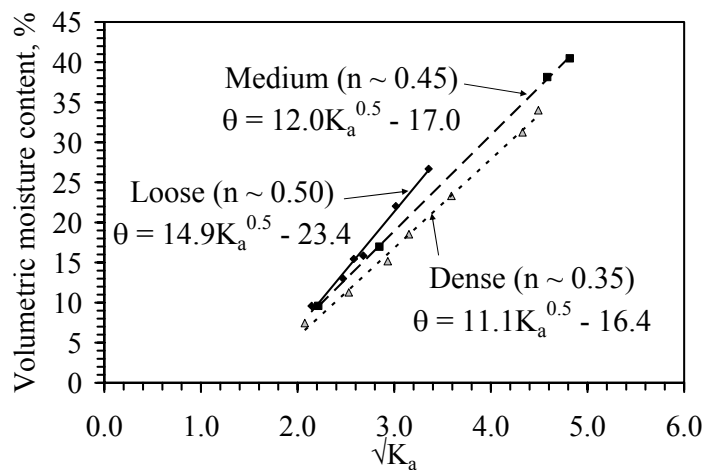


Figure 6.28: Embedded TDR calibration curves

The effect of pore water salinity on the TDR calibration was assessed to evaluate the initial osmotic potential in the soil. The salinity was changed by mixing air-dried soil with water having a known salinity concentration. The effects of increased salinity on TDR waveforms are shown in Figure 6.29(a). Increased salinity leads to attenuation of the signal as it passes through the waveguide, and can be significant enough that a reflection is not detected. Calibration curves for the TDR waveguides embedded in soils having different pore water salinity concentrations are shown in Figure 6.29(b). The TDR calibration curves are similar at low moisture contents. However, the calibration curves tend to deviate from linear with increasing water content, with a greater deviation for soils having higher salinity concentration. The salinity concentration for a given specimen can be assessed by plotting the moisture content and  $K_a$  at the end of an infiltration test (presumably having high  $\theta$ ) on Figure 6.29(b). The salinity can be assessed using the different trend lines. The salinity concentration may change throughout an infiltration test due to leaching of cations by the flowing water. Changes in salinity may reflect changes in osmotic suction, influencing tensiometer results.

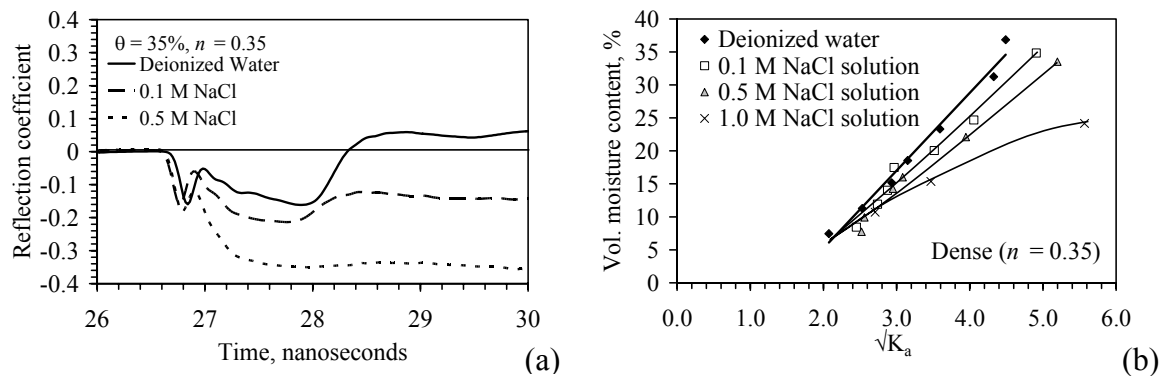


Figure 6.29: Effect of salinity on TDR measurements: (a) Waveforms; (b) Calibrations

To define calibration curves for the hydraulic characterization permeameter, moisture conditioned soil was compacted into the hydraulic characterization

permeameter, with the vertically oriented TDR waveguide in place before compaction. Results of the calibration program for clay with porosities of 0.35, 0.45, and 0.50 are shown in Figure 6.30. Accurate compaction of high water content specimens at high porosities values is very difficult due to the shape of the compaction curve. Accordingly, to obtain points on the calibration curve at high moisture contents, water was infiltrated through compacted specimens until reaching steady-state moisture flow. The average gravimetric water content was obtained from soil adjacent to the waveguide. The sensitivity of TDR in the hydraulic characterization permeameter is approximately half that of the situation when the waveguide is buried in the soil.

There is scatter in the calibration data due to slight variations in porosity between the specimens ( $n = 0.35$  to  $0.4$ ). It was initially expected that the electrical field would not be uniformly distributed between the soil and acrylic over a wide range of water contents, resulting in a non-linear calibration equation between dielectric permittivity and moisture content. However, a linear trend was observed indicating a uniform distribution over the range of moisture contents evaluated. The best-fit calibration factors for the hydraulic characterization and the prototype permeameters are summarized in Table 6.1.

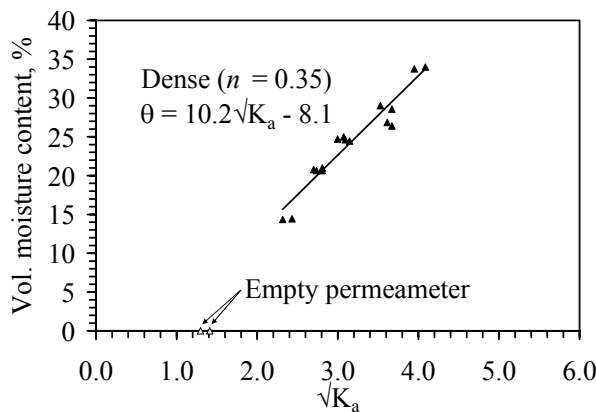


Figure 6.30: TDR calibration curve for hydraulic characterization permeameter

Table 6.1: Calibration equations for TDR in both centrifuge permeameters

Permeameter	Description	Porosity	Range of $\theta$ (%)	Parameters	
				a	b
Prototype	Embedded	0.5	9.6 - 26.7	14.9	-23.4
		0.45	9.6 - 40.5	12.0	-17.0
		0.35	7.5 - 34	1.1	-16.4
Hydraulic characterization	Vertical in permeameter wall	0.5	4.0 - 40.4	10.2	-8.1
		0.45	16.9 - 33.4	26.3	-35.0
		0.35	10.0 - 26.9	42.7	-65.0

Note: Linear calibration curves were used:  $\theta = a\sqrt{K_a} + b$

The sensitivity of the TDR measurements with respect to both centrifugation and the time travel analysis is important to the accurate determination of the hydraulic characteristics. The effect of the g-level on TDR measurements is shown in Figure 6.31(a). A negligible change in  $\Delta t$  is observed with centrifuge speed, which indicates that travel time analyses are not affected by the electromagnetic field in the centrifuge that is generated by the motor. Repeat measurements of the dielectric permittivity with time during steady-state water flow are shown in Figure 6.31(b). This data allows assessment of the accuracy of the TDR measurements. The c.o.v. is reasonably low (0.03) corresponding to an accuracy of  $\theta \pm 2\%$ , which is deemed acceptable

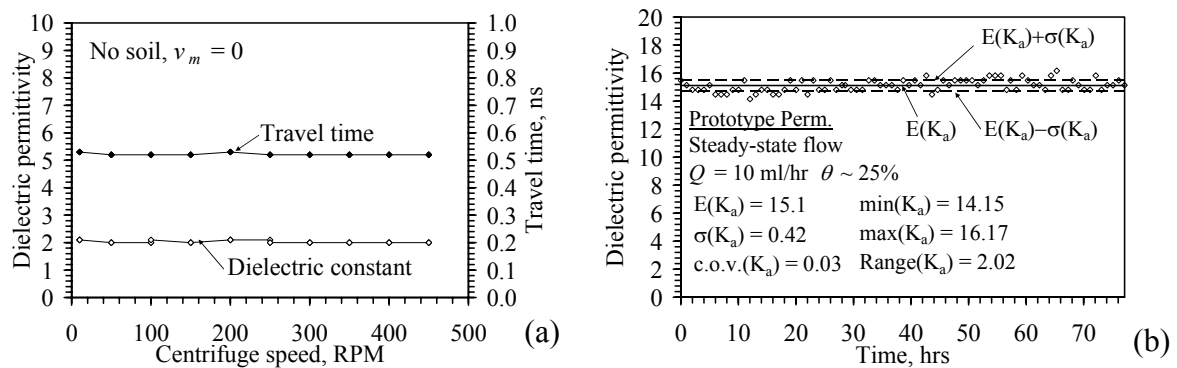


Figure 6.31: TDR sensitivity: (a) TDR during centrifugation in empty H.C. permeameter; (b) TDR measurements during steady-state flow in prototype permeameter

### 6.5.2 Tensiometers

Tensiometers are commonly used to measure suction below 80 kPa in unsaturated soils. Conventional tensiometers consist of a vacuum gauge connected via a water column to a water-saturated, high air-entry porous ceramic stone embedded within a soil mass. Due to continuity of suction at the interface between the soil and the ceramic, water will flow across the interface until the pressure within the reservoir is the same as the pressure within the soil (negative or positive). Accordingly, tensiometers have the advantage of providing a direct measurement of the matric suction.

Osmotic pressures in the soil may have a significant impact on the measurement of matric suction in saline soils using tensiometry. Ions in solution in the pore water tend to move from zones of high ionic concentration to low ionic concentration, which may result in an equivalent pressure in the water reservoir. If the water in the tensiometer reservoir is de-ionized, a potential gradient greater than that associated with the matric suction may develop, leading to higher suction measurements by the tensiometer. The TDR calibration for RMA Soil Type II indicates that osmotic potentials effects on the tensiometer readings should be negligible. Nonetheless, because distilled water is used in the infiltration tests, distilled pore water was also used to saturate the tensiometers.

Conventional tensiometers often experience cavitation at low suction values due to the large size of the water column, and also can be affected significantly by temperature. Several studies in the past two decades have led to innovations in the use of tensiometry (Ridley and Burland 1995; Sisson *et al.* 2002; Tarantino and Mongiovi 2003; Take and Bolton 2003). These “advanced” tensiometers consist of a miniature pressure transducer in contact with a small reservoir ( $< 1 \text{ mm}^3$ ) filled with de-aired water or another liquid. The water reservoir is also in contact with a water-saturated ceramic stone with a high air-entry value ( $> 300 \text{ kPa}$ ) and high hydraulic conductivity



( $> 10^{-7}$  m/s). The smaller size of the water reservoir limits nucleation of dissolved air bubbles under negative water pressures greater than 80 kPa, so cavitation can be avoided even for higher suctions. Suctions over 1000 kPa have been measured using these tensiometers, but they require complex saturation procedures, expensive machining, and cannot be disassembled after construction. A new tensiometer was designed for this study to make long-term measurements of suction values up to 200 kPa with simple saturation procedures and easy disassembly, for a cost less than 1000 dollars.

Two tensiometer designs were developed for this study, one for each of the permeameters. The tensiometer developed for the prototype permeameter is shown in Figure 6.32. A Druck PDCR 81 transducer was used to measure the pressure in a 1-ml water reservoir. The reservoir is formed between the brass housing of the tensiometer and a high-air entry ceramic porous stone. The brass housing of the tensiometer has  $\frac{1}{2}$ " NPT threads, and is screwed into the side-wall of the prototype permeameter.

The tensiometer has a continuous flushing channel that allows removal of air bubbles during saturation and in case cavitation occurs. The porous stone is sealed to the inside of a threaded brass pipe using epoxy, which allows the porous stones to be interchanged. This also allows the porous stones to be boiled in water during saturation without causing damage to the pressure transducer. To ensure saturation, the hydraulic conductivity of the porous stone in the tensiometer can be measured by connecting it to a pressure cell, shown in Figure 6.32(c), and connecting the flushing ports to pressurized, de-aired water lines. After obtaining a constant hydraulic conductivity of approximately  $3 \times 10^{-7}$  m/s (for a 5-bar stone) under a back pressure greater than 200 kPa, the tensiometer is ready for installation into a permeameter.

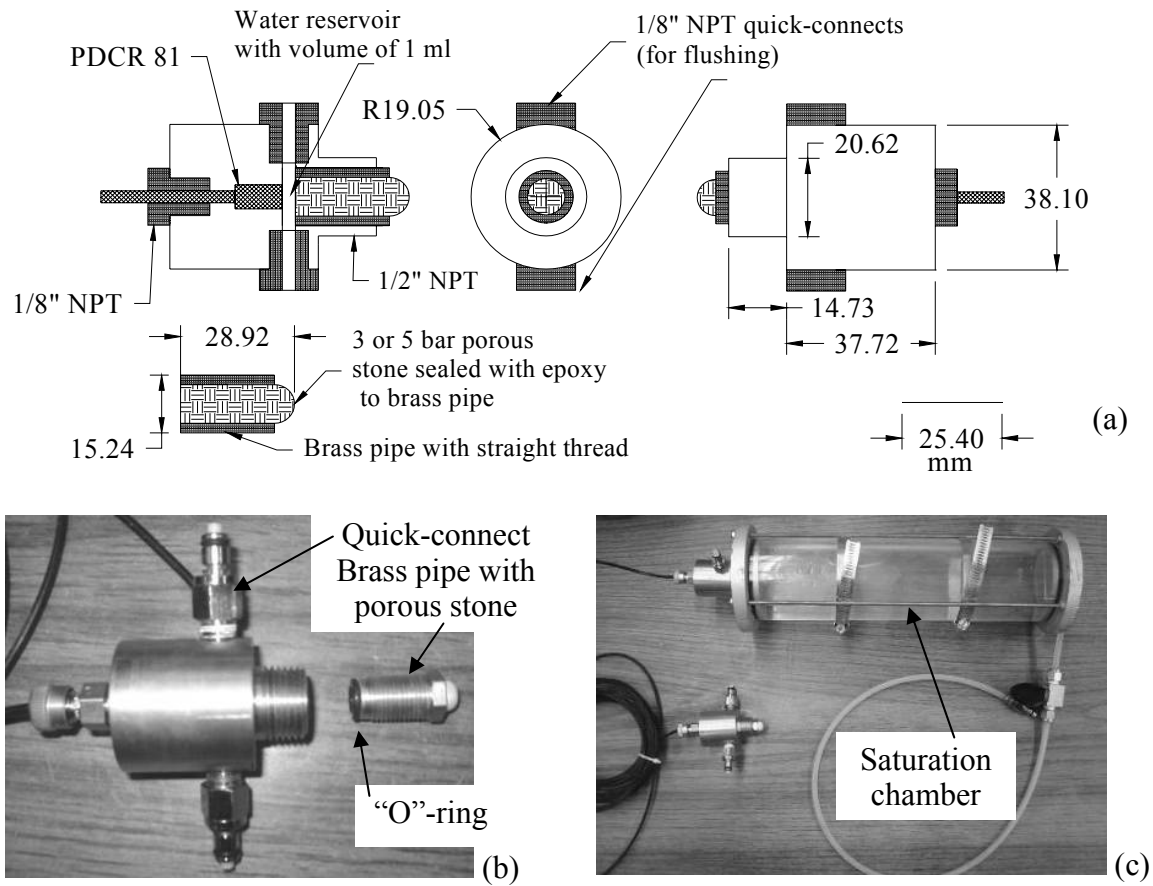


Figure 6.32: Flushing tensiometer for prototype permeameter: (a) Schematic; (b) Disassembled tensiometer; (c) Tensiometer with saturation chamber

The tensiometer design adopted for the hydraulic characterization permeameter, is shown in Figure 6.33(a). These tensiometers are similar in design to those for the prototype permeameter, as they have a brass housing, have a flushing path, and use the same porous stone-threaded brass pipe configuration, shown in Figure 6.33(b). However, in order to minimize the presence of small crevices around the pressure transducer, a vented Entran EPX-V01 pressure transducer, having a range of 700 kPa, was used in this tensiometer, as shown in Figure 6.33(c). This transducer has threads that allow it to be screwed directly into the brass housing of the tensiometer.

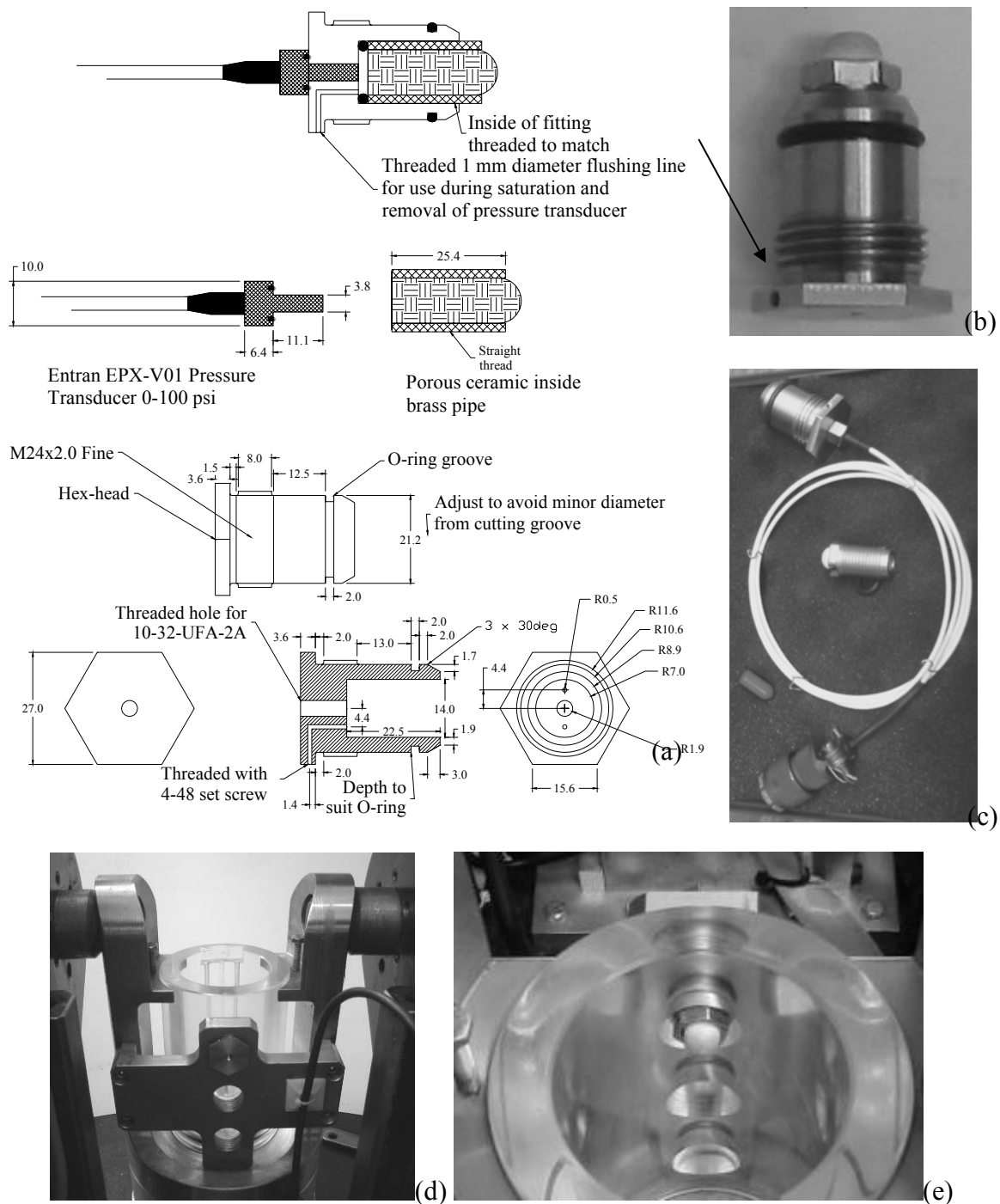


Figure 6.33: Tensiometer for the hydraulic characterization permeameter: (a) Schematic views; (b) Picture; (c) Tensiometer with transducer; (d) Bracket in swinging bucket; (e) Tensiometer in bracket and permeameter



Typical calibration curves for the advanced tensiometers are shown in Figure 6.35(a) and Figure 6.35(b). Experience indicates that the calibrations have a very stable slope, but the intercept may drift. Accordingly, the tensiometers were calibrated before each test during the saturation process. Different from traditional pressure transducers, it is necessary to wait for the voltage output to stabilize, as water must flow through the ceramic stone. A partially-saturated ceramic stone may lead to a slow response time, and also an inaccurate calibration if adequate time is not provided at each pressure increment. Because the tensiometers are vented, the suction measured is in reference to the ambient pressure during centrifugation. This is discussed in Appendix A.

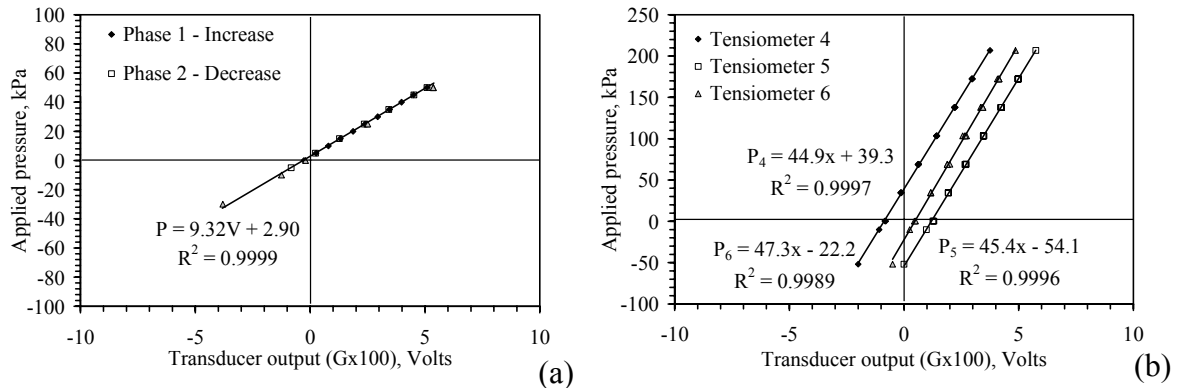


Figure 6.35: Tensiometer calibration curves: (a) Prototype permeameter tensiometer; (b) Hydraulic characterization permeameter tensiometer

### 6.5.3 Heat Dissipation Units

In the first design iteration of the centrifuge permeameter, heat dissipation units (HDUs) were used to infer matric suction. Use of HDUs was discontinued due to difficulties associated with noise in the signal during centrifugation, and because they do not have adequate resolution at suctions expected during infiltration testing (<50 kPa). Nonetheless, as the infrastructure for using heat HDUs has been developed, this section presents a brief discussion of HDUs to guide future researchers.

Heat dissipation units (HDUs) have been used in geotechnical applications to infer the soil suction through measurement of the thermal conductivity of a porous ceramic in hydraulic equilibrium with the soil of interest (Fredlund *et al.* 1992). They have been in use since the early 1970's (Phene *et al.* 1971), but have been gaining popularity only recently. The basis for the use of HDUs lies in the time response of a homogeneous material subject to a line heat source (Campbell *et al.* 1967):

$$\Delta T = T_f - T_o = \frac{q}{4\pi k} \ln(t_f - t_o) \quad (6.4)$$

where  $T_f$  is the final temperature at time  $t_f$ ,  $T_o$  is the offset temperature at time  $t_o$ ,  $q$  is the heat input in kW/hr, and  $k$  is the thermal conductivity of the ceramic. This equation is valid for a HDU when the heat pulse is lower than 3 kW/hr and is not applied for longer than 75 s (Flint *et al.* 2002). The thermal conductivity of porous materials is a function of their water content, making it a useful indicator of variables like suction.

HDUs consist of a steel needle embedded within a porous ceramic body. The steel needle contains both a heating coil and a thermocouple, shown schematically in Figure 6.36. For a given thermal input from the heating coil, the temperature increase in the ceramic depends on the thermal conductivity of the ceramic, which is a function of its water content. Dry ceramics tend to store heat (as air is an insulator), while wet ceramics tend to dissipate heat (as water is a conductor). If the ceramic is in contact with soil, the suction within the ceramic will come into equilibrium with the soil suction because of continuity. Accordingly, soil suction can be correlated with the temperature increase in the ceramic for a known thermal input. The calibration equation associating the temperature increase with suction for an HDU is sensitive only to the WRC of the ceramic, and is soil-independent. The characteristics of the ceramic are selected so that its WRC has a gradual curve in order to have appreciable changes in water content with changes in suction.

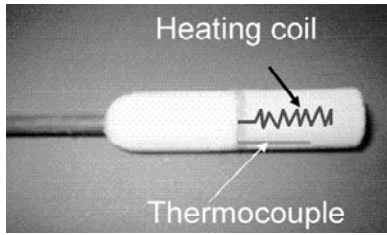


Figure 6.36: Heat dissipation unit

Model CS229 heat dissipation units, manufactured by Campbell Scientific, Inc. of Logan, Utah were used in this study. An 8-channel Campbell Scientific CE8 constant current source, shown in Figure 6.37(a), is used in this study to supply a heat pulse of 2.9 kW/hr to the heating coil for 30 seconds. The timing of the pulse is controlled using a +5V signal provided from an external power supply. The response of a thermocouple should be measured using a cold junction compensation circuit, or the temperature at the end of the thermocouple wires will affect the accuracy of the measurement. TC-mate units, obtained from Ectron Electronics, Inc of San Diego, CA and shown in Figure 6.37(b), were used to provide cold-junction compensation in the centrifuge permeameter.

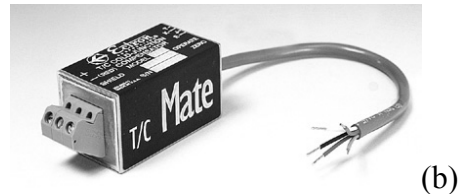


Figure 6.37: (a) Constant current source; (b) Cold-junction compensation module

A schematic of the HDU is shown in Figure 6.38(a). Similar to the TDR waveguides, fittings were designed for use with the different permeameters. A schematic of the fitting for the large-scale columns and the prototype permeameter is also shown in Figure 6.38(a). NPT threads are used to provide a hydraulic seal. The fitting for the HDU

in the hydraulic characterization permeameter shown in Figure 6.38(b) is similar to that for the tensiometer, with a circumferential “o”-ring seal.

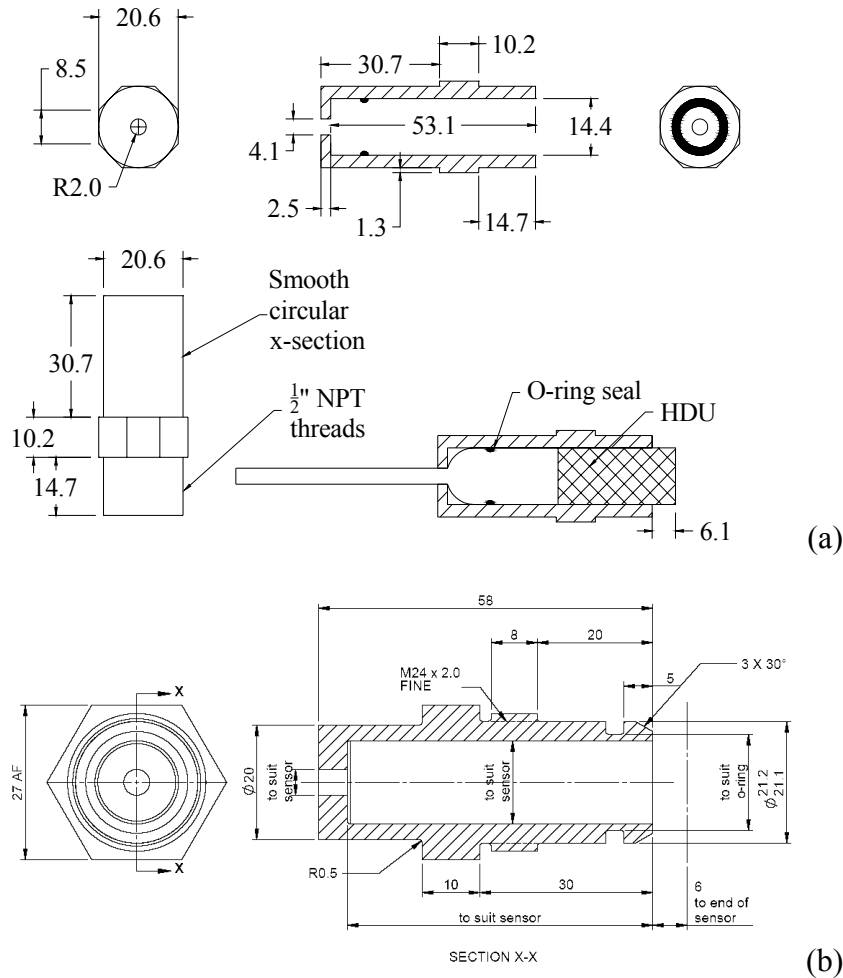


Figure 6.38: (a) Fitting for prototype permeameter; (b) Fitting for hydraulic characterization permeameter

Typical temperature responses for an HDU with different conditions (saturated, dry, and at an intermediate suction) are shown in Figure 6.39. During the 30 second heating period, the temperature was measured in 1 second increments. Afterwards, the control voltage is removed from the constant current source and the ceramic is allowed to cool. To prevent overheating of the ceramic, the time spacing between the 30 second



heat pulses was limited to at least 540 seconds. The temperature values at  $t = 2$  and 20 seconds were used to calculate the temperature increase during the heat pulse. These times were selected to eliminate timing uncertainties in the temperature response at early times, and to ensure that the heat response is contained within the ceramic.

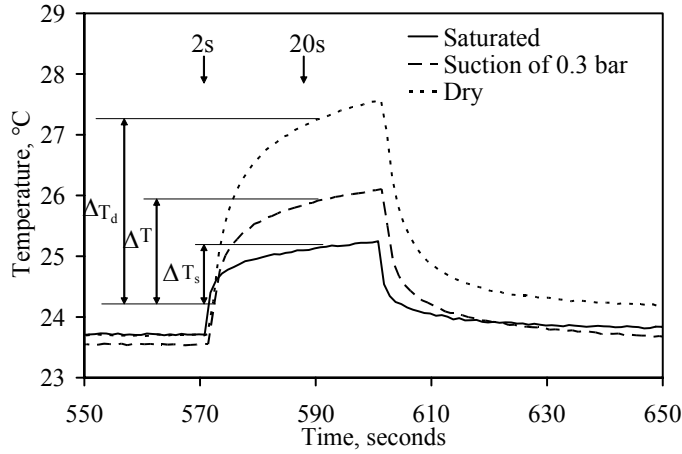


Figure 6.39: Typical HDU temperature responses during heating

Flint *et al.* (2002) also proposed a normalization of the temperature change using the temperature changes of a saturated (soaked in water) and dry ceramic (dried in an oven at 80 °C). The normalized temperature rise  $T^*$  is defined as:

$$T^* = \frac{\Delta T_d - \Delta T}{\Delta T_d - \Delta T_w} \quad (6.5)$$

where  $\Delta T_d$  is the temperature rise of a dry sensor,  $\Delta T_w$  is the temperature rise of a wet sensor, and  $\Delta T$  is the measured temperature rise. The values of  $\Delta T_d$  and  $\Delta T_w$  are sensor-specific, and vary due to differences in composition of the ceramic and alignment of the needle within the ceramic. Flint *et al.* (2002) calibrated several HDUs for a wide range of suctions with the results shown in Figure 6.40. Flint *et al.* (2002) observed that the response in  $T^*$  with suction followed a hyperbolic curve:

$$\psi = \psi_0 \left( T^{* \frac{1}{m}} - 1 \right)^{\frac{1}{n}} \quad (6.6)$$

where  $\psi_0$  is the suction at a dimensionless temperature rise of 1 equal to 56 kPa, and  $n$  and  $m$  are fitting parameters equal to 1 and 0.45, respectively. The calibration curve follows an S-shaped curve similar to the WRCs for soils presented in Chapter 2. These values vary with the ambient temperature. Flint *et al.* (2002) recommended determination of these values at a reference temperature of 20° C.

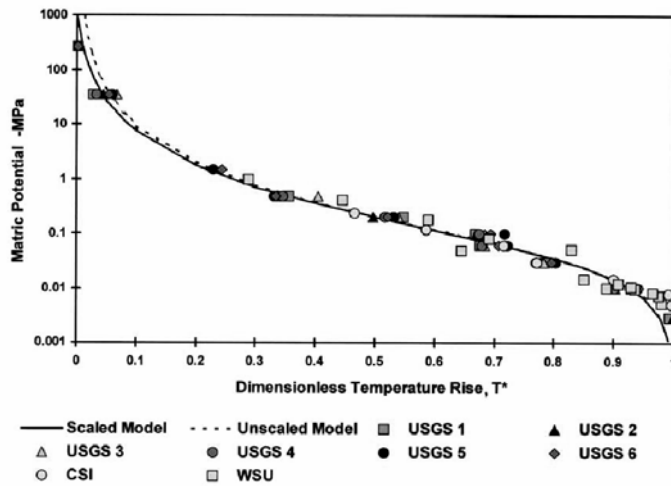


Figure 6.40: HDU calibration results reported by Flint *et al.* (2002)

The Flint *et al.* (2002) calibration curve was also investigated using additional calibration tests at UT. A pressure plate setup used to apply suctions to the HDU probes for calibration is shown in Figure 6.41(a). The HDUs were placed within silica flour slurry, which was used because it has high hydraulic conductivity when unsaturated. Water is allowed to drain from the HDUs and silica flour during suction increments up to 1000 kPa. Before making a temperature measurement, the outflow line from the cell was plugged and the pressure within the cell was decreased to atmospheric pressure. The calibration curve defined for an HDU is shown in Figure 6.41(b). This figure also

includes the calibration equation proposed by Flint *et al.* (2002). The HDU calibration curve indicates that it will have poor resolution below the air entry suction of the ceramic, as the water content of the ceramic does not change appreciably. Flint *et al.* (2002) reported that the air entry suction was approximately 10 kPa. Despite this shortcoming, HDUs have been used to infer suction values up to 300 MPa, making them useful in applications involving evaporation and clays of high plasticity.

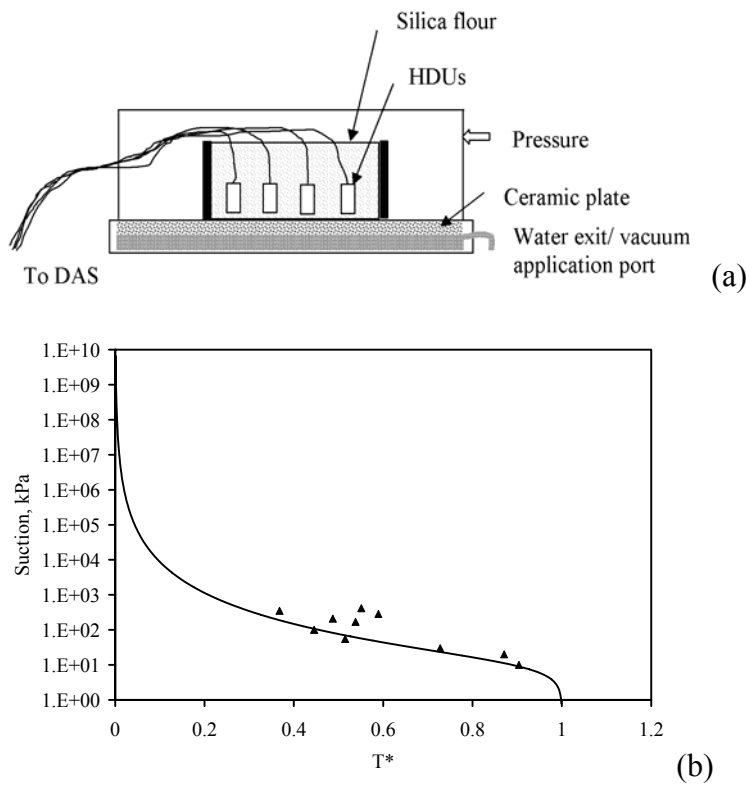


Figure 6.41: HDU calibration: (a) Calibration chamber; (b) Calibration curve

The responses of the HDUs in a high-g centrifuge test are shown in Figure 6.42. The HDU response during 1g shown for the first 3.9 hours in Figure 6.42(a) is consistent with the shape of the measurements shown in Figure 6.39. The voltage difference associated with the increase in temperature during the imposition of the heat pulse was

about 11 mV (after a gain of 1000). When the centrifuge was started at  $t = 3.9$  hrs, the signal from the HDUs is only slightly larger than the electromagnetic noise (approximately 6 mV). This noise arises from the DAS power supply as it passes through the slip ring stack. The noise tended to decrease to about 4 mV when reaching high angular velocities ( $>700$  RPM), possibly due to electrical resonance in the slip rings. The ambient temperature in the centrifuge was observed to increase by 5 degrees during centrifugation at 700 RPM, which was reflected in the HDU readings from  $t = 4.5$  to 6.0 hrs. The data shown in Figure 6.42(b) provides further indication that the noise tends to vary with the speed of the centrifuge. The noise is almost 6 mV at  $\omega = 200$  RPM.

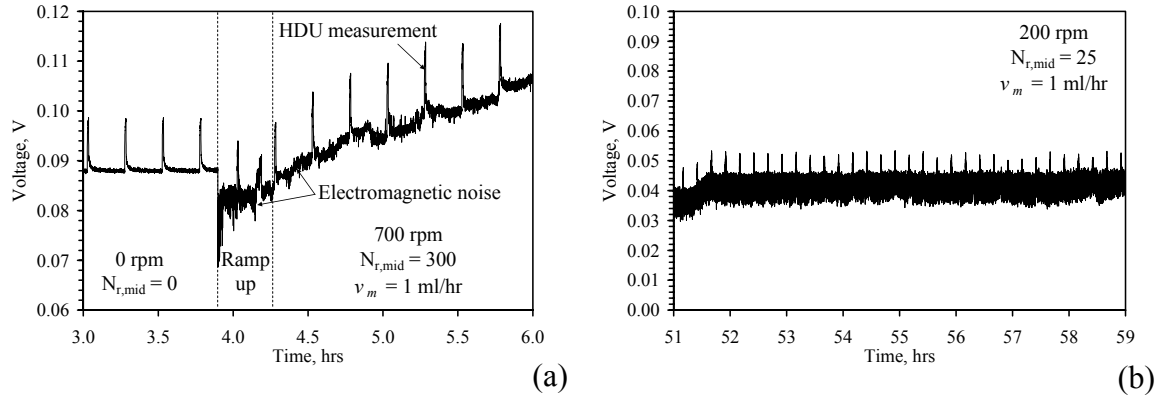


Figure 6.42: HDU measurements: (a) At rest and at high  $\omega$ ; (b) At low  $\omega$

## 6.6 DATA ACQUISITION SYSTEM AND AUXILIARY CENTRIFUGE COMPONENTS

The use of the instrumentation described in the previous section would not be possible without an on-board data acquisition system that is operational at high g-levels. The data acquisition system for the centrifuge permeameter has two components: the transducer interface data acquisition system and the time domain reflectometry (TDR) system. The transducer interface data acquisition system, shown in Figure 6.43, includes solid-state hardware (no moving disc-drives) developed by Neil Baker of  $G_{max}$ -Broadbent<sup>®</sup> LLC. The main processor in the data acquisition was obtained from

IOTech<sup>®</sup>. The data acquisition system has 32 analog input channels that can be used for various voltage-based transducers (load cells, LVDTs, pressure transducers, thermocouples). The data acquisition system also includes on-board amplification, filtering, and digitization. There are also 32 channels of digital input and output, and 2 channels of analog output (for CCD cameras). The output from the data acquisition system is a digital TCP-IP signal that is transmitted via an Ethernet cable. The digital signals may either be passed via Ethernet through a set of electrical slip rings, or they may be passed through a fiber optic rotary joint. If the fiber optic rotary joint is used, the TCP-IP signal is converted to photons using a media converter, passed through the joint, then reconverted to Ethernet outside of the centrifuge. Because the transmission of data from the spinning environment is digital, noise from the induction motor of the centrifuge is not added to the data and information is not lost. The data acquisition system is monitored using a software called Acqlipse<sup>®</sup>, developed by Neil Baker. This software allows plotting and storage of data from the 32 analog channels. The system is LABVIEW<sup>®</sup> compatible, which is needed to program the digital input-output channels.

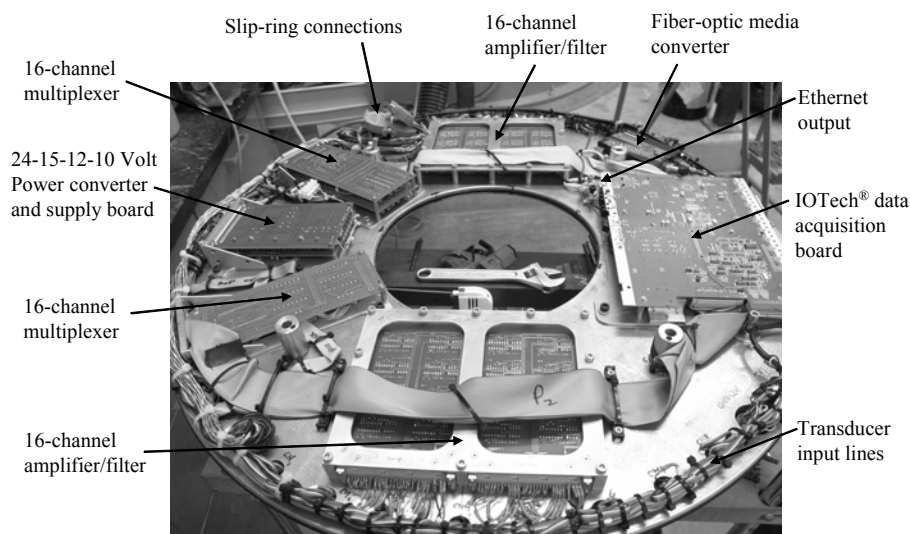


Figure 6.43: On-board data acquisition system

The gain for each channel is must be changed manually by flipping switches on the amplifier cards. The access port for the amplifier cards are shown in Figure 6.44(a). A gain of 100 was used for the tensiometers, and a gain of 10 was used for the outflow transducers. The transducers interface with the data acquisition system via Amphenol<sup>®</sup> connectors, shown in Figure 6.44(a), which are water-proof and robust under the centripetal acceleration. It is important to restrain instrumentation wires to avoid damage during centrifugation. Brackets were placed on the permeameter environment frame, as shown in Figure 6.44(b). These can be used to restrain wiring with cable stays.

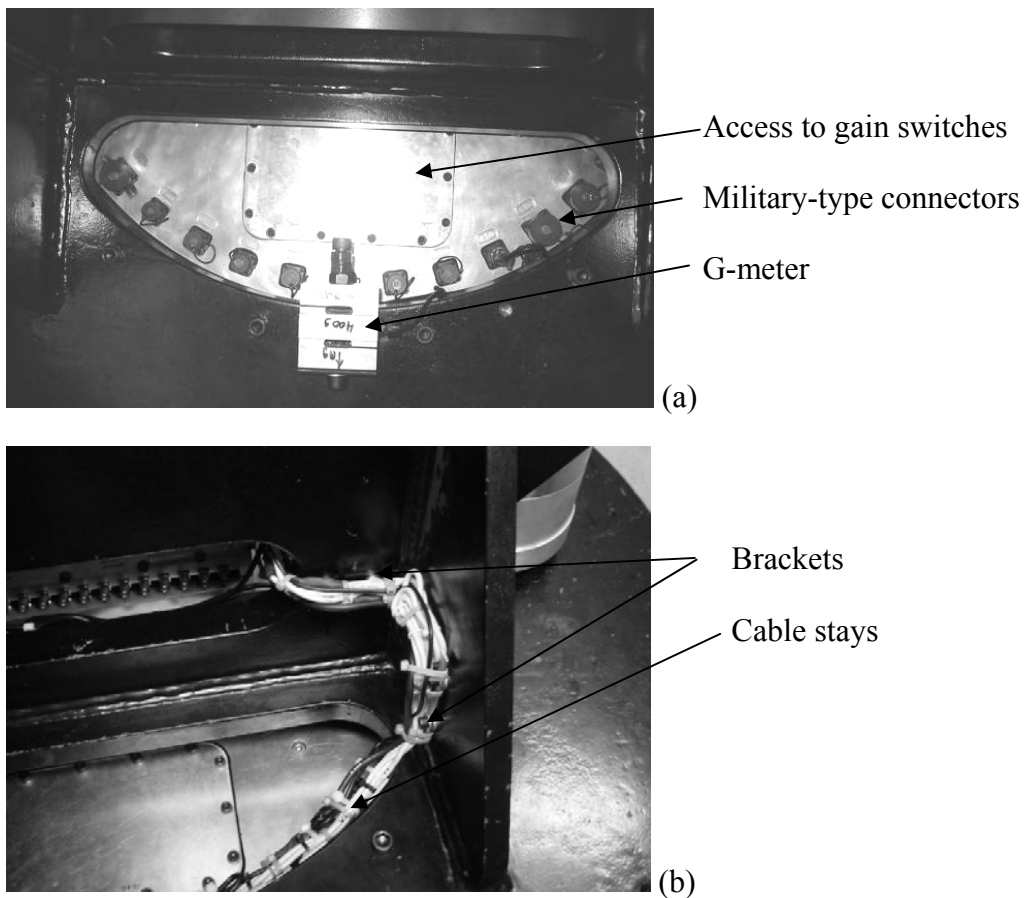


Figure 6.44: (a) User interface side of DAS; (b) Brackets and Cable stays

The Mini-TRASE® system was selected for the centrifuge permeameter as it is compact and robust (it was developed for field measurement applications). The cable tester has only one measurement port, so a coaxial multiplexer was also required to use multiple waveguides. The cable tester and coaxial multiplexer were installed on the central axis of the permeameter environment in an aluminum support frame, shown in Figure 6.45(a). A schematic of the aluminum container is shown in Figure 6.45(b).

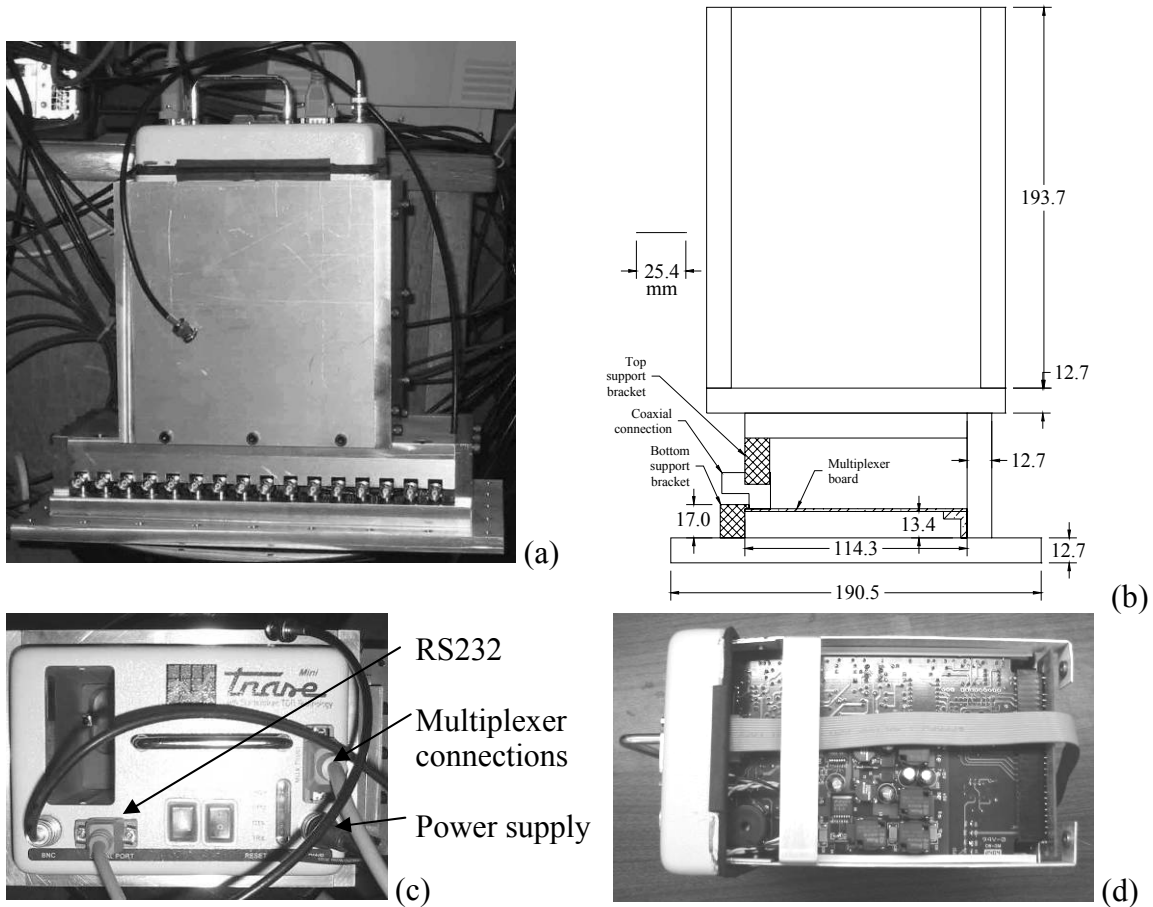


Figure 6.45: (a) Cable tester and multiplexer containment unit; (b) Top of cable tester; (c) Cross section schematic of the cable tester/multiplexer containment unit; (d) Side view of board within cable tester

The interface for the cable tester is shown in Figure 6.45(c). The 18V DC power supply and the RS232 communication cable were passed through the electrical slip ring

stack for communication with the cable tester during centrifuge operation. The RS232 connection permits real-time measurements during centrifugation. The cable tester also has on-board data storage and auto-measurement capabilities, so it can be independently operated. As the electrical boards in the cable tester are oriented vertically, the potential for bending of the boards, shown in Figure 6.45(d), was minimized using paper forms to support the boards and potting of sensitive components with non-conductive epoxy.

The ambient temperature in the centrifuge was measured using a Type T thermocouple. The transducer interface system does not provide cold-junction compensation, which is necessary to provide accurate measurements of temperature. Accordingly, a TC-Mate<sup>®</sup> cold junction compensation circuit was used the interface between the thermocouple and the transducer connections in the DAS. A picture of the TC-mate and thermocouple is shown in Figure 6.46(a), and the calibration equation for the thermocouple is shown in Figure 6.46(b).

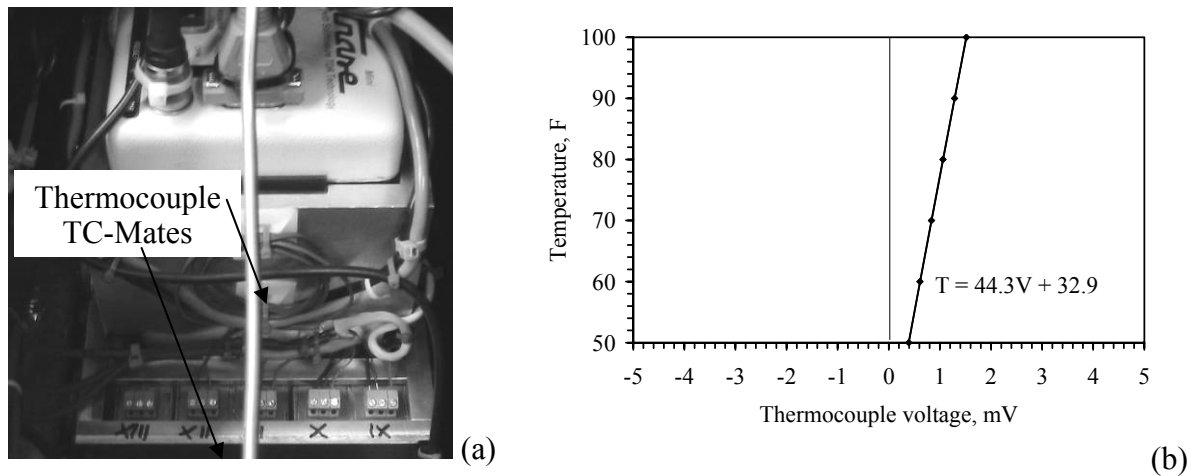


Figure 6.46: Temperature monitoring system: (a) Cold-junction compensation circuit; (b) calibration equation

A CCD camera is used for in-flight visualization of the permeameter and instrumentation to ensure their safety, shown in Figure 6.47(a) and Figure 6.47(b). In



addition, a stroboscope can be used for external visualization of the permeameter during centrifugation is shown in Figure 6.47(c). The stroboscope is mounted to an adjacent wall on a swinging arm, and is synchronized with the centrifuge RPM.

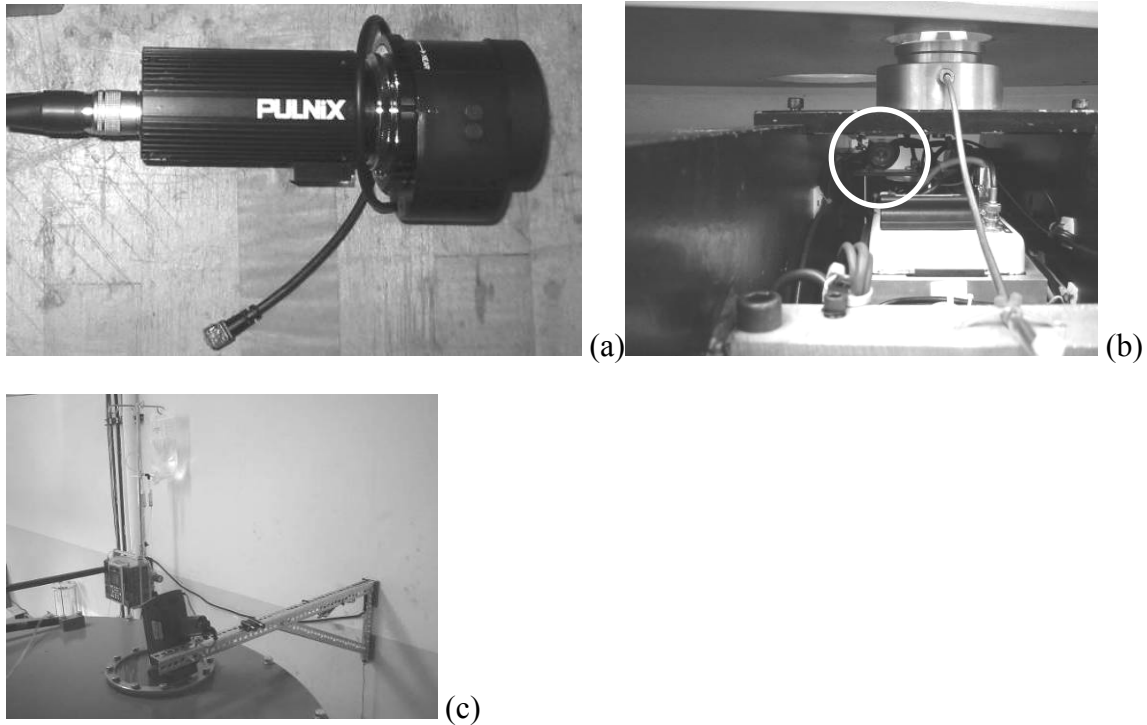


Figure 6.47: (a) CCD for in-flight visualization; (b) CCD installed in centrifuge; (c) Stroboscope for external visualization

Several additional components are necessary for running a safe centrifuge test, highlighted in Figure 6.48. These components include a slab to resist overturning in case of an emergency, a walking platform with a ladder, a work bench, power isolation for centrifuge maintenance, and a PLC controller box to drive the motor and detect faults (excess vibration, lid-interlock released, *etc.*). A drain is also included to collect fluids and dissipate temperature. A pressure panel is used for calibration of transducers and to supply water to the high-pressure fluid union. An analog output channel from the slip-rings is used to transmit images from the CCD camera to a television. A DVD-RW drive

is also attached to the television to record tests. The crane and hoist system used to change permeameter environments and for maintenance is shown in Figure 6.49.

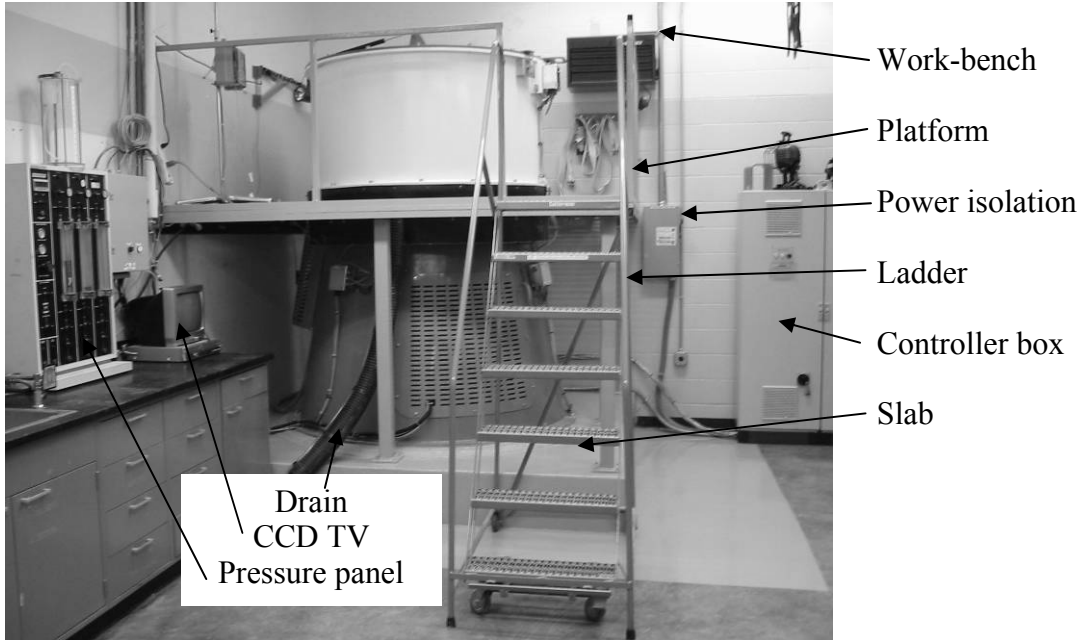


Figure 6.48: Centrifuge work area



Figure 6.49: Crane and hoist for exchange of centrifuge permeameter environments

## **Chapter 7: Testing Philosophy and Experimental Procedures**

### **7.1 OVERVIEW**

The goal of the experimental component of this study is to validate the centrifuge permeameter approach used to determine the K-function and WRC for a compacted soil specimen. This chapter focuses on the testing philosophy and assumptions behind the centrifuge permeameter approach, along with the experimental procedures adopted to obtain the hydraulic characteristics, validate the assumptions in the analysis, and interpret data from the instrumentation. The centrifuge permeameter testing philosophy is based on use of the hydraulic characterization permeameter, although the prototype permeameter was also used in this study to investigate boundary conditions and moisture profiles. The testing procedures used for both permeameters are the same, although they differ in specimen preparation, as will be discussed. Although typical results from the components of the centrifuge permeameter are presented in the last section of this chapter, the scope and results of the formal testing program are presented in Chapter 7.

The centrifuge permeameter testing philosophy is introduced in Section 6.2. The testing philosophy builds on lessons learned from the theoretical investigation of water flow in a centrifuge specimen (discussed in Chapters 2 and 3), and the capabilities of the permeameter and instrumentation (discussed in Chapter 5). Details of the data synthesis adopted to determine the hydraulic characteristics during steady-state infiltration are discussed, along with a summary of the important assumptions.

The testing procedures used to define the hydraulic properties of unsaturated soils with the centrifuge permeameter are described in Section 6.3. This includes a summary of the procedures adopted for preparation of compacted soil specimens and instrumentation installation in the hydraulic characterization and prototype

permeameters. Further, this section includes a description of the procedures adopted for control of the centrifuge speed and inflow rate during a steady-state infiltration test. The procedures adopted to interpret the readings of the instrumentation during a centrifuge infiltration test are also discussed. Section 7.4 also includes a presentation of procedures used to assess the consistency of  $K$  values that can be obtained using different combinations of inflow rate and centrifuge speed. In addition, previous studies indicate that hysteresis plays an important role in the measurement of the WRC and K-function. Accordingly, a simple set of procedures was adopted to use the centrifuge permeameter for investigation of hysteresis, and are presented in Section 6.4. The inflow rate and centrifuge speed can be controlled independently in the centrifuge permeameter, permitting wetting and drying during steady-state infiltration.

Although an optimal set of procedures is recommended in Section 7.3 for efficient determination of the hydraulic characteristics with the centrifuge permeameter, tests were also conducted in this study to assess the testing issues specific to the use of a centrifuge permeameter for hydraulic characterization. The procedures adopted to assess the validity of assumptions in the analysis, evaluate changes in the specimen during centrifugation, and quantify the time required for a centrifuge permeameter test are presented in Section 7.4. Procedures related to two simplifying assumptions used to interpret the instrumentation results are discussed. Specifically, these include the assumption of a negligible suction gradient during steady-state infiltration, and the validity of open flow boundary conditions (*i.e.*, negligible impedance to flow at the outflow boundary). Procedures are presented in Section 7.4 to quantify the effects of centrifugation the hydraulic characteristics. This includes measurement of settlement due to centrifugation as well as a comparison of the K-functions defined at different g-levels. Finally, Section 7.4 contains procedures used to quantify the testing time for hydraulic characterization.

Finally, hypothetical data expected from the individual instruments in the centrifuge permeameter are presented in Section 7.5 to highlight different scenarios anticipated during hydraulic characterization tests.

## 7.2 TESTING PHILOSOPHY

### 7.2.1 Bridging Theory and Measurement

A hydraulic characterization test in a centrifuge permeameter requires control of the inflow rate  $v_m$  and the centrifuge angular velocity  $\omega$ . These define the flow conditions imposed upon a soil specimen in the centrifuge permeameter, given by Darcy's law:

$$v_m = -K(\psi) \left[ \frac{\omega^2}{g} (r_0 - z_m) - \frac{1}{\rho_w g} \frac{d\psi}{dz_m} \right] \quad (7.1)$$

In Chapter 3, an analytical solution for the suction distribution in an unsaturated soil specimen in the centrifuge permeameter during steady-state flow of water was used to predict the variation in the hydraulic conductivity with  $z_m$ . Although this solution was obtained using a simple model for the K-function (Gardner's model) with generic parameters ( $\alpha$  and  $K_s$ ), it provides insight into the expected soil response during a hydraulic characterization test. Specifically, the solutions indicate that the suction head in the upper zone of the soil specimen is relatively constant. Further, its magnitude is negligible compared to that of the centrifuge elevation head. Larger values of  $\omega$  and smaller values of  $v_m$  lead to higher suction and lower hydraulic conductivity values in the upper zone of the specimen. The solutions also indicate that the suction in the upper zone of the specimen is essentially independent of the outflow boundary condition.

The hydraulic characterization permeameter developed in this study allows measurement of the important variables for determination of the WRC and K-function during water flow in the centrifuge. Specifically, TDR is used to measure the moisture content, tensiometers are used to measure the suction, and the outflow transducer is used

to measure the rate of outflow. Further, the particular geometry selected for the monitoring system was guided by the lessons learned from the theoretical solutions for the suction profiles discussed in the previous paragraph.

A schematic of the hydraulic characterization permeameter highlighting the dimensions and locations of the instrumentation is shown in Figure 7.1. The length of the permeameter was selected to permit free access on one side to the tensiometers, which require adequate spacing to screw into the support bracket. It also provides ample clearance for the TDR waveguide, the results of which are strongly affected by the presence of conductive materials in their zone of influence. Although the length of the permeameter compared to the length of the centrifuge arm is not significant ( $r_0/L_m \sim 5$ ), the analyses in Chapter 3 indicate that the g-level can be considered constant through the specimen, if it is necessary to make this assumption. Further, the permeameter length is adequate to develop a zone of constant suction in the upper portion of a soil specimen, as indicated by the analyses in Figure 3.8.

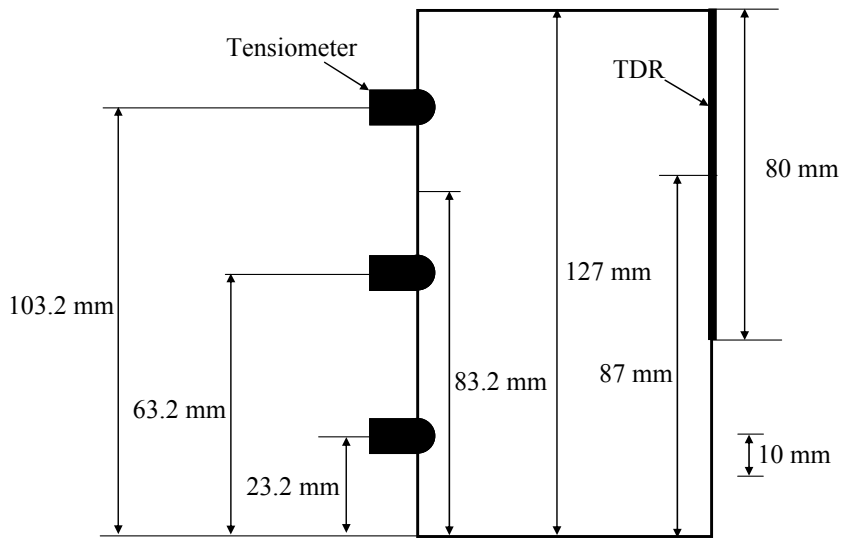


Figure 7.1: Instrumentation layout in the hydraulic characterization permeameter

As indicated in Figure 7.1, the TDR waveguide is oriented in the longitudinal direction at the top of the permeameter in a recess along the edge of the permeameter. Accordingly, the average moisture content in the upper 80 mm of the 127 mm-long specimen is inferred from the waveguide. Due to this configuration, the significant variation in moisture content expected near the base of the permeameter should not have a significant influence on the inferred moisture content. In addition to the TDR waveguide, three tensiometers are used to infer the suction profile. These tensiometers not only allow measurement of the suction at different points, but can be used to calculate the suction head gradient. Accordingly, it is not even necessary to assume that the suction head gradient in Equation (3.22) is negligible to calculate  $K$  like the UFA or SSC approaches. The tensiometers can also be used in conjunction with the outflow transducer to determine if steady-state water flow has been attained. Specifically, the suction measured by the tensiometer will change with changes in  $v_m$  or  $\omega$ , and will stabilize after reaching steady-state flow.

The average moisture content measured using the TDR can be associated with a height of  $z_m = 87$  mm from the base of the permeameter. Analyses of suction profiles similar to those shown in Figure 3.8 indicates that the suction is relatively constant for  $z_m/L_m > 0.3$  during steady-state flow at  $N_{r,mid} > 6$  and  $v_m < K_s$ . Accordingly, the moisture content along the length of the TDR waveguide should be relatively constant during steady-state flow. To match the TDR measurements, the suction at  $z_m = 87$  mm can be interpolated assuming a linear variation in suction between the locations of the upper two tensiometers. The suction profiles shown in Figure 3.8 have a slight inclination with  $z_m$ , so these two tensiometers can also be used to calculate  $d\psi/dz_m$  between the tensiometers.

For a set of imposed  $v_m$  and  $\omega$  values, a target estimate of the hydraulic conductivity can be made using Equation (3.22), as follows:

$$K_{\text{target}} = - \frac{v_m}{\frac{\omega^2}{g}(r_0 - z_m)} \bigg|_{z_m=87\text{mm}} = - \frac{v_m}{N_r} \bigg|_{z_m=87\text{mm}} \quad (7.2)$$

Following the discussion above, it is likely that the suction gradient near  $z_m = 87$  mm is negligible, so this target  $K$  value should be close to that present at steady-state flow. After measuring the suction and moisture content at steady-state corresponding to this target  $K$  value, the measured suction gradient can be used to calculate the actual  $K$  value at  $z_m = 87$  mm as follows:

$$K_{\text{measured}} = - \frac{v_m}{\frac{\omega^2}{g}(r_0 - z_m) - \frac{1}{\rho_w g} \frac{d\psi}{dz_m}} \bigg|_{z_m=87\text{mm}} = - \frac{v_m}{N_r - \frac{1}{\rho_w g} \frac{d\psi}{dz_m}} \bigg|_{z_m=87\text{mm}} \quad (7.3)$$

Points on the K-function and WRC can be determined by correlating the average moisture content, interpolated suction at  $z_m = 87$  mm, and  $K_{\text{measured}}$ . It should be noted that although transient measurements of the moisture content and suction can also be correlated, the moisture content is not likely to be uniform along the TDR waveguide.

### 7.2.2 Assumptions in the Centrifuge Permeameter Approach

Although the interpretation of the monitoring results to define the WRC and K-function described in the previous section is straightforward, there are still several assumptions that must be made in order to use this approach. Some assumptions are necessary to satisfy the theoretical basis of the data analysis while others are necessary for practical aspects of infiltration testing.

As discussed in Chapter 2, suction is defined as the difference between the pressure in the air and water phases. For simplicity, it is assumed that the pore air pressure in the specimen is equal to the atmospheric pressure. This assumption is valid if



the air can freely enter or exit the specimen during infiltration of water. The top cap of the permeameter was designed with a small gap between the soil and the water application holes, shown in Figure 6.13(c). An o-ring is not provided at the connection between the permeameter and the top cap, to allow air to escape around the edges of the cap. Release of air from the base of the permeameter is likely to be more of an issue, as a saturated wetting front passing through a dry soil may cause compression of the pore air. The pressure release port in the outflow reservoir, shown in Figure 6.16, was observed to release the air. However, as will be discussed in Appendix A, adequate time must be allowed for air release, particularly under high flow rates at low g-levels. In this situation, water occasionally was observed to enter the air release tube by capillarity, requiring an increase in the air pressure in the outflow reservoir to force the water out of the air release tube. Another issue that may affect the suction measurements is a change in air pressure near the permeameter due to Bernoulli effects during centrifugation. However, the swinging bucket provides some shielding of the tensiometers, and the vent hole in the tensiometers permits equilibration with the air pressure in the vicinity of the permeameter. Accordingly, it is assumed that changes in air pressure do not affect the suction measurements significantly.

An important assumption is that the suction profiles predicted by the analysis in Chapter 3 are reasonably representative of the soil and the conditions of the centrifuge permeameter test. Although measurements of the suction profile permit the use of Equation (7.3) to determine  $K_{measured}$ , in the case that a large suction gradient is present it is likely that the average moisture content measured by the TDR is not representative. The particular geometry of the permeameter and centrifuge as well as the range of  $v_m$  and  $\omega$  values that may be imposed by the centrifuge permeameter indicates that the shapes of

the profiles shown in Figure 3.8 can be expected during infiltration. Procedures used to assess the suction profiles are discussed in Section 7.4.

Important assumptions must be made about the boundary conditions. With respect to the inflow boundary, it is assumed that all water supplied to the top of the permeameter enters the specimen. In other words, it is assumed that water does not pond atop the permeameter. This can be assured that the inflow discharge velocity  $v_m$  divided by the centrifuge elevation head gradient ( $\sim N_{r,mid}$ ) is less than the hydraulic conductivity of the specimen when saturated. Although this seems intuitive,  $K_s$  is not known before the test for specimens compacted within the permeameter, and must be estimated using experimental data such as that shown in Figure 5.4 or using a predictive approach like the Kozeny-Carman model. If water is supplied to the specimen at a rate in excess of  $K_s$ , the ponding will not occur as water can “run off” the top surface (it does not have a water-tight seal). The water that runs off the top of the permeameter is trapped on a bowl-shaped ledge in the swinging basket around the base of the permeameter. The in-flight camera can be used to see if run-off collected on the ledge. Runoff was only observed for tests on dense specimens with high inflow rates at low centrifuge speeds. Another assumption is that the outflow boundary has a negligible effect on the suction profile. Even in the case that the base is close to saturation (as assumed in the theoretical suction profiles in Chapter 3), water should exit the specimen freely. Approaches used to assess the outflow boundary effects are described in Section 6.4.

An important assumption is the validity of the measurements of the TDR and tensiometers. As the instrumentation is located on the sides of the permeameter, they are influenced by water flow in the soil near the permeameter walls. Two extreme cases may occur: (i) the soil has high permeability (*e.g.*, sand or loosely compacted clay) in which case flow from the top fluid distribution cap passes preferentially through the inside of

the specimen and does not contact the boundaries, or (ii) the soil has extremely low permeability and flow occurs near the boundary of the permeameter. Evidence of preferential flow is typically noted in infiltration tests by negligible changes in TDR measurements to changes in the inflow rate. To minimize preferential flow for high permeability materials, several layers of filter paper are placed on the top of the soil (6 are typically used). The filter paper does not extend to the walls of the permeameter, so air can escape. Preferential flow was found to be minimal when the centrifuge test starts with a fully-saturated specimen as discussed in Section 6.5. Daniel *et al.* (1987) found that side wall leakage is an expected feature of using rigid-wall permeameters. However, the kneading compaction approach used in this study permitted uniform compaction across the area of the specimen, minimizing differences in hydraulic conductivity near the boundaries. A thin coat of vacuum grease on the permeameter walls was used in an early test, but this did not yield results different from tests in which it was not used. Its use was discontinued as it may affect compaction and TDR results.

An important requirement of this analysis is the validity of Darcy's law in the centrifuge. Although the centrifuge gradients can be relatively high, steady-state flow is used in this analysis. Accordingly, the seepage velocity should be constant throughout the specimen. As relatively low seepage velocities are imposed on the specimen to measure the hydraulic conductivity of unsaturated specimens, the Reynolds number will be small. This implies laminar flow, a requirement for the validity of Darcy's law.

Another assumption is that volume changes occurring due to increased stresses during centrifugation do not cause significant changes in the hydraulic conductivity. The analysis in Chapter 4 indicates that when the clay of low plasticity investigated in this study is compacted to a porosity of approximately 0.35, it should not deform significantly for the centrifuge angular velocities used in this study. These observations are also likely

to be representative of stiff-overconsolidated clays, rock cores, and cohesionless soils. However, different procedures may need to be adopted when investigating loosely compacted soils typical of landfill covers, soft clays, or organic soils. Procedures to assess this issue are described in Section 6.4.

Although not strictly an assumption, hysteresis in the hydraulic properties may influence the determination of the K-function and WRC in the centrifuge permeameter. This may result in a change in the shape of the K-function and WRC if wetting or drying from intermediate moisture content. An approach to assess the impact of hysteresis on the hydraulic properties is presented in Section 6.4.

### **7.3 SOIL PLACEMENT AND INSTRUMENTATION INSTALLATION PROCEDURES**

#### **7.3.1 Overview**

This study involves the determination of the hydraulic characteristics of a compacted clay of low plasticity. Consequently, kneading compaction was adopted to compact specimens with a target porosity of 0.35 at  $w_c = w_{c,opt}$ . The compaction conditions in Test I were different ( $n = 0.42$  and  $w_c = w_{c,opt} - 2\%$ ), but this test is included to investigate the suction profiles expected during centrifugation and boundary condition effects. The specific soil compaction procedures are the same as those used in the conventional hydraulic characterization tests discussed in Chapter 2. This section describes the procedures used to prepare the soil specimens and instrumentation for infiltration tests performed in both the hydraulic characterization and prototype permeameters.

#### **7.3.2 Hydraulic Characterization Permeameter**

The first step in preparing a specimen in the centrifuge permeameter is to clean and weigh the different permeameter components, shown in Figure 7.2. Each component

is weighed individually, as the mass of the compacted soil is defined by subtracting the mass of the permeameter from the permeameter and compacted specimen. A thin coat of vacuum grease is applied to the “o”-ring seals on the air release pipe and on the perimeter of the outflow support platen.

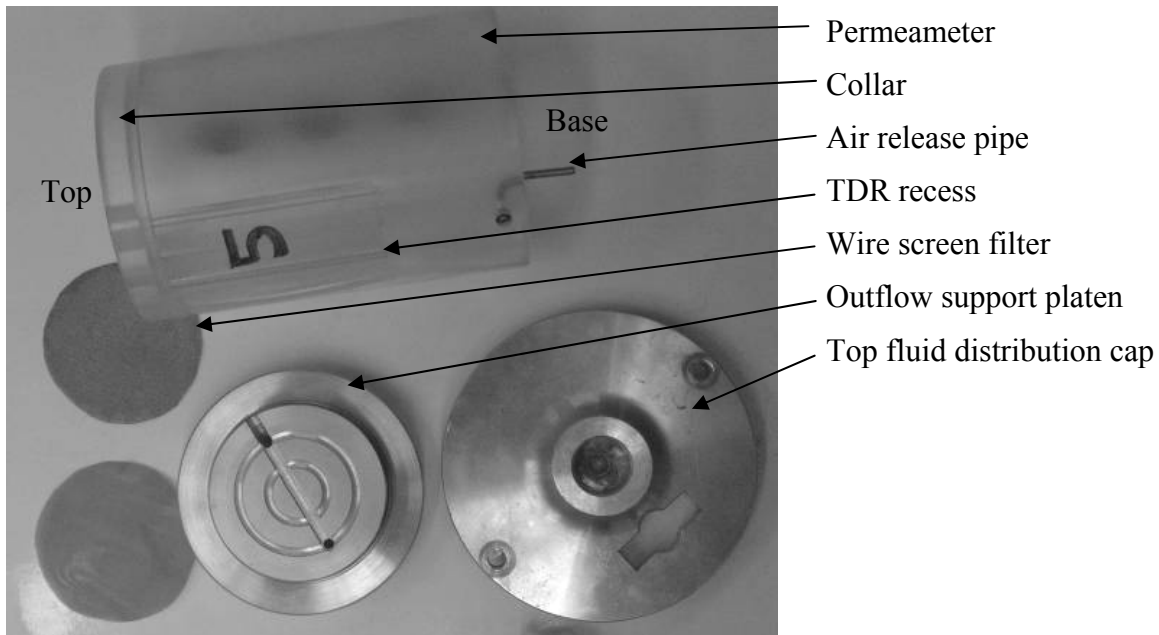


Figure 7.2: Hydraulic characterization permeameter components

The TDR waveguide is placed in its receptacle in the permeameter before compaction of soil as shown in Figure 7.3(a). This permits intimate contact between the TDR and soil to be obtained during compaction. Rubber stoppers are placed in the tensiometer holes, as shown in Figure 7.3(b). This permits soil to be compacted in the permeameter outside of the centrifuge. The braided wire mesh or the wire screen and filter paper are then placed at the bottom of the permeameter, shown in Figure 7.3(c). The braided wire mesh was used in early tests, but the tests presented later in Chapter 9 were performed with the combination of a wire screen and filter paper.

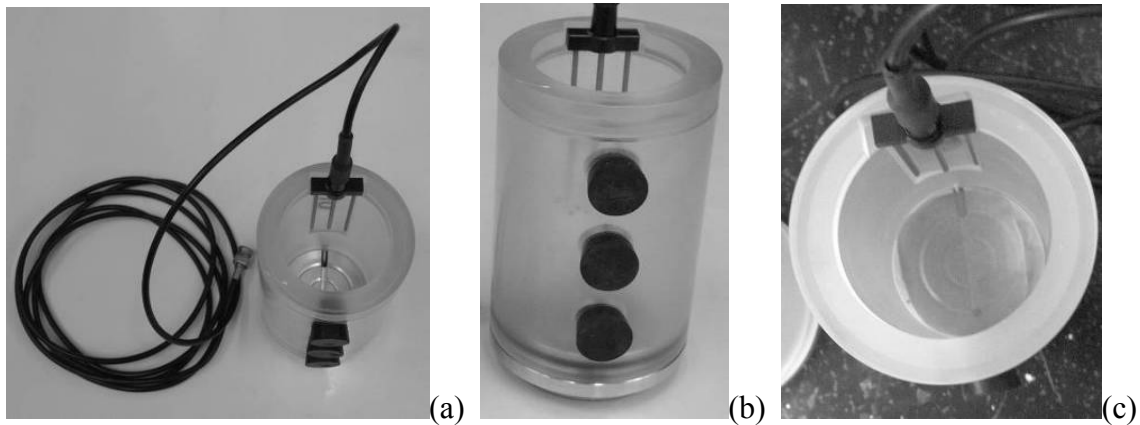


Figure 7.3: Assembled hydraulic characterization permeameter: (a) Installed TDR waveguide; (b) Rubber stoppers; (c) Outflow mesh

Before compaction, a target mass per lift was calculated using the water content of the soil and a target porosity. The soil was compacted in 6 lifts within the permeameter, using a piston compactor to densify the soil [Figure 7.4(a)]. The number of blows per lift was varied to reach different porosities. Marks on the side of the clear acrylic permeameter permitted verification of the required densification. The lifts were scarified after compaction [Figure 7.4(b)]. The collar allowed compaction of the top lift [Figure 7.4(c)].

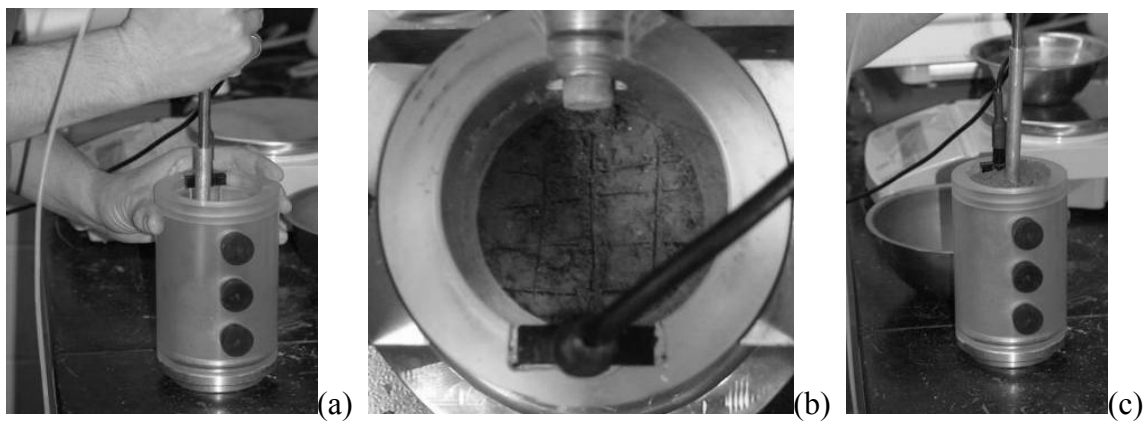


Figure 7.4: Compaction outside the centrifuge: (a) First lift; (b) Scarification; (c) Last lift

After compaction of the last lift, the collar was removed for preparation of the top surface [Figure 7.5(a)]. The collar was then replaced and 6 filter papers were placed atop the soil [Figure 7.5(b)]. Six filter papers were the most that could be used while still providing enough clearance so that the top fluid distribution cap could be mounted [Figure 7.5(c)].

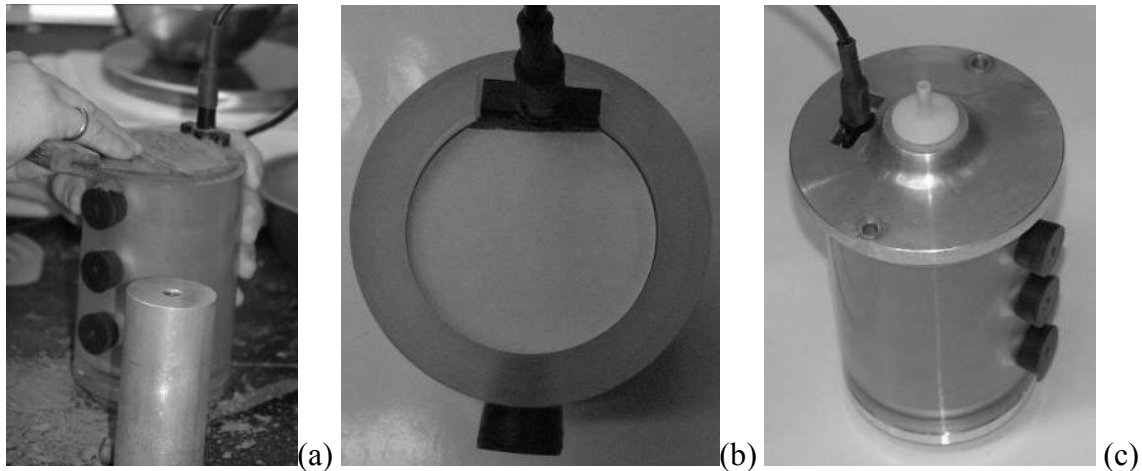


Figure 7.5: Post-compaction: (a) Preparation of the soil surface; (b) Placement of collar and filter papers; (c) Connection of inflow distribution cap

Most of the preliminary tests discussed in Chapter 6 were compacted directly in the centrifuge. This permits the suction sensors to be installed in the permeameter before compaction, as shown in Figure 7.6. However, it also requires climbing into the centrifuge several times, which is labor intensive. The suction sensors are also exposed to the air for a longer period of time. This approach was abandoned for the final series of tests used to verify the centrifuge permeameter approach. Initial saturation of the specimen minimizes preferential flow, limits buildup of air pressure during initial infiltration, and allows immediate installation of the tensiometers.

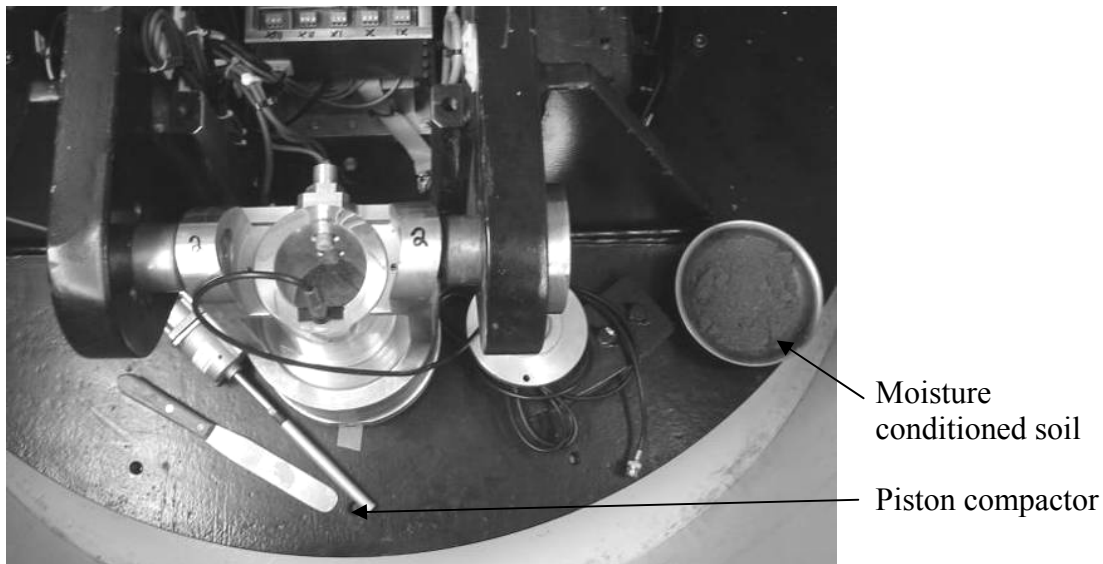


Figure 7.6: Compaction in the centrifuge

Experience from preliminary tests indicates that results from TDR and tensiometers were optimal for an infiltration test starting from saturated conditions, as preferential flow is minimized. Accordingly, the approach adopted in the formal testing program was to saturate the soil specimen outside of the centrifuge. The permeameter was placed within a water bath, and a constant infiltration rate was imposed on the top of the specimen, as shown in Figure 7.7(a). The water level was maintained at the base of the soil. This approach was found to lead to rapid saturation of the specimen, and should lead to a final suction distribution similar to the theoretical suction profile shown in Figure 2.19. After saturation, the rubber stoppers were removed, as shown in Figure 7.7(b). Although the suction in the soil is nearly zero at this point, the soil structure was maintained when the stoppers were removed.



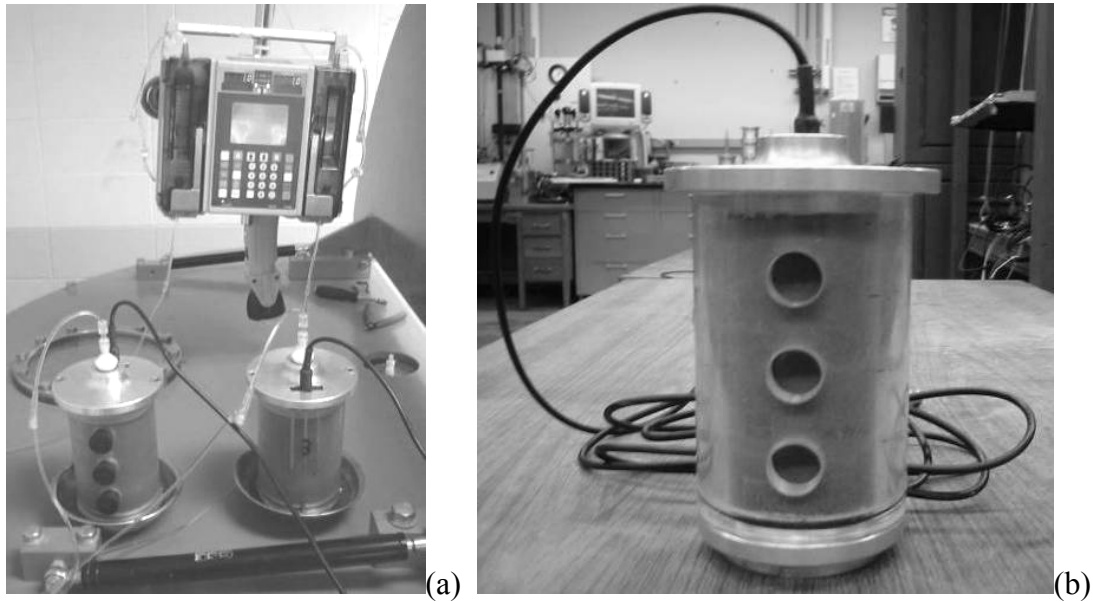


Figure 7.7: (a) Imposition of constant inflow rate outside centrifuge (with water bath);  
(b) Removal of rubber stoppers in tensiometer holes after saturation for  
installation in the centrifuge

Before installation of the permeameter into the centrifuge bucket, a nominal 10 ml of water was placed into the outflow reservoir, as shown in Figure 7.8(a). This permits the outflow transducer to have a positive pressure reading at the beginning of testing. If no water is present, the sensing membrane tends to deflect outwards during centrifugation causing a negative pressure reading. The permeameter was then installed in the centrifuge, as shown in Figure 7.8(b). The tensiometer holes were lined up with the holes in the support bracket, and the top cap was secured using two bolts.

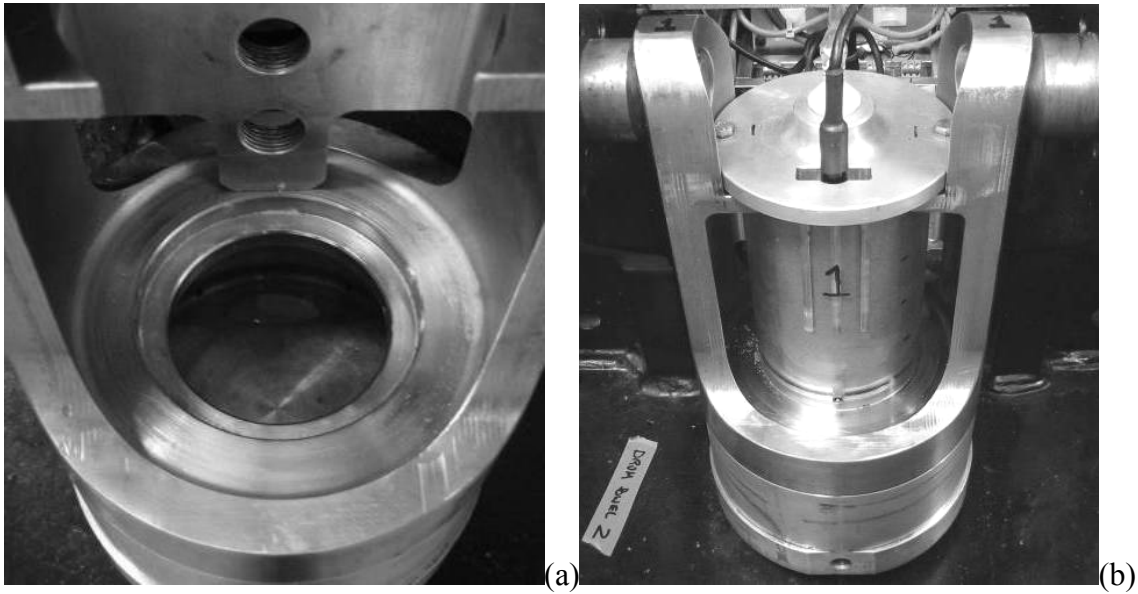


Figure 7.8: (a) Outflow reservoir with initial volume of water; (b) Placement of hydraulic characterization permeameter in the centrifuge bucket

As mentioned, the tensiometers were calibrated before each infiltration test. A working platform was placed on the edge of the permeameter, and the tensiometers were screwed into the calibration chamber. The front and back of the calibration chamber are shown in Figure 7.9(a) and Figure 7.9(b). This permits the on-board DAS to be used for all of the calibration measurements. Before calibration, all tensiometer components were boiled separately and then assembled under water. A positive water pressure of 200 kPa was applied to the tensiometers in the calibration chamber, and the vent holes were opened to flush water and any air bubbles from the tensiometer. The tensiometers were calibrated by varying the water pressure in the calibration chamber. A digital pressure gauge was used to verify the pressure in the chamber, as shown in Figure 7.9(b).

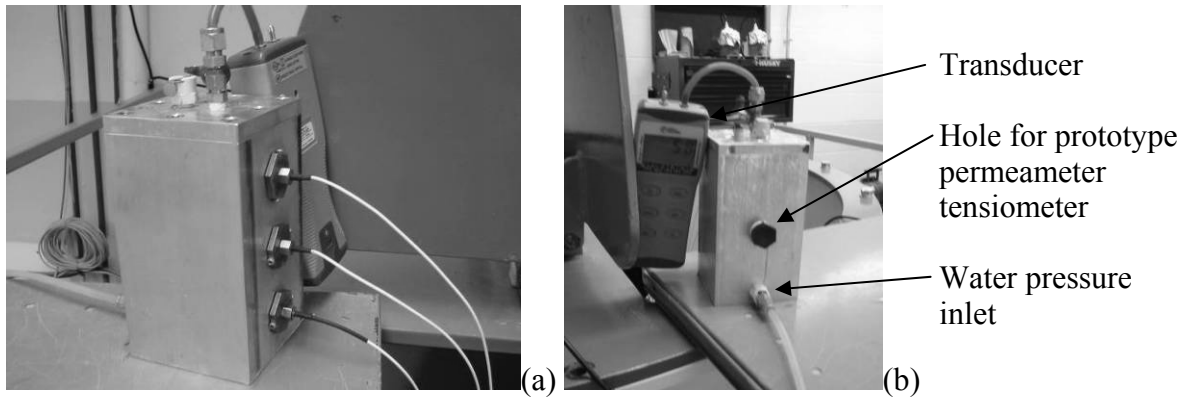


Figure 7.9: Calibration of tensiometers: (a) Tensiometer profile; (b) Pressure transducer

The support bracket and the aligned tensiometer holes in the permeameter are shown in Figure 7.10(a). After applying a small amount of vacuum grease to the tensiometers, they were screwed into the permeameters. This approach allows the ceramic stone of the tensiometer to be pushed directly into the exposed soil. The soil around this region deforms slightly, altering the density of the soil but also facilitating good contact between the soil and tensiometer. The tensiometers after installation are shown in Figure 7.10(b). It is important to secure the wires with cable stays to prevent pullout while still providing slack to allow the permeameter to swing up.

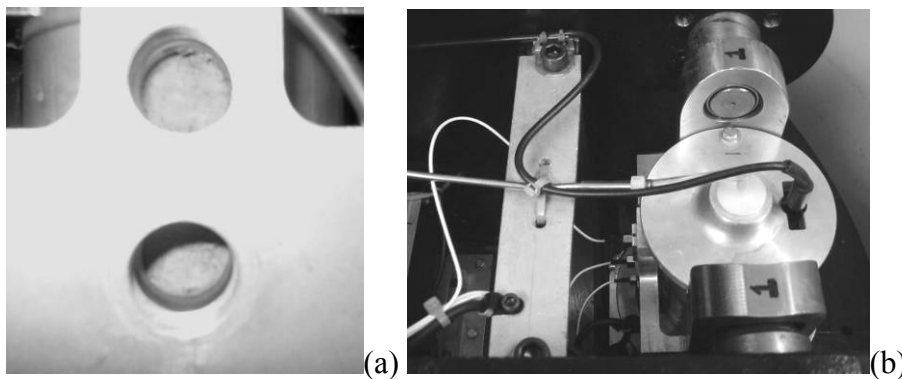


Figure 7.10: Installation of tensiometers (a) Support bracket and permeameter ready for tensiometer installation; (b) Installed tensiometers

### 7.3.3 Prototype Permeameter

The prototype permeameters, shown in Figure 7.11(a), were used in a single test to define moisture content and suction profiles in a longer soil specimen. These permeameters are larger in size, with an instrument layout shown in Figure 7.11(b). Five horizontally-oriented TDR waveguides were installed in the equally spaced ports, along with a single tensiometer in the lowest port.

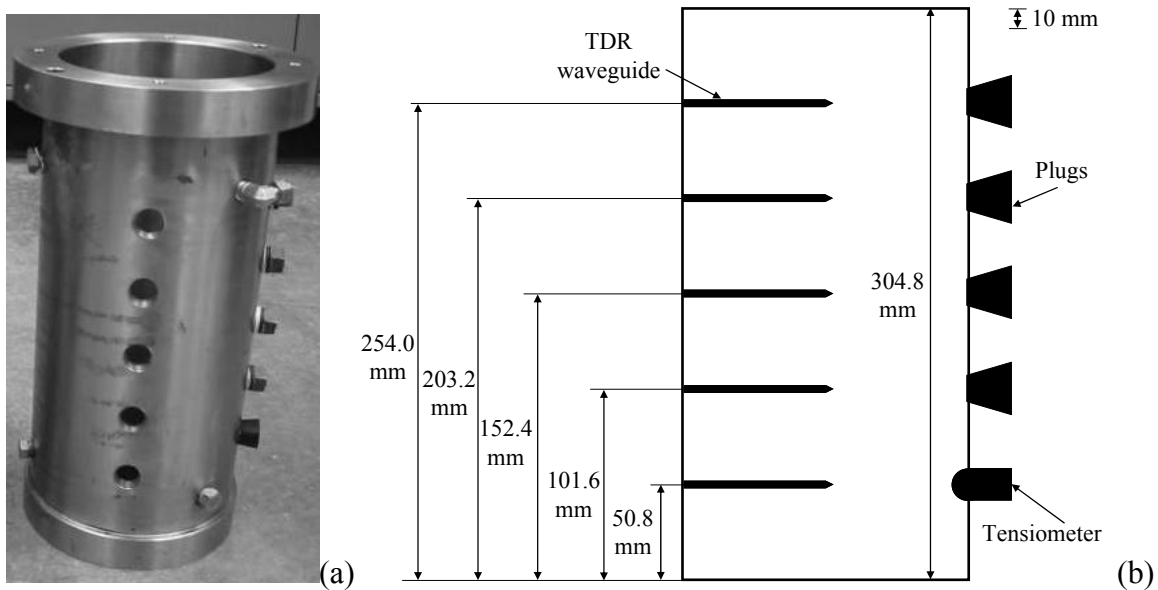


Figure 7.11: Prototype permeameter (a) Picture of empty TDR ports and plugged tensiometer ports (lower port plugged with rubber stopper); (b) Schematic of instrument spacing

Before compaction of soil in the prototype permeameter, it was necessary to plug the unused tensiometer ports, as shown in Figure 7.12(a). The TDR waveguide cables were passed through the ports, and the fittings were lightly screwed into the walls. During compaction, the TDR waveguides can be successively pulled into the permeameter. Different outflow boundary conditions are used in the two permeameters as shown in Figure 7.12(b), a nonwoven geotextile (left) and a wire screen and filter paper (right).

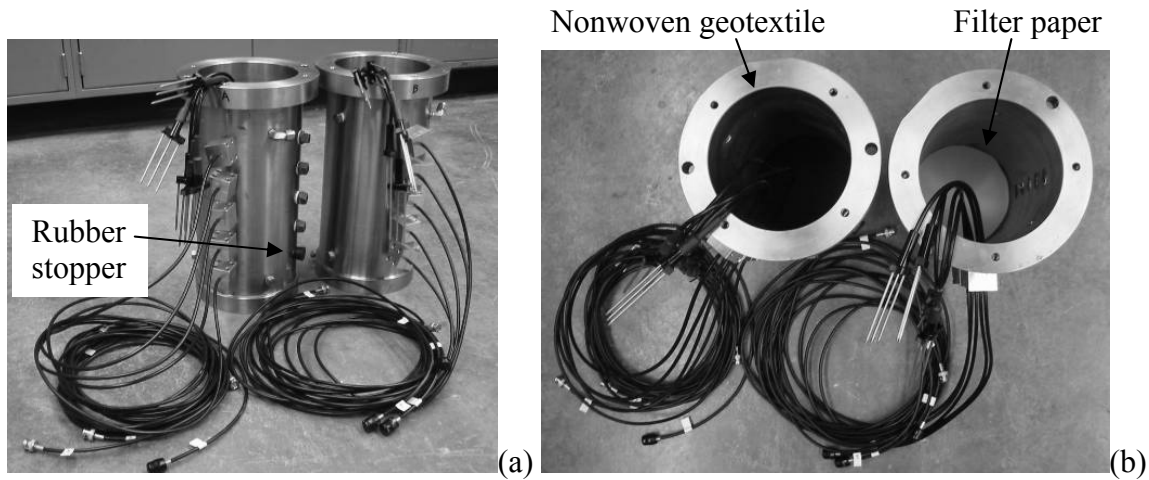


Figure 7.12: Prototype permeameter: (a) Installed TDR waveguides with rubber stopper for tensiometer; (b) Permeameters with different boundary conditions

Pictures of the compaction process for the prototype permeameter are shown in Figure 7.13. The soil in these tests was compacted to a porosity of 0.35 at the optimum water content using 25.4 mm-thick lifts. The TDR waveguides were installed at the interfaces between every other lift, at which time the cable was pulled back through the fitting, which was then tightened to the permeameter. The loose soil of the overlying lift was placed around the waveguides, which were slightly inclined upwards in order to ensure they are horizontal after compaction. Care was taken to maintain an adequate distance of the waveguide from the permeameter walls. The mass added and final height of each compacted lift from the surface was recorded to infer the local density distribution, and the entire permeameter and soil was weighed to infer the total density. After compaction fiberglass wicks were placed across the top surface to enhance lateral distribution of the inflow. Finally, the permeameter top cap was installed. The dimensions of the specimen allow the permeameter cap to press firmly against the fiber wicks. This provides good hydraulic contact between the wicks and soil and supports the soil surface when the centrifuge stops (important for sands and wet soils).

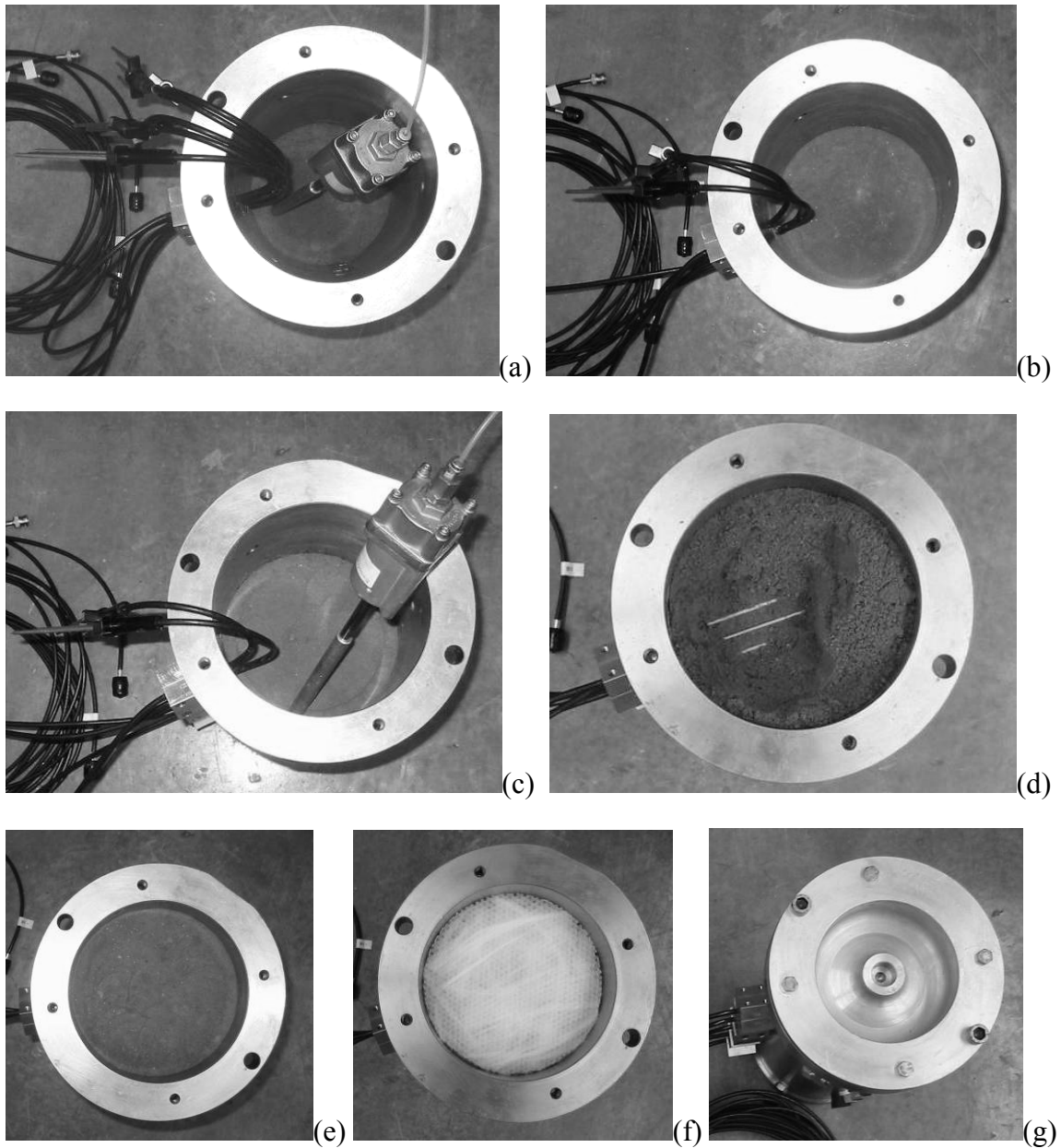


Figure 7.13: Compaction in the prototype permeameter: (a) First lift with TDR; (b) Finished lift; (c) Intermediate lift with no TDR; (d) Last lift with uppermost TDR (e) Prepared surface; (f) Fiber-glass wicks for inflow distribution; (g) Top fluid distribution cap

The outflow reservoir was detached from the hydraulic characterization permeameter, and the pivot points for the hydraulic characterization bucket were

removed, as shown in Figure 7.14(a). The permeameter was then lifted into the centrifuge, and the outflow reservoir was connected as shown in Figure 7.14(b). The yoke shown in the center of Figure 7.14(a) is designed to catch the top lip on the permeameter. In this way, all of the weight of the permeameter is “hung” from its top lip. A dowel behind the yoke ensures that the permeameter remains horizontal. A dowel behind the yoke ensures that the permeameter remains horizontal.

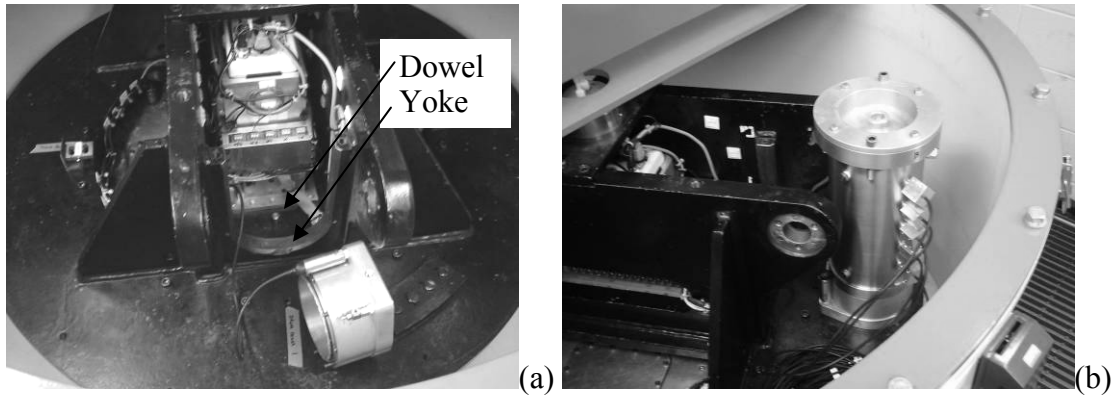


Figure 7.14: (a) Disconnected outflow reservoir; (b) Assembly of permeameter and reservoir in the centrifuge

The air release system in the prototype permeameter has a slightly different design than the hydraulic characterization permeameter. Because it was desired that the TDR waveguides exit from the top side of the permeameter when in a horizontal position, the air release port was on the bottom. Accordingly, if a vent were installed at this elevation, water exiting the specimen could have been released through the vent when the centrifuge was stopped. Accordingly, a tube was attached to the air release port and was extended to the top side of the permeameter, as shown in Figure 7.15(a). The permeameter was then installed horizontally in the centrifuge [Figure 7.15(b)]. Next, the tensiometer was saturated and calibrated using the calibration chamber, and was installed in the lowest port, as shown in Figure 7.16(a). The wires were then arrested with cable stays as shown in Figure 7.16(b), after which the permeameter was ready for testing.

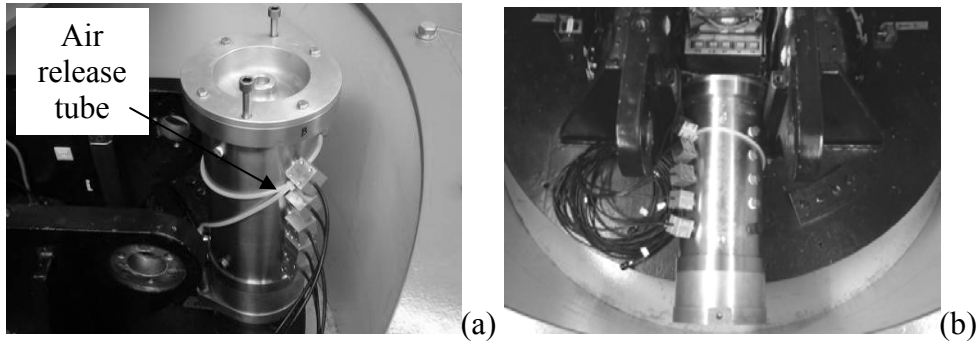


Figure 7.15: (a) Air release tube; (b) Placement of permeameter in the centrifuge

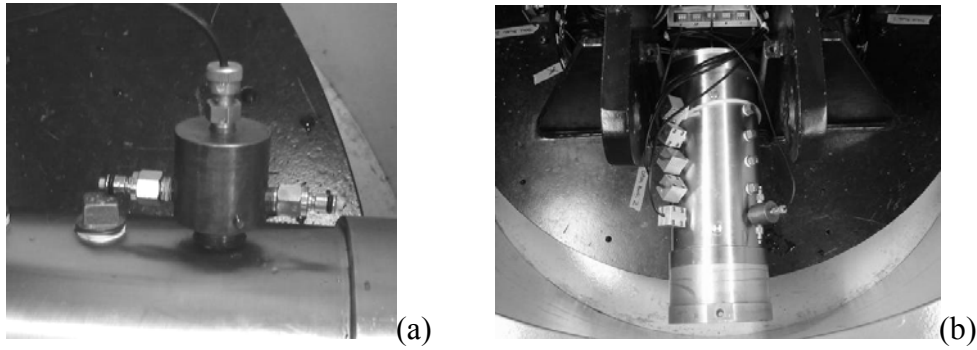


Figure 7.16: (a) Installation of tensiometer; (b) Permeameter ready for centrifugation

#### 7.4 PROCEDURES ADOPTED FOR HYDRAULIC CHARACTERIZATION

This section reviews different procedures that can be used to determine the K-function and WRCs, as well as constraints that must be considered when imposing values of flow rate  $Q$  and centrifuge speed  $\omega$  to reach a desired target value of hydraulic conductivity  $K_{target}$  using Equation (7.3). The flow rate  $Q$  and centrifuge speed  $\omega$  are referred to as the “control variables” for a centrifuge permeameter test.

The range of  $K_{target}$  values possible with the centrifuge permeameter is shown as a function of  $Q$  and  $\omega$  in Figure 7.17(a), and as a function of  $v_m$  and  $N_{r,mid}$  in Figure 7.17(b). Although the particular value of  $N_r$  at  $z_m = 87$  mm is used to calculate  $K_{target}$ , the value of  $N_{r,mid}$  is still used as it indicates that average g-level for the entire specimen. The curves



in these figures appear parallel as they are plotted on a log-log plot. However, each curve has a slope equal to the value of  $N_{r,mid}$  at  $z_m = 87$  mm.  $N_{r,mid}$  values less than 100 are shown in Figure 7.17(b) as these were the most commonly used g-levels in this study.

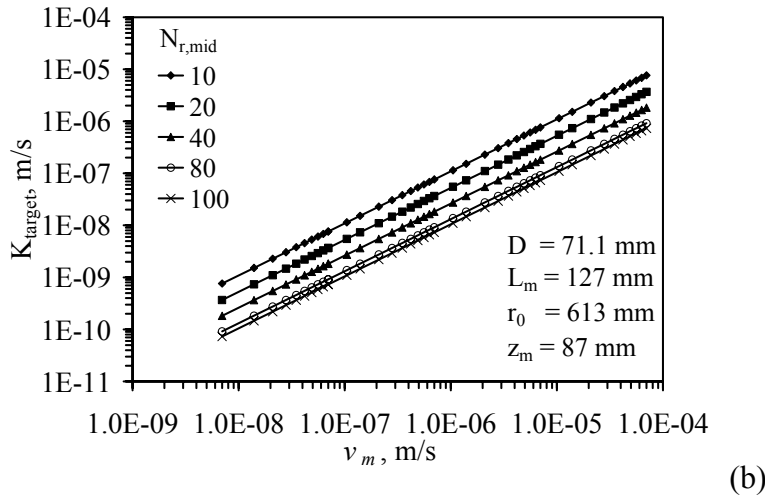
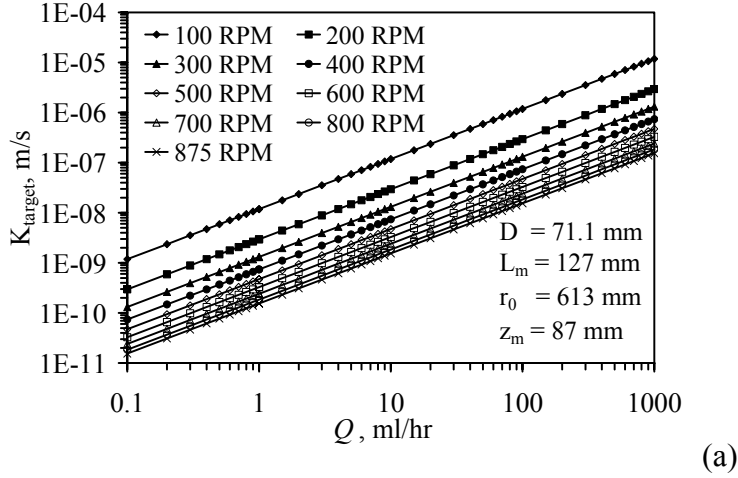


Figure 7.17: Ranges in  $K_{target}$  as a function of: (a)  $Q$  and  $\omega$ ; (b)  $v_m$  and  $N_{r,mid}$

$K_{target}$  values ranging from  $1 \times 10^{-5}$  to  $1 \times 10^{-11}$  m/s can be selected for an unsaturated specimen using the centrifuge permeameter. For example, imposing a flow rate of 10 ml/hr at an angular velocity of 100 RPM, the  $K_{target}$  value at  $z_m = 87$  mm will be  $1 \times 10^{-7}$  m/s. Lower  $K$  values could be obtained with a pump that delivers flow rates

below that used in this study. The moisture content and suction measured at  $z_m = 87$  mm corresponding to this target  $K$  value will depend on the soil being tested and its compaction conditions, as well as whether the soil is wetting or drying.

The particular combinations of  $Q$  and  $\omega$  depend on the characteristics of the soil being investigated. Specifically, the combinations of  $v_m$  and  $\omega$  that lead to values of  $K$  in excess of  $K_s$  should not be selected. Because the specimen is compacted within the permeameter,  $K_s$  is not necessarily known. Accordingly, the value of  $K_s$  must be measured using a centrifuge technique or estimated using the Kozeny-Carman model. The range of  $g$ -levels that can be used without causing excessive settlement should be estimated. This is necessary to obtain soil hydraulic characteristics representative of a specimen having the target compaction conditions. For example, the consolidation analysis in Chapter 4 indicates that negligible settlement and changes in  $K_s$  will be observed up to at least  $N_{r,mid}$  of 100. Starting a test from saturation has been observed to lead to less preferential flow through the specimen, and a shorter time to attain steady-state water flow. Accordingly, a centrifuge infiltration test will usually start from saturation with high values of  $v_m$  and low values of  $N_{r,mid}$ .

As discussed in Section 6.2, after reaching steady-state flow for a given combination of  $v_m$  and  $\omega$ , the moisture content and suction can be measured in the upper portion of the specimen, providing a single point on the  $K$ -function and WRC. Accordingly, different points on the  $K$ -function can be determined using three approaches: (i) maintaining  $\omega$  constant and varying  $Q$ ; (ii) maintaining  $Q$  constant and varying  $\omega$ , or (iii) varying both  $Q$  and  $\omega$ . A summary of the different testing sequences that can be taken is shown in Figure 7.18(a) and Figure 7.18(b) as functions of  $Q$  and  $\omega$ , and  $K$  and  $N_r$ , respectively. Approach (i) has the advantage of imposing negligible changes in “effective” stress during testing as  $\omega$  is constant. Further, the tensiometer

readings tend to shift slightly with increases in  $\omega$ . Approach (ii) has the advantage that a relatively high flow rate can be used to reach steady-state flow rapidly. A high flow rate can be used to have measurable outflow during a test. Shifts in the tensiometer readings are expected in this approach and be accounted for, but the analysis is not as straightforward as for constant  $\omega$ . Approach (iii) is used to reach the widest range in  $K$  values possible in a single test. Further, this approach can be conducted so that the time required to reach steady-state flow is similar for each combination of  $Q$  and  $\omega$ .

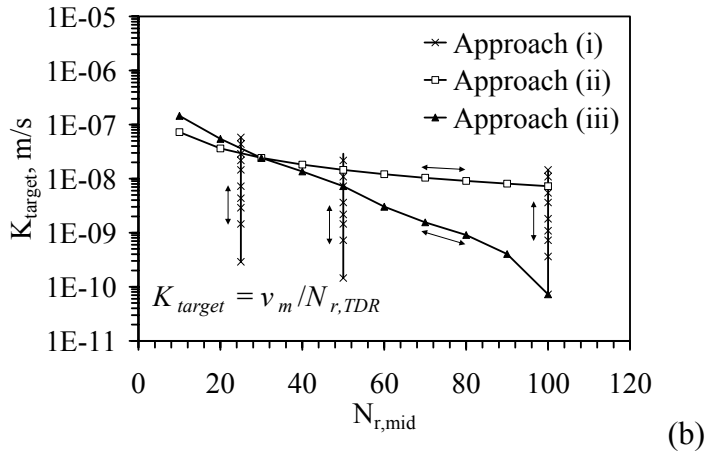
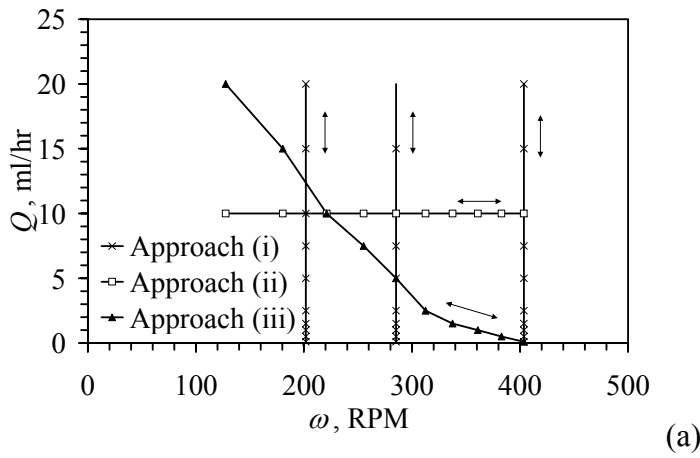


Figure 7.18: Test sequences for hydraulic characterization approaches in the centrifuge permeameter: (a)  $Q$  and  $\omega$ ; (b)  $K_{target}$  and  $N_{r,mid}$

In order obtain consistent  $K$ -function and WRC results using the centrifuge permeameter, the moisture content and suction should be constant for combinations of  $Q$  and  $\omega$  that result in the same  $K_{measured}$  values (assuming that the soil is not affected by hysteresis). This should only be the case when there is a sufficiently long zone of relatively constant suction (or moisture content and hydraulic conductivity). If this zone is shorter than the length of the TDR waveguide, then average moisture content measurements made by the vertical TDR may not be representative of the moisture content distribution. Accordingly, it is not guaranteed that consistent values of moisture content and suction will be obtained for a constant  $K_{target}$  for different combinations (but constant ratio) of imposed  $Q$  and  $\omega$  values in Equation (7.2). The length of the zone of constant suction will vary with  $Q$  and  $\omega$  as indicated by the curves in Figure 3.8. To investigate this issue, measurements of suction and moisture content in the upper portion of the specimen can be compared for constant  $K_{target}$  values such as those shown in Figure 7.19(a) (in terms of  $Q$  and  $\omega$ ) and in Figure 7.19(b) (in terms of  $v_m$  and  $N_{r,mid}$ ).

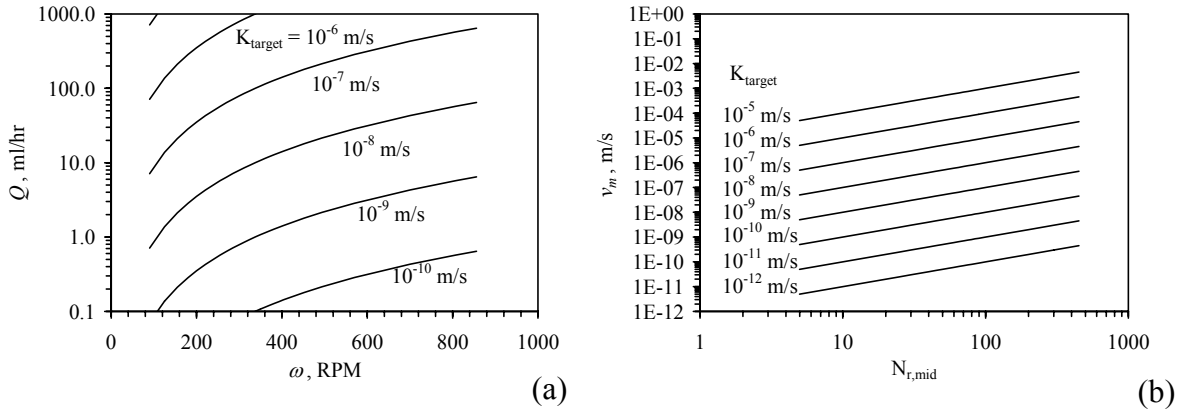


Figure 7.19: Contours of constant  $K_{target}$ : (a) Flow rate vs. RPM; (b)  $v_m$  vs.  $N_{r,mid}$

As the centrifuge speed and inflow rate can be controlled independently in the centrifuge permeameter, hysteresis can be investigated by wetting and drying of a soil specimen using steady-state water flow. Most studies in the past that investigated

hysteresis have used transient flow tests. In transient approaches, the amount of outflow/inflow typically changes with time making hysteresis measurements difficult, often with hydraulic characteristics that may be a function of the transient process. There have been few studies in the past on hysteresis using steady-state flow, so the findings of this study may give insight into the importance of hysteresis in unsaturated soils undergoing steady water flow. Hysteresis will be investigated in each of the three approaches described above by following a drying path (decreasing  $K_{target}$ ) and then subsequently following a wetting path (increasing  $K_{target}$ ).

A test will also be performed in a manner similar to the consistency test. Starting with a given  $K_{target}$  value the specimen will be dried at a constant g-level by decreasing the inflow rate. Next, the g-level can be increased simultaneously with an increase in the inflow rate to reach the same  $K_{target}$  as at the beginning of the test, as shown in Figure 7.20. Differences in the  $K_{measured}$  values corresponding to each of the  $K_{target}$  values can be attributed to hysteresis. Specifically, if hysteresis plays an important role, the moisture content and suction values corresponding to  $K_{measured}$  will be different after rewetting.

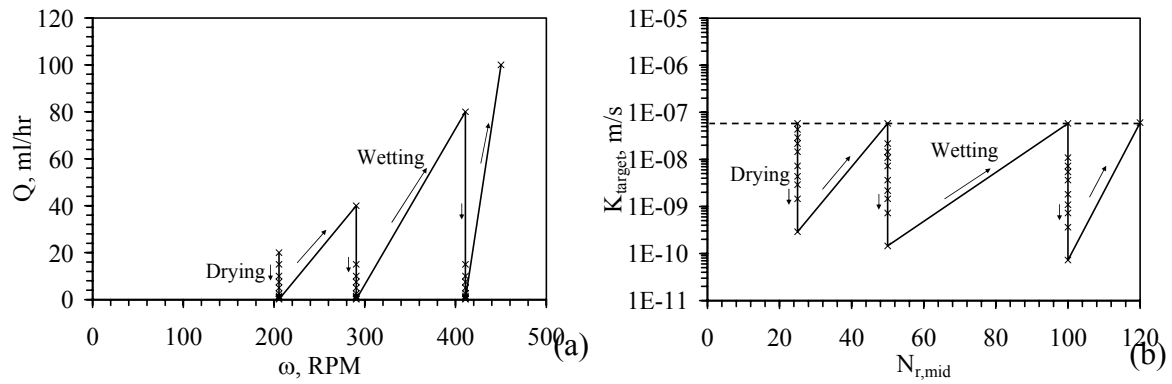


Figure 7.20: Hysteresis testing sequences: (a)  $Q$  vs.  $\omega$ , (b)  $K_{target}$  vs.  $N_{r,mid}$

## **7.5 PROCEDURES ADOPTED TO INTERPRET CENTRIFUGE TESTING ISSUES**

### **7.5.1 Procedures to Evaluate Suction Profiles during Centrifugation**

In order for the TDR measurement in the upper portion of the hydraulic characterization permeameter to be representative, it is assumed that the suction profile is constant in the upper portion of the specimen. This assumption is also the basis of the UFA and SSC approaches. Two experimental approaches are used in this study to quantify the moisture content and suction profiles in this study in order to verify this important assumption. In the hydraulic characterization permeameter, the three tensiometers can be used to quantify the shape of the suction profile at steady-state flow. If the assumption of a zero suction gradient in the upper portion of the specimen is valid, the suction readings obtained by the two upper tensiometers should be reasonably close (although not equal). Further, the shapes of the measured moisture content and suction profiles can be compared with those expected from analytical solutions. The analytical solutions can be obtained using the parameters obtained using the centrifuge permeameter results. The second experimental approach would be to use the prototype permeameter. This permeameter has five horizontally-oriented TDR waveguides, which can be used to quantify the shape of the moisture content profile. The moisture content profiles obtained using the prototype permeameter can also be compared with those obtained from 1-g column tests (such as that discussed in Chapter 4). By imposing a g-level on the centrifuge permeameter resulting in similitude of stresses, the centrifuge permeameter should have similar behavior as a large-scale column prototype.

### **7.5.2 Procedures to Evaluate Boundary Condition Effects**

It is assumed that the filter system and outflow support plate used in the centrifuge permeameter result in open-flow boundary conditions. Accordingly, the

outflow plate should allow free movement of water past the boundary. The boundary conditions will be assessed experimentally in this study by conducting tests in the centrifuge permeameter using different boundary conditions, such as a wire mesh with filter paper, a woven wire screen, or a nonwoven geotextile. Comparison of the suction profiles and hydraulic characteristics using these different outflow control materials can help assess the impact of the outflow boundary condition. Specifically, they may indicate if the boundaries influence the length of the zone in the specimen that has relatively constant suction, and if the base of the specimen is near saturation during steady-state water flow. Alternatively, numerical simulations using RichTexNg (Appendix B) can be used to evaluate the influence of different boundary conditions, and then compare the suction profiles with those obtained in the experimental program.

### **7.5.3 Procedures to Evaluate Centrifugation Effects on Hydraulic Characteristics**

As discussed in Chapter 4, settlement in the centrifuge can cause changes in  $K$ . The effects of settlement can be assessed by using Approach (i) to define the K-function at different g-levels. In other words, the K-function can be defined by maintaining  $\omega$  constant and by changing  $Q$ , then by defining the K-function in the same way but using a higher  $\omega$ . If the effects of settlement are minimal, then the shape of the K-function at each g-level should be similar. It is important to consider the effects of hysteresis, which will be discussed next. In general, this can be done by starting at a given value of  $K$ , drying the specimen by reducing  $Q$  and then subsequently rewetting the specimen by increasing  $Q$ . Then, a new combination of  $Q$  and  $\omega$  (albeit with a larger  $\omega$  than before) can be selected to start the next portion of the test from the same  $K$  value.

#### 7.5.4 Procedures to Evaluate Time Required for Hydraulic Characterization

The time required to determine the hydraulic characteristics of an unsaturated soil depends on the number of points desired on the K-function, whether or not hysteresis is investigated, the response time of the tensiometer, and the range of  $K_{target}$  values. The tests included in this study include at least points over a range of  $K_{target}$  values from  $10^{-4}$  to  $10^{-11}$  m/s, so they permit assessment of the contribution of each of these issues to the testing time. Further, the testing time required for the column infiltration tests presented in Chapter 5 can be used for comparative purposes. The experimental results from the centrifuge will also be compared with the results of a travel time analysis (length divided by discharge velocity) and scaling relationship associating the geometry of the 1-g columns and the centrifuge.

#### 7.6 INTERPRETATION OF INSTRUMENTATION RESULTS

The instrumentation used in the centrifuge permeameter can be used to gather a significant amount of information. The purpose of this section is to summarize the results expected from the different instruments during different scenarios expected during infiltration tests in the centrifuge. It is important to understand the expected changes in the measured values of moisture content, suction, and outflow during steady-state infiltration testing using the approaches described in Section 6.3. Assessment of the expected behavior helps proper interpretation of a hydraulic characterization test as many issues can arise during testing that may be reflected in the measured variables.

The expected changes in moisture content, suction, and outflow rate during infiltration tests conducted using Approach (i) (*i.e.*, constant  $\omega$  and varying  $Q$ ) are shown in Figure 7.21(a), and those expected using Approach (ii) (*i.e.*, constant  $Q$  and varying  $\omega$ ) are presented in Figure 7.21(b). In these figures, five phases typical of centrifuge infiltration testing are shown. The three initial phases are similar for both



approaches. Phase 0 signifies the initial conditions after compaction, Phase 1 involves saturation of the specimen outside of the centrifuge ( $Q > 0$  and  $\omega = 0$  and  $N_r = 1$ ). Assuming that the compacted specimen has high initial suction and low moisture content, saturation will involve and increase in moisture content and a decrease in suction. As the specimen is outside the centrifuge, no outflow is expected. During Phase 2, the inflow rate is maintained constant, but the centrifuge speed is increased ( $Q > 0$  and  $\omega > 0$ ). This will cause a decrease in moisture content and an increase in suction, both of which stabilize when at steady-state. Outflow will occur shortly after centrifugation is started due to the increase in the total hydraulic gradient. At steady-state flow, the increase in outflow volume reflected by the outflow transducer will be constant with time.

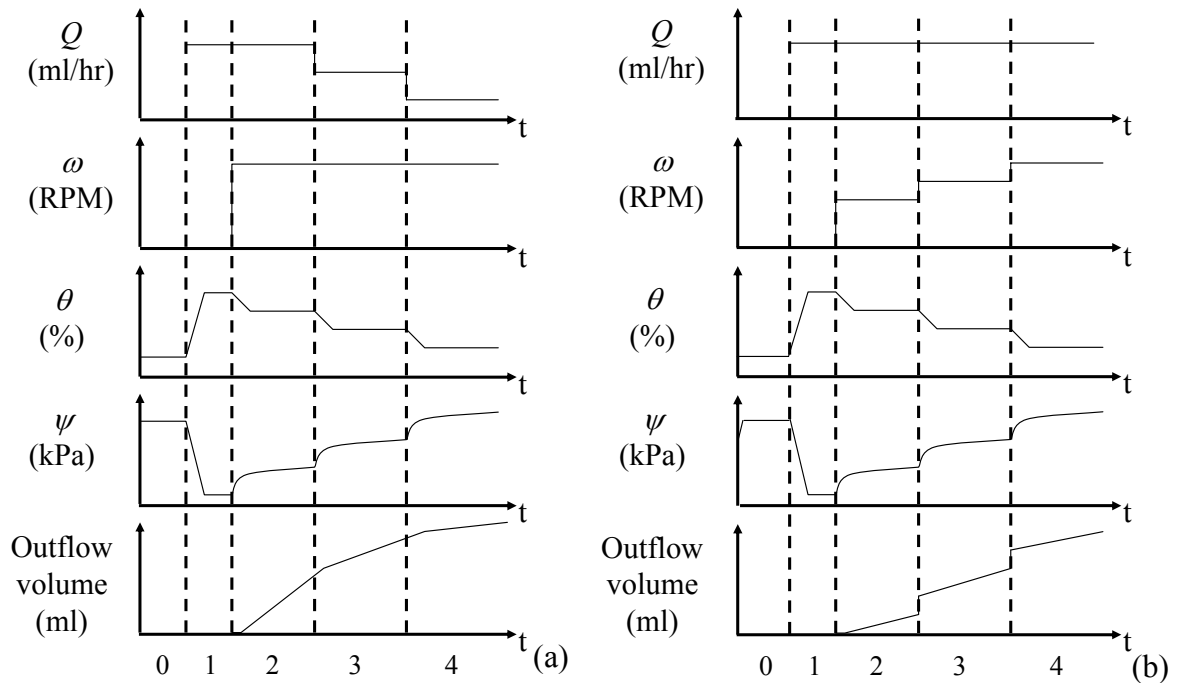


Figure 7.21: Hypothetical data from the different instruments in the centrifuge permeameter: (a) Constant  $\omega$  and varying  $Q$ ; (b) Constant  $Q$  and varying  $\omega$

Using Approach (i), the Phases 3 and 4 involve a decrease in the inflow rates while the centrifuge speed is maintained constant. A decrease in inflow is used in this

approach because the specimen is starting from near-saturated conditions. This will lead to gradual decreases in moisture content and suction which stabilize with time. The slope of the outflow volume with time will decrease with each decrease in the outflow rate. Using Approach (ii), the Phases 3 and 4 involve a decrease in the inflow rates while the centrifuge speed is maintained constant. This will lead to decreases in moisture content and suction similar to Approach (i), but outflow will shift at each change in  $\omega$ . Some of the tests indicate that changes in  $\omega$  will also lead to small shifts in the tensiometer data, although the shift decays with time. It is likely that the change in  $\omega$  causes minor changes in the weight of the fluid in the tensiometer, causing an increase in pressure. Unlike the outflow transducer, the sensing membrane in the tensiometer is perpendicular to the direction of increasing acceleration.

Close-ups of the variation in the outflow transducer data are shown in Figure 7.22(a) and Figure 7.22(b). During infiltration testing in the centrifuge permeameter, it is necessary to evaluate if steady-state water flow has been attained. This is done by ensuring that the slope of the outflow transducer output is constant with time. It is necessary to provide adequate time for transient water flow to occur due to changes in  $v_m$  or total hydraulic head so that the change in outflow volume with time is representative of the steady-state inflow imposed on the specimen. It should be ensured that the pressure measured by the outflow transducer is not due to a build-up in air pressure caused by compression of the pore air during application of a high flow rate. The air pressure relief hole may fill with a small amount of water, which must be expelled before the air pressure is relieved. Deviations from the expected outflow behavior associated with a build-up in air pressure are discussed in the next section.

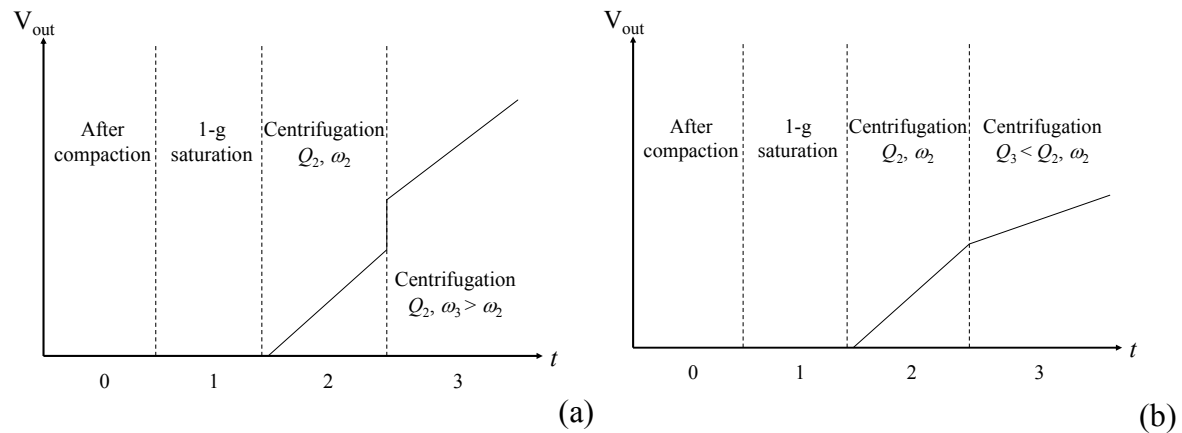


Figure 7.22: Hypothetical data from outflow transducer: (a) Constant  $\omega$  and varying  $Q$ ; (b) Constant  $Q$  and varying  $\omega$

A close-up of the TDR measurements expected after compaction, 1-g saturation, and during centrifuge is shown in Figure 7.23. It is expected that the different testing approaches will not change the anticipated trend of TDR measurements. However, the magnitude of the changes in moisture content will certainly change. Because the TDR measures the average moisture content along its length, adequate time must be provided to achieve equilibrium. Advanced analysis of the TDR waveform can be used to determine the transient position of wetting fronts along the length of the TDR waveguide, but this approach is complex with uncertain accuracy (McCartney and Zornberg 2006).

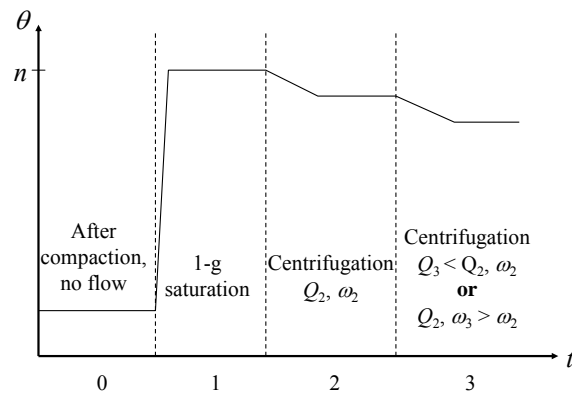


Figure 7.23: Hypothetical data from the TDR

Close-ups of the expected tensiometer results are shown in Figure 7.24(a) and Figure 7.24(b). Adequate time must be allowed for the tensiometer to equilibrate with the suction in the soil. Because steady-state water flow is used in this study, it is not necessary to have a very rapid tensiometer response. The suction time series can be monitored with time during an infiltration test. The tensiometers near the inlet of the permeameter will reach steady-state conditions before those closer to the base of the permeameter. It is particularly to start a test from near-saturated conditions, as the time required for the tensiometer to equilibrate with the initial suction in the specimen is minimized. The chances for cavitation are also minimized, as discussed in Appendix A.

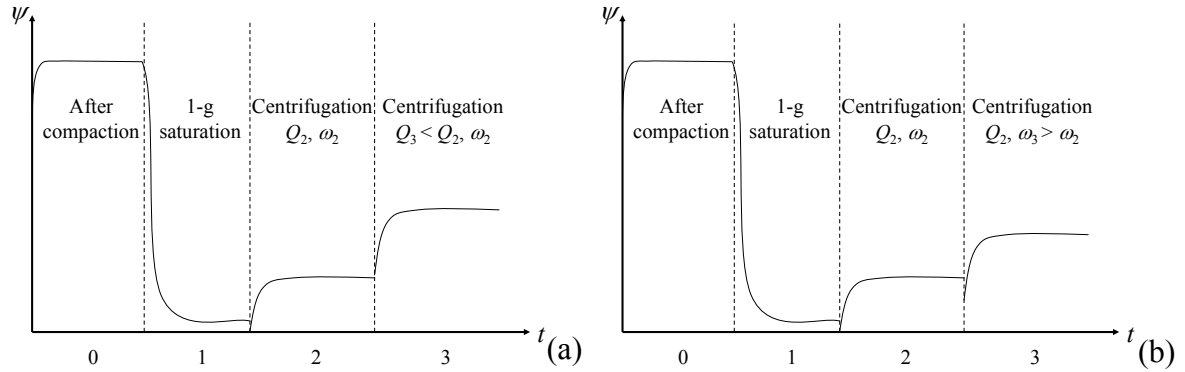


Figure 7.24: Hypothetical data from the tensiometer: (a) Constant  $\omega$  and varying  $Q$ ; (b) Constant  $Q$  and varying  $\omega$

## Chapter 8: Results from Infiltration Test in Prototype Permeameter

### 8.1 TESTING SCOPE

Test I was conducted in the prototype permeameter with the goal of investigating the moisture content profiles in a soil specimen during both transient and steady-state water flow, the suction at capillary breakthrough during transient water flow, and the impact of outflow boundary conditions on water flow through the specimen. An array of 5 TDR waveguides was used to infer the moisture content distribution with specimen length, and a tensiometer was installed at the base of the profile to infer the suction at the outflow face.

### 8.2 TEST I (POROSITY OF 0.4, $W_C = W_{C,OPT}$ )

Test I was conducted to evaluate the transient infiltration of water during centrifugation at a constant speed, as well as the moisture profiles at two different infiltration rates. The duration of the sub-stages and the different control variables are summarized in Table 8.1. The duration is significantly shorter than the column infiltration test described in Chapter 5.

Table 8.1: Summary of Test I

Stage number	Stage description	Sub-stage	Stage duration	$\omega$ (RPM)	$Q$ (ml/hr)	$v_m$ (m/s)	$N_{r,mid}$ ( $z = 0.15$ m)	$K_{target}$ ( $z = 0.15$ m) (m/s)
I	Staged infiltration (constant $\omega$ )	a	114.3	138	10	1.55E-07	10	1.54E-08
		b	37.3	138	1	1.55E-08	10	1.54E-09
		Stage duration	151.6					
		Elapsed time	151.6					

The control variables in Stage I-1 are shown in Figure 8.1. The cumulative inflow and the inflow rate during the two sub-stages are summarized in Figure 8.1(a), the target g-level

and centrifuge speed  $\omega$  are shown in Figure 8.1(b), and the ambient temperature and g-level measured using with the g-meter are shown in Figure 8.1(c).

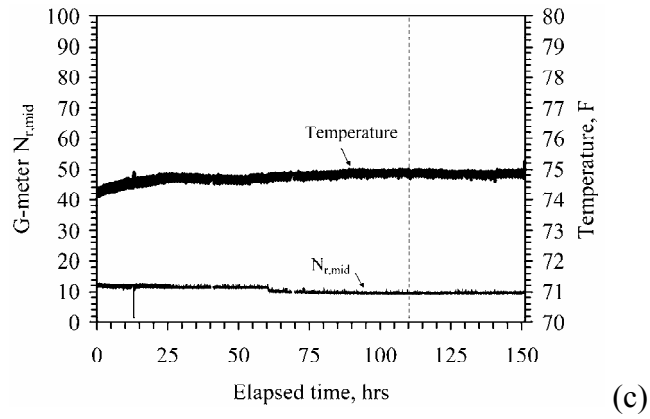
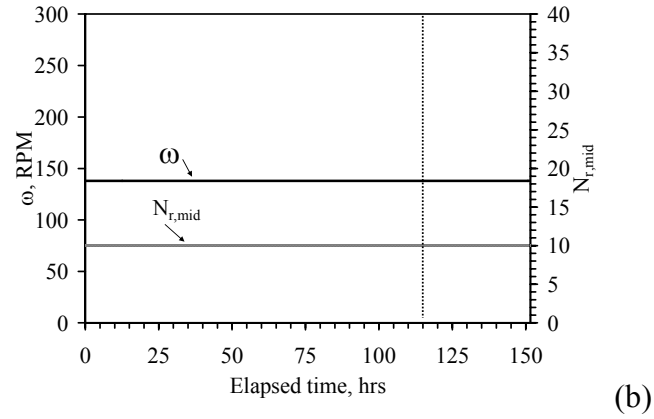
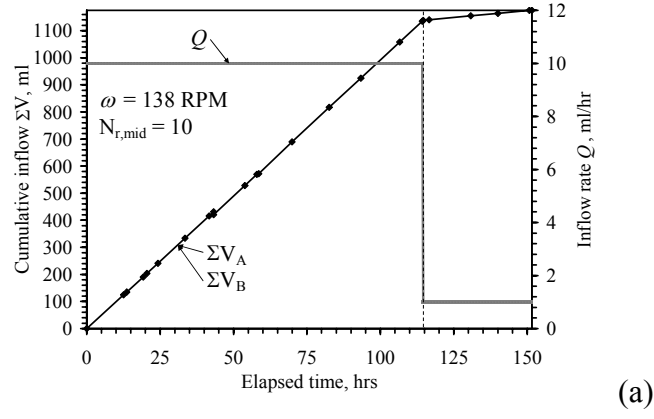


Figure 8.1: Test I time series: (a) Flow control variables  $\dot{Q}$  and  $\Sigma V$ ; (b) Centrifuge control variables  $\omega$  and  $N_r$ ; (c) G-meter and thermocouple results

The outflow transducer measurements in Test I are summarized in Figure 8.2. The initiation of outflow occurred after about 70 hrs of infiltration. Steady-state flow was observed soon after outflow was observed ( $t = 65$  hrs). A change in the slope of the outflow transducer reading was noted when the infiltration rate was decreased ( $t = 120$  hrs). Approximately 15 hours were required to reach steady-state flow at the lower rate.

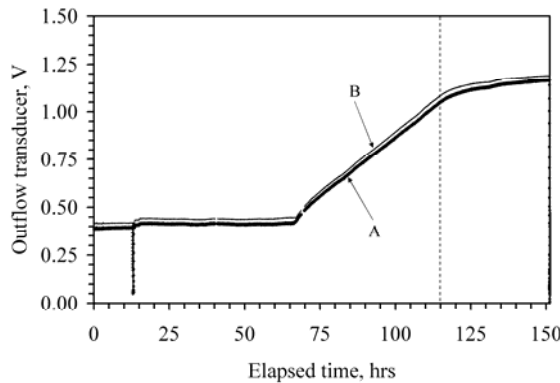
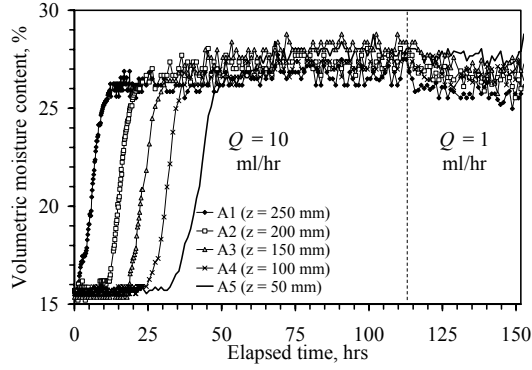


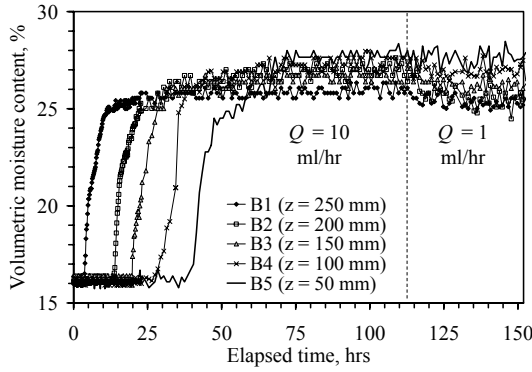
Figure 8.2: Outflow transducer measurements in Test I

The TDR measurements during Test I are shown in Figure 8.3(a) and Figure 8.3(b). A clear transition from dry to wet conditions is shown by each TDR waveguide as the wetting front passed through the specimen. Despite some scatter in the data, the moisture content is relatively uniform throughout the specimen at steady-state flow. The transitions in moisture content can be clearly seen in the moisture profiles, shown in Figure 8.4(a) and Figure 8.4 (b). Unlike the observations in the 1-g soil column discussed in Chapter 5, the moisture content at the base of the specimen does not show ponding above the outflow interface and is relatively uniform with height in the specimen. Although the moisture content is slightly higher at the base, it is still far from saturation (35%). It is possible that the transition to near saturation conditions ( $\psi_0 = 0$  kPa) occurs between  $z_m = 0$  and 50 mm, or it may be that the breakthrough suction is lower in the centrifuge than in 1-g. It should be noted that this data can be used to determine the K-

function of the soil using the instantaneous profile method, presented in Chapter 4. An advantage of the centrifuge test is that the boundary effects are less pronounced.

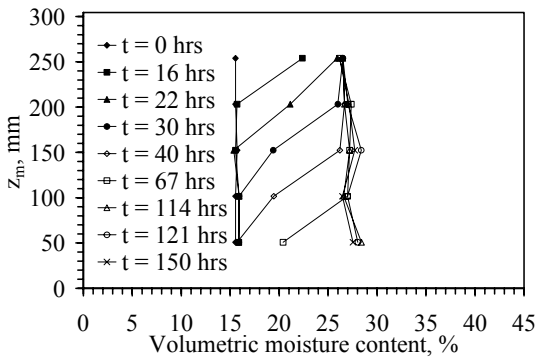


(a)

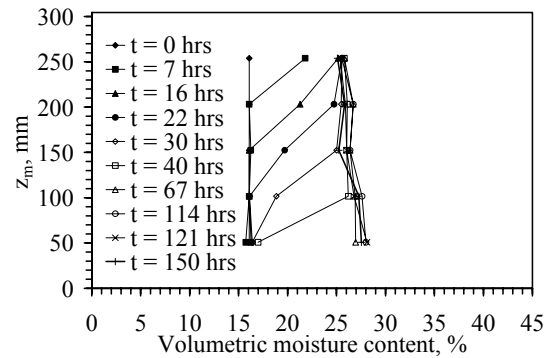


(b)

Figure 8.3: TDR measurements in Test I: (a) Specimen A; (b) Specimen B



(a)



(b)

Figure 8.4: Moisture content profiles in Test I: (a) Specimen A; (b) Specimen B



The suction at the base of the profile during Test I is shown in Figure 8.5. Cavitation occurred in Tensiometer B shortly after installation before centrifugation, and was immediately flushed using high water pressure. This high water pressure may have prevented an accurate measurement of the suction in the soil until about  $t = 100$  hrs. The initial suction was about 85 kPa. Cavitation did not occur in Tensiometer A until  $t = 37$  hrs. It was flushed under low pressure at  $t = 42$  hrs, which was approximately at the time that the wetting front passed the level of the tensiometer. However, the end of the wetting front was captured by the tensiometer at  $t = 50$  hrs. The suction at steady-state outflow was about 10 kPa, which is slightly higher than that observed in the 1-g column tests (3 kPa). A slight increase in suction was observed after the infiltration rate was decreased to 1.0 ml/hr at  $t = 113$  hrs.

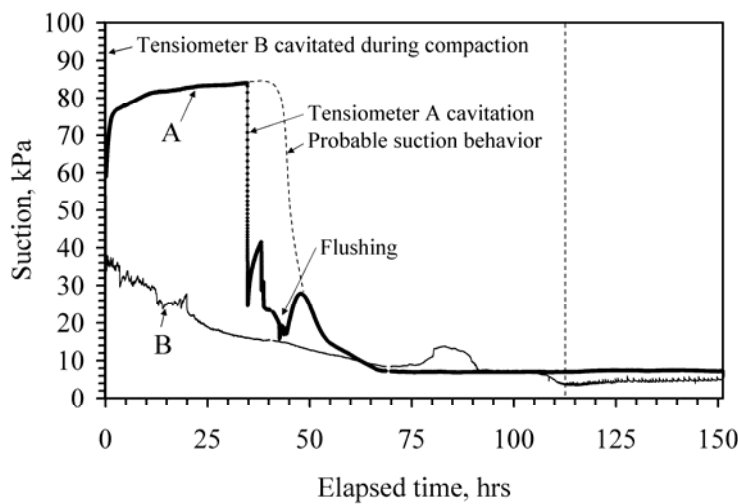


Figure 8.5: Tensiometer measurements in Test I

Overall, it is acknowledged that the tensiometer measurements for this test are particularly poor. However, the experience gained during this stage helped guide the development of the tensiometers for the hydraulic characterization permeameter used in Tests II through IV presented in the next chapter. Specifically, procedures for initial

saturation (*e.g.*, boiling, initial pressurization, and assembly underwater) and flushing of the tensiometer were refined, and the size of the water reservoir was decreased. The TDR measurements adequately reflect the behavior of the soil profile, despite some scatter. Although the derivative approach was used to analyze the TDR waveforms, the technique to select the beginning and end times by eye requires some experience.

The final moisture content profiles obtained using destructive gravimetric samples are shown in Figure 8.6. The shapes of these profiles are consistent with those observed with the TDR measurements at the end of the test (Figure 8.4). The measurement of the moisture content at the base indicates that the soil was not saturated at the outflow face.

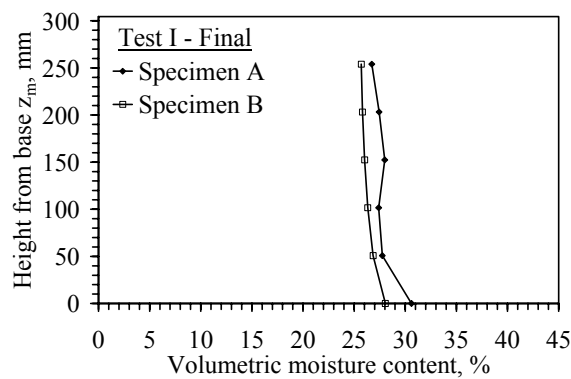


Figure 8.6: Final moisture content profile from destructive samples at the end of testing

## Chapter 9: Results from Hydraulic Characterization Tests

### 9.1 TESTING SCOPE

The testing program for verification and validation of the centrifuge permeameter includes three series of tests, each with two nearly identical specimens. This chapter includes an explanation of the results from these tests, while data will be synthesized to determine the hydraulic characteristics and assess the assumptions in Chapter 10. Each of the tests were performed with different motivations, and can be used together to validate and verify the centrifuge permeameter approach. The purposes of the three tests, labeled Tests II through IV, are summarized in Table 9.1. The tests were conducted in different stages to investigate the hydraulic characteristics and assumptions listed in Chapter 7, which permit investigation of different features of the hydraulic characteristics from a single soil specimen.

Table 9.1: Purpose of hydraulic characterization tests (with Test I included also)

Test name	Permeameter	Test motivation								
		Hydraulic characterization (Approach i)	Hydraulic characterization (Approach ii)	Hydraulic characterization (Approach iii)	Suction profiles	Boundary conditions	Darcy's law	Centrifuge effects on K and WRC	Hysteresis (constant K)	Hysteresis (wet/dry)
IA	Prototype				X	X				
IB	Prototype				X	X				
IIA	H.C.	X			X			X	X	
IIB	H.C.	X			X			X	X	
IIIA	H.C.	X	X	X	X		X	X		X
IIIB	H.C.	X	X	X	X		X	X		X
IVA	H.C.	X			X			X	X	
IVB	H.C.	X			X			X	X	

H.C. = Hydraulic characterization permeameter

These tests used a vertical TDR and a profile of three tensiometers. All of the tests used a filter paper and wire screen boundary condition. The compaction conditions in the different tests are summarized in Table 7.2. In general, a comparatively low target porosity was selected ( $n = 0.35$ ) to minimize the effects of settlement on the validation of

the testing approach. Three compaction water contents were selected in Tests II through IV ( $w_c = w_{c,opt} - 3\%$ ,  $w_c = w_{c,opt}$ , and  $w_c = w_{c,opt} + 3\%$ ) in order to obtain specimens with a range of different  $K_s$ . The  $K_s$  values for the specimens in Table 3 were estimated using the  $K_s$  vs.  $e$  and  $K_s$  vs.  $w_c$  curves presented in Chapter 4. A decrease in compaction water content was found to lead to a decrease in  $K_s$  of one order of magnitude. Variations in porosity between the specimens is not a major issue, as the WRC and K-function determined using conventional approaches in Chapter 5 were insensitive to density.

Table 9.2: Soil compaction conditions in testing program

Test name	$w_c$ (%)	$\pm w_{c,opt}$ (%)	Porosity $n$	$K_s$ (estimated) m/s
IA	10.2	-1.8	0.437	5.0E-08
IB	10.2	-1.8	0.417	5.0E-08
IIA	8.9	-3.1	0.360	1.0E-07
IIB	8.9	-3.1	0.360	1.0E-07
IIIA	11.8	-0.2	0.349	1.0E-08
IIIB	11.8	-0.2	0.343	1.0E-08
IVA	14.5	2.5	0.369	1.0E-09
IVB	14.5	2.5	0.362	1.0E-09

Note:  $w_{c,opt} = 12\%$

The ranges of centrifuge speed and inflow rates used in the tests are summarized in Table 7.3. The full speed capabilities of the centrifuge were not employed in this study (*i.e.*,  $\omega < 400$  RPM and  $N_{r,mid} < 120$ ). This was done to limit settlement and because a significant decrease in  $K_{target}$  is not obtained beyond  $N_{r,mid} = 120$  and 0.1 ml/hr (less than an order of magnitude decrease in  $K_{target}$  is obtained if using the maximum  $N_{r,mid}$  of 450). Although the time required to reach steady-state flow decreases for higher  $\omega$  values, the testing times for tests with  $N_{r,mid} < 120$  was deemed acceptable.

Table 9.3: Range of centrifuge and inflow conditions during each test

Test name	Centrifugation conditions			
	High K		Low K	
	$\omega$	Q	$\omega$	Q
	RPM	ml/hr	RPM	ml/hr
IA	138	30	239	1
IB	138	30	239	1
IIA	125	20	442	1
IIB	125	20	442	1
IIIA	125	20	403	0.1
IIIB	125	20	403	0.1
IVA	125	20	360	0.1
IVB	125	20	360	0.1

The discussion of results for each test includes time series for the: (i) control variables ( $\omega$  and  $Q$ ), (ii) target conditions ( $K_{target}$  and  $N_{r,mid}$ ), and (iii) instrumentation measurements (g-meter, thermocouple, TDR, tensiometer, and outflow transducer) during the entirety of each test. Each of the four tests has several sub-stages with different objectives (evaluation of testing approaches, evaluation hysteresis, or consistency tests). Accordingly, time series for the control variables, TDR, tensiometer, and outflow transducer measurements for each sub-stage are presented to guide an in-depth discussion on each sub-stage. Synthesized profiles of suction and moisture content at steady-state conditions also presented. For the hydraulic characterization tests, the test sequences are (plots of  $\omega$  vs.  $Q$  and  $K_{target}$  vs.  $N_{r,mid}$  showing the progression of the test).

The time series in the graphs are labeled “A” and “B” to denote the permeameter. The five TDR waveguides in the prototype permeameter and the three tensiometers in the hydraulic characterization permeameter are labeled with the permeameter name, a numeric designation (starting at the top), and the height from the specimen base. For example, the middle tensiometer in hydraulic characterization permeameter A is labeled as “A2 ( $z_m = 63.2$  mm)”. In the time series graphs, the stages of a test are separated by dotted vertical lines, while the different sub-stages are separated by dashed vertical lines.

## 9.2 TEST II (POROSITY OF 0.35, $W_C = W_{C,OPT} - 3\%$ )

The second test was conducted to analyze the hydraulic characteristics determined at different g-levels (characterization Approach *i*), to assess the effect of g-level on the K-function, to assess the impact of hysteresis on the hydraulic characteristics and to quantify the K-function of a specimen compacted dry of optimum. A summary of the duration and details for each of the stages in Test II is shown in Table 7.4.

Table 9.4: Summary of the test stages for hydraulic characterization Test II

Stage	Stage description	Sub-stage	Elapsed time (hrs)	$Q$ (ml/hr)	$\omega$ (RPM)	$N_{r,mid}$	$K_{target}$ (m/s)
II-1	Hydraulic characterization (constant $\omega$ )	a	12.2	20	125	10	1.5E-07
		b	6.4	10	125	10	7.6E-08
		c	7.8	5	125	10	3.8E-08
		d	9.2	1	125	10	7.6E-09
		Stage duration	35.7				
		Elapsed time	35.7				
II-2	Hydraulic characterization (constant $\omega$ )	a	2.6	41.5	180	20	1.5E-07
		b	4.0	20	180	20	7.3E-08
		c	3.9	10	180	20	3.7E-08
		d	12.8	5	180	20	1.8E-08
		Stage duration	23.3				
		Elapsed time	58.9				
II-3	Hydraulic characterization (constant $\omega$ )	a	1.7	83.5	255	40	1.5E-07
		b	2.3	20	255	40	3.7E-08
		c	8.0	10	255	40	1.8E-08
		d	16.9	5	255	40	9.1E-09
		e	4.8	1	255	40	1.8E-09
		Stage duration	33.9				
II-4	Hydraulic characterization (constant $\omega$ )	a	1.1	166	360	80	1.5E-07
		b	2.5	20	360	80	1.8E-08
		c	11.6	10	360	80	9.2E-09
		d	4.5	5	360	80	4.6E-09
		e	10.0	1	360	80	9.2E-10
		Stage duration	29.9				
II-5	Hydraulic characterization (constant $\omega$ )	a	8.5	1	442	120	6.1E-10
		Stage duration	8.5				
		Elapsed time	131.1				

Note: The first sub-stages in Stages II-1 to II-4 can be compared to assess hysteresis (constant K)

This test was performed to investigate the  $\omega$  and  $Q$  values and corresponding  $K$  and  $N_{r,mid}$  for each stage, as shown in Figure 9.1. At five different g-levels, the inflow rate is decreased gradually to define the WRC and K-function. After reaching steady-state flow at the lowest infiltration rate of 1 ml/hr, the infiltration rate and the g-level are both increased to obtain the same  $K_{target}$  of  $1.1 \times 10^{-7}$  m/s, as shown in Figure 9.1(b). As the  $K_{target}$  values are the same at the beginning of each stage, it is expected that the moisture content and suction should also be the same unless the soil is affected by wetting hysteresis.

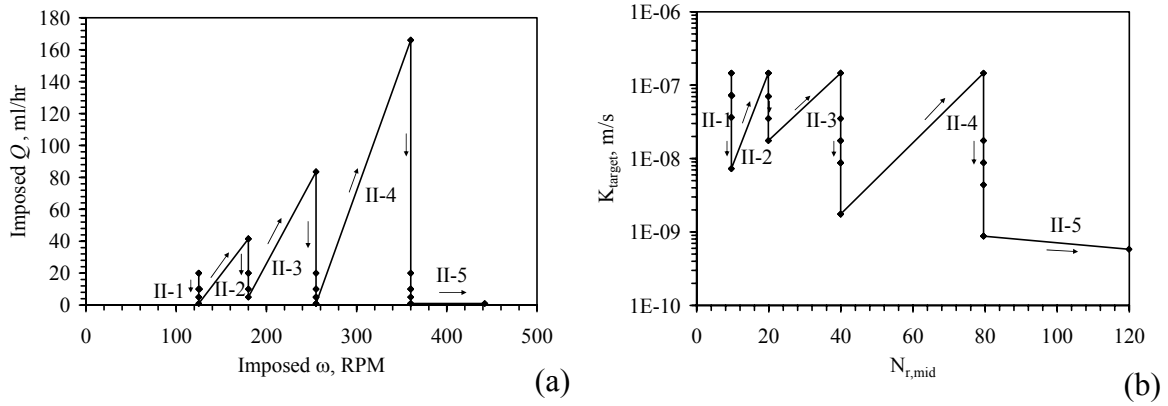


Figure 9.1: Test II: (a) Summary of imposed  $Q$  and  $\omega$  (arrows denote progression of the test); (b) Summary of steady-state imposed  $K$  values with  $N_{r,mid}$

Summaries of the control variables ( $Q$  and  $\omega$ ), the cumulative inflow volume, the actual g-level measured using the G-meter, and the temperature results for Test II are shown in Figure 9.2. The g-level was increased in five increments ranging from  $N_{r,mid} = 10$  to 120, as shown in Figure 9.2(b). During each of these periods of constant g-level, the flow rate was gradually decreased to attain different steady-state  $K_{target}$  values, as shown in Figure 9.2(a). The g-meter records are useful in showing times when the centrifuge was stopped, such as after  $t = 83$  hrs when the outflow reservoir was drained.

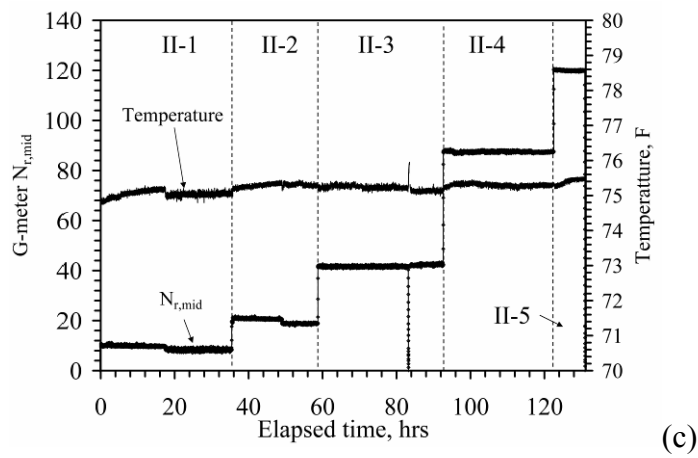
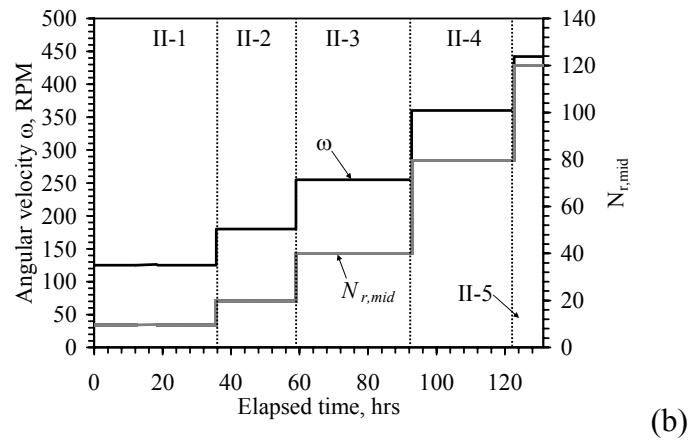
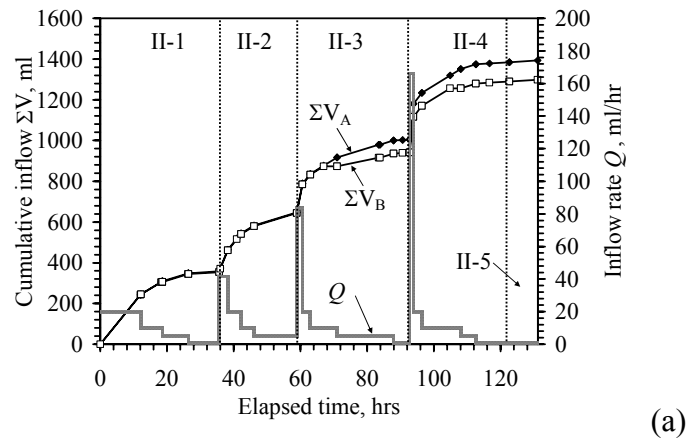


Figure 9.2: Test II time series: (a) Flow control variables  $Q$  and  $\Sigma V$ ; (b) Centrifuge control variables  $\omega$  and  $N_r$ ; (c) G-meter and thermocouple results



The infiltration rate was high ( $> 20$  ml/hr) at the beginning of each stage to achieve the same initial  $K_{target}$  value at each higher g-level. The outflow transducer results for Test II summarized in Figure 9.3 indicate that high flow rates did not result in compression of the pore air (smooth increases were observed). The inflow was paused for Permeameter B at three times during the test due to air bubbles in the pump [ $t = 67$ ,  $79$ , and  $t = 106$  hrs in Figure 9.2(a)], during which a flattening of the slope in the outflow data was observed. During Stage II-5, the same initial  $K_{target}$  as that selected for the other stages was not used as the outflow reservoir was nearly full. Instead a low infiltration rate of  $1$  ml/hr was imposed, reflected by a shallow slope at the end of the test.

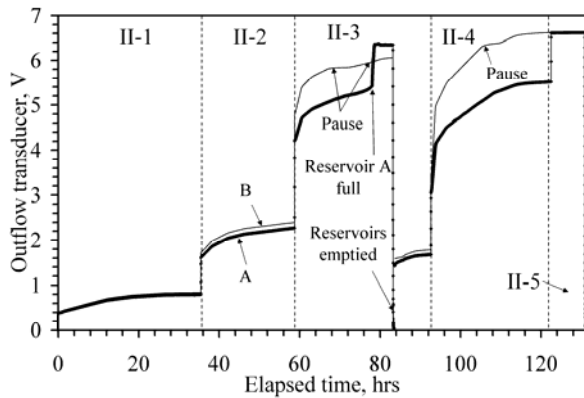


Figure 9.3: Summary of outflow transducer measurements during Test II

The TDR measurements, along with a 5-point moving average, shown in Figure 9.4 indicate a gradual decrease in moisture during each stage of the test (as the inflow rate is decreased in each stage). Increases in moisture content are observed during the periods of increased inflow at the beginning of each stage. Unlike the specimens in Test I, this test started from near-saturated conditions. The suction data shown in Figure 9.5 indicates that the suction increased during each phase, with slight decreases in suction at the beginning of each phase. The middle tensiometers were not working. However, the lower tensiometer follows the same trend as the upper tensiometer in both permeameters.

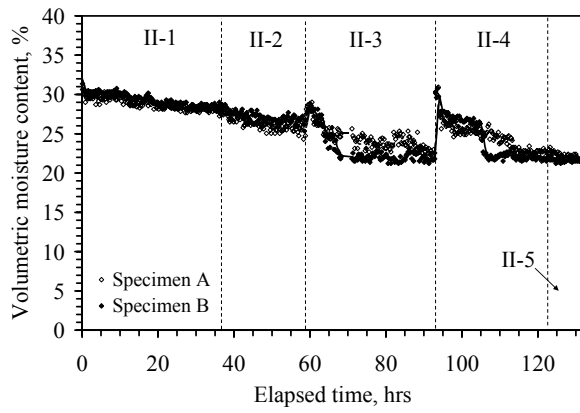
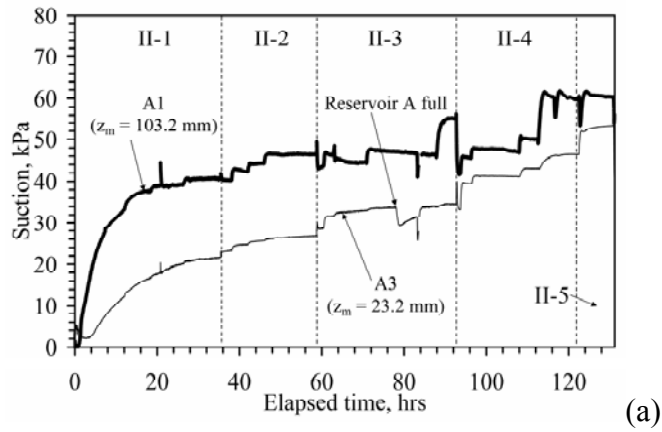
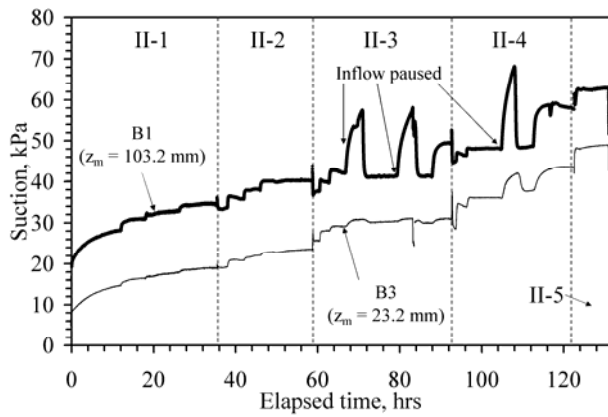


Figure 9.4: Summary of TDR measurements during Test II



(a)



(b)

Figure 9.5: Tensiometer measurements during Test II: (a) Specimen A; (b) Specimen B

In general, the suction magnitude is relatively low (less than 60 kPa) although this is expected during infiltration. At the times when the inflow was paused for Specimen B ( $t = 67, 79$ , and  $t = 106$  hrs), increases in suction were measured by the upper tensiometer. The tensiometer also shows that once the inflow was restarted after these pauses, the suction tended to return to the value before inflow stopped. The lower tensiometer results indicate that the suction at the base of the profile is generally greater than zero, which may imply that a saturated boundary condition is not present.

Stage II-1 was conducted to evaluate the transient infiltration of water during centrifugation, as well as the moisture profiles at two different infiltration rates. The control variables in Stage II-1 are shown in Figure 9.6. This figure clearly shows the decrease in inflow rate during each stage leads to a change in slope of the cumulative inflow curve. This behavior is closely mimicked by the outflow transducer data for this stage, shown in Figure 9.7. Steady-state infiltration was observed nearly immediately after infiltration started, as the specimen was saturated and the inflow rate was relatively high. Further, a gradual decrease in moisture content is observed during Sub-Stage, as shown in Figure 9.8. The scatter in the TDR results is less than that observed in Test 1.

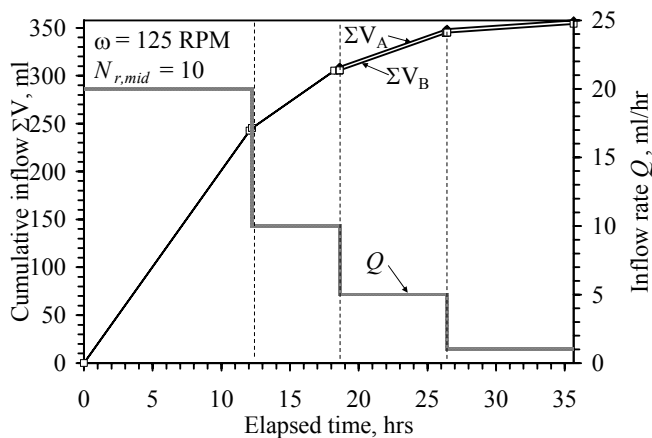


Figure 9.6: Control variables in Stage II-1

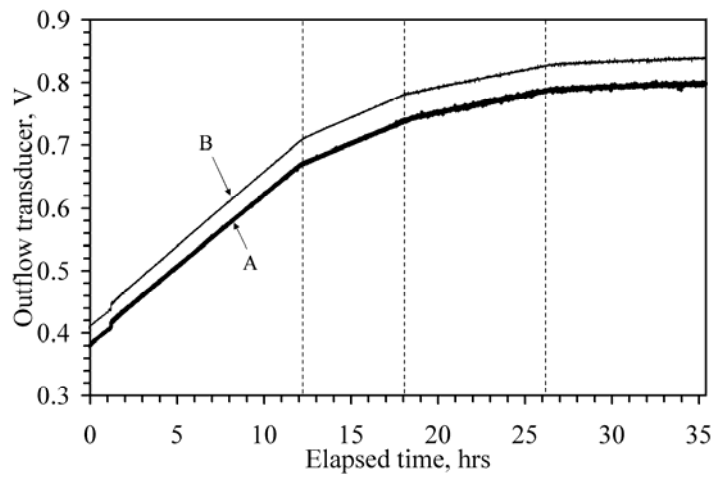


Figure 9.7: Outflow transducer measurements in Stage II-1

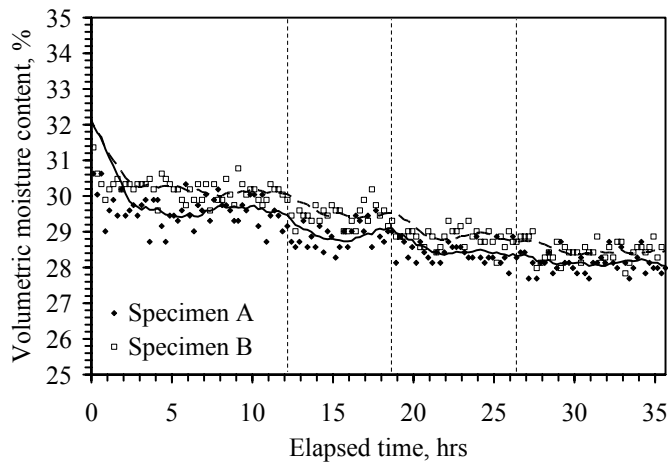


Figure 9.8: TDR measurements in Stage II-1

The suction values during this stage in Figure 9.9 show increases in magnitude after each decrease in the infiltration rate. The upper tensiometer reflects the changes in infiltration rate before the lower tensiometer. The suction profiles shown in Figure 9.10 indicate that a gradient in suction is present in the specimen. However, as the middle tensiometers were not functioning properly in this test, it is not clear if constant suction develops in the upper portion of the specimen.

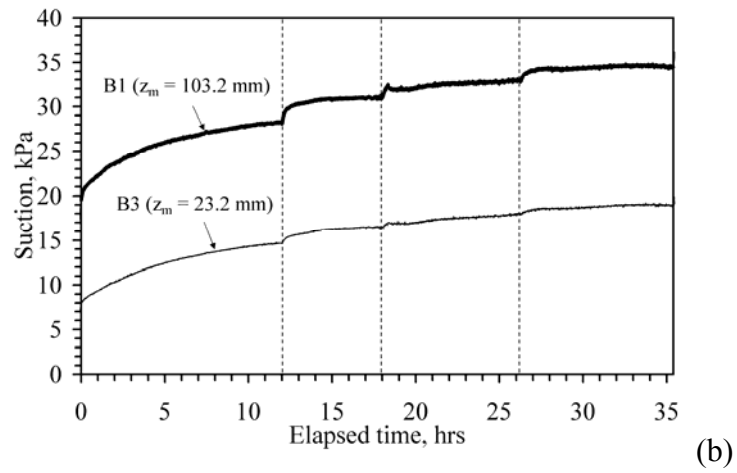
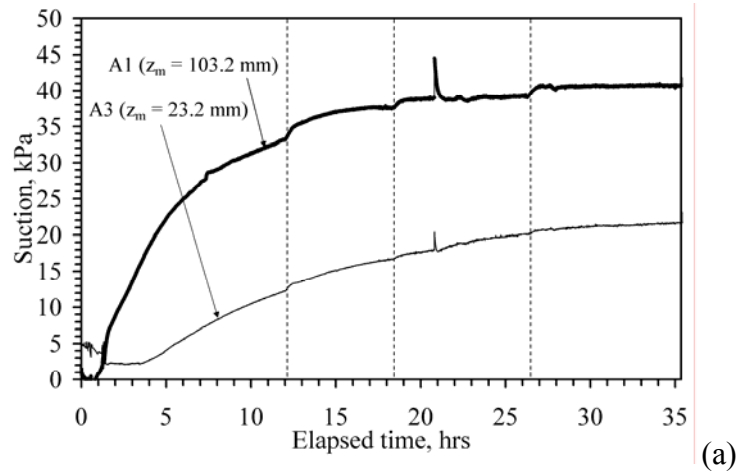


Figure 9.9: Tensiometer measurements in Stage II-1: (a) Specimen A; (b) Specimen B

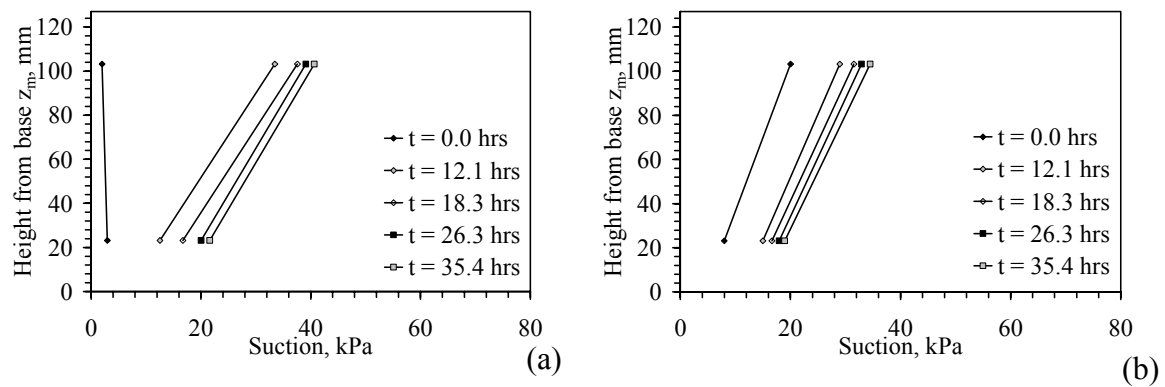


Figure 9.10: Suction profiles in Stage II-1: (a) Specimen A; (b) Specimen B

Stage II-2 was conducted with a similar purpose to Stage II-1 (hydraulic characterization Approach *i*) but at  $N_{r,mid} = 20$ . The control variables in Stage II-2 are shown in Figure 9.11. Similar to the previous stage, the outflow data in Figure 9.12 mirrors the inflow data. Although time was provided in the final phase of this stage to reach equilibrium at the lowest infiltration rate, the outflow data indicates that steady-state flow occurred soon after each change in the inflow rate. The TDR and tensiometer data for Stage II-2, shown in Figure 9.13 and Figure 9.14 respectively, show similar behavior to that noted in Stage II-1, with lower moisture content and higher suction.

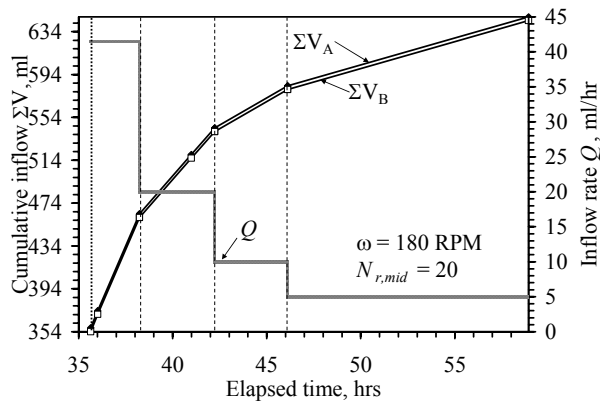


Figure 9.11: Control variables in Stage II-2

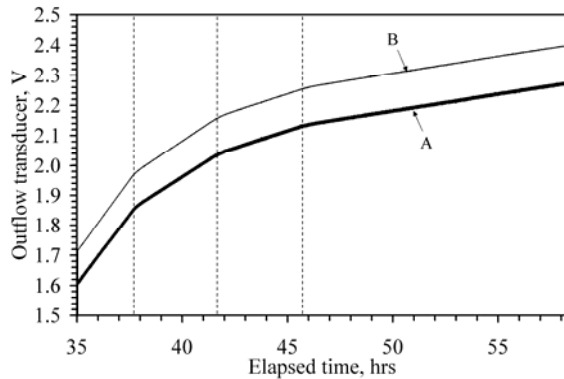


Figure 9.12: Outflow transducer measurements in Stage II-2

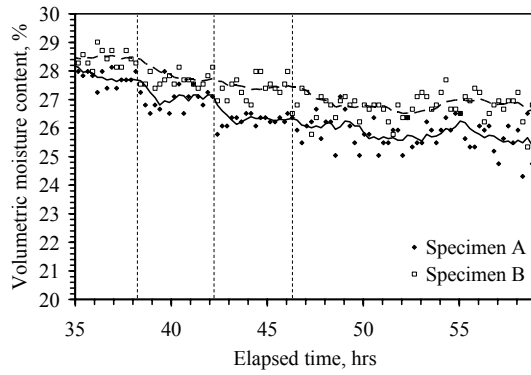


Figure 9.13: TDR measurements in Stage II-2

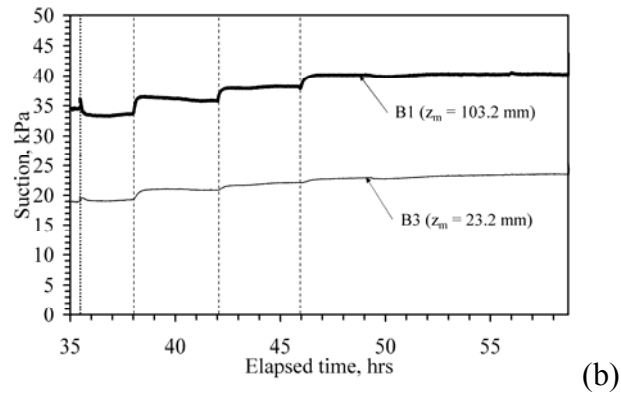
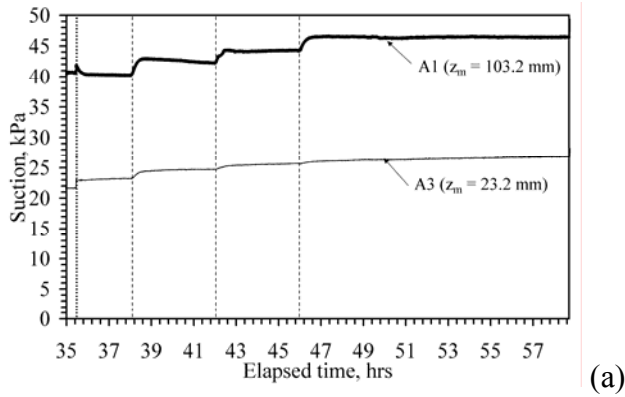


Figure 9.14: Tensiometer measurements in Stage II-2: (a) Specimen A; (b) Specimen B

The suction profiles in Figure 9.15 for Stage II-2 indicate that the top and bottom tensiometers showed similar changes in suction after steady-state flow occurs at each

infiltration rate. Although it is not possible to assess the suction gradient in the upper portion of the specimen as the middle tensiometer malfunctioned, a zero suction gradient throughout the entire specimen is clearly not observed even at this higher g-level.

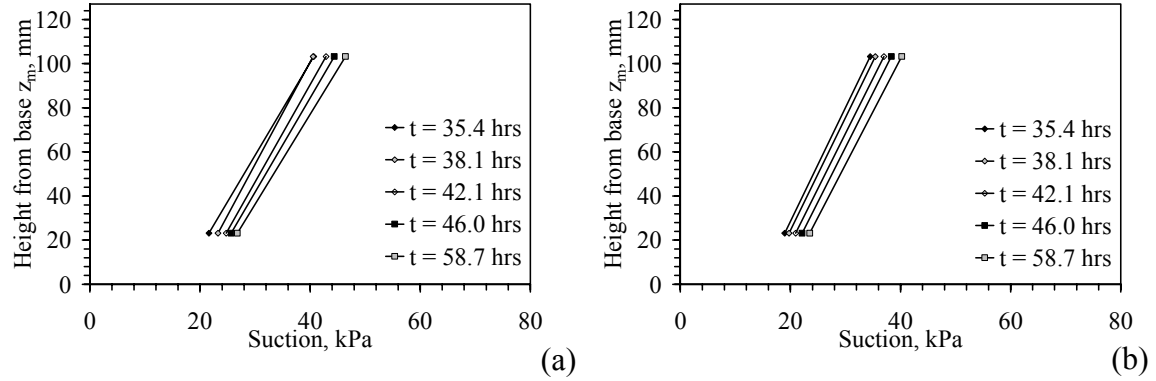


Figure 9.15: Suction profiles in Stage II-2

Stage II-3 is similar to Stage II-1 and II-2, but  $N_{r,mid}$  was increased to 40 g. The control variables in Stage II-3 are shown in Figure 9.16. The inflow was paused after  $t = 67$  hrs for Permeameter B. However, steady-state infiltration was attained by the time the next lower infiltration rate was applied (Sub-Stage II-3d), as indicated by the outflow data (Figure 9.17) and the TDR and tensiometer data (Figure 9.18 and Figure 9.19).

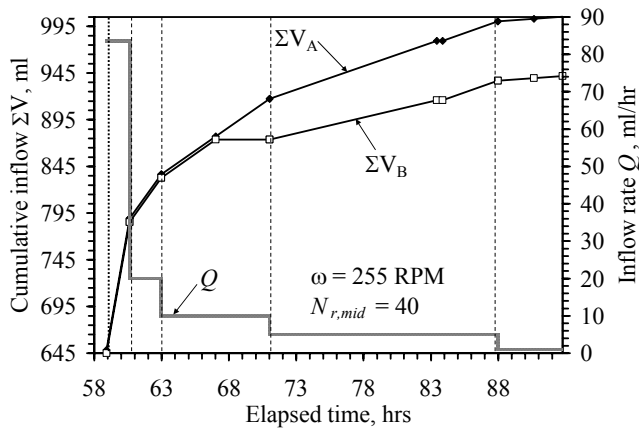


Figure 9.16: Control variables in Stage II-3



Two versions of the same plot but with different scales are shown for the outflow transducer in Stage II-3 in Figure 9.17. The reservoir for Permeameter A reached its capacity after  $t = 78$  hrs (during the middle of the night). The centrifuge was then stopped and the outflow was collected. When infiltration was restarted, the pressure on the transducer was much lower. Also during this stage, the inflow for Permeameter B was paused twice ( $t = 67$  and  $78$  hrs). These different phenomena are noted in the TDR data for Stage II-3, shown in Figure 9.18. At  $t = 67$  and  $78$  hrs, Specimen B shows a decrease in moisture content because inflow had stopped, while at  $t = 78$  hrs Specimen A showed an increase in moisture content because the outflow reservoir was full.

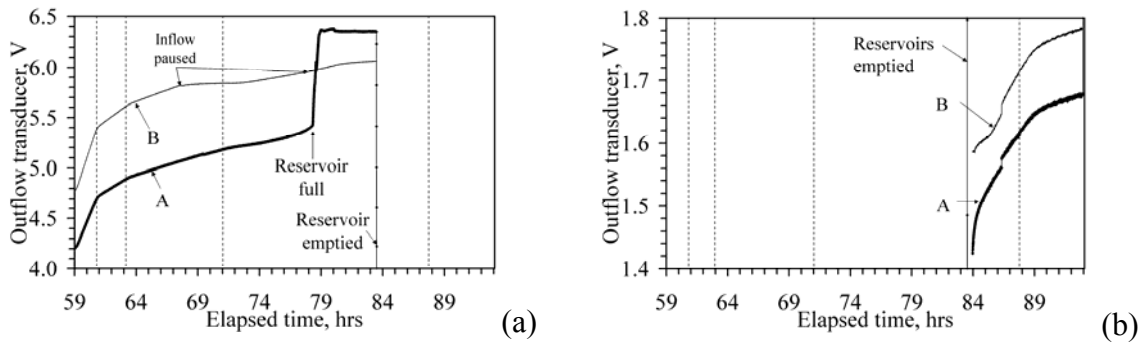


Figure 9.17: Outflow transducer in Stage II-3: (a) Before drainage; (b) After drainage

Further, in the tensiometer data for Stage II-3, shown in Figure 9.19, the upper tensiometer for Specimen A shows a decrease in suction at  $t = 78$  hrs because the outflow suction was likely near 0 (saturation). The upper tensiometer for Specimen B showed significant increases in suction during each of the two times when the inflow was paused due to air bubbles in the pump. Because the third infiltration rate (II-3c) was not reconvened after inflow was paused at  $t = 68$  hrs, the steady-state suction and moisture content values for the third infiltration rate (II-3c) were taken from  $t = 68$  hrs. Despite the pauses in inflow for Specimen B and the reservoir reaching its capacity in Specimen A, the steady-state moisture content and suction values were not impacted.

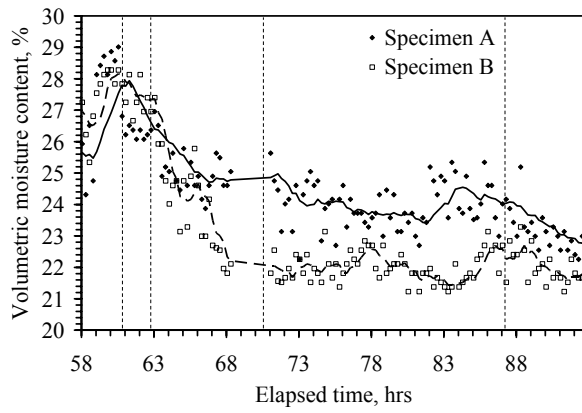
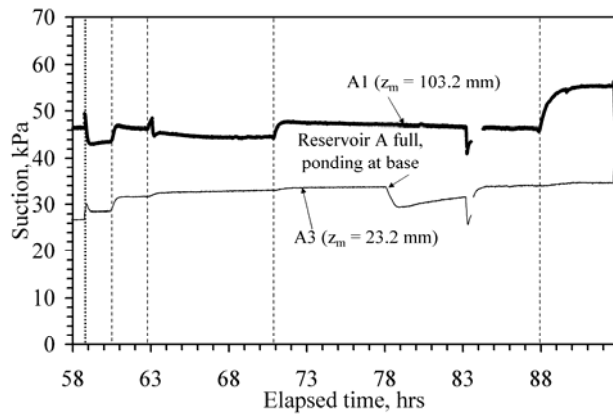
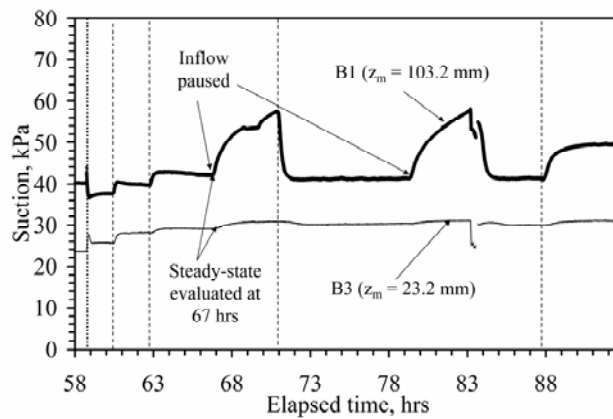


Figure 9.18: Summary of measured values in Stage II-3: (a) TDR; (b) Tensiometer; (c) Outflow transducer



(a)



(b)

Figure 9.19: Tensiometer measurements in Stage II-3: (a) Specimen A; (b) Specimen B

The suction profiles during Stage II-3 in Figure 9.20 indicate that the difference between the upper and lower tensiometers is similar to that during Stages II-1 and II-2. Despite the higher  $N_{r,mid}$ , a suction gradient is still observed between the tensiometers.

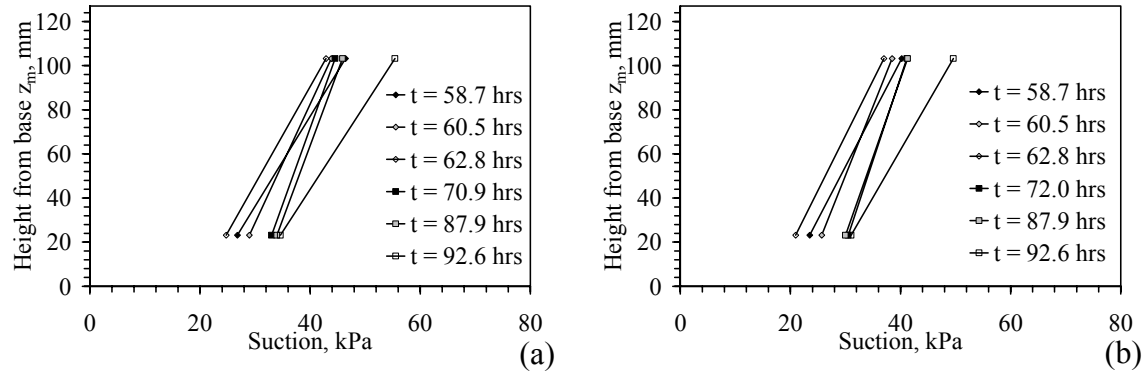


Figure 9.20: Suction profiles in Stage II-3

Stage II-4 is similar to the previous stages, but was conducted at  $N_{r,mid} = 80$ . The control variables in Stage II-4 are shown in Figure 9.21. Again, the inflow for Permeameter B was paused due to air bubbles during Sub-stage II-4c. The supply lines for the pump were changed after this, which led to more reliable pump performance. The pump supply lines should be changed after 10 days of continuous use.

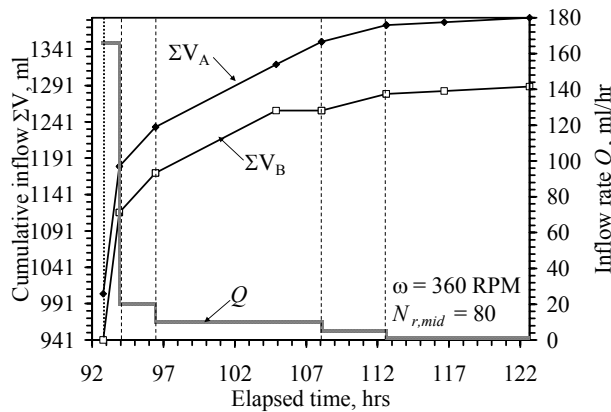


Figure 9.21: Control variables in Stage II-4

The outflow transducer results for Stage II-4 shown in Figure 9.22 are similar to those in the previous stages. As steady-state flow had been attained during the third infiltration stage (II-4c), the next infiltration rate was applied when flow was restarted at  $t = 108$  hrs. The TDR data shown in Figure 9.23 indicates a drop in moisture content in Specimen B when the inflow was paused, and a subsequent increase in moisture content during the fourth inflow rate. This is also noted in the tensiometer data in Figure 9.24.

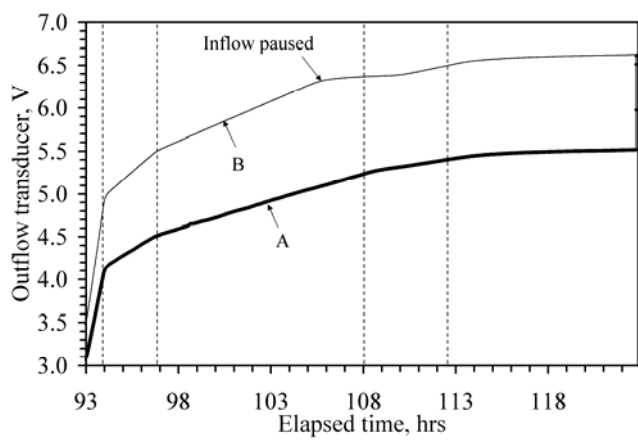


Figure 9.22: Outflow transducer measurements in Stage II-4

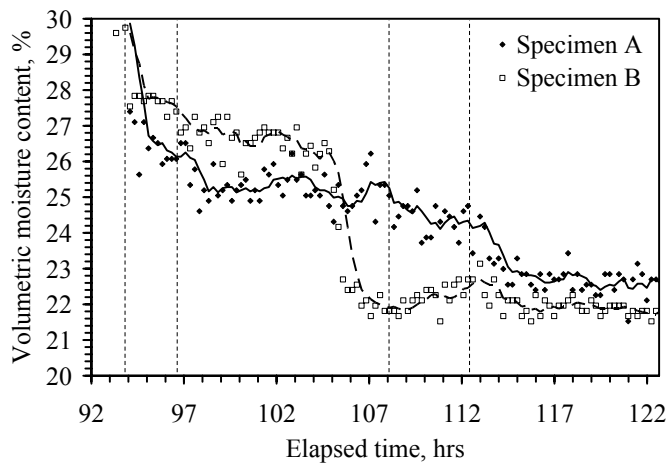


Figure 9.23: Summary of measured values in Stage II-4: (a) TDR; (b) Tensiometer; (c) Outflow transducer

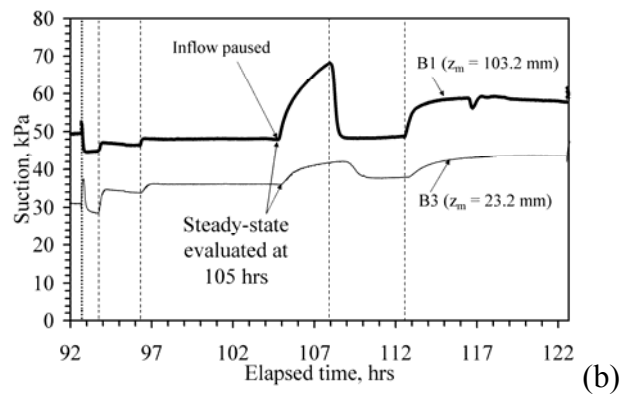
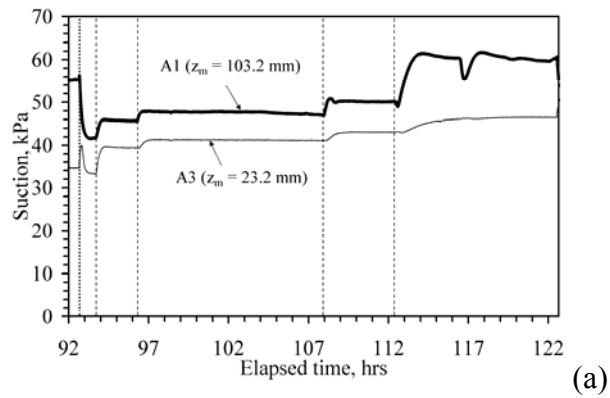


Figure 9.24: Tensiometer measurements in Stage II-4: (a) Specimen A; (b) Specimen B

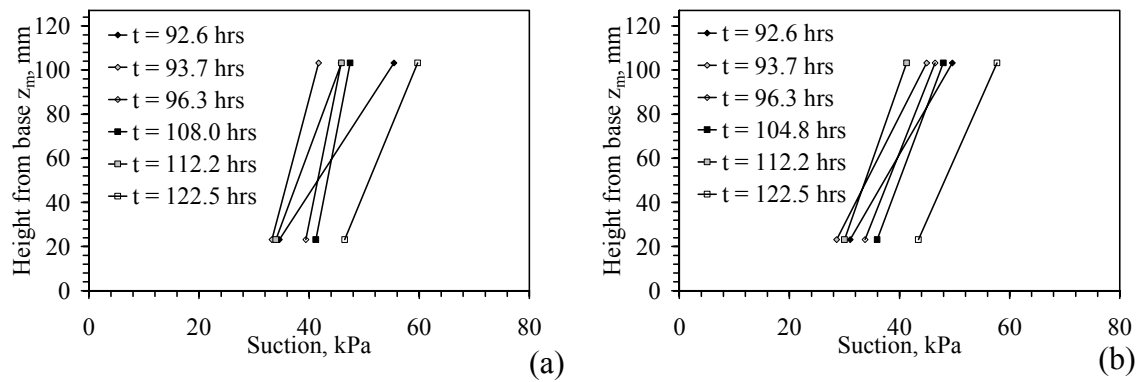


Figure 9.25: Suction profiles in Stage II-4

The suction profiles during Stage II-4 shown in Figure 9.25 indicate that the suction values at the top and bottom of the specimen are closer to each other than in the

previous stages, indicating that the suction profile is more uniform throughout the specimen for this higher  $N_{r,mid}$ . Nonetheless, a suction gradient is still observed.

Stage II-5 was conducted to evaluate one additional point on the K-function at a low rate and high g-level. The control variables in Stage II-5 are shown in Figure 9.26. The outflow data shown in Figure 9.27 indicate that the transducer was near voltage capacity ( $\sim 6.63\text{V}$ ), so it was not possible to investigate higher flow rates without stopping the centrifuge. The moisture content data shown in Figure 9.28 shows a slight decrease during this stage, and the suction data in Figure 9.29 shows a slight increase.

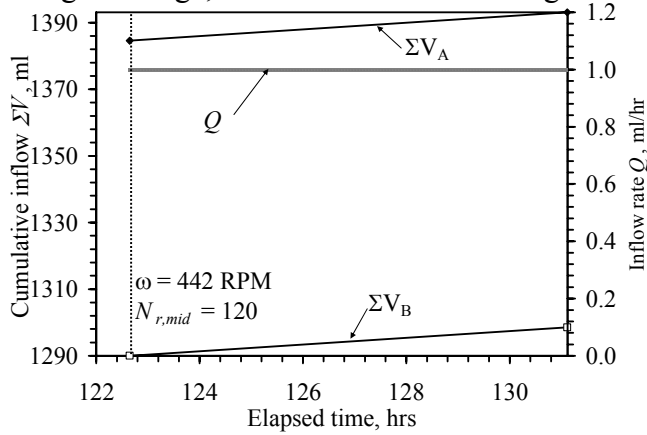


Figure 9.26: Control variables in Stage II-5

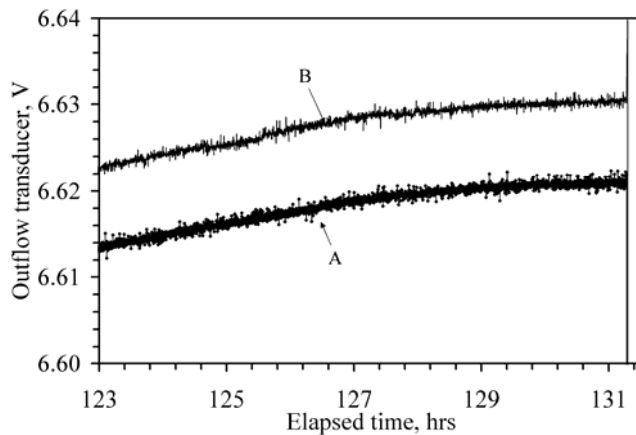


Figure 9.27: Outflow transducer measurements in Stage II-5

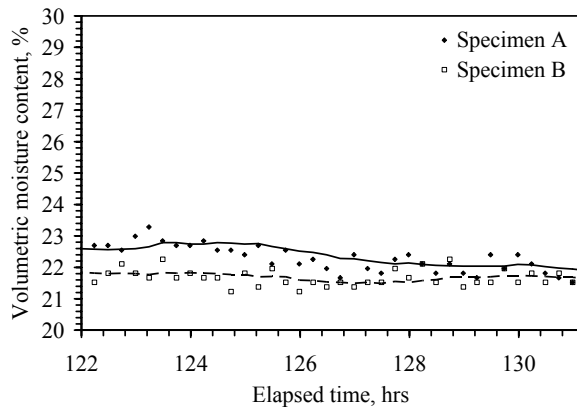
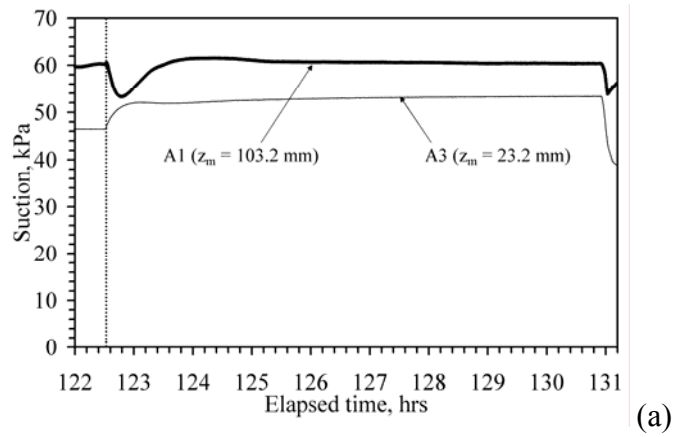
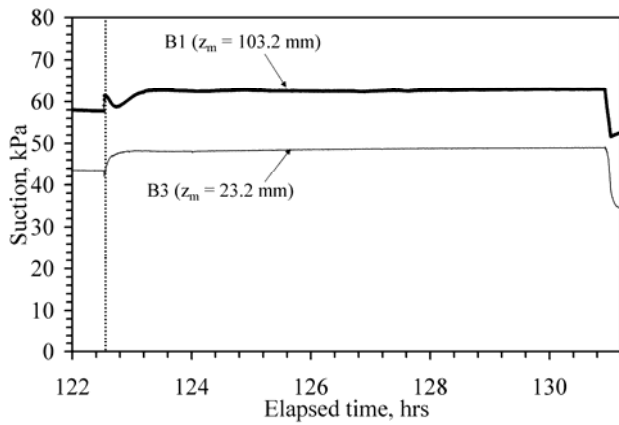


Figure 9.28: Summary of TDR values in Stage II-5



(a)



(b)

Figure 9.29: Tensiometer measurements in Stage II-5: (a) Specimen A; (b) Specimen B

The suction profiles during Stage II-5 are shown in Figure 9.30. Although conclusions about the suction gradient in the upper portion of the specimen cannot be made from this test as the middle tensiometer was not working, these results indicate that the suction values between the top and bottom of the specimen become closer for higher  $N_{r,mid}$ . Further, it is clear that the suction near the base of the profile is much greater than zero, indicating that a zero suction boundary condition may not be present.

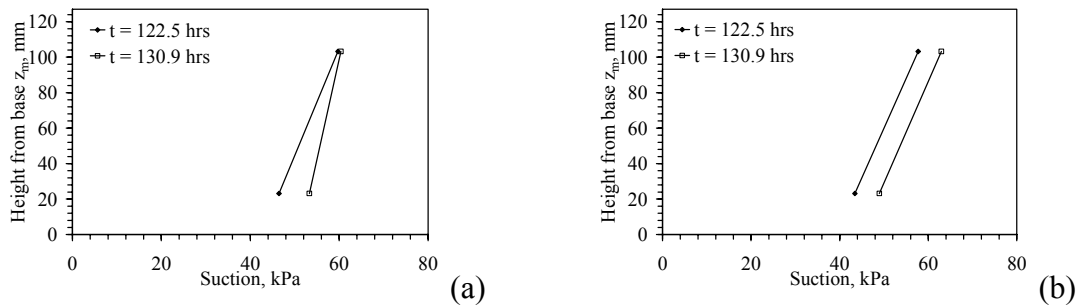


Figure 9.30: Suction profiles in Stage II-5

The moisture content profiles obtained using gravimetric samples at the end of Stage II-5 are shown in Figure 9.31. The moisture content values are relatively constant with height in the specimen and the values in the upper zone are consistent with the TDR results in Figure 9.28. The bottom of the specimen is slightly wetter than the upper portion of the specimen, consistent with the trends in the measured suction profiles.

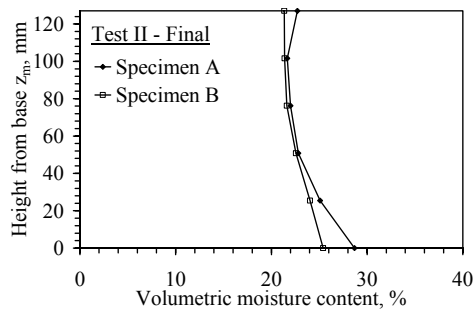


Figure 9.31: Final moisture content profile from destructive samples at the end of Test II



### 9.3 TEST III (POROSITY OF 0.35, $W_C = W_{C,opt}$ )

Test III includes 7 stages, summarized in Tables 7.7, 7.8 and 7.9. The goals of this test are to analyze the hydraulic characteristics using Approaches (i), (ii), and (iii), to assess the consistency of  $K_{measured}$  values obtained with the centrifuge permeameter, and to assess the role of hysteresis in the results from the three characterization approaches.

Table 9.5: Summary of the first five test stages for hydraulic characterization Test III

Stage	Stage description	Sub-stage	Elapsed time (hrs)	$Q$ (ml/hr)	$\omega$ (RPM)	$N_{r,mid}$	$K_{target}$ (m/s)
III-1	Hydraulic characterization (constant $\omega$ , varying $Q$ )	a	1.9	20	125	10	1.5E-07
		b	4.4	10	125	10	7.6E-08
		c	7.3	1	125	10	7.6E-09
		Stage duration	13.5				
		Elapsed time	13.5				
III-2	Hydraulic characterization (constant $\omega$ , varying $Q$ )	a	4.2	5	180	20	1.8E-08
		b	17.3	2.5	180	20	9.2E-09
		c	15.1	1	180	20	3.7E-09
		Stage duration	36.6				
		Elapsed time	50.1				
III-3	Hydraulic characterization (constant $\omega$ , varying $Q$ )	a	15.4	10	255	40	1.8E-08
		b	2.7	5	255	40	9.1E-09
		c	4.7	2.5	255	40	4.6E-09
		d	12.7	1	255	40	1.8E-09
		Stage duration	35.5				
III-4	Hydraulic characterization with hysteresis (constant $\omega$ , varying $Q$ )	Stage duration	85.6				
		Elapsed time	85.6				
		a	5.6	20	360	80	1.8E-08
		b	2.2	10	360	80	9.2E-09
		c	3.8	5	360	80	4.6E-09
		d	12.5	1	360	80	9.2E-10
		e	5.0	5	360	80	4.6E-09
		f	3.8	10	360	80	9.2E-09
III-5	Centrifuge consistency test (constant K)	g	2.0	20	360	80	1.8E-08
		Stage duration	34.9				
		Elapsed time	120.5				
		a	4.6	10	255	40	1.8E-08
		b	8.6	5	180	20	1.8E-08
III-5	Centrifuge consistency test (constant K)	c	5.7	2.4	125	10	1.8E-08
		Stage duration	18.9				
		Elapsed time	139.4				

Note: First sub-stage in Stages II-2 to II-4 allows investigation of hysteresis (constant K)

Stages III-1 through III-4 are similar to stages II-1 through II-4 in Test II, in which  $N_{r,mid}$  was maintained constant and the inflow rate is varied [Approach (i)]. Stage III-4 is unique in that the inflow is decreased then increased, which allows investigation of drying and wetting (hysteresis). Stage III-5, combined with the last Sub-stage in Stage III-4, allows investigation of the consistency of  $K_{measured}$  values obtained in the centrifuge permeameter, in which a constant  $K_{target}$  is used in each sub-stage by imposing different combinations of  $Q$  and  $\omega$ . If the centrifuge permeameter approach is consistent, the moisture content and suction should be constant, and  $K_{measured}$  should be the same. This is in contrast to the hysteresis investigation in Test II, in which the same  $K_{target}$  was imposed at the beginning of each stage (after drying the specimen in the previous stage).

Table 9.6: Summary of Stage III-6 for hydraulic characterization Test III

Stage	Stage description	Sub-stage	Elapsed time (hrs)	$Q$ (ml/hr)	$\omega$ (RPM)	$N_{r,mid}$	$K_{target}$ (m/s)
III-6	Hydraulic characterization with hysteresis (varying $\omega$ and $Q$ )	Outflow drained	3.3	0	0	1	0.0E+00
		a	5.9	20	125	10	1.5E-07
		b	10.6	15	180	20	5.5E-08
		c	6.7	10	220	30	2.5E-08
		d	3.6	7.5	255	40	1.4E-08
		e	4.4	5	285	50	7.3E-09
		f	7.7	2.5	312	60	3.1E-09
		g	6.4	1.5	338	70	1.6E-09
		h	8.5	1	360	80	9.2E-10
		i	9.9	0.5	385	91	4.0E-10
		j	29.3	0.1	403	100	7.3E-11
		k	29.9	0.5	385	91	4.0E-10
		l	14.8	1	360	80	9.2E-10
		m	11.8	1.5	338	70	1.6E-09
		n	8.2	2.5	312	60	3.1E-09
		o	10.0	5	285	50	7.3E-09
		p	5.4	7.5	255	40	1.4E-08
		q	18.4	10	220	30	2.5E-08
		r	8.6	15	180	20	5.5E-08
	s	6.6	20	125	10	1.5E-07	
	Stage duration	209.9					
	Elapsed time	349.3					

Stage III-6 was conducted to investigate the use of Approach (iii) to determine the hydraulic characteristics. As summarized in Table 7.8,  $Q$  is decreased and  $\omega$  is increased during each sub-stage to dry the specimen to reach a wide range of  $K_{target}$  values. The same  $Q$  and  $\omega$  values are then applied in reverse to investigate wetting. Stage 7 was conducted to evaluate the use of Approach (ii) to determine the hydraulic characteristics. As summarized in Table 7.9, the inflow rate was maintained constant at  $Q = 5$  ml/hr during each sub-stage, and  $N_{r,mid}$  was varied to reach different  $K_{target}$  values.

Table 9.7: Summary of Stage III-7 for hydraulic characterization Test III

Stage	Stage description	Sub-stage	Elapsed time (hrs)	$Q$ (ml/hr)	$\omega$ (RPM)	$N_{r,mid}$	$K_{target}$ (m/s)
III-7	Hydraulic characterization with hysteresis (varying $\omega$ and constant $Q$ )	Outflow drained	0.4	0	0	1	0.0E+00
		a	9.8	5	125	10	3.8E-08
		b	5.1	5	180	20	1.8E-08
		c	10.4	5	220	30	1.2E-08
		d	6.1	5	255	40	9.1E-09
		e	5.8	5	285	50	7.3E-09
		f	11.4	5	312	60	6.1E-09
		g	4.6	5	338	70	5.2E-09
		h	3.3	5	360	80	4.6E-09
		i	2.2	5	383	90	4.1E-09
		j	2.6	5	360	80	4.6E-09
		k	3.2	5	338	70	5.2E-09
		l	7.2	5	312	60	6.1E-09
		m	2.8	5	285	50	7.3E-09
		n	4.1	5	255	40	9.1E-09
		o	4.1	5	220	30	1.2E-08
		p	5.1	5	180	20	1.8E-08
		Stage duration	88.1				
		Elapsed time	437.4				

Summaries of the control variables for Test III are shown in Figure 9.32. The test sequence in Figure 9.32(a) is similar to that used in Test II [Approach (i)], while those shown in Figure 9.32(b) and Figure 9.32(c) are representative of Approaches (iii) and (ii) respectively. The arrows in these figures indicate the test sequence. Similarly, the

related values of  $K_{target}$  and  $N_{r,mid}$  corresponding to these curves are shown in Figure 9.33. In particular the curves in Figure 9.33(b) for Stage III-5 highlight the constant  $K_{target}$  portion of the test, used to investigate the consistency of the centrifuge approach.

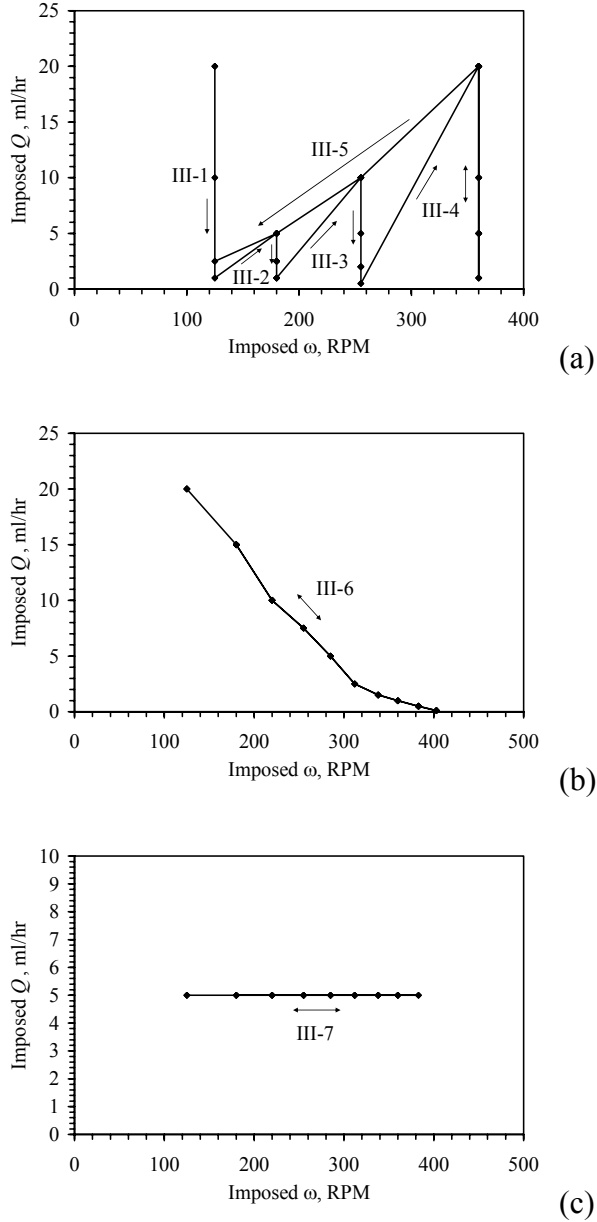


Figure 9.32: Summary of imposed  $Q$  and  $\omega$  for Test III (arrows denote progression of test): (a) First five stages; (b) Stage III-6; (c) Stage III-7

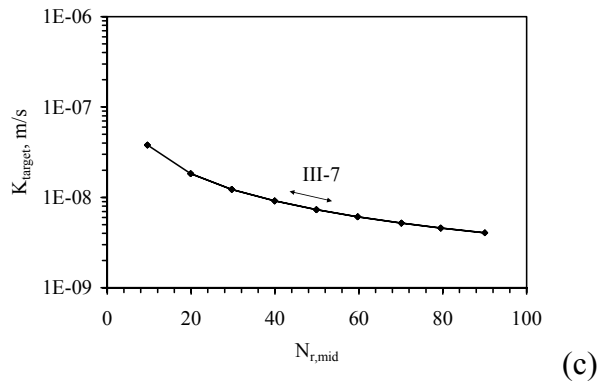
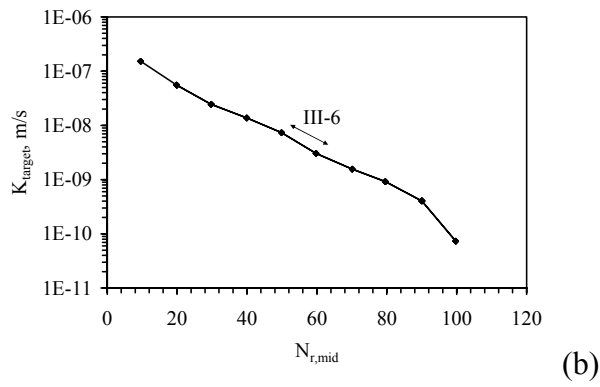
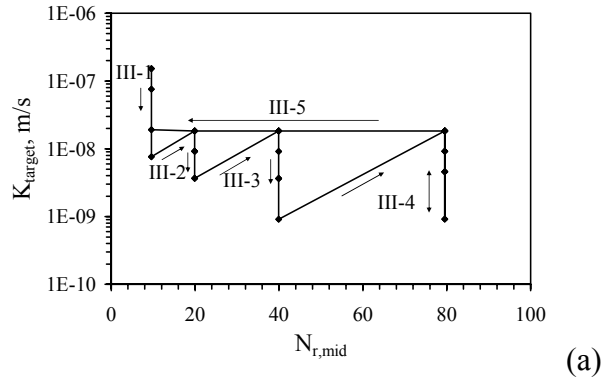
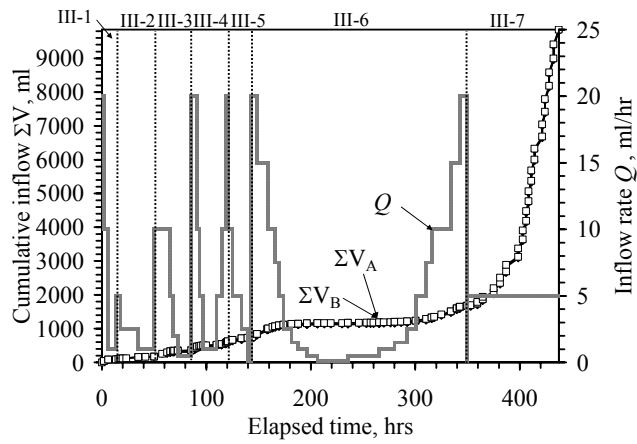
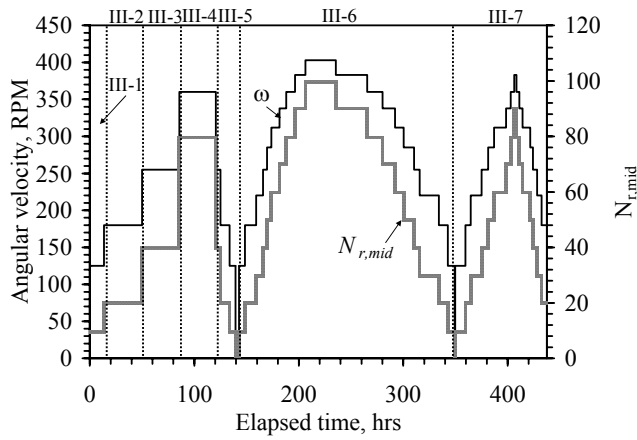


Figure 9.33: Summary of  $K_{target}$  values with  $N_{r,mid}$  in Test III (arrows denote progression of test): (a) First five stages; (b) Stage 6; (c) Stage III-7

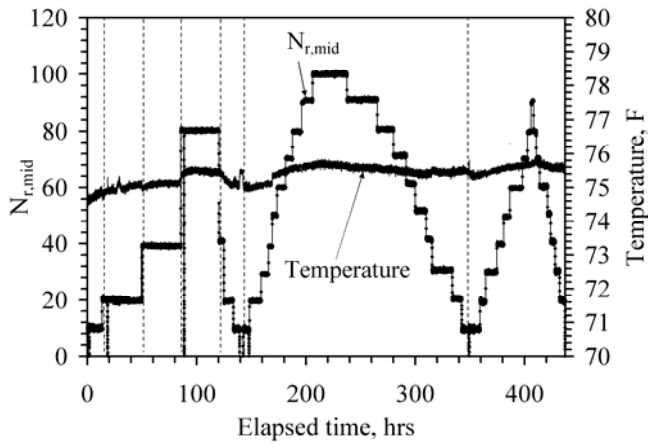
Summaries of the control variables for Test III are shown in Figure 9.34. The details of each of the individual stages of the test will be discussed in more detail later, but these figures illustrate both the duration of the test, and the values investigated.



(a)



(b)



(c)

Figure 9.34: Test III time series: (a) Flow control variables  $Q$  and  $\Sigma V$ ; (b) Centrifuge control variables  $\omega$  and  $N_r$ ; (c) G-meter and thermocouple results

A summary of the outflow transducer data for Test III is shown in Figure 9.35. The interesting aspects of this test include the outflow during infiltration at low  $N_{r,mid}$  (III-1, III-6a, III-7a), during which the outflow measurements were significantly affected compression of the pore air. The outflow transducer results during Stages III-6 and III-7 is different than the typical results observed in Test II. Specifically, each change in  $N_{r,mid}$  causes a shift in the transducer reading. As will be discussed later, the outflow transducer in Permeameter A reached its capacity during Stage III-6 ( $t = 190$  to  $t = 290$  hrs).

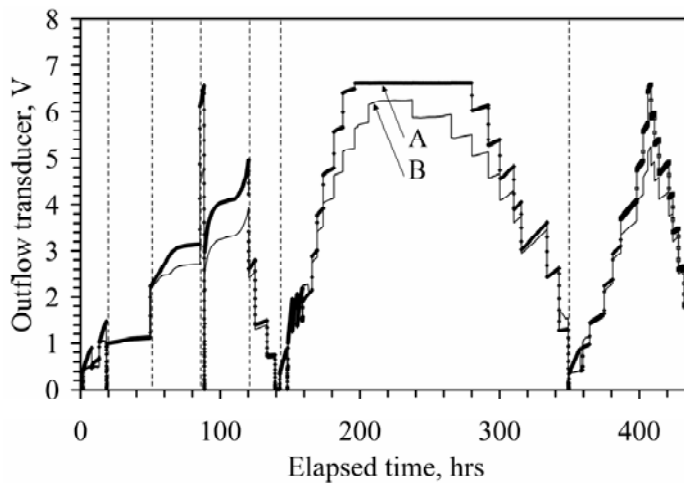


Figure 9.35: Summary of outflow transducer measurements during Test III

The TDR data during Test III in Figure 9.36 indicate that the range of moisture contents (22 to 34%) is wider than that observed in Test II. The scatter in the TDR data is relatively low for Test III. The moisture content is consistently greater than 20% during infiltration testing (relatively wet). The tensiometer measurements in Figure 9.37 indicate that the suction values follow the same trends as the moisture content values measured using TDR. Unlike Test II, all three tensiometers in each permeameter were functional through the full duration of Test III, and cavitation was not noted. This provides an opportunity to assess the suction profiles during steady-state moisture flow.

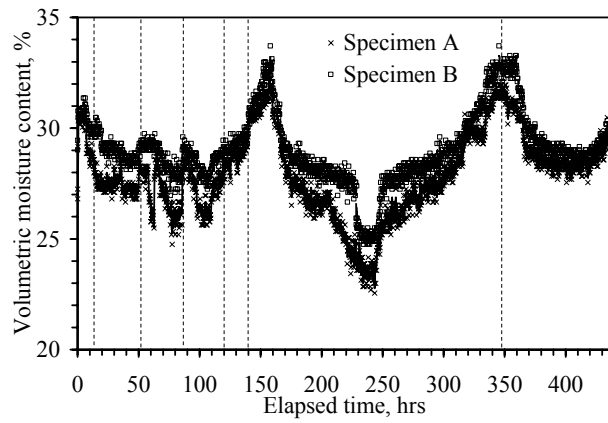
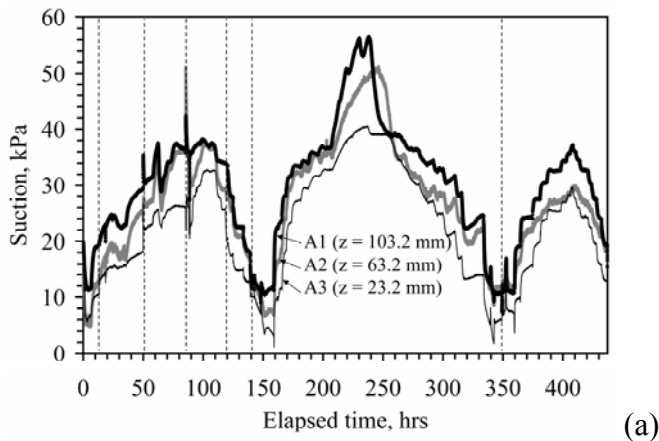
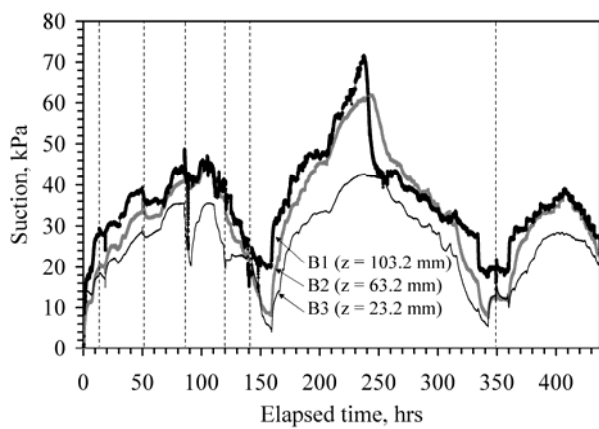


Figure 9.36: Summary of TDR measurements during Test III



(a)



(b)

Figure 9.37: Tensiometer measurements during Test III: (a) Specimen A; (b) Specimen B



Stage III-1 was conducted in a similar fashion as those described in Test II, allowing evaluation of the hydraulic characteristics using constant  $N_{r,mid}$  with varying  $Q$  [Approach (i)]. The control variables in Stage III-1 are shown in Figure 9.38.

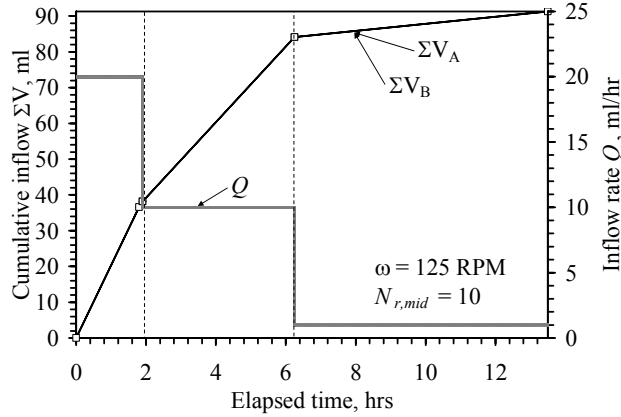


Figure 9.38: Control variables in Stage III-1

Although the inflow variables were well controlled (no pauses in inflow), the outflow transducer data for Stage III-1 shown in Figure 9.39 indicate erratic behavior different from that observed in Test II. Specifically, compression of the pore air occurred during infiltration at low  $N_{r,mid}$  (10) and high inflow rates (20 ml/hr). Outflow transducer B shows periodic dissipation of the compressed air, while transducer A shows a gradual build-up of pressure followed by a single release of air at  $t = 8$  hrs. With the exception of the Sub-stage III-1c, the infiltration rates and  $N_{r,mid}$  imposed during this stage led to  $K_{target}$  values in excess of  $K_s$  for this specimen, so the results from the first two phases of this stage are not useful for hydraulic characterization.

The TDR data for Stage III-1 shown in Figure 9.40 indicate that the specimen was relatively wet during the initial two infiltration phases, but a decrease in moisture content occurred during the final infiltration phase, which corresponds to the fact that steady-state outflow was attained after  $t = 12$  hrs.

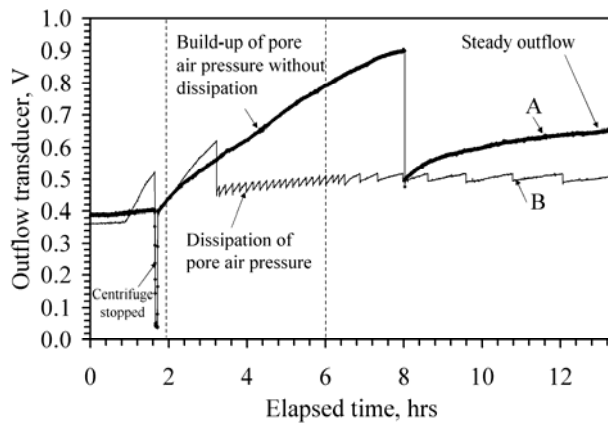


Figure 9.39: Outflow transducer measurements in Stage III-1

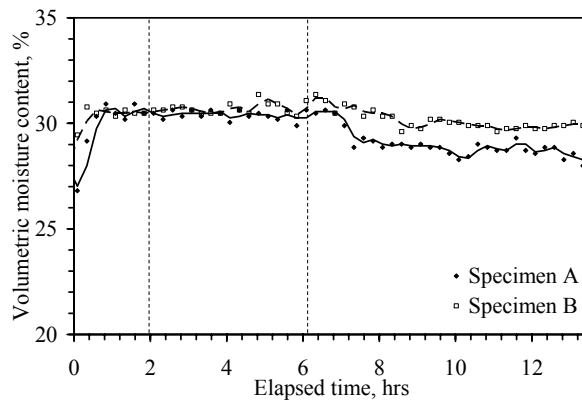


Figure 9.40: TDR measurements in Stage III-1

The suction data during Stage III-1 in Figure 9.41 indicate that the base of the specimen was nearly saturated during the first two stages. An increase in suction was noted in the tensiometer data, corresponding to the decrease in moisture content inferred by TDR. The initial suction in the two permeameters is different because the tensiometers were installed at different times in the two specimens. The suction profiles shown in Figure 9.42 indicate that the suction is relatively uniform in the lower portion of the specimen, but the suction is greater in the upper portion. This is due to

inconsistencies in the outflow during this stage. This stage was not particularly useful for hydraulic characterization due to the non-uniformity in suction and air pressure build-up.

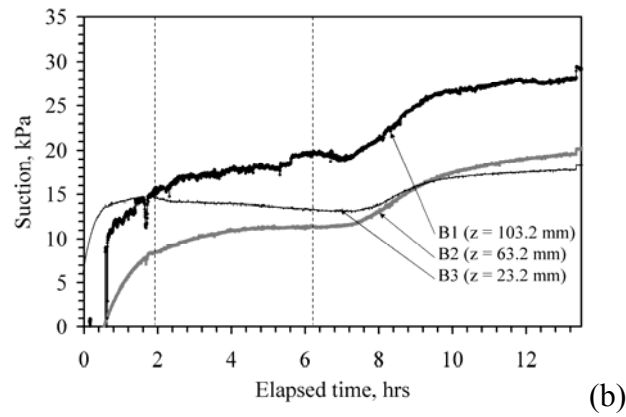
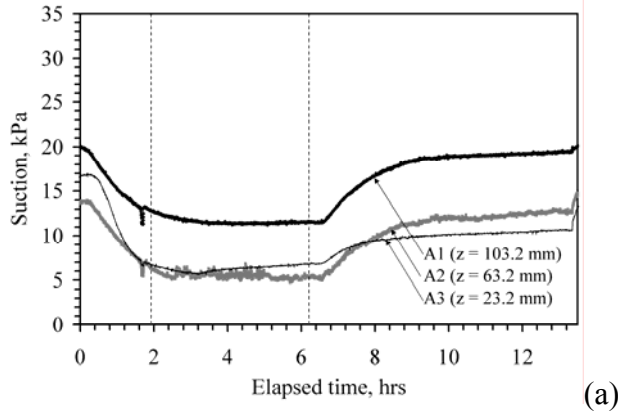


Figure 9.41: Tensiometer measurements in Stage III-1: (a) Specimen A; (b) Specimen B

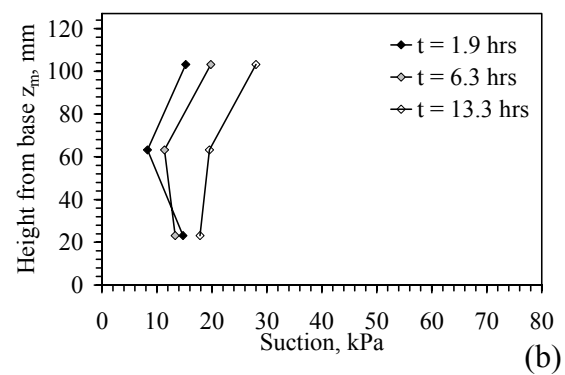
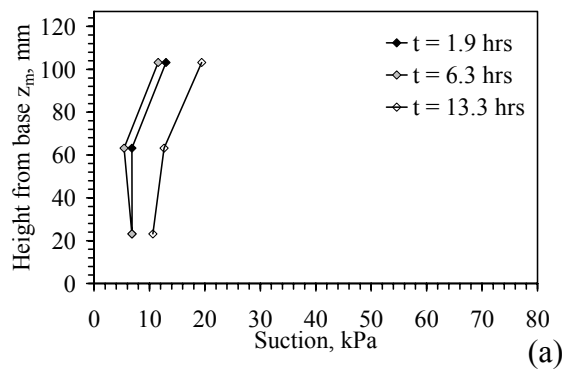


Figure 9.42: Suction profiles in Stage III-1: (a) Specimen A; (b) Specimen B

Stage III-2 was in a similar manner to Stage III-1, but  $N_{r,mid} = 20$ . The control variables in Stage III-2 are shown in Figure 9.43. Similar to the outflow results in Stage III-1, the outflow transducer data in Figure 9.44 indicates that the combination of  $Q$  and  $\omega$  in Sub-stage III-2b led to compression of the pore air. The test was stopped  $t = 18.4$  hrs to investigate the outflow results, which permitted measurement of the outflow during this stage and purging of water from the air release tubes. The combinations of  $Q$  and  $\omega$  in Sub-stages III-2b and III-2c led to more uniform outflow.

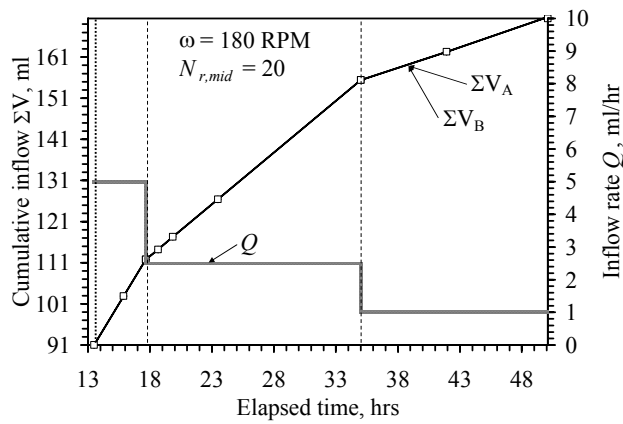


Figure 9.43: Control variables in Stage III-2

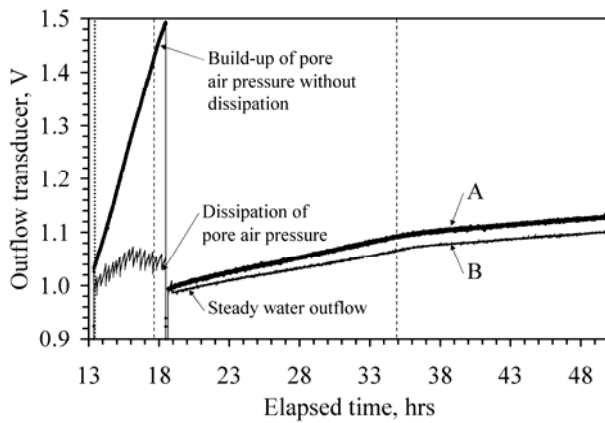


Figure 9.44: Outflow transducer measurements in Stage III-2

The TDR data during Stage III-2 shown in Figure 9.45 indicates a gradual decrease in moisture content with time. The suction data during this stage, shown in Figure 9.46, indicate that the suction was still increasing at the end of Sub-stage III-2a, but constant suction values were attained at the end of Sub-stages II-2b and II-2c. The higher suction values attained in the middle of Sub-stage II-2b ( $t = 25$  hrs) may be due to continued dissipation of the pore air pressure.

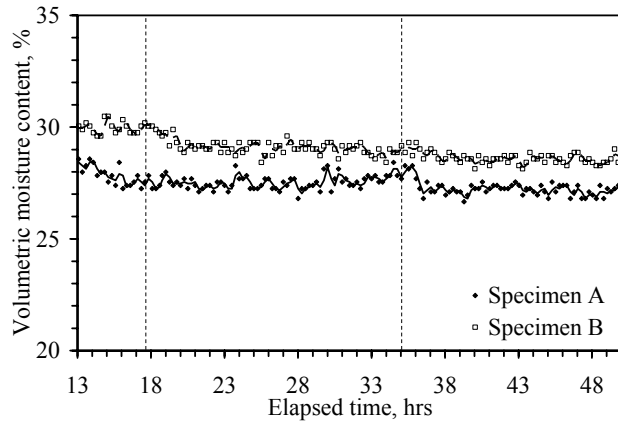


Figure 9.45: TDR measurements in Stage III-2

The suction profiles during Stage III-2 shown in Figure 9.47 indicate that there is a gradient in suction throughout the specimen. Although the suction profiles at earlier times ( $t = 13.3$  and  $17.7$  hrs) are affected by compression of the pore air during infiltration, the suction profiles obtained at the end of this stage in Permeameter A indicate that the suction is relatively uniform in the upper portion of the specimen. However, because  $N_{r,mid}$  is still relatively low in this stage (20), a gradient in suction is still observed, especially in Permeameter B. This is consistent with discussion in Chapter 3, in which a zone of relatively constant suction was observed to increase in length when the  $v_m$  was small,  $N_{r,mid}$  was high, or when  $\psi_0$  was greater than zero. Further, as the suction gradient is measured, this stage is useful for hydraulic characterization.

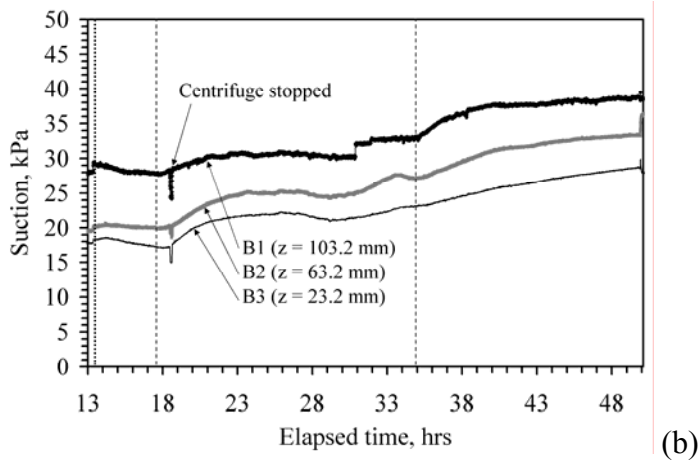
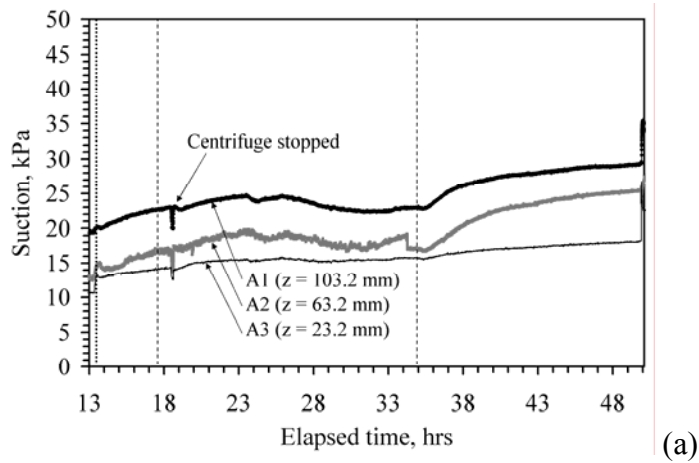


Figure 9.46: Tensiometer measurements in Stage III-2: (a) Specimen A; (b) Specimen B

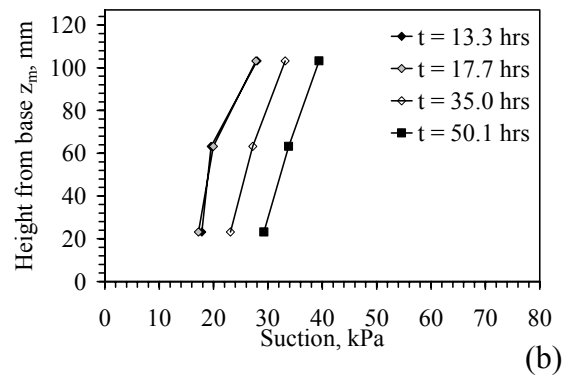
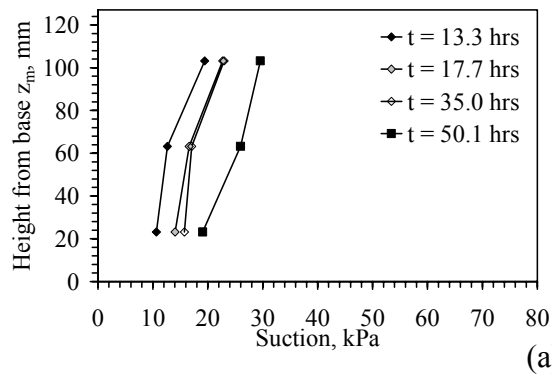


Figure 9.47: Suction profiles in Stage III-2: (a) Specimen A; (b) Specimen B

Stage III-3 was similar to the first two stages of Test III, and the stages in Test II. The control variables in Stage III-3 are shown in Figure 9.48. A pause in the inflow rate occurred after  $t = 57$  hrs due to an air bubble, but the pump was restarted shortly afterwards. The outflow during Stage III-3, shown in Figure 9.49, closely followed the inflow (even during the pause in inflow), and steady-state flow was observed for all of the imposed flow rates. The pause in inflow was also indicated in the TDR data for Permeameter A in Figure 9.50 and the tensiometer data in Figure 9.51. The tensiometer data indicates that a constant suction was observed at the end of each sub-stage.

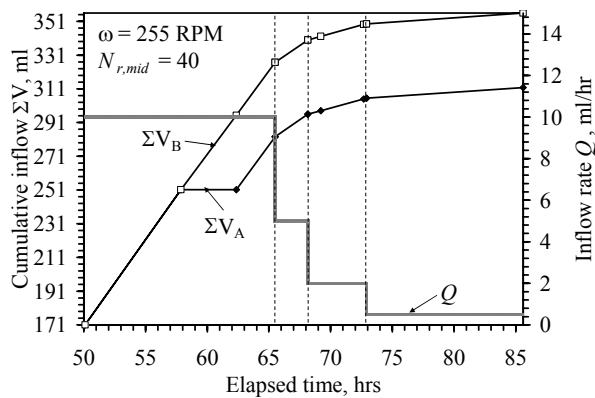


Figure 9.48: Control variables in Stage III-3

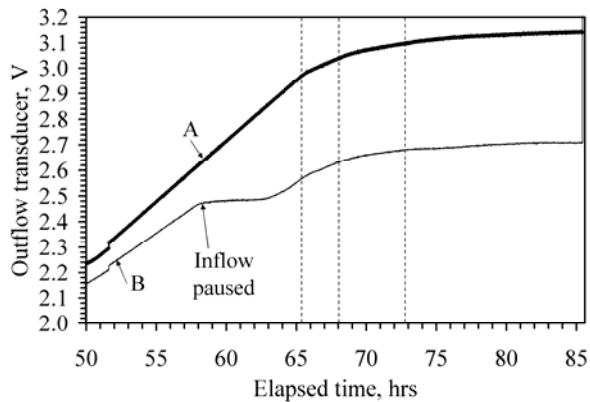


Figure 9.49: Outflow transducer measurements in Stage III-3

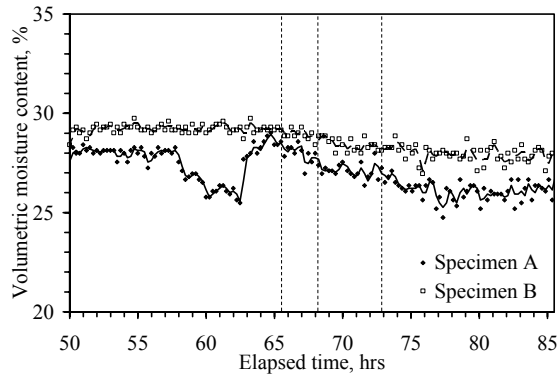


Figure 9.50: TDR measurements in Stage III-3

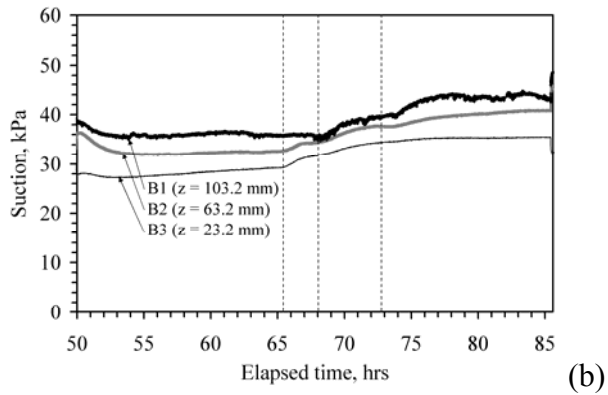
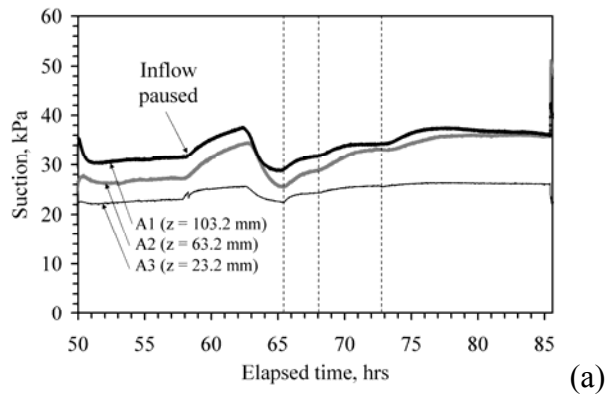


Figure 9.51: Tensiometer measurements in Stage III-3: (a) Specimen A; (b) Specimen B

The suction profiles during the latter portions of Stage II-3, shown in Figure 9.52, indicate that the suction in the upper portion of the specimen is relatively uniform. This



indicates that  $K_{target}$  is similar to  $K_{measured}$  in this stage (*i.e.*, negligible suction head gradient compared to the centrifuge elevation head gradient) and that correlating the TDR moisture content with  $K_{target}$  is reasonable. A difference in suction is observed between the lower two tensiometers indicating that the UFA approach (*i.e.*, correlation of average moisture content throughout the entire specimen with  $K_{target}$ ) is not valid. The suction at the base of the profile is likely greater than zero.

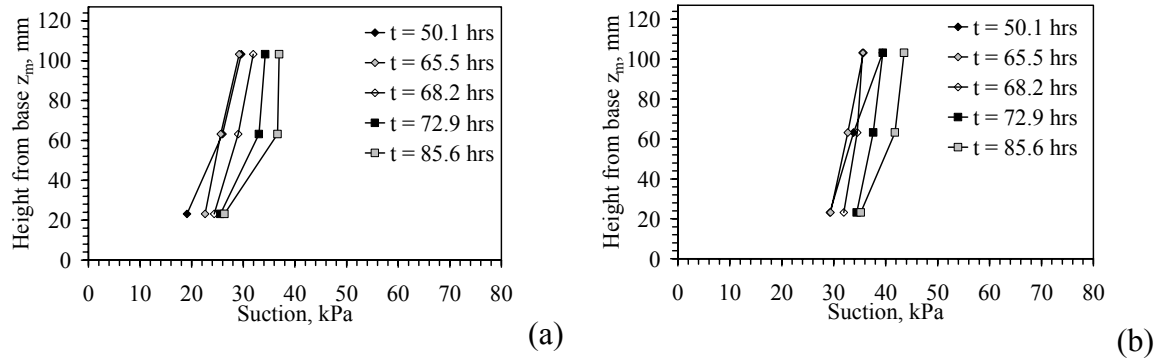


Figure 9.52: Suction profiles in Stage III-3: (a) Specimen A; (b) Specimen B

Stage III-4 was conducted to continue the investigation of characterization Approach *i*, but with the added objective of investigating hysteresis. The control variables in Stage III-4 are shown in Figure 9.53. The specimen was first dried, then wetted.

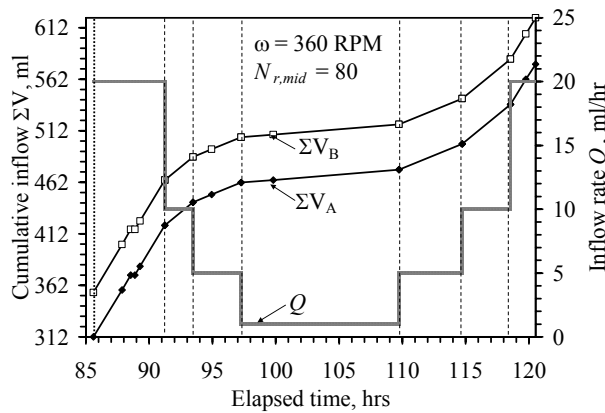


Figure 9.53: Control variables in Stage III-4

The outflow transducer results for Stage III-4, shown in Figure 9.54, also followed the inflow data. The outflow was drained from the reservoir at  $t = 88$  hrs, which led to a shift in the magnitude of the outflow measurements. The TDR measurements for this stage, shown in Figure 9.55, indicate a gradual decrease in moisture content throughout the drying phases of this test (approximately 4%), then an increase during the wetting phases (approximately 3%).

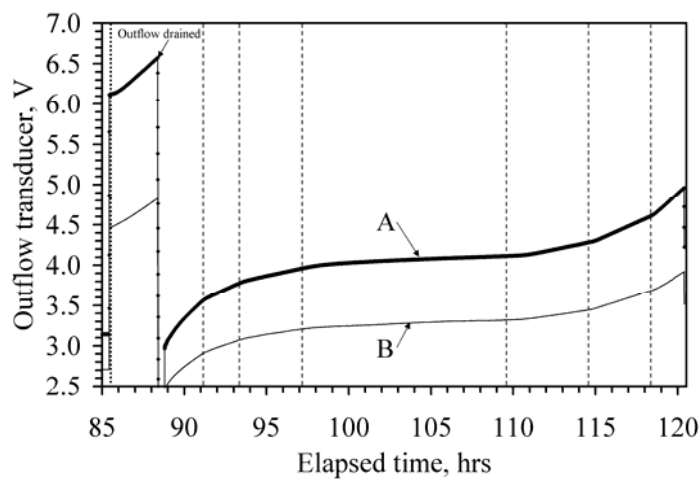


Figure 9.54: Outflow transducer measurements in Stage III-4

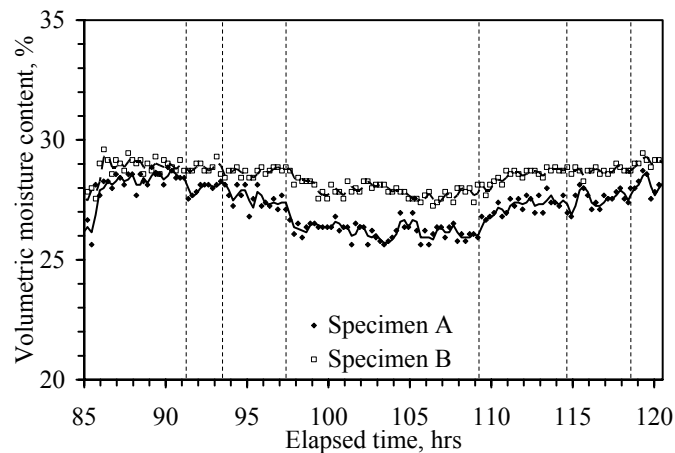


Figure 9.55: TDR measurements in Stage III-4

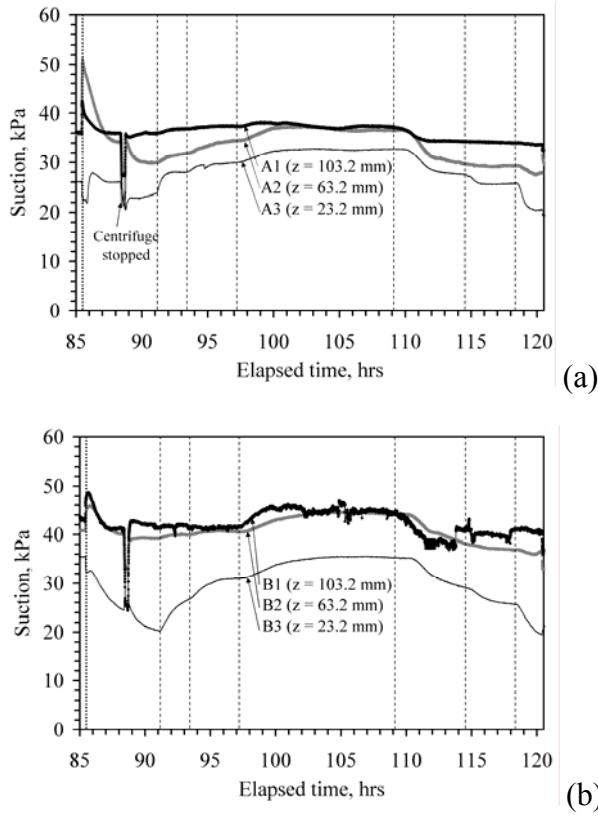


Figure 9.56: Tensiometer measurements in Stage III-4: (a) Specimen A; (b) Specimen B

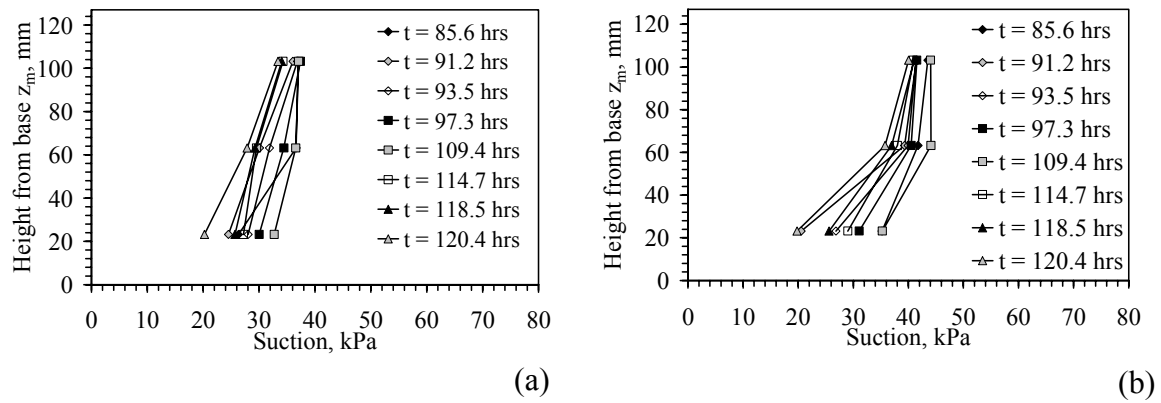


Figure 9.57: Suction profiles in Stage III-4: (a) Specimen A; (b) Specimen B

The tensiometer results for Stage III-4 shown in Figure 9.56 show an increase in suction during the drying sub-stages (approximately 5 kPa), and a decrease in suction

during the wetting sub-stages (approximately 5 kPa), which is consistent with the trends in the TDR data. During the first sub-stage, the relatively high inflow rate led to a decrease in suction at the base of the profile but led to little changes in the upper portion of the profile. The tensiometers show a slight in magnitude when the centrifuge was stopped to empty the outflow reservoir at  $t = 88$  hrs. This shift is associated with an increase water pressure in the tensiometer reservoir due to its self-weight in the g-field. This pressure dissipates through the ceramic into the specimen, so the tensiometer measurements at steady-state should be representative of the suction in the specimen. Relatively uniform suction in the upper zone of the specimen is observed in Figure 9.57.

Stage III-5, in combination with the last phase of Stage III-4, was conducted to investigate the consistency of the centrifuge permeameter results. Specifically, after reaching a  $K_{target}$  of  $1.83 \times 10^{-8}$  m/s at the end of Stage III-4, the centrifuge speed and inflow rate were proportionally decreased to maintain a constant  $K_{target}$ . The control variables in Stage III-5 are shown in Figure 9.58. The outflow measurements during this stage, shown in Figure 9.59, indicate shifts in magnitude during the decreases in  $N_{r,mid}$ , and a decrease in slope with the lower inflow rates. The TDR data during Stage III-5, shown in Figure 9.60 is relatively constant, although a slight increase is noted.

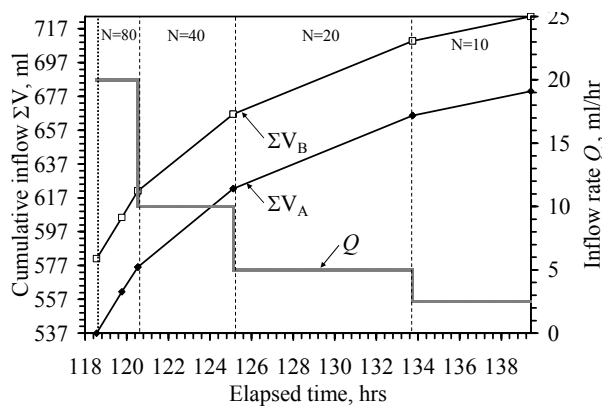


Figure 9.58: Control variables in Stage III-5

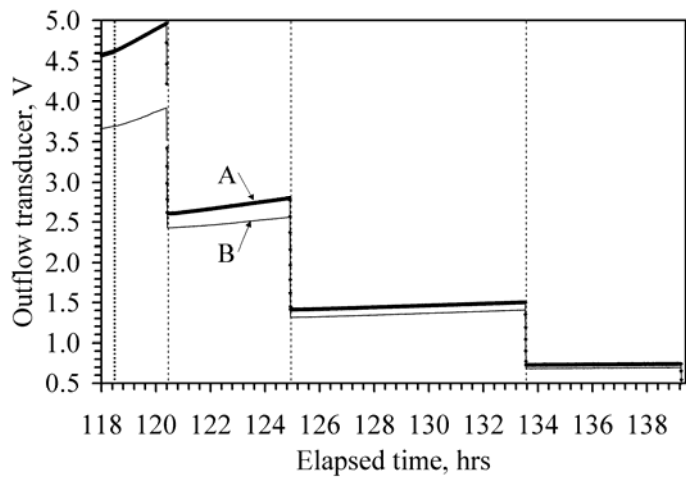


Figure 9.59: Outflow transducer measurements in Stage III-5

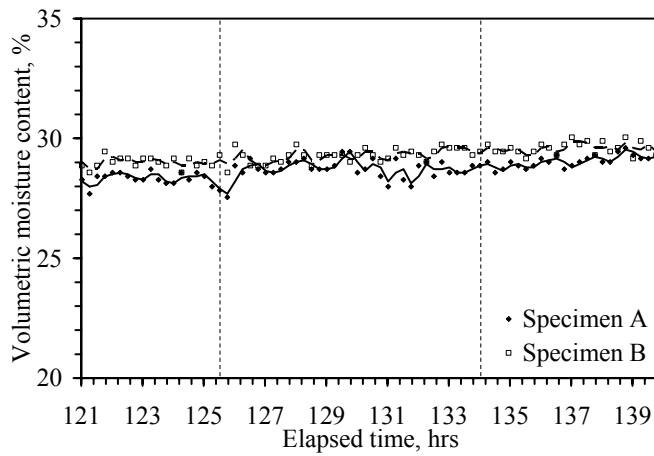


Figure 9.60: TDR measurements in Stage III-5

The suction data during the consistency test in Stage III-5, shown in Figure 9.61, indicates that the suction is not constant during this stage despite the constant  $K_{target}$ . A decrease in suction of about 4 kPa was noted at each change in  $K_{target}$ . These results will be discussed in more detail in Chapter 10. The suction profiles during this stage, shown in Figure 9.62, show a clear transition from a negligible suction gradient in the upper portion of the specimen at higher  $N_{r,mid}$  to a more significant gradient at lower  $N_{r,mid}$ .

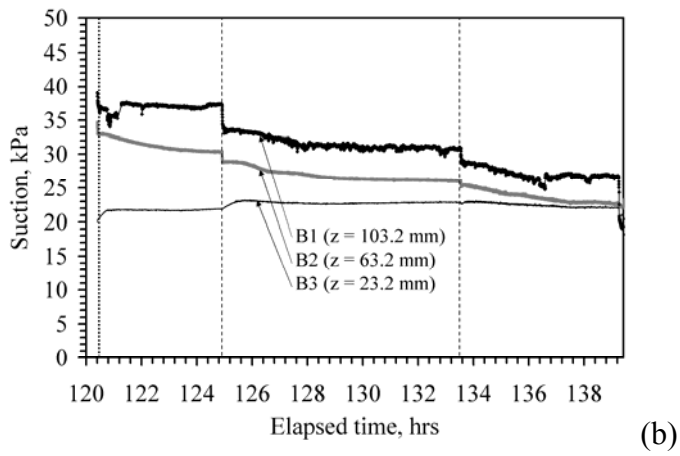
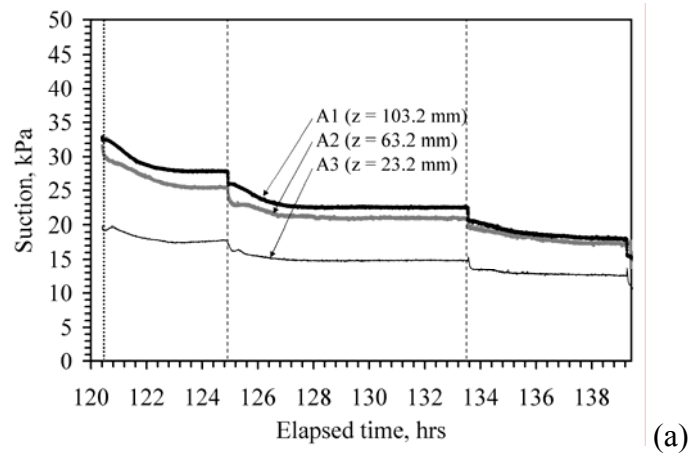


Figure 9.61: Tensiometer measurements in Stage III-5: (a) Specimen A; (b) Specimen B

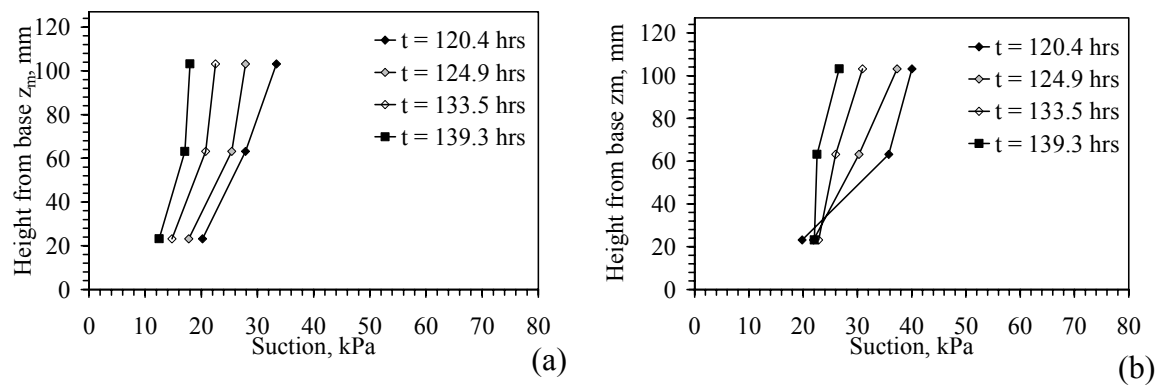
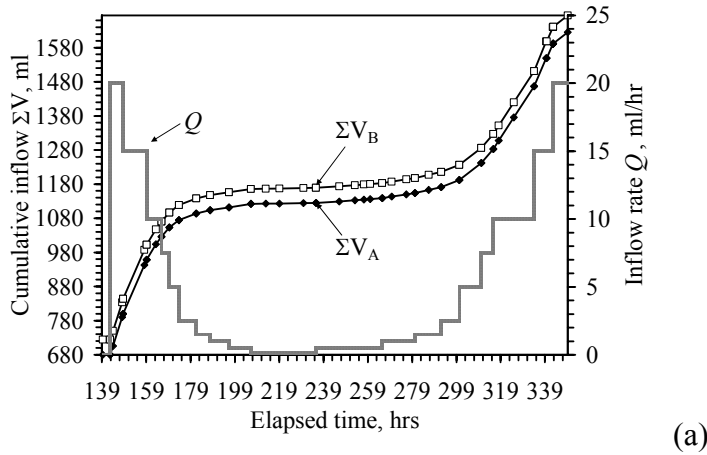
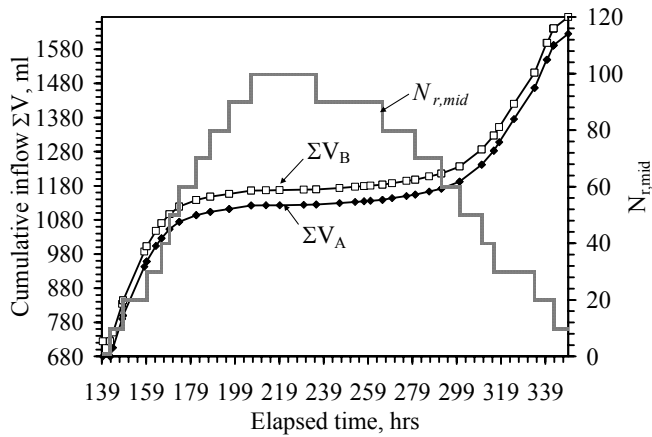


Figure 9.62: Suction profiles in Stage III-5: (a) Specimen A; (b) Specimen B

Stage III-6 was conducted to investigate the use of characterization Approach (iii), in which  $Q$  and  $\omega$  were varied to obtain a wide range in  $K_{target}$ . In addition, the soil was dried then wetted to investigate the role of hysteresis. This stage was the longest of all the hydraulic characterization stages (8 days). The cumulative inflow and inflow rate during Stage III-6 are shown in Figure 9.63(a), and the cumulative inflow and g-level are shown in Figure 9.63(b). The stages in which lower  $K_{target}$  values were investigated had a longer duration than those focusing on higher  $K_{target}$  values, and wetting paths required longer times to reach steady-state flow than drying paths.



(a)



(b)

Figure 9.63: Control variables in Stage III-6: (a) Inflow rate; (b)  $N_{r,mid}$

The outflow transducer data for Stage III-6 is shown in Figure 9.64. In the early phases of this stage, when high flow rates and low  $N_{r,mid}$  values were imposed, compression of the pore air was noted (between  $t = 139$  and  $150$  hrs). During infiltration at the lowest  $K_{target}$  values, outflow transducer A indicated negligible changes in magnitude, as the transducer was at voltage capacity ( $\sim 6.63V$ ). However, the transducer in permeameter B indicated steady-state changes, so similar behavior was expected in the other permeameter. This is indicated by the higher offset in the reading from transducer A from the corresponding drying phase earlier in the test, after  $N_{r,mid}$  was decreased low enough that saturation stopped (around  $t = 275$  hrs).

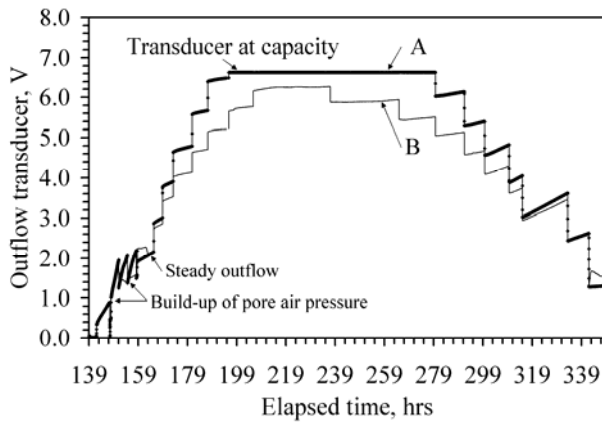


Figure 9.64: Outflow transducer measurements in Stage III-6

The TDR data during Stage III-6 shown in Figure 9.65 indicate a relatively large decrease in moisture content during the drying phase of this stage ( $\sim 7\%$ ), and an increase in moisture content of similar magnitude during rewetting. The specimen initially becomes wetter in the first sub-stage, as outflow from the permeameter is prevented due to pore air compression. The suction data for this stage shown in Figure 9.66 indicate similar behavior with time, with a maximum suction of  $70$  kPa. During drying, upper tensiometer showed a decrease in suction first, followed by the lower tensiometers.



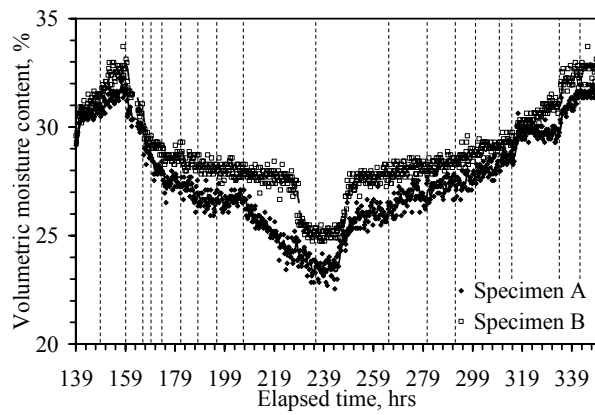
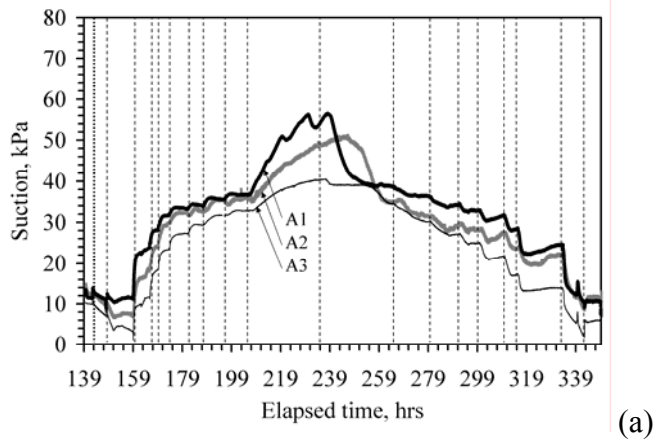
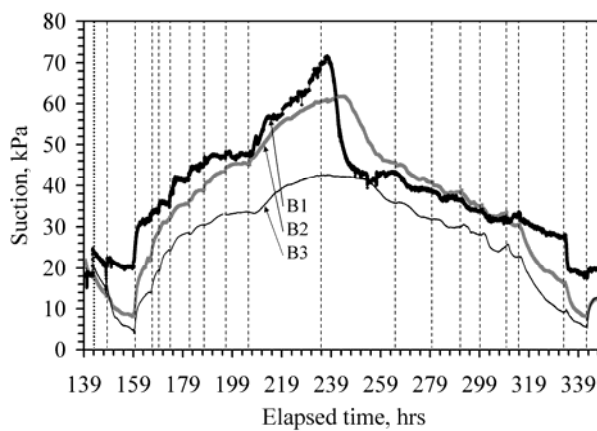


Figure 9.65: TDR measurements in Stage III-6



(a)



(b)

Figure 9.66: Tensiometer measurements in Stage III-6: (a) Specimen A; (b) Specimen B

The suction profiles in Figure 9.67 for this stage indicate that the suction is generally uniform throughout the specimen during drying. The suction profile at  $t = 235.6$  hrs, corresponding to the driest conditions, indicates that the suction profile is not uniform through the specimen, which is not consistent with other profiles measured in this study. This may indicate that steady-state flow had not been reached at this infiltration rate (*e.g.*, the suction was still increasing at  $z_m = 63.2$  mm). During rewetting, the suction in the middle of Specimen A was less than that at the top, while the suction in the middle of Specimen B was slightly greater than that at the top. The suction profile throughout the upper portion of the specimen is relatively uniform, on average.

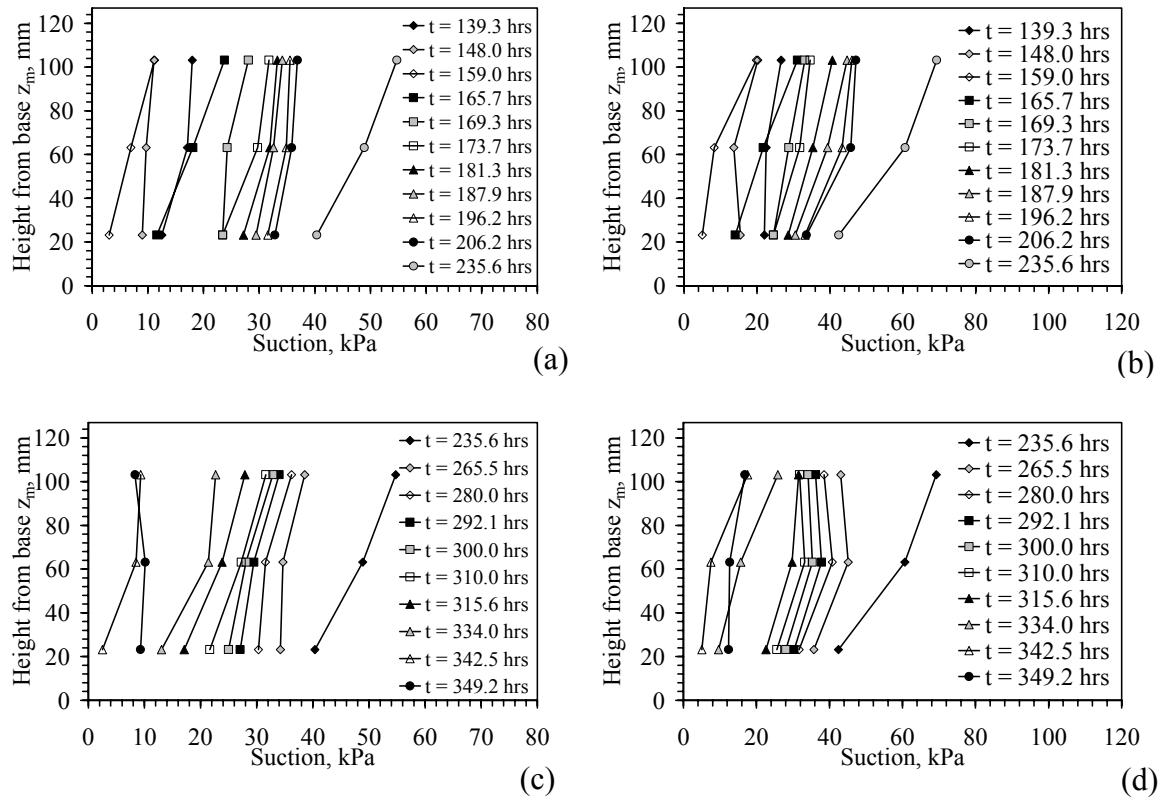


Figure 9.67: Suction profiles in Stage III-6: (a) Specimen A drying; (b) Specimen B drying; (c) Specimen A wetting; (d) Specimen B wetting

Stage III-7 was conducted to evaluate the characterization Approach (ii), in which the inflow rate was maintained constant while  $N_{r,mid}$  was varied to dry and wet the specimen. The control variables in Stage III-7 are shown in Figure 9.68. The outflow data for this stage, shown in Figure 9.69, indicates the advantages of this approach: steady-state flow was rapidly obtained, it was easy to evaluate when steady-state outflow was obtained, and only one variable was varied. However, Approach (ii) does not lead to as wide a range in  $K_{target}$  values as Approach (iii).

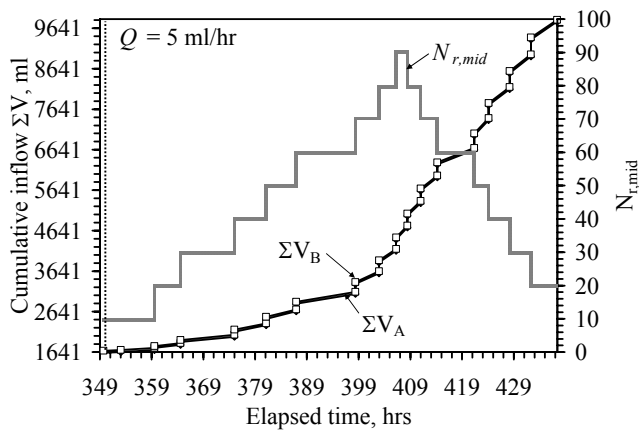


Figure 9.68: Control variables in Stage III-7

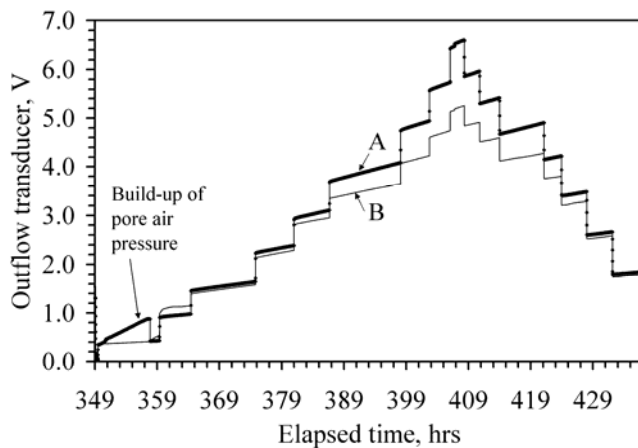


Figure 9.69: Outflow transducer measurements in Stage III-7

The TDR data shown in Figure 9.70 indicates that the specimen had an increase in moisture content during the first phase of this stage, similar to that observed at the beginning of Stage III-6. This is due to compression of the pore air during flow at  $Q = 5$  ml/hr and low  $\omega$  of 125 RPM ( $N_{r,mid} = 10$ ). As the range of hydraulic conductivity values imposed during Stage III-7 is smaller than in Stage III-6.

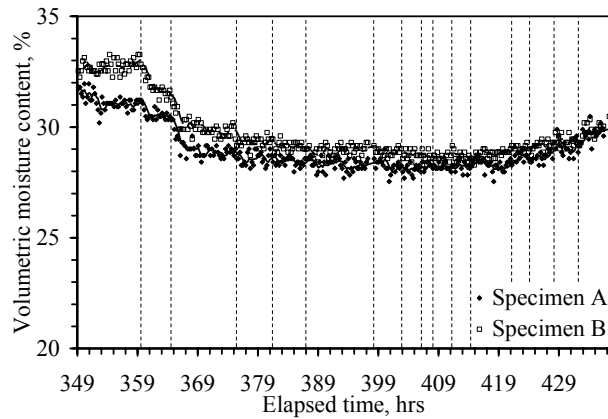
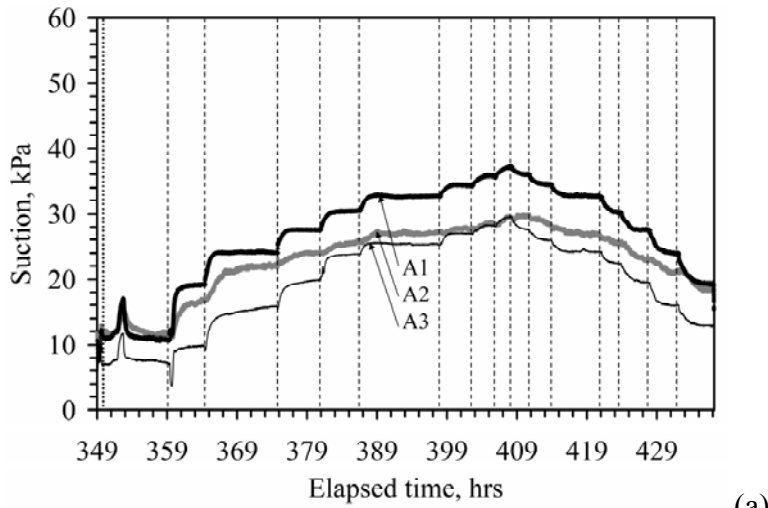
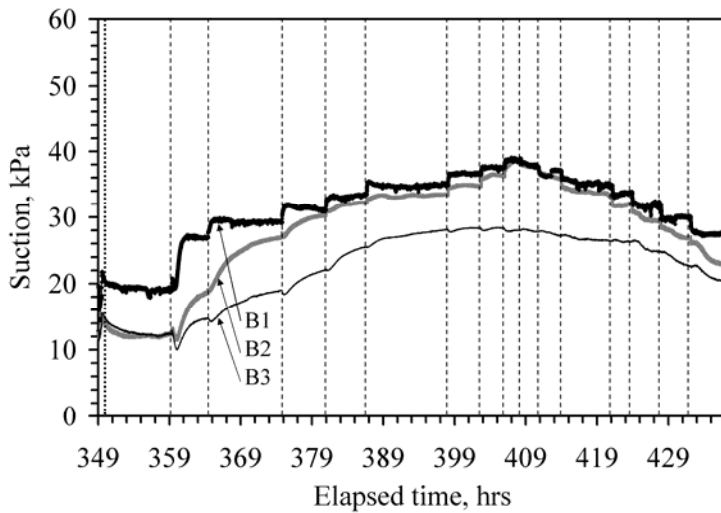


Figure 9.70: TDR measurements in Stage III-7

The suction measurements during Stage III-7 are shown in Figure 9.71. The middle tensiometer followed different trends in both of the permeameters. Specifically, the middle tensiometer in permeameter A followed the same trend as the other tensiometers, but had a magnitude similar to the lower tensiometer through this test. This does not lead to the expected suction profiles, shown in Figure 9.72. This may be due to drift in the tensiometer calibration through the test. The data from this permeameter is still useful for hydraulic characterization, but the hydraulic gradient in the upper portion of the specimen is likely overestimated. In contrast, the middle tensiometer in Permeameter B had a magnitude similar to the upper tensiometer which was consistent with the other tests at higher  $N_{r,mid}$  values. In fact the suction became more uniform in the upper zone of the specimen with increasing  $N_{r,mid}$ .



(a)



(b)

Figure 9.71: Tensiometer measurements in Stage III-7: (a) Specimen A; (b) Specimen B

In general, the difference in suction between the top and bottom of the specimen decreases with increasing  $N_{r,mid}$  (e.g.,  $t = 408.3$ ). The final moisture content profiles obtained using destructive gravimetric samples are shown in Figure 9.73. Consistent with the suction measurements, the moisture content profile was relatively uniform in the specimen. The moisture content in the upper portion of the specimen is consistent with that inferred using TDR (at the end of Stage III-7 in Figure 9.70).

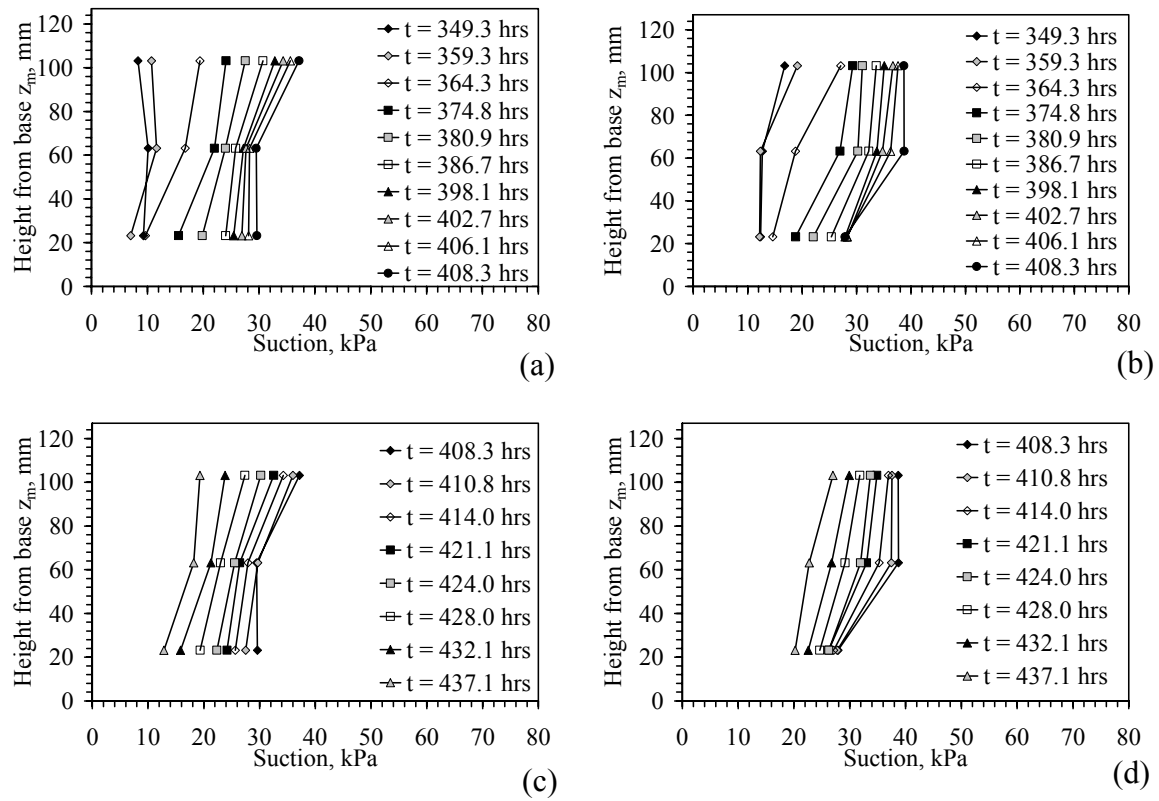


Figure 9.72: Suction profiles in Stage III-7: (a) Specimen A drying; (b) Specimen B drying; (c) Specimen A wetting; (d) Specimen B wetting

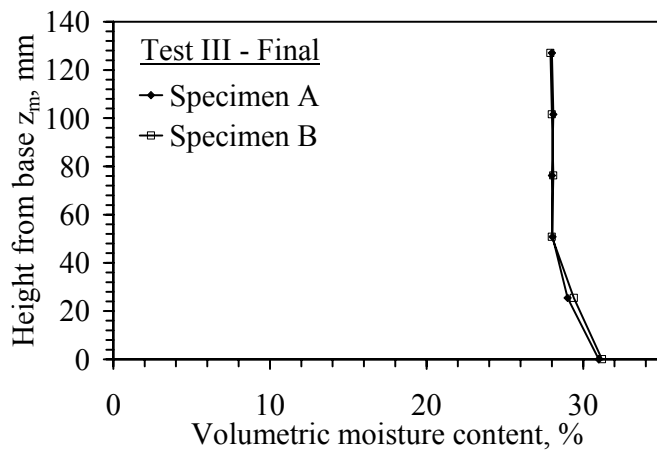


Figure 9.73: Final moisture content profile from destructive samples at end of Test III

#### 9.4 TEST IV (POROSITY OF 0.35, $W_C = W_{C,OPT} + 3\%$ )

Test IV was performed to investigate the impact of a higher compaction moisture content (and soil with lower  $K_s$ ). This had implications on the selected control variables ( $Q$  and  $\omega$ ). The stages of this test, summarized in Table 7.10, allow determination of the hydraulic characteristics by varying  $Q$  but maintaining  $\omega$  constant [Approach (i)], assessment of the consistency of centrifuge permeameter results (similar to Stage III-5) and assessment of hysteresis by changing  $Q$  at constant  $N_{r,mid}$  (similar to Stage III-4).

Table 9.8: Summary of the test stages for hydraulic characterization Test IV

Stage	Stage description	Sub-stage	Elapsed time (hrs)	$Q$ (ml/hr)	$\omega$ (RPM)	$N_{r,mid}$	$K_{target}$ (m/s)
IV-1	Hydraulic characterization (constant $\omega$ )	a	2.4	20	255	40	3.7E-08
		b	7.9	10	255	40	1.8E-08
		c	13.7	5	255	40	9.1E-09
		d	11.7	1	255	40	1.8E-09
		Stage duration	35.8				
		Elapsed time	35.8				
IV-2	Hydraulic characterization (constant $\omega$ )	a	3.4	20	360	80	1.8E-08
		b	8.7	10	360	80	9.2E-09
		c	4.1	5	360	80	4.6E-09
		d	4.2	1	360	80	9.2E-10
		Stage duration	20.5				
		Elapsed time	56.3				
IV-3	Darcy's law investigation (constant K)	a	16.5	0.5	255	40	9.2E-10
		Stage duration	16.5				
		Elapsed time	72.8				
IV-4	Hysteresis investigation (constant $\omega$ and varying $Q$ )	a	7.3	1	360	80	9.2E-10
		b	6.2	0.5	360	80	4.6E-10
		c	10.8	0.1	360	80	9.2E-11
		d	5.8	1	360	80	9.2E-10
		e	3.7	5	360	80	4.6E-09
		f	1.9	10	360	80	9.2E-09
		Stage duration	35.8				
		Elapsed time	108.5				

Note: Comparison between Stages II-2 to II-4 allows investigation of hysteresis (constant K)

The test sequence for Test IV is shown in Figure 9.74(a), and the  $K_{target}$  and  $N_{r,mid}$  values are shown in Figure 9.74 (b). The hydraulic characteristics were determined using Approach (i) in Stage IV-1 at  $N_{r,mid} = 40$ , and in Stage IV-2 at  $N_{r,mid} = 80$ . A consistency test was conducted using constant  $K_{target}$  in Stage IV-3 at  $N_{r,mid} = 40$ , and hysteresis was investigated at  $N_{r,mid} = 80$  in Stage IV-4 using wetting and drying.

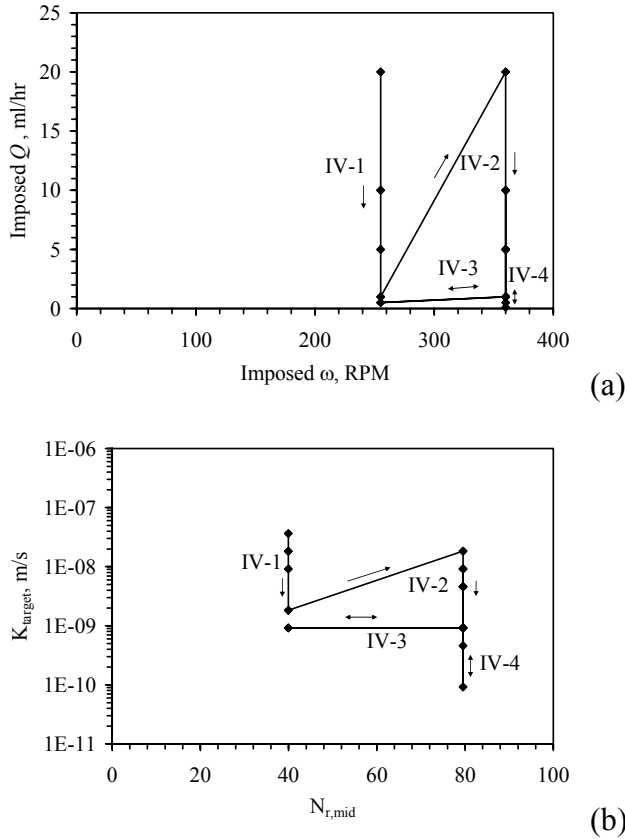


Figure 9.74: Test IV: (a) Summary of imposed  $Q$  and  $\omega$  (arrows denote progression of the test); (b) Summary of steady-state imposed  $K$  values with  $N_{r,mid}$

A summary of the control variables during Test IV is shown in Figure 9.75. It should be noted that relatively high  $N_{r,mid}$  values ( $<40$ ), combined with low inflow rates ( $<20$  ml/hr), were used in order to reach  $K_{target}$  values below  $K_s$ , as this specimen is



compacted wet of optimum. The G-meter results in Figure 9.75(c) indicate that the target  $N_{r,mid}$  was attained, and there was negligible temperature generation during the test.

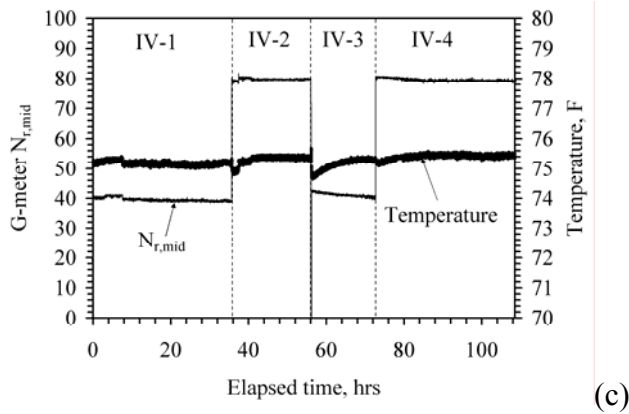
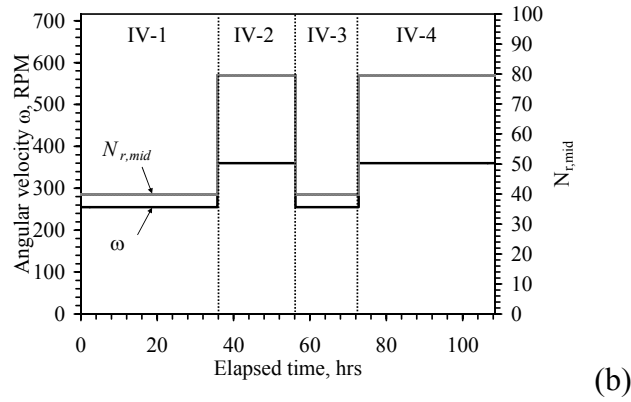
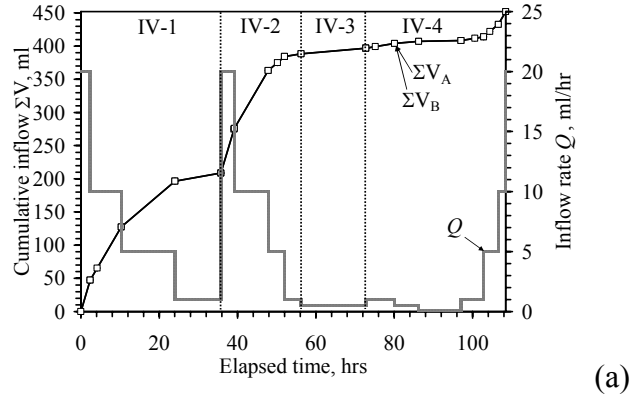


Figure 9.75: Test IV time series: (a) Flow control variables  $Q$  and  $\Sigma V$ ; (b) Centrifuge control variables  $\omega$  and  $N_r$ ; (c) G-meter and thermocouple results

The outflow transducer results for Test IV shown in Figure 9.76 are similar to those observed in other tests, although the outflow from Permeameter A was generally less than that from Permeameter B despite the same inflow applied to each permeameter. An interesting aspect of the test is that the moisture content during Test IV, shown in Figure 9.77, changed less than 3% during this test despite the wide range of  $K$  values imposed during the test.

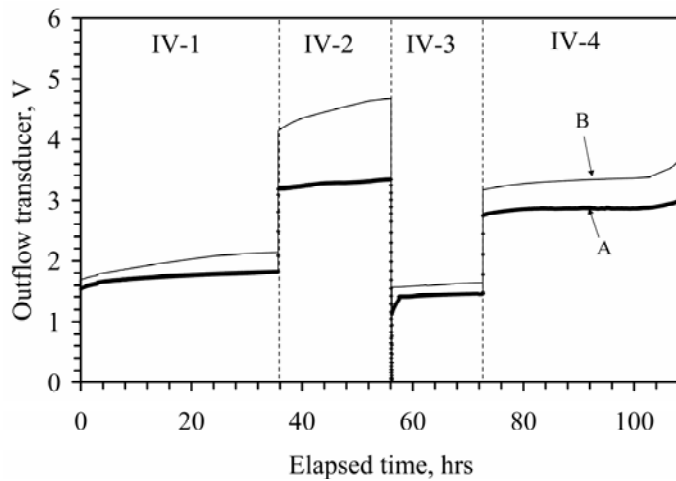


Figure 9.76: Summary of outflow transducer measurements during Test IV

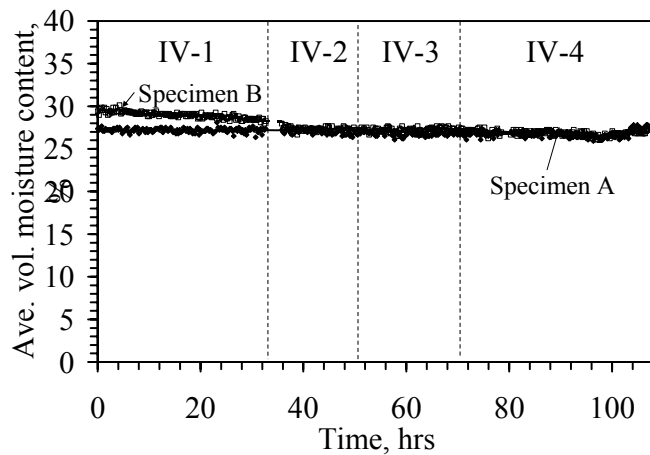


Figure 9.77: Summary of TDR measurements during Test IV

The suction data from Test IV is shown in Figure 9.78. Similar to the TDR data, the suction data did not vary significantly during this test except during Stage IV-4. Similar to Test II, the middle tensiometer was malfunctioning during this test. However, unlike Test II, the tensiometer started giving reasonable results after a certain period of centrifugation (*e.g.*, in Stage IV-3 for Specimen A and in Stage IV-1 for Specimen B). Although there was more scatter in this tensiometer than in the upper and lower tensiometers, it follows the same trends as the other tensiometers and provides some insight into the suction profiles during testing.

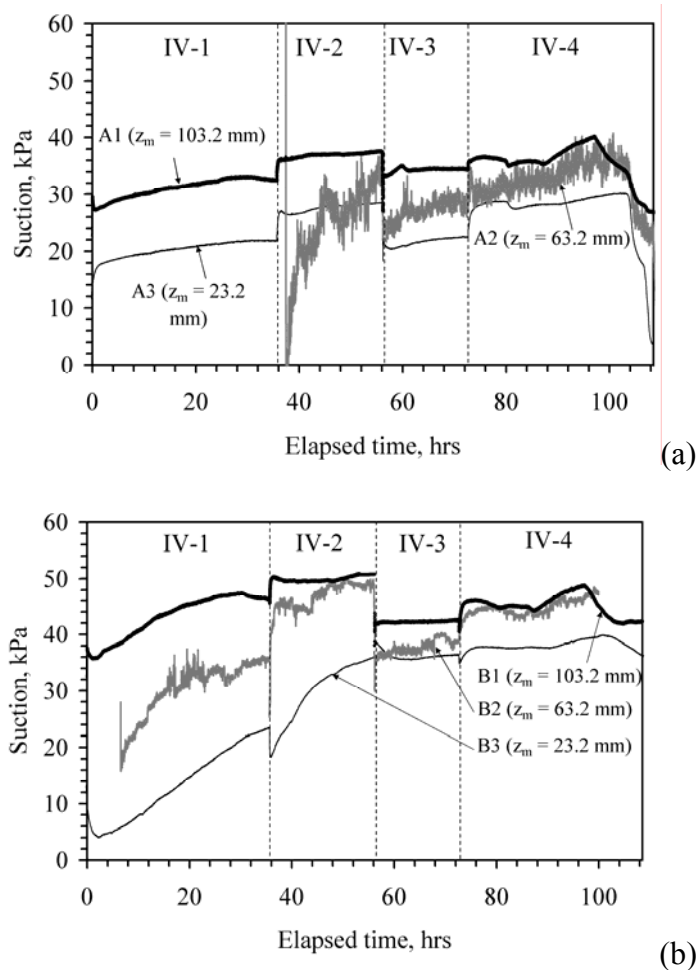


Figure 9.78: Tensiometer measurements in Test IV: (a) Specimen A; (b) Specimen B

Stage IV-1 was conducted to evaluate the determination of hydraulic characteristics using varying  $Q$  but a constant  $N_{r,mid}$  of 40. The control variables in Stage IV-1 are shown in Figure 9.79. The outflow results for this stage, shown in Figure 9.80, indicate that the outflow generally follows the inflow, although the magnitude of changes in the outflow transducer for Permeameter A is smaller than in Permeameter B.

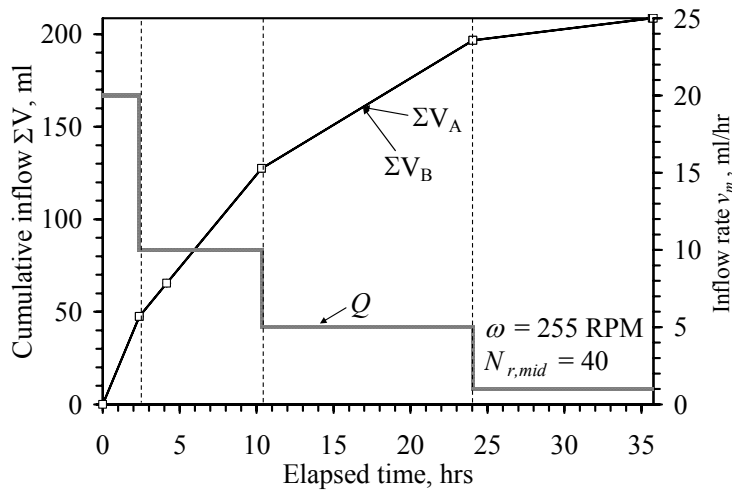


Figure 9.79: Control variables in Stage IV-1

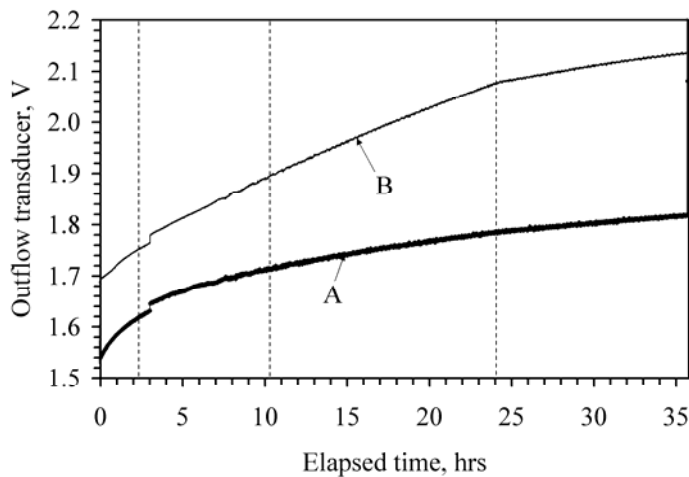


Figure 9.80: Outflow transducer measurements in Stage IV-1

The TDR results for Stage IV-1 are shown in Figure 9.81. The moisture content did not change significantly for Specimen A, but there was a slight decrease in moisture content in Specimen B. This may have been due to different initial moisture content conditions in the two specimens. The scatter in these measurements appears high, but the scale is relatively narrow in this figure.

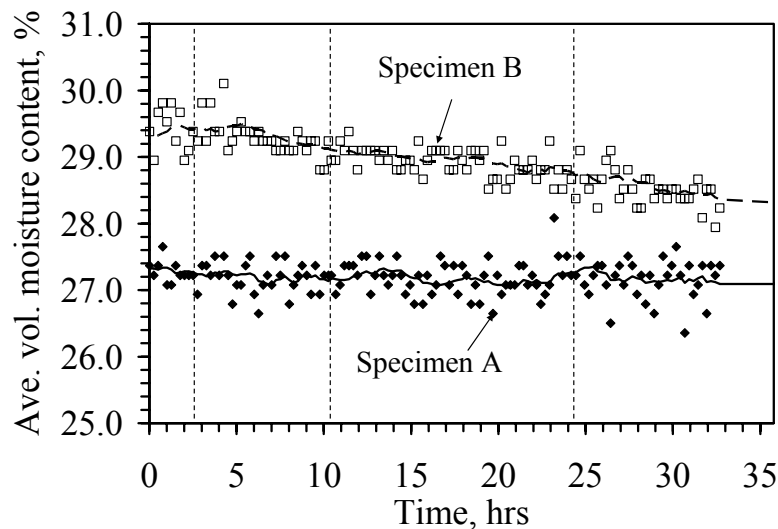


Figure 9.81: TDR measurements in Stage IV-1

Similar to the observations from the TDR measurements, the suction measurements during this stage, shown in Figure 9.82, indicate that the suction change in Specimen A are less than those observed in Specimen B. The suction profiles shown in Figure 9.83 indicate that the suction increases linearly with height. Further, the suction varied by about 40 kPa throughout the specimen, which indicates a high suction gradient. The middle tensiometer in Specimen B fell into line with a straight line between the upper and lower tensiometers. Although the middle tensiometer results for Specimen A in Stage IV-1 were shown in Figure 9.78, they were not shown in this figure due to high

variability. Nonetheless, the data in Figure 9.78 indicates that the middle tensiometer stabilized at the end of this stage.

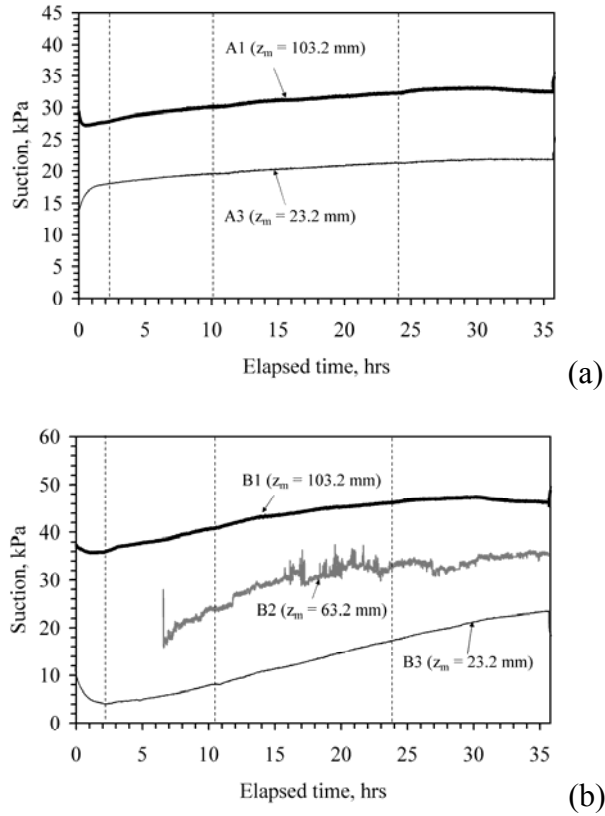


Figure 9.82: Tensiometer measurements in Stage IV-1: (a) Specimen A; (b) Specimen B

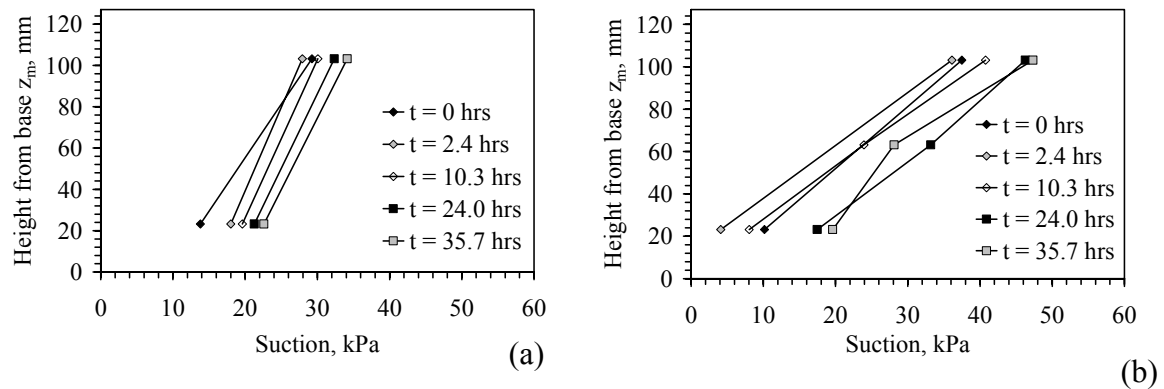


Figure 9.83: Suction profiles in Stage IV-1: (a) Specimen A; (b) Specimen B

Stage IV-2 was conducted to evaluate the determination of the hydraulic characteristics using Approach *i*, but using higher  $N_{r,mid}$ . The control variables in Stage IV-2 are shown in Figure 9.84. The outflow transducer results during Stage IV-2 shown in Figure 9.85 follow the inflow data, although the changes in outflow in Specimen A were relatively small compared to those in Specimen B.

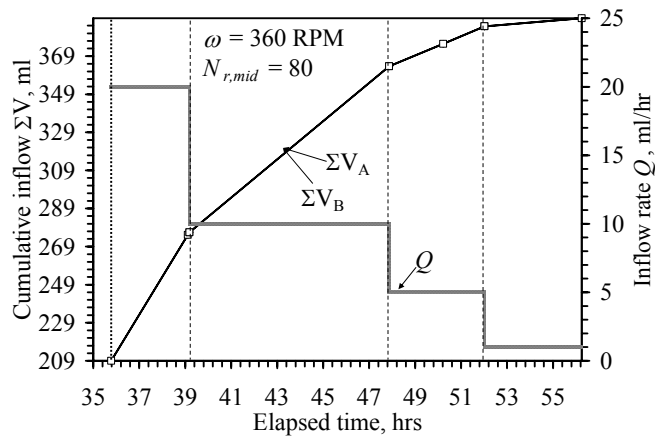


Figure 9.84: Control variables in Stage IV-2

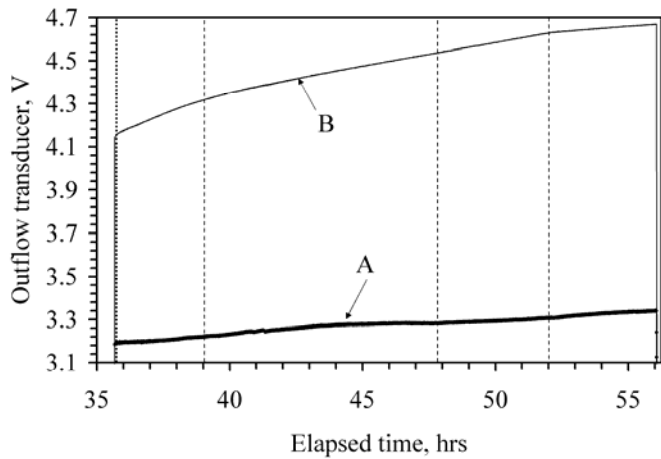


Figure 9.85: Outflow transducer measurements in Stage IV-2

The TDR results for Stage IV-2, shown in Figure 9.86, are similar to those observed during Stage IV-1, with only a slight decrease in moisture content. The scatter during this stage is higher than in Stage IV-1.

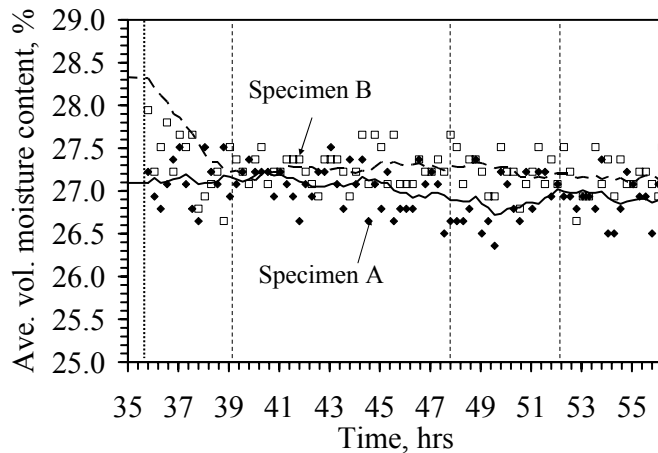


Figure 9.86: TDR measurements in Stage IV-2

The upper tensiometer measurements in both specimens, shown in Figure 9.87, show a large increase in suction when  $N_{r,mid}$  is increased from 40 to 80 at the beginning of this stage. However, the upper tensiometers show relatively little change during each variation in the inflow rate during this stage. In contrast, the lower tensiometer measurements tended to show an increase with each change in inflow rate. This indicates that the suction profile becomes more uniform with each decrease in the inflow rate. The middle tensiometer measurements in Specimen B indicate that the suction in the upper portion of the specimen is relatively uniform, which is expected compared to the results of the other tests at  $N_{r,mid} > 80$ . There was too much scatter in the middle tensiometer measurements in Specimen A during this stage to be used in this analysis. The suction profiles in Figure 9.88 indicate that the suction in the upper zone of the specimen became more uniform later in the test (for lower  $K_{target}$ ).



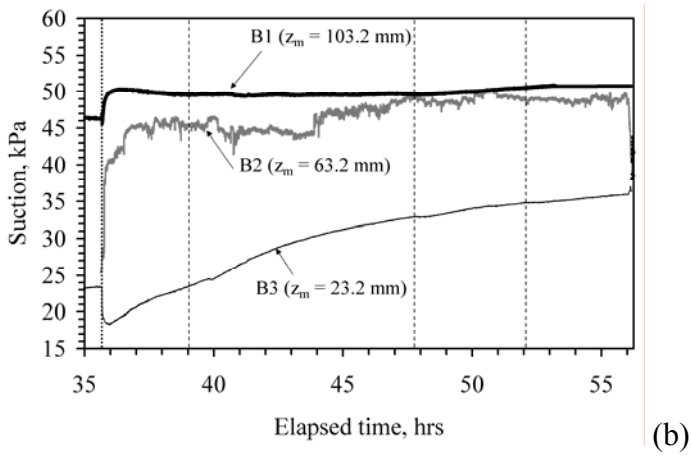
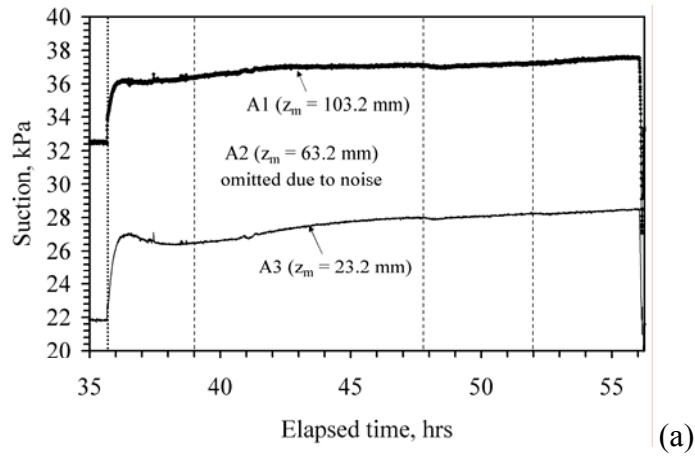


Figure 9.87: Tensiometer measurements in Stage IV-2: (a) Specimen A; (b) Specimen B

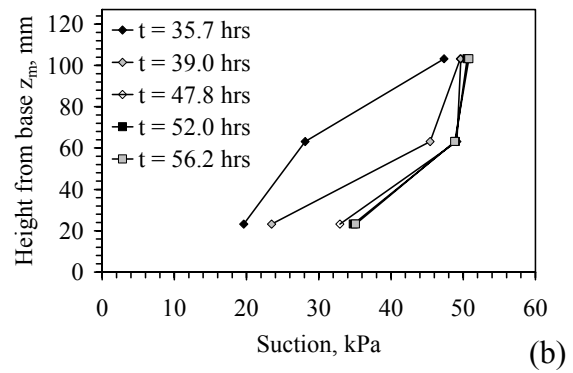
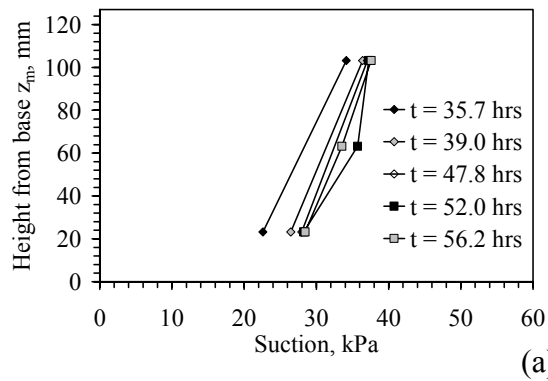


Figure 9.88: Suction profiles in Stage IV-2: (a) Specimen A; (b) Specimen B

Stage IV-3 was conducted to investigate the effect of varying  $Q$  and  $\omega$  to reach the same  $K_{target}$  as that in the last phase of Stage IV-2. The control variables in Stage IV-3 are shown in Figure 9.89. The outflow transducer results for permeameter A, shown in Figure 9.90, indicate that the decrease in  $N_{r,mid}$  and decrease in flow rate resulted in some compression of the air phase at the beginning of the stage. However, the outflow eventually reached steady-state flow in each of the permeameters.

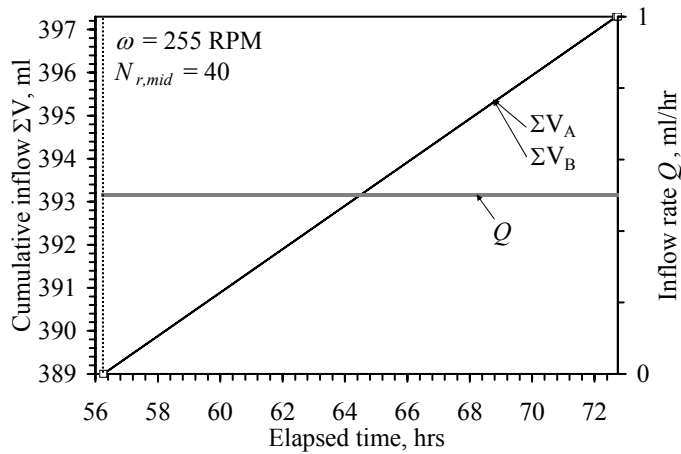


Figure 9.89: Control variables in Stage IV-3

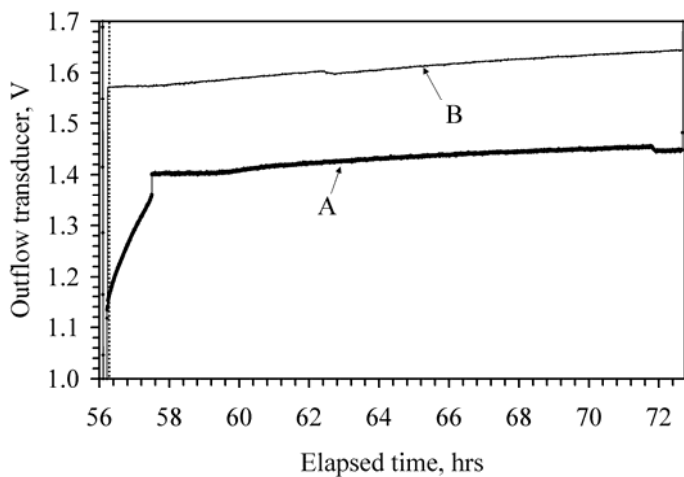


Figure 9.90: Outflow transducer measurements in Stage IV-3

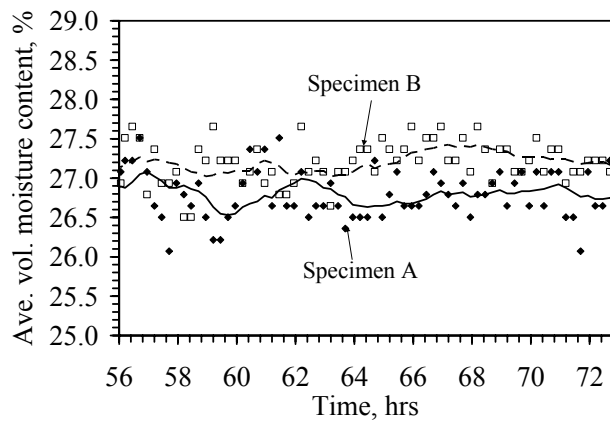
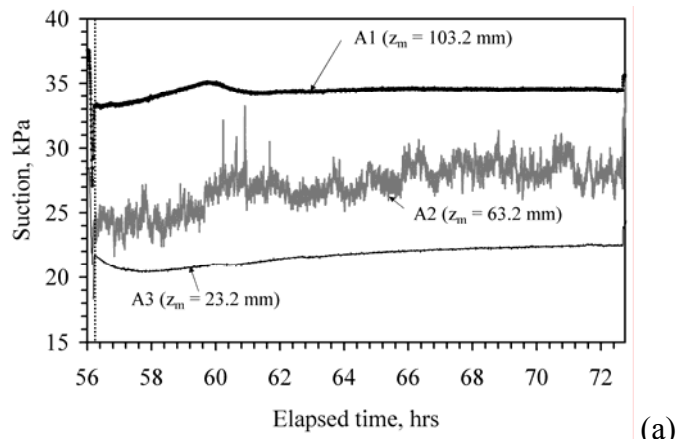
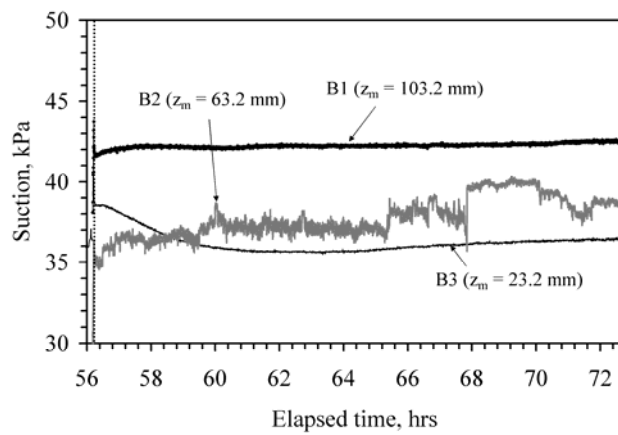


Figure 9.91: TDR measurements in Stage IV-3



(a)



(b)

Figure 9.92: Tensiometer measurements in Stage IV-3: (a) Specimen A; (b) Specimen B

The TDR results for Stage IV-3 shown in Figure 9.91 indicate that the moisture content did not vary significantly in either specimen during this stage, although there is significant scatter. Similarly, the upper tensiometer measurements in this stage, shown in Figure 9.92, indicate a negligible change in suction. The lower tensiometers in Specimen A indicate a linear increase in suction with height, while those in Specimen B indicate a uniform suction in the upper zone of the specimen, as seen in the profiles in Figure 9.93.

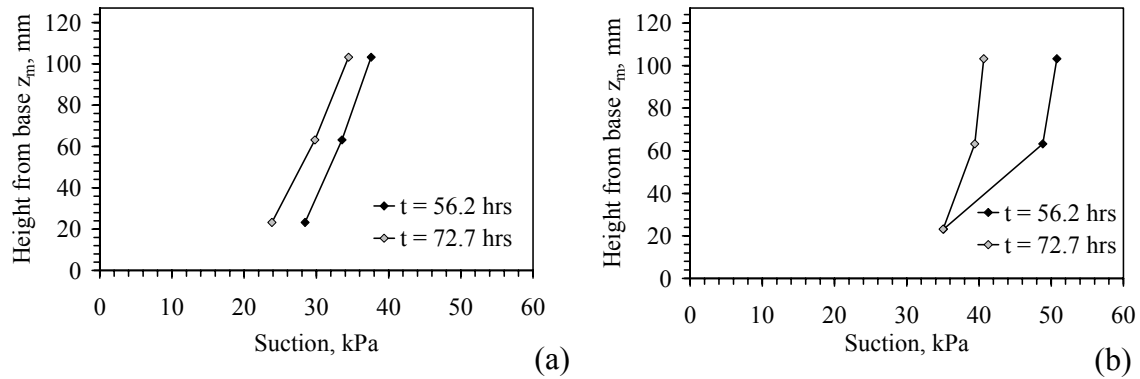


Figure 9.93: Suction profiles in Stage IV-3: (a) Specimen A; (b) Specimen B

Stage IV-4 was conducted to investigate drying and wetting of the specimen at constant  $\omega$ . The control variables in Stage IV-4 are shown in Figure 9.94.

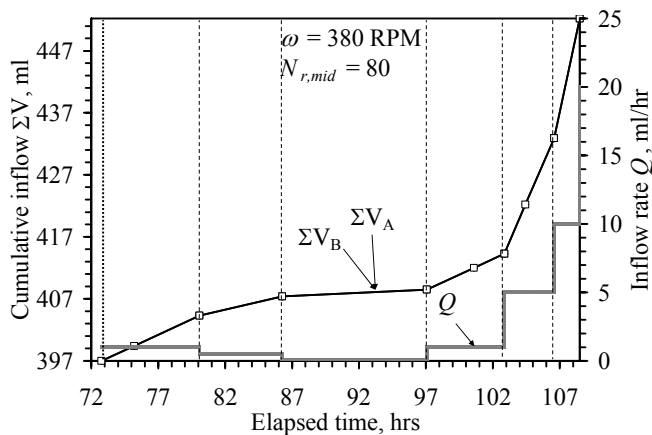


Figure 9.94: Control variables in Stage IV-4

The outflow transducer results for Stage IV-4 shown in Figure 9.95 mimic the changes in inflow rate. Unlike the previous three stages of this test, the TDR results during this stage, shown in Figure 9.96, indicate changes in the moisture content due to the changing flow conditions. The moisture content decreases during the first four drying stages, and then shows an increase at the end of the test.

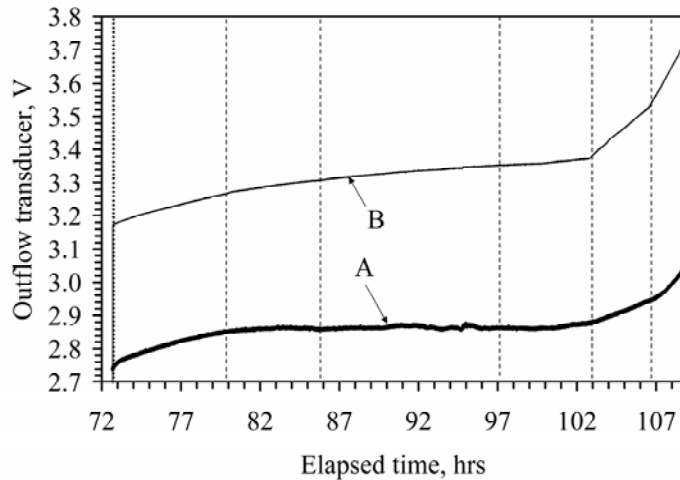


Figure 9.95: Outflow transducer measurements in Stage IV-4

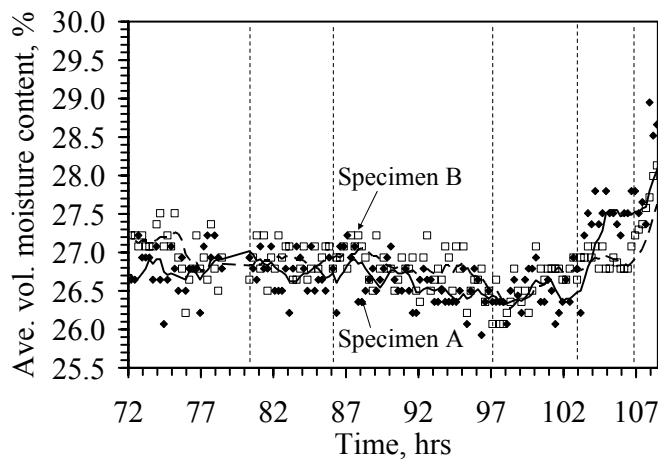


Figure 9.96: TDR measurements in Stage IV-4

The tensiometer results during this stage, shown in Figure 9.97, follow a similar trend to the TDR measurements. The upper tensiometer shows slight increases in suction during the first two infiltration stages, a greater increase in suction during the third stage, then a decrease in suction during the wetting stages. Despite the higher variability noted in the middle tensiometer, the suction profiles shown in Figure 9.98 indicate that the suction in the upper portion of the specimen is relatively constant. The middle tensiometer in Specimen B stopped working in the middle of the fourth phase of Stage IV-4, but provides similar measurements to those in Specimen A.

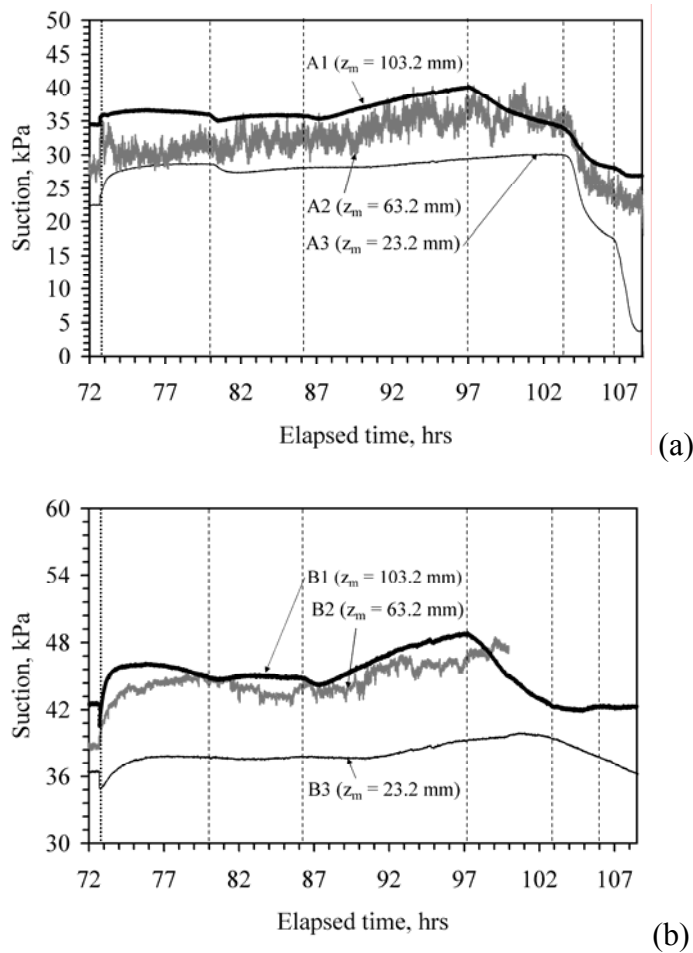


Figure 9.97: Tensiometer measurements in Stage IV-4: (a) Specimen A; (b) Specimen B

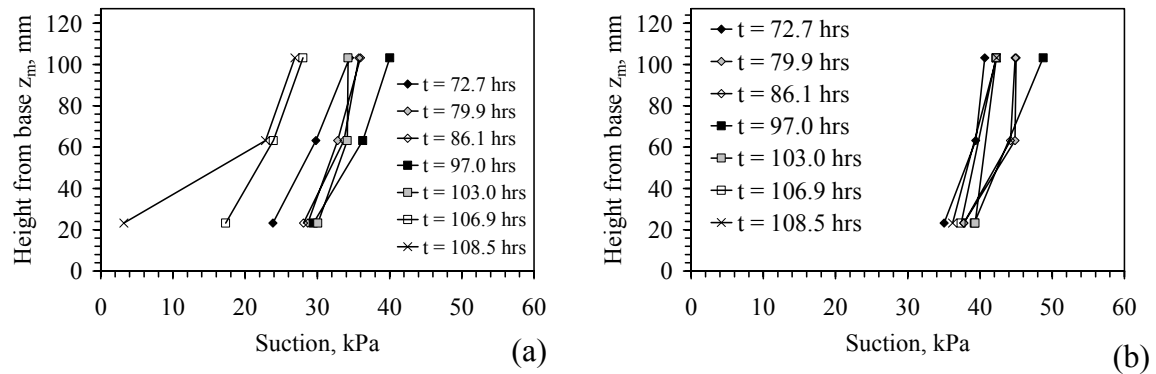


Figure 9.98: Suction profiles in Stage IV-4: (a) Specimen A; (b) Specimen B

The final moisture content profiles obtained using destructive gravimetric samples are shown in Figure 9.99. The moisture profiles are consistent with the shapes of the suction profiles at  $t = 108.5$  hrs. Similar to the previous tests, the moisture content inferred using TDR is consistent with the moisture content measurements in the upper portion of the specimen.

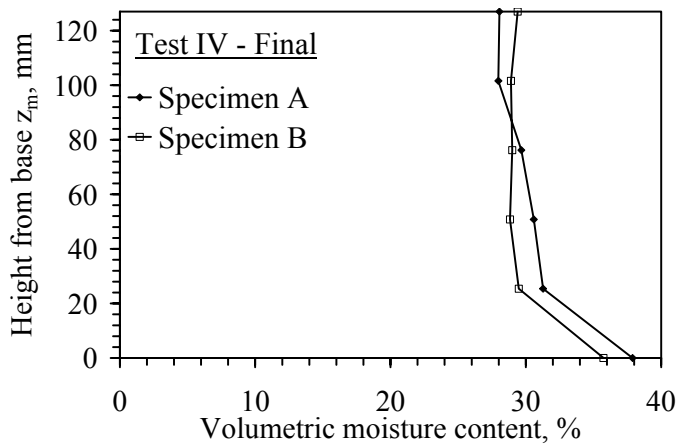


Figure 9.99: Final moisture content profile from destructive samples at end of Test IV

## **Chapter 10: Determination of the Hydraulic Characteristics of Unsaturated Soils using the Centrifuge Permeameter**

### **10.1 OVERVIEW**

This chapter synthesizes the results from the experimental testing program to determine the WRC and K-function of the low plasticity clay and includes an evaluation of the lessons learned by comparing the results from the different centrifuge permeameter tests. Section 10.2 includes a discussion of the calculation of the WRC and K-function determined from a centrifuge permeameter infiltration test. This includes a discussion of the role of the suction head gradient and a comparison between the target hydraulic conductivity ( $K_{target}$ ) calculated using Equation (7.2) and the measured hydraulic conductivity ( $K_{measured}$ ) calculated using Equation (7.3). Based on this discussion, the results obtained from Tests II through IV are then presented and discussed. This section also includes an assessment of the repeatability of the centrifuge permeameter approach through comparison of the results from both permeameters during a given test. Section 10.3 focuses on lessons learned from comparison of the hydraulic characteristics from the different tests. This also includes an investigation of the hydraulic characteristics defined using the three different approaches, focusing on the range of hydraulic conductivity, moisture content, and suction values obtained during testing. A discussion of the impact of soil compaction conditions (*e.g.*, compaction water content) is also presented.

### **10.2 DETERMINATION OF THE HYDRAULIC CHARACTERISTICS**

#### **10.2.1 Determination of the WRC**

In an ideal centrifuge permeameter test, the WRC can be determined by correlating the average moisture content from the TDR corresponding to a height of  $z_m = 87$  mm with the suction interpolated from the two upper tensiometers. This was the case



in Test III, but was not necessarily the case in Tests II and IV because the middle tensiometer was not functional throughout the full duration of the tests. Accordingly, a parametric analysis was performed using the data from Test III to evaluate changes in the WRC if different values of suction are used. Specifically, WRCs determined for the drying path of Stage III-7 are shown in Figure 10.1. The WRCs were determined by correlating the TDR moisture content with the interpolated suction at  $z_m = 87$  mm, the suction at the elevation of each of the tensiometers, and the average suction for the entire profile. The WRC defined with the suction from the top tensiometer shows the highest suctions for any given moisture content, while the WRC defined with the bottom tensiometer shows the lowest suction across the range of moisture content. The interpolated suction value at  $z_m = 87$  mm is generally consistent with the suction from the upper tensiometer (within 4 kPa). Accordingly, for the situations in which the middle tensiometer is not working, the upper tensiometer can be used to define the suction used in determination of the WRC.

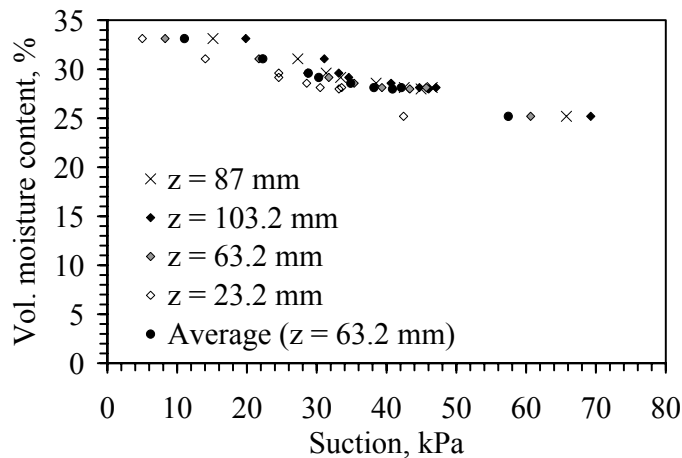


Figure 10.1: WRC determined for different suction values in drying path of Stage III-6

### 10.2.2 Determination of the K-function

Although the imposed values of  $Q$  and  $\omega$  in a centrifuge infiltration test were selected to attain a given  $K_{target}$  using Equation (7.2), the measured suction values from the centrifuge permeameter allow direct determination of  $K_{measured}$  by substituting the  $g$ -level and calculated suction head gradient into Equation (7.3). However, the suction profiles observed during most of Test III indicate that the calculation of the suction head gradient is potentially sensitive to the height at which the suction value is measured. This is specifically a concern for the calculation of  $K_{measured}$  using the data from Tests II and IV, where the middle tensiometer was not functional. The suction values corresponding to different combinations of  $Q$  and  $\omega$  at steady-state flow for Test III are summarized in Figure 10.2(a). These data indicate that the suction values from the two upper tensiometers are generally closer in magnitude than the suction values from the upper and lower tensiometers. The suction head gradient calculated using the two upper tensiometer suction values is generally lower than that calculated using the upper and lower tensiometer suction values, as shown in Figure 10.2(b). However, the data in this figure indicate that the difference in magnitude is not significant, and the trend in the two gradients with time is consistent (except at low suctions). Accordingly, the suction values from the top and middle tensiometers should be used when available to calculate the gradient as they best capture the behavior in the vicinity of  $z_m = 87$  mm, but estimates of the gradient made using the top and bottom tensiometers will not yield significantly different results.

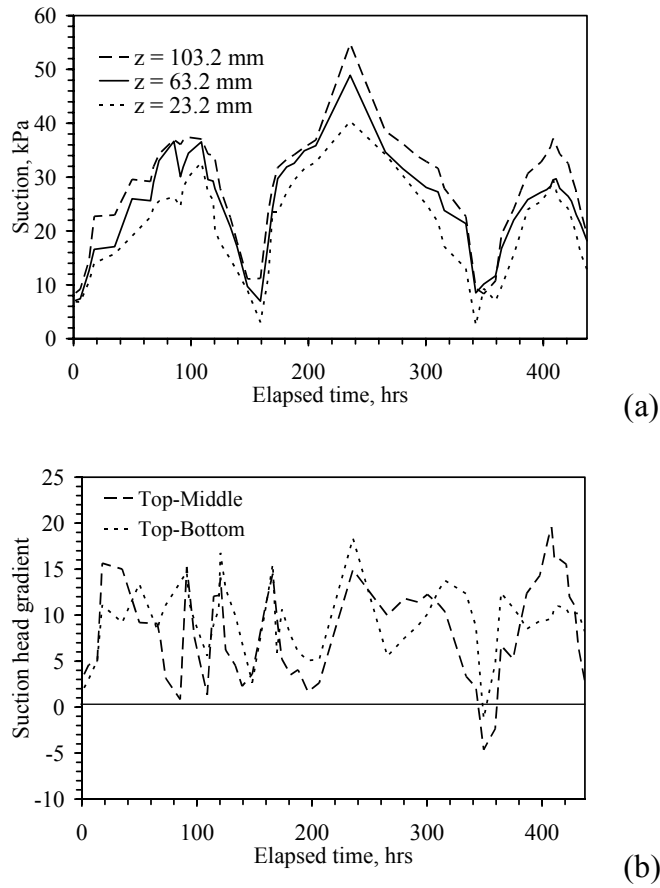


Figure 10.2: (a) Suction values measured at different elevations at steady-state water flow during Test III; (b) Suction head gradient values for different elevations

Although the centrifuge permeameter allows quantification of the suction head gradient to calculate  $K_{measured}$ , the suction head gradient may be small compared to that of the g-level (which is the gradient in the centrifuge elevation head). A comparison between the suction head gradient (defined using the top and middle tensiometers) and the g-level at steady-state during Test III are shown in Figure 10.3. With the exception of the stages of the test with low g-levels, the magnitude of  $N$  at  $z_m = 87$  mm is 5 to 10 times that of the suction head gradient. However, in some instances during infiltration at  $N_{r,mid} = 10$  (e.g., at  $t = 5, 150$ , and  $350$  hrs), the suction gradient and centrifuge elevation

head gradient are of the same magnitude. At these times, the suction varies linearly with height and the outflow boundary is likely saturated. As the two gradient terms shown in Figure 10.3 have opposite signs in the denominator of Equation (7.3), the magnitude of the denominator will be small and the calculated value of  $K_{measured}$  may be unrealistically high. Nonetheless, for the stages of Test III at higher g-levels, the magnitude of the suction head gradient,  $K_{measured}$  should be similar to  $K_{target}$ .

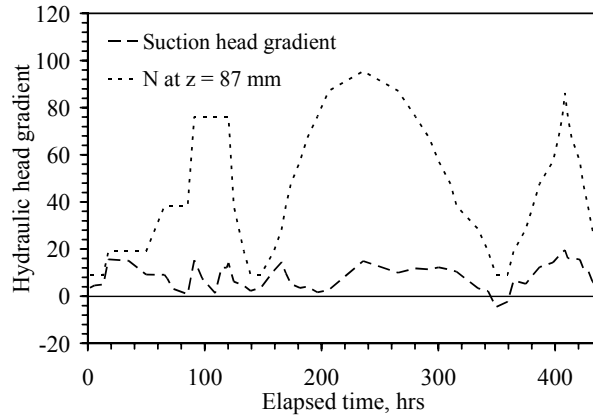


Figure 10.3: Comparison between suction head gradient and centrifuge elevation head gradient ( $N$ ) at steady-state water flow during Test III

A comparison of the K-functions calculated without the suction head gradient ( $K_{target}$ ) and with the suction head gradient ( $K_{measured}$ ) during Stage III-6 is shown in Figure 10.4(a). Very little difference is noted in the K-functions for this particular test, except perhaps at low suctions. A similar comparison for Stages III-1 and III-3 shown in Figure 10.4(b) indicates that during Stage III-1, which was conducted at low  $N_{r,mid} = 10$ , the suction gradient plays a more prominent role in the determination of K. However, during Stage III-4, which was conducted at a higher  $N_{r,mid} = 40$ , the suction head gradient does not play a significant role in the calculation of the hydraulic conductivity.

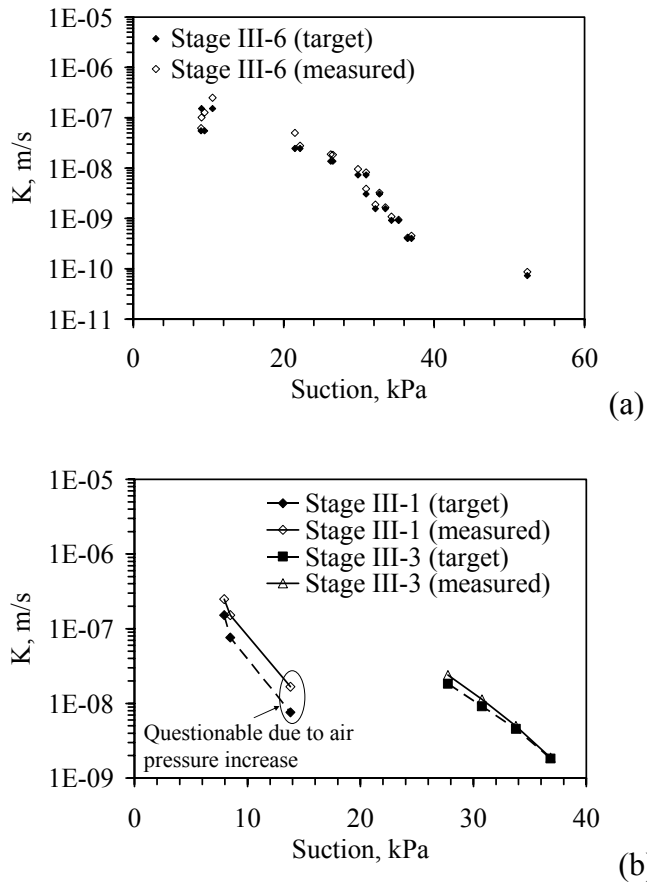
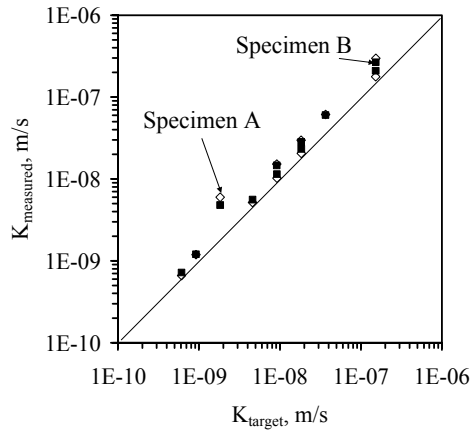
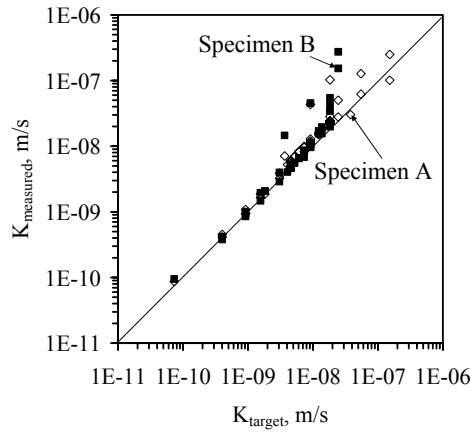


Figure 10.4:  $K$ -functions with  $K_{target}$  and  $K_{measured}$ : (a) Stage III-7; (b) Stage III-1

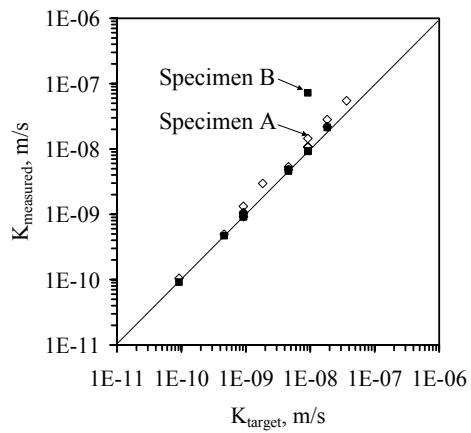
This same analysis was extended to the other tests, shown in Figure 10.5 as plots between  $K_{target}$  from Equation (7.2) and  $K_{measured}$  from Equation (7.3). The  $K$  values calculated from both equations are similar for  $K_{target}$  less than  $5 \times 10^{-8}$  m/s. In general, the predictions of hydraulic conductivity using Equation (7.3) are slightly greater than in Equation (7.2). In particular, the values of  $K_{measured}$  during Test II are consistently higher, as the difference between the upper and lower tensiometer results were the most significant during this test. This indicates that the soil compaction conditions (or soil type in general) may have an influence on the calculation of  $K$ .



(a)



(b)



(c)

Figure 10.5: Comparison between  $K_{target}$  (without suction head gradient) and  $K_{measured}$  (with suction head gradient): (a) Test II; (b) Test III; (c) Test IV; Note:  $K_{measured}$  values calculated using the upper and middle tensiometers in Test III and using the upper and lower tensiometers in Tests II and IV

## 10.3 EVALUATION OF HYDRAULIC CHARACTERISTICS FROM CENTRIFUGE TESTS

### 10.3.1 Summary of K-function and WRC Results

The results from Specimen A during Test II are presented in Figure 10.6, with the K-functions plotted as a function of suction [Figure 10.6(a)], moisture content [Figure 10.6(b)], and degree of saturation [Figure 10.6(c)]. Because the middle tensiometer was not functional during this test,  $K_{target}$  was used to define the K-function. Overall, these results reflect the fact that infiltration occurs under relatively wet conditions (suction less than 60 kPa and degree of saturation greater than 50%). This observation is consistent with the other results presented in this section for this soil, and is considered representative for a compacted clay of low plasticity having a wide range in pore sizes.

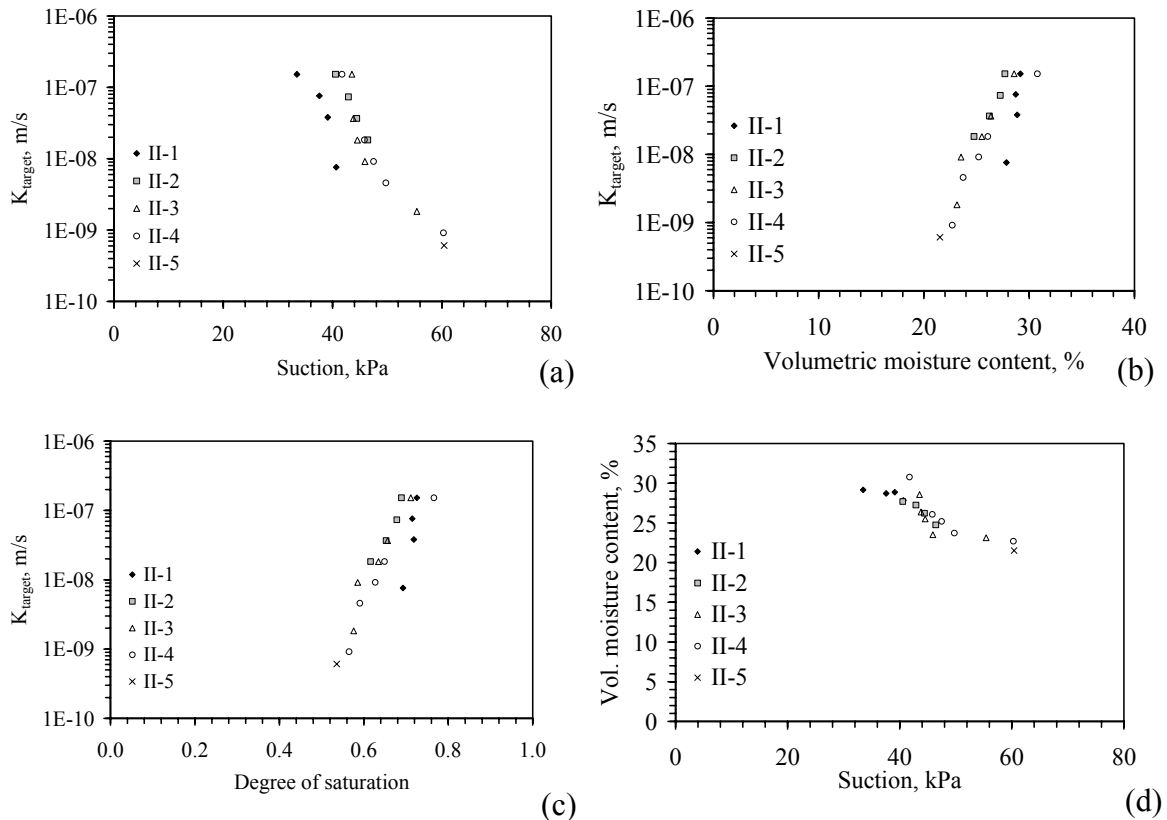


Figure 10.6: Test II results for Specimen A: (a)  $K-\psi$ ; (b)  $K-\theta$ ; (c)  $K-S_r$ ; (d) WRC

The K-functions follow log-linear trends with respect to each of the dependent variables.  $K$  was observed to drop by more than 2 orders of magnitude during a drop in suction from about 35 kPa to about 60 kPa, and for a decrease in moisture content from 30 to 22%. The WRC shown in Figure 10.6(d) also follows a log-linear trend. An “S” shape is not observed in the WRC, but this may be due to the fact that a natural scale is used for suction. The results for Specimen B, presented in Figure 10.7, show similar results, although there is more scatter in the suction and moisture content values obtained during this test. Although not as smooth as the data for Specimen A, the slope and bounds of the hydraulic characteristics are similar for Specimen B.

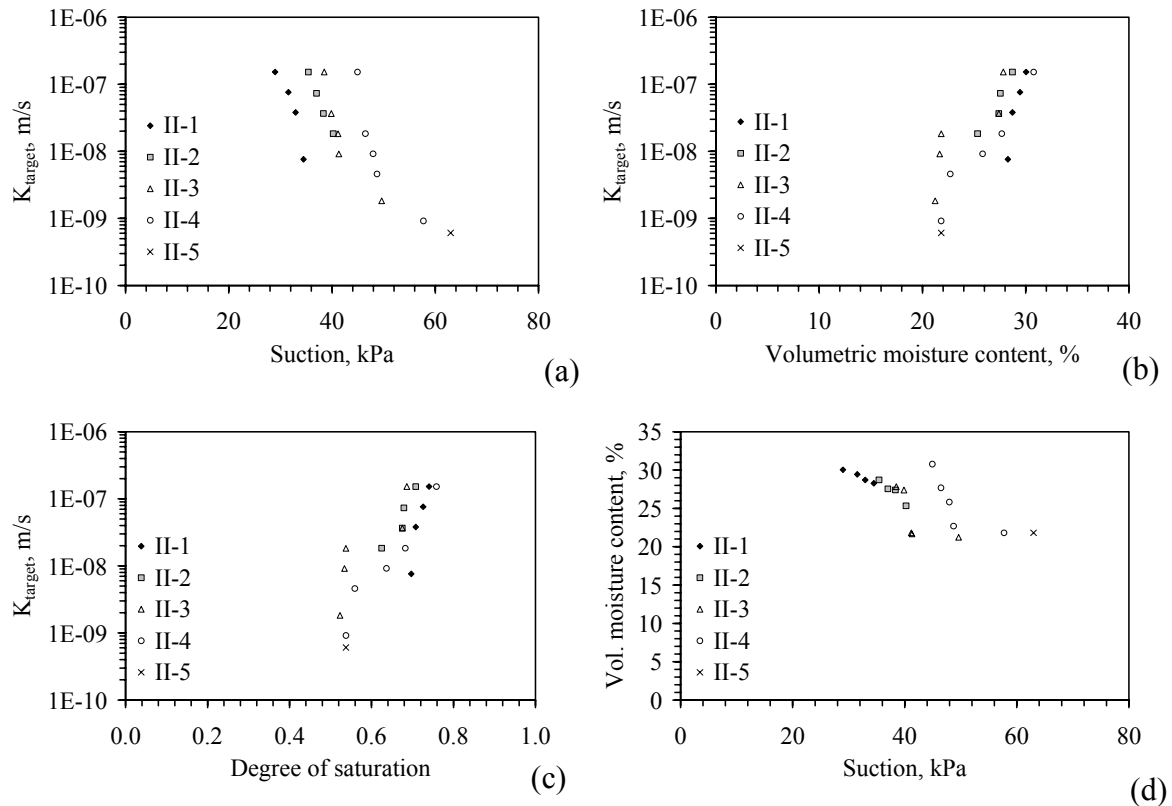


Figure 10.7: Test II results for Specimen B: (a)  $K$ - $\psi$ ; (b)  $K$ - $\theta$ ; (c)  $K$ - $S$ ; (d) WRC



The  $K$ -functions obtained during all of the stages of Test III, shown in Figure 10.8, illustrate the widest range in suction, moisture content, and  $K_{measured}$  values obtained using the centrifuge permeameter. The suction observed during steady-state infiltration was ranged from 9 to 52 kPa for  $K$  values ranging from  $5 \times 10^{-11}$  to  $2 \times 10^{-7}$  m/s. This corresponds to a range in volumetric moisture content from 24 to 32%, which is relatively wet (degree of saturation greater than 0.65). Similar to Test II, the maximum suction during infiltration is less than 60 kPa. Lower suctions were measured in this test than in Test II, but the  $K$  values corresponding to these suctions may be unreliable due to problems with air compression during outflow at low  $N_{r,mid}$ . The WRC shown in Figure 10.8(d) has a shallow slope, with a decrease in moisture content of 8% corresponding to a decrease in suction of 44 kPa.

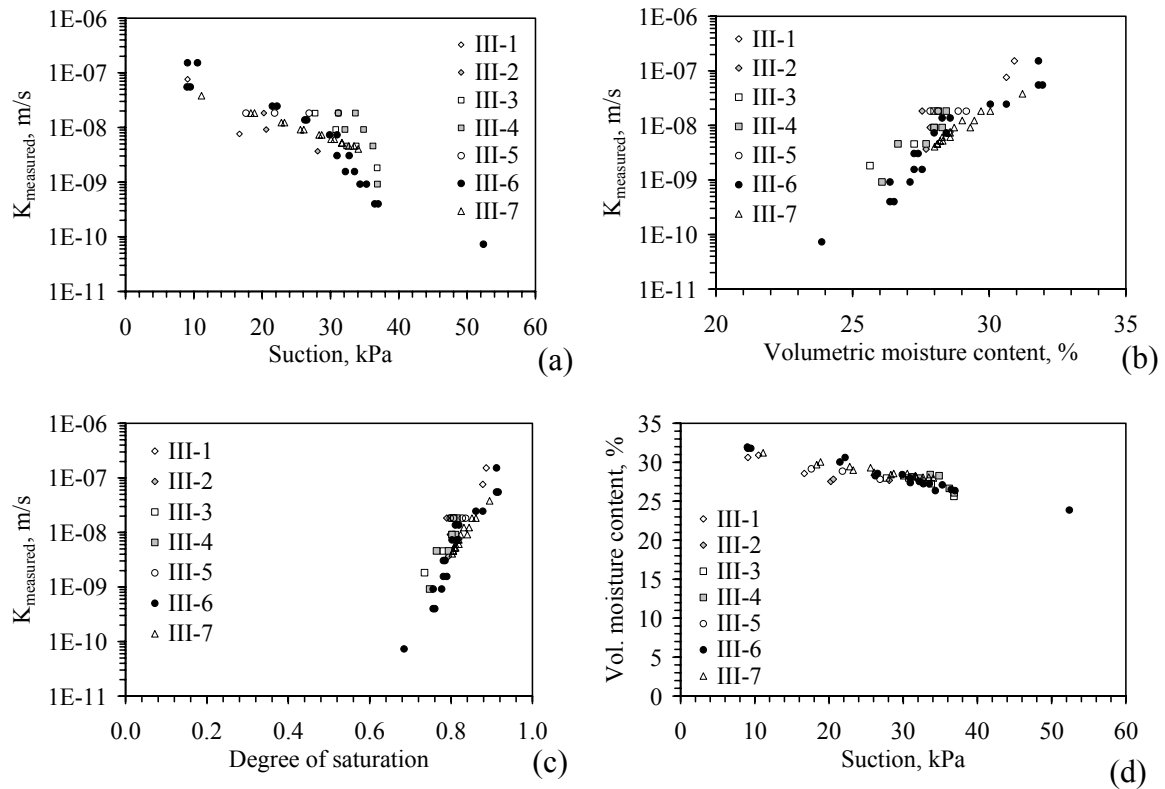


Figure 10.8: Test III results for Specimen A: (a)  $K$ - $\psi$ ; (b)  $K$ - $\theta$ ; (c)  $K$ - $S$ ; (d) WRC

The results for Specimen B during Test III shown in Figure 10.9 are similar to those in Specimen A. The highest suction measured during this test was 66 kPa, which is about 14 kPa greater than that observed in Specimen A (corresponding to the lowest  $K_{target}$  in Stage III-6). Although this suction value does not fall into line with the overall trend of the K-function with suction in Figure 10.9(a), this inconsistency in shape is also observed for the K-function when plotted as a function of moisture content in Figure 10.9(b). Although non-linearity in the K-function may occur for steady-state flow at high suctions, this could be caused by improper distribution of the relatively low inflow rate.

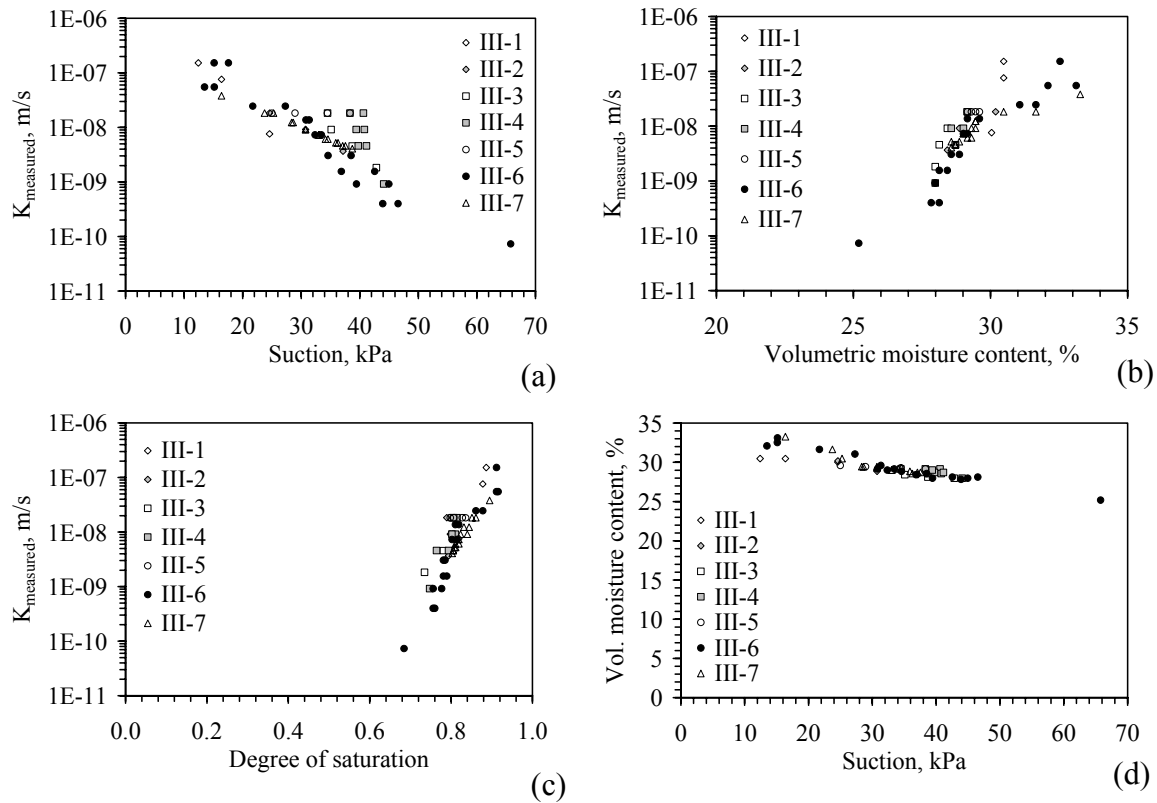


Figure 10.9: Test III results for Specimen B: (a) K- $\psi$ ; (b) K- $\theta$ ; (c) K-S; (d) WRC

The hydraulic characteristics for Specimens A and B during Test IV are presented in Figure 10.10 and Figure 10.11. The K-functions plotted as a function of suction, shown in Figure 10.10(a) and Figure 10.11(a), show a decreasing trend despite some

scatter likely due to the definition of the hydraulic characteristics over wide range of constant  $N_{r,mid}$  values [Approach (i)]. The suction values were lower in this test than in Tests II and III, ranging from 27 to 40 kPa.

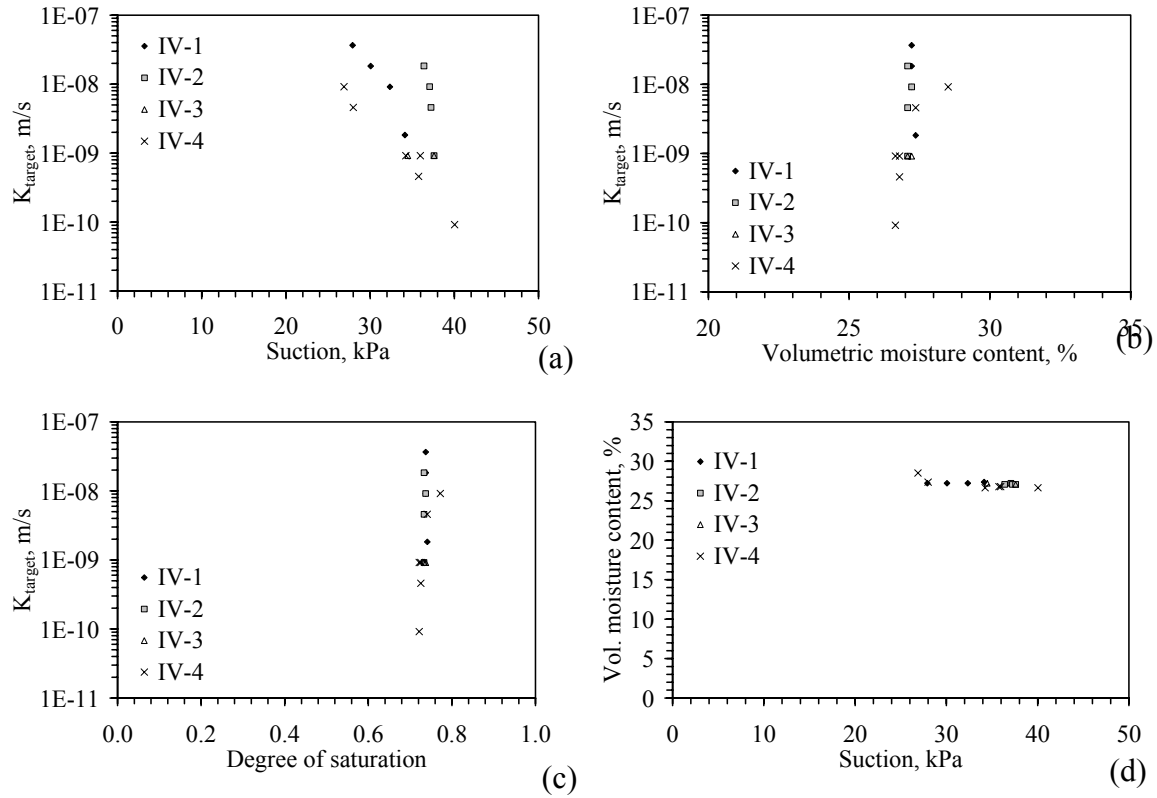


Figure 10.10: Test IV results for Specimen A: (a) K- $\psi$ ; (b) K- $\theta$ ; (c) K-S; (d) WRC

Unlike the results from Tests II and III, the K-function for Test IV plotted as a function of moisture content in Figure 10.10(b) and Figure 10.11(b) shows a relatively small change in moisture content (3%) for  $K_{target}$  values ranging from  $3.7 \times 10^{-8}$  m/s to  $9 \times 10^{-11}$  m/s. This may be due to low sensitivity of the TDR measurements compared to the suction measurements, but the different behavior may arise from the difference in the compaction conditions. Another possibility is that the flow pattern in the soil was such that the TDR did not capture a realistic value of the moisture content. The WRCs shown

in Figure 10.10(d) and Figure 10.11(d) indicate that the moisture content does not vary significantly with suction. This could, in theory, lead to a steep K- $\theta$  relationship.

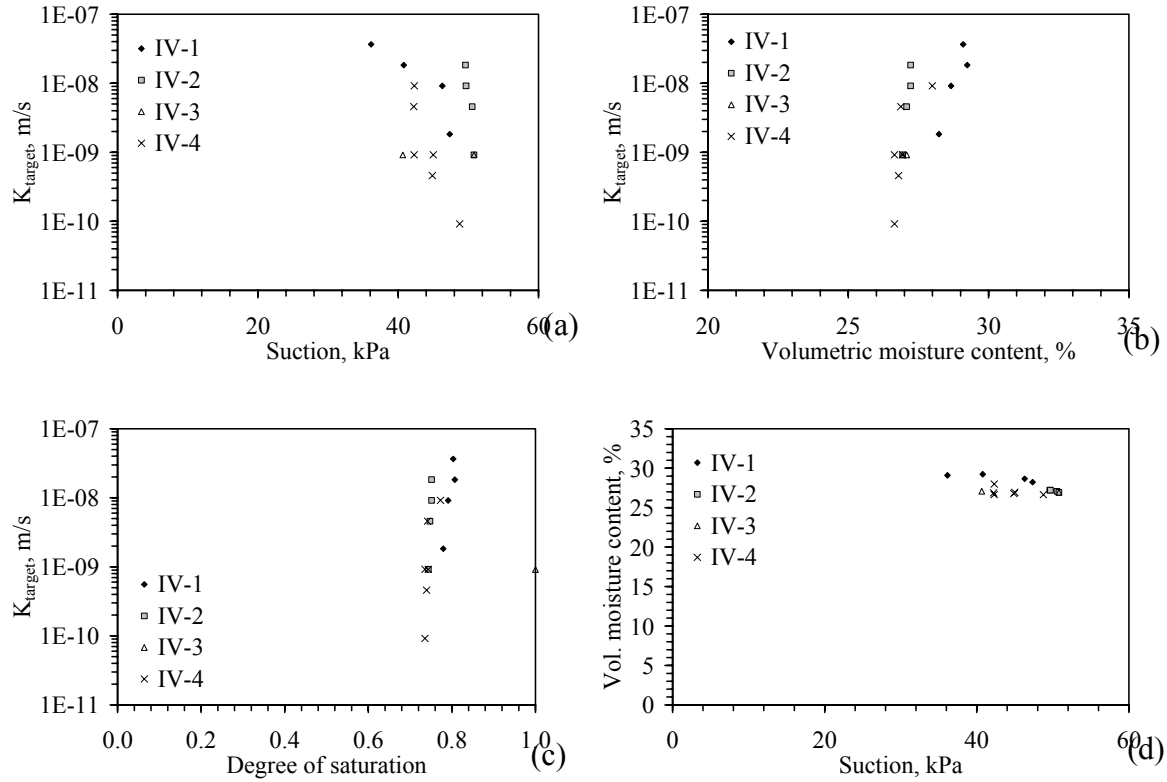


Figure 10.11: Test IV results for Specimen B: (a) K- $\psi$ ; (b) K- $\theta$ ; (c) K-S; (d) WRC

### 10.3.2 Repeatability of Hydraulic Characteristics from the Centrifuge Permeameter

One advantage of the centrifuge permeameter approach is that two specimens are tested simultaneously. A comparison of the K-function and WRC from two permeameters is shown in Figure 10.12(a) and Figure 10.12(b). The data from Stage III-6 was selected as it reflects the greatest difference observed in this study. Although there are likely differences in compaction conditions between any two specimens, the WRC and K-functions for both specimens follow similar trends. The  $K_{measured}$  values vary at most by an order of magnitude and the WRC varies between 3% moisture content, both of which

can be deemed acceptable when comparing the results from conventional tests. These differences may arise from the calibration of the tensiometers and TDR, as the hydraulic characteristics rely heavily on the quality of measurements from these instruments.

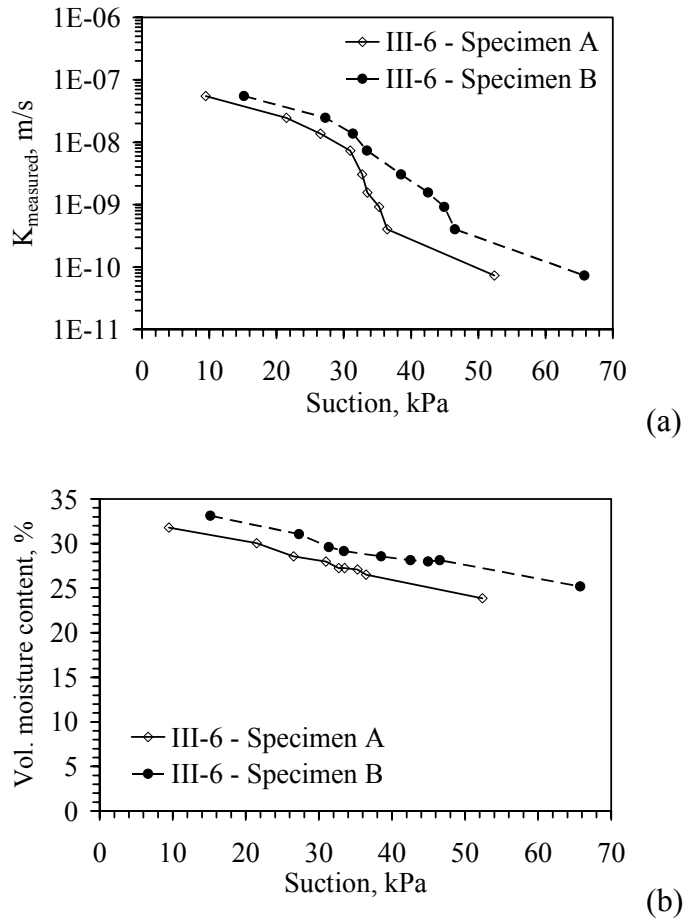


Figure 10.12: Repeatability assessment: (a) K-function; (b) WRC

### 10.3.3 Evaluation of Testing Approaches to Determine Hydraulic Characteristics

The K-function and WRC defined for Specimen A during three of the stages in Test III are shown in Figure 10.13(a) and Figure 10.13 (b). A different approach was used to determine the hydraulic characteristics in each of these testing stages. The shapes of the K-function and WRC are relatively the same for each of the different approaches.

The range of  $K_{measured}$  values is the widest for Approach (iii), while Approach (ii) shows the shallowest slope in  $K_{measured}$  with suction. The use of Approach (i) was observed to lead to the steepest K-function with suction. The adoption of Approach (i) in Test IV may be another reason that the relatively steep K-functions were observed.

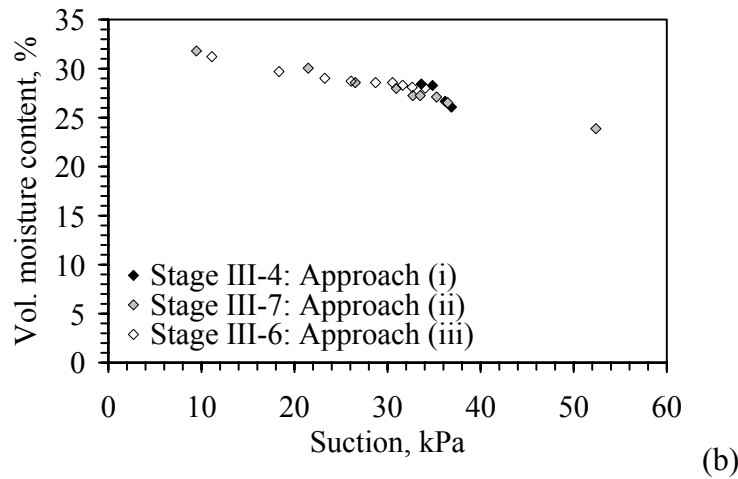
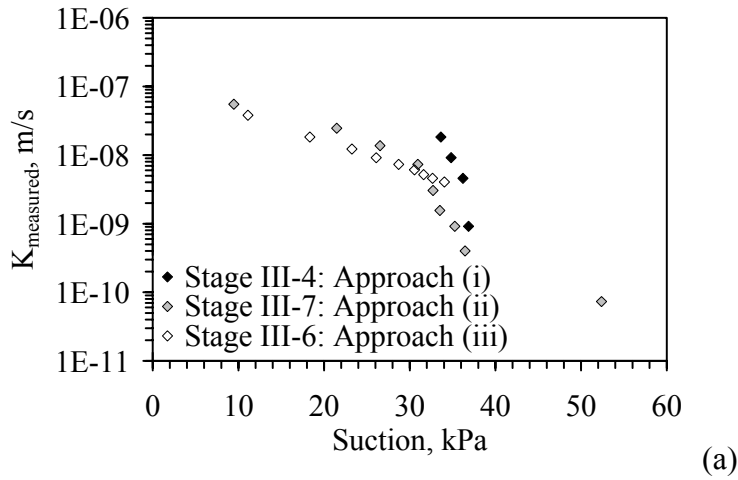


Figure 10.13: Comparison of characterization approaches: (a) K-function; (b) WRC

### 10.3.4 Consistency of Hydraulic Characteristics from the Centrifuge Permeameter

The consistency of the moisture content and suction values obtained for combinations of  $Q$  and  $\omega$  that yield the same values of  $K_{target}$  in Equation (7.3) was

investigated in Test III (Stage III-5) and Test IV (Stage IV-3). The results of the analysis for Stage III-5 are shown in Figure 10.14. The data indicates that the moisture content is relatively constant with each change in  $N_{r,mid}$  (and proportional change in  $Q$ ) but the suction at the top of the specimen increased with  $N_{r,mid}$ . Nonetheless, the change in suction is not significant, and is tending toward a constant value with  $N_{r,mid}$ . Similar observations were made during Stage IV-3. Accordingly, the centrifuge permeameter approach will lead to consistent results for  $N_{r,mid} > 40$  for the clay used in this study.

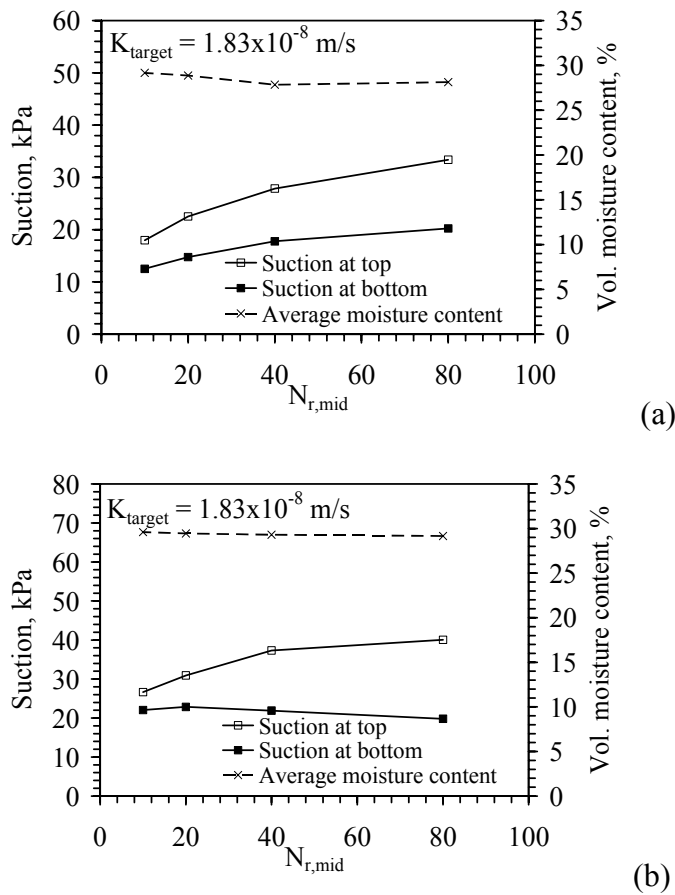


Figure 10.14: Consistency tests during Stage III-5: (a) Specimen A; (b) Specimen B

The consistency test results can also be summarized by plotting the values of  $K_{measured}$  with the measured suction and moisture content values, and comparing the

values with  $K_{target}$ , as shown in Figure 10.15. The difference in suction values occurs due to different suction profiles at each of the combinations of  $Q$  and  $\omega$ . However, the  $K_{measured}$  values are within an order of magnitude of the target values.

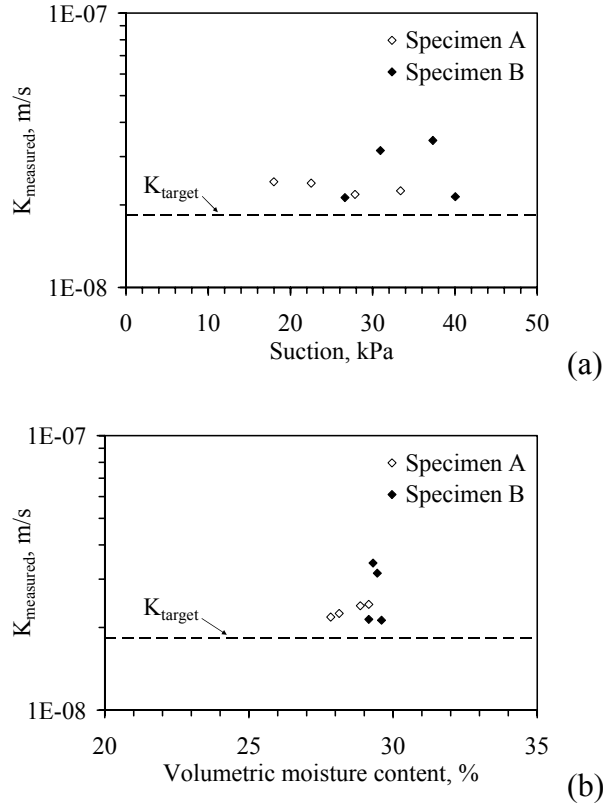


Figure 10.15: Consistency tests for Specimen A during Stage III-5: (a)  $K$ - $\psi$ , (b)  $K$ - $\theta$

### 10.3.5 Effect of Hysteresis on the Hydraulic Characteristics

The different testing approaches considered in this study provide an excellent opportunity to assess the role of hysteresis in the hydraulic properties. The transitions between each stage in Test II allow investigation of the change in suction and moisture content for constant  $K_{target}$  values, as shown in Figure 10.16. This allows assessment of the impact of wetting hysteresis on the hydraulic properties. This data indicates that there is a clear variation in moisture content ( $\pm 1.5\%$ ) and suction ( $\pm 5$  kPa) with increasing



$N_{r,mid}$ , although it appears that the curves are approaching a constant value asymptotically. This test represents the most extreme hysteresis situation, as a significant change in  $K_{measured}$  of several orders in magnitude was imposed on the specimen.

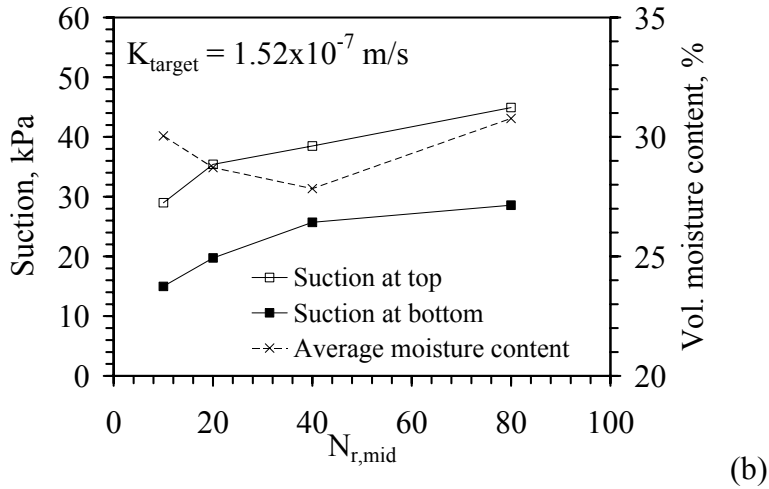
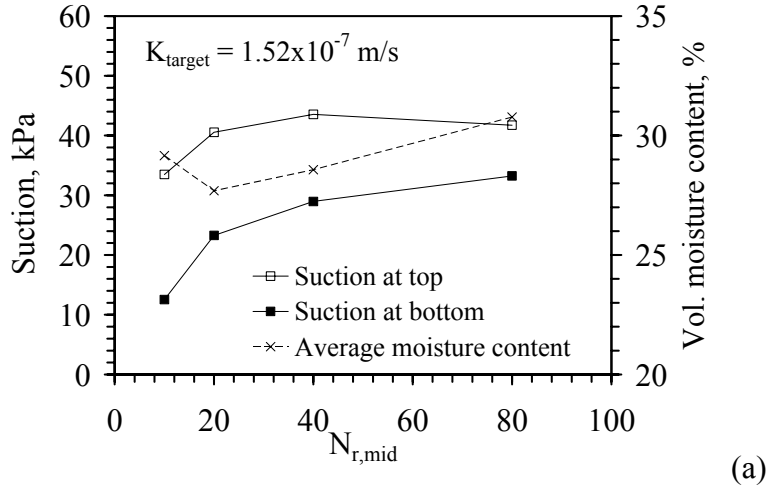


Figure 10.16: Constant  $K_{target}$  hysteresis test: (a) Specimen A; (b) Specimen B

Similar to the consistency tests, the impact of hysteresis on the constant  $K_{target}$  tests can be summarized by plotting the values of  $K_{measured}$  with the measured suction and moisture content values, and comparing the values with  $K_{target}$ , shown in Figure 10.17 for Specimen A in Test III. The  $K_{measured}$  values are within an order of magnitude of the

target values. The suction values show a similar range to those observed in the consistency evaluation in Figure 10.15. The K-function plotted as a function of suction indicates that the  $K_{measured}$  values are approaching  $K_{target}$  as the suction increases.

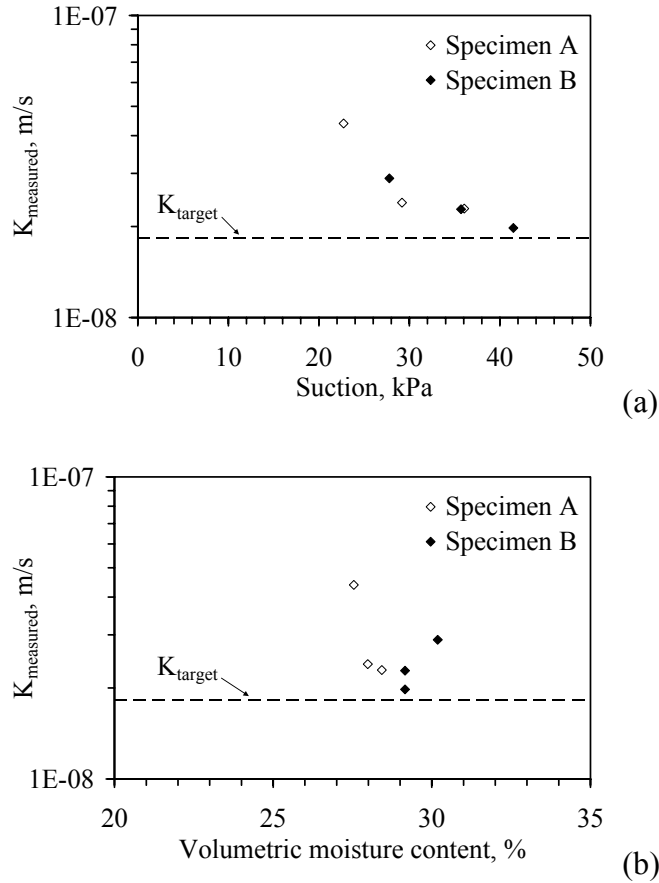


Figure 10.17: Hysteresis tests for Specimen A during Stage III-5: (a)  $K-\psi$ , (b)  $K-\theta$

During Test III, hysteresis was investigated using each of the three characterization approaches (constant  $\omega$  and varying  $Q$ , constant  $Q$  and varying  $\omega$ , varying both). In these tests, the specimen was dried then gradually rewetted, as shown in Figure 10.18. Except in the case of Approach (i), hysteresis had a negligible effect. Hysteresis may have played a more prominent role in Approach (i) as  $Q$  is changed for a

constant  $\omega$  between stages of the test. Accordingly, this test has the highest potential for air entrapment to occur when the inflow rate is increased during the wetting path.

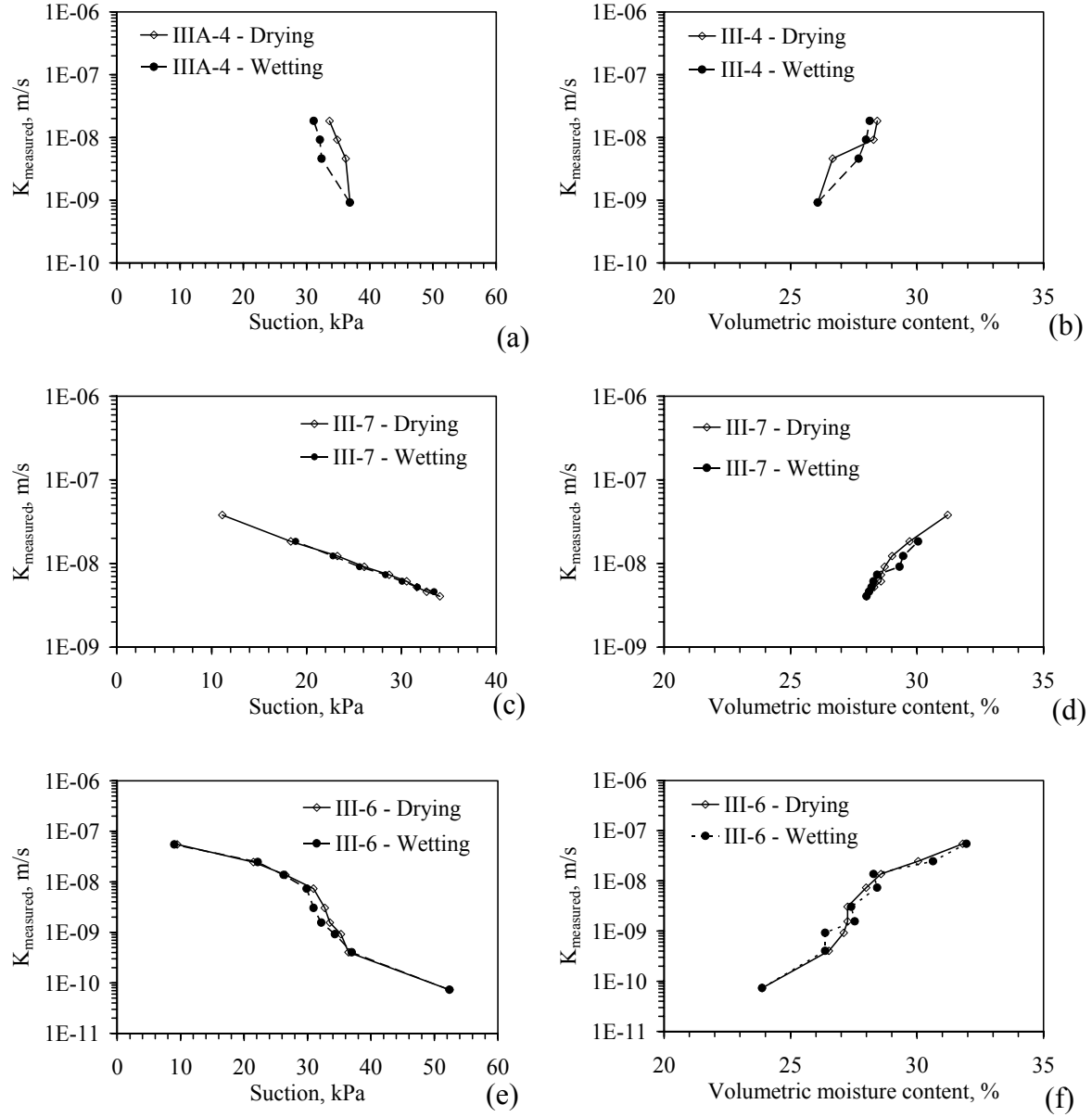


Figure 10.18: K-function hysteresis: (a)  $K$ - $\psi$  Approach (i); (b)  $K$ - $\theta$  Approach (i); (c)  $K$ - $\psi$  Approach (ii); (d)  $K$ - $\theta$  Approach (ii); (e)  $K$ - $\psi$  Approach (iii); (f)  $K$ - $\theta$  Approach (iii)

Hysteresis played a greater role in the definition of the WRC, shown in Figure 10.19, especially in Approaches (i) and (ii). Overall, the amount of hysteresis is influenced by the instrumentation, the characteristics of the soil, and the magnitude of the changes in inflow rate or g-level leading to wetting or drying.

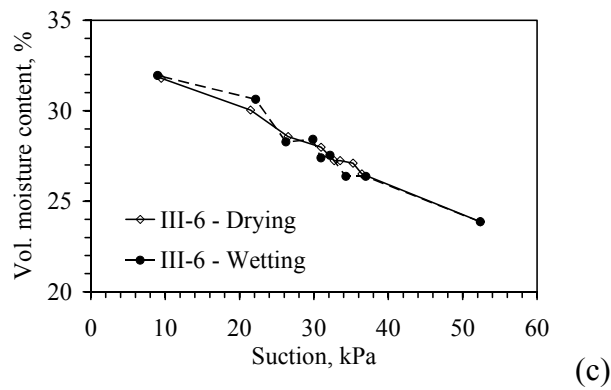
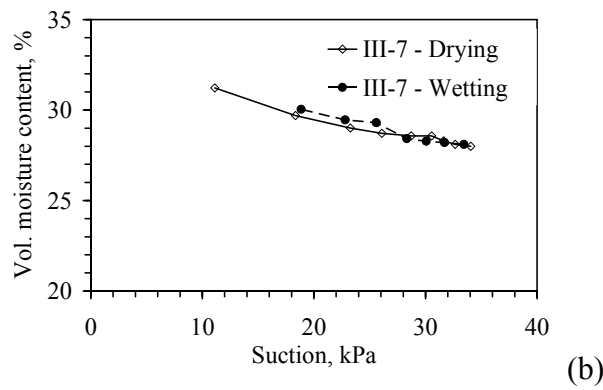
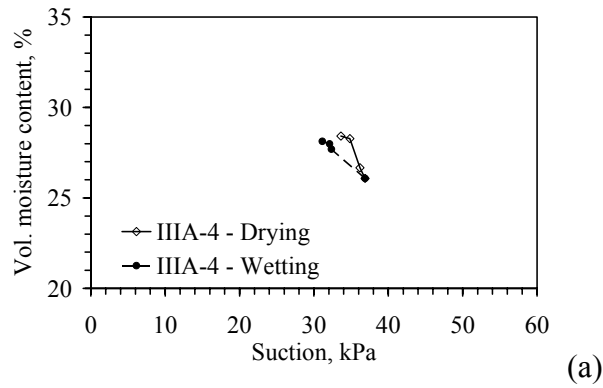


Figure 10.19: Hysteresis in WRCs: (a) Approach (i); (b) Approach (ii); (c) Approach (iii)

### 10.3.6 Effect of Compaction Conditions on Hydraulic Characteristics

The K-function and WRC from Tests II through IV allow assessment of the impact of compaction water content on the K-function, are shown in Figure 10.20(a) and Figure 10.20(b). The specimen compacted dry of optimum has higher suctions for the same  $K_{target}$  value, and appears to be approaching a higher  $K_s$  value. Nonetheless, the slopes of the three K-functions are relatively similar. The retention curves for these specimens are similar, which is consistent with the observations made in Chapter 5 that different compaction conditions have a negligible impact on the WRC unless near saturation. The similar shapes for the WRC indicate that the predicted K-functions for the different soils should have similar slopes, although the K-function is anchored on the ordinate axis by  $K_s$ . Compaction wet of optimum moisture content (or at optimum) is known to result in lower  $K_s$  than compaction dry of optimum (Mitchell *et al.* 1965).

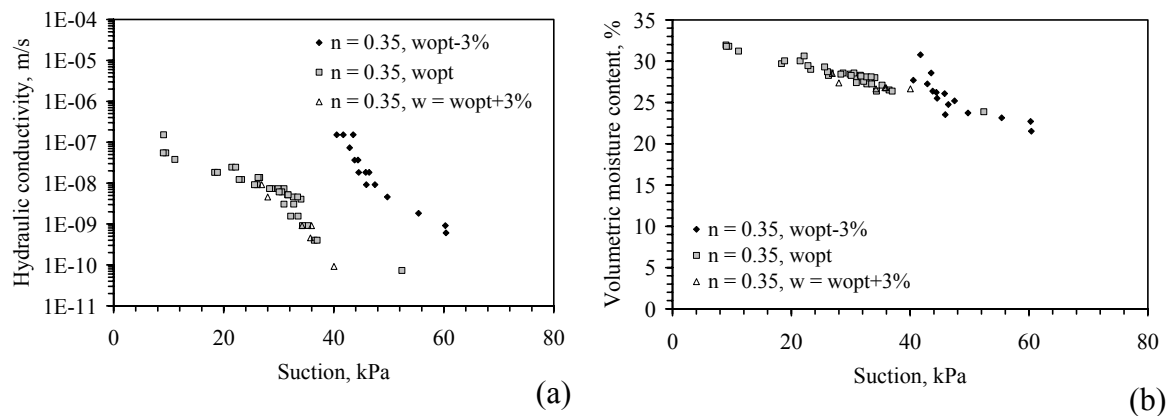


Figure 10.20: Effect of compaction water content; (a) K-function; (b) WRC

## Chapter 11: Verification of the Centrifuge Permeameter Results

### 11.1 OVERVIEW

This chapter includes a comparison of the results from the centrifuge permeameter with those from the conventional tests presented in Chapter 5. Also, this chapter includes a comparison between the results obtained with the centrifuge permeameter and those obtained from predictive models.

### 11.2 COMPARISON BETWEEN CENTRIFUGE AND CONVENTIONAL TEST RESULTS

The K-functions from the 1-g infiltration column study presented in Chapter 4 are shown in Figure 11.1. Despite the differences in density (the columns were constructed at a porosity of 0.50), the transient and steady-state K-functions follow a similar trend with decreasing moisture content. An important quantity from the K-function is its slope, so these tests would yield similar results. The  $K$  values from the centrifuge permeameter correspond to higher moisture contents, which can be associated with the greater density of the soil (more small pores, so greater water retention). The results from the transient column analysis show a wider range in  $K$  values, but a greater amount of scatter is noted.

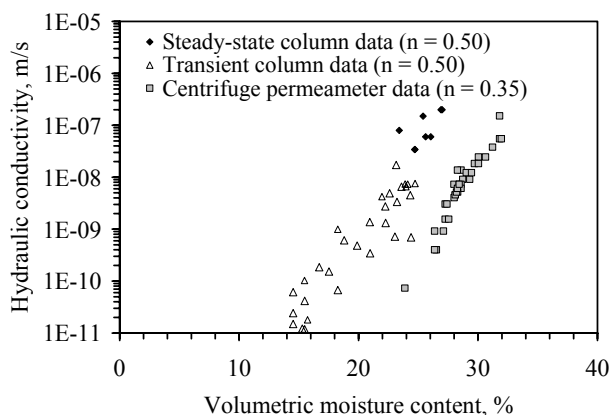


Figure 11.1: K-functions with centrifuge and column infiltration tests

A comparison between the WRC obtained using steady-state flow in the centrifuge permeameter (Stage III-6) and the pressure plate and hanging column tests is shown in Figure 11.2. The WRCs follow a similar trend with suction, although the WRC from the pressure plate and hanging column tests show slightly lower moisture contents for the same suction values (approximately 2% lower). Nonetheless, this data indicates that a consistent shape is still obtained on a natural suction scale.

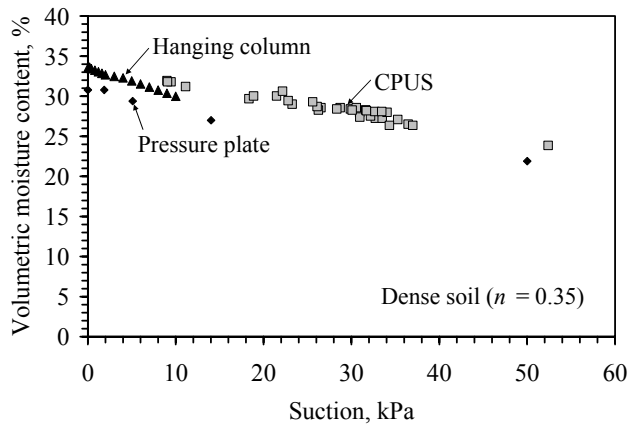


Figure 11.2: Comparison of WRC from the centrifuge and pressure plate tests

The K-functions determined using the centrifuge (Stage III-6) and pressure plate tests are shown in Figure 11.3. Again, there is a significant difference in porosity between the soil specimens used in these tests, so the soil in the pressure plate will dry faster due to the greater number of large pores. Nonetheless, the slopes of the K-functions are remarkably similar for except near saturation. The difference in moisture content for a given K value measured by these tests may be due to (i) uncertainty related to the estimation of the average moisture content of the specimen during pressure plate testing; (ii) the fact that infiltration is used for characterization in the centrifuge permeameter while pressurization of the pore air is used in the pressure plate, and (iii) outflow boundary impedance in the pressure plate test, which tends to decrease the estimated value of  $K$ .

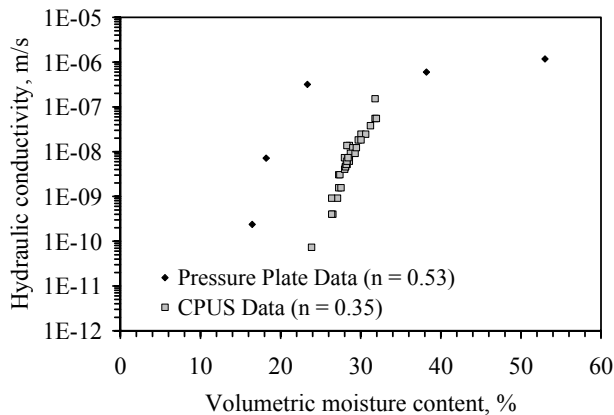


Figure 11.3: Comparison of K-functions from the centrifuge and pressure plate tests

### 11.3 COMPARISON BETWEEN CENTRIFUGE RESULTS AND PREDICTIVE MODELS

Once a K-function has been obtained experimentally, it is useful to provide a mathematical representation of the variation in  $K$  with moisture content or suction. The K-functions were first fitted with the Gardner model, which is a simple exponential function, which is particularly useful in the determination of analytical solutions. The K-function fits for the data are shown in Figure 11.4. The Campbell model fits well, although the  $K_s$  value used in the equation is likely not representative of the actual  $K_s$ , and is only a fitting parameter. The linearity of the K-function on a semi-log plot is likely because of the narrow range in suction values during infiltration, but Campbell model will give representative results in restricted situations. The results for the soils compacted wet of optimum and at optimum have similar parameters, which is likely because soils compacted at or wet of optimum typically have similar behavior.



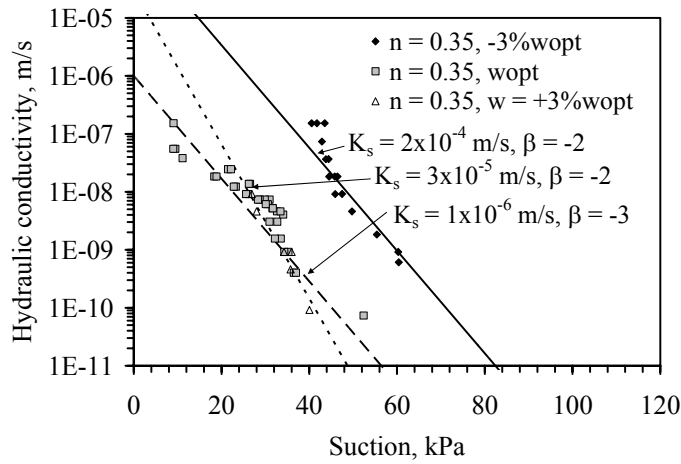


Figure 11.4: Centrifuge data with fitted Campbell model K-functions

The van Genuchten-Mualem (1980) model can be used to predict the K-function from the shape of the WRC. The fitted WRC using the van Genuchten model is shown in Figure 11.5(a). A reasonable fit is obtained for the WRC data. However, the predicted K-function shown in Figure 11.5(b) overestimates the  $K$  values, particularly at comparatively high suction, although the experimental K-function does follow the same slope as the predicted K-function up to 30 kPa. Similar observations were made for the other K-functions obtained with the centrifuge permeameter. The van Genuchten-Mualem model also provided a poor fit for the data from conventional tests presented in Chapter 5. Even if the predicted K-function were to be scaled linearly to a  $K$  value other than  $K_s$ , as suggested by Khaleel et al. (1995), the predicted K-function would not provide a good fit. This highlights the importance of determining the K-function experimentally rather than relying on predictive relationships.

Overall, the comparison between the hydraulic characteristics from the centrifuge permeameter and those from conventional tests indicates that the approach used for the centrifuge permeameter provides reasonable results. The K-function and WRC results

are only representative of the relatively narrow range of suction and moisture content values observed. For instance, the current configuration of the centrifuge permeameter cannot be used to predict the hydraulic characteristics for modeling evaporation from soils under high suctions. Nonetheless, the centrifuge permeameter is particularly suited for applications in which continuous, steady-state water flow is expected. Continuous water flow will occur in the vadose zone where water is routinely cycling upward and downward in response to infiltration and evaporation. Steady-state seepage in unsaturated soils also occurs from perched water tables and in dams above the phreatic surface.

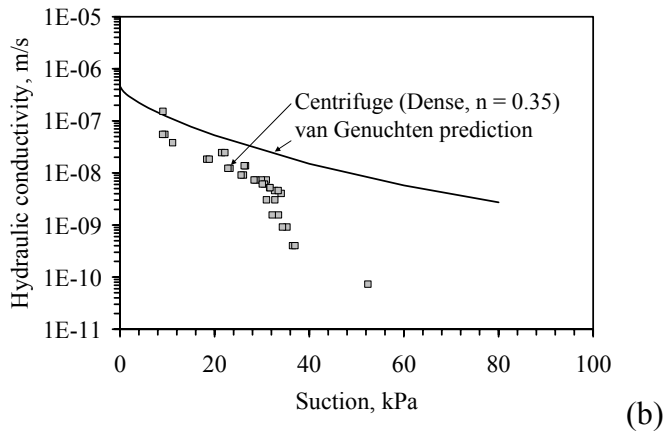
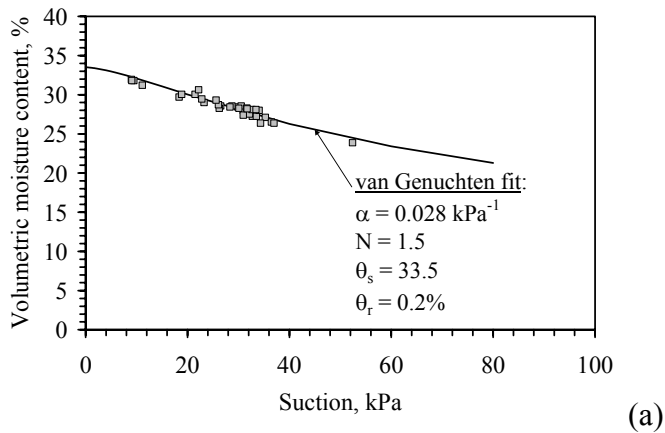


Figure 11.5: (a) Fitted WRC using the van Genuchten model; (b) K-function predicted using the van Genuchten-Mualem model using the WRC parameters

## Chapter 12: Evaluation of Centrifuge Testing Issues

### 12.1 OVERVIEW

This chapter includes an evaluation of the validity of the assumptions necessary in the analysis and an assessment of different issues specific to centrifuge testing. Section 8.4 includes an assessment of the different issues specific to determination of the hydraulic characteristics using a centrifuge permeameter. The shapes of the moisture content and suction profiles and the validity of open flow boundary conditions are assessed. The results from the consistency tests on the K-function and WRC values for different combinations of the control variables (inflow rate  $Q$  and centrifuge speed  $\omega$ ) are also analyzed. Two experimental issues specific to centrifuge testing are discussed in this section, the effect of the g-level and increased stress on the hydraulic characteristics, and the role of hysteresis in steady-state infiltration. This section also includes an evaluation of required test duration for a centrifuge test, an analysis of the different variables that contribute to the testing time, and a comparison between the testing times of the centrifuge and conventional tests.

### 12.2 SUCTION AND MOISTURE CONTENT PROFILES DURING CENTRIFUGATION

The key assumption of previous centrifuge permeameter approaches to determine the hydraulic characteristics of unsaturated soils (*e.g.*, the unsaturated flow apparatus, UFA and the steady-state centrifugation method, SSC) is that the moisture content and suction profiles are uniform throughout the specimen. This is not necessarily a key assumption in this study as the suction profile is measured using tensiometry. Nonetheless, the hydraulic conductivity calculation is greatly simplified if the suction head gradient is negligible (*e.g.*,  $K_{target}$ ). If the suction gradient is negligible, the

tensiometers can be eliminated from the equipment layout, which may be useful for rapid hydraulic characterization tests. Further, a uniform distribution in moisture content is important from a measurement standpoint, as the vertical TDR waveguide infers the average moisture content along its length. A non-uniform distribution in moisture content in the soil along the length of the TDR waveguide may lead to biased measurements.

The moisture content profiles observed during Test I in the prototype permeameter (*e.g.*, Figure 8.4) indicate that the moisture content distribution is highly non-linear during transient infiltration, but is relatively constant through the specimen during steady-state infiltration. The TDR observations are consistent with the observations from gravimetric water content measurements at the end of this test and reported in the technical literature (*e.g.*, Figure 8.6 and Figure 5.38). The zone near the outflow face of the permeameter was found to have slightly higher moisture content due to boundary effects. Nonetheless, this higher moisture content at the base was much less significant than that observed in the 1-g column infiltration tests described in Chapter 4. Overall, the observations from Test I indicate that the moisture content measurements made using the vertical TDR waveguide in Tests II through IV can be considered representative of the average moisture content.

The suction profiles measured during the hydraulic characterization permeameter tests provide additional information. Specifically, the measurements tend to support the development a constant suction gradient in the specimen during steady-state water flow, but only during specific situations. A comparison is made in Figure 12.1 between the suction profile measured at the driest point of Stage III-6 and the theoretical solution to Richards' equation in the centrifuge. The suction profiles are similar for the parameters shown in the figure, although the suction value measured by the middle tensiometer does not match perfectly with the theoretical suction profile. Further, the theoretical solution

with a suction at the outflow boundary of 13 kPa matches the data well, indicating that the suction at the outflow face is not necessarily saturated during steady-state flow.

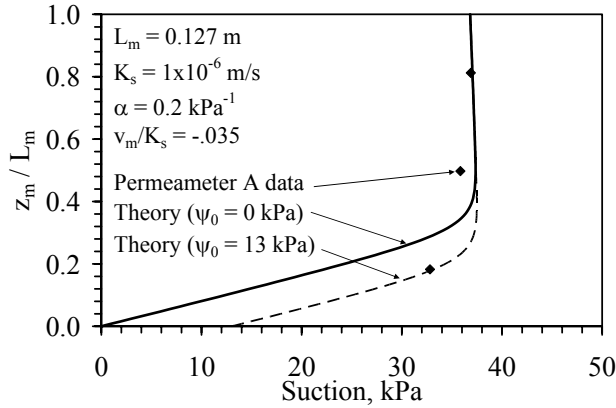


Figure 12.1: Theoretical and measured suction profiles with boundary condition effects

During the infiltration tests in the small permeameter, the two upper tensiometers gave similar suction measurements only during combinations of high  $N_{r,mid}$  values ( $> 40$ ), and low inflow rates ( $< 20$  ml/hr). In reality, the combinations of control variables that will result in a negligible suction gradient will depend on the characteristics of the soil, the uniformity of inflow distribution, and outflow boundary conditions. Nonetheless, the suction profiles indicate that the average moisture content measurements of the vertical TDR are representative of the moisture content in the upper zone of the specimen.

### 12.3 BOUNDARY CONDITION EFFECTS

Another important assumption for hydraulic characterization of unsaturated soils using the centrifuge permeameter is that the bottom boundary is freely draining and does not have a significant impact on the suction profiles in the specimen (open flow). The two permeameters in Test I had different bottom boundary conditions (filter paper and wire screen for one and a nonwoven geotextile for the other). Nonetheless, the results from both permeameters in Test I are relatively consistent, and were freely-draining

during steady-state infiltration. The suction measured by the tensiometers near the interface (at a height of 50 mm) indicates that the suction at breakthrough was about 10 kPa, and the moisture content profiles indicate that only the TDR near the interface showed only slightly higher moisture content values than the rest of the profile.

This observation is in contrast with the observations from the 1-g column infiltration tests. Profiles of degree of saturation at steady-state flow are shown in Figure 12.2(a) for the 1-g column and in Figure 12.2(b) for the centrifuge permeameter (during Stage III-6). The initial moisture content profiles are also shown for reference. The moisture profiles in the 1-g column indicate that a capillary break influenced the moisture profile, causing accumulation of water at the interface between the soil and the geosynthetic drainage layer at the base of the profile. Although the degree of saturation in the upper portion of the profile is low and relatively constant (approximately 0.58), the degree of saturation near the base is greater than 0.95. The degree of saturation distribution at steady-state flow in the centrifuge indicates that a capillary break did not influence the outflow of water from the profile. The entire soil profile has a degree of saturation of about 0.58. There is a slight inclination in the saturation profile near the base, indicating that the capillary break occurred but only had a small zone of influence.

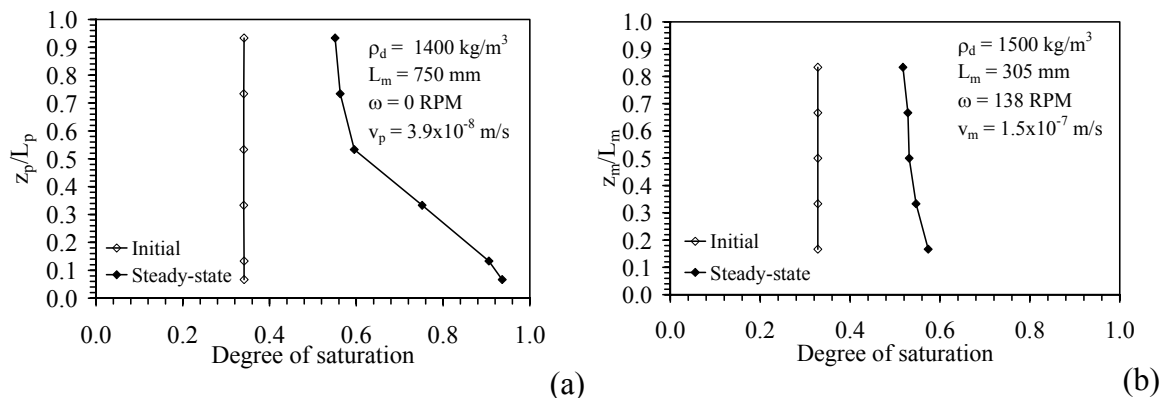


Figure 12.2: Boundary effects on moisture content profiles: (a) Column; (b) Centrifuge

The bottom tensiometers consistently showed suction values greater than 20 kPa during Tests II through IV. The moisture profiles observed in the hydraulic characterization tests are likely closer to the profiles with  $\psi_0 > 0$  shown in Figure 3.8(c) than to the profile with a saturated bottom boundary. This indicates that the outflow boundary was freely-flowing, because if it were not, a zero-suction condition would have likely developed at the interface. Conditions that indicate a zero-suction boundary condition were noted in some tests where compression of the pore air was observed, occurring only at low  $N_{r,mid}$  values ( $< 40$ ) and high flow rates ( $> 20$  ml/hr). Further, the suction at the base tended to follow the trend in the upper tensiometer, indicating that the zone of soil affected by the boundary condition changes with  $N_{r,mid}$ . This behavior is consistent with the theoretical suction profiles in Figure 3.8(a).

As discussed in Section 3.5, the water pressure must be zero for water to exit from a porous media (*i.e.*, in order to develop a convex meniscus). This conceptual discussion is valid for a soil without support or filter material, and it may only be valid for the first occurrence of outflow from the soil. For instance, if water is continually supplied to the outflow face, the air-water meniscus at the outflow face may not necessarily need to be at saturation. Although the capillary break effect is a transient water flow phenomenon, the suction at capillary breakthrough may have some indication as to the suction at the outflow interface. One hypothesis is that steady-state flow occurs at the capillary breakthrough suction as long as water is continuously drained from the filter material. Another similar hypothesis is that the zero-suction boundary is not in the soil into the filter material, making the outflow face of the soil have a suction value greater than zero. These hypotheses provide some indications as to why the suction at the base of the permeameter was significantly greater than zero.

The RichTexNg program, presented in Appendix B, was developed to analyze the impact of different boundary conditions. Although not the focus of this study, this program is presented to highlight an approach that can be used in future studies to investigate boundary conditions. The results of a simulation predicting the moisture content profiles during transient drainage of an initially saturated specimen with  $v_m = 0$  (no inflow) and  $N_{r,mid} = 10$  are shown in Figure 12.3. The outflow boundary condition used in this analysis is a freely-draining boundary (*e.g.*,  $K_{outflow} = K_{soil}$ ). This figure indicates that the bottom of the soil gradually becomes de-saturated during centrifugation. This may also occur for a freely-draining boundary condition for steady-state flow.

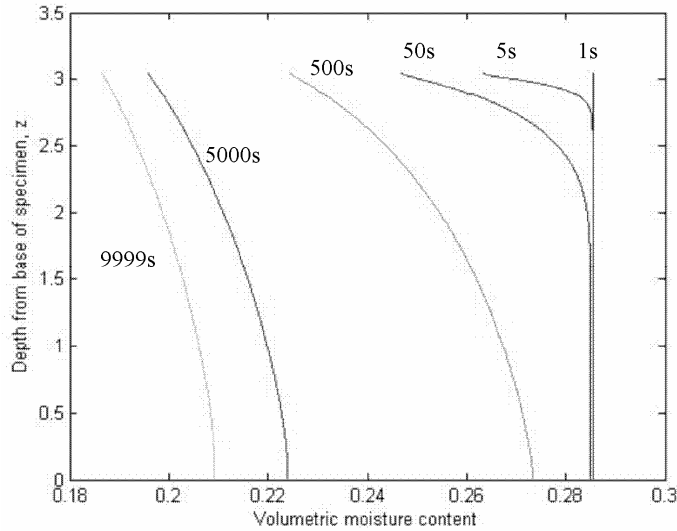


Figure 12.3: RichTexNg results showing de-saturation of the bottom boundary ( $v_m = 0$ )

#### 12.4 IMPACT OF CENTRIFUGATION ON THE HYDRAULIC CHARACTERISTICS

The centrifuge can induce significant body forces on a soil specimen. Even though the focus of this study is on the determination of the hydraulic characteristics of unsaturated soils, the deformation of the soil during centrifugation and corresponding changes in hydraulic characteristics were also evaluated in this study. Accordingly, the



stress-deformation properties of the RMA Soil Type II are investigated in this section. The deformation characteristics of both saturated and unsaturated soil specimens are considered. Conventional consolidation data was used to assess the deformation of saturated specimens under the effective stresses expected in the centrifuge, while linear elasticity was used to estimate the deformation of an unsaturated specimen under compacted conditions. Specimens used in infiltration tests in the centrifuge will likely have deformation characteristics bounded between these two conditions.

A one-dimensional oedometer test was performed on a saturated soil specimen, compacted at the optimum moisture content (12%) to porosity of 0.35. This curve portrays the worst-case settlement conditions for the soil, as it is saturated. The porosity – effective stress relationship is shown in Figure 12.4. As the soil is compacted (*i.e.*, remolded), a clear preconsolidation pressure was not observed.

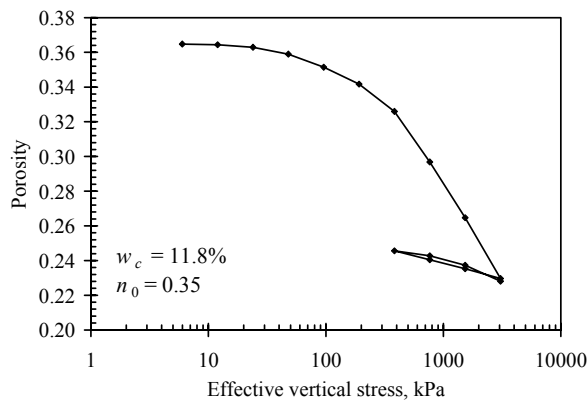


Figure 12.4: Results from oedometer test on a saturated, compacted specimen

The shape of the  $n$ - $\log \sigma'$  curve is too nonlinear to use a single value of  $C_c$  and  $C_R$ . Accordingly, the variation in the slope of the  $n$ - $\log \sigma'$  curve with effective stress was calculated, as shown in Figure 12.5. The data in this figure can be used to calculate settlements using a piece-wise linear formula:

$$\Delta S = \sum_{i=2} C_i (1-n) L \log \left( \frac{\sigma_i}{\sigma_{i-1}} \right) \quad (12.1)$$

where  $\sigma_i'$  and  $\sigma_{i-1}'$  are the effective stresses at the previous and current loading increments,  $L$  is the length of the specimen, and  $C_i$  is the slope of the  $n$ -log  $\sigma'$  curve.

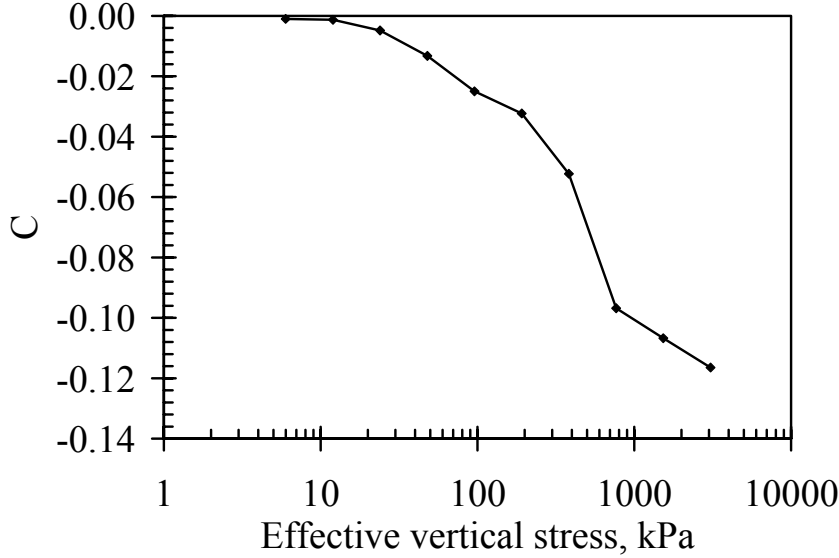


Figure 12.5: Incremental change in slope for the  $n$ -log  $\sigma'$  curve in Figure 12.4

The vertical effective stress in a centrifuge specimen is straightforward to calculate. The buoyant unit weight is used to calculate the effective stress, as follows:

$$\sigma'(z_m) = \rho' \omega^2 (r^2 - r r_i) = \rho' \omega^2 \left[ z_m^2 - r_0 z_m - L_m (r_0 - z_m) \right] \quad (12.2)$$

where  $r_i$  is the inlet radius equal to  $r_0 - L_m$ ,  $\rho'$  is the buoyant soil density and  $\sigma'(z_m)$  is the effective stress at each value of  $z_m$ . Plots of the vertical effective stress with the normalized specimen height are shown in Figure 12.6. For the geometry of the centrifuge permeameter and for clay compacted to a porosity of 0.35 at  $w_c = w_{opt}$ , the vertical stress varies nearly linearly with height. However, this curve is quadratic for larger specimens.

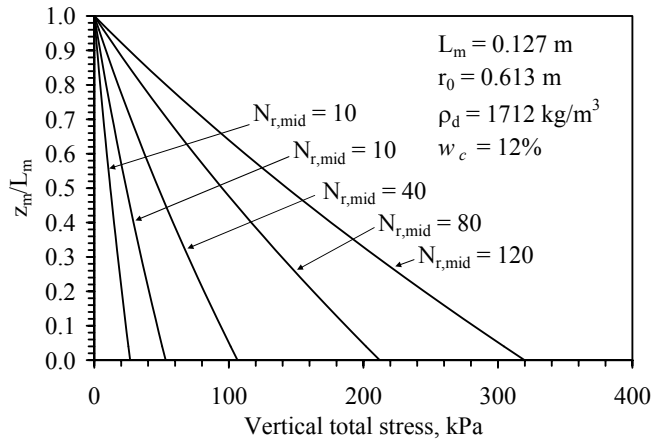


Figure 12.6: Effective stress profiles (Note: geometry is for centrifuge permeameter)

The changes in porosity with height for different g-levels are shown in Figure 12.7(a), using the data in Figure 4.32 and Equation (12.1). A change in porosity of about 0.02 was noted for the g-levels shown in this Figure. The relationships for  $K_s$  vs.  $n$  shown in Figure 5.4 indicate that this upper bound estimate of settlement should result in less than an order of magnitude change in  $K_s$ . The surface settlement with g-level for a saturated specimen is shown in Figure 12.7 (b). The settlements shown in this figure indicate that 3 mm of settlement over the length of the specimen (127 mm) can be expected for testing up to  $N_{r,mid} = 120$ .

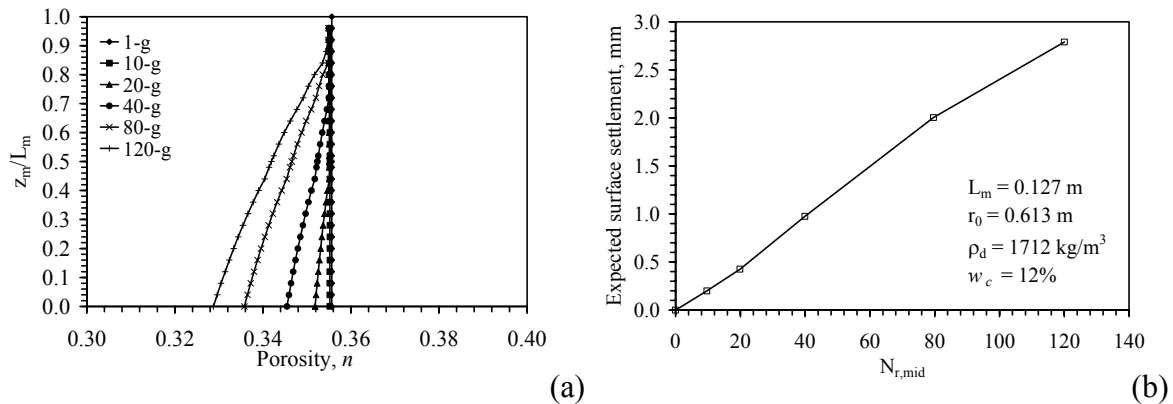


Figure 12.7: Calculations using e-log  $\sigma'$  curve (a) Void ratio; (b) Surface settlement

Unlike saturated soils, unsaturated soils have an increased stiffness due to the increased inter-particle contact stress related to the suction (Cho and Santamarina 1996). In unsaturated soils, volume changes can arise due to the changes in the two independent stress state variables, the net normal stress  $\sigma_n = \sigma - u_a$  and the matric suction  $\psi = u_a - u_w$ . A schematic of a stress-deformation surface for unsaturated soils is shown in Figure 12.8 (Fredlund 2006). It is difficult to obtain the independent relationships between porosity and net normal stress and between void ratio and suction. This makes the stress-deformation path during centrifuge loading even more complex, as both the suction and net normal stress change with g-level and inflow rate.

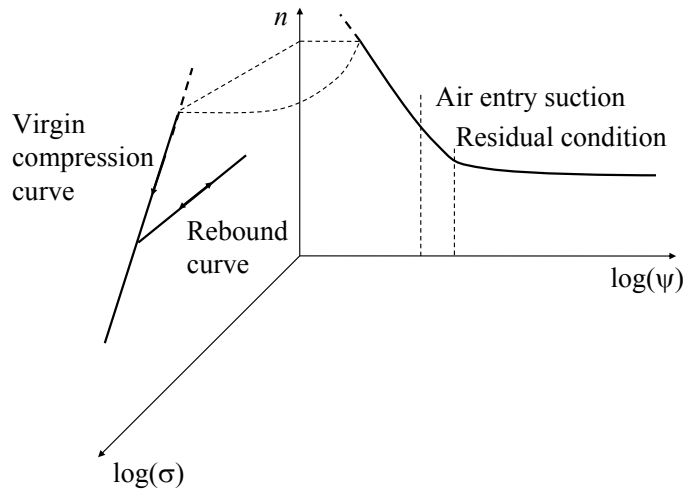


Figure 12.8: Schematic stress-deformation surface for unsaturated soils (Fredlund 2006)

If air pressure is equal to zero, then the total stress is equal to the net normal stress. The centrifuge acceleration increases the total stress on the specimen in a manner similar to the effective stress. Assuming that the suction remains constant for an unsaturated soil and that the air pressure is negligible, changes in total stress will drive settlement. The net normal stress in the centrifuge can be calculated using the total unit weight of the soil, as follows:

$$\sigma_n(z_m) = \rho_t \omega^2 (r^2 - rr_i) = \rho_t \omega^2 [z_m^2 - r_0 z_m - L_m (r_0 - z_m)] \quad (12.3)$$

where  $\rho_t$  is the total density of the soil. The net normal stress distribution with height for a specimen compacted to a porosity of 0.35 and  $w_c = w_{c,opt}$  is shown in Figure 12.9.

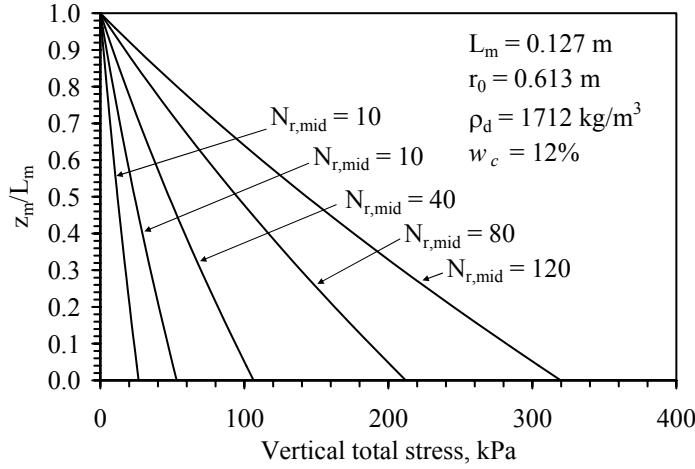


Figure 12.9: Net normal stress profiles (Note: geometry is for centrifuge permeameter)

In the case that there is no infiltration during centrifugation, water will tend to flow out of the specimen, leading to an increase in suction throughout the specimen. The final distribution in suction for a constant g-level is given by Equation (5.7). In the case of steady-state infiltration during centrifugation, the suction is constant throughout the profile, predicted using Equation (3.21). A lower bound on the deformation expected during centrifugation can be obtained through investigation of a compacted specimen, having constant suction. Settlement of an unsaturated soil specimen during centrifugation can be estimated using linear elasticity. In this case, the constrained stiffness can be used to relate volume changes with net normal stress, as follows:

$$\varepsilon_z = M \sigma_{n,r} \quad (12.4)$$

where  $\sigma_{n,r}$  and  $\varepsilon_z$  are the net normal stress and strain in the longitudinal direction, and M is a function of suction. Models have been proposed to estimate the constrained stiffness

of unsaturated soils (Mendoza *et al.* 2005) as well as the shear modulus of unsaturated soils (Cho and Santamarina 1996; Vassalo *et al.* 2006). The models differ in that the model of Mendoza *et al.* (2005) only considers the effect of suction on the constrained stiffness, while the models of Cho and Santamarina (1996) and Vassalo *et al.* (2006) consider both the effects of suction and net normal stress on the shear modulus. The latter two studies normalize the effects of suction and net normal stress so that the models are dimensionally correct, while that of Mendoza *et al.* (2005) does not. It is necessary to assume a value of Poisson's ratio to estimate the constrained modulus for the unsaturated soil specimen. Although the approaches that consider the impact of both suction and net normal stress on the shear wave velocity have a more theoretically correct basis, the motivation of this discussion is to only to obtain a preliminary estimate of the elastic settlement for purposes of determining how much the hydraulic conductivity will change during centrifugation. Accordingly, the simpler model of Mendoza *et al.* (2005) was used in this study. This model is empirically based on controlled-suction oedometer tests performed on a CL clay having properties similar to the clay used in this study. The model is given by:

$$M_{\max} = \alpha_M f(e) [\ln(\psi_0)]^{n_M} \quad (12.5)$$

where  $M_{\max}$  is the constrained modulus for small strains with units of kPa,  $\alpha_M$  and  $n_M$  are fitting parameters that were found to be 30000 and 1.35 from the oedometer tests, and  $f(e)$  is the void ratio function defined by Hardin and Black (1968), given by:

$$f(e) = \frac{(2.397 - e)^2}{1 + e} = \frac{(2.397 - 1.397n)}{1 - n} \quad (12.6)$$

The variation in constrained modulus with suction is shown in Figure 12.10. The empirical model shows a nonlinear increase in modulus with suction on a log-log scale.

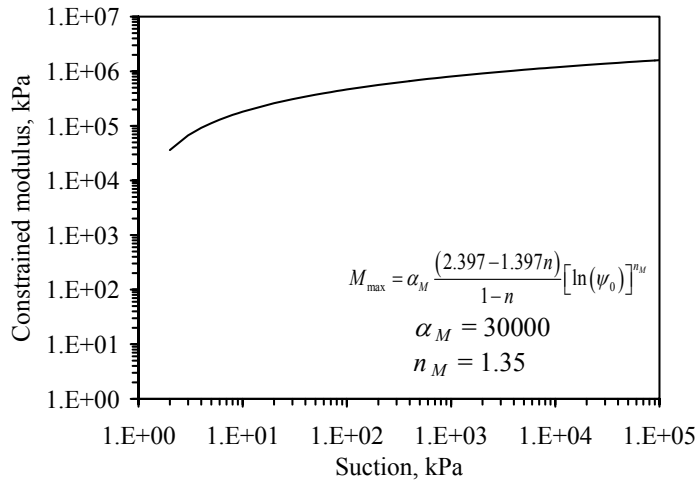


Figure 12.10: Constrained modulus predicted from the model of Mendoza *et al.* (2005)

Tensiometer measurements indicate that the initial suction in a specimen of RMA Soil Type II compacted to a porosity of 0.35 and  $w_c = w_{c,opt}$  is approximately 120 kPa. Using this suction value and neglecting friction on the container sides, the strain distribution in a centrifuge specimen is calculated using the estimated value of  $M_{\max}$  and Equation (12.4), as shown in Figure 12.11. An increase in strain with depth is observed.

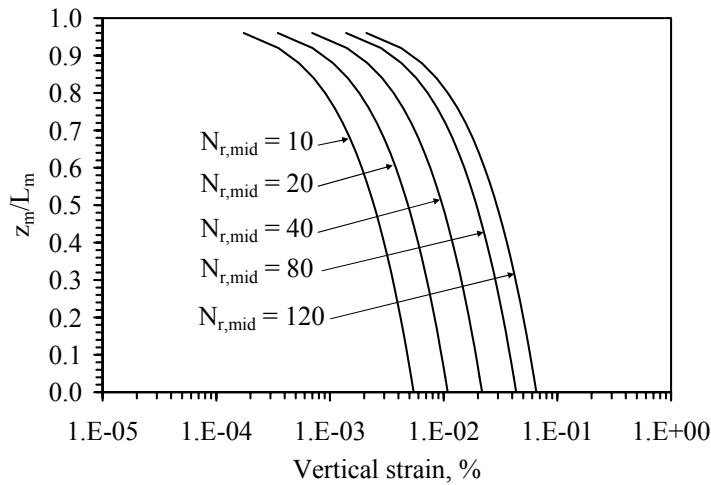


Figure 12.11: Calculated strains with specimen height (for a constant suction of 120 kPa)

The surface settlement was calculated by integrating the strain distribution, as shown in Figure 12.12. The settlement for an as-compacted specimen is on the order of 0.32 mm at a g-level of 120, about 10 times less than that of a saturated specimen. The settlement for a specimen during infiltration (with a suction of 10 kPa) is 0.85 mm. This corresponds to a change in porosity of 0.03. The relationships for  $K_s$  vs.  $n$  shown in Figure 5.4 indicate that this settlement will cause a negligible change in  $K_s$ . It is assumed that changes in  $K_s$  with  $n$  reflect changes in soil structure, so the K-function should shift by a similar amount. Also, the changes in  $e$  are not expected to have an appreciable effect on the WRC except perhaps near saturation (indicated by the data in Figure 5.17).

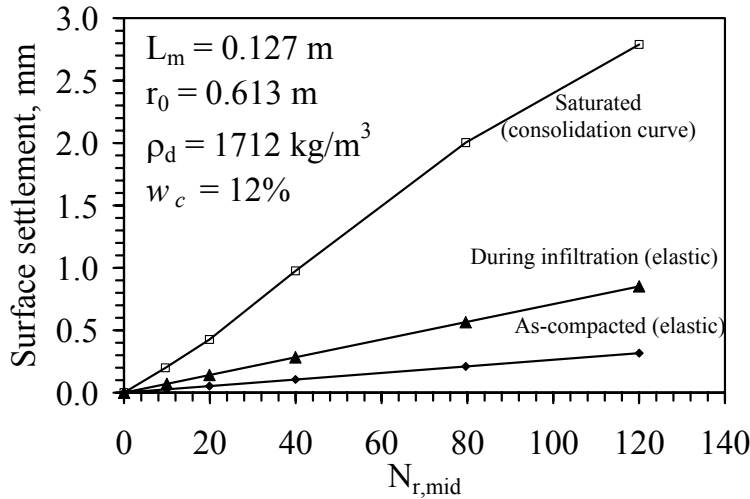


Figure 12.12: Bounds on expected surface settlement with  $N_{r,mid}$

A hydraulic characterization test in the centrifuge permeameter was performed on a specimen having similar conditions to those shown in Figure 12.4 ( $n = 0.35$ ,  $w_c = w_{opt} - 3\%$ ). The surface of the specimen observed after infiltration in the centrifuge permeameter at  $N_{r,mid} = 120$  is shown in Figure 12.13. A minimum suction of 10 kPa was observed in this specimen during infiltration. Approximately 0.76 mm of surface settlement was observed for the 127 mm-long specimen. This is slightly lower than the



surface settlement calculated for a specimen using the elastic approach and a suction of 10 kPa in the constrained modulus relationship from Mendoza *et al.* (2005). Based on the observed settlement,  $K_s$  is expected to change by less than an order of magnitude. The specimen shown in Figure 12.13 shows less settlement near the permeameter wall due to side friction, but the area of influence seems to be small.

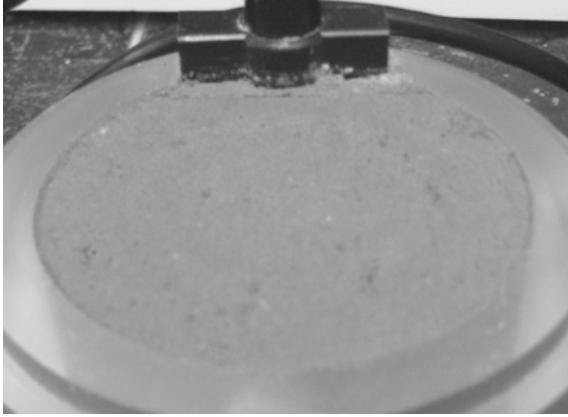


Figure 12.13: Surface of a dense specimen ( $n = 0.35$ ) after infiltration at 120 g

Centrifuge testing on a given soil having a certain density should involve: (i) consideration of the deformation of a saturated and an unsaturated specimen under the maximum centrifuge acceleration expected in a test; (ii) consideration of the change in  $K_s$  for the predicted change in porosity, and evaluate if this change is appreciable; (iii) minimizing cracking due to arching over instrumentation; (iv) quantification of any volume changes and reporting the hydraulic characteristics as corresponding to the actual (tested) density if different from the initial (target) density.

The hydraulic characteristics defined for different  $N_{r,mid}$  values using Approach *i* in Test II are shown in Figure 12.14. This figure indicates that the hydraulic characteristics have similar shapes and magnitude for  $N_{r,mid} > 20$  when plotted as a function of suction, moisture content, and degree of saturation. The difference between

the data above and below  $N_{r,mid} = 20$  is likely due to the non-uniform suction distribution and the effects of the outflow boundary at low  $N_{r,mid}$ . The similarity of the K-functions at higher  $N_{r,mid}$  values indicates that the increased stresses due to centrifugation do not have a significant effect on the hydraulic characteristics, either by settlement or by changes in capillarity.

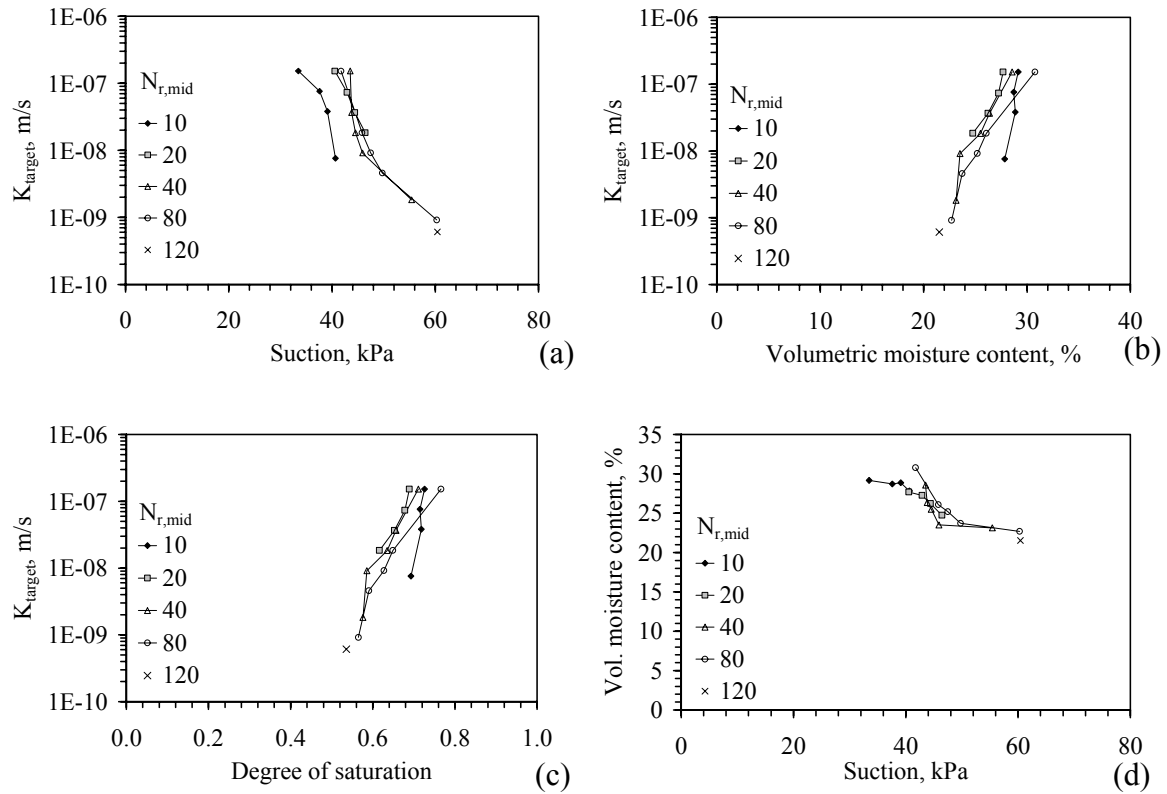


Figure 12.14: Effect of g-level on the K-function: (a)  $K-\psi$ ; (b)  $K-\theta$ ; (c)  $K-S$ ; (d)  $\psi-\theta$

A summary of the expected surface settlement using elastic analyses (by calculating the confined modulus for the average minimum suction of 10 kPa observed during infiltration) the bounds on the surface settlement from elastic analysis of an as-compacted specimen and the  $n-\log \sigma'$  curve, and the observed settlement during the different centrifuge permeameter tests is shown in Table 12.1. The settlement was

measured at the end of the test using a Vernier caliper. This measured settlement indicates that deformation in the specimen is negligible. However, because the stress distribution in the specimen is highly nonlinear, there may be some change in void ratio lower in the specimen that is not evident at the surface. Friction on the permeameter sidewall also contributes to a lack in visible surface settlement. Pictures of the surface settlement at the end of Test III are shown in Figure 12.15. Negligible settlement was observed during this test.

Table 12.1: Summary of expected and observed settlements

Test name	Calculated settlement values			Observed settlement *
	Low (Elastic, $\psi_{\text{initial}} = 120 \text{ kPa}$ )	Expected (Elastic, $\psi_{\text{min}} = 10 \text{ kPa}$ )	High (Saturated $e\text{-log}\sigma'$ )	
	mm		mm	
IA	0.10	0.25	1.50	0.22
IB	0.10	0.25	1.50	0.27
IIA	0.20	0.50	2.50	0.84
IIB	0.20	0.50	2.50	0.64
IIIA	0.25	0.63	2.40	0.64
IIIB	0.25	0.63	2.40	0.76
IVA	0.30	0.75	2.00	0.76
IVB	0.30	0.75	2.00	0.69

\* Observed settlement is an average across the specimen area, and is sensitive to the smoothness of the upper surface

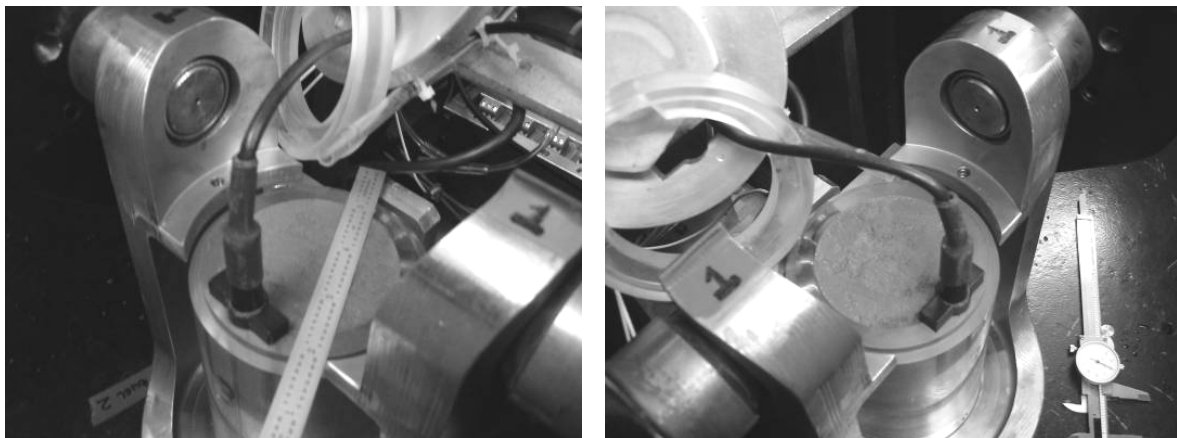


Figure 12.15: Views of the top of the soil specimen at the end of Test III

## 12.5 EVALUATION OF TESTING TIMES FOR HYDRAULIC CHARACTERIZATION

Although the use of steady-state water flow in a centrifuge permeameter permits the use of simplifying assumptions to determine the hydraulic characteristics, the time required to perform the test is still an important issue to consider. To fully determine the shape of the K-function and WRC, several different steady-state flow rates must be applied to a specimen. In this sense, rapid attainment of steady-state water flow allows the hydraulic characteristics to be defined for a soil in a reasonable time. However, the time required to reach steady-state flow depends on the hydraulic conductivity of the soil as well as the imposed flow rate and centrifuge acceleration. Clays with low saturated hydraulic conductivity may require a prohibitively long time to reach steady-state water flow. As mentioned in Chapter 3, the same steady-state suction profiles attained at steady-state water flow in a 1.35 meter soil profile can be obtained in a 0.127 m permeameter in a much shorter time. This shorter time is not only due to the shorter length of the specimen, but also because the driving force for water flow is scaled up by the g-level. The travel time  $t_{travel}$  required for water entering the top of a specimen of length  $L_m$  to reach the bottom is given by:

$$t_{travel} = \frac{L_m}{(v_m/n)} = \frac{nL_m}{KN_{r,mid}} \quad (12.7)$$

where  $v_m/n$  is the seepage velocity. This equation assumes that the suction gradient is negligible during centrifugation. Although this is certainly not the case during transient water flow, this assumption does allow the travel time to be estimated without the use of a numerical solution for Richards' equation. To calculate the travel time, a value of hydraulic conductivity must still be assumed. The simplest case to start from would be centrifugation of an initially saturated specimen. If an infiltration rate and g-level are applied to this specimen such that the imposed hydraulic conductivity is below  $K_s$ , then a

saturated “wetting front” will pass through the specimen. The hydraulic conductivity at the point of this front will always equal the saturated hydraulic conductivity.

Substituting different values of  $K$  into Equation (12.7) allow travel time curves to be defined for a constant  $\omega$  (or  $N_{r,mid}$ ), as shown in Figure 12.16. These curves indicates that more than 100 hrs are required to reach steady-state flow through a specimen having a saturated hydraulic conductivity less than  $10^{-9}$  m/s. This duration is certainly better than a similar column test conducted in 1-g, but may still be unfeasible.

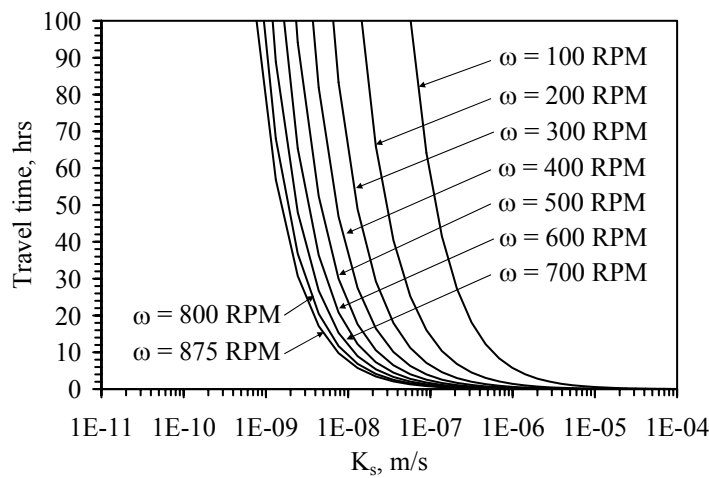


Figure 12.16: Estimated travel times for soils with different initial  $K_s$  values

Scaling relationships are another important resource to highlight the benefit of decreased testing time in a centrifuge environment. Scaling relationships can be defined using dimensional analysis (Buckingham 1914; Butterfield 1999a) or direct comparison of the geometrical, kinematic, and dynamic variables in a centrifuge model and a 1-g prototype (Dell’Avanzi *et al.* 2004). Variables that do not depend on gravity can be scaled 1:1, such as suction, volumetric moisture content, intrinsic permeability, density, viscosity, and temperature. Of particular interest to this study are scaling relationships

for length, acceleration, hydraulic conductivity, discharge velocity, and travel time. The length scale factor  $\lambda$  is defined as:

$$\lambda_L = \frac{L_p}{L_m} \quad (12.8)$$

where  $L_p$  is the length of the 1-g prototype and  $L_m$  is the length of the centrifuge model. The acceleration scale factor relationship was defined in Equation (3.6), where the g-level  $N_r$  is the scale factor. It is conventional in geotechnical modeling to assume that the length scale factor is equal to  $N_{r,mid}$ . The scaling relationship for the transit time of flow through a specimen during steady-state flow can be defined using the length of the model and the seepage velocity:

$$\lambda_t = \frac{\left( \frac{L_p}{v_p / n} \right)}{\left( \frac{L_m}{v_m / n} \right)} = \frac{L_p}{L_m} \frac{v_m}{v_p} = \frac{L_p}{L_m} \frac{KN_{r,mid}}{K} = \lambda_L N_{r,mid} = N_{r,mid}^2 \quad (12.9)$$

This equation indicates that tests involving steady-state water flow in a 1-g setting can require much longer times than in the centrifuge. However, data from a 1-g test can be used to estimate the time required to reach steady-state flow in the centrifuge. Specifically, the time to reach steady state flow in column experiments can be scaled down by  $N_{r,mid}^2$  to estimate the time required to reach steady state flow in the centrifuge.

The times for definition of the hydraulic characteristics using the centrifuge permeameter are summarized in Table 12.2. In most of the stages at least three points on the K-function and WRC were defined using steady-state water flow. Approximately 4 to 13 hours were required to reach steady-state water flow for each combination of inflow rate and g-levels investigated in the different stages, with an average of 7.5 hours. Except for the tests that included an investigation of hysteresis, the tests were started from near-saturated conditions and initially involved drying (by imposing lower  $K$  values). Starting

from near-saturated conditions yielded the lowest time to reach steady-state flow, as inflow is not required to fill empty void spaces, but is immediately seen as outflow.

Table 12.2: Summary of testing times in hydraulic characterization tests

Centrifuge stage number	Approach	Hysteresis path	Number of points on K-function and WRC	Stage duration (hrs)	Stage duration (days)
II-1	<i>i</i> (constant $\omega$ , varying $Q$ )	Drying	4	36	1.5
II-2	<i>i</i> (constant $\omega$ , varying $Q$ )	Drying	4	23	1.0
II-3	<i>i</i> (constant $\omega$ , varying $Q$ )	Drying	5	34	1.4
II-4	<i>i</i> (constant $\omega$ , varying $Q$ )	Drying	5	30	1.2
II-5	<i>i</i> (constant $\omega$ , varying $Q$ )	Drying	1	8	0.4
III-1	<i>i</i> (constant $\omega$ , varying $Q$ )	Drying	3	14	0.6
III-2	<i>i</i> (constant $\omega$ , varying $Q$ )	Drying	3	37	1.5
III-3	<i>i</i> (constant $\omega$ , varying $Q$ )	Drying	4	35	1.5
III-4	<i>i</i> (constant $\omega$ , varying $Q$ )	Drying	4	24	1.0
III-4	<i>i</i> (constant $\omega$ , varying $Q$ )	Wetting	3	11	0.5
III-5	Darcy's law (constant $K$ )	N/A	3	19	0.8
III-6	<i>iii</i> (varying $\omega$ and $Q$ )	Drying	10	93	3.9
III-6	<i>iii</i> (varying $\omega$ and $Q$ )	Wetting	9	114	4.7
III-7	<i>ii</i> (varying $\omega$ , constant $Q$ )	Drying	9	59	2.4
III-7	<i>ii</i> (varying $\omega$ , constant $Q$ )	Wetting	7	29	1.2
IV-1	<i>i</i> (constant $\omega$ , varying $Q$ )	Drying	4	36	1.5
IV-2	<i>i</i> (constant $\omega$ , varying $Q$ )	Drying	4	20	0.9
IV-3	Darcy's law (constant $K$ )	N/A	1	17	0.7
IV-4	<i>i</i> (constant $\omega$ , varying $Q$ )	Drying	3	24	1.0
IV-4	<i>i</i> (constant $\omega$ , varying $Q$ )	Wetting	3	11	0.5

The factors that contributed to the time required to reach steady-state water flow include the magnitude of the imposed flow rate (longer testing times for lower  $v_m$ ), the magnitude of the g-level (faster for higher g-levels), the response time of the tensiometer, and whether the soil was wetted or dried. The testing time was not sensitive to the soil compaction conditions, although the three soils had different  $K_s$  values. Wetting requires more time to reach equilibrium, likely because the tensiometers require a longer time to equilibrate for wetting than for drying. The total time of a centrifuge permeameter test

depends on the number of points desired on the K-function and WRC, the range of steady-state K values desired, and whether wetting and drying is investigated.

The three characterization approaches used in the centrifuge permeameter approach have in different testing times. A strict comparison is not possible as the different approaches led to different ranges of steady-state  $K$  values. Approaches *i* and *iii* lead to longer testing times than Approach *ii*. These approaches require equilibration under a new flow rate at each intermediate testing phase. Of the factors listed above, the testing time was found to be most sensitive to low flow rates. Accordingly, Although Stage III-6 only required 8.7 days to determine both the wetting and drying paths, the majority of the testing duration is attributed to the lowest imposed  $K$  values.

In general, the required testing time is significantly less than that predicted using a travel time analysis (Figure 12.16). This is likely because it is not required for a “front” to pass through the soil before fully attaining steady-state water flow. However, the required testing times are consistent with those obtained using the UFA and SSC approach for coarse-grained soils summarized in Table 5.4.

The testing times observed in the centrifuge permeameter are much shorter than those required in the 1-g column tests summarized in Table 5.4. The difference in testing times can be attributed to the differences in the lengths of the centrifuge permeameter and columns, the driving force (1-g vs.  $N_{r,mid}$ ), the boundary condition effects, the compaction conditions, and the initial degree of saturation. The large-scale columns were affected more significantly by the capillary break than the centrifuge permeameter tests. In the large-scale columns, water had to accumulate in a significant length of the soil profile to reach the capillary breakthrough suction in order for outflow to occur. The density of the soils played a more important role in the time required to reach steady-state water flow,



as the columns were started from as-compacted conditions. Looser soil has higher moisture storage capacity, so more fluid must be supplied before steady flow occurs.

Table 12.3 summarizes the scaling factor ( $N_{r,mid}$ ) required to satisfy geometric similarity between the large-scale columns and the centrifuge permeameter, along with the actual testing time and the testing time scaled by  $N_r^2$  [Equation (12.9)]. For the longer columns (C, D, E), the scaled times to reach steady-state flow are consistent with those obtained experimentally in the centrifuge permeameter (less than 1 day). Similarity is attained using a low  $N_{r,mid}$  for the shorter columns, so the scaled testing time is still high. The suction profiles in the centrifuge tests conducted at  $N_{r,mid} = 10$  had similar suction profiles to those observed in the column tests.

Table 12.3: Scaled testing times for large-scale columns

Column test - stage number	$N_{r,mid}$ (equivalent)	Actual time until steady-state (hrs)	Scaled time until steady-state (hrs)
A	2.4	136	24
B	2.4	150	27
C-1	5.9	946	27
C-2	5.9	302	9
D-1	10.6	1795	16
D-2	10.6	450	4
E-1	11.8	1990	14
E-2	11.8	450	3
F	1.1	359	318
G	1.1	209	185
H	1.1	222	196
I	1.1	103	91

## **Chapter 13: Summary and Conclusions**

### **13.1 SUMMARY OF RESEARCH OBJECTIVES**

The goal of this study was to develop and verify a centrifuge permeameter used to determine the hydraulic characteristics of unsaturated soils. By providing a new experimental approach with the capability of determining the hydraulic characteristics in a reasonable time frame using straightforward interpretation of the data, this study helps promote the use of experimentally-derived hydraulic characteristics in geotechnical engineering practice.

The objectives of this study stated in the introduction were reached as follows:

- Quantitative variables were defined for the variables governing the hydraulic behavior of unsaturated soils, specifically the volumetric moisture content (volume of water storage in the soil pores), the suction (the pressure difference between the air and water in the soil pores), and hydraulic conductivity (impedance to water flow).
- A literature review was presented to summarize the experimental and predictive techniques that have been used to determine the hydraulic characteristics of unsaturated soils, the variables that affect the hydraulic characteristics, and typical results for different soils obtained with different methods. Specific focus was placed on the use of transient or steady-state water flow in experimental approaches.
- A firm theoretical background was developed for water flow in unsaturated soils in a field setting and a centrifuge permeameter setting, focusing on the spatial distribution in suction and moisture content in soil profiles undergoing steady-state water flow.
- A clay of low plasticity was selected to verify the use of the centrifuge permeameter. The hydraulic and mechanical properties of this clay were investigated to assess the

impact of porosity, saturated hydraulic conductivity, and increased stresses (during centrifugation) on the hydraulic characteristics of the unsaturated clay.

- The water retention curve (WRC) for an unsaturated, compacted clay of low plasticity were determined using transient tests (hanging column, pressure plate, and evaporation tests), while the K-function was determined using transient tests (analysis of the outflow data from the pressure plate) and steady-state tests (infiltration column tests). The K-function was also estimated using predictive models that involve parameters determined from fitting smooth curves to the experimental WRCs.
- The centrifuge permeameter was developed to impose inflow rates and centrifuge speeds to reach target hydraulic conductivity values ranging from  $1 \times 10^{-5}$  to  $1 \times 10^{-11}$  m/s. Inflow was found to be controlled well using an infusion pump, was reliably transferred from the stationary environment to the spinning centrifuge at high g-levels, and was well distributed across the top surface of the specimen using an infiltration distribution cap. Outflow was collected in a reservoir, and was monitored satisfactorily with time using a pressure transducer. Trends in the outflow transducer were found to follow the imposed inflow rate at steady-state water flow.
- Instrumentation was developed and validated that allow simultaneous determination of the suction and moisture content profiles during steady-state flow, permitting thorough analysis of the hydraulic characteristics with a minimum number of assumptions. A time domain reflectometry (TDR) system was developed to measure the average moisture content of the specimen.
- The theoretical distribution of the suction profiles indicate a zone of constant moisture content in the upper portion of the specimen, which permitted the use of a vertically-oriented TDR waveguide to measure the average moisture content in the upper portion of the specimen. The TDR setup was found to provide minimal

disturbance of the water flow path and caused negligible settlement in the specimen. Tensiometers were developed for this study to measure the suction profile in the specimen. The tensiometers were used to reliably measure suctions over 100 kPa, and were used to measure suctions up to 65 kPa during long-duration infiltration tests.

- The layout of the instruments permits non-destructive and non-intrusive measurements. A data acquisition system was developed and tested to provide continuous measurements during centrifugation. The data acquisition and visualization tools were found to be fully functional under g-levels up to 600 g.
- The lessons learned from the theoretical investigations of water flow in unsaturated soils were synthesized to develop a testing approach used to determine the hydraulic characteristics of an unsaturated soil specimen in the centrifuge permeameter. Specifically, a target hydraulic conductivity value was calculated by assuming that the suction gradient in the specimen is zero. Different combinations of inflow rates and centrifuge speeds were selected to reach a wide range of target hydraulic conductivity values. Specimens of the clay were compacted and saturated outside of the centrifuge before the hydraulic characterization test was performed.
- The hydraulic characteristics were defined for the clay compacted at three different water contents to a relatively low porosity of 0.35. The centrifuge permeameter allows measurement of the suction distribution with the specimen length, so the assumption of a zero suction gradient can be assessed. Similarly, the impact of the outflow boundary on the suction profile can be assessed.
- The effect of centrifugation on the hydraulic characteristics was assessed by determining the WRC and K-function at a constant g-level by changing the inflow rate. This was then repeated for different g-levels. Also, the surface settlement was

measured periodically throughout the tests, which permits an assessment of the settlement of the unsaturated clay during centrifugation.

- Hysteresis in the hydraulic characteristics during steady-state water flow was assessed by imposing a combination of steady inflow rates and centrifuge speeds that gradually dried the specimen (to reach lower hydraulic conductivity values), then subsequently wetted the specimen (to return to high hydraulic conductivity values).
- Compare the results from the centrifuge permeameter approach with those from conventional testing approaches.
- The development of the centrifuge permeameter permitted the use of steady-state water flow to determine the hydraulic characteristics of unsaturated soils in a reasonable time frame with straightforward interpretation of the results.

### **13.2 CONCLUSIONS FROM HYDRAULIC CHARACTERIZATION**

- Moisture content profiles measured using TDR and gravimetric sampling indicate that the moisture content is uniformly distributed in the upper portion of the specimen during steady-state infiltration. For the clay tested in this study, this is particularly the case for g-levels greater than 40, infiltration rates less than 20 ml/hr, and target hydraulic conductivity values less than the saturated hydraulic conductivity.
- Tensiometer measurements in the hydraulic characterization permeameter indicate that the suction profile becomes more uniform with height in the specimen as the g-level increases and as the inflow rate decreases.
- The suction gradient was observed to be negligible in the upper portion of the specimen compared to the g-level in the calculation of the hydraulic conductivity. However, the suction gradient is not negligible when considering the full length of the soil specimen due to boundary condition effects.

- The use of a target hydraulic conductivity value, calculated by assuming that the suction gradient is negligible, was found to be acceptable for the compacted clay.
- The key assumption in the UFA and SSC centrifuge permeameter approaches is partially correct. Specifically, the assumption of a zero suction gradient, which was found to be valid in the upper portion of the specimen, permits a straightforward calculation of the hydraulic conductivity. However, the use of the average moisture content throughout the specimen to define the K-function is inaccurate as the moisture content is not necessarily uniform throughout the specimen.
- Open flow boundary conditions were found to be satisfactorily attained, with the suction and moisture content in the specimen reaching equilibrium with the imposed, steady water flow. The outflow boundary was observed to cause negligible impedance to moisture flow, and can be considered freely-draining, except in the case when compression of the pore air occurred. Compression of the pore air was observed when imposing high inflow rates at low g-levels.
- The outflow boundary condition was observed to play a minimal role in the determination of the hydraulic characterization of unsaturated soils using the centrifuge permeameter. This is in contrast to steady-state infiltration column tests performed at 1-g, where the outflow boundary had a significant impact on the suction and moisture content distributions in the specimen height.
- The suction profiles measured during steady-state infiltration indicate that the zone of the specimen near the base (0 to 23.2 mm) had a lower suction than in the upper zone of the specimen (63.2 to 127 mm). Also, a slight increase in moisture content was observed near the outflow face of the specimen. However, because only three points on the suction profile were obtained, conclusions as to the particular value of suction at the outflow face cannot be made. Specifically, evidence of a saturated bottom

boundary was not observed. Even if the bottom boundary is saturated, the height of saturated soil is small. Specifically, the lower tensiometer, which is 23.2 mm from the base of the profile, typically measured suction values greater than 10 kPa (a water pressure head equal to -1.0 m of water).

- It is likely that the suction boundary condition changed with the imposed infiltration rate and g-level. Specifically, the suction measured by the lower tensiometer followed the same trend as the upper tensiometer, indicating that the suction at the outflow face changes with g-level and infiltration rate during steady-state flow.
- The difference between the suction values measured by the upper and lower tensiometers tended to decrease with increasing g-level (above 40) and decreasing inflow rate (below 20 ml/hr), indicating that the suction profile is more uniform in such situations in the clay tested in this study.
- For the soil investigated in this study, when the same target hydraulic conductivity was imposed on the specimen (by using constant a constant ratio between the inflow rate and g-level), the measured suction and moisture content gave the same values for g-levels greater than 40. Above this g-level, the suction profile is consistently uniform in the upper portion of the specimen.
- The moisture content and suction values observed in the clay specimen during steady-state infiltration in the centrifuge permeameter reflect value closer to saturated conditions (moisture content near porosity and suction close to zero) than those observed in hydraulic characteristics presented in the technical literature.
- Although the inflow rate and g-level were imposed to reach target hydraulic conductivity values ranged over four orders of magnitude, the corresponding suction values only ranged from 10 to 60 kPa, and the degree of saturation ranged from 0.65 to 0.95.

- Tendencies in the WRC or K-function toward a residual condition were not observed in the range of target hydraulic conductivity values investigated. This indicates that the water phase was continuous, and that steady-state infiltration occurs under nearly-saturated conditions.

### **13.3 CONCLUSIONS FROM EVALUATION OF TESTING ISSUES**

- Negligible surface settlement was observed in a series of infiltration tests on compacted clay specimens in the centrifuge permeameter, despite the significant increase in total stress due to centrifugation.
- The WRCs and K-functions obtained by changing the inflow rate at different g-levels were similar, indicating that centrifugation has a negligible effect on the hydraulic characteristics.
- Negligible hysteresis was observed in the WRC and K-function for the low plasticity clay investigated in this study when the target hydraulic conductivity was changed in gradual increments using different combinations of g-level and infiltration rates. This is not consistent with the observations in the technical literature. However, this can be explained by the fact that steady-state infiltration was used in this study, and that the suction increments were relatively small.
- Hysteresis played a more significant role when large changes in target hydraulic conductivity (several orders of magnitude) were imposed. In this case, the changes in moisture content and suction were more extreme, and entrapment of air was likely.
- Centrifugation was found to decrease the time required to reach steady-state water flow and uniform moisture content profile in a soil specimen from several months (for conventional tests) to less than a week.
- Testing time was found to be sensitive to the instrumentation response time, and the hydraulic conductivity value being imposed. Testing time was dominated more by



the infiltration rate imposed rather than the g-level. The focus of this study was on validation of the centrifuge permeameter approach, so production testing using the centrifuge permeameter could be more expeditious.

#### **13.4 CONCLUSIONS FROM VERIFICATION OF CENTRIFUGE RESULTS**

- The K-functions and WRCs determined using the centrifuge permeameter are similar to those determined using conventional techniques, despite different specimen densities. Due to the relatively low suctions measured in the centrifuge permeameter tests, only the results from low suctions in the pressure plate, hanging column, infiltration column were used for comparison.
- Different from the conventional characterization tests, the results of the centrifuge permeameter are particularly sensitive to the performance and calibration of the instrumentation (tensiometers and TDR). The calibration of the TDR equipment was found to be sensitive to the density of a compacted soil, which may change during centrifugation. The calibration curve of the tensiometers may drift during long duration tests, changing the magnitude of the measured suction.
- The moisture contents measured by the centrifuge permeameter were higher than those obtained using conventional techniques for the soil used in this study, which may be due to the use of steady-state water flow.
- The slopes of the K-functions (when plotted either as a function of suction or moisture content) were consistent for the different tests, regardless of compaction conditions. Often the change in  $K$  with increasing suction (or decreasing volumetric moisture content) is more useful in design than the actual position of the K-function when plotted as a function of suction or moisture content. In other words, the position of the K-function will change as the saturated hydraulic conductivity of the specimen changes (*e.g.*, during volume changes). However, if the slope of the K-

function is constant, then only the change in hydraulic conductivity with changing suction or moisture content is necessary for a design.

- The K-functions were found to have a similar shape to the Campbell model, with a log-linear decrease in hydraulic conductivity with suction. However, the fitting parameters for this model are not realistic. Specifically, a saturated hydraulic conductivity that was not representative of the soil was used in the model to obtain a good fit to the data.
- K-functions predicted from the shape of the WRC were found to provide a poor fit to the K-functions determined using the centrifuge permeameter. Major inaccuracies may result when using estimates of the K-function from theory instead of measured K-functions in geotechnical engineering projects.

### **13.5 RECOMMENDATIONS FOR FUTURE RESEARCH**

A recommendation for future research would be to compare the experimental results with numerical solutions to Richards' equation in the centrifuge using different boundary conditions (constant suction, constant flow rate, constant impedance). The program RichTexNg provided in the appendix is particularly suited for this research. Several studies have used the assumption of open flow boundary conditions (Conca and Wright 1990; 1998). However a mathematical representation for this boundary condition has not been developed for analytical or numerical solutions to Richards' equation (Simunek and Nimmo 2005; Bear *et al.* 1986).

The development of a K-function from the centrifuge permeameter suitable for design purposes is an important topic of future research. This likely will depend on an in-depth investigation of the physics of the K-function, such as the value of K when there is occluded air, a continuous air phase, and when the water phase is occluded. A possible K-function that fits the experimental data is shown in Figure 13.1.

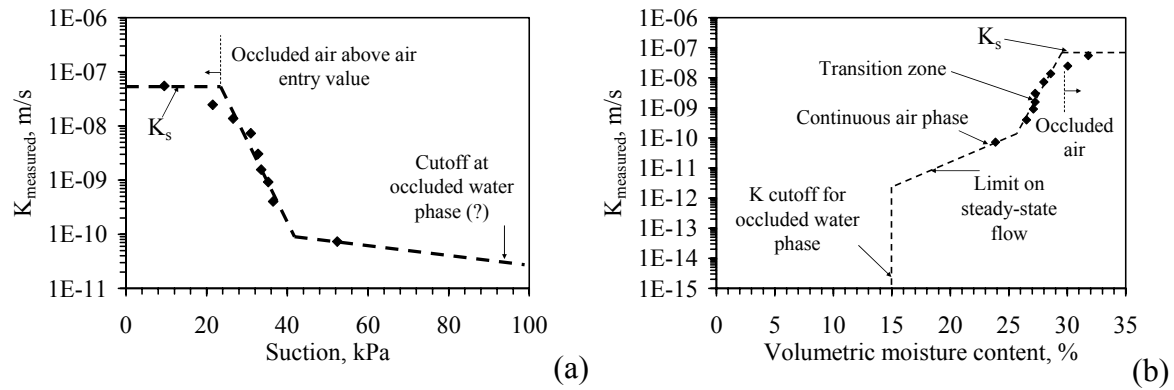


Figure 13.1: Design K-function: (a)  $K-\psi$ , (b)  $K-\theta$

The impact of increased stresses during centrifugation on the hydraulic properties should be assessed using improved settlement measurements. Specifically, surficial settlement measurements or internal settlement distribution using photographic or electromagnetic techniques can be implemented. The distribution of strain throughout the length of the specimen would permit a better understanding of the void ratio that is controlling the measurement of the hydraulic conductivity. Alternatively, calculation of the expected settlement can also be improved through better estimation of the stiffness of an unsaturated soil. Placing bounds on the expected settlement using consolidation test results and elastic deformation analysis is useful in estimating the possible impact of volume change on the hydraulic characteristics.

The calibration and interpretation of the instrumentation results can still be improved. The TDR calibration curves can be refined by adding additional data from soils with different densities and compaction water contents. Further research is required to quantify changes in the electrical field around the TDR waveguide due to the presence of the acrylic permeameter (with constant dielectric permittivity) and the soil (with variable dielectric permittivity). As the suctions measured during infiltration testing are generally less than 100 kPa, the upper limit of the tensiometers (*e.g.*, the suction at

cavitation) is acceptable. However, there are still unresolved issues related to drift in the intercept value of the tensiometer calibration equation. This has been noted at the beginning of different tests during calibration of the tensiometers. This offset likely occurs each time the tensiometer is powered on or off. Further, drift in the calibration equation with time during centrifugation may lead to the differences in hydraulic characteristics determined during different stages of a long-term test.

The analysis of the K-function and WRC can be enhanced by using transient variation in moisture content and suction during changes in infiltration. This can be done using inverse analysis or the instantaneous profile method. It is clear that there is a significant amount of information in the transient variation in the suction and moisture content time series. Drying stages (*e.g.*, without infiltration) are useful to investigate the hydraulic characteristics at higher suction values.

The centrifuge permeameter can also be used to investigate water flow or volume change in scale models of soil profiles, as the stress profiles in the centrifuge can be used to replicate those in field soil profiles. Possible applications include infiltration into retaining walls, infiltration into expansive soil profiles, infiltration into soil profiles to predict groundwater recharge rates, and modeling of landfill cover systems.

The centrifuge permeameter can also be used to investigate capillary pressure and relative permeability curves for multi-phase flow situations. In particular, the centrifuge permeameter can be used to determine the capillary pressure required for removal of oil or contaminants from a specimen, or it can be used to determine the residual saturation of contaminants. Tensiometry and TDR can be used to evaluate the assumptions made in studies in the petroleum literature for the determination of oil-water capillary pressure curves. The centrifuge is also useful for pore water sampling. Soil cores can be spun in the centrifuge to expel pore water, which can be collected for chemical analysis.

## **Appendix A: Lessons Learned from Preliminary Tests**

### **A.1 OVERVIEW OF PRELIMINARY TESTS**

This section includes an assessment of TDR, tensiometry, and outflow transducer measurements, focusing on situations in which reliable and unreliable results may be obtained. Data from these instruments are used to interpret undesirable scenarios that may be encountered during testing, such as problems with air-pressure release, imposed infiltration rates being greater than the capacity of the soil, and leaks. In addition, soil preparation conditions resulting in poor performance of the centrifuge permeameter approach are discussed, focusing on conditions associated with settlement, prohibitive testing times, a change in the experimental layout, or improved measurement quality.

Several preliminary tests were conducted in this study with the goals of understanding the data obtained from the instrumentation during different types of infiltration tests, verifying the functionality of the instrumentation and plumbing during centrifugation, and checking the validity of some of the assumptions listed in Section 6.2. These tests were not conducted in a systematic manner, and in some cases were not useful to determine the hydraulic characteristics of the soils being tested. Nonetheless, the lessons learned from these preliminary tests build confidence in both the procedures adopted in the hydraulic characterization testing program (the scope and results of which are presented in Chapter 9) as well as the results obtained from these tests. A summary of the different tests is presented in Table A.1, including the compaction conditions as well as the test motivation and comments concerning the observations made during each test. It should be noted that each test included two nearly identical specimens, which were very useful in assessing problems and investigating variability in results.

As will be discussed in the next section, early tests were conducted with heat dissipation units (HDUs) to measure the suction. This approach was abandoned early due to interference between the electrical noise and the small signal of the HDU. Nonetheless, they were still included (and monitored) in most of the early tests because they are necessary to provide a hydraulic seal on the back side of the permeameters. Most of the early tests were conducted with the braided-wire mesh as an outflow filter. This approach led to satisfactory filtration, but was abandoned because small particles were observed in the filter after infiltration testing. The hydraulic characteristics inferred when using this filter were not significantly different from those obtained when using a filter paper and wire screen, but it was unclear if they were gradually becoming less permeable with time as more particles become collected in the pores of the filter. Filter paper was used in later tests as it can be replaced to ensure repeatable conditions.

The early tests were conducted to verify the plumbing and to obtain the optimal procedures to restrain the cables during testing. Several improvements were made to the centrifuge during these tests to better secure wires and connectors. The two early tests were conducted without an air escape port due to delays in machining, but allowed investigation of the sealing capabilities of the permeameter. In the first test, a build-up of air pressure was observed in the outflow transducer concurrent with leaks from the side of the permeameter. Leaks were not observed in the second test.

Many of the early tests were conducted to investigate the sensitivity of the TDR. In early tests, build-up of air pressure in the outflow reservoir caused water to accumulate in the specimen. This resulted in large changes in moisture content inferred using TDR. However, once the air-release port was installed and water was permitted to freely enter the outflow reservoir, changes in moisture content observed during the tests were smaller. In fact, these changes in were so small that the sensitivity was deemed too low.

Table A.1: Summary of test conditions for preliminary centrifuge permeameter tests

Test name	Starting date	Soil conditions					Measurement details			Motivation	Comments
		Relative compaction <sup>1</sup>	Compaction water content	$\pm w_{opt}$ <sup>2</sup>	Porosity $n$	$K_s$	Outflow boundary condition	Moisture content monitoring	Suction monitoring		
		(%)	(%)	(%)		m/s					
1a	9/28/2006	79.9	11.1	-0.9	0.44	5.2E-07	Braided wire mesh	Vertical TDR	HDU profile	Plumbing check with soil	No air escape, leak at HDU port
1b	9/28/2006	80.0	11.1	-0.9	0.44	5.1E-07	Braided wire mesh	Vertical TDR	HDU profile	Plumbing check with soil	No air escape, leak at HDU port
2a	10/1/2006	89.4	14.3	2.3	0.37	1.9E-08	Braided wire mesh	Vertical TDR	HDU profile	Plumbing check with soil	No leaks, but no air escape (port installed after test)
2b	10/1/2006	80.2	14.3	2.3	0.44	4.8E-07	Braided wire mesh	Vertical TDR	HDU profile	Plumbing check with soil	No leaks, but no air escape (port installed after test)
3a	10/13/2006	80.1	12.7	0.7	0.44	4.9E-07	Braided wire mesh	Vertical TDR	HDU profile	HDU check	No leaks, but no air escape (port installed after test)
3b	10/13/2006	80.1	12.7	0.7	0.44	4.8E-07	Braided wire mesh	Vertical TDR	HDU profile	HDU check	Settlement, cracking around HDUs, high noise in HDUs
4a <sup>3</sup>	10/28/2006	N/A	N/A	N/A	N/A	N/A	None	None	None	Outflow pressure transducer calibration	Inflow = Outflow
4b <sup>3</sup>	10/28/2006	N/A	N/A	N/A	N/A	N/A	None	None	None	Outflow pressure transducer calibration	Inflow = Outflow
5a	11/1/2006	83.0	12.0	0.0	0.42	1.8E-07	Braided wire mesh	Vertical TDR	HDU profile	HDU check	High noise in HDUs, low TDR sensitivity
5b	11/1/2006	80.2	12.0	0.0	0.44	4.7E-07	Braided wire mesh	Vertical TDR	HDU profile	HDU check	High noise in HDUs, low TDR sensitivity
6a <sup>4</sup>	11/18/2006	N/A	N/A	N/A	0.40	1.2E-04	Braided wire mesh	None	HDU profile	Inflow fluid distribution	Inflow is distributed uniformly
6b <sup>4</sup>	11/18/2006	N/A	N/A	N/A	0.40	1.2E-04	Braided wire mesh	None	HDU profile	Inflow fluid distribution	Inflow is distributed uniformly
7a <sup>4</sup>	11/21/2006	N/A	N/A	N/A	0.40	1.2E-04	Braided wire mesh	Vertical TDR	HDU profile	TDR sensitivity test using high K soil	Low TDR sensitivity
7b <sup>4</sup>	11/21/2006	N/A	N/A	N/A	0.40	1.2E-04	Braided wire mesh	Vertical TDR	HDU profile	TDR sensitivity test using high K soil	Low TDR sensitivity
8a	11/24/2006	86.4	12.2	0.2	0.39	5.5E-08	Braided wire mesh	Vertical TDR	HDU profile	TDR sensitivity test for low K soil	Low TDR sensitivity
8b	11/24/2006	87.5	12.2	0.2	0.39	3.7E-08	Braided wire mesh	Vertical TDR	HDU profile	TDR sensitivity test for low K soil	Low TDR sensitivity
9a	12/1/2006	92.0	12.2	0.2	0.39	5.5E-08	Braided wire mesh	Vertical TDR	HDU profile	TDR sensitivity test for low K soil	Low TDR sensitivity
9b	12/1/2006	92.1	12.2	0.2	0.39	3.7E-08	Braided wire mesh	Vertical TDR	HDU profile	TDR sensitivity test for low K soil	Low TDR sensitivity
10a	12/6/2006	70.0	12.3	0.3	0.51	1.5E-05	Braided wire mesh	Vertical TDR	HDU profile	TDR sensitivity test for low K soil	Improved TDR sensitivity due to enlarged recess
10b	12/6/2006	69.9	12.3	0.3	0.51	1.5E-05	Braided wire mesh	Vertical TDR	HDU profile	TDR sensitivity test for low K soil	Improved TDR sensitivity due to enlarged recess
11a	12/12/2006	80.3	12.3	0.3	0.44	4.6E-07	Filter paper/wire screen	Vertical TDR	HDU profile	Hydraulic characterization	Successful test
11b	12/12/2006	80.3	12.3	0.3	0.44	4.5E-07	Filter paper/wire screen	Vertical TDR	HDU profile	Hydraulic characterization	Successful test
12a	3/1/2007	90.1	12.0	0.0	0.37	1.4E-08	Filter paper/wire screen	Vertical TDR	Tensiometer profile	Hydraulic characterization	Tensiometer cavitation, leaks, excessive inflow
12b	3/1/2007	90.1	12.0	0.0	0.37	1.4E-08	Filter paper/wire screen	Vertical TDR	Tensiometer profile	Hydraulic characterization	Tensiometer cavitation, leaks, excessive inflow

<sup>1</sup>  $\rho_{d,max} = 1900 \text{ kg/m}^3$

<sup>2</sup>  $w_{opt} = 12\%$

<sup>3</sup> No soil (N/A - not applicable)

<sup>4</sup> Monterey sand #30 (Dr = 50%) used in these tests

To meet this shortcoming, several of the preliminary tests focused on new designs for the TDR receptacle with the goal of increasing the sensitivity. In the first permeameter design, the two outer prongs of the TDR waveguide were fully embedded in the permeameter wall in the design of the first TDR recess. In addition, only half of the

central, conducting prong of the TDR waveguide was exposed to the soil. In this case, the TDR measurements were dominated by the acrylic. When submerged in water alone, a TDR waveguide will infer a dielectric permittivity of approximately 80, whereas a value of about 20 was obtained when the TDR waveguide and permeameter were submerged in water together (without soil). The permeameters were milled to maximize the area of the TDR waveguide in contact with the soil.

New permeameters were also constructed, consistent with the design shown in Chapter 5. The TDR measurements were also sensitive to the initial moisture content in the soil before starting an infiltration test. Test 6 was conducted to investigate the uniformity of moisture distribution in the specimen, and it was determined that an even amount of water was passed through each hole in the top distribution cap. However, it was determined that preferential flow paths tended to form in the specimen when starting from as-compacted conditions. In this case, infiltrating moisture will only reach the sides of the permeameter by diffusion. This is especially the case for loose soils and soils with high hydraulic conductivity, such as the sand used in test 7a. It was determined that using a layer of filter papers at the top of the specimen would aid in diffusion of the inflow across the area of the specimen, and that starting from saturated conditions would minimize the number of preferential flow paths forming in the specimen. The final preliminary test focused on the performance of the relatively new tensiometer system, which required provisions to deal with cavitation, as will be discussed next.

## **A.2 INTERPRETATION OF INSTRUMENTATION RESULTS**

A set of data from the outflow transducer is shown in Figure A.1 for an infiltration test into a permeameter without soil. This figure also shows the output from the g-meter. In the first part of the test, a known volume of water was placed in the outflow reservoir ( $V_i = 10$  ml), and the speed was ramped up to 700 RPM ( $N_{r,mid} = 400$ ).



Next, a constant inflow of 100 ml/hr was applied to the permeameter. This was close to the highest inflow rate expected in the experimental program. After reaching steady-state flow conditions, the centrifuge speed was decreased in increments. This figure indicates that the slope of the outflow curve is constant during steady-state outflow at a constant g-level, but the slope is not the same at different g-levels. The behavior noted in Figure A.1 is consistent with the expected behavior of the outflow transducer described above.

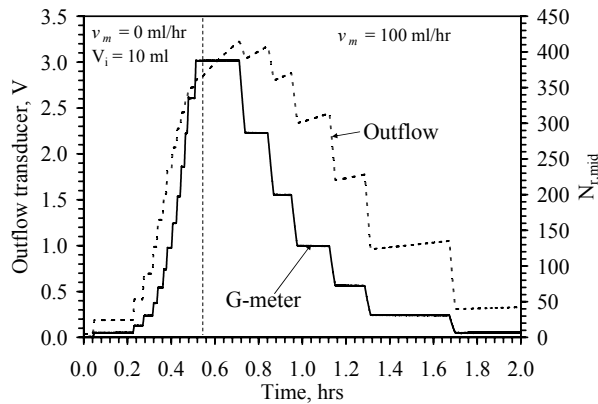


Figure A.1: Actual outflow data from an infiltration test without soil

Some differences occur when a test is conducted with soil. As mentioned, a delay in the steady-state slope is expected due to transient flow under changes in the control variables. However, more importantly, when a high infiltration rate is applied to a very dry soil specimen during centrifugation, compression of the pore air may occur. Differences in actual measurements from those expected will be observed because the pressure in the air requires some time to diffuse through the specimen, and additional time may be required for the air to exit through the pressure relief hole in the outflow reservoir. Specifically, compression of the pore air may cause a false increase in the pressure measured by the outflow transducer, which mimics the pressure increase observed during steady-state water flow. In this case, the measurements of the outflow transducer are characterized by a sawtooth pattern, as shown in Figure A.2, which occurs

due to air incrementally being pushed through the relief hole. In this case, the centrifuge was stopped and the air-release pipe was cleared. Steady-state outflow was soon observed after this time. The slope of the steady-state outflow was much less than that observed after this time. The slope of the steady-state outflow was much less than that during the increments of air-pressure build-up. The sawtooth pattern observed in Figure A.2 can also be characterized by fewer (but larger) jumps, so adequate time should be maintained at each inflow increment to ensure that the outflow is reasonable.

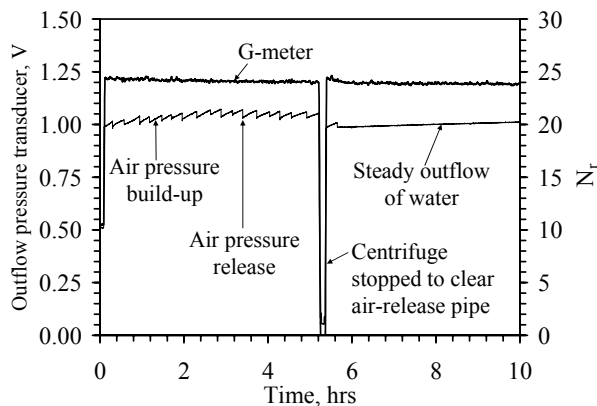


Figure A.2: Outflow transducer results indicating compression of the pore air

Another important issue with the outflow transducer that may be encountered are measurements at the high outflow volume or pressure ranges. Specifically, the outflow transducer can be used to indicate when the reservoir may become full, as shown in Figure A.3(a). In the test portrayed in this figure, steady-state water flow is supplied to the outflow reservoir. At  $t = 78$  hrs, the outflow transducer for Specimen *A* shows an increase in magnitude as the reservoir reached its capacity. After this, the water level entered into the permeameter (effectively increasing the height of the water column on the transducer). The outflow transducer may also reach its capacity when there is a large volume of water in the reservoir at high  $g$ -levels, as shown in Figure A.3(b). Outflow transducer B does not show a response to changes in outflow (steady-state during this test) or to changes in  $g$ -level (signified by the shifts in magnitude). However, once the  $g$ -

level is reduced the pressure on the transducer will eventually be less than the capacity, after which consistent results are observed between the two transducers.

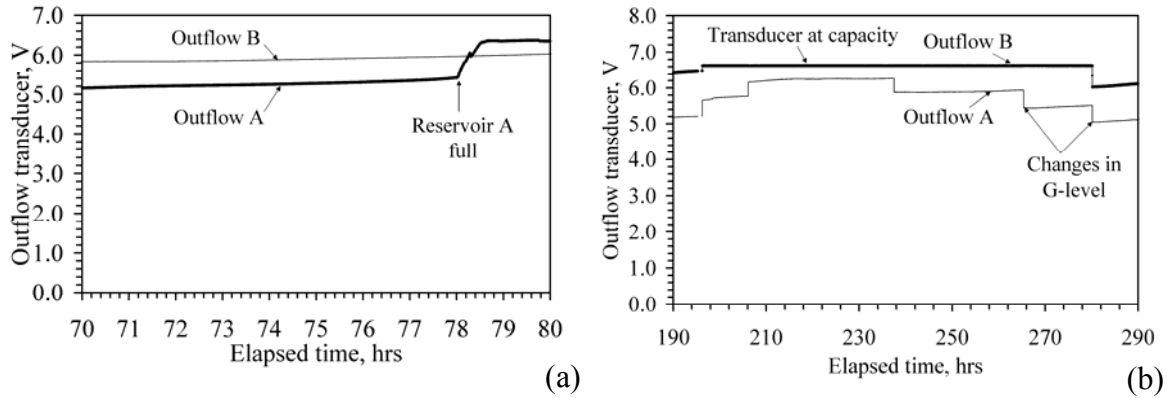


Figure A.3: High outflow measurements: (a) Reservoir full; (b) Transducer capacity

As mentioned, the main inconsistency between the actual and expected TDR measurements is the sensitivity to changes in flow conditions. Although this inconsistency may be due to insensitivity in the system, care must be taken to ensure that the moisture content of the soil does not vary significantly over the changes in flow conditions imposed on the specimen. This is particularly the case for clays and dense soils. An example of a test with particularly insensitive TDR measurements is shown in Figure A.4. The data in Figure A.4(a) indicates that several inflow rates were applied at  $N_{r,mid} = 50$ . A decrease in the inflow rate by a factor of 5 did not lead to a significant change in moisture content throughout this period of the test as shown in Figure A.4(b).

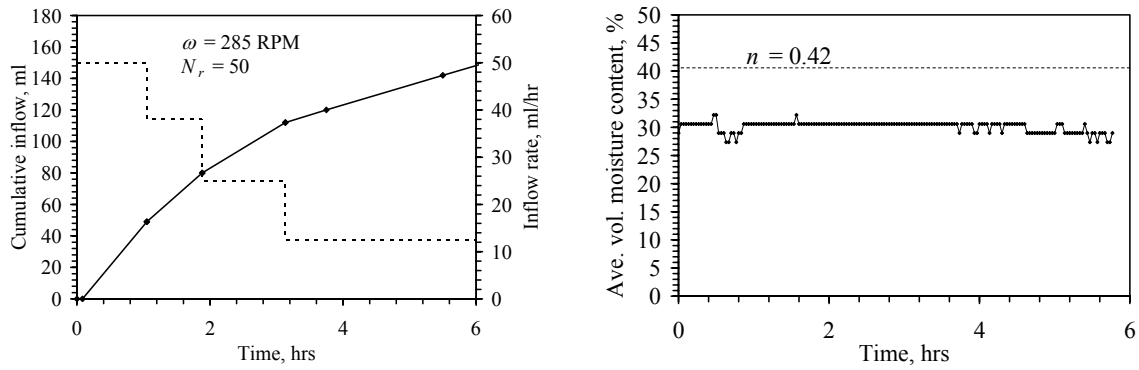


Figure A.4: Infiltration test on sand; (a) Inflow data; (b) Volumetric moisture content

After the TDR recesses were enlarged, more consistent changes in moisture content with changes in inflow rate were observed. The TDR results from a test in which the centrifuge speed was constant but the infiltration rate was increase is shown in Figure A.5. This figure indicates that steady-state flow occurs relatively quickly at each infiltration rate, although a significant amount of time was provided for the slowest flow rate at the beginning of the test. The data in this figure indicate that the moisture content of the soil only varied from 24 to 28% during increases in flow rate from 1 to 40 ml/hr.

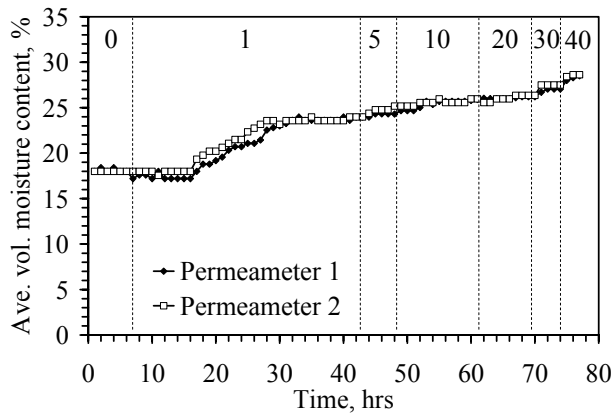


Figure A.5: Changes in moisture content inferred from TDR during an infiltration test  
(Note:  $\omega = 200 \text{ RPM}$ ,  $N_r = 25$ , dashed lines separate different  $v_m$  in ml/hr)

The TDR measurement system for the hydraulic characterization permeameter may not be suitable for all soils. As the TDR is on the side of the permeameter, water must be evenly distributed across the area of the specimen for the TDR to properly infer the moisture content in the upper portion of the soil.

Another necessary condition when performing a steady-state infiltration test is that the tensiometers measurements must reach an equilibrium value. The time required to reach equilibrium is both a function of the change in suction imposed by a change in g-level or flow rate, and the hydraulic conductivity of the ceramic stone in the tensiometer. Even though the soil may reach steady-state flow rapidly, the tensiometer may require additional time to respond. This has been minimized in this study by using a thin ceramic stone, but it is still an important aspect to consider. Equilibration of the tensiometer should also be assessed by comparing the outflow transducer results with those of the tensiometer. The results from the tensiometer during an infiltration and drainage test shown in Figure A.6 indicate that the response is consistent with that expected. The initial response time for the transducers was approximately 50 hours, but the tensiometer responded well during subsequent changes.

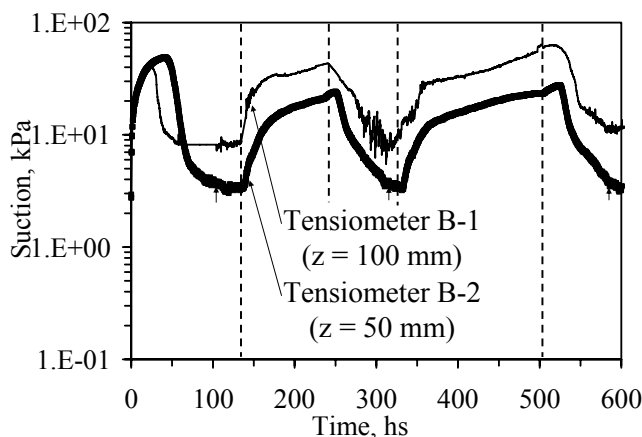


Figure A.6: Tensiometer data from an infiltration/drainage test

In general, the tensiometers have been found to be reliable if they are calibrated prior to each test to measure the offset (*i.e.*, the intercept value for the calibration curve, shown in Figure 6.35). Cavitation of the tensiometer may be an issue if the suction in the soil is high, which may either occur when using the tensiometer to measure the initial suction in a compacted specimen, when using the centrifuge at very low flow rates and high speeds, and during evaporation. Cavitation of the tensiometers may occur if (a) the suction in the soil is higher than the point at which water will boil and air bubbles are able to nucleate; or (b) the tensiometer was not properly saturated (*e.g.*, there was dissolved air present before installation of the tensiometer). The data from a tensiometer during initial equilibration with the suction in a compacted soil is shown in Figure A.7(a) and Figure A.7(b). After reaching a suction of approximately 105 kPa, cavitation occurred. After initial cavitation, a sawtooth pattern is observed in the data, which indicates that water is continuously being drawn from the tensiometer until more air comes out of solution.

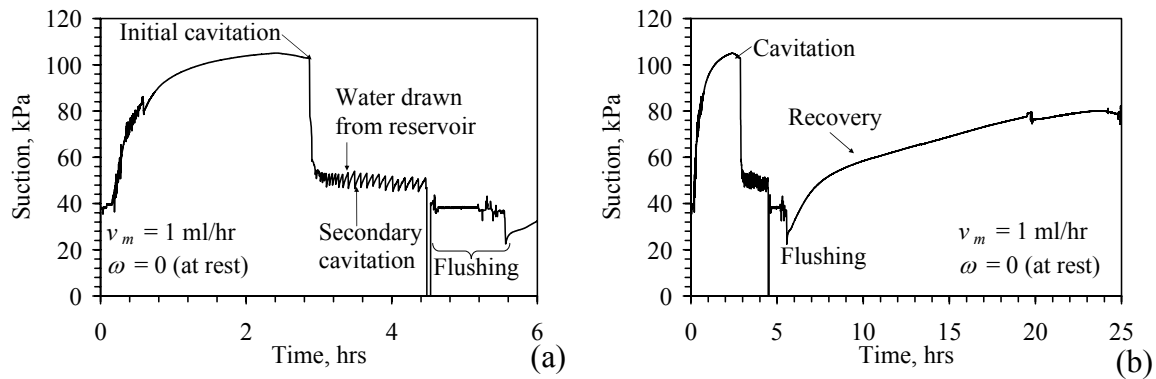


Figure A.7: Tensiometer cavitation: (a) Cavitation behavior; (b) Behavior after flushing

In the case of cavitation in the tensiometers in the prototype permeameter, water can be passed through the water reservoir at high pressure through the flushing ports. However, in the case of cavitation of the tensiometers in the hydraulic characterization

permeameter, a different approach had to be taken. Specifically, the small set screws in the side of the tensiometer were loosened. The screw facing upward was then fully removed, and the syringe assembly shown in Figure A.8 was threaded into the open flushing hole. The syringe was used to pass de-aired water through the tensiometer. The loosened screw on one side of the tensiometer was then tightened, and the other screw was carefully replaced, taking care not to entrap air bubbles. This was done by placing a bead of water in the hole, then diagonally setting the screw into place. This approach worked well to recover tensiometers that have experienced cavitation, as indicated from the data in Figure A.7(b).

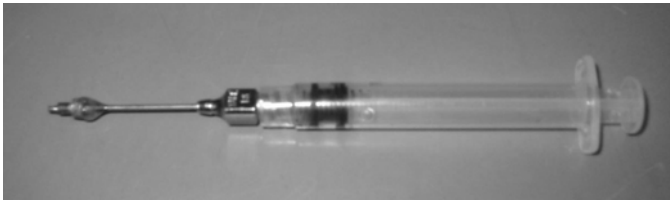


Figure A.8: Flushing needle for an installed tensiometer

Additional inconsistencies between the actual and expected tensiometer measurements have been observed due to erratic shifts in the tensiometer readings. These shifts were observed to occur when water came into contact with the vent port, likely causing a temporary short-circuit. This has been avoided in recent tests, but it is common to see small shifts similar to those in Figure A.7(b) at  $t = 20$  hrs. Even when large shifts observed during testing preclude quantitative measurement of suction, the measurements can still be used to qualitative assessment of moisture migration trends.

Unlike the conventional hydraulic characterization tests described in Chapter 5, direct observation of the specimen in the centrifuge is not possible. Accordingly, many techniques must be used, including the measurements by the instrumentation, the cameras and strobe-lights, as well as the lessons learned from the preliminary tests discussed

above. In addition, the presence of two identical specimens in the centrifuge setup allows comparison of the individual results, which increases confidence in the overall results. As an example, the data obtained from the TDR waveguides in the first infiltration test are shown in Figure A.9. Because the air-release ports were blocked in this test, the moisture content tended to increase more than it would have during a typical infiltration test (the sensitivity of the embedded TDR was also very low in this test). Steady-state conditions were observed during the early part of the test where  $v_m = 10$  ml/hr. However, subsequent increases in moisture content led to inconsistent increases in moisture content in the two permeameters. A leak was observed via the CCD camera in Permeameter 2 during this interval. After reaching an infiltration rate of 50 ml/hr, the TDR in permeameter 1 inferred a decrease in moisture content. This occurred because the amount of water backed-up in the permeameter was significant enough to overcome the air pressure in the outflow reservoir. After inflow was stopped, air was able to slowly seep out of the reservoir and the specimen dried. Although this test yielded poor results, important lessons were learned about infiltration in the centrifuge permeameter.

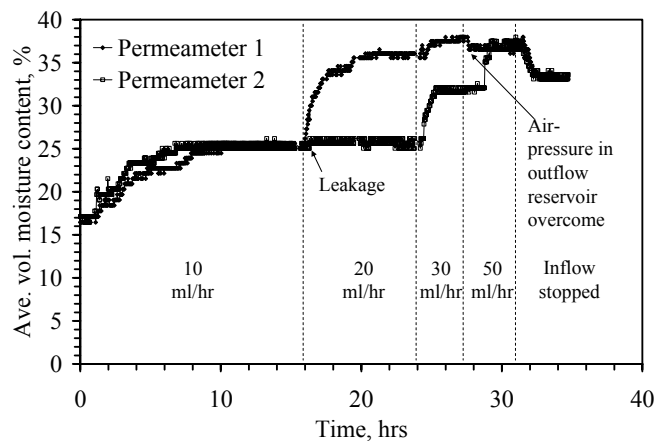


Figure A.9: TDR data indicating a leak and air-pressure build-up



## Appendix B: Solution to Richards' Equation in the Centrifuge

### B.1 OVERVIEW

This appendix describes a program used to solve Richards' equation in the centrifuge, shown in Equation (3.20) above. The goal of this program is to determine one-dimensional changes in suction and moisture content for a specimen undergoing transient moisture flow in a centrifuge field, subject to a range of boundary conditions. Particular boundary conditions that will be investigated include a constant inflow boundary condition at the top surface of the specimen, and either a saturated boundary condition or open flow boundary condition at the base of the specimen. An open flow boundary condition indicates that the suction at the base of the specimen is not purposely controlled. The impedance of the outflow plate will control the particular suction boundary condition on the specimen for a given inflow rate.

As discussed in Chapter 3, Richards' equation can be derived by combining the continuity equation with Darcy's law. Dropping the subscripts and distributing the hydraulic conductivity results in Richards' equation in the centrifuge [Equation (3.20)]:

$$\frac{d\theta}{dt} = \frac{d}{dz} \left[ \frac{K\omega^2}{g} (r_0 - z) - \frac{K}{\rho g} \frac{\partial \psi}{\partial z} \right] \quad (\text{B.1})$$

Distributing the derivatives:

$$\frac{d\theta}{dt} = \frac{d}{dz} \left[ \frac{K\omega^2}{g} (r_0 - z) \right] - \frac{d}{dz} \left[ \frac{K}{\rho g} \frac{\partial \psi}{\partial z} \right] \quad (\text{B.2})$$

$K$  is a function of both time and space, as it is a function of the suction  $\psi$ . Use the product rule to differentiate the first term on the right hand side:

$$\frac{d\theta}{dt} = \frac{\omega^2}{g} \left[ \frac{dK}{dz} (r_0 - z) - K \right] - \frac{d}{dz} \left[ \frac{K}{\rho g} \frac{\partial \psi}{\partial z} \right] \quad (\text{B.3})$$

To use the suction form of Richards' equation, the derivative on the left hand side can be expanded using the chain rule. The slope of the retention curve can be represented by the variable  $C(\psi)$ , which has units of 1/kPa:

$$\frac{d\theta}{dt} = \frac{d\theta}{d\psi} \frac{d\psi}{dt} = C(\psi) \frac{d\psi}{dt} \quad (\text{B.4})$$

Substituting Equation (B.4) into Equation (B.3):

$$C(\psi) \frac{d\psi}{dt} = \frac{\omega^2}{g} \left[ \frac{dK}{dz} (r_0 - z) - K \right] - \frac{d}{dz} \left[ \frac{K}{\rho g} \frac{\partial \psi}{\partial z} \right] \quad (\text{B.5})$$

This equation can be solved by treating both  $K$  and  $\psi$  as independent functions of  $z$ , which, as will be shown, is relatively straightforward. However, this solution may result in numerical instability, as  $K$  can be written directly as a function of the primary variable  $\psi$ . In this case, the product rule can be used to differentiate the two terms in brackets on the right hand side:

$$C(\psi) \frac{d\psi}{dt} = \frac{\omega^2}{g} \left[ \frac{dK}{dz} (r_0 - z) - K \right] - \frac{1}{\rho g} \left[ \frac{dK}{dz} \frac{\partial \psi}{\partial z} + K \frac{\partial^2 \psi}{\partial z^2} \right] \quad (\text{B.6})$$

Also, the spatial derivatives of  $K$  can be replaced with spatial derivatives of suction using the chain rule:

$$C(\psi) \frac{d\psi}{dt} = \frac{\omega^2}{g} \left[ \frac{dK}{d\psi} \frac{\partial \psi}{\partial z} (r_0 - z) - K \right] - \frac{1}{\rho g} \left[ \frac{dK}{d\psi} \left( \frac{\partial \psi}{\partial z} \right)^2 + K \frac{\partial^2 \psi}{\partial z^2} \right] \quad (\text{B.7})$$

Rearranging this equation results in the complete form of Richards' equation in the centrifuge:

$$C(\psi) \frac{d\psi}{dt} = \frac{-K\omega^2}{g} + \left[ \frac{\omega^2}{g} \frac{dK}{d\psi} \right] \frac{\partial \psi}{\partial z} - \left[ \frac{1}{\rho g} \frac{dK}{d\psi} \right] \left( \frac{\partial \psi}{\partial z} \right)^2 + \frac{K}{\rho g} \left( \frac{\partial^2 \psi}{\partial z^2} \right) \quad (\text{B.8})$$

Solution of this form of Richards' equation requires a complex algorithm due to the quadratic term in the suction derivative. Accordingly, this appendix covers only the solution to Richards' equation in the simplified form of Equation (B.5).

## A.2 FINITE DIFFERENCE MODEL

Replace the time and space derivatives in Equation (B.5) with finite difference approximations (from Taylor series expansions of the derivatives). The subscripts in the terms signify spatial node numbers, while the superscripts denote the time step number. The hydraulic conductivity values are obtained from the previous time step.

$$C_i \left[ \frac{\psi_i^j - \psi_i^{j-1}}{\Delta t} \right] = \frac{\omega^2}{g} \left[ \frac{K(\psi_i^{j-1}) - K(\psi_{i-1}^{j-1})}{\Delta z} (r_0 - z_i) - K(\psi_i^{j-1}) \right] - \frac{1}{\Delta z \rho g} \left[ K(\psi_i^{j-1}) \left( \frac{\psi_{i+1}^j - \psi_i^j}{\Delta z} \right) - K(\psi_{i-1}^{j-1}) \left( \frac{\psi_i^j - \psi_{i-1}^j}{\Delta z} \right) \right] \quad (\text{B.9})$$

Rearranging:

$$\begin{aligned} \psi_{i-1}^j \left[ \frac{K(\psi_{i-1}^{j-1})}{\Delta z} \right] - \psi_i^j \left[ \frac{K(\psi_{i-1}^{j-1})}{\Delta z} + \frac{K(\psi_i^{j-1})}{\Delta z} - C_i \frac{\Delta z \rho g}{\Delta t} \right] + \psi_{i+1}^j \left[ \frac{K(\psi_i^{j-1})}{\Delta z} \right] \\ = C_i \frac{\psi_i^{j-1} \Delta z \rho g}{\Delta t} - \Delta z \omega^2 \rho \left[ \frac{K(\psi_i^{j-1}) - K(\psi_{i-1}^{j-1})}{\Delta z} (r_0 - z_i) - K(\psi_i^{j-1}) \right] \end{aligned} \quad (\text{B.10})$$

## B.3 BOUNDARY CONDITIONS

### A.3.1 Inflow boundary

For inflow boundary conditions, use the continuity equation combined with Equation (B.4):

$$C(\psi) \frac{d\psi}{dt} = - \frac{dv}{dz} \quad (\text{B.11})$$

Discretization of the derivatives in Equation (B.11):

$$C_N \left[ \frac{\psi_N^j - \psi_N^{j-1}}{\Delta t} \right] = - \frac{v_N - v_{N-1}}{\Delta z} \quad (\text{B.12})$$

Let  $v_N$  equal the prescribed influx, and determine  $v_{N-1}$  using Darcy's law:

$$C_N \left[ \frac{\psi_N^j - \psi_N^{j-1}}{\Delta t} \right] = - \frac{1}{\Delta z} \left[ v_{in} - K(\psi_N^{j-1}) \left( \frac{\omega^2 (r_0 - z_N)}{g} - \frac{1}{\rho g} \frac{\psi_N^j - \psi_{N-1}^j}{\Delta z} \right) \right] \quad (\text{B.13})$$

Rearranging:

$$\psi_{N-1}^j \left[ \frac{K(\psi_N^{j-1})}{\Delta z} \right] - \psi_N^j \left[ \frac{K(\psi_N^{j-1})}{\Delta z} - C_N \frac{\Delta z \rho g}{\Delta t} \right] = C_N \frac{\psi_N^{j-1} \Delta z \rho g}{\Delta t} - v_{in} \rho g - K(\psi_N^{j-1}) \rho \omega^2 (r_0 - z_N) \quad (B.14)$$

### A.3.2 Outflow boundary

For outflow boundary conditions, use the continuity equation combined with

Equation (B.4):

$$C(\psi) \frac{d\psi}{dt} = - \frac{dv}{dz} \quad (B.15)$$

Discretization of the derivatives in Equation (B.15):

$$C_N \left[ \frac{\psi_N^j - \psi_N^{j-1}}{\Delta t} \right] = - \frac{v_2 - v_1}{\Delta z} \quad (B.16)$$

Let  $v_1$  equal the outflow (see options below), and determine  $v_2$  using Darcy's law:

$$C_1 \left[ \frac{\psi_1^j - \psi_1^{j-1}}{\Delta t} \right] = - \frac{1}{\Delta z} \left[ -K(\psi_2^{j-1}) \left( \frac{\omega^2 (r_0 - z_2)}{g} - \frac{1}{\rho g} \frac{\psi_2^j - \psi_1^j}{\Delta z} \right) - v_{out} \right] \quad (B.17)$$

Rearranging:

$$-\psi_1^j \left[ \frac{K(\psi_2^{j-1})}{\Delta z} - C_1 \frac{\Delta z \rho g}{\Delta t} \right] + \psi_2^j \left[ \frac{K(\psi_2^{j-1})}{\Delta z} \right] = C_1 \frac{\psi_1^{j-1} \Delta z \rho g}{\Delta t} - K(\psi_2^{j-1}) \rho \omega^2 (r_0 - z_2) - v_{out}^{j-1} \rho g \quad (B.18)$$

There are several options that can be used for a bottom boundary condition in

Equation (B.18) (Bear *et al.* 1984):

1. Unit gradient: It can be assumed that the moisture content

$$\frac{dh}{dz} = 0 \quad \text{or} \quad K(\psi_{out}^{j-1}) = K(\psi_1^{j-1}) \quad (B.19)$$

2. Outflow equal to a constant value:

$$K(\psi_{out}^{j-1}) = K_{sat,plate} \quad (B.20)$$

where  $K_{sat,plate}$  is the hydraulic conductivity of the plate, typically assumed greater than that of the soil or similar to the soil

3. Outflow is equal to the change in moisture storage of the profile in a given time

interval:

$$v_{out}^j = \frac{1}{\Delta t} \int_0^{r_0 - r_1} \theta^{j-1} dz \quad (B.21)$$

#### B.4 MATRIX FORMAT

Equations (B.10), (B.14), and (B.18) can be assembled into matrix form to solve

for the most recent values of the suction profile (*i.e.*, time step  $j$ ):

$$\begin{bmatrix} a_{1,1} & a_{1,2} & 0 & 0 & 0 \\ a_{2,1} & a_{2,2} & a_{2,3} & 0 & 0 \\ 0 & \dots & \dots & \dots & 0 \\ 0 & 0 & a_{N-1,N-2} & a_{N-1,N-1} & a_{N-1,N} \\ 0 & 0 & 0 & a_{N,N-1} & a_{N,N} \end{bmatrix} \begin{Bmatrix} \psi_1^j \\ \psi_2^j \\ \dots \\ \psi_{N-1}^j \\ \psi_N^j \end{Bmatrix} = \begin{Bmatrix} b_1 \\ b_2 \\ \dots \\ b_{N-1} \\ b_N \end{Bmatrix} \quad (B.22)$$

Where the terms in the above matrix are defined as follows:

$$a_{1,1} = - \left[ \frac{K(\psi_2^{j-1})}{\Delta z} - C_1 \frac{\Delta z \rho g}{\Delta t} \right] \quad (B.23)$$

$$a_{1,2} = \frac{K(\psi_2^{j-1})}{\Delta z} \quad (B.24)$$

$$a_{i,i-1} = \frac{K(\psi_{i-1}^{j-1})}{\Delta z} \quad (B.25)$$

$$a_{i,i} = - \left[ \frac{K(\psi_{i-1}^{j-1})}{\Delta z} + \frac{K(\psi_i^{j-1})}{\Delta z} - C_i \frac{\Delta z \rho g}{\Delta t} \right] \quad (B.26)$$

$$a_{i,i+1} = \frac{K(\psi_i^{j-1})}{\Delta z} \quad (B.27)$$

$$a_{N,N-1} = \frac{K(\psi_N^{j-1})}{\Delta z} \quad (B.28)$$

$$a_{N,N} = - \left[ \frac{K(\psi_N^{j-1})}{\Delta z} - C_N \frac{\Delta z \rho g}{\Delta t} \right] \quad (B.29)$$

$$b_1 = C_1 \frac{\psi_1^{j-1} \Delta z \rho g}{\Delta t} - K(\psi_2^{j-1}) \rho \omega^2 (r_0 - z_2) - v_{out}^{j-1} \rho g \quad (B.30)$$

$$b_i = C_i \frac{\psi_i^{j-1} \Delta z \rho g}{\Delta t} - \Delta z \rho \omega^2 \left[ \frac{K(\psi_i^{j-1}) - K(\psi_{i-1}^{j-1})}{\Delta z} (r_0 - z_i) - K(\psi_i^{j-1}) \right] \quad (\text{B.31})$$

$$b_N = C_N \frac{\psi_N^{j-1} \Delta z \rho g}{\Delta t} - v_{in} \rho g - K(\psi_N^{j-1}) \rho \omega^2 (r_0 - z_N) \quad (\text{B.32})$$

## B.5 SOLUTION (MODIFIED PICARD ITERATION)

To solve this system of equations, first estimate a value of the slope of the WRC:

$$C_{est,i} = \begin{cases} \frac{d\theta}{d\psi} & \text{from the van Genuchten model if } \psi_k - \psi_{k-1} < 10^{-10} \\ \frac{\theta_i^j - \theta_j^{j-1}}{h_i^j - h_i^{j-1}} & \text{if } \psi_k - \psi_{k-1} > 10^{-10} \end{cases} \quad (\text{B.33})$$

Then, solve Equation (B.22) using the Thomas Algorithm. This will give the most updated values of suction with space. Use the WRC to determine the corresponding updated values of  $\theta_i^j$ . As a check for convergence, define an estimate of the moisture content:

$$\theta_{est} = \theta_i^{j-1} + C_{est,i} (\psi_i^j - \psi_i^{j-1}) \quad (\text{B.34})$$

Then, define the mass balance as:

$$mb_i^j = \theta_i^j - \theta_{est} \quad (\text{B.35})$$

The sum of squares can be used to minimize the mass balance:

$$SSQ^j = \sum_{i=1}^N mb_i^j \quad (\text{B.36})$$

Iterate with a new value of  $C_{est,i}$  until  $SSQ < 10^{-6}$

## B.6 RICHTEXNG

```
%-----
%
% RichTexNg.m
%
% by John McCartney
%
% This program uses a modified Picard iteration technique
% to solve Richards' equation in a centrifuge environment
%
% -----
%
clear all, close all, nfig = 0;
%
%*****
% PARAMETER DEFINITION
%*****
% A. Geometry Parameters
% Outside radius in m
ro=0.194;
% Inside radius in m
ri=0.16352;
% Specimen cross sectional area in m2
A=0.0022913;
%
% B. Given Parameters
% Acceleration due to gravity in m/s2
g=9.81;
% Angular velocity of centrifuge
omega=136;
% Density in kg/m3
rho=1000;
%
% C. van Genuchten parameters
% Alpha in 1/kPa
a=0.332;
% N
N=1.335;
m=1-1/N;
% Pore connectivity, l
l=0.5;
% Saturated volumetric moisture content
qs=0.4;
```

```

% Residual volumetric moisture content
qr=0.01;
% Saturated hydraulic conductivity in m/s
Ks=1.2E-6;
% Impedance of the outflow plate in m/s
Kplate=1.2E-6;
%
%-----
% Problem Solution
% -----
%
%*****
% TIME INPUT
%*****
% Define the starting time:
tstart=0;
% Number of time points desired for integration:
nt=100;
% Define the time spacing in seconds:
dt=0.001;
% Define a time vector for plotting
t=zeros(nt,1);
for k=2:nt
    t(k)=t(k-1)+dt;
end
%
%*****
% SPATIAL INPUTS
%*****
% Define the upper and lower space points:
zmin=0;
zmax=ro-ri;
% Now define the spatial spacing:
% nx is the total number of points including the boundaries
nz=501;
%
% Spacing for z:
dz=(zmax-zmin)/(nz);
% Build a vector of z values:
z=zeros(nz,1);
for j=1:nz
    if j==1
        z(j)=dz;
    else
        z(j)=z(j-1)+dz;
    end
end

```



```

    end
end
%
%*****
% INITIAL CONDITIONS AND HYDRAULIC PROPERTY INITIALIZATION
%*****
%
% Define the initial head value in the column in m, assume this is constant with depth:
Yinitial=0.1;
%
% Initialize the hydraulic property matrices
q=zeros(nz,nt);
Se=zeros(nz,nt);
K=zeros(nz,nt);
C=zeros(nz,nt);
%
% Initialize the iteration hydraulic property matrices
Ctemp=zeros(nz,1);
Cest=zeros(nz,1);
qest=zeros(nz,1);
mb=zeros(nz,1);
%
% The solution will be presented in a matrix. The rows will be the x values, while each
column
% will be a new time level. Initialize the solution matrix to zero.
Y=zeros(nz,nt);
for i=1:nz
    Y(i,1)=Yinitial;
    if Y(i,1)>0
        q(i,1)=qr+(qs-qr)*(1+(a*Y(i,1))^N)^-m;
        C(i,1)=a*(1/N-1)*N*(qs-qr)*(a*Y(i,1))^(N-1)*(1-(a*Y(i,1))^(1/N-2));
    else
        q(i,1)=qs;
        C(i,1)=0;
    end
    Se(i,1)=(q(i,1)-qr)/(qs-qr);
    K(i,1)=Ks*((Se(i,1))^l)*(1-(1-(Se(i,1))^(1/m))^m)^2;
    % Estimate the gradient in C for the next time step
    Cest(i)=C(i,1);
end
%*****
% BOUNDARY CONDITIONS AND SOLUTION INITIALIZATION
%*****
%
% Initialize solution vectors

```

```

p1=zeros(nz,1);
p2=zeros(nz,1);
p3=zeros(nz,1);
RHS=zeros(nz,1);
Qout=zeros(nt,1);
%
%*****
% BOTTOM BOUNDARY
%*****
% Flow B.C.
Qout(1)=-Kplate*(rho*omega^2*(ro-z(2))-(Y(2,1)-Y(1,1))/dz);
p1(1)=0;
p2(1)=-1/dz*K(2,1)+(rho*g*dz/dt)*Cest(1);
p3(1)=1/dz*K(2,1);
RHS(1)=-K(2,1)*(rho*omega^2*(ro-z(2)))-
Qout(1)*rho*g+(rho*g*dz/dt)*Y(1,1)*Cest(1);
%
% Constant head B.C.
%p1(1)=0;
%p2(1)=1;
%p3(1)=0;
%RHS(1)=0;
%
%*****
% TOP BOUNDARY
%*****
% Flow B.C.
Qin=0;
p1(nz)=1/dz*K(nz,1);
p2(nz)=-1/dz*K(nz,1)+(rho*g*dz/dt)*Cest(nz);
p3(nz)=0;
RHS(nz)=-((Qin*rho*g+K(nz,1)*(rho*omega^2*(ro-
z(nz))))+(rho*g*dz/dt)*Y(nz,1)*Cest(nz);
%
% Constant head top B.C.
%p1(nz)=0;
%p2(nz)=1;
%p3(nz)=0;
%RHS(nz)=-30.5;
%
% Enter the initial coefficients
for i=2:nz-1
    p1(i)=1/dz*K(i,1);
    p2(i)=-1/dz*(K(i,1)+K(i-1,1))+(rho*g*dz/dt)*Cest(i);
    p3(i)=1/dz*K(i,1);

```

```

    RHS(i)=-dz*rho*omega^2*K(i,1)+(ro-z(i))*rho*omega^2*(K(i,1)-K(i-...
    1,1))+(rho*g*dz/dt)*Y(i,1)*Cest(i);
end
%*****
% CALCULATED VALUES
% *****
% Initialize the water storage (W) and Average water content(Aveq)
W=zeros(nt,1);
Aveq=zeros(nt,1);
for i=1:(nz/2)
    W(1)=W(1)+dz/3*(q(2*i-1,1)+4*q(2*i,1)+q(2*i+1,1));
end
Aveq(1)=sum(q(1:nz,1))/nz;
%
%*****
% SOLUTION
%*****
%
% Subscripts
% i is for space
% j is for time
% n is for Picard iteration
%
% Enter the desired number of iterations:
ni=1000;
ntime=0;
for j=2:nt
    niterate=0;
    ntime=ntime+1
    for n=1:ni
        %*****
        % THOMAS ALGORITHM
        %*****
        for i=1:nz
            sub(i)=p1(i);
            diag(i)=p2(i);
            sup(i)=p3(i);
        end
        for i=2:nz
            ratio=sub(i)/diag(i-1);
            diag(i)=diag(i)-ratio*sup(i-1);
            RHS(i)=RHS(i)-ratio*RHS(i-1);
        end
        sol(nz)=RHS(nz)/diag(nz);
        for i=1:nz-1

```

```

nmi=nz-i;
nmi1=nz-i+1;
sol(nmi)=(RHS(nmi)-sup(nmi)*sol(nmi1))/diag(nmi);
end
%*****
% CALCULATE UPDATED HYDRAULIC PROPERTIES
%*****
for i=1:nz
    Y(i,j)=sol(i);
    if Y(i,j)>0
        q(i,j)=qr+(qs-qr)*(1+(a*Y(i,j))^N)^-m;
        C(i,j)=a*(1/N-1)*N*(qs-qr)*(a*Y(i,j))^(N-1)*(1-(a*Y(i,j))^(1/N-2));
    else
        q(i,j)=qs;
        C(i,j)=0;
    end
    Se(i,j)=(q(i,j)-qr)/(qs-qr);
    K(i,j)=Ks*((Se(i,j))^l*(1-(1-(Se(i,j))^(1/m))^m)^2;
    %
    % Calculate updated values of C
    if abs(Y(i,j)-Y(i,j-1))<10^(-10)
        Ctemp(i)=C(i,j-1);
    else
        Ctemp(i)=(q(i,j)-q(i,j-1))/(Y(i,j)-Y(i,j-1));
    end
    qest(i)=q(i,j-1)+Cest(i)*(Y(i,j)-Y(i,j-1));
    mb(i)=q(i,j)-qest(i);
end
%-----
%Convergence Check:
%-----
SSQ=sum(mb.^2);
if SSQ<10^-6
    % Calculate new water storage, average q and outflow
    for i=1:(nz/2)
        W(j)=W(j)+dz/3*(q(2*i-1,j)+4*q(2*i,j)+q(2*i+1,j));
    end
    Aveq(j)=sum(q(1:nz,j))/nz;
    Qout(j)=W(j)-W(j-1);
    %-----
    % OPTION A: ADVANCE IN TIME
    %-----
    for i=1:nz
        Cest(i)=C(i,j);
    end
end

```

```

%*****
% BOTTOM BOUNDARY
%*****
% Flow B.C.
p1(1)=0;
p2(1)=-1/dz*K(2,j)+(rho*g*dz/dt)*Cest(1);
p3(1)=1/dz*K(2,j);
RHS(1)=-K(2,j)*(rho*omega^2*(ro-z(2)))-...
Qout(j)*rho*g+(rho*g*dz/dt)*Y(1,j)*Cest(1);
%
% Constant head B.C.
%p1(1)=0;
%p2(1)=1;
%p3(1)=0;
%RHS(1)=0;
%
%*****
% TOP BOUNDARY
%*****
% Flow B.C.
p1(nz)=1/dz*K(nz,j);
p2(nz)=-1/dz*K(nz,j)+(rho*g*dz/dt)*Cest(nz);
p3(nz)=0;
RHS(nz)=- (Qin*rho*g+K(nz,j)*rho*omega^2*(ro-...
z(nz)))+(rho*g*dz/dt)*Y(nz,j)*Cest(nz);
%
% Constant head B.C.
%p1(nz)=0;
%p2(nz)=1;
%p3(nz)=0;
%RHS(nz)=-30.5;
%
for i=2:nz-1
    p1(i)=1/dz*K(i,j);
    p2(i)=-1/dz*(K(i,j)+K(i-1,j))+(rho*g*dz/dt)*Cest(i);
    p3(i)=1/dz*K(i,j);
    RHS(i)=-dz*rho*omega^2*K(i,j)+(ro-z(i))*rho*omega^2*(K(i,j)-K(i-...
    1,j))+(rho*g*dz/dt)*Y(i,j)*Cest(i);
end
break
else
    niterate=niterate+1
    %-----
    % OPTION B: ITERATE
    %-----

```

```

for i=1:nz
    Cest(i)=Ctemp(i);
end
%*****
% BOTTOM BOUNDARY
%*****
% Flow B.C.
p1(1)=0;
p2(1)=-1/dz*K(2,j-1)+(rho*g*dz/dt)*Cest(1);
p3(1)=1/dz*K(2,j-1);
RHS(1)=-K(2,j-1)*(rho*omega^2*(ro-z(2)))-Qout(j)*rho*g+(rho*g*dz/dt)*...
Y(1,j-1)*Cest(1);
%
% Constant head B.C.
%p1(1)=0;
%p2(1)=1;
%p3(1)=0;
%RHS(1)=0;
%*****
% TOP BOUNDARY
%*****
% Flow B.C.
p1(nz)=1/dz*K(nz,j-1);
p2(nz)=-1/dz*K(nz,j-1)+(rho*g*dz/dt)*Cest(nz);
p3(nz)=0;
RHS(nz)=-(Qin*rho*g+K(nz,j-1)*rho*omega^2*(ro-...
z(nz)))+(rho*g*dz/dt)*Y(nz,j-1)*Cest(nz);
% Constant head B.C.
%p1(nz)=0;
%p2(nz)=1;
%p3(nz)=0;
%RHS(nz)=-30.5;
for i=2:nz-1
    p1(i)=1/dz*K(i,j);
    p2(i)=-1/dz*(K(i,j)+K(i-1,j))+dz/dt*Cest(i);
    p3(i)=1/dz*K(i,j);
    RHS(i)=-dz*omega^2/g*K(i,j)+(ro-z(i))*omega^2/(g)*(K(i,j)-K(i-...
    1,j))+dz/dt*Y(i,j)*Cest(i);
end
end
end

```

## Glossary

Centrifuge permeameter: A system used to determine the hydraulic characteristics of unsaturated soils or the modeling of flow through layered, unsaturated soils. This system includes a permeameter to hold a soil specimen, a geotechnical centrifuge, the ability to control the impinging infiltration rate of the soil specimen, instrumentation to measure outflow of water, matric suction, and volumetric moisture content, and a data acquisition system for in-flight measurements.

Control variables: the centrifuge angular velocity ( $\omega$ ) and the inflow rate ( $Q$ )

HDU: Heat dissipation unit, a device used to infer suction in unsaturated soils.

Hysteresis: Phenomenon that results in a change in shape of the hydraulic characteristics upon cyclic wetting and drying.

K-function: The relationships between hydraulic conductivity and suction or between hydraulic conductivity and volumetric moisture content.

Matric Suction: The difference between the pore air and pore water pressures. This is equal to the negative of the pore water pressure in the case that the air pressure is equal to zero (atmospheric).

Tensiometer: A device used to measure pore water pressures in unsaturated soils.

TDR: Time domain reflectometry, a technology used to infer the bulk dielectric permittivity of a soil, which can be correlated with volumetric moisture content.

Unsaturated soil: A soil containing both air and water in its pore spaces.

Volumetric Moisture Content: The volume of water in the soil voids divided by the total volume of the soil.

Water Retention Curve: The relationship between volumetric moisture content and matric suction.

## References

- ASTM D 698. Standard Test Methods for Laboratory Compaction Characteristics of Soil Using Standard Effort (12,400 ft-lbf/ft<sup>3</sup> (600 kN-m/m<sup>3</sup>)). The American Society for Testing and Materials. West Conshohoken, PA.
- ASTM D 854. Standard Test Methods for Specific Gravity of Soil Solids by Water Pycnometer. The American Society for Testing and Materials. West Conshohoken, PA.
- ASTM D 4318. Standard Test Methods for Liquid Limit, Plastic Limit, and Plasticity Index of Soils. The American Society for Testing and Materials. West Conshohoken, PA.
- ASTM D 2216. Standard Test Methods for Laboratory Determination of Water (Moisture) Content of Soil and Rock by Mass. The American Society for Testing and Materials. West Conshohoken, PA.
- ASTM D 6527. Standard Test Method for Determining Unsaturated and Saturated Hydraulic Conductivity in Porous Media by Steady-State Centrifugation. The American Society for Testing and Materials. West Conshohoken, PA.
- ASTM D 6836. Standard test methods for determination of the soil water characteristic curve for desorption using a hanging column, pressure extractor, chilled mirror hygrometer, and/or centrifuge. American Society for Testing and Materials. West Conshohocken, Pennsylvania.
- Bear, J., Corapcioglu, Y. and J. Bulkarishna. 1984. "Modeling of centrifugal filtration in unsaturated deformable porous medium." *Adv. in Water Resour.* 7(4), 150-167.
- Benson, C. and Gribb, M. 1997. "Measuring unsaturated hydraulic conductivity in the laboratory and field." *Unsaturated Soil Engineering Practice*. Houston, S. and Wray, W. eds. 113-168.
- Briggs, L.J., and J.W. McLane. 1907. "The moisture equivalents of soils." USDA Bureau of Soils Bulletin 45. U.S. Gov. Printing Office, Washington, DC.
- Brooks, R.H., and Corey, A.T. 1964. "Hydraulic properties of porous medium." Colorado State University Fort Collins. Hydrology Paper No. 3. March.
- Burdine, N.T. 1953. "Relative permeability calculations from pore-size distribution data." *Pet. Trans. of the Amer. Inst. of Mining and Metal. Eng.* 198, 71-77.



- Butters, G. and Duchateau, P. 2002. "Continuous flow method for rapid measurement of soil hydraulic properties: I. Experimental considerations." *Vadose Zone Journal*. 1, 239–251.
- Campbell, G. 1974. "A simple method for determining unsaturated conductivity from moisture retention data." *Soil Science*. 117(6), 311-314.
- Childs, E. and Collis-George, N. 1950. "The permeability of porous materials." *Proc. Roy. Soc. London. A*, 201, 392-405.
- Chiu, T., and Shackelford, C. 1998. "Unsaturated hydraulic conductivity of compacted sand-kaolin mixtures." *Jour. Geotech. Geoenv. Eng.*. 126(11), 990-1001.
- Conca, J., and Wright, J. 1992. "Diffusion and flow in gravel, soil, and whole rock." *Applied Hydrogeology*. 1, 5-24.
- Darcy, H. 1856. *Les Fontaines Publiques de la Ville de Dijon*. Dalmont, Paris. 647 p.
- Dell'Avanzi, E., Zornberg, J.G., and Cabral, A.R. 2004. "Suction profiles and scale factors for unsaturated flow under increased gravitational field." *Soils and Foundations*. 44(3), 1-11.
- Eching, S., and Hopmans, J. 1993. "Optimization of hydraulic functions from transient outflow and soil water pressure data." *Soil Sci. Soc. Am. J.* 57, 1167-1175.
- Flint, A.L., Campbell, G.S., Ellet, K.M., and Calissendorff, C. 2002. "Calibration and temperature correction of heat dissipation matric potential sensors." *Soil Sci. Soc. Am. J.* 66, 1439-1445.
- Forbes, P. L. 1994. "Simple and accurate methods for converting centrifuge data into drainage and imbibition capillary pressure curves." *Log Analyst*. 35(4), 31–53.
- Fredlund, D.G. 1992. "Background, Theory, and Research Related to the Use of Thermal Conductivity Sensors for Matric Suction." *Advances in Measurement of Soil Properties: Bringing Theory into Practice*. Special Pub. 30. SSSA, Madison WI.
- Fredlund, D.G. and Xing, A. 1994. "Equations for the soil-water characteristic curve." *Can. Geotech. Jour.* 31, 521-532.
- Fredlund, M.D., Wilson, G.W., and Fredlund, D.G. "Indirect procedures to determine unsaturated soil property functions." *Proc. 50<sup>th</sup> Canadian Geot. Conference*. Ottawa, Ontario, Canada, Oct. 20-22 1997.
- Gardner, R.A. 1937. "The method of measuring the capillary pressures in small core samples." *Soil Science*. 43, 277-283.

- Gardner, W. 1956. "Calculation of capillary conductivity from pressure plate outflow data." *Soil Sci. Amer. Proc.* 20, 317-320.
- Gardner W. 1958. "Some steady-state solutions of the unsaturated moisture flow equation with applications to evaporation from a water table." *Soil Science.* 85, 228-232.
- Hassler, G. L. and Brunner, E. 1945. "Measurements of capillary pressure in small core samples." *Trans. AIME.* 160, 114-123.
- Haines, W.B. 1930. "Studies in the physical properties of soil. V. The hysteresis effect in capillary properties, and the modes of moisture distribution associated therewith." *J. Agric. Sci.*, 20, 97-116.
- Henry, E.J. and Smith, J.E. 2003. "Surfactant induced flow phenomena in the vadose zone: A review of data and numerical modeling." *Vadose zone Jour.* 2,154-157.
- Hillel, D. 1998. *Environmental Soil Physics.* Academic Press.
- Hoffman, R. N. 1963. "A technique for the determination of capillary pressure curves using a constantly accelerated centrifuge." *Soc. Pet. Eng. J.* 3, 227-235.
- Hopmans, J.W., and J.H. Dane. 1986a. "Temperature dependence of soil hydraulic properties." *Soil Sci. Soc. Am. J.* 50:4-9.
- Hopmans, J.W., and J.H. Dane. 1986b. "Temperature dependence of soil water retention curves." *Soil Sci. Soc. Am. J.* 50:562-567.
- Hwang, S.I. and Powers, S. (2003). "Using Particle Size Distribution Models to Estimate Soil Hydraulic Properties." *Soil Sci. Amer. Proc.* 67:1103-1112.
- Khaleel, R. Relyea, J.F., Conca, J.L. 1995. "Evaluation of van Genuchten-Mualem relationships to estimate unsaturated hydraulic conductivity at low water contents." *Water Resour. Res.* 31(11), 2659-2668.
- Khanzode, R.M., Vanapali, S.K., and Fredlund, D.G. 2002. "Measurement of soil-water characteristic curves for fine-grained soils using a small-scale centrifuge." *Can. Geotech. Jour.* 39, 1209-1217.
- Kleppe, J.H. and Olson, R.E. 1985. "Desiccation cracking of soil barriers." *Hydraulic Barriers in Soil and Rock.* ASTM STP 874. 263-267.
- Klute, A. 1986. *Water Retention: Laboratory Methods.* *Methods of Soil Analysis, Vol. 1: Physical and Mineralogical Methods.* SSSA. Madison, WI. 635-662.
- Klute, A. and Dirksen, C. 1986. "Hydraulic conductivity and diffusivity: Laboratory methods." In *Methods of Soil Analysis, Vol. 1.* 9, 687-732.

- Kong, L.-W. and Tan, L.-R. 2000. "A simple method of determining the soil water characteristic curve indirectly. Unsaturated Soils for Asia. 341-345.
- Kunze, R.J. and Kirkham, D. 1962. "Simplified accounting for membrane impedance in capillary conductivity determinations." Soil Sci. Amer. Proc. 26, 421-426.
- Leij, F.J., Alves, W.J., and van Genuchten, M. (1996). "The UNSODA unsaturated soil hydraulic database." EPA/600/R-96/095. EPA and US Sal. Lab. Riverside, CA.
- Lu, N., Wallyace, A. Carrera, J., and Likos, W.J. 2006. "Constant flow method for concurrently measuring soil-water characteristic curve and hydraulic conductivity function. ASTM Geot. Test. Jour. 29(3), 1-12.
- Marshall, T.J. 1958. "A relation between permeability and size distribution of pores." Journal of Soil Science. 9, 1-8.
- McCartney, J.S., Kuhn, J.A., and Zornberg J.G. 2005. "Geosynthetic drainage layers in contact with unsaturated soils." 16th ISSMGE. 12-16 Sept. 2005. Osaka, Japan.
- McCartney, J.S. and Zornberg, J.G. 2006. "TDR System for Hydraulic Characterization of Unsaturated Soils in the Centrifuge." TDR 2006. Purdue University, West Lafayette, Indiana. September 18-20, 2006.
- McCartney, J.S., and Zornberg, J.G. 2007a. "Effect of Wet-Dry Cycles on Capillary Break Formation in Geosynthetic Drainage Layers." Geosynthetics 2007. Washington, DC. January 16-19, 2007.
- McCartney, J.S. and Zornberg, J.G. 2007b. "Hydraulic Interaction between Geosynthetic Drainage Layers and Unsaturated Low Plasticity Clay." GeoDenver 2007. Denver, CO. February 18-21, 2007.
- Meerdink, J. S., Benson, C. H., and Khire, M. V. 1996. "Unsaturated hydraulic conductivity of two compacted barrier soils." Jour. Geotech. Geoenv. Eng., ASCE. 122(7), 565-576.
- Meyer, P.D. and Gee, G.W. 1999. "Flux-based estimation of field capacity." Jour. Geotech. Geoenv. Eng. ASCE. 125(7), 595-599.
- Miller, D. Yesiller, N., Yaldo, K., and Merayyan, S. (2002). "Impact of soil type and compaction conditions of soil water characteristic." Jour. Geotech. Geoenv. Eng., ASCE. 128(9), 733-742.
- Millington, R. and Quirk, J. 1961. "Permeability of porous solids." Trans. Faraday Soc. 57, 1200-1207.

- Mitchell, R. 1994. "Matric suction and diffusive transport in centrifuge models." *Can. Geotech. Jour.* 31, 357-363.
- Mitchell, J.K. 1979. *Fundamentals of Soil Behavior*. John Wiley, New York.
- Mitchell, J.K., Hooper, D., and R. Campanella. 1965 "Permeability of Compacted Clay." *Jour. of Soil Mech. and Foundation Division. ASCE.* 91(4), 41-65.
- Moore, R. 1939. "Water conduction from shallow water tables." *Hilgardia*, 12, 383-426.
- Mualem, Y. 1978. "Hydraulic conductivity of unsaturated porous media: generalized macroscopic approach." *Water Resources Res.* 14, 325-334.
- Mualem, Y. 1976) "A new model for predicting the hydraulic conductivity of unsaturated porous media." *Water Resources Res.* 12, 513-522.
- Nachabe, M. 1998. "Refining the definition of field capacity in the literature." *Jour. of Irrig. and Drain. Eng.* 124(4), 230-232.
- Neilsen, D., Kirkham, D., and Perrier, E. 1960. "Soil capillary conductivity: comparison of measured and calculated values." *Soil Sci. Amer. Proc.* 24, 157-160.
- Nimmo, J., and Akstin, K. 1988. "Hydraulic conductivity of a sandy soil at low water content after compaction by various methods." *Soil Sci. Soc. Am. J.* 52, 303-310.
- Nimmo, J. 1990. "Experimental testing of transient unsaturated flow theory at low water content in a centrifugal field." *Water Resour. Res.* 26, 1951-1960.
- Nimmo, J., Rubin, J., and Hammermeister, D. 1987. "Unsaturated flow in a centrifugal field: Measurement of hydraulic conductivity and testing of Darcy's law." *Water Resour. Res.* 23(1), 124-134.
- Nimmo, J. R., Akstin, K. C., and Mello, K. A. 1992. "Improved apparatus for measuring hydraulic conductivity at low water content." *Soil Sci. Soc. Am. J.* 56, 1758-1761.
- Nimmo, J. R. and Mello, K. A. 1991. "Centrifugal techniques for measuring saturated hydraulic conductivity." *Water Resour. Res.* 27, 1263-1269.
- Olson, R.E., and L.J. Langfelder 1965. "Pore water pressures in unsaturated soils." *Jour. of the Soil Mech. and Found. Div. ASCE*, 91(SM4), 127-151.
- Olson, R.E., and Daniel, D.E. 1981. "Measurement of the Hydraulic Conductivity of Fine Grained Soils." *Permeability and Groundwater Contaminant Transport*, ASTM STP 746. T.F. Zimmie and C.O. Riggs, Eds., ASTM. 18-64.

- Parker, J.C., Kool, J.B., and van Genuchten, M.T. 1985. "Determining soil hydraulic properties from one-step outflow experiments by parameter estimation: II Experimental studies." *Soil Sci. Soc. Am. J.* 49,1354-1359.
- Parent, S.E. and Cabral, A.R. 2004. Procedure for the design of inclined covers with capillary barrier effect. *Proc. 57th Can. Geotech. Conf. Québec, October, 24-28.*
- Poulovassilis, A. (1962). "Hysteresis of pore water, an application of the concept of independent domains." *Soil Science.* 93: 405-412.
- Poulose, A., Nair, S.R., Singh, D.N. 2000. "Centrifuge modeling of moisture migration in silty soils. *Jour. Geotech. Geoenv. Eng.* 126(6), 748-752.
- Poulsen, T.G., Moldrup, P., Yamaguchi, T. and Jacobsen, O.H. (1999) "Predicting saturated and unsaturated hydraulic conductivity in undisturbed soils from soil water characteristics." *Soil Sci.* 164, 877-887.
- Richards, L.A. 1952. "Water conducting and retaining properties of soils in relation to irrigation." *Proc. Int. Symp. On Desert Research.* 523-546.
- Ridley, A.M. and Burland, J.B. 1995. "A pore pressure probe for the in-situ measurement of soil suction". *Proc. of Conf. on Adv. in Site Invest. Prac.. I.C.E.:London.*
- Roscoe, K.H. 1968. "Soils and model tests." *J. Strain. Anal.* 3, 57-64.
- Shoop S.A. and Bigl S.R. 1997. "Moisture migration during freeze and thaw of unsaturated soils: modeling and large scale experiments." *Cold Regions Science and Technology.* 25(1), 33-45.
- Siddiqui, S., Drnevich, V., and Deschamps, R. 2000. "Time domain reflectometry development for use in geotechnical engineering," *Geotech. Test. Jour.* 23(1), 9-20.
- Sigda, J.M., and Wilson, J.L. 2005. "Are faults preferential flow paths through semiarid and arid vadose zones." *Water Resour. Res.* 39(8), 1225-1239.
- Simunek, J., and Nimmo, J.R. 2005. "Estimating soil hydraulic parameters from transient flow experiments in a centrifuge using parameter optimization technique." *Water Resour. Res.* 41(4)
- Sisson, J.B., Gee, G., Hubbell, J.M., Bratton, W.L., Ritter, J.C., Ward, A.L., and Caldwell, A.C. 2002. "Advances in tensiometry for long-term monitoring of soil water pressures." *Vadose Zone Jour.* 1, 310-315.
- Stormont, J.C. and Anderson, C.E. 1999. "Capillary barrier effect from underlying coarser soil layer." *Jour. Geotech. Geoenv. Eng.* 125(8), 641-648.

- Suwansuwat, S. and Benson C. 1999. "Cell size for water content-dielectric permittivity calibrations for time domain reflectometry." *Geotech. Test. Jour.* 22, 3-12.
- Take, W.A., and Bolton, M.D. 2003. Tensiometer saturation and the reliable measurement of matric suction. *Geotechnique* 53(2), 159-172.
- Tan, C.S. and Scott, R.F. 1985. "Centrifuge scaling considerations for fluid-particle systems." *Geotechnique*. 35(4), 461-470.
- Tarantino, A. and Mongiovì, L. 2003. "Calibration of tensiometer for direct measurement of matric suction." *Géotechnique*. 53(1), 137-141.
- Taylor, R.N. (1987). "Discussion, Tan and Scott (1985)." *Geotechnique*. 37(1), 131-133.
- Tinjum, J., Benson, C., and Blotz, L. "Soil-Water Characteristic Curves for Compacted Clays." (1997). *Jour. Geotech. Geoenv. Eng.* 123(11)1060-1069.
- Topp, G., Davis, J., and Annan, A. 1980. "Electromagnetic determination of soil water content: Measurement in coaxial transmission lines." *Water Resour. Res.* 16, 574-582.
- Topp, G.C. and Miller, E.E. 1966. "Hysteretic moisture characteristics and hydraulic conductivities for glass-bead media." *Soil Sci. Soc. Am. Proc.* 30, 156-162.
- van Dam, J., Stricker, J., and Droogers, P. 1994. "Inverse method to determine soil hydraulic functions from multistep outflow experiments." *Soil Sci. Soc. Am. J.* 58, 647-652.
- van Genuchten, M. 1980. "A closed-form equation for predicting the hydraulic conductivity of unsaturated soils." *Soil Sci. Soc. Am. J.* 44, 892-898.
- Wang, X. and Benson, C.H. 2004. "Leak-free pressure plate extractor for the soil water characteristic curve." *Geotech. Testing Journal*. 27(2), 1-10.
- Watson, K. 1966. "An instantaneous profile method for determining the hydraulic conductivity of unsaturated porous materials." *Water Resour. Res.* 2(4), 709-715.
- Wendroth, O., Ehlers, W., Hopmans, J., Kage, H., Halbertsma, J., and Wosten, J. 1993. "Reevaluation of the evaporation method for determining hydraulic functions in unsaturated soils." *Soil Sc. Soc. Am. J.* 57, 1436-1443.
- Wildenschild, D., Jensen, K.H., Hollenbeck, K.J., Illangasekare, T.H., Znidarcic, D., Sonnenborg, T., and Butts, M.B. 1997. "A two stage procedure for determining unsaturated hydraulic characteristics using a syringe pump and outflow observations." *Soil Sc. Soc. Am. J.* 61, 347-359.

- Wind, G. 1968. "Capillary conductivity data estimated by a simple method." *Water in the Unsaturated Zone*. Vol. 1, Proc. Wageningen Symp. June 1966. IASH. UNESCO, Paris. Ritjema, P. and Wassnik, H. eds.. 181-191.
- Young, M., Karagunduz, A. Simunek, J. and Pennell, K. 2002. "A modified upward infiltration method for characterizing soil hydraulic properties. *Soil Sci. Soc. Am. J.* 66, 57–64.
- Zegelin, S. J. White, I. and Jenkins, D. R. 1989. "Improved field probes for soil water content and electrical conductivity measurements using time domain reflectometry," *Water Resour. Res.* 25, 2367–2376.
- Zornberg, J.G., LaFountain, L., and Caldwell, J.C. 2003. "Analysis and design of evapotranspirative cover for hazardous waste landfill." *Jour. of Geotech. And Geoenv. Eng. ASCE*. 129(5), 427-438.
- Zornberg, J.G. and McCartney, J.S. 2003. Analysis of monitoring data from the evapotranspirative test covers at the Rocky Mountain Arsenal. Geotechnical Research Report, USEPA, Region 8, December 2003, 227 pg.

## **Vita**

John McCartney is the son of Robert and Bonita McCartney, and was born in Denver, Colorado on June 12, 1979. John attended Denver East High School, and graduated in May 1997. John attended the University of Colorado at Boulder from 1997 to July 2003, and earned concurrent BS and MS degrees in Civil Engineering. During his MS degree, John was an intern at the Colorado Department of Public Health and the Environment. He participated in a research program on stewardship of waste containment facilities, and discovered his passion for geotechnical and geoenvironmental engineering. John received the Ketchum award from the Department of Civil, Architectural and Environmental Engineering at the University of Colorado at Boulder, given to the top undergraduate student from the department graduating in May. In 2002, John also received the Colorado ASCE section outstanding senior award, the Association of Drilled Shaft Contractors award, and was an honorable mention for the Colorado Engineering Council Silver Medal award. John received the National Science Foundation Graduate Research Fellowship to support the first three years of his PhD, and has received support from the W.M. Keck Foundation at UT and TXDoT. John spent one year of his PhD studies at CU before moving to The University of Texas at Austin. To date, John has published 20 papers in international conferences, 2 book chapters, and 5 technical articles in international journals. John has also applied for a US patent for the Centrifuge Permeameter for Unsaturated Soils with Dr. Zornberg and Th. Broadbent and Sons, LLC.

Permanent address: 608 N. Assembly Dr., Fayetteville, AR 72701

This dissertation was typed by John Scott McCartney.